



HAL
open science

Development of a thin-film polymer barrier on a dense substrate by using interfacial polymerization combined with molecular modelling - Application to high-pressure hydrogen storage tanks

Méryll Barraco

► **To cite this version:**

Méryll Barraco. Development of a thin-film polymer barrier on a dense substrate by using interfacial polymerization combined with molecular modelling - Application to high-pressure hydrogen storage tanks. Material chemistry. Université Savoie Mont Blanc, 2023. English. NNT : 2023CHAMA062 . tel-04382507

HAL Id: tel-04382507

<https://hal.science/tel-04382507v1>

Submitted on 6 Dec 2024

HAL is a multi-disciplinary open access archive for the deposit and dissemination of scientific research documents, whether they are published or not. The documents may come from teaching and research institutions in France or abroad, or from public or private research centers.

L'archive ouverte pluridisciplinaire **HAL**, est destinée au dépôt et à la diffusion de documents scientifiques de niveau recherche, publiés ou non, émanant des établissements d'enseignement et de recherche français ou étrangers, des laboratoires publics ou privés.

THÈSE

Pour obtenir le grade de

DOCTEUR DE L'UNIVERSITÉ SAVOIE MONT BLANC

Spécialité : **Matériaux, Mécanique, Génie civil, Electrochimie**

Arrêté ministériel : 25 Mai 2016

Présentée par

Méryll BARRACO

Thèse dirigée par **David BROWN**, Professeur des Universités et codirigée par **Sylvie NEYERTZ**, Maîtresse de Conférences, USMB

Préparée au sein du Laboratoire d'Électrochimie et Physico-chimie des Matériaux et des Interfaces dans l'École Doctorale I-MEP2 – Ingénierie – Matériaux, Mécanique, Environnement, Énergétique, Procédés, Production.

Développement d'un film polymère barrière sur un substrat dense en couplant la technique de polymérisation interfaciale et la modélisation moléculaire - Application aux réservoirs de stockage d'hydrogène à haute pression

Thèse soutenue publiquement le **18 décembre 2023**, devant le jury composé de :

Madame Anne JONQUIERES

Professeure des Universités, Université de Lorraine, Rapporteur

Madame Maria Grazia DE ANGELIS

Professeure des Universités, University of Edinburgh, Rapporteur

Monsieur Jean-Louis BARRAT

Professeur des Universités, Université Grenoble Alpes, Président et Examineur

Madame Catherine MARESTIN

Chargée de recherche, Université Claude Bernard Lyon 1 - CNRS, Examinatrice

Monsieur David BROWN

Professeur des Universités, Université de Savoie Mont-Blanc, Directeur de thèse

Madame Sylvie NEYERTZ

Maîtresse de Conférences, Université de Savoie Mont-Blanc, Co-directrice de thèse

Monsieur Nieck BENES

Professeur des Universités, University of Twente, Invité

Development of a thin-film polymer barrier on a dense substrate by using interfacial polymerization combined with molecular modelling - Application to high-pressure hydrogen storage tanks

Méryll Barraco*

**DPI, P.O. Box 902, 5600 AX Eindhoven, the Netherlands.*

Acknowledgement: This research forms part of the research programme of DPI, project DINGOES #845.

Table of Contents

Chapter 1 : State of the Art	1
1) A. Environmental challenges	2
1) A. 1. Current situation	2
1) A. 2. The interest of hydrogen	5
1) A. 3. Hydrogen fuel cell cars	9
1) B. Storage tanks	13
1) B. 1. The need to reduce the volume	14
1) B. 1. 1. Solid state storage	15
1) B. 1. 2. Liquid state storage.....	18
1) B. 1. 3. High pressure gas storage.....	21
1) B. 2. The different high-pressure hydrogen gas storage tanks.....	23
1) B. 3. The depressurization problem.....	31
1) C. Inner liners.....	38
1) C. 1. Existing barrier materials.....	39
1) C. 2. Membrane manufacturing	50
1) D. Abbreviations list.....	61
Chapter 2 : Background and Theory	64
2) A. Interfacial polymerization	65
2) A. 1. Basic principles	65
2) A. 2. Interfacial polymerization parameters	70
2) A. 2. 1. Solvents.....	71
2) A. 2. 2. Monomers	72
2) A. 2. 3. Experimental conditions	74
2) A. 2. 4. Substrates	75
2) B. Molecular modelling.....	76

2) B. 1. General principles.....	76
<hr/>	
2) B. 2. Molecular dynamics potentials.....	80
2) B. 2. 1. Bending potential.....	81
2) B. 2. 2. Torsional potential.....	82
2) B. 2. 3. Out-of-plane potential	83
2) B. 2. 4. Van der Waals interactions (VdW).....	84
2) B. 2. 5. Coulombic interactions	87
2) B. 3. Available MD parameters and conditions	88
2) C. Abbreviations list.....	91
<hr/>	
Chapter 3 : Molecular Modelling - Hydrogen Potentials	93
<hr/>	
3) A. Justification and Abstract.....	94
<hr/>	
3) B. Introduction.....	95
<hr/>	
3) C. Computational details	96
3) C. 1. H ₂ LJ-based models.....	97
3) C. 1. 1. Single-site LJ models: LJ-1S	97
3) C. 1. 2. Two-site LJ model: LJ-2S.....	98
3) C. 1. 3. Two-site LJ + quadrupole moment: LJ-2S-q±	98
3) C. 1. 4. Three-sites LJ + quadrupole moment: LJ-3S-q±	99
3) D. Details of the MD simulations	99
<hr/>	
3) E. Results and discussion	104
3) E. 1. Phase diagram at -50°C, 20°C and 90°C	104
3) E. 2. Gas solubilities at -50°C, 20°C and 90°C.....	109
3) E. 3. Gas diffusion coefficients at -50°C, 20°C and 90°C	111
3) F. Conclusions	113
<hr/>	
3) G. Supporting information.....	115
<hr/>	
3) H. Acknowledgments.....	123
<hr/>	
3) I. Abbreviations list.....	123

Chapter 4 : Molecular Modelling - Monomer Potentials 125

4) A. Graphical abstract..... 126

4) B. Pure monomers 127

4) B. 1. General presentation..... 127

4) B. 1. 1. Hexachlorocyclotriphosphazene (HCCP)..... 127

4) B. 1. 2. Phloroglucinol (Phg)..... 130

4) B. 2. Molecular dynamics models - monomers 131

4) B. 2. 1. Phloroglucinol 132

4) B. 2. 2. HCCP 135

4) B. 3. Molecular dynamics models - mixture 136

4) C. Fragments of combined monomers..... 139

4) C. 1. Definition of a fragment 139

4) C. 2. Generation of different conformers 144

4) C. 3. Extraction of partial charges for the fragments..... 153

4) C. 3. 1. HCCP_1_Cl..... 154

4) C. 3. 2. HCCP_2_Cl..... 155

4) C. 3. 3. HCCP_2_Cl_1_P..... 160

4) C. 3. 4. HCCP_3_Cl..... 163

4) C. 3. 5. Phg_2_OH 166

4) C. 3. 6. Phg_3_OH 169

4) C. 4. Set of optimized partial charges 171

4) D. Supporting information..... 174

4) E. Acknowledgments 176

4) F. Abbreviations list 176

Chapter 5 : Molecular Modelling - Cross-linked Polyphosphazene Networks 178

5) A. Graphical abstract..... 179

5) B. The algorithm to mimic polymerization 180

5) B. 1. Definition of the main “reaction” criterion	181
<hr/>	
5) B. 2. The iterative reaction/relaxation procedure	184
<hr/>	
5) B. 3. Algorithmic instability and change of C-O-P potential	189
<hr/>	
5) C. <i>Effect of the monomer ratio on the polymer networks</i>	190
<hr/>	
5) C. 1. Network formation with different monomer ratios in the mixture and variable R_{max}	190
<hr/>	
5) C. 1. 1. Phg:HCCP 1:1 ratio and variable R_{max}	190
<hr/>	
5) C. 1. 2. Variable Phg:HCCP ratios and $R_{max} = 2.8 \text{ \AA}$	192
<hr/>	
5) C. 1. 3. Variable Phg:HCCP ratios and $R_{max} = 3.0 \text{ \AA}$	194
<hr/>	
5) C. 2. Mechanical tests	198
<hr/>	
5) C. 2. 1. Phg:HCCP 1:1 ratio and variable R_{max}	199
<hr/>	
5) C. 2. 2. Variable Phg:HCCP ratios and $R_{max} = 2.8$ or 3.0 \AA	200
<hr/>	
5) C. 3. Hydrogen uptake	202
<hr/>	
5) C. 3. 1. Methods and models	203
<hr/>	
5) C. 3. 2. H_2 solubility, diffusion and permeability as a function of the Phg:HCCP ratio	206
<hr/>	
5) D. <i>Supporting information</i>	214
<hr/>	
5) E. <i>Acknowledgments</i>	221
<hr/>	
5) F. <i>Abbreviations list</i>	221
<hr/>	
Chapter 6 : Experimental - Interfacial Polymerization	223
<hr/>	
6) A. <i>Graphical abstract</i>	224
<hr/>	
6) B. <i>Test monomers</i>	225
<hr/>	
6) B. 1. Piperazine and trimesoyl chlorine	225
<hr/>	
6) B. 2. Silicon wafer with titanium layer	228
<hr/>	
6) B. 3. Silicon wafer with alumina layer	233
<hr/>	
6) B. 4. Silicon wafer with clean titanium layer	235
<hr/>	
6) C. <i>Monomers for polyphosphazene networks</i>	237
<hr/>	
6) C. 1. Hexachlorocyclotriphosphazene (HCCP) and phloroglucinol (Phg)	237
<hr/>	
6) C. 2. Fabrication procedure via IP	239

6) C. 2. 1. Material fabrication	239
<hr/>	
6) C. 2. 2. Results and discussion	242
<hr/>	
6) C. 3. Bulk polymerization	249
6) C. 3. 1. Procedure.....	250
<hr/>	
6) C. 3. 2. Results and discussion	251
<hr/>	
6) C. 4. Conclusion of the studies on Phg-HCCP monomers	257
<hr/>	
6) D. Supporting information.....	261
<hr/>	
6) E. Acknowledgments	263
<hr/>	
6) F. Abbreviations list	263
<hr/>	
Chapter 7 : Experimental - Interfacial Polymerization on Hydrogen Tank Substrates	265
<hr/>	
7) A. Graphical abstract.....	266
<hr/>	
7) B. Free-standing films.....	267
<hr/>	
7) B. 1. Testing the changes in the procedure	268
<hr/>	
7) B. 2. Test results	269
<hr/>	
7) C. Hydrogen tank substrates	275
<hr/>	
7) C. 1. Polyamide supports and first tests	277
7) C. 1. 1. IP on supports using previous protocol	279
<hr/>	
7) C. 1. 2. First tests.....	280
<hr/>	
7) C. 2. Addition of a surface treatment	282
7) C. 2. 1. Mechanical treatment	283
<hr/>	
7) C. 2. 2. Chemical treatment	284
<hr/>	
7) C. 2. 3. First tests with surface treatment.....	286
<hr/>	
7) C. 3. Definition of a new process	289
7) C. 3. 1. Vacuum plasma.....	290
<hr/>	
7) C. 3. 2. Atmospheric plasma	294
<hr/>	
7) C. 4. Treatment parameters for IP on dense organic substrates.....	300
7) C. 4. 1. Polyamide FLE40 substrate	300

7) C. 4. 2. Polyamide F136 substrate.....	308
7) C. 4. 3. Estimation of the film/substrate hydrogen permeability	314
7) D. Supporting information.....	317
7) E. Acknowledgments	322
7) F. Abbreviations list	322
Chapter 8 : Conclusion and Perspectives.....	324
8) A. General conclusion and remarks	325
8) A. 1. Molecular modelling.....	325
8) A. 2. Interfacial polymerization	329
8) B. Future work	331
8) B. 1. Molecular modelling.....	331
8) B. 2. Interfacial polymerization.....	332

Abstract

It is now accepted worldwide that human civilization must switch from fossil to renewable energy sources and decarbonized forms of transportation, which include hydrogen cars. These fuel-cell-powered vehicles use lightweight storage tanks made from plastic and fibre-reinforced composite materials that contain hydrogen gas at very high pressures, *i.e.* up to 800 bar. To reduce H₂ depressurization problems, it is hereby proposed to incorporate an additional thin-film polymer barrier into the wall of such reservoirs. This new polymer layer must be stable over the range of H₂ pressures and temperatures consistent with the harsh operating conditions. The syntheses were carried out by interfacial polymerization (IP), which produces thin, robust and defect-free films by localized polymer network formation at the interface of two immiscible solvents. They were characterized by elemental analysis, infrared, visible and ultra-violet spectroscopy, nuclear magnetic resonance spectroscopy, Raman spectroscopy, ellipsometry, scanning electron microscopy, gravimetry and permeation measurements. In parallel, molecular modelling techniques were used to study in detail the static and dynamic properties of the barriers at the atomistic level. This involved mainly molecular dynamics (MD), but also density functional theory (DFT), energy minimization (EM), test-particle insertion (TPI) as well as grand-canonical Monte Carlo (GCMC) simulations. This complementary approach was aimed at saving time and reducing the costly laboratory experiments.

The study involved an in-depth investigation of cyclomatrix polyphosphazene films based on two monomers, phloroglucinol (Phg) and hexachlorocyclotriphosphazene (HCCP), which had previously shown promising barrier performances for H₂. In order to further decrease their H₂ permeability and coat them onto the walls of storage tanks, several steps were carried out in both the molecular modelling and experimental approaches.

The main goal of the molecular modelling simulations was to optimize the IP parameters leading to a defect-free film with high barrier properties. As such, the models for each component had to be built and validated with respect to available experimental data. The first step involved selecting the H₂ model in the literature which was the most appropriate for the wide range of temperatures and pressures relevant to storage tanks (to cover all possibilities: $-50^{\circ}\text{C} < T < +90^{\circ}\text{C}$; $0 < P < 2000$ bar). In a second step, the force fields for both Phg and HCCP monomers were optimized. These were subsequently used in a third step to build models for different fragments of linked reactants and calculate some of the additional force-field parameters to be used for the cross-linked networks. In a fourth step, a range of *in-silico* model polyphosphazenes were created from mixtures of the monomers at several pre-specified monomer ratios. All these model networks were tested for their mechanical properties as well as for their hydrogen sorption

and barrier capacities. This gave indications as to which mixture ratios were likely to lead to the best properties.

For the experimental part, a series of polyphosphazene HCCP-Phg thin-films were first synthesized on porous substrates by IP in order to confirm previous findings. They were characterized in detail to assess the effects of the various process parameters on the reproducibility of the results. They showed promising barrier properties since a very low permeability coefficient for H₂ (1.8×10^{-17} cm³(STP) cm cm⁻² s⁻¹ Pa⁻¹) could be obtained. It was then attempted to synthesize such films directly on a polyamide dense support, which is the material currently used as an inner liner for hydrogen storage tanks. A novel deposition process, including a plasma surface treatment and a deprotonation step, was developed and thin layers were grown on industrially-provided dense supports.

Résumé

La civilisation humaine doit maintenant effectuer la transition des énergies fossiles aux énergies renouvelables et décarboner son industrie des transports, ce qui inclut les voitures à hydrogène. Ces véhicules utilisent des piles à combustibles et sont équipés de réservoirs à H₂ comprimé (jusqu'à 800 bar) constitués de plastiques et de composites renforcés par des fibres de verre. Afin de réduire les problèmes de dépressurisation du H₂, il est proposé d'incorporer aux réservoirs un film mince de polymère à propriétés barrières. Ce nouveau polymère doit être stable dans la large gamme de températures et de pressions de H₂. Les synthèses ont été réalisées par polymérisation interfaciale (IP), qui produit des films minces, résistants et sans défauts en formant un réseau polymère à l'interface de deux solvants non miscibles. Ils ont été caractérisés par analyse élémentaire, spectroscopie infrarouge, visible et ultraviolet, spectroscopie à résonance magnétique nucléaire, spectroscopie Raman, ellipsométrie, microscopie électronique à balayage, gravimétrie et mesures de perméance. En parallèle, des simulations de modélisation moléculaire ont été menées afin d'étudier les propriétés statiques et dynamiques de ces matériaux barrières à l'échelle atomique. La technique principale était la dynamique moléculaire (DM), mais la théorie fonctionnelle de la densité (DFT), la minimisation énergétique (EM), l'insertion de particules-tests (TPI) ainsi que les simulations de Monte Carlo dans l'ensemble grand-canonique (GCMC) ont également été utilisées. Cette approche complémentaire avait pour objectif de gagner du temps et de réduire le coût expérimental.

L'étude a porté sur des films polyphosphazène basés sur deux monomères cycliques, le phloroglucinol (Phg) et l'hexachlorocyclotriphosphazène (HCCP), qui avaient précédemment montré de bonnes capacités barrières. Pour réduire leurs perméabilités à H₂ et pouvoir les déposer sur les parois des réservoirs, plusieurs étapes ont été considérées en modélisation et au niveau expérimental.

Le but de la modélisation moléculaire était d'optimiser les paramètres IP afin d'obtenir des films sans défauts et avec de bonnes capacités barrières. Il a donc fallu construire des modèles pour chaque composant et les confronter aux données expérimentales disponibles. La première étape a consisté à sélectionner dans la littérature un modèle de H₂ valide sur la large gamme d'utilisation de températures et de pressions des réservoirs (pour inclure toutes les possibilités : $-50^{\circ}\text{C} < T < +90^{\circ}\text{C}$; $0 < P < 2000 \text{ bar}$). Dans la seconde étape, les champs de forces des monomères Phg et HCCP ont été optimisés. Ils ont ensuite été utilisés dans la troisième étape pour construire des modèles de monomères liés, et calculer les paramètres additionnels nécessaires pour les réseaux réticulés. Dans la quatrième étape, de nombreux polyphosphazènes modèles ont été créés à partir de ratios différents de monomères. Leurs propriétés mécaniques, de sorption et barrières à l'hydrogène ont ensuite été testées afin d'indiquer les ratios susceptibles de conduire expérimentalement aux meilleures propriétés.

Dans la partie expérimentale, plusieurs films minces de polyphosphazène HCCP-Phg ont d'abord été synthétisés par IP sur des supports poreux pour vérifier les résultats précédents. Ils ont été caractérisés en détail afin d'estimer l'effet des différents paramètres sur la reproductibilité. Leurs capacités barrières sont prometteuses puisqu'un coefficient de perméabilité à l'hydrogène assez bas ($1.8 \times 10^{-17} \text{ cm}^3 \text{ (STP) cm cm}^{-2} \text{ s}^{-1} \text{ Pa}^{-1}$) a pu être obtenu. Il a ensuite été tenté de synthétiser ces films sur un substrat de polyamide dense qui est le matériau utilisé comme liner intérieur dans les réservoirs. Un nouveau protocole de dépôt, incluant un traitement de surface par plasma et une étape de déprotonation, a été développé et des films minces ont pu être déposés sur des supports denses fournis par des industriels.

Chapter 1 : State of the Art

1) A. Environmental challenges

“*The Earth is a fine place and worth fighting for*” said Ernest Hemingway in 1940 [1] and it is easy to understand because our planet allows us both to live and to evolve. However, since the mid 1900’s, our influence on the climate is the main cause of the observed warming and this increase of the temperature already results in profound alterations to human and natural systems. Therefore, the precariousness of the current situation must be taken into account in order to find solutions to improve it.

1) A. 1. Current situation

Since the 20th century, it is known worldwide that the climatic changes to the planet are moving it out of the relatively stable Holocene period into a new geological era, often termed Anthropocene. Indeed, as Figure 1.1 extracted from the “AR6 Synthesis Report: Climate Change 2023” written by the Intergovernmental Panel on Climate Change (IPCC) [2] clearly shows, there is a massive problem of pollution reflected in the increase of greenhouse gases (GHG) emissions, which are linked to the global surface temperature and human activities.

It can be seen that the increase in emissions of the three major GHGs in the recent decades, *i.e.* CO₂, CH₄ and N₂O (bottom and middle part), led to an increase of the global surface temperature by ~1.1°C (upper part) since 1850–1900. If there were previous “warm” periods, especially ~6500 years ago during the Holocene interglacial period, the recent warmest period is clearly induced by humans (upper part, right panel). Indeed, climate models and observations all confirm that the recent temperature changes are attributed to the total human influence. This can be separated into changes in GHG concentrations and other effects of human origin. In comparison, the effects of the more “natural” causes, such as solar, volcanic activity and internal climate variability, are very low [2].

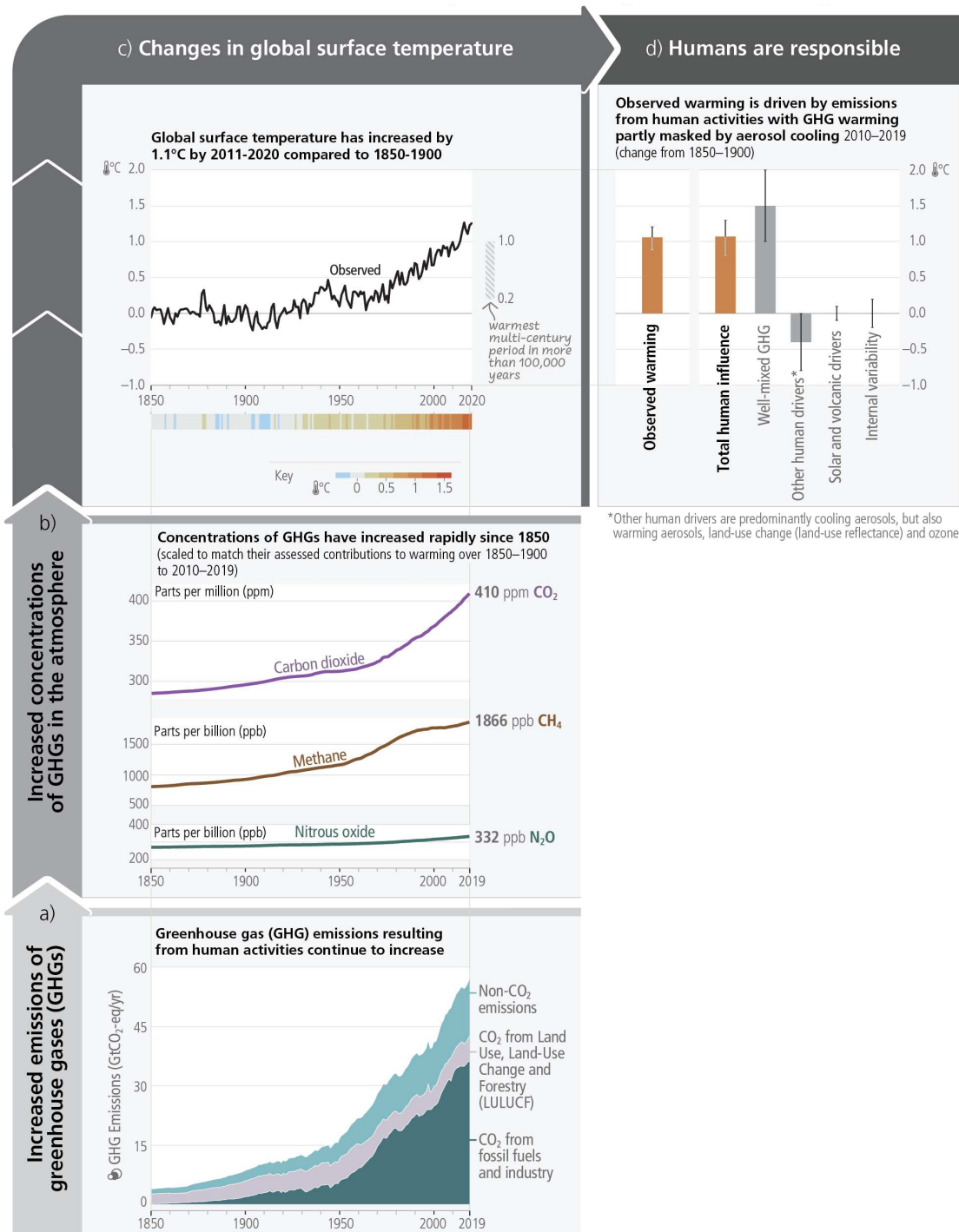


Figure 1.1 The causal chain due to human activities, from the emissions to the resulting warming of the climate system. In panel a), the non-CO₂ emissions correspond to CH₄, N₂O and fluorinated gases (HFCs, PFCs, SF₆ and NF₃) [2]. In panel c), the global surface temperature is defined as the averaged combined land and ocean surface temperature.

This climate change can be observed in the atmosphere, ocean, cryosphere and biosphere and means that numerous ecosystems are at risk of severe consequences. This is particularly true for the warm-water

tropical reefs and the arctic ecosystems. However, all the human and natural systems are affected by this global warming, which induces extreme climate events such as droughts, floods, other extreme weather phenomena, sea-level rises and decreases in the biodiversity. If those incidents are the most well-known, they do not hide the unprecedented risks to vulnerable persons and populations. Indeed, in addition to environmental degradation and pollution, many regions remain characterized by significant poverty, food and water insecurity, health concerns and severe inequality in income distributions leading to inequality in access to resources [2, 3].

These limited number of observations give an idea of the damage caused by mankind over a relatively short period of time in geological terms. Therefore, in order to respond to the climate challenges, the interconnectivity across the global community is required. One example of that large involvement is the Paris Agreement (December 2015) involving 190 Parties [4]. This was set-up to fight climate change, accelerate and scale up the actions as well as estimating the required investments [4]. One of its main goals is to limit global warming to at the most 2°C above pre-industrial levels. Consequently, several priorities were identified to achieve this objective, such as:

- Use of new technologies
- Reduced deforestation
- Improved sustainable agricultural methods
- Changes in individual and collective behaviour
- Clean energy sources

The last recommendation has been identified as a key-challenge by many countries, amongst which France, which has set as a target the reduction of its CO₂ emissions from ~310 Mt in 2015 to ~90 Mt in 2050 [5]. Indeed, energy systems are one of the main GHG emitting sectors accounting for about 66% of all discharges and with CO₂ representing ~88% of these emissions and the manufacturing and transportation being the two main energy consumers (31% and 26%, respectively). Almost 70% of this energy consumption is based on fossil-fuel resources, such as coal, oil and gas [6, 7]. These natural resources exist in a limited supply because they require several million years to form whereas renewable energies (RE) are almost available in a continuous way [5]. Consequently, a growing number of policies have driven the growth of RE technologies in recent years [6]. These include those related to hydrogen H₂ and there are many worldwide companies that are currently investing in this technology (Air Liquide, Hydrogen Europe, H₂ Mobility Deutschland, DSM, etc.) [8-11].

1) A. 2. The interest of hydrogen

In a future where sustainable energy systems based on renewable resources must prevail, hydrogen environmentally-harmless energy carriers are crucial. Indeed, it is a strategic opportunity for the transition to a “zero carbon” economy because they will allow to decarbonize industries and transport [12].

Before discussing the place of hydrogen in the energy industry, it is important to introduce the chemical compound itself. Hydrogen is the smallest chemical element and the most abundant in the universe, for example, all the stars are constituted largely of hydrogen gas. Then, H₂ is the only non-carbonaceous fuel, which means that it does not produce CO₂ during its combustion and this is a major advantage for the energy field. The general characteristics of H as an atom and those of the H₂ molecule are reported in Table 1.1 as well as the main applications of this molecule in Table 1.2.

Table 1.1 The general properties of hydrogen as an atom and as a H₂ molecule [13].

Symbol	Atomic number	Block	Family
H	1	s	Non metal
CAS number	Electron configuration	Relative atomic mass	Density (T = 25°C; P = 1.013 bar)
133.74.0	1s ¹	1.008 g/mol	0.08 kg/m ³
Melting point (P = 1.013 bar)	Boiling point (P = 1.013 bar)	Electronegativity	Atomic radius (non-bonded)
13.84 K (-259.16°C)	20.22 K (-252.78°C)	2.2	1.10 Å

Table 1.2 Domains where H₂ is largely used [14].

Automotive	Due to its carbon-free combustion, hydrogen is a very interesting fuel for vehicles. These vehicles have an on-board hydrogen tank and a fuel-cell to respectively store the hydrogen and produce electricity (detailed latter).	Laboratories	Amongst the numerous uses of hydrogen in laboratories, the most known is its involvement as carrier gas in gas chromatography or other analytical instruments: it helps to move the substance under study through the processes.
Chemicals	This element is also largely involved in synthesis processes, <i>e.g.</i> amines or alkanes from alkenes via hydrogenation reactions or alcohol production from a mixture of hydrogen and carbon monoxide.	Metal	If it is mixed with protective inert gases, <i>e.g.</i> nitrogen, it can eliminate traces of oxygen on metals or be used with heat treatments to improve mechanical properties for example.
Electronic components	Another use as carrier gas is in semiconductor processes.	Oil & Gas	Hydrogen is used in refineries to remove sulphur from petroleum products. It can also be used to crack long-chain hydrocarbons into lighter hydrocarbons and/or to remove aromatic compounds from mixtures during the oil-refining process.
Industries	It is also an element largely present in various industries such as the well-known fertilizer production with ammonia plants		
Food	Hydrogenation reaction to form amines are also used to make fatty acids.	Photonics	When its purity is very high, it can be used in the fabrication of optic fibres.
Glass	Mixed with nitrogen, it can produce an atmosphere which prevents oxygen reacting with tin in the bath for the glass production process. Again, it is used in the heat treatment of hollow glass and optic fibres.	Space	More and more liquid hydrogen is introduced in rocket or launcher propellant. In combination with an oxidizer such as liquid oxygen, it gives the highest specific impulse necessary for the rocket propellants.

Concerning its sources, H₂ is generally produced from hydrocarbons, steam-methane reforming, or water electrolysis. It should be noted that it also exists in its natural state, H₂, in the seabed as well as in the large terrestrial massifs of peridotite and intraplate areas at the heart of the continents [15]. However, using these sources is far from being viable. Finally, as hydrogen is (almost) inexhaustible and mostly non-polluting, its use in any form is very interesting.

Most of the time, it is not a source but a vector, which means that it must first be produced. Currently, several production techniques with different costs exist and they all involve the extraction of H₂ from primary resources such as natural gas, water or biomass (Figure 1.2).

Method	Steam natural gas reforming (the most widely employed)
Principle and chemical equations	<p>Steam reacts with natural gas in the presence of a nickel-based catalyst and produces syngas (synthesis gas), from where H₂ is separated from the other components by pressure swing adsorption (PSA). If sulphur compounds are present, this reforming step is preceded by a desulphurization step in order to avoid poisoning the catalyst.</p> $C_n H_m + nH_2O \rightarrow nCO + (n + \frac{1}{2}m)H_2 \quad (1.1)$ $CO + H_2O \rightarrow CO_2 + H_2$
Diagram	<pre> graph LR CH4[CH4] --> Desulfurization Desulfurization --> Reformer[Reformer 850-900°C] Steam[Steam] --> Reformer Fuel[Fuel] --> Reformer Reformer --> ShiftConversion[Shift Conversion] ShiftConversion --> PSA[PSA System] PSA --> H2[H2] PSA --> CO2[CO2] Reformer --> HeatRecovery[Heat Recovery] HeatRecovery --> Reformer </pre>
Major drawback	Rejection of CO ₂ , which is one of the main greenhouse gases.
Main prospects	These CO ₂ emissions can be reduced by CO ₂ capture and storage: H ₂ produced by this reforming+CO ₂ neutralization, is called “Blue hydrogen”.

Methods	Electrolysis of water (the most expensive)	Gasification from biomass
Principle and chemical equations	<p>H_2O is introduced at the anode where it is split into oxygen and protons H^+. The latter travel through the membrane to the cathode where they combine with the electrons to form H_2.</p> $2H_2O \rightarrow O_2 + 4H^+ + 4e^-$ $4H^+ + 4e^- \rightarrow 2H_2$ <hr/> $2H_2O \rightarrow 2H_2 + O_2$ <p style="text-align: right;">(1.2)</p>	<p>Biomass is converted into a gaseous fuel in a gasification medium such as air or oxygen and/or steam, at temperatures between 500 and 1400 °C and pressures from between 1 to 33 bar.</p> $Biomass + Air + Steam \rightarrow H_2 + CO_2 + CO + N_2 + CH_4 + H_2O + otherCH_s$ <p style="text-align: right;">(1.3)</p>
Diagram		
Major drawback	In addition to the higher costs, this method has lower yields than gas reforming for example.	Variable H_2 production due to the seasonal availability of biomass and the feedstock impurities. Even if it is less than reforming, there is still rejection of CO_2 .
Main prospects	Increased use of renewable energy sources, such as hydro, solar and wind. The H_2 produced this way is called « Green H_2 ».	Production of H_2 from bacteria or algae can be considered and natural biological processes, such as photosynthesis, can consume the CO_2 .

Figure 1.2 Hydrogen production methods [16-19].

Therefore, depending on how it is produced, hydrogen can be “renewable”. Water electrolysis with renewable electricity is the cleanest way to obtain H_2 . In addition, its versatile, clean, and safe features contribute to the “zero carbon transition” across the whole energy chain, as stated in Figure 1.3:

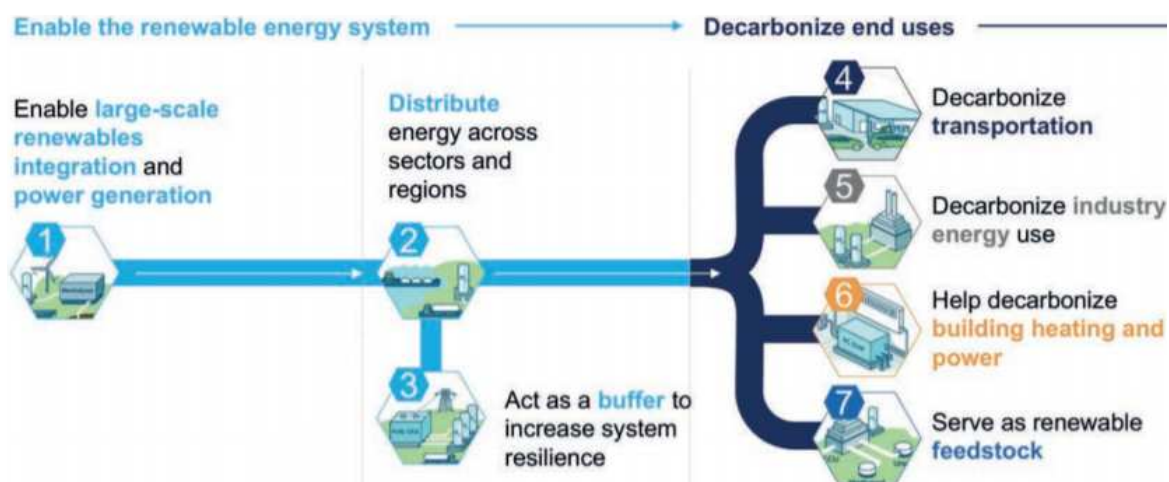


Figure 1.3 The seven roles of hydrogen in the energy transition [20].

Hydrogen is also expected to significantly improve air quality in cities. Fuel cell applications, in transport emit no particulates, no NO_x/SO_x and make almost no noise [20].

1) A. 3. Hydrogen fuel cell cars

Transportation is responsible for 23% of the GHG emissions worldwide, making it one of the major problems, and therefore an important lever for the reduction of those emissions [21]. Due to its advantageous properties, hydrogen is increasingly emerging as a logical solution for that purpose. As stated in Table 1.2, it can be used as an energy source in fuel cell electric vehicles (FCEVs) and it is estimated that 5 kg of H₂ are sufficient to power a car for over 600 km. This means that these vehicles contain three times more energy *per* kg than petrol or diesel. However, one of the major drawbacks of this configuration is that 5 kg corresponds to a huge volume of ~60 m³ of gas at ambient temperature and pressure [22]. Consequently, FCEVs and others vehicles intending to use hydrogen, have to solve this problem.

At the emergence of these technologies, research first focused mainly on using H₂ directly as a fuel for conventional and common combustion engines, such as those developed by BMW, Ferrari, Fiat, Ford, etc. However, this approach was rapidly discarded due to issues with NO_x emissions and the need to develop high-pressure hydrogen injection technologies [23]. Then, efforts concentrated on hydrogen fuel cells which led to a maturing of the technology, with numerous prototypes developed by the same car manufacturers as well as new actors such as Hyundai, Nissan, Renault or Toyota with its second generation of FCEV already available on the market (Figure 1.4.A). Some of the other car dealers propose their vehicles for fleets operated by professionals and local authorities [24-31]. These engines are quite reliable with their battery-powered models having a range of 400 to 600 km, combined with a short hydrogen refuelling times (3 to 5 minutes) which is close to that of internal combustion engines. This is why mass-

produced hydrogen-powered cars are rolling off the production lines with, for example in France, an expected ramp-up to ~200000 FCEVs in 2028 [21]. In captive fleets such as taxis, one in 10 cars sold could be an FCEV by 2028. Public transports such as buses or trains (Figure 1.4.B), are already or will be in the future involved in hydrogen technologies. This commitment is not exclusive to land-transports and some hydrogen-powered ferries and boats are being deployed [20].

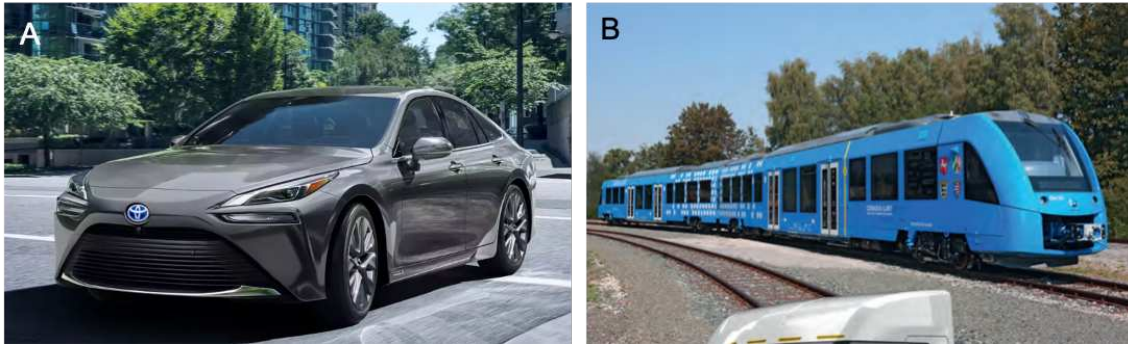


Figure 1.4 The Toyota Mirai 2023 (A) and the train built by Alstom (B) [21, 32].

Very often all-electric and hydrogen vehicles are put in the same category, but there are both similarities and differences. First of all, both work with electricity and not petrol nor diesel. Indeed, a “traditional petrol car” uses an inflammable mixture of air and petrol which, when ignited in the pistons of the engine, creates high pressures that drive the motor and, in turn, the wheels. This combustion releases CO_2 . In an electric motor, it is just an electric current and magnetic field which drive the motor and hence the wheels. However, if rechargeable batteries store the electricity that is supplied to the electric motor in all-electric cars, this electricity is directly produced onboard using the fuel cell powered by H_2 in FCEVs (Figure 1.5). Therefore, the amount of energy stored onboard is determined by the number and capacity of hydrogen fuel tanks for the FCEVs whilst the power and energy are closely related to the capacities of the batteries for the all-electric cars [33].

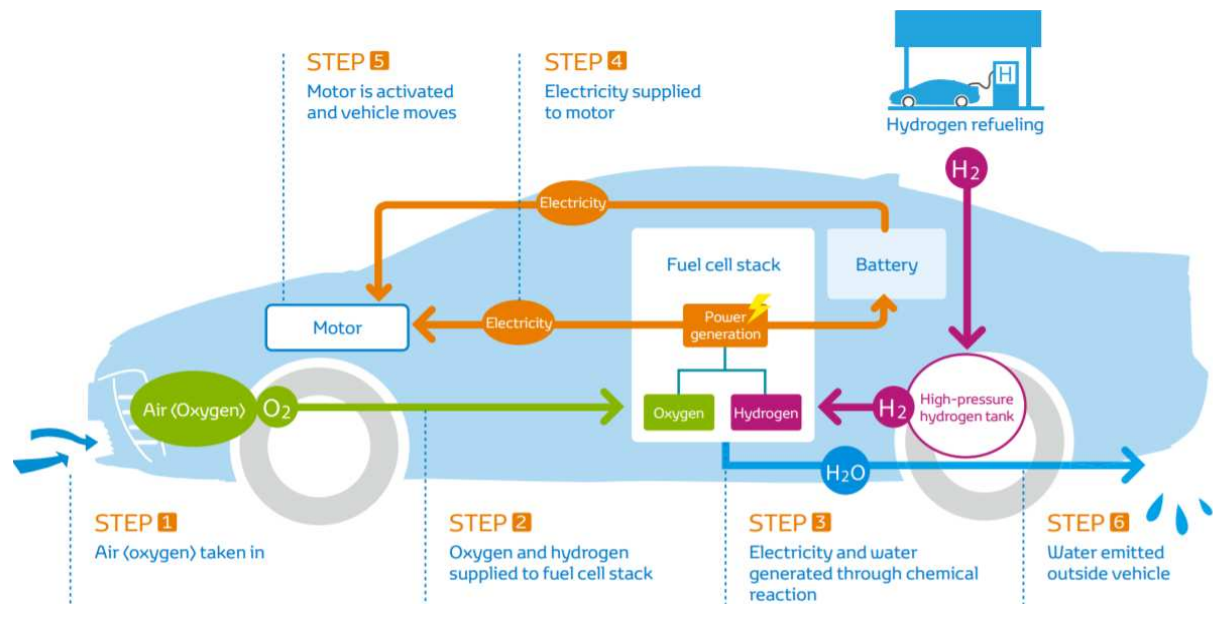


Figure 1.5 Energy operations in a hydrogen Toyota Mirai. The battery is used only for the auxiliary functions and is supplied by the fuel cell stack too [34].

Figures 1.6 and 1.7 give the basic principle of an hydrogen fuel cell as well as the chemical reactions when the cell is supplied with hydrogen and oxygen and produces electricity and water.

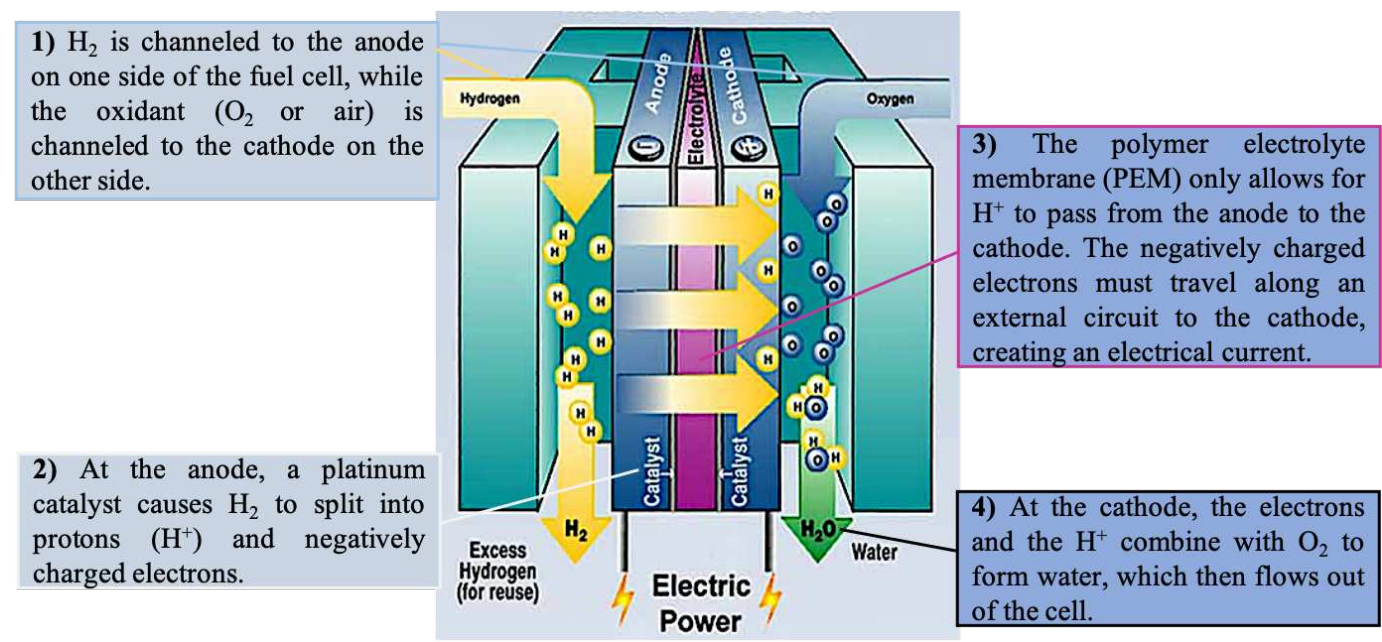


Figure 1.6 Schematic operation of a hydrogen fuel cell [35].

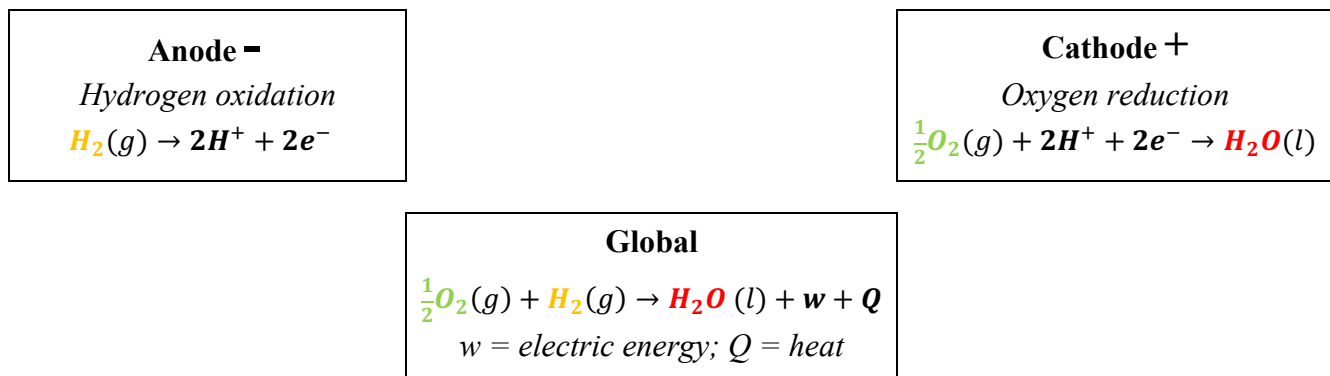


Figure 1.7 The chemical equations involved in a fuel cell [36].

As shown by Figure 1.7, the global reaction produces heat which can also be recovered and gives a total energy yield of around 60%. For comparison, the conventional petrol engines have an efficiency of 35% [21]. Table 1.3 summarizes the main differences invoked above between the three types of cars considered.

Table 1.3 Differences between the 3 main types of small vehicles available on the market [37].

	Petrol car	All-electric car	Hydrogen car
Engine	Combustion	Electric	Electric
Supply mode	Petrol	Battery	Fuel cell
Energy creation	Onboard - Engine cylinders	External – Power plant	Onboard – Fuel cell
Storage	Petrol tank	Battery	Hydrogen tank
“Recharge” mode	Gas station	Power grid	H ₂ station

Contrary to what seems to be a recent innovation, research and tests on electric and hydrogen cars date back to the 1960s, e.g. General Motors and its Electrovan prototype in 1966 [38]. The “innovations” in the “Zero Emission Vehicles” concern more the battery for the all-electric vehicle and the fuel cell and/or the hydrogen reservoir for the FCEV. Battery research is mainly focused on the aims of improving the power and autonomy as well as the composition and the replacement of toxic elements such as the lead or lithium-ion batteries. For the FCEV, due to the presence of a battery, the major challenges are the power and the yield of the fuel cells. More specifically, the number and the size (weight) of the hydrogen tanks are also a concern and, of course, an axis of improvement. Indeed, as already stated above, initial research

focused on “hydrogen as fuel”, then on a hybrid vehicle with a battery and a fuel cell, and, at the end, on vehicles operating only with the fuel cell and a small battery for the auxiliary functions such as electric windows, radio, warning lights, etc. In such a vehicle, H₂ had to be stored onboard like petrol in an internal combustion car. Therefore, several possibilities were tested with a H₂ storage in the liquid or in the solid form at first and then, in the gas form under pressures of 350 to 700 bars [23]. Indeed, in spite of all their advantages, the development of hydrogen technologies still comes up against several difficulties [37]:

- The need for a sufficiently extensive distribution network.
- An improved yield for the fuel cell, which is better than a petrol engine but still lower than a battery.
- The origin/production of H₂: even if there are alternative decarbonized techniques such as electrolysis, it is currently mostly of fossil origin (Figure 1.2).
- The storage of H₂.

This last point is critical because one of the major impediments for the transition to hydrogen-based vehicles, is the lack of satisfactory H₂ storage alternatives. This is actually also an issue for all other energy fields. As stated before, hydrogen in gaseous form occupies a lot of space at room temperature and pressure. For example, in the first generation of Toyota Mirai, there were 2 tanks of 5 kg each, containing H₂ at a pressure of ~700 bar which would correspond to a volume of gas at atmospheric pressure of ~120 m³. Even if pressurization reduces the volume to ~0.122 m³, this is still not negligible and there was only space for 4 seats and a small car boot [34]. However, in recent years, storing hydrogen in various materials has been extensively studied, which led to only one tank instead of two [32].

1) B. Storage tanks

“*The man who moves a mountain begins by carrying away small stones.*”– Confucius [39]. This sentence can be applied at different levels of the environmental challenge as Figure 1.8 schematizes:

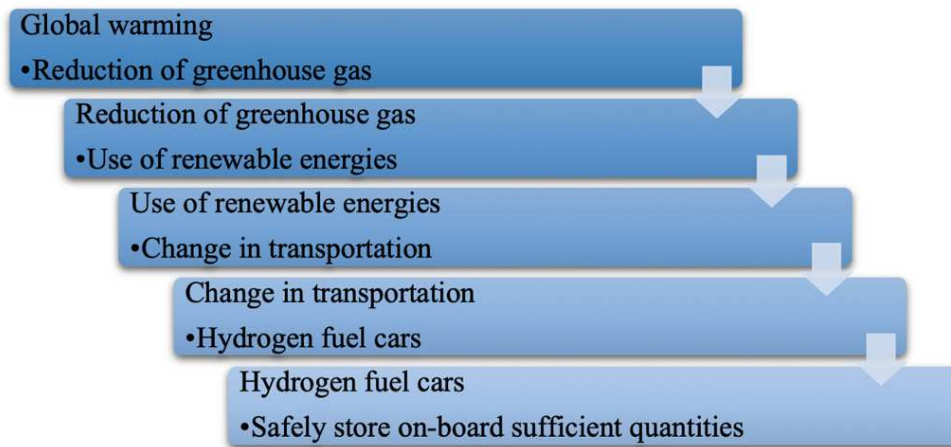


Figure 1.8 The different levels of the environmental challenge with the “mountain” on the left and the “small stones” on the right.

The last level, *i.e.* the storage of H_2 has long been a technical barrier to the development of the FCEVs but recent progress offers attractive solutions. Nevertheless, more work is needed to obtain a good adequacy between the requested technical and economical specifications and the certified storage.

1) B. 1. The need to reduce the volume

Hydrogen is a very light gas and thus, for an equivalent mass, it occupies a large volume at atmospheric pressure. This means that this volume must be greatly reduced. However, in light vehicles particularly, the overall size of the hydrogen tank is a constraint. In addition, hydrogen storage systems should be able to provide high storage capacities, high volumetric densities, effective heat transfers, long lifetimes or many adsorption/desorption cycles of H_2 , high mechanical strengths and durability, safety under normal uses and acceptable risks under extreme conditions [22]. There are standards associated to their designs, such as those published by the ISO/TC 197 technical committee [40].

Accordingly, volume reduction and storage techniques are closely linked. There are three mains techniques to increase the densities of stored H_2 [41]:

- Storage of hydrides in the solid form.
- Storage at very low temperatures in the liquid form.
- High pressure storage in the gaseous form.

Their common feature is that there are two typically controlled thermodynamic parameters, *i.e.* the temperature and the pressure. For the gaseous phase, their relationship can be approximated by the equation for the ideal gas:

$$PV = nRT \quad (1.4)$$

where P is the pressure, V is the volume, n is the number of moles of gas, R is the ideal gas constant, and T is the absolute temperature in Kelvin. n and V are linked to the density ρ through the molar mass M :

$$\rho = \frac{nM}{V} \quad (1.5)$$

and rewriting Eq. 1.4 as in Eq. 1.6 shows clearly that the density ρ will increase when either the pressure P increases or the temperature T decreases:

$$\frac{n}{V} = \frac{P}{RT} \quad (1.6)$$

The storage techniques are, therefore, primarily governed by thermodynamics. To emphasize their differences, a description along with its drawbacks and advantages will be provided hereafter for each of them.

1) B. 1. 1. Solid state storage

The first technique mentioned is the storage within a solid substrate, which has been explored since the 1960s. At the start, research focused on finding the most suitable solid material for the storage of hydrogen molecules. Indeed, as water in a sponge, H_2 can be kept with or within another material in a hydride form under certain conditions and released under other conditions. Due to the very small sizes of H or H_2 , many different materials can be used since the solid storage techniques involve mechanisms of absorption and adsorption. This is the case for instance of carbon-based materials such as graphite nanofibres, metal-organic frameworks (MOF), hollow-glass microspheres (HGM) or alloys [42]. These materials are then used in various solid-state techniques such as physisorption, chemical hydrides, complex metal and metal hydrides, which are summarized in Figure 1.9. For mobile applications such as cars, the magnesium hydrides and alanates ($NaAlH_4$) are preferred. On the other hand, for stationary applications, alloy-based hydrides, *e.g.* calcium-nickel or iron-titanium, are favoured [43].

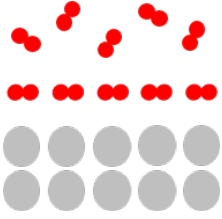
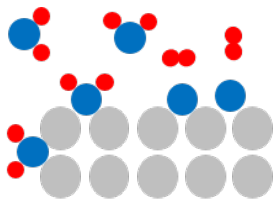
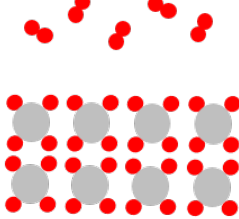
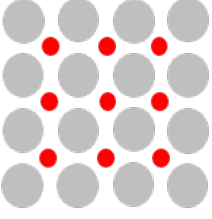
Physisorption	Chemical hydrides	Complex metal hydrides	Metal hydrides
 <p>Hydrogen is bonded to the surface of the material, either by hydrogen molecules or by hydrogen atoms.</p>	 <p>Hydrogen can be stored through the reaction of selected materials such as alanates or imides with water. One molecule of these materials can bind four to six hydrogen atoms to itself.</p>	 <p>H_2 molecules are dissociated into hydrogen atoms that are incorporated into the solid lattice framework. Depending on the bonding mechanism between the hydrogen and this framework, two types of hydrides exist: ionic and covalent bonds give “complex metal” and metallic/interstitial are named “metal”.</p>	

Figure 1.9 The different solid-state hydrogen storage techniques [22, 44-46].

The complex or simple metal hydrides are the most common. Basically, the metal matrix is filled with absorbed hydrogen atoms, as displayed by Figure 1.10 [47]. The penetrants are usually located in tetrahedral or octahedral interstitial sites (Figure 1.11) [48].

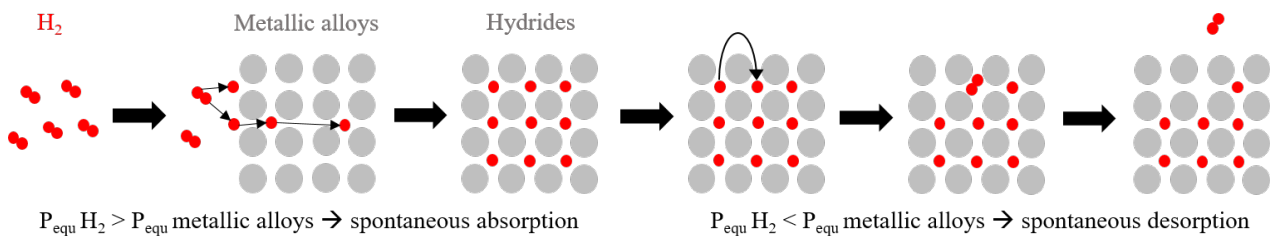


Figure 1.10 The mechanisms of hydrogen absorption/desorption in metallic alloys.

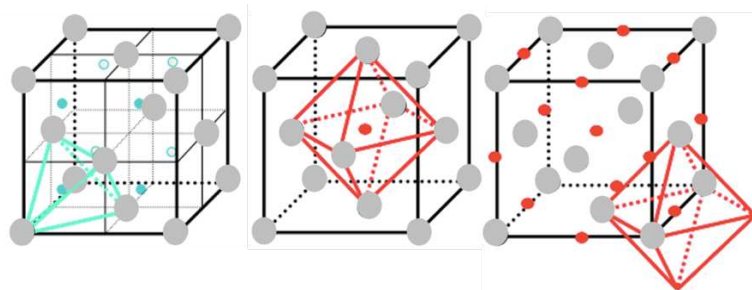


Figure 1.11 Interstitial sites on a face-centered cubic structure, with tetrahedral sites in blue and the octahedral sites in red.

Many metals in the periodic table can make “metal hydrides” but the lightest ones such as magnesium are preferentially used [47]. The storage capacity of a hydrogen-absorbing material, *i.e.* in which the hydrogen is stored within the bulk of the material (both chemical or metal hydrides), is typically reported as gravimetric capacity in wt%: this corresponds to the ratio of the mass of hydrogen stored within the material to the total mass of the material **plus** hydrogen. As an example, different hydrogen capacities are displayed in Figure 1.12 for some selected metal hydrides [49].

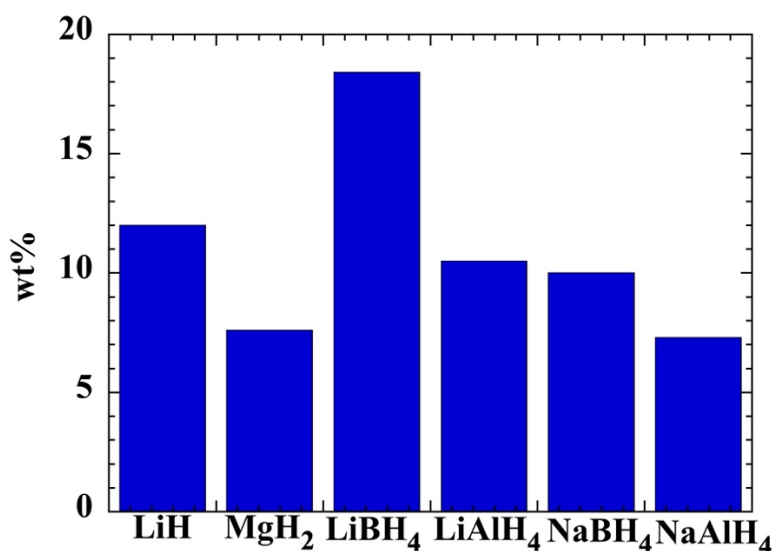


Figure 1.12 The capacity to store hydrogen of some selected metal hydrides.

The solid-state approach is mainly used for stationary applications in the “hydrogen energy” field. A good illustration of its efficiency is the management of electricity networks. Indeed, within the context of a complex balance between production and consumption, if there is too much electricity for the current demand, the surplus electricity in the network could be used to produce H₂ by electrolysis of water (Figure 1.2). This newly formed H₂ can then be stored in the networked tanks with solid storage [50] or be used by industries that require a lot of hydrogen such as ammonia plants or oil refineries. Hydrogen-absorbing solid materials are therefore one of the main studied storage techniques. Their main features are summarized in Figure 1.13 [22, 45, 47-50].

+	➤ <i>Manufacture quite safe</i> : metallic hydride can be handled at ambient temperature and pressure, they neither explode nor burn.
	➤ <i>Stable even when not used</i> : in the “standby” mode of the reservoir, hydrogen does not evaporate into the environment.
	➤ <i>Easy-to-use</i> : solid storage systems can be easily transported and installed.
	➤ <i>Highest volumetric densities</i> : due to the atomic ratios of two H atoms for one atom of metal alloy, densities of $\sim 106 \text{ kg/m}^3$ can be reached for e.g. MgH_2 . Liquid storage densities are more around 70 kg/m^3 and gas storage densities around 42 kg/m^3 at 700 bars.
	➤ <i>Easy to fill</i> : metallic reservoirs operate at a pressure range of 8 to 30 bars which corresponds to an electrolyser’s output pressure (H_2 production) and means that they often do not require the use of compressors.

-	➤ <i>Heavy</i> : weight is the major problem. Metals are quite heavy and, even if the lightest are preferred, tanks are too heavy for a light car despite their high volumetric densities.
	➤ <i>Thermal cycle necessary</i> : the absorption reaction is exothermic. It is therefore necessary to evacuate this heat from the tank or recover it for the desorption, which is endothermic.
	➤ <i>Temperature limits</i> : heavy metals can release hydrogen at low temperatures while light metals must be heated.
	➤ <i>Cost</i> : most of the materials available with high storage capacity are very expensive.
	➤ <i>Impurities sensitivity</i> : a potential reduction of the storage capacity can appear since the uptake and release processes take place at the molecular level, where impurities can also be captured and kept in the interstitial sites instead of hydrogen atoms.

Figure 1.13 The advantages and disadvantages of the metal hydride and more generally of the solid-state storage approach.

1) B. 1. 2. Liquid state storage

The second technique is the storage in the liquid form or liquefaction. Historically, it was developed even before the solid approach (at the end of the 19th century) and research accelerated during the cold war [51]. At ambient temperature and pressure, hydrogen is a gas since its boiling point is very low, *i.e.* 20.22 K (-252.78°C) [13]. However, if the temperature decreases, the density increases (Eq. 1.6) and it is then possible to consider liquid or cryogenic storage. Here again, at least three different liquefaction processes exist: two are already used and one is under study. The two well-established ways are based on Joule-Thomson expansion [52, 53] and several steps follow one another: this begins with a pre-cooling of the gaseous hydrogen by a mechanical refrigeration unit and a liquid nitrogen heat exchanger. During this first

step, the temperature goes down from ~ 300 K ($\sim 27^\circ\text{C}$) to 80 K (-193°C). Then, two refrigeration cycles are possible. They are referred to as “Claude cycle” and “Bayton cycle”, and are presented in Figure 1.14. For each of them, compressors and turbines work together to compress and expand the cold gas under adiabatic conditions. This succession of compression-expansion cycles allows the cooling to continue. Finally, there is a low-speed gas isenthalpic expansion, *i.e.* it does not exchange work nor heat with the external environment. As a result, of this last step, the temperature goes down from 80 K to 20 K (-253°C) and hydrogen condenses to a liquid [54].

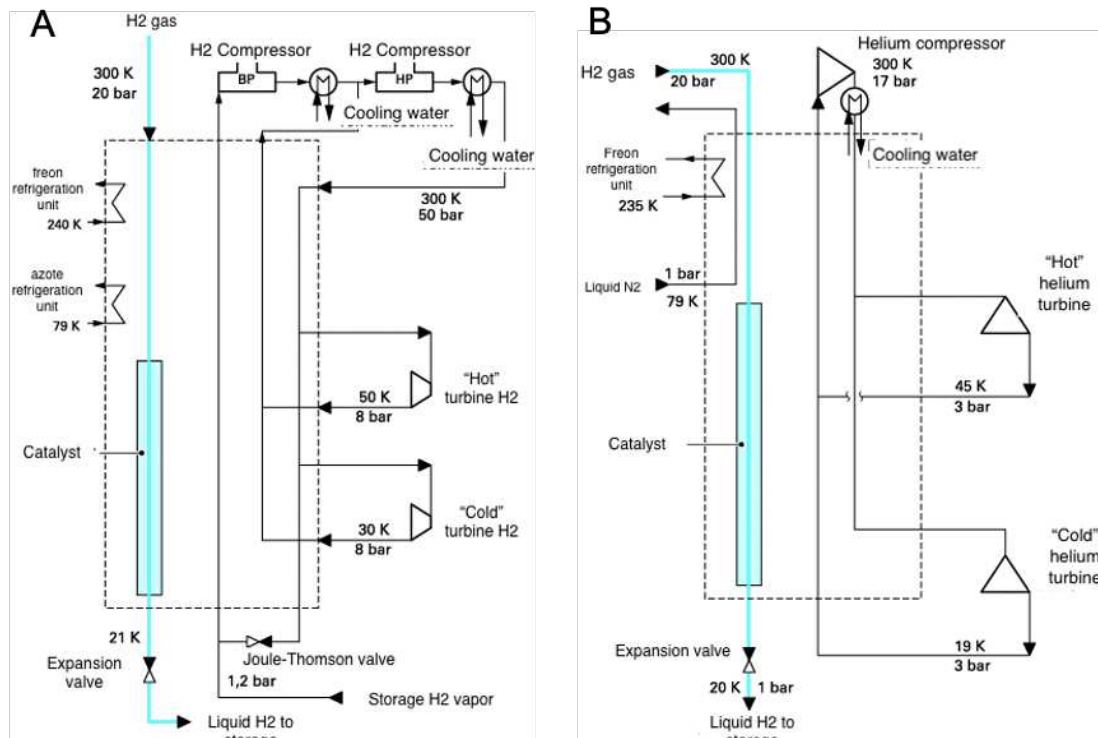


Figure 1.14 Claude’s cycle with two compressors and two turbines in series (A) and Bayton’s cycle with one compressor and two turbines in series (B) [54].

The third liquefaction process, which is still at the experimental stage, is simpler than both previous methods. It is named “liquefaction by magnetothermal effect process” and uses magnetic refrigeration based on the “magnetocaloric effect”. This phenomenon means that magnetic materials are heated when subjected to a magnetic field and cooled when it is removed [55, 56]. It allowed William Francis Giauque to win the chemistry Nobel prize in 1949 for developing a magnetic refrigeration device to approach absolute zero [57].

Whatever the method, storing liquid hydrogen requires a lot of energy because it needs to reach very low temperatures and pressures ranging from 1 bar to 3.5 bar [22]. In addition, tanks must be perfectly insulated in order to maintain liquid hydrogen at this temperature. This is the main problem with this type

of storage: if hydrogen starts to boil off due to heat transfer through the tank wall, it becomes gaseous and ultimately leaks. Currently, evaporation rates of hydrogen can reach 2-3% by volume *per* day, and the onset of evaporation is usually observed after 3-4 days in parked cars [22]. This issue can be limited by constructing the tank walls using materials with low thermal conductivities. However, at cryogenic temperatures (-253°C), materials may behave very differently and their thermal conductivities and other properties can change drastically. Another solution would be to evacuate the air between the tank wall layers or by placing a multi-layered insulation at the inner tank face [22]. Nonetheless, delaying the boil-off effects and solving this “insulation” problem is one of the main research objectives in tank wall design.

Due to the large amount of energy necessary for liquefaction and the continuous boil-off of H_2 , the use of liquid hydrogen storage systems is limited. However, it is exploited in applications where the cost of hydrogen is not an issue and the gas is consumed in a short time, *e.g.* for the air and space field, are the main beneficiaries of this technique [58]. For instance, the tanks in the Ariane launcher are designed and manufactured by Air Liquide and contain 28 tons of liquid hydrogen that will provide fuel to the central engine (Figure 1.15). These tanks are made from different materials such as polyester felt fabrics, covered with an aluminium liner. They weigh only 5.5 tons when they are empty and their casing is not more than 1.3 mm thick [41, 59].

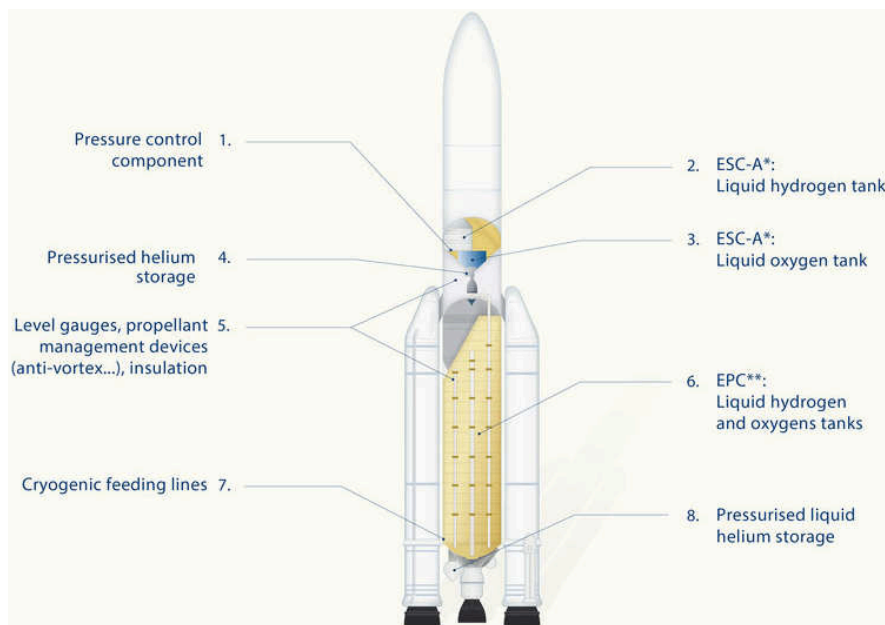


Figure 1.15 An Ariane rocket tank [60].

The main characteristics of the liquid storage approach are summarized in Figure 1.16:

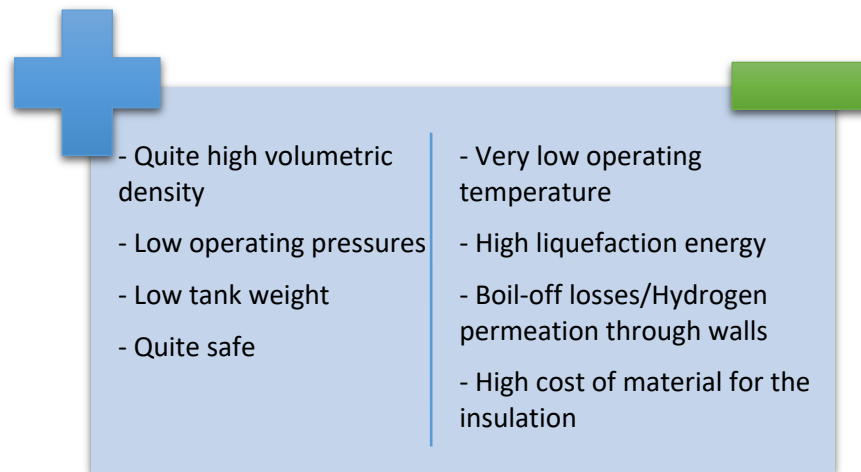


Figure 1.16 The advantages and disadvantages of the liquid storage approach [22].

Another issue, which will also be present in the compressed hydrogen storage, is the hydrogen embrittlement (HE), *i.e.* corrosion cracking due to hydrogen stress. It can be caused by the boil-off and/or the hydrogen gas permeation through the tank walls. As for gas storage, multilayer tanks can help to prevent this problem [22].

1) B. 1. 3. High pressure gas storage

The third and last technique to store H₂ is in the gas phase at high pressures. Indeed, hydrogen is commercially-available as a compressed gas which means that storing it under high pressure is feasible and a commonly used technique. The following example using the ideal gas approximation, Eqs. 1.4 and 1.5, illustrates how the volume can be reduced. It should be remembered that 5 kg of H₂ means almost 600 km of autonomy.

What is the volume of 5 kg of H₂ at ambient temperature (~298 K) and pressure (~101325 Pa)?

$$n = \frac{m}{M} = \frac{5000}{2.016} \approx 2480 \text{ moles} \quad (1.7)$$

$$V = \frac{nRT}{P} = \frac{2480 \times 8.314 \times 298}{101325} \approx 60 \text{ m}^3 \quad (1.8)$$

Now, what happens when it is compressed to 700 bars (700×10⁵ Pa):

$$V = \frac{nRT}{P} = \frac{2480 \times 8.314 \times 298}{700 \times 10^5} \approx 0.09 \text{ m}^3 \quad (1.9)$$

The volume decreases and, by extension, the density increases from ~0.08 kg/m³ to ~56 kg/m³.

While, the liquid state is generally required when a very large quantity of fuel is necessary, *e.g.* tons or even tens of tons, gas storage under high pressures is more suitable for quantities not exceeding a few kilograms or tens of kilograms. It is already used by certain vehicles to store on-board hydrogen [61]. Depending on the production technique and installation, it is also used in the refuelling stations. For example, when there are on-site electrolyzers to produce hydrogen, the gas must be stored temporarily in high-pressure bottles as shown in Figure 1.17.

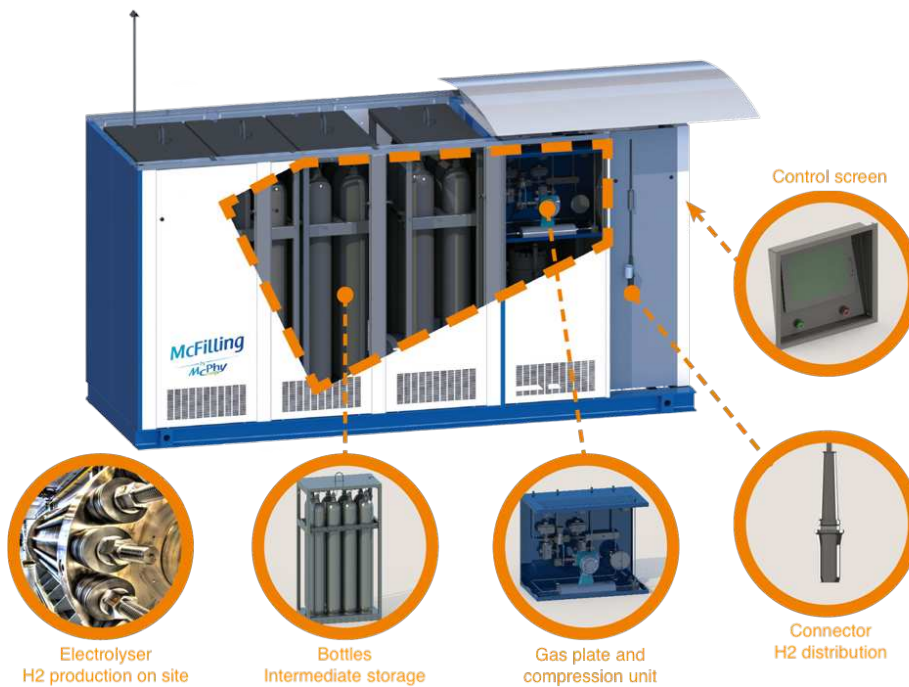


Figure 1.17 Hydrogen station equipped with an electrolyser [62].

However, when compared to other techniques, the major drawback of gaseous storage for transportation applications is the limited amount of hydrogen that may be stored in a reasonable volume [41]. Its advantages and disadvantages are summarized in Figure 1.18.

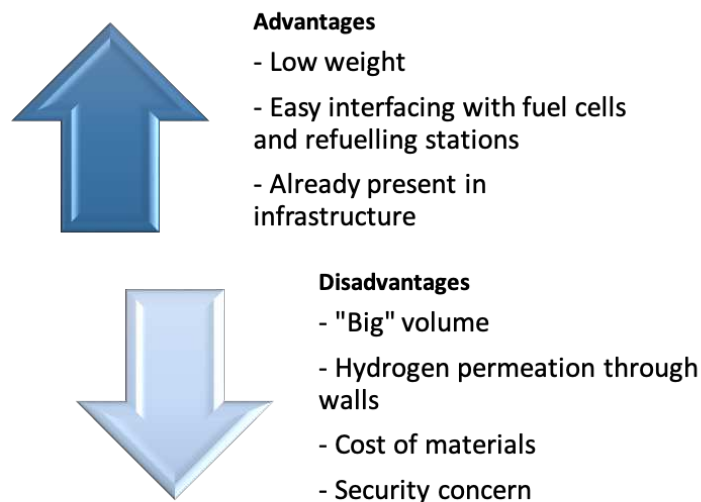


Figure 1.18 The advantages and drawbacks of the gaseous storage approach [22].

All three solid, liquid and gaseous techniques to store H_2 have their good and bad points, and much research has been carried out to improve their capacity and uses since before the 1960s. Hybrid solutions using two of them have also been considered: these include, for example, a new system aimed at improving loading/unloading characteristics by combining a high-pressure tank and absorbing alloys, which improves the volumetric density [63]. However, gaseous storage remains preferable for cars and different types of tanks are proposed for the “zero carbon transition”.

1) B. 2. The different high-pressure hydrogen gas storage tanks

Different high-pressure tanks operating between 300 bar and 700 bar are currently available and certified on the market and can be categorized into four main types as outlined by Figure 1.19 [63]. The more recent ones are based on new lightweight materials such as carbon-fibre reinforced composites [48], but different types of tanks have been studied over the last decade. Actually, a fifth type is also under study: a pressure vessel, which is fully made in composite without liner and is therefore ~20% lighter than the most recent commercial tanks. However, it is only able to handle low-pressure ranges, which leaves it at the experimental stage for now [64].

Figure 1.20 provides a quick historical timeline of the main steps in the development of these technologies for hydrogen and other small molecules.

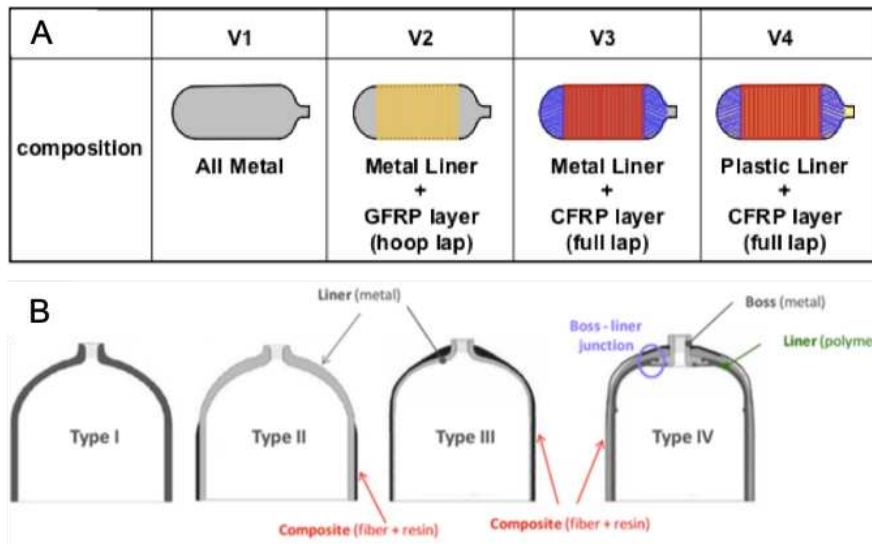


Figure 1.19 The different types of tanks where GFRP refers to “Glass Fibre Reinforced Plastic” and CFRP refers to “Carbon Fibre Reinforced Plastic” (A) [63]. A closer representation of types I (or V1), II (or V2), III (or V3) and IV (or V4) (B) [46].

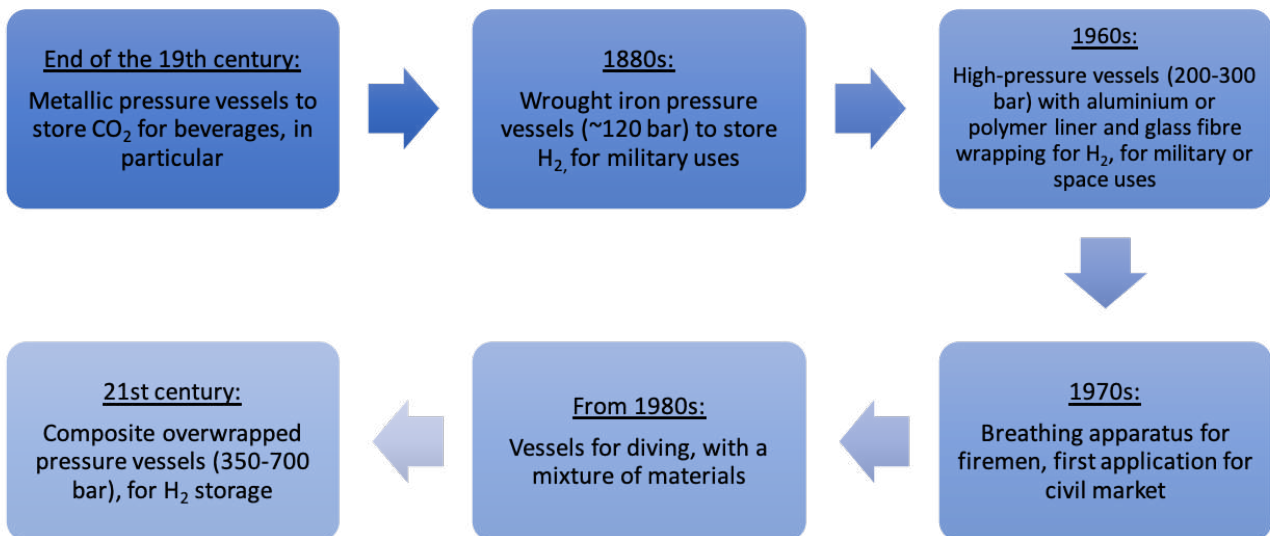


Figure 1.20 Historical timeline of the different tanks [46].

Nowadays, the 700 bar tanks designed at the beginning of the 21st century are, therefore, the current and upper limit of what it is economically and technologically viable. Indeed, the density as function of the pressure is plotted in Figure 1.21 and this corresponds to the compressibility of hydrogen gas. To compare, the density for liquid hydrogen is added to the Figure, but at much lower temperature and atmospheric pressure. There is clearly an inflection at around 700 bars, beyond which the density increases less and less with pressure. The gain in quantity of gas stored decreases and is less interesting above this pressure but, inversely, the mechanical resistance of the tanks has to be increased to resist such conditions. Therefore,

the pressure of 700 bars was defined as the standard pressure for the composite tanks, mostly type IV (Figure 1.19) which have been developed for fuel cell vehicles [55].

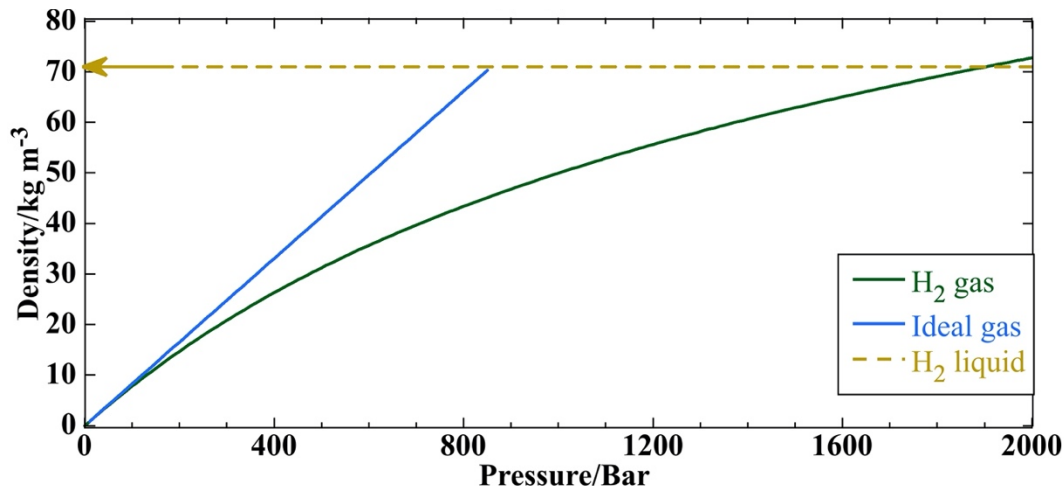


Figure 1.21 Density of compressed hydrogen gas as a function of pressure, at 20°C. The ideal gas approximation is also shown as well as the density of liquid hydrogen at -253.15°C and atmospheric pressure [65, 66].

Amongst the four types of tanks shown in Figure 1.19, the ones designed for hydrogen storage are mostly based on the carbon composite types V3 and V4, whereas the types V1 and V2 are preferably used for compressed natural gas. The reason behind this choice is simply the pressure range used. It is much higher for hydrogen cars than the natural gas vehicles, these latter being normally compressed to 200-250 bar [63]. However, the development of different types of tanks has also been guided by requirements that can be categorized as follow [40, 63, 67]:

- ✓ Safety
- ✓ Performance (storage capacity, weight, volume, quick uptake and release of fuel, etc.)
- ✓ Balanced cost-effectiveness
- ✓ Technical adaptation to the infrastructures
- ✓ Mechanical resistance
- ✓ Handling at room temperature and pressure

The safety can be evaluated with a “safety factor”, whose limits depend on the different standards defined for the hydrogen technologies. This is one of the requirements that weighs heavily on the costs of developing, manufacturing and using the tanks [40, 68].

For the performance, some “certified” tanks are available on the market, *i.e.* they have been validated by the US Department of Energy (DOE) [69]. To be “valid”, an on-board hydrogen storage system stated to *attain a range greater than 500 km on a single filling* should have a storage capacity of at least 7.5 wt% in gravimetric capacity or 70 kg m⁻³ in volumetric density. To achieve such performances, the use of type III fully-wrapped vessels with a metallic liner and type IV fully-wrapped vessels with a non-metallic liner is inevitable. Indeed, types I and II cylinders have insufficient storage efficiencies, *e.g.* only about 1 wt% of H₂ can be stored in type I [70].

The mechanical resistance depends on several properties such as the design, materials and use of the tanks. Besides the lifetime of the reservoir itself, this resistance is very important in the event of an accident (impact, crushing, fire, etc.). Wrapping the tank with any kind of protection is limited by the constraints of the weights and sizes of the vehicles [61]. Performance tests are carried out to ensure that the high-pressure hydrogen systems and their components are fully capable of avoiding failure, rupture or leakage under extreme conditions, including extensive fuelling frequencies, physical damage and harsh environmental conditions [46, 70].

To meet the specifications, the materials sought for the manufacture of the tanks must have some key characteristics such as [22]:

- ✓ A very high tensile strength. It limits the maximum allowable operating pressures and, therefore, the storage capacity.
- ✓ A low density and weight. Thicker walls are required when the working pressures increase to meet the corresponding “safety factors”.
- ✓ Non-reactivity with hydrogen and good mechanical resistance

As stated above, the different available were designed to meet the requirements evoked. Due to the very high pressures used, the shape is for now limited to a cylinder, which is more robust than other shapes [67].

Indeed, **Type I or VI** (Figure 1.19) were the first tanks developed. They are cylindrical bottles made essentially in steel and assembled inside metal frames, *i.e.* an all-metal construction. However, even if there is only one layer and if low-stress steels are used, they are still very heavy for mobile applications. Their major drawback is their weight *per* kg of H₂ stored. For example, a standard steel cylinder of 1.50 m of height and diameter of 0.23 m contains 740 g of H₂ and weighs ~67 kg at 200 bars [48] with a maximum gravimetric density of ~1.7wt% [67]. Moreover, as almost all the parts exposed to hydrogen are metallic, they are subject to embrittlement (as for liquid storage), *i.e.* the hydrogen-stress corrosion cracking.

Research has been carried out on the atomic-level processes responsible for this embrittlement, in order to prevent the failures resulting from long exposure to this gas [48]. Stainless steels and aluminium alloys are most often used as they have the advantages of being relatively light and avoiding quite well this damage [61].

Type II or V2 tanks (Figure 1.19) consist of two-layer reservoirs with a thick metallic inner liner which is overwrapped in the hoop direction by a glass fibre reinforced plastic composite (GFRP) [46, 63]. This composite outer protection is made using a filament winding technique, which allows different types of angles and positions for the fibre (Figure 1.22). At a typical pressure of 200 bars, this type of tank has a gravimetric density of ~ 2.1 wt% [67].

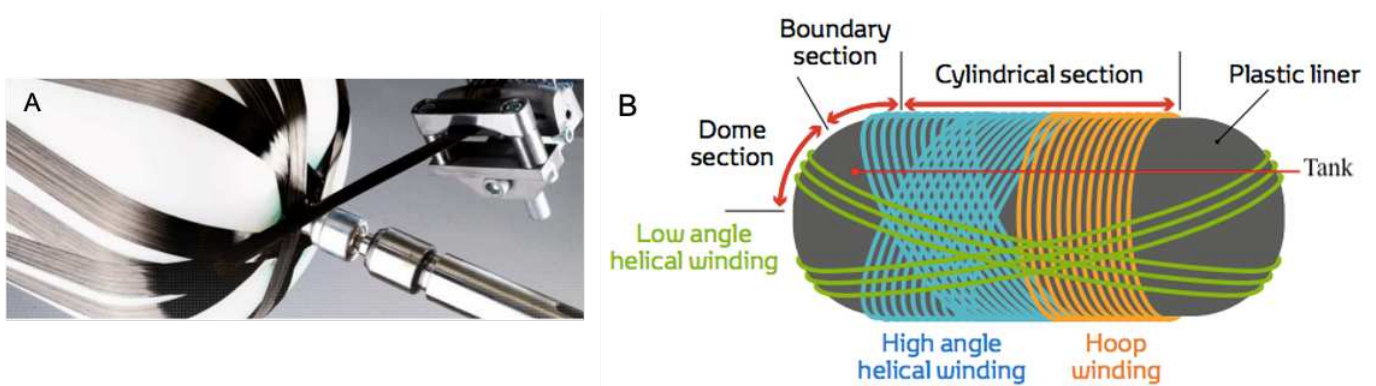


Figure 1.22 Filament winding (A) [61] and the different angles obtained by filament winding (B) [34].

When a type II tank is overwrapped by a carbon fibre reinforced plastic (CFRP), it is then referred to **type III or V3** (Figure 1.23). Here, the metallic liner contributes at around 5% to the mechanical resistance [63]. Indeed, the principle aim of this metallic liner is to be leakproof whereas the full-wrap composite layer provides the resistance to pressure. With this configuration, these two functions are managed separately. However, the metallic liner can also help withstanding fatigue due to repeated filling-emptying cycles. Indeed, during these cycles, the tanks are subjected to temperatures varying from 65-85 °C for the liner and 40-60 °C for the boss liner junction. The metallic liner also simplifies the connection with the operating circuit [46]. Compared to the partially-wrapped composite layer of the previous type, the overwrapped composite layer of type III leads to a gravimetric density around 4.2 wt% for a pressure of 700 bars [67].

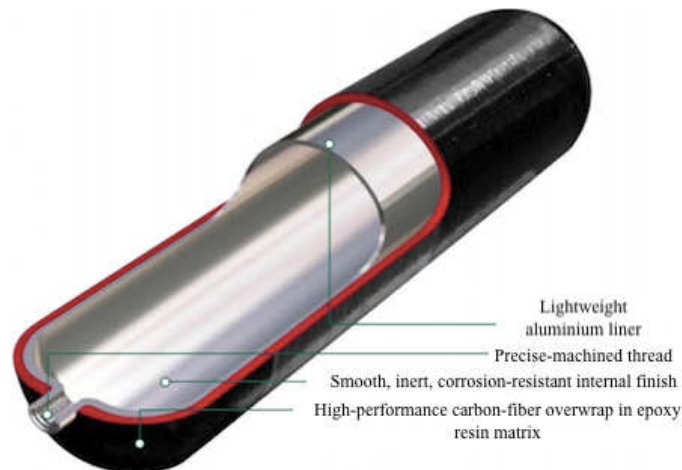


Figure 1.23 The G-Stor™ Pro Type 3 AF Cylinder by Luxfer, which is a type III tanks [71].

Finally, when the liner is a polymer or (more rarely) an extremely thin metal liner (Figure 1.24) [63], the tank becomes a **Type IV or V4**, which consists of three layers much lighter layers than the steels used in **type I** and **II** bottles [58, 61]:

- ❖ An inner polymer liner, which is used for sealing and has the advantages of being cheaper, lighter and insensitive to hydrogen embrittlement. However, this kind of liner is less impermeable to H_2 than metal enclosures.
- ❖ A first over-wrap layer with a carbon-fibre composite, which corresponds to the resistant structure, *i.e.* it compensates for almost all of the stresses exerted by the pressure on the container walls.
- ❖ An outer layer made of a glass-fibre composite and aimed as external protection, *i.e.* it provides the shock resistance and protection against environmental aggressions and prevents the humidity or corrosion damage. Moreover, it allows the tank to be marked.

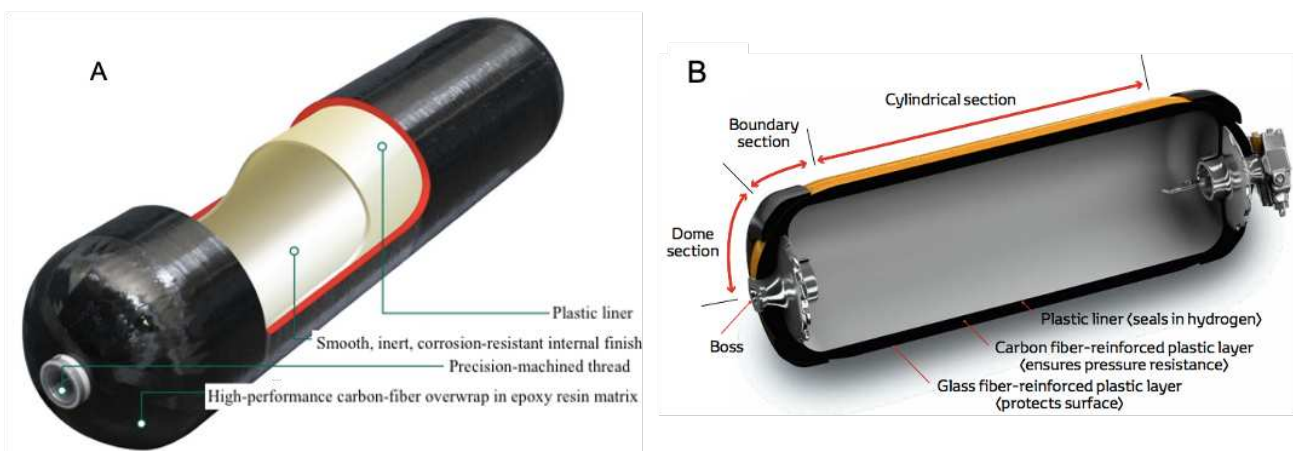


Figure 1.24 The G-Stor™ Go Type 4 AF Cylinder by Luxfer, which is a type IV tanks (A) [71]. A Toyota pressure tank (B) [34].

Due to their lightweight, advanced technology and good storage capacity, *i.e.* 5.7wt% for a pressure of 700 bars [67], the current tanks for small vehicles are mainly based on **type IV**. The commonly-used materials for the three layers are [46, 58]:

- ❖ For the metallic parts (if existing): aluminum alloys, which are thin enough to fulfil the weight requirement and quite resistant to HE. Some other low-stress and stainless steels, such as inox or chrome molybdenum, can also be used.
- ❖ For the polymer parts: high density polyethylene (HDPE) treated with an appropriate surface treatment, which can reduce hydrogen permeation by 80–90% as compared to untreated polyethylene. Polyamide-based materials are also increasingly used [22, 72].
- ❖ For the composite parts: glass, aramid or carbon fibres are embedded in epoxy, polyester or phenolic resins. The former are preferred because of their good mechanical properties, stability and compatibility with the filament winding process.

All the different parts of the tanks, liner and outer layers, have their own role and specificities in order to meet the requirements [40] and ensure the proper functioning of the tank, as summarized in Table 1.4.

Table 1.4 Summary of the different layers which can be part of gaseous hydrogen storage tanks, with the inner two layers in metal and/or polymer and the outer part in composite [46, 58, 61].

Metallic parts (liner and boss)	Polymer parts (liner of type IV)
As already stated, H ₂ affects metallic materials with consequent degradation of the mechanical properties and premature cracks. This comes from the H atom dissolution and trapping in metals, <i>i.e.</i> hydrogen embrittlement. To try to mitigate this issue, research has been made to have a better understanding of the mechanisms in order to improve the alloy manufacturing and the assembling of the components, especially.	A high purity of H ₂ is required to guarantee the performance and the reliability of fuel cells, as the draft standard ISO 14687-2 states [73]. This requirement is also an advantage for the polymer liner which, if not sensitive to HE, is nevertheless less impermeable to hydrogen than the metallic parts. The large pressure variations, to which the reservoir may be subject, can lead to deformations, which are accentuated by a gas with contaminants.
Composite parts (types II, III and IV)	
Depending on the type of tanks, different composites are used but they are all obtained by filament winding of the fibre embedded in the resin. The difference, beside the composition, is how this part is wrapped around the inner part: for type II pressure vessels, it is with a circumferential angle (hoop), whereas for types III and IV , it is a combination of circumferential, helical and polar angles. These different angles allow the final structure to resist the internal pressure.	

As mentioned before, a very high mechanical resistance is necessary whatever the type of tanks. Even composite overwrapped pressure vessels (COPV) can be subjected to a broad range of impacts such as falls or impacts during handling, transportation and car accidents. Although tests are made to ensure the performance of the high-pressure hydrogen system, there is little information available to understand the effects of mechanical shocks on these vessels and their consequences. Indeed, a surface impact can create “discrete” damages in the outer composite layers, such as fibre breaks, delamination and matrix cracking, but also more in the inner part with deformations of *e.g.* the metallic liner of a type III tank (Figure 1.25).

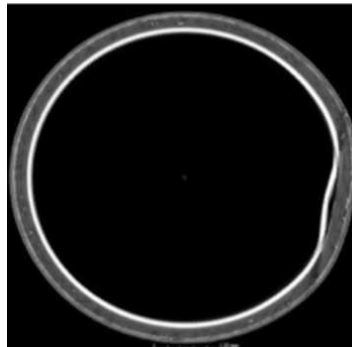


Figure 1.25 Deformation of a metallic liner after a mechanical impact on the external surface of the COPV [46].

On the other hand, if the shock is too big, it results in “distinct” damages such as mechanical failure which can cause hydrogen leakage. In extreme cases, the gas released can form a jet fire which can impinge on objects and emit thermal radiations. In tank manufacturing, barrier walls can be installed to mitigate the hazards caused by this hydrogen jet flame. However, it is important to ensure that they do not create unexpected additional hazards [70].

Furthermore, even if it is not directly linked to the mechanical resistance, another deformation can also appear in the tank walls. Although the mechanism is not fully understood, it is attributed to the solubility and diffusion of hydrogen in the materials and its accumulation at the interfaces. All along its life, the hydrogen tank is subject to emptying and refuelling cycles or, in other words, to quick uptake and release of fuel which, in some cases, may lead to permanent deformations of the plastic liner (Figure 1.26)

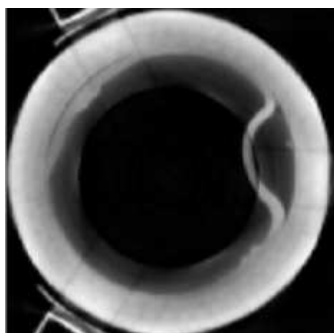


Figure 1.26 X-Ray tomography of a polymer-lined COPV with permanent deformation after rapid venting [46].

Therefore, **type IV** high-pressure gas tanks currently used in cars need to be improved on two main points: a further reduction of the volume and avoid, if not eliminate, H_2 permeation through the tank walls.

1) B. 3. The depressurization problem

There are two main ways for gas molecules to escape from a gas container due to the pressure difference between the container and the exterior: either effusion or permeation. Effusion (Figure 1.27) is the passage of gas through a small hole or a leak. For a gas cylinder without any damage, this could occur, for example, at a bad seal or at the valve [74].

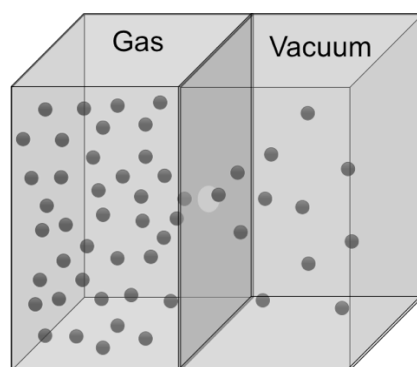


Figure 1.27 Gas effusion. The molecules move from a high-pressure region (left) to a low-pressure one (right) through a pinhole.

The other main transport mechanism is gas permeation. This is an inherent phenomenon for all gases in contact with polymers and it results from the dissolution and diffusion of gas molecules in the polymer matrix. For safety reasons, there are maximum allowable rates defined in standards and regulations [46], but even these requirements are not sufficient to prevent the problems caused by permeation in the hydrogen storage vessels. So, if the plastic liner and composite layers are not, unlike metals, subject to hydrogen embrittlement, the permeation of H_2 still leads to their hardening of materials and a significant

reduction in ductility which, in turns, induces cracks and ruptures during a rapid depressurization. Even the carbon composites with their high yield stress and a low density are susceptible to hydrogen leaks, which reduces their effective capacity during operation. This is, therefore, the role of the liners incorporated as inner layer in the **types III and IV** (Fig. 1.19), is to reduce these hydrogen leaks and prevent cracking of other wall elements [22]. However, the different materials used as liners are still not completely impermeable and this why improving the tanks by incorporating hydrogen-barrier coatings is studied.

In order to manage this depressurization problem, it is important to understand the notions at the basis of permeation, because hydrogen diffusivity, solubility and permeability are important parameters for selecting the materials suitable for liner purposes [75]. For the gas, all these transport properties are connected and depend on its nature (polarity and molecular size) as well as on the pressure and temperature which are imposed by the external usage conditions. For example, dihydrogen gas with one non-polar H-H bond has a distinct permeation behaviour compared to a molecule like water with a permanent dipole. It is also a very small molecule, which gives it a different diffusive behaviour from CO₂, although the latter is also non-polar [76].

The following equations 1.10-1.13 define each transport property and show how they are interconnected [74-76]. The flux J defined as:

$$J = \frac{Q}{A \cdot t} \quad (1.10)$$

with Q being the amount of gas that permeates through the polymer (the inner liner in the present case) in a time t and across a surface area A . Then the permeability coefficient P_c is defined as the flux divided by the pressure gradient:

$$P_c = J \cdot \frac{l}{\Delta p} \quad (1.11)$$

with Δp being the pressure difference on either side of the layer of thickness l . It can be expressed in a variety of different units. The most widely used, although non-SI, is the *barrer* ($= 10^{-10} \text{ cm}^3 \text{ (STP) cm cm}^{-2} \text{ s}^{-1} \text{ cmHg}^{-1}$), where the standard cubic centimetre at standard temperature and pressure (STP) conditions represents an amount of gas as an equivalent volume, *i.e.* that which the n moles of gas *would occupy if it were an ideal gas* and if it were kept under STP conditions, $V(\text{STP}) = nRT^{\text{STP}}/P^{\text{STP}}$. For example, 1 mole of gas at the (SI) standard temperature of 273.15 K and standard pressure of 1 bar (10^5 Pa) would have an equivalent volume of about $22711 \text{ cm}^3(\text{STP})$. Another common unit of the permeability coefficient is $\text{mol m m}^{-2} \text{ s}^{-1} \text{ Pa}^{-1}$.

The permeability coefficient, defining the ability of a species to penetrate and permeate a membrane [77], is also related to the diffusion coefficient, D , and solubility coefficient, S_c :

$$P_c = D \cdot S_c \quad (1.12)$$

The diffusion coefficient describes the physical movement of penetrant molecules through the polymer free volume of the polymer, whereas the solubility coefficient is defined as the concentration of penetrant in the polymer divided by the applied gas pressure:

$$S_c(p) = \frac{C(p)}{p} \quad (1.13)$$

Finally, to complete all these equations, it is also important to mention the permselectivity α . Even if this parameter is not useful in mobile applications like hydrogen cars, where there is only one gas, it is still part of the equations of permeation. It describes the material's ability to selectively separate gas i in favour of gas j according to their different permeabilities in the liner:

$$\alpha_{ij} = \frac{P_{c_i}}{P_{c_j}} = \frac{D_i S_{c_i}}{D_j S_{c_j}} \quad (1.13)$$

In fact, all these properties can be summarized by the two main notions, *i.e.* sorption and permeation, as described in Figure 1.28 [78]:

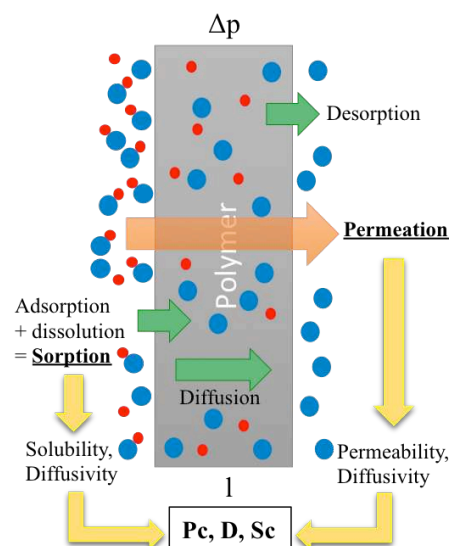


Figure 1.28 Sorption and permeation regroup all the other concepts linked to the transport properties.

Another main impact to the gas permeabilities is the properties and characteristics of the polymer layer used as the matrix. Its chemical structure, processing conditions and other factors define its properties,

such as crystallinity, orientation and cross-linking degree, which in turn affect the permeation of any gas absorbed in it. Table 1.5 provides an overview of the main effects of the polymer characteristics [79].

Table 1.5 General factors affecting gas permeability in polymers [76].

Properties	Impacts
Density	Linked to the free volume between the polymer chains, the higher the density, the lower is the permeability. Solubility is usually enhanced in denser systems but it is the opposite for diffusivity.
Crystallinity	Crystallinity in polymers reduces gas permeability significantly compared to amorphous structures. The crystallinity is strongly related to the chain movements and density: as the degree of crystallinity increases, the density increases as well and the permeability decreases.
Molecular mass	It does not have too much effect except at the very low range of molecular masses.
Orientation/alignment of polymer molecules	An extruded polymer with chain alignment in the direction of extrusion may have a lower permeability than the same solution-cast polymer.
Cross-linking degree	Often, the higher the degree of crosslinking, the lower the permeability, especially for permeants that are larger than the distance between crosslinks.
Glass transition temperature - T_g	Also linked to free volume and chain movements: permeation rates above T_g are much higher than below T_g .
Plasticizers	Small plasticizer molecules penetrate between the polymer chains and reduce the density as well as decreasing the T_g , resulting in an increase of the permeability.
Humidity	For hydrophobic polymers, such as a special grade of HDPE, the water-repellent property tends to decrease permeability. However, hydrophilic polymers may absorb water, causing swelling and, therefore, increasing the free volume and leading to an increase in gas permeation. However, water can also act as an anti-plasticizer by blocking permeation channels, thus leading to lower gas diffusion.
Fillers	Usually, inorganic fillers such as silica or clay provide a physical barrier to diffusion and decrease the permeability. However, the effect depends on the type, shape, and amount of filler as well as the interaction with the polymer.
Thickness	In principle, does not affect the permeability, diffusion, or solubility coefficients except for very low thicknesses with boundary effects. In practice, different values may be obtained for films of variable thickness: this can be due to differences in drawing, orientation, and crystallinity as well as the pressure gradient along this thickness.

To illustrate the effect and complexity of one of the main factors, *i.e.* the crystallinity, a semi-crystalline such as high-density polyethylene (HDPE) is a good example. Indeed, it has distinct amorphous and crystalline regions and, as such, the prediction of the permeation properties is complicated. Hydrogen permeability will depend on the relative amounts of each phase as well as on the size, shape, and distribution of the crystalline phase. The report written by M. C. Kane in 2008 [76], provides evidence that diffusion only takes place in the amorphous regions, which act like an amorphous liquid above T_g , whereas the crystalline regions act as a barrier and restrict permeation. Indeed, rubbery materials have free volume between the molecular chains where H_2 can easily penetrate and permeate through the material. It is then possible to predict the gas permeability based on the free-volume fraction calculated from the occupied volume and density.

To illustrate the different links between pressure, temperature and permeation, Fujiwara *et al.* [75] measured the hydrogen permeability of HDPE for pressures up to 900 bar (90 MPa) and at 30°C. Results are provided in Figure 1.29.

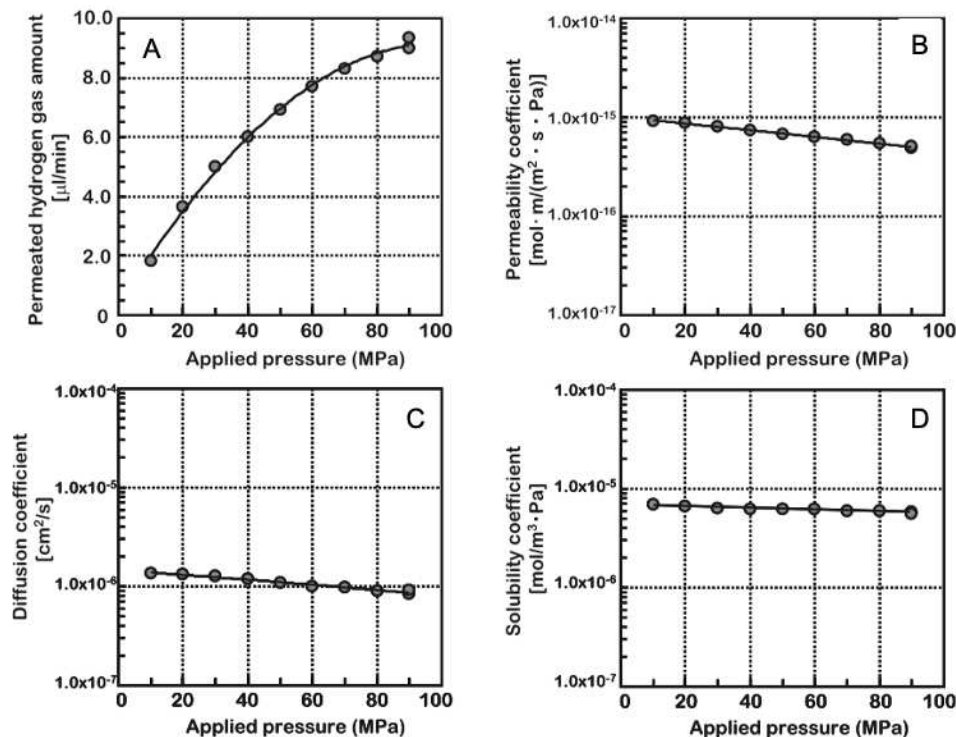


Figure 1.29 High-pressure permeation tests in HDPE at 30°C. The influence of the applied gas pressure on the amount of permeated hydrogen gas (A), permeability coefficient (B), diffusion coefficient (C) and solubility coefficient (D) are shown [75].

The amount of permeated hydrogen gas (Figure 1.29.A) increases as the pressure increases. The permeability coefficient (Figure 1.29.B) decreases with increasing pressure, reaching at 90 MPa almost half

of the P_c at 10 MPa. The diffusion and solubility coefficients also decrease as the pressure increases (Figure 1.29.D), a slightly larger rate of decrease for the diffusion coefficient. Consequently, D has the largest effect on the permeability coefficient [75].

This confirmed the assumption published in the 2008 report by the SRNL laboratory (USA), where different polymers used for hydrogen transport were compared [76]. In gaseous permeation through polymers, two kinds of materials are studied: the ones for use as barrier materials, *i.e.* with a low permeability and the ones for use as membrane separation materials, *i.e.* with a high permselectivity and if possible a high permeability. For the barrier application, materials typically have flexible carbon-carbon backbones with highly polar pendant groups, while for separations, they usually have more rigid backbone structures, such as aromatic compounds. The aim of the study was to demonstrate whether the main factor in determining the hydrogen permeability coefficient, at a given temperature, is predominantly controlled by the changes in diffusion (physical movements) or by those in solubility (molecular interactions). Therefore, the H_2 solubility and permeability coefficient were measured in different semi-crystalline polymers such as HDPE, polyetherketoneketone (PEKK), polyethylene terephthalate (PET) and polyvinildine fluoride (PVDF). The solubility coefficient was found to be the same for all these polymers, although their permeability coefficient was not. This confirms that the variations are mainly due to the diffusion coefficient. In other words, there are only very weak attractive interactions between the polymer and the non-polar permeating hydrogen gas and, therefore, diffusion is the limiting factor. Diffusion being related to the free volume, the latter is really influential and varies because the temperature and pressure influence the motion of H_2 through the polymer chains, as explained in Figure 1.30 [79].

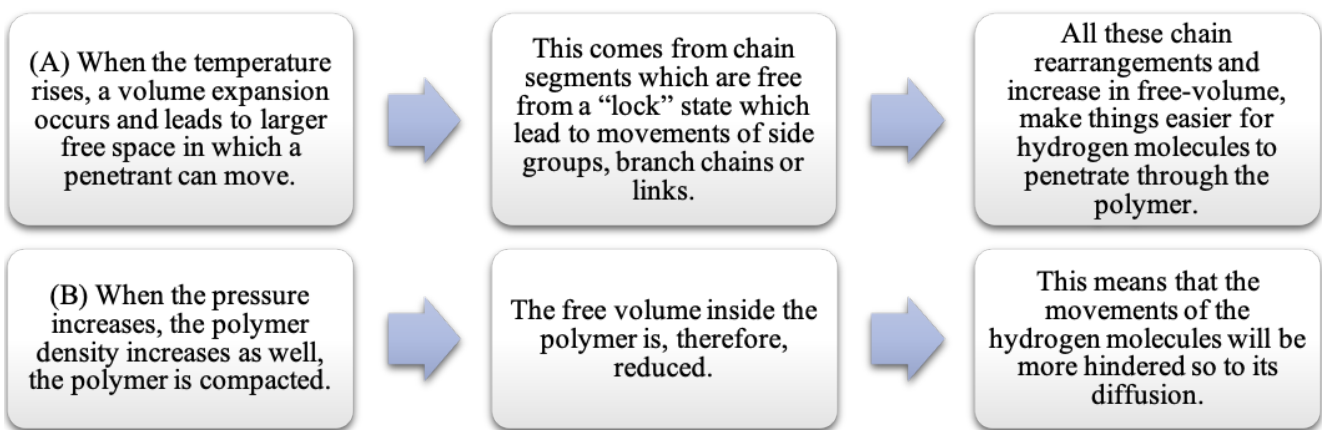


Figure 1.30 Effects of temperature (A) and pressure (B) on the polymer chains, free-volume and hydrogen permeation in a polymer.

It is clear that the properties of the polymer influence largely the permeation of the gas, which gives indications to better understand the depressurization problem. Indeed, this phenomenon can lead to plastic liner blistering because of the gas absorbed by the polymer at high pressure: if this pressure suddenly drops and the decompression rate exceeds the rate by which this gas can escape by diffusion, internal fractures and stresses are generated within the component and end up damaging the liner [80]. As stated above, they are dependent on the pressure difference, *i.e.* that between the initial and the final tank pressure, the temperature, the liner material properties, the depressurization rate and the hydrogen purity. Yersak *et al.* [81] developed a predictive model of the depressurization-induced blistering of type IV tank liners (HDPE or polyamide PA), and compared their results to depressurization experiments. Figure 1.31 displays experimental samples obtained after depressurization at different rates, *i.e.* 1, 3, 5 and 13 h at 50°C. They clearly show the blistering phenomena.

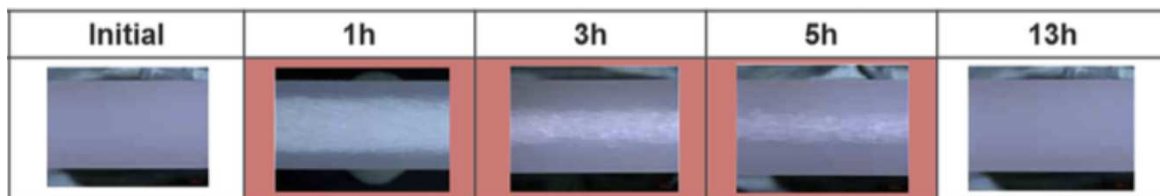


Figure 1.31 Cross-section of a HDPE 3 mm-thick monolayer liner, before and after depressurization at different rates and at 50°C [81]. The blistering corresponds to the whitening.

According to these pictures, the extent and intensity of blistering seems to increase as the depressurization rate increases: the “1 h” correspond to the highest depressurization rate and the “13 h” to the slowest. The same experiment was carried out with different polyamide liners and they show that:

- ❖ The blistering behaviour is not the same for all kinds of PA: some of them have blisters whilst others not.
- ❖ PA has a better blistering resistance than HDPE. Since PA has a lower hydrogen diffusivity than HDPE at 50 °C, as well as a lower solubility and a higher yield stress, a combination of these properties are beneficial for blistering resistance.

Depending on the conditions, the blister initiation within the material can lead to permanent deformation (Figure 1.26) or even to the complete failure of the component, as shown in Figure 1.32 [80].

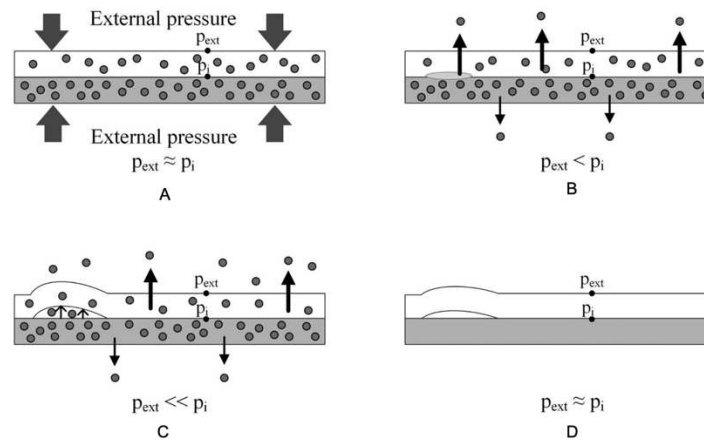


Figure 1.32 The liner collapse or permanent deformation in a liner/composite assembly of a hydrogen gaseous storage tank. It starts with the compression phase (A) then a depressurization phase during (B) and at the end (C) followed by the complete desorption (D) [80, 82].

During the compression phase, an equilibrium is established between the gas dissolved in the material and the liner/composite interface, *i.e.* there is no pressure gradient. During the decompression phase, a pressure gradient appears if the rate is faster than the diffusion rate of the hydrogen gas through the material. This implies driving forces which, if they are too large, can detach the liner/composite interface, thus leading to the collapse of the liner. Then, the trapped H_2 fills these cavities created by this delamination and continues to increase the damage until the pressure gradient disappears. After the complete desorption, this opening between liner and composite interface may get smaller, but it is too late and the permanent deformation of the liner is already in place [80, 82].

If the materials currently used as liners, *i.e.* mostly HDPE and PA, are resistant enough to allow the commercialization of the tanks, they can still be improved to counter the depressurization problem and blistering behaviour.

1) C. Inner liners

Thomas A. Edison said “*There’s a way to do it better - find it*” [83] and hydrogen permeation through containment materials is still an issue that requires consideration. Many researchers around the world, *e.g.* the French CEA or Toyota Motor Corporation, are trying to develop innovative and suitable liners using polyamides or polyurethanes. Indeed, these materials are known for their high strength, good blocking performance and heat resistance [70]. Another solution is the development of a thin-barrier coating in a gas containment system, which could reduce the depressurization rates and therefore avoid the loss of

fuel. It would also diminish the risk from potentially dangerous build-ups of inflammable gases. This coating should thus be a membrane with barrier properties.

1) C. 1. Existing barrier materials

By definition, a membrane is a layer of thin material separating two environments and being impermeable (to a certain extent) to one or several molecules [84]. Barrier materials are not exclusive to H_2 , and therefore, some examples of various membranes used as a barrier for different gases in different forms, *e.g.* liners or coatings, will be given in this section. The list is not exhaustive and highlights only the main materials or systems for liners for hydrogen storage, transport and infrastructure.

One well-known example of barrier membranes is in composite gas cylinders for breathing gas, *i.e.* a mixture of nitrogen and oxygen [74]. Similarly to a tank of type IV, the inner liner is a thermoplastic copolyester/elastomer with polytetramethylene oxide (PTMO) and polybutylene terephthalate (PBT). Silvanus *et al.* [74] evaluated the permeability properties of the tank in a diving application, in order to calculate how long the gas cylinders can be stored without the risk of attaining undesired nitrogen/oxygen ratios. The rates of gas permeation through the composite container at pressures up to 300 bars, both with and without the liner, were investigated during a period of 136 days to 1240 days. The results are presented in Table 1.6, in terms of the permeability coefficient for both gases and of the O_2/N_2 permselectivity.

Table 1.6 Gas diffusion through a container for breathing apparatus [74].

	O_2	N_2
Permeability coefficients (Barrer)	0.62 - 0.90	0.44 - 0.56
Permselectivity O_2/N_2	1.5 - 3.3	

The permeability coefficient as well as the permselectivity vary depending on the pressure and oxygen permeates faster than nitrogen. Moreover, they noticed cracks in the liner caused an accentuated drop in the oxygen fraction and pressure [74].

Another example of an oxygen barrier material is the one used in the beverage bottling field. In order to replace the easily-breakable and relatively heavy glass bottles, polyethylene terephthalate (PET) containers are a common alternative. However, like many other polymers, it is less impermeable to gases such as O_2 . Therefore, Deilmann *et al.* [85] attempted to improve PET barrier properties using a plasma-deposited silicon oxide film (SiO_x). The improvement was found to depend on the coating composition.

Indeed, they investigated the effects of different oxygen fluxes of a pulsed hexamethyldisiloxane (HMDSO) oxygen plasma used to coat the PET substrates. Different fluxes gave different layer compositions and the barrier properties were studied using oxygen permeation measurements of the modified PET. The results were presented using a “barrier improvement factor” (BIF), defined as the ratio of the oxygen permeation flux of untreated PET, J_{PET} , to that of the treated material, J , as in Equation 1.15.

$$BIF = \frac{J_{PET}}{J} \quad (1.15)$$

with $J_{PET} = 68.2 \text{ cm}^3 \text{ m}^{-2} \text{ day}^{-1}$. When the BIF is plotted as a function of the oxygen flux (Figure 1.33), low-oxygen fluxes give layers without (or almost without) barrier improvement whereas for oxygen fluxes above 400 standard cubic centimetres *per* minute (sccm), the BIF is above 60, which corresponds to a permeation flux of $J \approx 1 \text{ cm}^3 \text{ m}^{-2} \text{ day}^{-1}$:

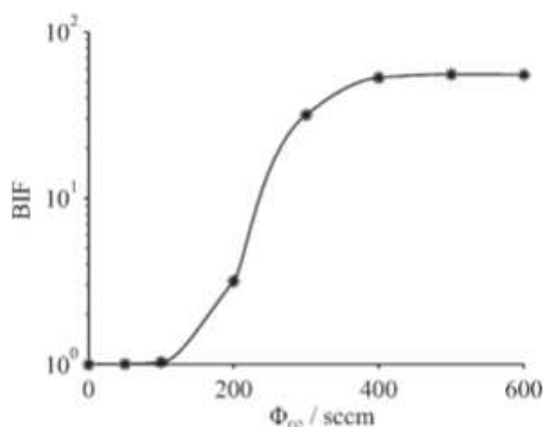


Figure 1.33 Barrier improvement factor for several PET foils coated with different SiO_x obtained by using various oxygen fluxes, ϕ_{O_2} , expressed in standard cubic centimetres *per* minute [85].

Various copolymers of PET and polyethylene naphthalate (PEN) have also been studied by Pang *et al.* [86] as oxygen barrier materials and, depending on the amount of each component, permeability coefficients as low as $8.7 \times 10^{-13} \text{ cm}^3(\text{STP}) \text{ cm cm}^{-2} \text{ s}^{-1} \text{ cmHg}^{-1}$ or $7.4 \times 10^{-13} \text{ cm}^3(\text{STP}) \text{ cm cm}^{-2} \text{ s}^{-1} \text{ cmHg}^{-1}$ were found at 30°C for the PEN alone.

Some of the materials cited have also been studied for hydrogen barrier materials. They are not only necessary to prevent leakage from storage tanks, but are also required for transport systems, such as pipelines, and hydrogen separation.

For pipeline applications, the report written by M. C. Kane [76] suggests the use of semi-crystalline thermoplastic polymers, such as polyethylene and polyphenylene sulfide (PPS). However, the selection of

the material is not only governed by the need for good barrier properties but also by a good resistance to the environmental conditions, such as sunlight, oxygen and humidity. As polyethylene meets all these requirements, the effect of its crystallinity ratio on hydrogen permeation was investigated in two distinct samples: a highly amorphous polyethylene, *i.e.* LDPE with 30vol% of crystallinity, and a highly crystalline polyethylene, *i.e.* HDPE with 90vol% of crystallinity, both of them at 20°C. The solubility and permeation coefficients were calculated, as well as the flux which they attributed to the leakage rate, *i.e.* the amount of hydrogen lost under typical service conditions. These conditions are a thickness of 0.525 cm, a surface area of 3173 cm² and a pressure difference of $p_0 - p_1$ where $p_0 = 1.03 \times 10^7$ Pa and $p_1 = 9.97 \times 10^4$ Pa. The main results are given in Table 1.7:

Table 1.7 Hydrogen permeability coefficients and fluxes through a LDPE with a low-crystallinity and a HDPE with a high crystallinity [76].

Parameters	Low crystallinity	High crystallinity
Permeability coefficient - cm ³ cm cm ⁻² Pa ⁻¹ s ⁻¹	29.4×10 ⁻¹⁴	4.20×10 ⁻¹⁴
Flux of H ₂ through the pipe walls - cm ³ s ⁻¹ m ⁻¹ (upper values) and mol s ⁻¹ m ⁻¹ (lower values)	0.018	0.003
	8.09×10 ⁻⁷	1.16×10 ⁻⁷

In agreement with the results shown before, the flux of hydrogen through the material is divided by a factor of six when the crystallinity ratio increases from 30% to 90%. Increasing the crystallinity seems therefore a good approach to enhance the barriers properties of PE. A similar behaviour is expected for PPS [76].

In 2007, Acharya *et al.* [87] studied the permeability of H₂ and CO₂ through polymer blends of polysulphone (PSF) and polycarbonate (PC). Due to their common ring structure, PC alters the free volume of PSF, which promotes a relatively fast permeation. Therefore, different ratios were tested and permeation measurements were carried out for both gases (Figure 1.34).

S. no.	Sample (PSF + PC) (in barrer)	P (H ₂)	P (CO ₂) (in barrer)	P (H ₂)/ P (CO ₂)
1	100	13.45	5.33	2.52
2	90% + 10%	19.15	11.44	1.67
3	75% + 25%	21.45	13.20	1.62
4	50% + 50%	25.11	21.45	1.17

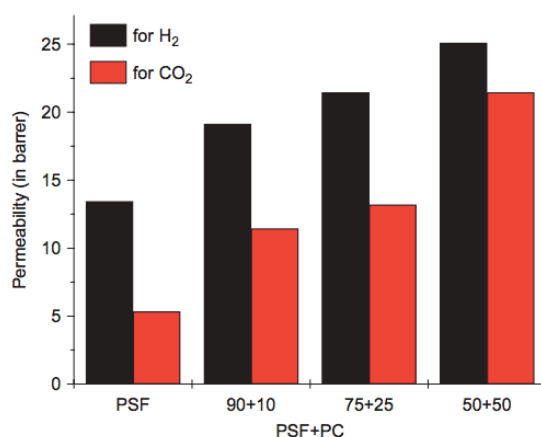


Figure 1.34 Hydrogen and carbon dioxide permeabilities data for various PSF and PC polymers blends [87].

The permeability of both gases increases as the content of PC increases. This can be explained by the increase of the free volume. Consequently, at higher concentrations of PC, the layer allows both gases to pass more freely but, as hydrogen is smaller than carbon dioxide, this leads for a 50/50 PSF/PC ratio to a permeability coefficient of 25.11 barrer for H₂ compared to 21.45 barrer for CO₂. This also results in a minimal H₂/CO₂ permselectivity of 1.17 for this equimolar ratio [87]. Since this material was investigated for gas separation applications, the fact that the hydrogen permeability is higher than that of CO₂ is here an advantage. However, this shows clearly that, what can be good for gas separations involving hydrogen, is not always suitable for barrier applications.

Materials more specific to hydrogen storage tanks have also been developed and a commonly studied component is graphene. Indeed, graphene or graphene oxide display very good properties when associated in different structures with polymers, such as excellent mechanical resistances, electrical conductivities and impermeabilities to various gases and/or liquids [88-97]. In 2014, Layek *et al.* [98] published a study about layer-structured graphene oxide (GO)/polyvinyl alcohol (PVA) nanocomposite-coated PET films for hydrogen gas barrier properties. However, producing graphene is difficult and samples with too many defects are obtained. The same authors proposed to use reduced graphene oxide (rGO) instead of graphene and suggested that a stacked multi-layered GO/PVA nanocomposite-coated PET had better barrier properties. As proof, they measured the hydrogen permeation of several samples:

- PET uncoated.
- PET coated only with PVA (named P3) or GO (named G3).
- PET coated with various ratios of GO/PVA (named PG3, PG6 and PG9, where the number correspond to the volume of the solution).

The results were reported in the form of hydrogen gas transmission rates (GTR) and permeability coefficients (Figure 1.35).

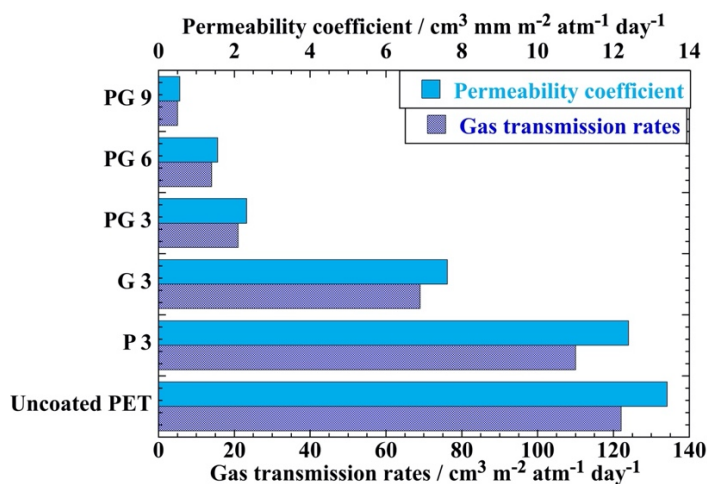


Figure 1.35 H_2 transmission rates and permeability coefficients of uncoated PET and PET coated with 3 ml of PVA solution (P3), 3 ml of a GO solution (G3) as well as 3 ml, 6 ml and 9 ml of a mixture of GO/PVA solution (PG3, PG6 and PG9) [98].

For uncoated PET, the hydrogen gas transmission rate is $122 \text{ cm}^3 \text{ m}^{-2} \text{ atm}^{-1} \text{ day}^{-1}$. Coating with a solution of either GO or PVA alone decreases the GTR and this is even better with the mixture and with an increase in the quantity of solution. Similar observations hold for the permeability coefficient. It was deduced that this is probably due firstly to a better attachment of the layer-structured GO/PVA nanocomposite on the PET surface compared to the layer-structured GO only and secondly, to the brick wall structure of the GO/PVA nanocomposite systems. As schematised in Figure 1.36, this system can be seen as a wall where the GO will act as a brick, whereas the crosslinker PVA acts as the mortar.

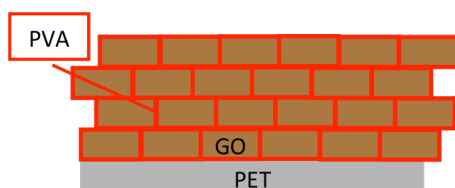


Figure 1.36 Schematic representation of the structure of a PET coated with a GO/PVA nanocomposite [98].

Another study about graphene oxide by Li *et al.* [99] focused on a modified graphene oxide(mGO)/polyethyleneimine (PEI) film for use as a hydrogen barrier. The GO was modified by ethylene glycol diglycidyl ether (EDGE) in order to introduce new groups at its surface, which then reacted with PEI to form covalent bonds and obtain a mGO/PEI film. Modifying the functionalization time, pH and feed ratios were found to affect the composition of the functional groups introduced on the GO surface. This in turn affected the hydrogen barrier properties of the films. To understand why, the hydrogen transmission rate was measured of a PET film both used as a comparison and a substrate for the mGO/PEI film (Figure 1.37).

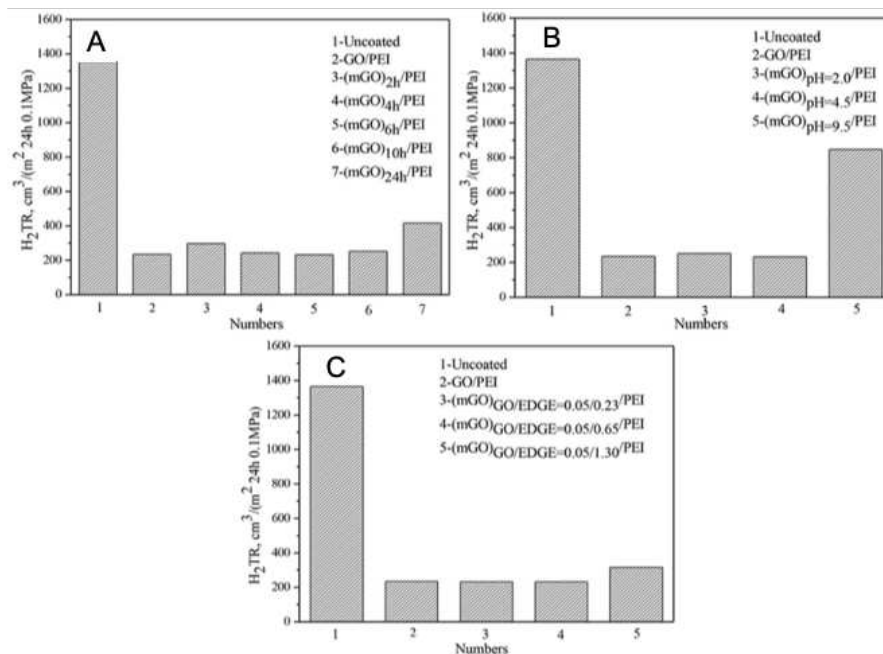


Figure 1.37 Hydrogen transmission rate (H₂TR) of a mGO/PEI film with GO modified under different conditions: different functionalization times (A), different pH values (B) and using EDGE with different feed ratios (C) [99].

The H₂TR is much lower for any modified GO/PEI than for the PET substrate alone. Concerning the different preparation conditions:

- For the functionalization time, 6 h gives the lowest H_2TR with $232 \text{ cm}^3 \text{ m}^{-2} 24 \text{ h}^{-1} 0.1 \text{ MPa}^{-1} = 232 \text{ cm}^3 \text{ m}^{-2} \text{ day}^{-1} \text{ bar}^{-1}$.
- When the pH is acid (pH = 2 and pH = 4.5), the barrier properties are better than in an alkaline environment (pH = 9.5).
- When EDGE is in excess (0.65 or 1.30) the H_2TR is higher than for a ration of GO/EDGE = 0.05:0.23.

In addition to their good hydrogen barrier properties, the mGO/PEI films have better acid, alkali and salt resistances compared to unmodified GO [99].

More recently, Seo *et al.* [100] also used GO to prepare a nanocomposite with MXene (an inorganic compound based on a transition metal, here Ti_3AlC_2) as a nanofiller and poly(ethylene-co-acrylic acid) (EAA) as a resin in order to coat a nylon 6 substrate and attempt to enhance its H_2 barrier properties. With a low permeability coefficient of $0.03 \text{ cm}^3 \text{ mm m}^{-2} \text{ day}^{-1} \text{ atm}^{-1}$, this inorganic-organic hybrid material showed an improvement of almost 90% compared to nylon 6 alone [100]. This example shows that nanofiller-polymer matrices are an effective way to improve the barrier properties. Indeed, if the tank liners are nowadays mostly based on HDPE, more and more PA-based polymers with fillers tend to be seen as a real asset for this application. In 2020, Sun *et al.* [79] studied PA6 filled with lamellar inorganic components (LIC), more precisely silicate nanofillers. The hydrogen permeability was tested under various temperature and pressure conditions and compared between LIC/PA6 and pure PA6: the lowest values at $-10^\circ\text{C}/50\text{MPa}$, were respectively, $1.1 \times 10^{-17} \text{ mol m}^{-1} \text{ s}^{-1} \text{ Pa}^{-1}$ for LIC/PA6 and $4.7 \times 10^{-17} \text{ mol m}^{-1} \text{ s}^{-1} \text{ Pa}^{-1}$ for PA6. This means that the hydrogen barrier property is improved by the introduction of LIC in PA6, and it is most likely due to an increase of the crossing path of the permeating molecules, as shown in Figure 1.38.

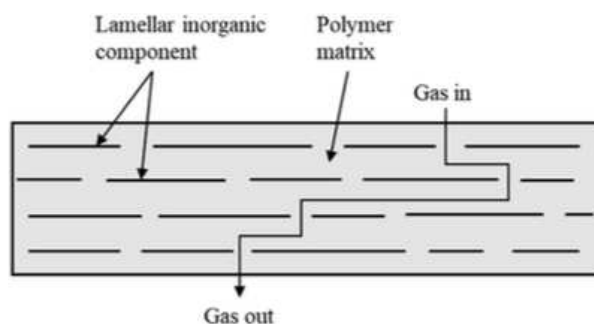


Figure 1.38 The barrier effect of lamellar inorganic filler components with respect to gas transmission [79].

In 2013, the Sandia National Laboratories published a report about polymer-based materials used in high-pressure hydrogen applications [101] and, Balasooriya *et al.* [80] updated this list in 2022. The most often used [101-104] are summarized in Table 1.8. Some of them have been quoted before.

Table 1.8 Typical materials used in high-pressure hydrogen infrastructures. The H_2 solubility coefficient (S_c), diffusion coefficient (D) and permeability coefficient (P_c) are also given for several polymers at room temperature and 1 atm.

Applications	Description	Common materials	Permeation properties		
Compressed hydrogen pressure vessels	Type III	Metallic liner/composite shell (glass fibres in epoxy resin)	PA	$P_c / 10^{-9} \text{ mol m}^{-1} \text{ s}^{-1} \text{ MPa}^{-1}$	0.14
	Type IV	HDPE or PA liner/composite shell (glass/carbon fibres in epoxy resin)	HDPE	$S_c / \text{mol m}^{-3} \text{ MPa}^{-1}$	4.3
Pipelines	High-pressure distribution (> 10 MPa)	HDPE or PA		$D / 10^{-10} \text{ m}^2 \text{ s}^{-1}$	1.9
Piping, tubing	Low-pressure distribution (< 10 MPa)	HDPE, PP, PVC and CPVC		$P_c / 10^{-9} \text{ mol m}^{-1} \text{ s}^{-1} \text{ MPa}^{-1}$	0.82
Mechanical compressors	Seals and coatings	PEEK and PTFE composite	PTFE	$P_c / 10^{-9} \text{ mol m}^{-1} \text{ s}^{-1} \text{ MPa}^{-1}$	3.2
Dispensing hoses		Nitrile rubber, FKM and PC	PP	$P_c / 10^{-9} \text{ mol m}^{-1} \text{ s}^{-1} \text{ MPa}^{-1}$	3.1
Flange connectors (low pressure)	O-rings, gaskets	Nitrile rubber, FKM, PTFE	FKM	$S_c / \text{mol m}^{-3} \text{ MPa}^{-1}$	19
				$D / 10^{-10} \text{ m}^2 \text{ s}^{-1}$	1.9
				$P_c / 10^{-9} \text{ mol m}^{-1} \text{ s}^{-1} \text{ MPa}^{-1}$	3.4
Threaded connectors (high pressure)	O-rings	Nitrile rubber, FKM	PEEK	$S_c / \text{mol m}^{-3} \text{ MPa}^{-1}$	20
Valves	Pistons	PEEK		$D / 10^{-10} \text{ m}^2 \text{ s}^{-1}$	0.3
	O-rings, fitting, etc.	Nitrile rubber, FKM, PTFE	$P_c / 10^{-9} \text{ mol m}^{-1} \text{ s}^{-1} \text{ MPa}^{-1}$	0.61	
	Seals and gaskets	Nitrile rubber, FKM, PTFE, EPM, fluorosilicone, silicone, Neoprene, PA, PEEK	Neoprene	$S_c / \text{mol m}^{-3} \text{ MPa}^{-1}$	10
				$D / 10^{-10} \text{ m}^2 \text{ s}^{-1}$	9.3
Valve seats	PA, PTFE, PCTFE, PI	PCTFE	$P_c / 10^{-9} \text{ mol m}^{-1} \text{ s}^{-1} \text{ MPa}^{-1}$	9.2	
				$P_c / 10^{-9} \text{ mol m}^{-1} \text{ s}^{-1} \text{ MPa}^{-1}$	0.31

Most materials are often the same polymer, whatever the application. However, if the examples given were for only one polymer layer on the liner, some innovative multi-layer films have also been investigated over the last decades.

An active electrochemical tri-layer barrier has been proposed by Lessing *et al.* [105, 106]. It can be applied to the polymer liner and is based on almost the same principle as the proton-exchange membrane (PEM) fuel cells. It is constituted of a cathode, a dense electrolyte and a polymer anode as shown in Figure 1.39. It uses an electrochemical reaction to block any hydrogen that diffuses out of the storage tank.

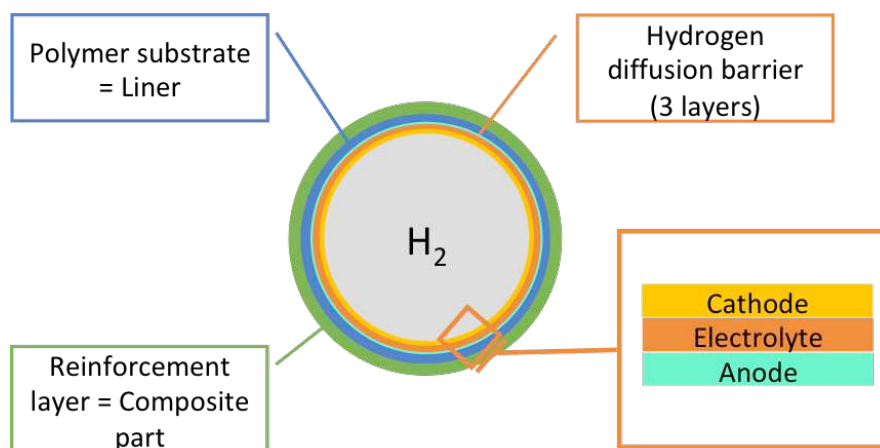


Figure 1.39 Cross-sectional representation of a cylindrical gaseous storage tank with an active hydrogen barrier consisting of a three-layer assembly of a cathode, electrolyte and anode [105, 106].

The total thickness of the active layer is between 6 and 75 μm and the two electrode layers can be formed of polyaniline, polypyrrole (PPy) or blends of PA/PPy. Its principle is:

- When the storage tank is pressurized, H_2 diffuses into the cathode layer and reaches the cathode/electrolyte interface.
- The electrolyte being quite impermeable to H_2 , a majority of H_2 stays at this point or goes back into the storage tank.
- A small proportion of gas passes through the electrolyte and reaches the anode layer where it is converted into H^+ and e^- . Both are sent back inwards, the first via the proton-permeable electrolyte layer and the second via an external circuit.
- Once contacting the cathode, the electrons combine with the protons to reform hydrogen which returns to the tank.

Although still under study, this elaborated active barrier already shows a significant reduction in permeation as Figure 1.40 demonstrates. Due to its electrochemical principle, a small electrical current can

be applied to improve its performance and during the test, the layer was spin-coated on a polymer substrate whose nature is not specified.

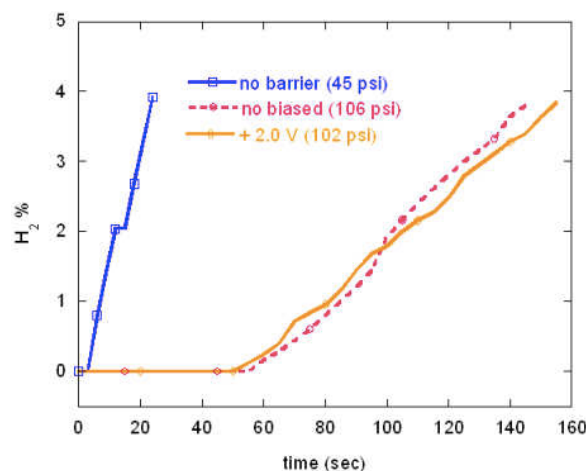


Figure 1.40 H₂ permeability tests of an innovative three-layer assembly of a cathode, electrolyte and anode coated on a polymer substrate. The measurements were done on three different samples: without the layer (“no barrier”), with the layer and without current (“no biased”) and with the layer plus a small current (“+2.0V”) [107].

However, polymers are not the only class of materials that can be involved in gas storage. Indeed, glass is also an exceptionally efficient barrier against hydrogen. Storing hydrogen in hollow glass microspheres and glass capillary arrays was reported in 2007 [108]. The process of encapsulation, *i.e.* trapped H₂ in glass spheres, was first used (Table 1.9) and then, the researchers considered glass capillary arrays. Two structures were tested: a bundle of cylindric capillaries packed in a 2D hexagonal lattice (Figure 1.41.A) and an array of fused hexagonal capillaries, *i.e.* honeycomb structure (Figure 1.41.B).

Table 1.9 Encapsulation process of hydrogen in hollow glass microspheres.

Step 1	Step 2	Step 3	Step 4
<p>Hollow glass microspheres are placed at pressure P_1 in a hydrogen rich atmosphere and heated.</p>	<p>When the temperature is between 100°C and 400°C, hydrogen permeates into the hollow cores through the thin glass shells.</p>	<p>When the hydrogen partial pressure in the microspheres P_2 becomes close to the external pressure P_1, the system is cooled and the hydrogen remaining outside the microspheres is removed. As the permeation is lower at room temperature, the hydrogen within the microspheres is trapped.</p>	<p>Then, to extract this trapped H_2, the filled microspheres are placed in a low-pressure vessel and heated again.</p>

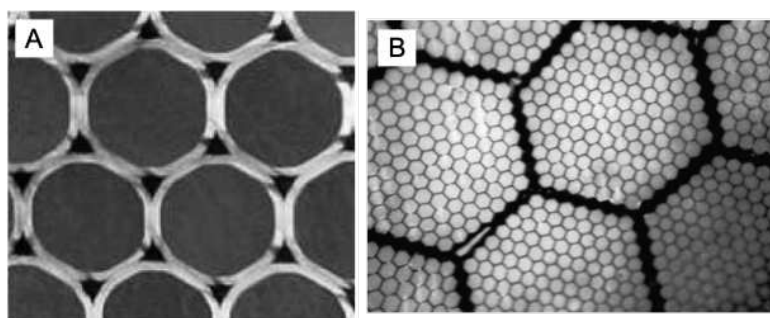


Figure 1.41 Cross-sections of two different capillary arrays: cylindric capillaries parked in hexagonal lattice (A) and honeycomb array of fused hexagonal capillaries (B) [108].

Although the H_2 permeabilities of these specific systems were not measured, it was shown that capillary arrays can be fabricated more easily than hollow microspheres and are very resistant to external pressure. The permeation of these glass capillaries arrays coated either with an epoxy resin or with a glass lacquer was measured in 2018 [109]. The first had better barrier properties than the second, with permeability coefficients of $370 \times 10^{-18} \text{ mol m}^{-1} \text{ Pa}^{-1} \text{ s}^{-1}$ and $930 \times 10^{-18} \text{ mol m}^{-1} \text{ Pa}^{-1} \text{ s}^{-1}$, respectively. In

addition, epoxy resins with two different degrees of cross-linking were tested and the results suggested that the higher the cross-linking, the lower the hydrogen permeability [109].

Glass storage systems demonstrate that the materials exploited in gaseous storage applications are not limited to the polymers or the original metallic layers, but other structures and components can also present good performances. Nevertheless, for mobile applications, certain considerations such as the weight or the refuelling time need to be taken into consideration [108, 109].

Figure 1.42 summarizes all the examples given in this Section. For each of them, the H₂ permeability coefficient given is always for the optimal case, *i.e.* when the different conditions, concentrations, and structures are optimal. For more fluidity, all the values have been converted to the same unit.

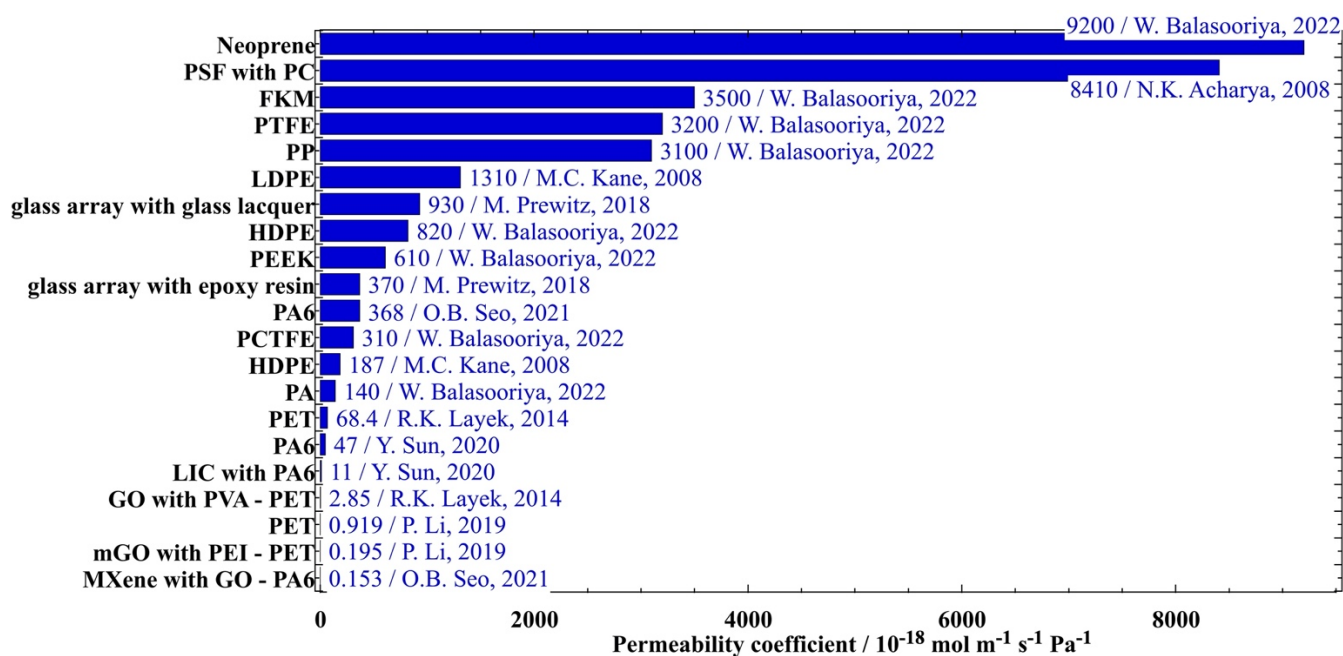


Figure 1.42 Examples of materials used or studied for hydrogen gaseous applications. Note that the temperatures, the pressures, the layer thicknesses and the measurement methods may be slightly different [76, 79, 80, 87, 98-100, 109].

Furthermore, before becoming a part of a tank or piping system, these materials need to be fabricated in the form of membranes or films and this step can affect the properties of the final product. It is therefore essential to make the most judicious choice amongst all the existing manufacturing techniques.

1) C. 2. Membrane manufacturing

A membrane is a thin layer of material. Consequently, its fabrication needs to combine good mechanical resistance and a suitable thickness, amongst other requirements. The fabrication techniques

depend on the material, on the shape of the membrane as well as on the final application [110]. In terms of shape, a film is flat most of the time, but it can also be a hollow fibre, as shown in Figure 1.43. This second shape does not correspond to the one needed in this project, thus the method of fabrication will not be discussed. However, more information can be found in Refs [111-113].

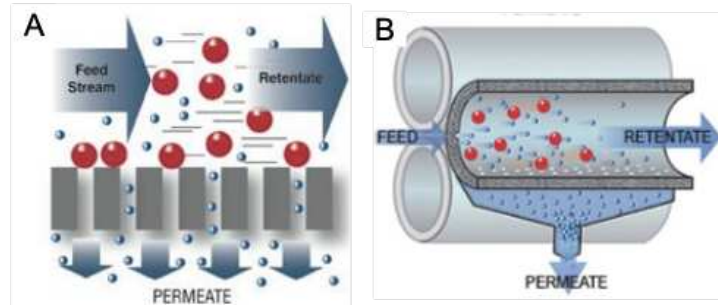


Figure 1.43 Visual comparison between flat and hollow fibre membranes [114].

Whatever their shape, the structure of polymeric membranes can be separated into several categories (Figure 1.44).

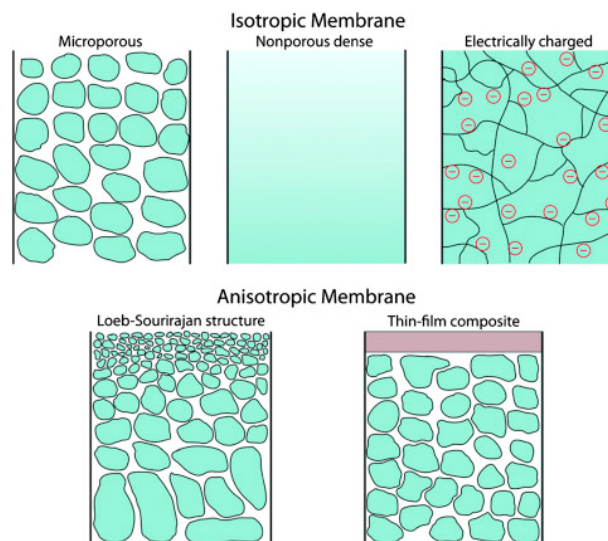


Figure 1.44 Different types of polymeric membranes structures [115-117].

Nowadays, there are 10 main techniques to manufacture thin films, and 8 of them can be separated into two different approaches called “top-down” and “bottom-up”, as displayed in Figure 1.45 [118]. The remaining two, as well as an additional novel method, are not classified in the same way and will be treated at the end of the Section.

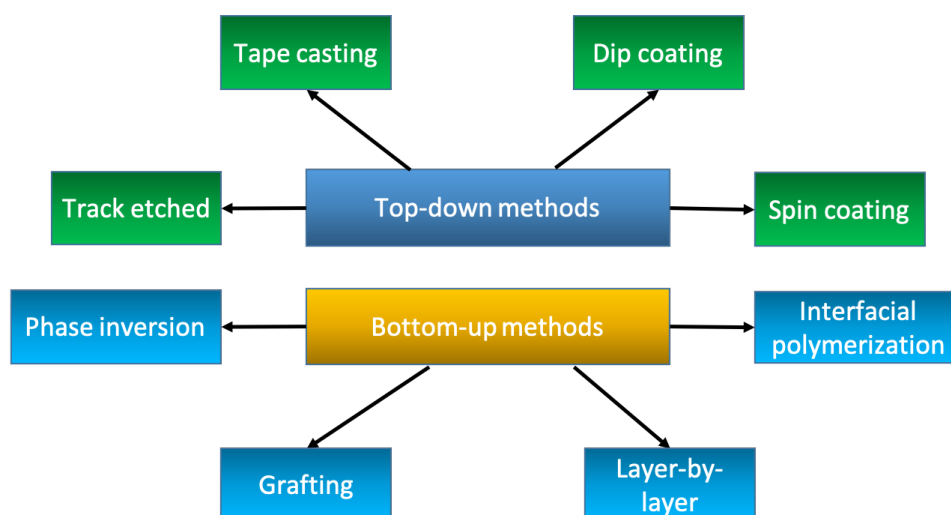


Figure 1.45 Membrane fabrication techniques classed as “top-down” or “bottom-up” approaches [116, 118-120].

The top-down approaches work at the macroscale level and use “external” parameters such as gravity, shaving or centrifugal force, in order to control the formation of the layer. The bottom-up techniques are more based on intrinsic interactions and therefore take place at microscale level, *i.e.* at the scale of the atoms, ions and molecules [118].

The top-down methods usually involve the coating of a polymer solution onto a substrate, followed by solvent evaporation to obtain the films. The substrate brings mechanical strength to the thin layer and is mainly porous. Amongst the most widely used materials for support, polyacrylonitrile (PAN), polysulfone (PS) and alumina can be cited. Porous substrates have the advantage of being easier to coat due to the penetration of the polymer solution inside the pores. However, they have the disadvantage of making it difficult to control the thickness, which must be able to avoid defects: thicknesses from 20 nm to 1000 nm can be obtained with this approach. Therefore, a pre-wetting is often required to reduce the solution penetration and most of the films obtained by these techniques are called “thin-film composite membranes” (TFCMs) [118].

The first “top-down” approach is the “track-etched” [120]. Although 60 years old, it is continuously improved and its basic principle is divided into two steps: tracking and etching (Figure 1.46).

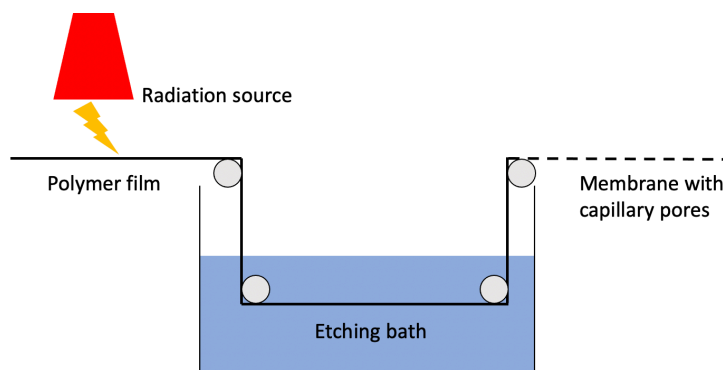


Figure 1.46 The track-etched method process [120].

During the first phase, a thin polymer film is exposed to high-energy particle radiations which affect its surface by breaking the polymer chains, leaving “tracks” which are then etched during the second phase in a chemical bath such as *e.g.* caustic soda. This converts them into clean and cylindrical pores. The pores size and density are controlled, either by modifying the speed of the film or the immersion time in the etching bath.

The second “top-down” approach is the “tape casting” or “doctor blade casting” method. Well-known for its use to manufacture ceramic substrates, it can also be applied for membrane production due to its relatively easy process (Figure 1.47) [118, 121].

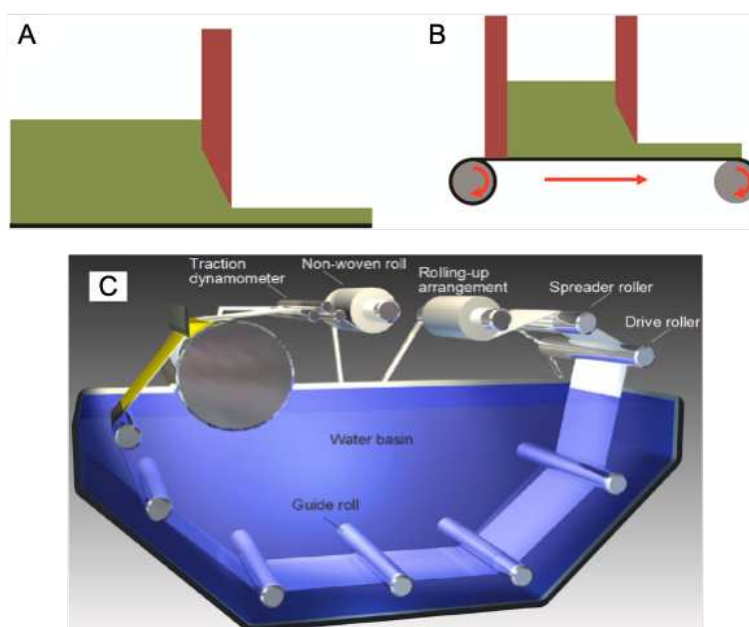


Figure 1.47 Doctor blade casting representation with the typical procedure (A), the continuous procedure (B) and the continuous apparatus (C). In A and B, the polymer solution is in green and the blade is in brown [118, 121].

The polymer solution is poured onto the substrate where a “doctor blade” slides along it in order to spread the solution, and the film is cast after solvent evaporation. When a coagulation bath, *e.g.* water, is inserted in the process, a precipitation occurs and a different kind of membrane structure can be obtained. The thickness is controlled by the gap between the blade and the substrate but also by process parameters such as the velocity, the composition and the viscosity of the solution as well as those related to the coagulation bath (temperature or concentration).

A very similar method to tape casting is spin coating, which is the third “top-down” approach. A polymer solution is poured onto a circular substrate which starts to spin in order to eject the excess solution through centrifugal force. The liquid layer becomes thinner and thinner until the desired thickness is achieved. When the solvent is evaporated, a thin and quite uniform polymeric film is produced with a thickness depending on the solution concentration and/or spinning rate. The viscosity of the initial solution is also an important parameter for a smooth running of the process. Figure 1.48 gives a representation of this technique.

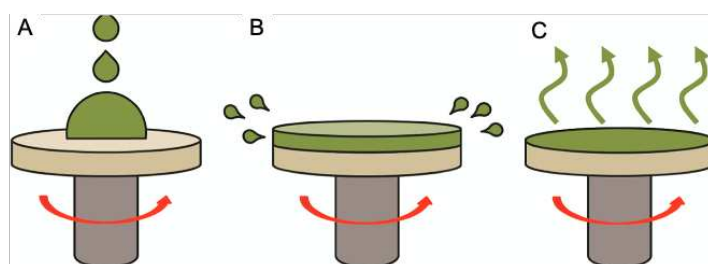


Figure 1.48 The spin coating procedure with the polymer being deposited on a substrate (A) which spins to form a uniform layer (B). The thin polymer film is then obtained after evaporation (C) [118].

The fourth and final “top-down” approach is the dip coating method, which is also similar to the two previous ones [118, 121]. In this case, the porous substrate is immersed into the polymer solution for a period of time, then removed, drained by gravitational forces and then, the solvent is evaporated. The polymer film remains coated on the surface of the substrate, as shown in Figure 1.49. The film formation is affected by the properties of the casting solution, such as the viscosity, the pH, the concentration, etc., the substrate itself, the speed of casting as well as the solvent evaporation rate.

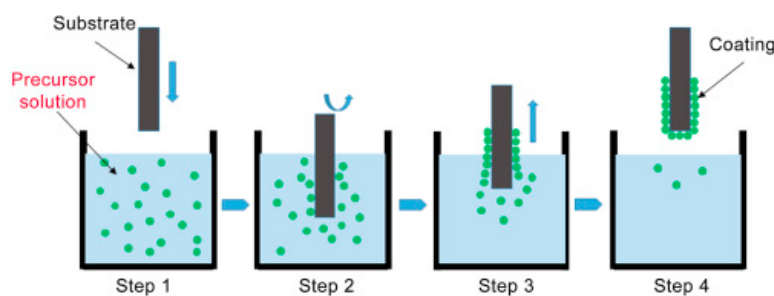


Figure 1.49 The dip-coating technique with the polymer solution being named “precursor solution” [122].

Compared to the “top-down” approach, the “bottom-up” category contains techniques allowing for a more diverse production in terms of types of films. Consequently, they have been more intensively studied over the last years and very recent methods have been developed.

The first “bottom-up” approach is the grafting method. Indeed, an effective way to form thin films *in-situ* is to chemically graft the polymer on the substrate. In that case, there are two possibilities: “grafting-from” and “grafting-to”. The “grafting-from” involves a surface-initiated polymerization process, *i.e.* the polymer chains grow *from* functional monomers present on the surface. In the “grafting-to”, a pre-synthesized polymer is connected *to* the treated surface via active sites, as shown in Figure 1.50.A and B [119, 123]. A thin-film formation technology which combines these two possibilities, was also developed in 2019 as shown in Figure 1.50.C [118].

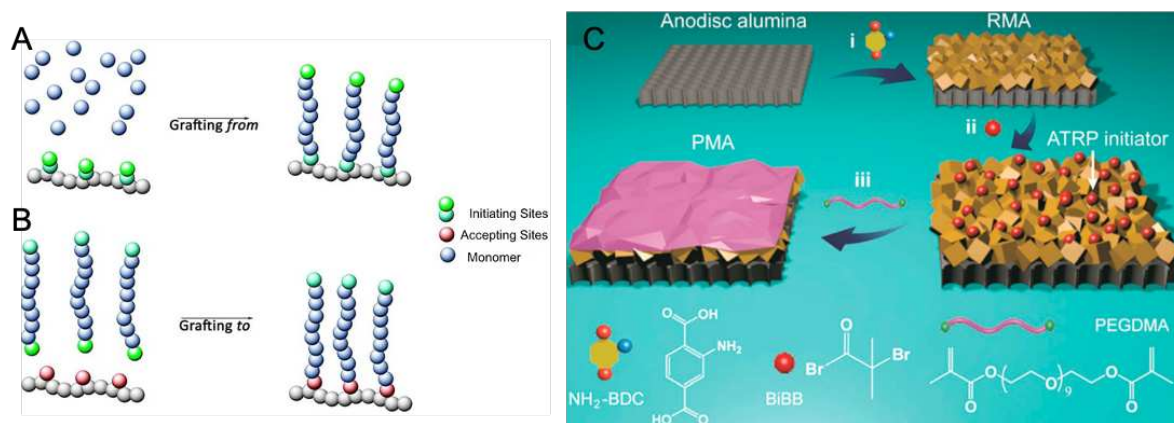


Figure 1.50 The grafting techniques with the “grafting-from” (A) and “grafting-to” (B) methods. Also shown is the fabrication of a polymer on a metal-organic framework (MOF) membrane (C). Step (i) is the coating of an anodisc alumina layer by a $\text{NH}_2\text{-BDC}$ solution. Step (ii) is the initiation of the grafting by atom-transfer radical-polymerization (ATRP). Step (iii) is a final grafting with macro-crosslinkers. RMA and PMA refer, respectively, to, RawMOF/anodisc and PolymerMOF/anodisc [118, 124].

Whatever the grafting method used, this is more considered as a “surface modification technique” rather than as a “fabrication technique”.

The second “bottom-up” approach is the “layer-by-layer” (LBL) or self-assembly technique [118, 119]. Under the influence of interaction forces such as electrostatic forces, hydrogen bonds and hydrophilic-hydrophobic properties, the film is spontaneously assembled as seen in Figure 1.51. Due to the variety of molecular interactions, many different materials can be formed by the LBL self-assembly technique. For example, polyelectrolyte multilayer membranes (PEMs) are often prepared via this method.

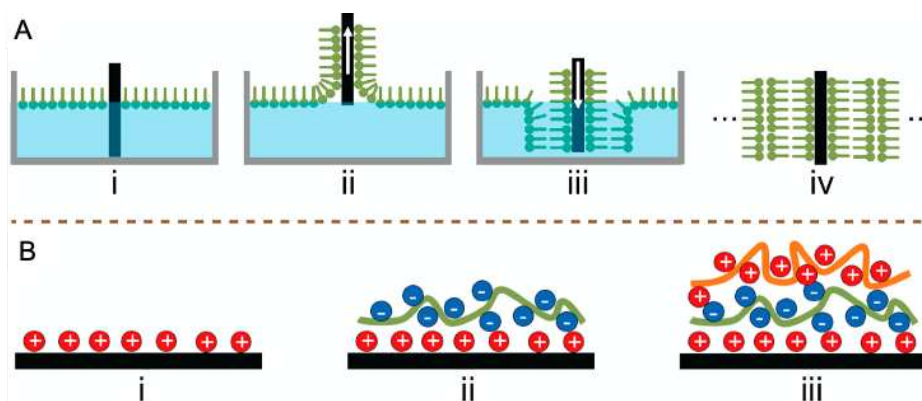


Figure 1.51 Formation of a typical Langmuir-Blodgett (LB) self-assembly films based on hydrophilic-hydrophobic properties (A) or on electrostatic forces with the formation of a polyelectrolyte multilayers (PEMs) (B) [118].

So, in the LB films formation (Figure 1.51.A), amphiphilic molecules with hydrophobic tails and hydrophilic heads form a monolayer at the air/liquid interface (step i), which is then transferred onto the solid substrate just by dipping it several times, *i.e.* a monolayer is added at each insertion/extraction (steps ii and iii). When the desired layer thickness is obtained, the substrate is completely removed from the solution (step iv). The formation by charged-surfaces (Figure 1.51.B) follows the same principle. A solid substrate with a charged surface (step i) is immersed into a solution containing ions with the opposite charge, which adsorb on the surface and reverse the charge sign (step ii). This newly created charge-surface is then exposed to another solution containing the opposite ions and another layer is adsorbed onto this substrate (step iii). A layer of opposite sign can again be added and so on, until the desired layer thickness is produced. With these self-assembly processes, the thickness of the film can be as low as $\sim 15\text{nm}$, which is thinner than for most of the other fabrication techniques. However, it is a laborious process and relatively time- and solution-consuming, which makes it difficult to transpose to large-scale production.

The third “bottom-up” approach, *i.e.* the phase inversion process is actually the main industrial way to produce membranes [117, 125, 126]. An initial homogeneous polymer solution is converted from a liquid to a solid state by changing its thermodynamic parameters such as the temperature, or by placing it in the presence of a non-solvent. Consequently, the polymer is no longer soluble, which induces a demixing into polymer-rich and polymer-poor phases. The film is formed in the polymer-rich phase and pores are created inside due to the polymer-poor phase. Four basic processes exist in phase inversion (Figure 1.52).

Non-solvent-induced phase separation (NIPS)	Thermally-induced phase separation (TIPS)	Precipitation from vapour phase	Precipitation by controlled evaporation
Most widely used. A polymer solution is cast on a substrate, submerged in a coagulation bath which is solvent-free. The solvent from the polymer solution leaves, demixing and precipitation takes place.	The polymer solution is prepared at high temperature, then a cooling of the system decreases the solvent quality. Heat transfer-induced demixing and phase separation occur. The solvent is continuously removed until reaching the desired membrane thickness.	The polymer solution is cast on a substrate or on another film, which is placed in a vapour atmosphere of a high concentration of the same solvent. Therefore, there is no solvent evaporation from the polymer solution into the atmosphere and the film is formed by diffusion of the non-solvent into the cast layer.	The polymer solution is a solvent dissolved in highly volatile nonsolvent mixture. Due to this volatility, the evaporation of the solvent occurs and causes the composition of the solution to have a higher non-solvent and polymer content. Then, the polymer precipitates and forms the film.

Figure 1.52 Basic processes of phase inversion techniques [125-127].

The first two processes, *i.e.* NIPS and TIPS, are the most widely-used. To illustrate the phase inversion principle, both are schematized in Figure 1.53.

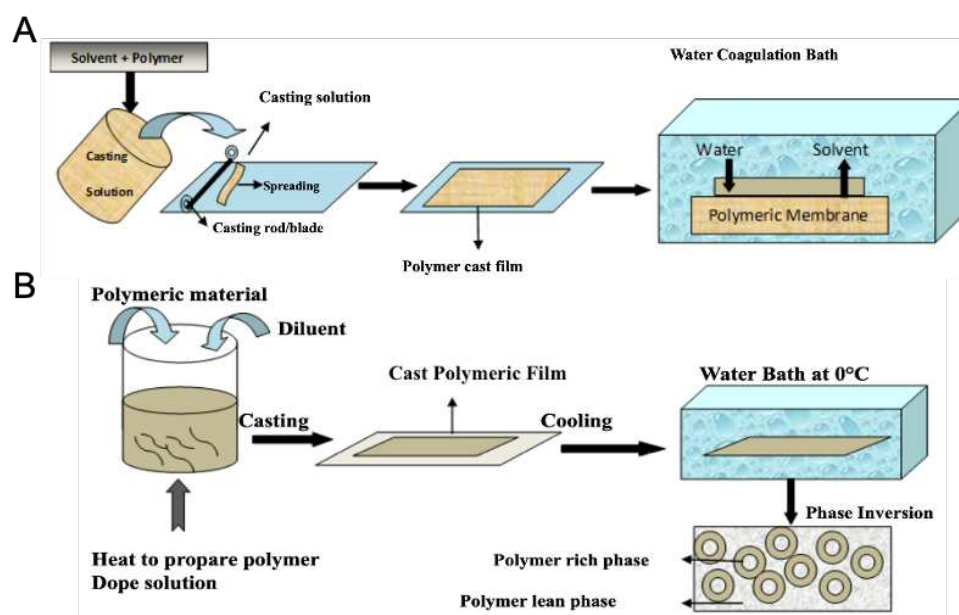


Figure 1.53 Illustration of the non-solvent-induced phase separation (A) and thermally-induced phase separation (B) technique [127].

The fourth “bottom-up” approach, *i.e.* the interfacial polymerization technique is the subject of this project. It will thus be detailed in the next Chapters.

Some techniques cannot really be categorized as “top-down” or “bottom-up” approaches. These include sintering, extrusion plus stretching and 3D printing. All of them have the advantage of being solvent-free compared to the previous ones. Sintering [117, 120] is a physical process mostly used for materials available in powder form such as minerals or poorly soluble polymers (Figure 1.54). It starts by compressing the powder to have particles of graded size, and when the temperature is increased, the interface between these particles disappears to produce a porous structure. The pore size depends on the initial particle sizes and distribution: the lowest value that can be obtained is 0.1 μm .

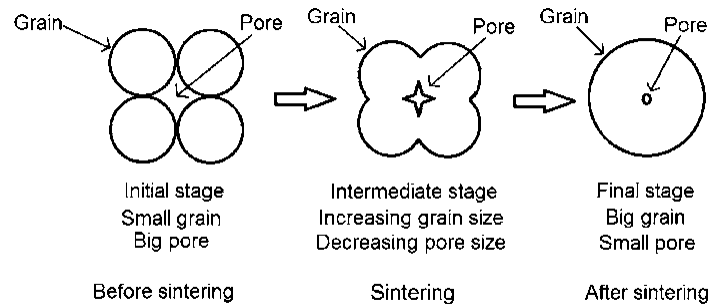


Figure 1.54 The sintering process [128].

The extrusion plus stretching is also a physical process, adapted mostly to semi-crystalline polymers [117, 125]. The polymer is heated above its melting point, extruded into thin sheets where the crystalline regions are oriented. These sheets are then stretched in a transverse direction, which stretches the amorphous regions to obtain a porous structure. As for any extrusion process, the polymer properties, *i.e.* its crystallinity, its melting point, its tensile strength, etc. have to be taken into account to control the properties of the final films. Figure 1.55 provides a representation of this technique.

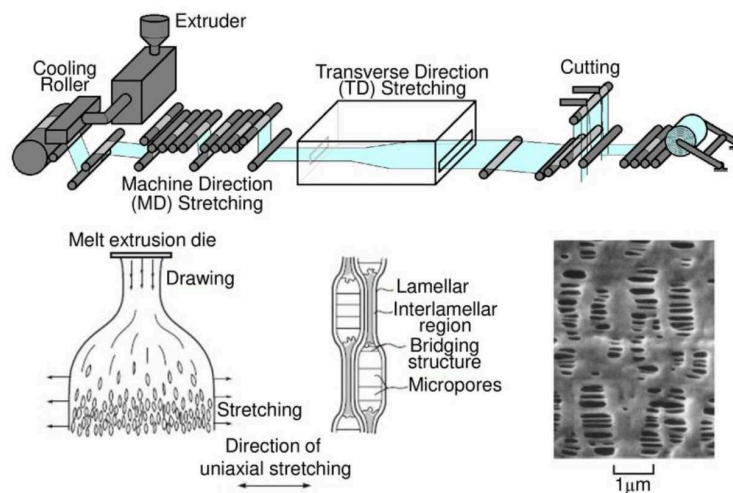


Figure 1.55 Extrusion and stretching process of a semi-crystalline polymer [129].

Finally, a study published in 2017 suggested that 3D printing, also called additive manufacturing (AM), can be used to fabricate thin films [130]. There are several existing AM methods but photopolymerization (Figure 1.56) is the most popular. It is separated into four processes.

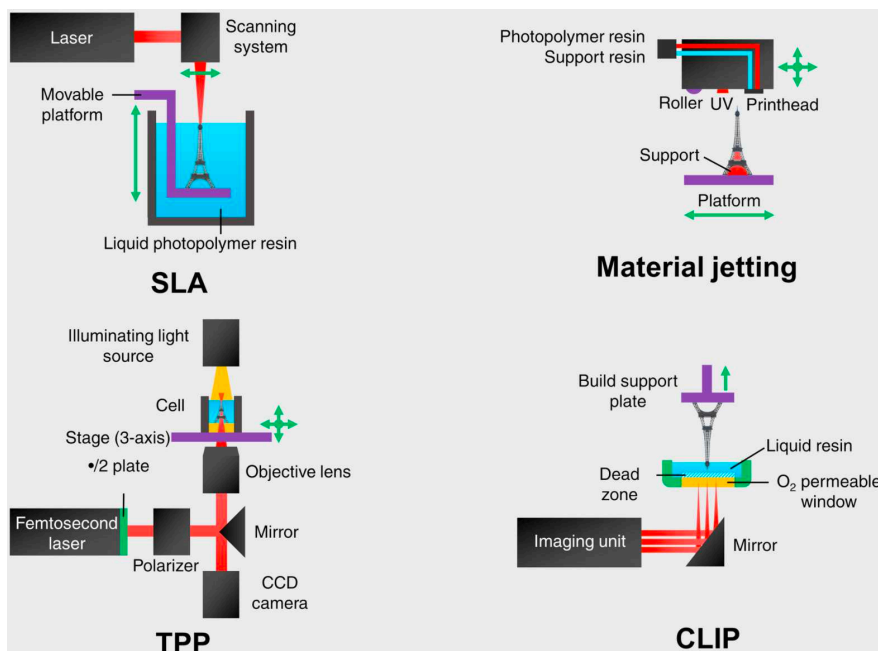


Figure 1.56 The different AM techniques of photopolymerization, where SLA stands for “stereolithography”, TPP for “two-photon polymerization” and CLIP for “continuous liquid interface production” [130].

This approach sounds very interesting because it allows the production of films of different shapes, types and designs, unlike more “conventional” techniques. However, 3D printing is very complex and needs more research to be applied at an industrial scale

The variety of membranes leads to a large range of fabrication techniques. The choice of the right process has to take into account the final application, the properties wanted and the material used. To obtain a highly cross-linked thin film with potentially good H₂ barrier properties, interfacial polymerization (IP) which, as noted above is part of the “bottom-up” approach, is a wise choice. Its process, parameters, advantages and disadvantages will be described in-depth in the following part of this manuscript.

1) D. Abbreviations list

➤ AM	Additive manufacturing
➤ BIF	Barrier improvement factor
➤ CEA	Commissariat à l'énergie atomique et aux énergies alternatives
➤ CFRP	Carbon Fibre Reinforced Plastic
➤ COPV	Composite Overwrapped Pressure Vessels
➤ CPVC	Chlorinated poly(vinylchloride)
➤ CR	Neoprene
➤ DOE	Department of Energy
➤ EAA	Poly(ethylene-co-acrylic acid)
➤ EDGE	Ethylene glycol diglycidyl ether
➤ EPM	Ethylene propylene copolymer
➤ FKM	Fluoroelastomer
➤ FCEVs	Fuel cell electric vehicles
➤ GFRP	Glass Fibre Reinforced Plastic
➤ GHG	Greenhouse gases
➤ GO	Graphene oxide
➤ GRT	Gas transmission rates
➤ HDPE	High density polyethylene
➤ HE	Hydrogen embrittlement
➤ HGM	Hollow-glass microspheres
➤ HMDSO	Hexamethyldisiloxane
➤ IPCC	Intergovernmental Panel on Climate Change
➤ LB	Langmuir-Blodgett
➤ LBL	Layer-by-layer
➤ LIC	Lamellar inorganic components
➤ MOF	Metal-organic frameworks
➤ NIPS	Non-solvent-induced phase separation
➤ PA	Polyamide
➤ PAN	Polyacrylonitrile
➤ PBT	Polybutylene terephthalate
➤ PC	Polycarbonate

➤ PCTFE	Polychlorotrifluoroethylene
➤ PEI	Polyethyleneimine
➤ PET	Polyethylene terephthalate
➤ PEEK	Polyetherketoneketone
➤ PEM	Proton-exchange membrane
➤ PEMs	Polyelectrolyte multilayers
➤ PEN	Polyethylene naphthalate
➤ PI	Polyimide
➤ PP	Polypropylene
➤ PPS	Polyphenylene sulfide
➤ PPy	Polypyrrole
➤ PS	Polysulfone
➤ PSA	Pressure swing adsorption
➤ PSF	Polysulphone
➤ PTFE	Polytetrafluoroethylene
➤ PTMO	Polytetramethylene oxide
➤ PVA	Polyvinyl alcohol
➤ PVC	Poly(vinylchloride)
➤ PVDF	Polyvinildine fluoride
➤ RE	Renewable energies
➤ rGO	Reduced graphene oxide
➤ SiO _x	Silicon oxide
➤ sccm	Standard cubic centimetres per minute
➤ STP	Standard temperature and pressure
➤ TFCMs	Thin-film composite membranes
➤ TIPS	Thermal induced phase separation

Chapter 2 : Background and Theory

2) A. Interfacial polymerization

Nowadays, producing a thin-film is no longer a major challenge in the membrane field. All the existing methods have their advantages and disadvantages but the interfacial polymerization (IP) is a suitable and well-known technique to synthesize such layers. Indeed, it is encountered in a large industrial-scale production of hollow nanospheres, nanofibres and highly cross-linked ultra-thin layers. Because of a wide range of usable monomers and a good flexibility in terms of surface topology, an impressive collection of polymers can be synthesized with easily-tailored properties [131-133]. It also allows for the preparation of defect-free, ultrathin films of metal organic frameworks, organic-inorganic hybrids and bio-hybrids [131]. Polymer films obtained by this method have been used for membrane applications, mostly nanofiltration (NF) and reverse osmosis (RO), and to a lesser extent for gas separations [134].

2) A. 1. Basic principles

First, as can easily be deduced from its name, one of IP must-have features is an interface obtained by the combination of two immiscible phases, which can be categorized into three groups: liquid/solid, liquid/gas, and liquid/liquid [135]. Second, the polymerization is a polycondensation reaction between two highly reactive monomers that are dissolved in those phases and the film is therefore created at the interface. It is most often created between two liquids (Figure 2.1) which, traditionally, were organic and aqueous. However, recent works have shown that non-aqueous interfacial polymerization is also possible, *e.g.* for the synthesis of microcapsules [136] or thin polymer films [133], which greatly extends the chemistry of the precursors.

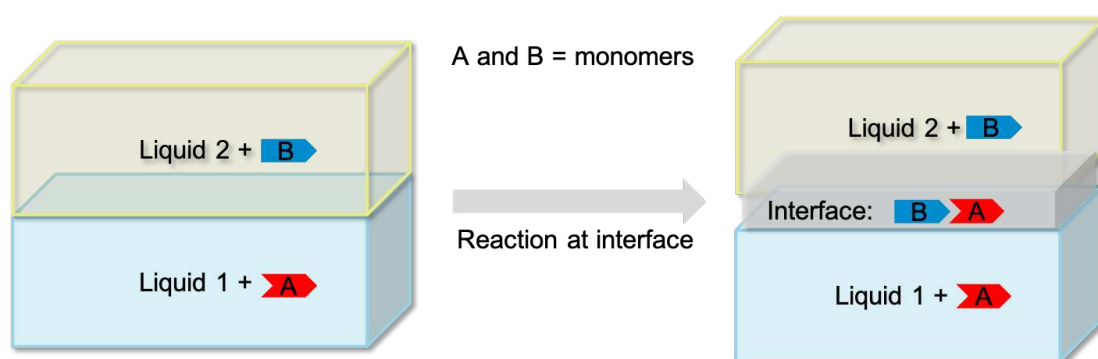


Figure 2.1 A schematic illustration of the polycondensation occurring at the interface between a solvent 1, containing the dissolved monomer A, and a solvent 2, containing the dissolved monomer B [131].

Before going into details about interfacial polymerization, it is useful to recall the basics of polycondensation reactions.

The process of polymerization can be divided into two categories: chain polymerization and step-polymerization. Polycondensation belongs to the second category. Even if both types of polymerizations lead to long chains, the presence or the absence of by-products is the main difference. Indeed, “polycondensation” is a chemical reaction for producing a polymer by linking single or multiple kinds of monomers to form high molecular-weight polymers, while releasing either water, a low carbon-number alcohol or other low molecular-weight molecules [137]. The polymers formed by this mechanism usually have two functional groups, whose functionality is defined as the number of covalent bonds that a monomer molecule or monomeric unit in a macromolecule or oligomer molecule can form with other reactants [138]. However, the by-products can have a concentration and mass that negatively affect the reaction mechanism. The remedy is to perform the reaction at a higher temperature and to maintain a high vacuum, which will effectively remove the by-products generated during the reaction, thereby favouring the production of higher molecular-weight polymers [139]. As an example, Figure 2.2 gives the global scheme of the polycondensation reaction to make nylon 66 [140].

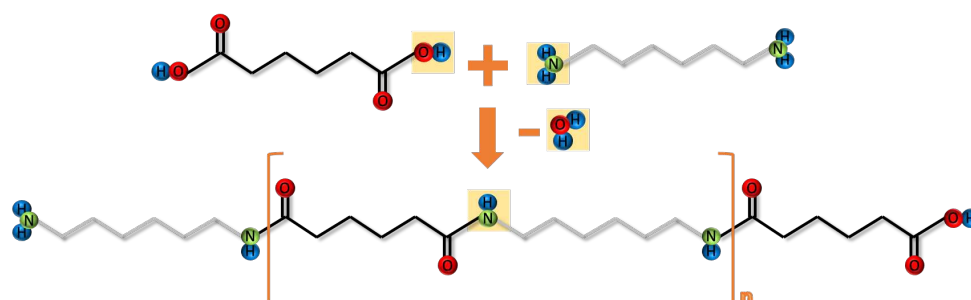


Figure 2.2 Polycondensation of the polyamide (nylon) 66 with hexamethylenediamine and adipic acid precursors [140].

An interfacial polymerization occurs with two monomer reactants and two immiscible solvents and generally results in a fast chain growth followed by the polymer precipitation at the liquid-liquid interface [131]. Indeed, it is the separation of the monomer precursors in each solvent phase that results in the localized reaction and the formation of the thin polymer. As it is confined to the interface, reactants will more likely encounter the growing polymer chain rather than the other monomers. Compared to bulk polymerization, higher molecular weights can be obtained under mild reaction conditions and the precipitation of the polymer at the interface might occur for a given molecular-weight range resulting in distinct polydispersities [141, 142]. The growth of the layer is controlled and determined mainly by the

diffusion of the monomers. Due to the localized interface, the monomer reactions take place within a reaction-diffusion boundary layer which separates the two phases. The more the network grows, the more the rate of polymerization slows down as it is limited by the diffusion of the monomers through this new layer. With time and increasing thickness, this acts more and more as a barrier until diffusion is no longer possible and the reaction stops. This behaviour can be named “self-limiting” [143].

The formation of polyhedral oligomeric silsesquioxane (POSS) covalently bonded with imides is a good example of what it is possible to do by IP [144]. Moreover, this polymerisation results in a novel organic-inorganic hybrid material. The following text and Figures explain this synthesis:

- 1) Preparation of the different monomers: for this reaction, the precursors are the POSS (Figure 2.3) and a selection of dianhydrides, amongst which the pyromellitic dianhydride (PMDA) and the hexafluoroisopropylidene diphthalic anhydride (6FDA) shown in Figure 2.4. Many others dianhydrides can be used but only these two will be discussed here.

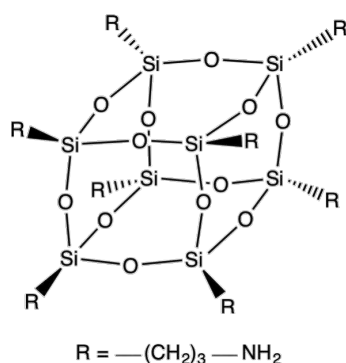


Figure 2.3 Chemical formula of octa(aminopropylsilsesquioxane) [144].

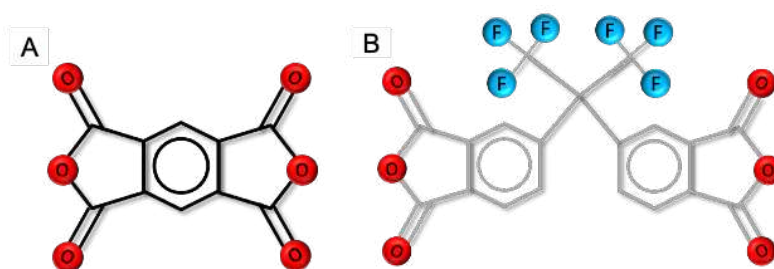


Figure 2.4 Chemical formulas of the PMDA (A) and 6FDA (B) dianhydrides [144].

- 2) Solubilization of the monomers: there are two different solvents and each reactant is dissolved in one of them. The POSS is dissolved in an aqueous solution whereas the dianhydride (here, the 6FDA) is dissolved in an organic phase (Figure 2.5). The POSS can be soluble in water due to its amine groups (corresponding to the R in the chemical formula) which are partly protonated.

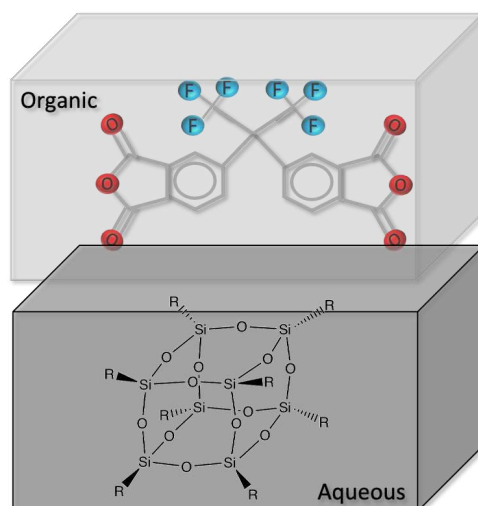


Figure 2.5 Schematic diagram of the different monomers dissolved in the immiscible solvents.

- 3) Polycondensation: At room temperature, the contact between both solutions leads to the reaction between a carbonyl group of 6FDA and the amine groups on the POSS. This reaction forms a polyPOSS-(amic acid) with bridges between the arms of the POSS and the dianhydride molecules (Figure 2.6).

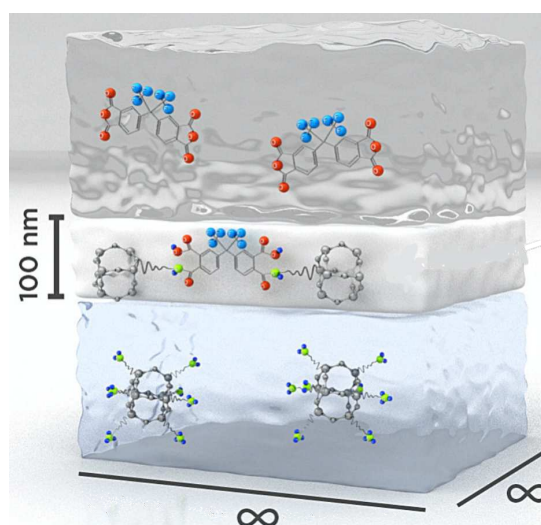


Figure 2.6 Interfacial polycondensation leading to a polyPOSS-(amic acid) network [144, 145].

- 4) Thermal imidization: at high temperature, another condensation reaction converts this acid into a polyimide with the formation of imide bridges (Figure 2.7). This step is a thermal treatment of 2 h at 300°C under an atmosphere of air.

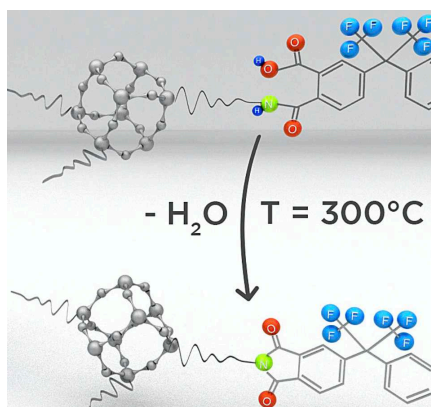


Figure 2.7 Thermal imidization leading to the polyPOSS-imide network [144, 145].

Over the entire process, residual reactants are washed off from the sample surfaces and the solvents are evaporated under dry nitrogen atmosphere. All these steps lead to the formation of a polyPOSS-imide film (Figure 2.8).

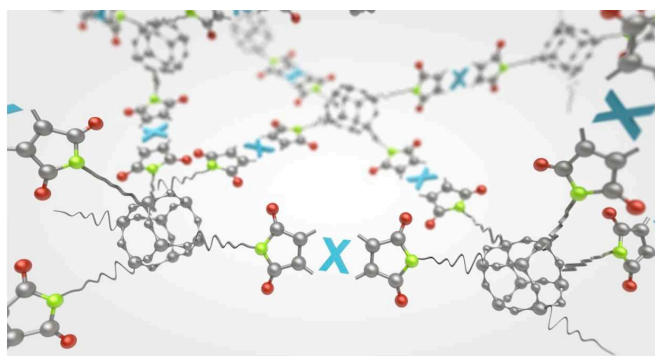


Figure 2.8 Poly(POSS-imide) network based on alternating POSS and imide groups [146].

The synthesis of the polyPOSS-imide film is one example of a “free-standing film” that can be accomplished with IP. As with other polymerization techniques, different polymers can be synthesized with this method, but a very interesting aspect is that they can have different forms. Indeed, it is also possible to make films “on top of a porous substrate” to, among other things, bring mechanical strength to the film [131]. Figure 2.9 shows a summary of the synthesis of a thin cyclomatrix polyphosphazene film on top of a polydimethylsiloxane (PDMS) slab [147].

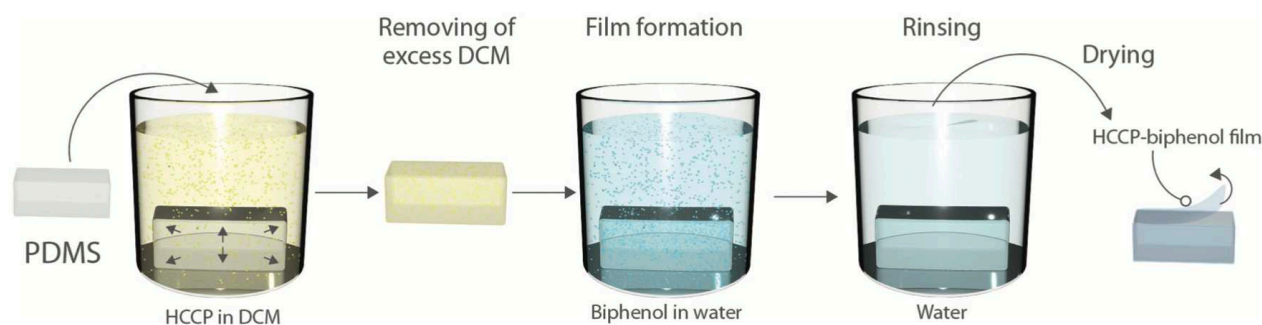


Figure 2.9 Preparation of hyper-cross-linked polyphosphazene films on the surface of PDMS slabs with hexachlorocyclotriphosphazene (HCCP) in dichloromethane (DCM) and biphenol in water as reactants [147].

This highlights another advantage of IP, *i.e.* the post-functionalization. Usually, the layer synthesized with this method has a gradient in its chemical composition, charge and number of residual groups as a function of the layer thickness. This number as well as the composition of the unreacted residual groups depend not only on the monomers used but also on their properties such as their size, their concentration, their diffusivity, etc. and on which monomer is supplied in excess. For example, in the polyPOSS-imide synthesis, the excess of amine groups on the POSS in the aqueous phase results in residual amine groups [148], while in the HCCP-biphenol film, the unreacted chloride groups can be used to post-functionalize the HCCP moiety [147]. However, nothing prevents both monomers from remaining with partially unreacted residual groups. Post-functionalization can be achieved using heat treatment, second exposure to one of the IP solutions or another chemical preparation [149, 150]. For example, if they have at least 2 reactive functionalities, the POSS silsesquioxane cages may be used to synthesize high molecular-weight linear polymers with silsesquioxanes directly incorporated along the chain backbone [151]. This step allows to improve the properties of the film without a modification of the polymerization process.

The performances and properties of the formed polymer can be tailored depending on a large number of parameters which will be briefly discussed in the next Section.

2) A. 2. Interfacial polymerization parameters

Although the IP is a useful and easy-to-use technique, there are a lot of different interconnected and sometimes sensitive parameters which can affect the film properties [143, 152-154]. Among those, the most interesting are often: the molecular weight and the polydispersity, the degree of branching or cross-linking, the thickness, the layer roughness, the density, the chemical composition and the residual group content, the mechanical strength as well as the final performance of the polymer, in particular, a gas barrier capacity

[155-158]. These properties depend to a great extent on the many parameters presented in Figure 2.10. This list is non-exhaustive but gives a good overview.

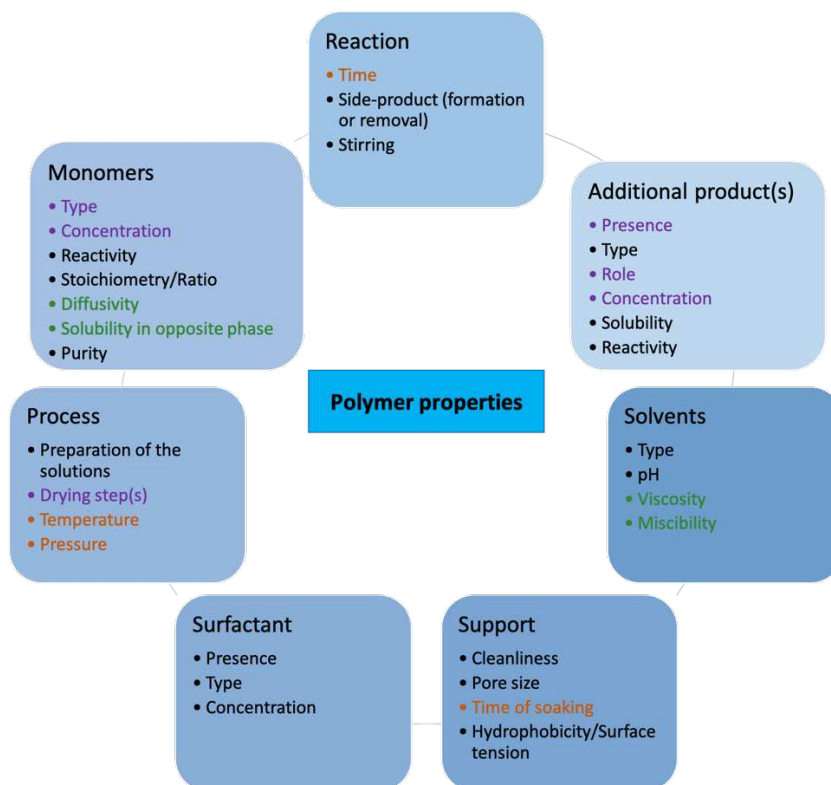


Figure 2.10 Main parameters of the interfacial polymerization that affect the film formation and its properties. They are categorized to take into account all that is involved in the reaction and the colours highlight a strong interdependency. For example, the green shows that the miscibility and viscosity of the solvent influence the diffusivity and solubility of the monomer in the opposite phase. Similarly, the reaction or soaking times are linked together as well as with the temperature and the pressure (orange).

Due to these many parameters, the fact that they overlap and that some of them cannot be controlled *in situ* (e.g. the purity of the monomers), the implementation of the IP can be very complex. For example, the pore size of the support as well as the time of soaking can impact the diffusion of the monomers on the support, which can in turn impact the thickness of the membrane or its homogeneity (creation of defects, polymer not continuous with a patchy distribution, etc.). However, certain trends and effects are already known and can help to carry out interfacial polymerizations.

2) A. 2. 1. Solvents

If the most important aspect about the solvents involved in IP is their immiscibility, this is not the only parameter that influences the final membrane. Indeed, the formation of the film first requires a liquid-

liquid interface which is as stable as possible and therefore it is obtained by using a pair of solvents that are not very miscible, such as a polar and a non-polar solvent. But the choice of the specific solvents affects the reaction as well. For example, the less viscous the solvent, the faster the monomers will diffuse [159, 160], which in turn affects the thickness, extent of cross-linking of the film and its performances [161]. For the polar liquid, the easiest and logical choice is water because of its abundance and high polarity as well as ecological and economic advantages. However, the use of a non-aqueous solvent such as DMSO can have interesting benefits which will be discussed later on.

Besides the choice of the solvents themselves, their interactions with each other also affect the behaviours of the monomers. For example, although the solvent combinations are chosen to be as immiscible as possible, small amounts of solvent can dissolve in the other phase [136]. This exchange at the interface can disturb the reaction zone and affect the diffusivity, reactivity and solubility of the monomer reactants in either phase. This is partly the reason why, when adding the solutions, the densest should be added first in order to avoid mixing as much as possible. Along with the problems related to immiscibilities, the quantities of the solvents are also a limitation of the technique. Indeed, a large amount of liquid means different steps of washing, purification, re-usage and sometimes heavy processes in terms of safety. Then, the incompatibility of the solvents implies that each of the reactants should be compatible with at least one of the phases and not or little with the other, which is not straightforward either [131]. Nevertheless, a substantial variety of chemistries is so far available for IP and the recent work about non-aqueous reactions extends even more the libraries of precursors [133].

2) A. 2. 2. Monomers

If an interface is essential, the monomers are just as important. They are selected based on their final application, *i.e.* the target polymer and its properties, but they can be limited due to the solvents used, even if the situation improves when the monomers belong to the same family [157]. For example, for the polyPOSS-imide film above, the length and flexibility of the imide bridge, represented by the symbol X in Figure 2.8, can be varied by using different dianhydride precursors during the first step.

Most of the time, the reaction involves di-, tri- or multi-functionalized monomers. As one of the solvents contains a nucleophile reactant, *e.g.* amines or alcohols, and the other contains an electrophile reactant, *e.g.* acid chlorides or isocyanates, the reaction is often a nucleophilic addition [146]. If two of the monomer functions react, this results in the formation of a linear polymer chain, whereas a branched polymer is obtained if more than two functions react. The network degree of branching or cross-linking depends mainly on the number, reactivity and local concentration of the functional groups. Indeed, unlike bulk polymerization, the stoichiometry of the monomers set for the interfacial polymerization reaction is

not necessarily in agreement with the final composition of the film. Therefore, this local behaviour, *i.e.* the reactivities, ratios and concentrations of the reactants *at the interface*, is very important and requires optimization before use. Naturally, this is related to the global characteristics of the monomers: size, diffusivities, solubilities in either phase, concentration and reactivity [131].

Some general trends about the influence of the monomer behaviours on the polymer properties are already known and can be applied whatever the combination of reactants used. The polymerization kinetics are mainly affected by reactivity: the more reactive a monomer, the faster the rate of film formation, *e.g.* it can occur in a matter of seconds or minutes. Inversely, the less reactive, the slower it will be, *e.g.* hours or even days [131]. This kinetic aspect is closely linked to the film thickness. In the case of a low reactivity and a slow polymer formation, thick films (up to several μm) can be produced. On the other hand, the thickness is also related to the diffusion of the monomers through the new layer which, when it is limited, decelerates the film growth and restricts the thickness to sub- μm range, *e.g.* a few tens of nanometres. However, although this rate of formation decreases as the film forms, the properties are not final and may still vary with longer reaction times because of the densification and network cross-linking [162]. To change this polymerization kinetics, the concentrations of the monomers can also be used: higher concentrations correspond to higher rates of polymerization. Nevertheless, in practice, varying the concentrations is not always easy, feasible and sometimes even possible as an optimal concentration may be required for the good progress of the reaction. Moreover, a limit in accelerating the rate of film formation means that there is also a maximum concentration above which nothing changes [143].

Indubitably, the solubility of reactants also affect the structure of the polymer and, therefore, its performance. For example, monomers with high reactivity and low solubility in the opposite phase are required to obtain a well-defined and dense film. Inversely, if the solubility is too high, the layer formed can be corrugated [161]. In addition to solubility, the diffusion in the other solution affects the thickness and rigidity of the polymer network and depends on the size and flexibility of the monomers. Consequently, when large and rigid molecules are involved in the reaction, the mass transport limitations of these molecules are more pronounced due to film formation, and thinner and less flexible polymer networks are obtained [148, 163, 164]. Moreover, the diffusion of the monomers along the area of the film formation allows for continued polymer growth and usually, inherently ultrathin defect-free layers are synthesized with potentially unlimited lateral dimensions.

These relatively low thicknesses and defect-free properties are two of the main attractive aspects of interfacial polymerization.

2) A. 2. 3. Experimental conditions

The main conditions applied are the temperature and the reaction time. The effect of the former on the course of the reaction was investigated [160, 165, 166]. If IP is generally performed at ambient temperature, it is conceivable to set a different temperature to one or both phases. For example, if the temperature of the organic phase is increased in an aqueous IP, this improves the diffusion of monomers to the opposite phase. In turn, this impacts the interface and therefore changes the morphology of the film and its cross-linking degree, which definitely affect its performances such as the permeability [160, 165, 166].

As noted before, the reaction time has much influence on the thickness of the layer as well as on its extent of branching. An increasing time means that these two properties are increased, but it eventually also slows down the growth of the film because the monomers can no longer pass through it. However, the material can still densify after this stage by progressive establishment of covalent bonds. The polymer properties are, therefore, not completely defined until the very end of the reaction [162, 167, 168]. Nevertheless, at some point, the thickening film will eventually always stop the reaction when the diffusion of monomers through the formed membrane is no longer possible.

The experimental conditions also include the incorporation of additives such as catalysts, surfactants or other additional products to adjust the pH. Among the common compounds used, an acid acceptor is often necessary to remove the acids formed as side-products during an interfacial polycondensation reaction [169, 170]. This removal of by-products can lead to the use of more complex assemblies with refrigerants and/or specific atmospheres, *e.g.* nitrogen/anhydrous. Indeed, similarly to other synthesis techniques, it is always better to remove the by-products in order to have larger yields. Furthermore, applying stirring to create more liquid-liquid interface leads to more product formation [146]. This also improves the homogeneity of the solutions and accordingly the solubility and diffusivity of the monomers. Another regular additive is a catalyst which, for example, in the case of aqueous IP, can enhance the transport of the reactants to the opposite phase and increase the cross-linking degree [147, 171-173]. Although the IP is most of the time carried out in a unique step, a preliminary phase to activate one or both of the monomers can be added, which also involves the use of additives such as a strong base.

Finally, the preparation of each solution and related steps of the process are part of the experimental conditions as well. Indeed, depending on the solvents, monomers and additives involved, this preparation can be more or less long, difficult and feasible and can add small steps which are necessary and potentially critical. This difficulty will be further discussed in this thesis.

2) A. 2. 4. Substrates

If the free-standing films prepared by IP have a good mechanical strength considering their thicknesses (sub- μm), it is unfortunately not sufficient for many applications. The parade is to use a film support, whose main function is to provide the mechanical properties that the thin film alone lacks. The properties of this support are thus very important to know.

For harsh conditions such as high temperatures and pressures, the layer is often prepared on top of a porous inorganic substrate. However, nowadays, porous polymeric supports are preferred because of their low cost and large range of processabilities [174]. They can have different forms and thicknesses, such as hollow fibres and flexible or rigid flat sheets. If this shape guides the course of the reaction, the other important features which influence the formation and performances of the film are the morphology of the support such as its porosity and pore size distribution, and its surface properties such as its roughness, chemistry and hydrophilicity [175-178].

A smooth substrate with small pores is the best choice to obtain a well-defined defect-free film. Indeed, in aqueous IP, the porosity and pore size distribution control the stability of the interface, how many monomers will be available and how they will diffuse to the reaction zone. A low porosity means less solution present, more difficulties to wet and a slower diffusion of the monomers. On the other hand, pores that are too large could lead to a too fast evaporation or a loss of solution, which will empty the pore and result in a no solution/no interface/no layer situation (or with lots of defects). The upper size limit for a pore to have a good interface is considered to be 100 nm [146]. This parameter can be tuned in to give the required properties of the layer. For example, it was proved that for PA films, reducing the pore size improves its rejections of salts and, therefore, its selectivity [179, 180]. When the reaction is a non-aqueous IP, the wetting or soaking of the substrate by an aqueous solution is obviously not achievable. Fortunately, it is also possible to use an organic phase but this goes hand-in-hand with a greater difficulty in maintaining a stable interface [131].

In the course of the IP reaction, the pores must be filled and this defines the “soaking time”. Long soaking times are associated to low pore sizes. However, the filling of the pores can impact several parameters such as the diffusion of the monomers on the substrate (which is different than the diffusion through the membrane or to the opposite phase) or the thickness, continuity and homogeneity of the layer. If the soaking time is too short, a patchy distribution of the monomers can occur and the spaces without reactants will not react to form the film, which will result in defects in the formed layer. On the other hand, depending on the type of solvent and the resistance of the support, an excessively long soaking time could damage the support [133, 146].

It is clear that the chemistry and the surface tension of the substrate influence how the film is connected to the support. In the case of aqueous IP, if the surface is hydrophilic, the layer will be well attached and not undergo delamination. Consequently, hydrophilic substrates are wetted more easily whereas hydrophobic supports could need a pre-wetting and the liquid might remain confined inside the pores [175-178]. For non-aqueous IP, the behaviour is the same even if the hydrophobicity is in this case defined by the surface tension: the higher the surface tension, the better the wetting and, therefore, a better connection of the film to the support.

To summarize the above overview, interfacial polymerization is an easy-to-use, large-scale and one of the main techniques to produce thin polymeric films with high cross-linking densities and impressive properties. The possibility to tune their performances is provided by the wide range of monomers that can be used and by many interconnected parameters which can be adjusted almost unlimitedly. Of course, an in-depth study of all these functionalities would be long and costly. A very interesting alternative is to mix experimental trials with molecular modelling in order to optimize some of the parameters and/or select the best candidate monomers.

2) B. Molecular modelling

The choice to combine two approaches such as experiments and molecular modelling, which are as different as they are complementary, may be surprising at first glance but it has already proven its effectiveness in the field of gas permeation in particular [181-183]. This Section introduces the basic notions and the related programs associated to molecular modelling.

2) B. 1. General principles

Molecular modelling allows to study the static and dynamic properties of different systems at the atomistic level. The most well-known computational technique on the atomic scale is molecular dynamics (MD) simulations, which has been developed since the appearance of computers. The first MD simulations of simple gases were performed in the late 1950s [184] and since then, this technique has become substantially more popular and visible in chemistry, physics or biology [184-186]. Computer experiments are, in many ways, similar to real laboratory experiments: they also involve sample preparation, validation steps and modification of the process parameters (temperature, pressure, concentration, etc.) [187]. These simulations are even more powerful as these conditions are precisely known and mostly controlled. Indeed, as the MD captures the position and motion of every atom in the system at any time, this allows to define for example, the initial conformation of the molecules or polymers, *i.e.* which atoms are bonded to which

other atoms, the concentration or density of each substance, which other molecules are present in its environment, the temperature, the pressure, etc. The corresponding experiments are difficult to set up in general, as they cannot be controlled as well, and this is even more the case with interfacial polymerization and its multiple parameters (Figure 2.10) [184].

The assumptions of classical mechanics, *i.e.* Newtonian mechanics, lie behind a classical MD simulation [188]. Applying this to a set of interacting points representing the atoms in the system, it is possible to predict how every one of them will move with time under the influence of forces originating from interatomic interactions [184]. Understanding the motion of the atoms will then allow the extraction of different static and dynamic properties, including transport properties, for the system under study. The Newton's laws of motion [188] are solved numerically for all the atoms in the system, and therefore, give their positions as a function of time, with each position allowing for the estimation of the next. This principle is detailed in the loop given in Figure 2.11. The integration algorithm leads to a trajectory describing the atomic-level configuration of the system at every point during the simulation time, and in turn, it gives the necessary information to extract the desired properties.

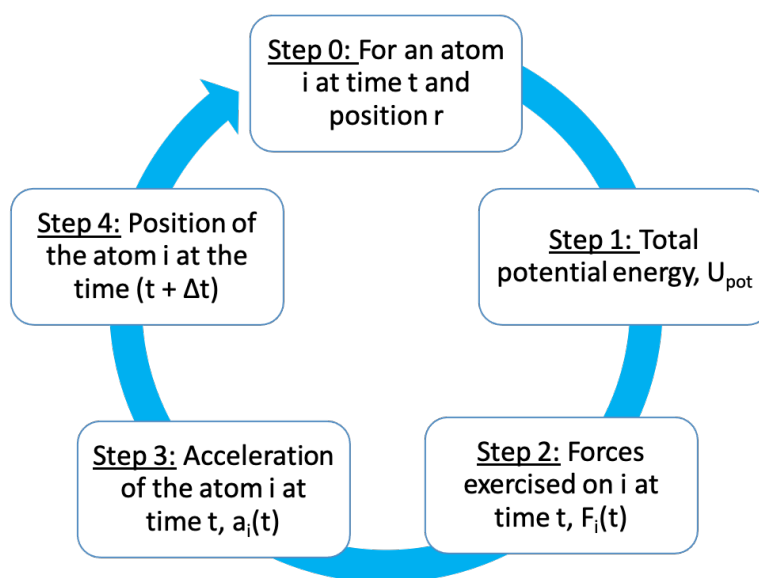


Figure 2.11 Process for the determination of each position of an atom i : MD integration algorithm [189].

At the beginning, before any motion, the atoms have initial vector positions r_i at time t (Step 0). Then, the total potential energy U_{pot} is calculated as a function of the force field chosen (Step 1, detailed later) and its derivative with respect to the vector position r_i (Eq. 2.(2.1) gives the vector force exercised on the atom i , $F_i(t)$ (Step 2):

$$F_i(t) = -\frac{\partial U_{pot}(r_i(t))}{\partial r_i(t)} \quad (2.1)$$

According to Newton's 2nd law, "the change of motion of an object is proportional to the force impressed and is made in the direction of the straight line in which the force is impressed." [188]. It means that the force $F_i(t)$ is related directly to the vector acceleration of this same atom $a_i(t)$ through Eq. 2.2 and mass m_i (Step 3):

$$F_i(t) = m_i a_i(t) \quad (2.2)$$

Moreover, the acceleration is of course linked to the velocity vector v_i and position r_i via the following time differential equations (Eqs. 2.3 and 2.4):

$$v_i(t) = \frac{dr_i(t)}{dt} \quad (2.3)$$

$$a_i(t) = \frac{dv_i(t)}{dt} = \frac{d^2r_i(t)}{dt^2} \quad (2.4)$$

Due to the acceleration and following Eqs 2.5 and 2.6 from the so-called leap-frog algorithm (Figure 2.12), based on the Verlet algorithm [190], estimations of the next position at time t plus time step Δt , $r_i(t+\Delta t)$ can be obtained (Step 4):

$$v_i\left(t + \frac{\Delta t}{2}\right) \approx v_i\left(t - \frac{\Delta t}{2}\right) + \frac{d^2r_i(t)}{dt^2} \Delta t \approx v_i\left(t - \frac{\Delta t}{2}\right) + \frac{F_i(t)}{m_i} \Delta t \quad (2.5)$$

$$r_i(t + \Delta t) \approx r_i(t) + v_i\left(t + \frac{\Delta t}{2}\right) \Delta t \quad (2.6)$$

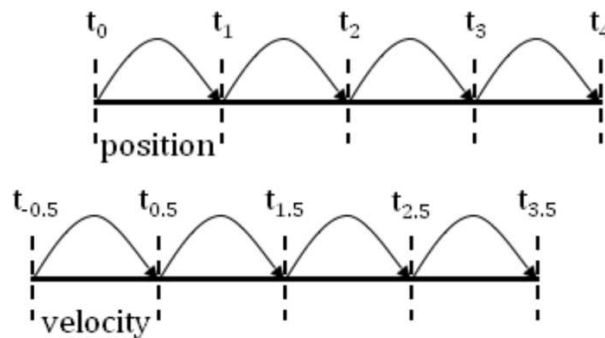


Figure 2.12 The leap-frog algorithm based on the Verlet algorithm [191].

The algorithm uses the position r_i at time t , velocity at time $t - \frac{\Delta t}{2}$ and the forces $F_i(t)$ to update the positions for time $t + \Delta t$. Finally, once this new position is known, the loop can be repeated again and again to build the trajectory which will then be used to determine the microscopic and macroscopic properties of interest [184, 189, 192].

In an MD simulation, several approximations are made to solve Newton's equations of motion and follow the previous loop:

- Atoms are considered as point masses, *i.e.* an object with dimensions assumed to be so small that it can be defined by a point whose differences in position, velocity and acceleration of its different parts are negligible [193]. Moreover, the electrons are considered to be in their ground state *i.e.* the lowest electronic energy. This means that no electronic degrees of freedom (no change in electronic state) are therefore taken into account.
- The repetition of the loop above is performed in successive discrete time steps (Δt) for a defined time of simulation (t_{tot}). These time-steps must be smaller than the characteristic time for the fastest vibrational motions in the system. However, its definition is a compromise between having a stable and good quality integration of the equations of motion (*i.e.* a small time step) and minimizing the computational time to do the simulation of t_{tot} (*i.e.* a longer time step to reach faster t_{tot}). Among the highest frequency vibrations, there are all the bond stretching modes. Removing these high-frequency low-amplitude vibrations using a rigid constraint, which keeps the atoms forming a bond (i and j) at a fixed distance of b_0 (equilibrium bond length), through Eq 2.7 (where r_{ij} is the separation/bond vector between the atoms i and j), allows for the possibility of using a longer time step, for the same quality of the numerical integration, and also diminishes problems of equipartition of kinetic energy amongst the different degree of freedom [194, 195]. In general, a time-step of the order of 10^{-15} s (1 fs) is compatible with all the previous requirements [189, 196].

$$|r_{ij}|^2 - b_0^2 = 0 \quad (2.7)$$

Finally, the most time-consuming part in an MD simulation is the calculation of the forces acting on every atom (Step 1). The forces arising from the interactions of each particle with all its surrounding neighbours have to be calculated according to the chosen force-field. Here, the *gmq* program was used to accomplish this task [194]. This program was designed for MD simulations of dense materials such as the ones produced in this work, and has already proven its suitability many times [181, 197-199]. The interactions described in Figure 2.13 make up the force field and are summed to give the total potential

energy, U_{pot} . They can be classified under two different labels, *i.e.* the “bonded” and “non-bonded” interactions, as shown in Eq. 2.8 [189, 192, 194, 200, 201]:

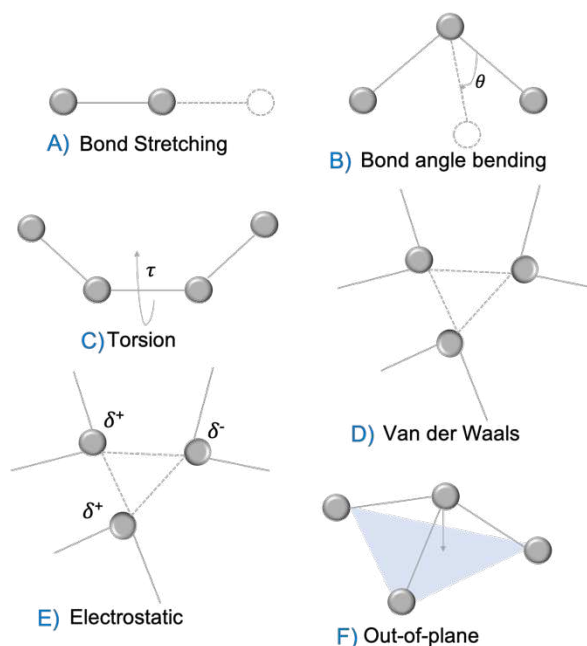


Figure 2.13 Main interactions occurring in molecules and corresponding to the typical potentials used in MD simulations (Eq. 2.8) [202].

$$\begin{aligned}
 U_{pot} = & \sum_{\theta} U_{bend}(\theta) + \sum_{\tau} U_{tors}(\tau) + \sum_{i-sp^2} U_{oop}(i) + \left(\sum U_{bond} \right) + \sum_{(i,j)_{nb}} U_{vdw}(r) \\
 & + \sum_{(i,j)_{nb}} U_{coul}(r) = \sum U_{bonded} + \sum U_{non-bonded}
 \end{aligned} \tag{2.8}$$

All these potentials are described by several physical constants and variable parameters (detailed later). The variable terms depend on the chemical nature and position of the atoms, and they define the “specific” force-field for the molecules of interest. Such parameters can be obtained from experimental data and *ab initio* calculations [203], if not available already in the literature as for the hydrogen gas [189]. In that latter case, they have to be tested if different values are provided in the literature.

The bond stretching U_{bond} potential (Figure 2.13.A) is generally replaced by a rigid constraint, but the possibility of using such a flexible potential exists.

2) B. 2. Molecular dynamics potentials

The typical MD potentials used by *gmq* are separated into 2 main categories: “bonded” and “non-bonded” (Eq. 2.8). The “bonded” part refers to the interactions involving closely-connected atoms while

the “non-bonded” part, described by Van der Waals and Coulombic interactions, depends on the distance r between two interacting sites. The latter is applied between atoms in different molecules or between atoms in the same molecule as long as they are separated by more than two or three bonds [204]. The potentials in Eq. 2.8 are detailed hereafter, starting with the “bonded” potentials.

As noted above, the chemical bonds are usually kept at a fixed length by a rigid constraint but, if not, Eq 2.9 can be used with k_b being the force constant of the bond:

$$U_{bond}(|r_{ij}|) = \frac{1}{2}k_b(|r_{ij}| - b_0)^2 \quad (2.9)$$

2) B. 2. 1. Bending potential

The angle-bending deformation is related to the angle θ , defined by three consecutive atoms: i, j and k (Figure 2.13.B). The energy can be determined using Eqs 2.10 and 2.11, where k_θ is a constant indicating the flexibility of the angle (energy units), θ_0 is the equilibrium bond angle and r_{ij} and r_{kj} are the separation vectors between the concerned atoms.

$$U_{bend}(\theta) = \frac{1}{2}k_\theta(\cos \theta - \cos \theta_0)^2 \quad (2.10)$$

$$\cos \theta = \frac{(\vec{r}_{ij} \cdot \vec{r}_{kj})}{|\vec{r}_{ij}||\vec{r}_{kj}|} \quad (2.11)$$

The aim of such a potential is to keep the bending angle close to its equilibrium value. Examples of the bending energy as a function of the bending angle are given in Figure 2.14:

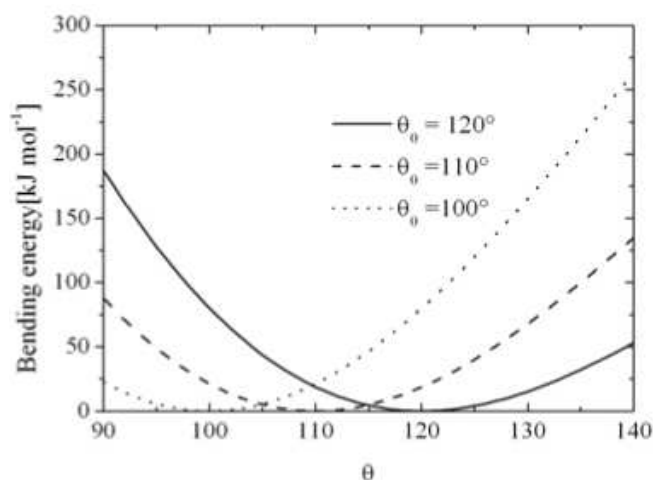


Figure 2.14 The bending potential as function of the bending angle θ for different values of θ_0 [187].

2) B. 2. 2. Torsional potential

The torsional, angle τ is defined by an atom quadruplet i, j, k and l , where the torsional motion is a rotation around the j - k bond (Figure 2.13.C). The potential energy can be calculated with Eq. 2.12 which uses a polynomial function with C_m coefficients of order n . Eq. 2.13 gives the expression to calculate the torsion angle from the separation vectors.

$$U_{tors}(\tau) = \sum_{m=0}^n C_m \cos^m \tau \quad (2.12)$$

$$\cos \tau = -\frac{(\vec{r}_{ij} \times \vec{r}_{jk}) \cdot (\vec{r}_{jk} \times \vec{r}_{kl})}{|\vec{r}_{ij} \times \vec{r}_{kl}| |\vec{r}_{jk} \times \vec{r}_{kl}|} \quad (2.13)$$

Usually, the atoms of the “bonded” potentials do not interact through the “non-bonded” ones. However, for the torsional energy involving 4 atoms and a rotation around a bond, this distinction is not entirely true. Indeed, two possibilities may occur. Either the atoms are separated by more than two bonds are considered as “non-bonded”, therefore only a part of U_{tors} is described by Eq. 2.12 whilst non-bonded interactions between the end atoms i and l make up the rest. Or the atoms separated by more than three bonds are considered as “non-bonded”, and this time, Eq. 2.12 represent the total torsional energy: i and l do not interact through the non-bonded potentials.

Finally, in the convention used in *gmq* [194], the dihedral angle varies from -180° to $+180^\circ$ and when $\tau = 0^\circ$ defines the *trans* conformation *i.e.* all the four atoms are in the same plane but i and l are each on one side of the central bond: they are at a maximum distance apart from each other (Figure 2.15, left). The *cis* conformation (Figure 2.15, right) is at $\pm 180^\circ$.

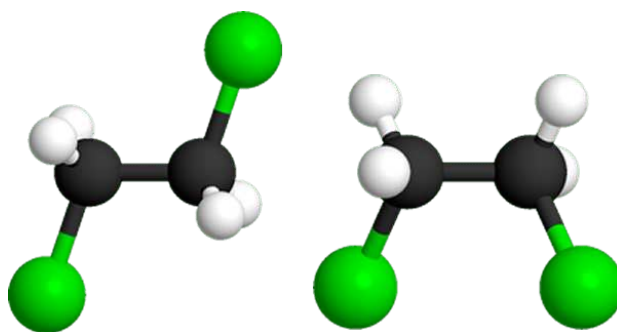


Figure 2.15 The *trans* conformation (left) and *cis* conformation (right) for the torsion defined by the four green and black atoms [205].

The torsional potential varies with the angle τ , as shown by Figure 2.16.

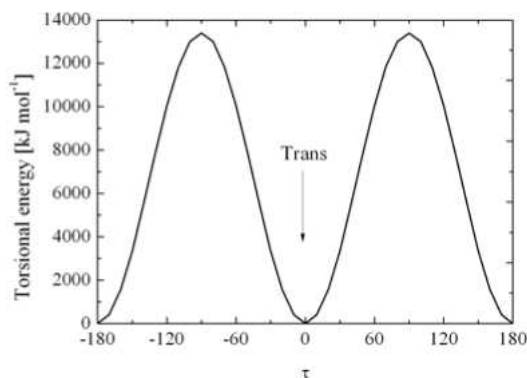


Figure 2.16 A torsion potential as a function of the torsion angle τ [187].

For the bends, the torsions and the “non-bonded” potentials, the symmetry is assumed, *i.e.* the torsion type defined with i, j, k and l is the same as the torsion type with l, k, j and i atoms.

2) B. 2. 3. Out-of-plane potential

As for the previous case, this potential involves four atoms i, j, k and l , whose central atom i is bonded to the three others (Figure 2.13.F). The central trivalent sp^2 atom can move out of the plane formed by the other three atoms to which it is bonded to. Therefore, the out-of-plane potential restricts this motion and keeps the sp^2 structures as close as possible to planar by acting upon the perpendicular distance s between i and the plane of j, k and l . Eq. 2.14 gives the harmonic form of the potential and Equation 2.15 the relation between s and the separation vectors.

$$U_{oop}(i) = \frac{1}{2}k_{oop}s^2 \quad (2.14)$$

$$s = \vec{r}_{ij} \cdot \frac{(\vec{r}_{jk} \cdot \vec{r}_{jl})}{|\vec{r}_{jk}||\vec{r}_{jl}|} \quad (2.15)$$

k_{oop} is a force parameter in kg s^{-2} [206]. An example of the variation of the out-of-plane potential with the distance s is given in Figure 2.17.

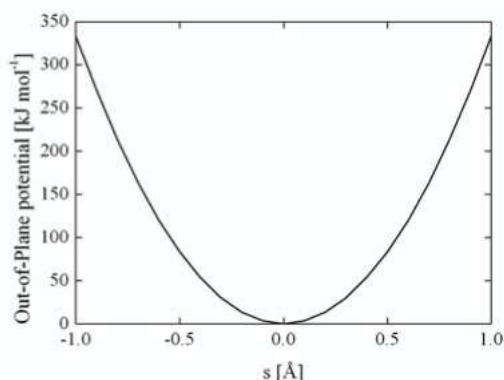


Figure 2.17 The out-of-plane potential as a function of the perpendicular distance s between atom i and the plane of atoms j , k and l [187].

In the case where one of the out-of-plane atoms is a pendant hydrogen, it is possible to keep it in the plane of the other heavy atoms and to maintain it aligned on the bisector of the angle formed by the other three atoms using special constraints [194]. This removes all the degrees of freedom of the hydrogen and, therefore, reduces any problems of equipartition whilst maintaining a reasonable time step.

A molecule is a number of atoms connected by a network of bonds whose atoms interact with their neighbours in the same molecule through the above “bonded” potentials and with the atoms of the same molecule or of another molecule via the “non-bonded” potentials within the already-stated conditions (Eq. 2.8).

Van der Waals and Coulombic potentials each present two main contributions: a repulsive and an attractive part. The first one prevents two atoms from occupying the same region of the space, while the second tends to keep the molecules together in a preferred packing structure in the absence of containing walls [194]. They are quite computationally expensive.

2) B. 2. 4. Van der Waals interactions (VdW)

Even if the Van der Waals interactions can be described by several forms within the *gmq* package, here, it is the Lennard-Jones 12-6 form which is most often used. As Eq. 2.16 shows, this potential involves the separation vectors, the distance at which the potential is zero σ and its well-depth ϵ . The $(\sigma/r_{ij})^{12}$ term approximates the Pauli repulsion at short ranges (due to the overlap between the electronic orbitals of the atoms) and the $(\sigma/r_{ij})^6$ term the attraction at longer distances.

$$U_{vdw}(|\vec{r}_{ij}|) = 4\varepsilon \left(\left(\frac{\sigma}{|\vec{r}_{ij}|} \right)^{12} - \left(\frac{\sigma}{|\vec{r}_{ij}|} \right)^6 \right) \quad (2.16)$$

The behaviour of this potential is shown in Figure 2.18.

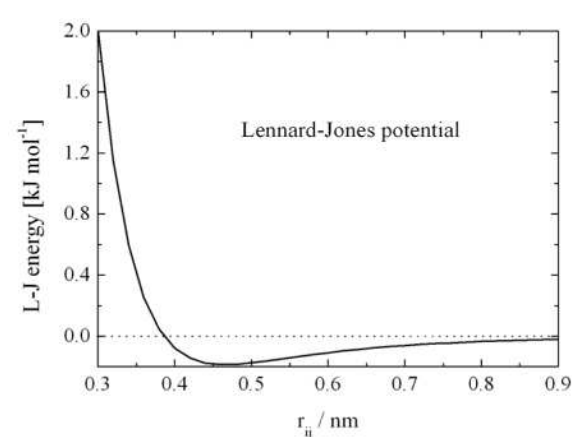


Figure 2.18 The Lennard-Jones 12-6 potential as a function of the distance between the concerned atoms [187].

According to their definition, the “non-bonded” potentials should be applied to any particles regardless of their distance apart. In practice, Van der Waals interactions are generally calculated explicitly out to a certain restricted range, *i.e.* they are ignored beyond a certain cut-off distance, R_c [190]. The Lennard-Jones form energy reaches relatively small values within short distances (Figure 2.18). Therefore, the interactions between atoms further apart are less important and the limit chosen to evaluate specifically the Van der Waals energy is the “cut-off distance” R_c (Figure 2.19). The *gmq* package makes long-range corrections that estimate the contribution to the potential energy and the pressure of the VdW potential beyond this R_c [194].

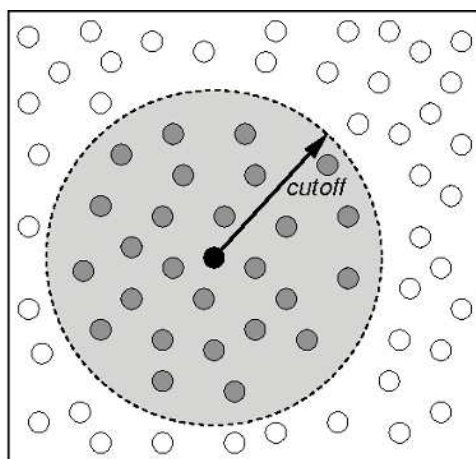


Figure 2.19 Representation of the Van der Waals cut-off distance R_c [207].

This limit in distance is complementary with the notion of “periodic boundary conditions” (PBC), which are generally used to avoid boundary artefacts. Even if the time-step is chosen to be a compromise between reduced computational time and a good quality of the integration of the equations of motions, the number of atoms in the system also affect the computing costs. Indeed, more there are atoms in the system, more the computer time *per* time-step will be long. This limits the number of atoms to a value that is relatively small compared to macroscopic samples, *i.e.* typically between a few thousands and 100000 atoms. Small systems leads to significant edge effects if they are confined by walls: the particles close to the borders have a smaller number of neighbours than the particles that are located in the middle of the box and, therefore, they experience different forces. These effects are improved by the use of PBC. With these conditions, the primary simulation box is replicated through all directions of the space to form a three-dimensional virtual infinite lattice. When one particle moves in the original simulation box, all “images” of that particle (*i.e.* replication of this one) in other virtual boxes move in the same way. Therefore, if one particle leaves the primary simulation box (A) by a boundary, its image from the neighbouring periodic box (B) will enter box A through the opposite side (Figure 2.20). As such, the number of particles remains constant in the primary MD box during the simulation and, in principle, surface effects are removed with this “infinite framework” [189, 208].

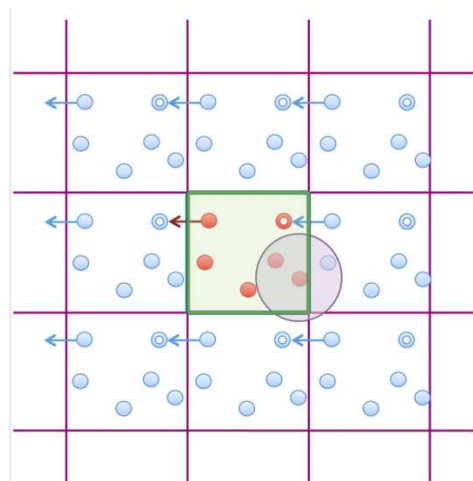


Figure 2.20 Illustration of the periodic boundary conditions in two dimensions with a particle (red circle) which leaves the primary simulation box (green square) and its image (red hollow circle) which enters in this box through the opposite face. The purple circle represents the cut-off distance, R_c [208].

As mentioned above, a finite interaction range for the particles is defined. This means that each atom only interacts with particles and images in the region defined by the R_c cut-off distance (purple circle in Figure 2.20). This reduces the number of forces to be calculated and therefore the computational costs. This spherical cut-off should be less than half the length of the box size to avoid interactions of atoms with their own images or different images of the same atom [208].

2) B. 2. 5. Coulombic interactions

The Coulombic potential describes the pair interaction between two sites having a non-zero charge, *i.e.* electrically-charged particles with partial charges q_i and q_j . Eq. 2.17 gives the form of the Coulombic potential with ϵ_0 corresponding to the vacuum permittivity. The electrostatic interactions are long-range in nature and they are evaluated in *gmq* by using the Ewald summation method [209].

$$U_{coul}(|\vec{r}_{ij}|) = \frac{q_i q_j}{4\pi\epsilon_0 |\vec{r}_{ij}|} \quad (2.17)$$

Due to the $1/r$ nature of the charge-charge interactions, this potential has a slow convergence. Unlike the VdW interactions where the LJ 12-6 form (more precisely the $1/r^6$ term) allows it to diminish more rapidly, it cannot be summed entirely in the restricted volume defined by the spherical cut-off (real space) No appropriate corrections for the contributions beyond this can be made. The Ewald sum solves this problem. In order for the potential to converge faster, this sum divides it into two parts: a real space term and a reciprocal space term. Three parameters have to be tuned to optimize the convergence of the Ewald

sum: R_c , α and K_{max} . The first is the cut-off distance in the real space, the second is the Ewald separation parameter and the third is the reciprocal space cut-off, which limits the number of reciprocal space vectors used in the sum. Typically, in the tuning procedure, R_c is initially set to the highest value allowed, *i.e.* half the box length. The value of α determines the proportion of the Ewald sum that is performed in the real space and the reciprocal space: with $\alpha = 0$, the entire sum is calculated in the real space (lower limit). A low value of α is appropriate for large box sizes. For smaller box sizes, α should be increased but more of the Ewald sum will have to be done in the reciprocal space so K_{max} must increase too. Therefore, these three parameters have to be adjusted to optimize to convergence of the U_{coul} potential to a reasonable tolerance without rendering the simulations too costly [190, 194, 209, 210].

2) B. 3. Available MD parameters and conditions

All MD simulations reported here were carried out using *gmq* [194]. They are run in a primary MD box which can be designed and adapted as a function of the system. The purpose is to perform all the steps of the MD algorithm (Figure 2.11) as efficiently as possible [200]. Taking into account the force field defined, the presence or not of rigid constraints, the code-specific parameters and the boundary conditions, the program integrates the equations of motion of a set of particles of varied complexity. All the parameters and conditions are organised in a series of input files which are the informations fed to the program, while the output files provide the desired results, *e.g.* the total energy, the energies corresponding to the different potentials involved, the density, the pressure, the temperature, etc.

One of the main input files contains the information about the atom types such as their name or molar masses as well as the force fields used, *i.e.* the potentials taken into account, their parameters for each interaction, etc. Another input file is associated to the initial box size and shape as well as the initial configurations, *i.e.* the atoms present with their connectivity (the other atoms to which they are bonded to), their coordinates (positions) and their velocities at the time t . A third one contains the informations about the conditions of the simulations, *e.g.* the time-step, the required temperature and pressure, the cut-off distance and Ewald parameters, etc.

At the end of a simulation, the output files include the thermodynamic data and the molecular configurations which are stored regularly over the total simulation time. They also output the shape and size of the MD box which are defined by a matrix h of basis vectors $\{a,b,c\}$, *e.g.* vector a is given by the matrix elements h_{11} , h_{21} , h_{31} .

The *gmq* package allows to study a system under different sets of conditions:

- *NVT*: constant number of atoms N and controlled temperature T but with a constant volume V which means that the density is fixed but the pressure is not controlled.
- *NPT*: constant number of atoms N , controlled pressure tensor \mathbf{P} and temperature T .
- *NpT*: constant number of atoms N , controlled isotropic pressure p and controlled T .
- *NVE*: N and V constant as well as the total energy E (this mode is especially used to check energy conservation).

The conditions that are neither constant nor controlled in a set are variable and change according to the course of the simulation.

Although working at a constant V and N in the system is straightforward, controlling the temperature and pressure requires special methods. In *gmq*, when T has to be maintained close to a required value T_{req} , it is coupled to an external heat bath at the required temperature using the loose-coupling technique of Berendsen *et al.* [211]. The loose-coupling is defined by Eq. 2.18 where τ_T is the relaxation time determining the rate of the heat flow.

$$\dot{T}(t) = \frac{-1}{\tau_T} (T(t) - T_{req}(t)) \quad (2.18)$$

The difference between the temperatures decreases exponentially with the relaxation time. The ability to control the rate of change of the required temperature allows *gmq* to perform gradual heating or cooling simulations.

Concerning the pressure tensor, it is linked to the box size and shape, which means that it can be controlled by modifying the h matrix defined by the box vectors. A loose-coupling method is again used according to Eq. 2.19:

$$\dot{h}(t) = \frac{P(t) - P_{req}(t)}{\tau_P \mu} \quad (2.19)$$

with μ being a pre-defined constant and, as for the temperature, τ_P being the relaxation time which defines the rate at which the h matrix responds to the difference between the required pressure tensor $P_{req}(t)$ and the measured pressure tensor $P(t)$. Controlling the rate of change of the required pressure tensor allows for the ramping up or down of its components (Figure 2.21). This means that mechanical tests, such as compression in one or more directions, can be performed by MD simulations.

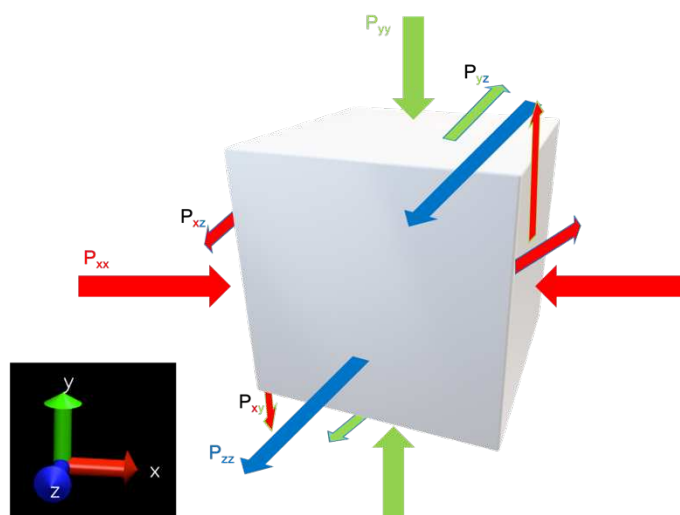


Figure 2.21 The different pressure tensor components (coloured arrows), applied to the MD box (white cube). The subscript letters indicate the face and direction to which the pressure is applied: for example, P_{xx} means on face x, direction x whereas P_{xy} is still on face x but in the direction of y.

The different conditions are therefore controllable by the user, depending on what is simulated. The *gmq* package can perform MD simulations of materials in different states (solid, liquid and gaseous), mixtures of different models, *e.g.* several reactants together (prerequisite for modelling IP) or a gas in a polymer phase (prerequisite for studying model transport properties), thermal and/or mechanical tests, etc.

Molecular dynamics is a very useful tool to complement existing experimental results, but it can also avoid long, expensive and dangerous laboratory experiments. It can help in the selection of a suitable material for a defined application or be a guide for the experimental process when this one is complex and vast. This is the case for the main objective of this work, which is to develop a novel robust coating for high-pressure containment vessels of type IV capable of providing H_2 barrier properties under a wide range of temperature, pressure, stress and strain conditions (cf. Chapter 1). To reach such a goal, the IP syntheses were supported by molecular modelling. The simulations were carried out to guide the experiments by exploring in particular the effects that the stoichiometry of the film, *i.e.* the ratios of the monomers at the interface, had on its mechanical and barrier properties. This meant that all components involved (hydrogen, monomers and network polymers) were modelled and, as such, that an appropriate force field had to be fed into *gmq* for each of them. Some force fields had to be developed (monomer fragments or network), while others based on the literature had to be tested and adapted if necessary (hydrogen and pure monomers).

2) C. Abbreviations list

➤ 6FDA	Hexafluoroisopropylidene diphthalic anhydride
➤ DCM	Dichloromethane
➤ DMSO	Dimethyl sulfoxide
➤ HCCP	Hexa chloro cyclotriphosphazene
➤ IP	Interfacial polymerization
➤ LJ	Lennard-Jones
➤ MD	Molecular dynamics
➤ NF	Nanofiltration
➤ PBC	Periodic boundary conditions
➤ PDMS	Polydimethylsiloxane
➤ PMDA	Pyromellitic dianhydride
➤ POSS	Polyhedral oligomeric silsesquioxane
➤ RO	Reverse osmosis
➤ VdW	Van der Waals
➤ VMD	Visual Molecular Dynamics

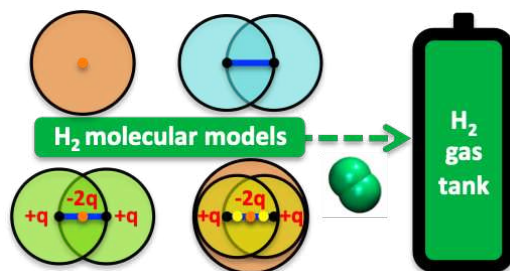
Chapter 3 : Molecular Modelling - Hydrogen Potentials

3) A. Justification and Abstract

In the literature, many force fields exist for the key permeant of this project, *i.e.* molecular hydrogen H_2 . Therefore, the first step is to find an existing empirical model compatible with the *gmq* code and which fits as closely as possible the experimental data for hydrogen. Some of these existing force fields have been simulated and compared with selected experimental data in order to select the best match.

This chapter compares eight classical H_2 molecular models in the gas phase taken from the existing literature. All the models are based on Lennard-Jones (LJ) 12-6 terms for the van der Waals interactions, and hence they are easier to transfer to multiphase molecular simulations than more sophisticated potentials. The H_2 potentials tested include one-site, two-site, three-site and five-site models, with the sites being either the H atoms, the centre-of-mass of the H_2 molecule or massless sites. For the multi-site models, high-frequency H-H stretching modes can lead to poor equipartition of the kinetic energy and the timestep for molecular dynamics (MD) simulations should be reduced to maintain a stable numerical integration of the equations of motion. As such, only those models with rigid bonds are considered. In the present case, 600 MD simulations of H_2 gas were carried out over a large range of temperatures (-50°C to $+90^\circ\text{C}$) and at densities corresponding to a pressure range of 50 to 2000 bar, which include the operating conditions of on-board storage tanks in hydrogen-fuelled vehicles.

Most of the models under study were found to reproduce reasonably well the experimental pVT phase diagram as well as the solubility. Discrepancies only became significant at the highest densities tested and these could be used to rank the different models. All model diffusion coefficients were essentially indistinguishable from experimental results, and as such, kinetically-dominated dynamic properties could not be used as a criterion for the choice of model. Among the eight models tested, two of them, *i.e.* the two-site model of Yang and Zhong and the one-site model derived from Buch performed very well over the range of conditions tested. They represent a good compromise between realism, simplicity and computational efficiency.



This chapter is adapted from:

Méryll Barraco, Sylvie Neyertz, Nieck E. Benes and David Brown, *Comparison of Eight Classical Lennard-Jones-Based H_2 Molecular Models in the Gas Phase at Temperatures and Pressures Relevant to Hydrogen On-Board Storage Tanks*, J. Phys. Chem. A, 127 (2023) 6335-6346, <https://doi.org/10.1021/acs.jpca.3c03212>.

3) B. Introduction

Molecular dynamics (MD) simulation studies of hydrogen H₂ have been carried out for a long time and many classical models of varying complexity already exist [212-229]. However, in recent years, there has been a large increase in theoretical studies of hydrogen technologies and storage due to environmental challenges: there is definitely a need for improved energy efficiencies, cleaner energy sources and decarbonized transports [230, 231]. Among them are the fuel-cell electric vehicles (FCEVs), whose major challenges are the power and yields of the fuel cells as well as the number and sizes of the high-pressure hydrogen tanks [46, 58, 63, 232].

The more recent hydrogen tanks are made of stacked layers with a polymeric inner layer in direct contact with H₂, and have large working ranges of temperature and pressure: indeed, they must be able to resist temperatures ranging from -40°C to 80°C and H₂ pressures ranging from 60 bar to 800 bar [46, 62, 71, 233, 234]. Within this context, the use of classical MD simulations is a powerful tool to complement experimental efforts, due to its capacities to model the static and dynamic behaviour of systems at the atomistic level under a large variety of operating conditions. MD simulations are based on Newtonian mechanics for a set of interacting sites and can predict how every atom in a system will move with time from the physics governing interatomic interactions [184, 200]. Computer experiments are, in many ways, similar to real laboratory experiments: MD involves sample preparations, statistical analyses, validation steps and can undergo modifications of the process parameters (temperature, pressure, concentration, etc...) [189]. The latter is particularly appropriate when harsh conditions of temperature and pressure have to be tested [235], since MD simulations are both cheaper and much less dangerous to carry out than laboratory experiments. Modelling can then be used to provide key information on molecular mechanisms, which in turn will help experimentalists to focus on the most interesting systems.

In a classical MD simulation, the total potential energy is calculated using different mathematical equations, which represent each type of intramolecular and intermolecular interactions in the system. They are usually referred to as “force fields”, “potentials” or “models”. Their parameters depend on the chemical nature of the atoms and can be obtained from experimental data, *ab initio* calculations or from the literature [189] (cf. Chapter 2). As mentioned above, many classical molecular models of H₂ exist [212-229], but they are based on different numbers of sites, different potential equations and different parameters. Some of them are difficult to transfer to the typical force-fields implemented in most MD codes, and as such, the focus here is rather on those based on the simple Lennard-Jones (LJ) 12-6 form for Van der Waals interactions. In addition, only the models with rigid-bond are considered since the H₂ stretching modes have such a high frequency that the MD timestep would have to be lower than 1 fs to maintain a stable numerical

integration of the equations of motion [190]. Flexible-bond diatomic models can also lead to severe problems of equipartition of kinetic energy due to the very poor coupling between their high-frequency low-amplitude stretching modes and their slower translational and rotational modes [236]. Consequently, only models with “non-bonded” interactions are taken into account (cf. Chapter 2, Equation 2.8)

In this work, eight classical LJ-based rigid-bond models available in the literature for hydrogen [212, 215, 217, 218, 221, 222, 225, 228], have been assessed over the -50°C to 90°C temperature range and at densities corresponding to the 50-2000 bar pressure range of the real gas, in order to find those which give the best agreement with experimental H_2 gas data. Indeed, the focus is made on the transport properties of this gas under an extended range of conditions pertinent to hydrogen on-board storage tanks for FCEVs. Although it is known that at low temperatures, quantum effects should be taken into account for a proper representation of H_2 [227, 237], it will be shown that such conditions allow for a classical treatment. This amounted to a total of 600 MD simulations. Comparisons of H_2 models have already been reported in the literature, but they apply to sets of different models, different conditions and properties as well as specific mixtures [227, 238]. In the present work, the thermodynamic, solubility and diffusivity data obtained from the models are compared to the corresponding experimental data in order to allow a ranking of the eight models under study.

3) C. Computational details

All simulations were carried out using the *gmq* package [194]. As noted above, the H_2 potentials tested were those compatible with typical force-fields for molecular materials [239], which are implemented in most MD codes, including *gmq*. All selected multi-site models had rigid bonds, *i.e.* they could be simulated with a typical timestep of 1 fs [190]. The above restrictions eliminated, for example, those models that do not use van der Waals interactions based on the Lennard-Jones 12-6 representation as well as polarizable and flexible-bond models [213, 214, 223, 224, 227, 229]. Indeed, as a reminder, the high-frequency low-amplitude vibrational motions can cause a poor equipartition of the kinetic energy between the rotational and translational degrees of freedom, which means very long relaxation times. Moreover, this can create situations where the rotational and translational temperatures are higher than the temperature calculated from all degrees of freedom, *i.e.* the bond vibrations are underpopulated. Or inversely, the two first temperatures are lower than the third, *i.e.* the bond vibrations are overpopulated. Both of these situations can persist for a very long time and therefore impact the average pressure and potential energy. This was actually noticed in this work about gaseous hydrogen: at low densities, the rotational and translational temperatures were not always the same (detailed later) due to the problem of equipartition, which is worsened as the collision frequency diminishes.

Of course, sophisticated models can usually yield very accurate predictions, *e.g.* it has been shown that a Mie potential with a softer repulsion of the hydrogen atom outperforms some of the traditional LJ potentials for a number of thermodynamic properties [227]. However, within the context of hydrogen on-board storage tanks, the objective here is to aim for models which are significantly less difficult to transfer to multiphase simulations, while still being suitable at reproducing reasonably well the pVT phase diagram as well as the solubility and mobility of H_2 in its gas phase.

3) C. 1. H_2 LJ-based models

The H_2 force-fields tested included one-site, two-site, three-site and five-site models. Sites can either be the H atoms, the centre-of-mass (COM) of the H_2 molecule or massless sites. In a specific force-field, sites can be associated to a LJ and/or an electrostatic interaction. Bonds between the H atoms in the multi-site models are rigid. The different types are schematically presented in Figure 3.1 and the eight models under study are introduced hereafter by order of increasing complexity.

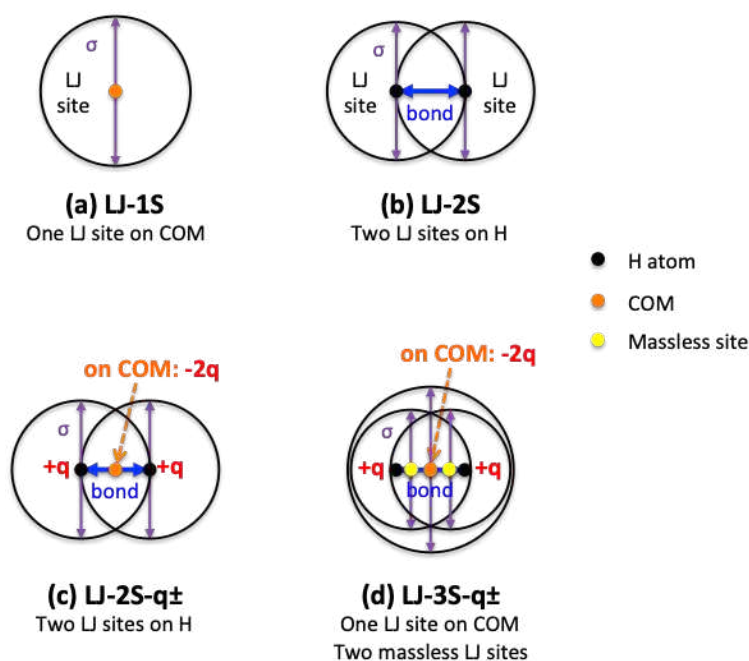


Figure 3.1 A schematic representation of the different H_2 LJ-based models.

Details about these different types of models are given in the following text.

3) C. 1. 1. Single-site LJ models: LJ-1S

The simplest model of diatomic H_2 uses a single-site Lennard-Jones 12-6 potential placed at the COM of the molecule and is generally referred to as a “LJ-1S model” (Figure 3.1.a). A LJ potential is

defined by its well depth ε and the distance σ at which the potential is equal to zero (cf. Chapter 2). Values of $\varepsilon/k_B = 37.0$ K, with k_B being Boltzmann's constant, and $\sigma = 2.928$ Å were initially proposed by Hirschfelder, Curtiss and Bird (model HCB LJ-1S) [212]. A slightly different value of $\sigma = 2.95$ Å was later proposed by Maitland *et al.* (model Ma LJ-1S) [215], and used for H₂ solubility in amorphous polymers [240-242]. Köster *et al.* [225] fitted a single-site LJ 12-6 model to the speed of sound and the pVT data of H₂ over the 50-250 K temperature range with parameters of $\varepsilon/k_B = 25.84$ K and $\sigma = 3.0366$ Å (model Kö LJ-1S). The last LJ-1S model tested is derived from the work of Buch [218] on orientational effects in hydrogen at low temperatures and has parameters of $\varepsilon/k_B = 34.2$ K and $\sigma = 2.96$ Å (model Bu LJ-1S). In its original form, it was supplemented by a small quadrupole-quadrupole interaction term. However preliminary tests showed problems attaining equipartition between the different modes due to a slow exchange of kinetic energy between the rotational and translational degrees of freedom, and, as done elsewhere [227], the weak quadrupole interaction was discarded.

3) C. 1. 2. Two-site LJ model: LJ-2S

The anisotropic nature of the interactions between diatomic molecules can be introduced by using a “LJ-2S model” with the two sites of the LJ 12-6 potential being placed on the atomic H positions (Figure 3.1.b). Yang and Zhong [221] have proposed such a potential for H₂ with $\varepsilon_{\text{HH}}/k_B = 10.00$ K and $\sigma_{\text{HH}} = 2.72$ Å along with a H-H bond length of 0.74 Å (model YZ LJ-2S). It was fitted to the experimental pVT curve and the self-diffusion coefficients of H₂ over the 80-300 K range at pressures up to 600 bar [221].

3) C. 1. 3. Two-site LJ + quadrupole moment: LJ-2S- q_{\pm}

The two-site LJ model can be further supplemented by taking into account the quadrupole moment of H₂, thus being referred to as a “LJ-2S- q_{\pm} ” model (Figure 3.1.c). This is the case for Marx and Niebala [216], whose model had a quadrupole moment of $Q/(4\pi\varepsilon_0k_B)^{1/2} = 54.2$ (K Å⁵)^{1/2} along with LJ 12-6 interactions between the H atoms defined as $\varepsilon_{\text{HH}}/k_B = 36.7$ K and $\sigma_{\text{HH}} = 2.958$ Å, *i.e.* they were very close to those of a LJ-1S model. This led to confusion as these parameters ended up being either used on “LJ-1S- q_{\pm} ” [225, 243] or “LJ-2S- q_{\pm} ” [227] models along with various partial charges of $q = 0.615 \times 10^{-26}$ esu [243], $q/e = 0.120746$ [225], or $q/e = 0.468$ [227]. Within this context, it is not surprising that large deviations from experimental results were reported [227]. As such, we rather selected two other LJ-2S- q_{\pm} potentials. The first one, proposed by Bouanich (model Bo3 LJ-2S- q_{\pm}) [217], is based on a two-site LJ 12-6 potential placed on the atomic positions with parameters $\varepsilon_{\text{HH}}/k_B = 11.2544$ K and $\sigma_{\text{HH}} = 2.68259$ Å as well as a H-H bond length of 0.7508 Å. It is supplemented by partial charges $q/e = 0.1108$ on the H atoms and this is

neutralised by a charge of $-2q$ on the COM. It was parametrized using the experimental second-virial coefficients over the 98-773 K range [217]. The second one, proposed by Siepmann and coworkers within the framework of the TraPPE force-field (model Si3 LJ-2S- q_{\pm}) [228], has parameters $\varepsilon_{\text{HH}}/k_B = 8.06$ K and $\sigma_{\text{HH}} = 3.03$ Å as well as a H-H bond length of 0.741 Å. It is supplemented by partial charges $q/e = 0.47$ on the H atoms and a countercharge of $q/e = -0.94$ on the COM. It was fitted to the experimental vapor-liquid coexistence curve of H₂ in its near-critical region, *i.e.* around 33 K, in order to account for nuclear quantum effects [228]. The Si3 LJ-2S- q_{\pm} model has been used to address adsorption and diffusion of H₂ in nanoporous materials [228, 244].

3) C. 1. 4. Three-sites LJ + quadrupole moment: LJ-3S- q_{\pm}

Belof *et al.* [222, 245] have developed both a polarizable and non-polarizable potential for H₂ from first principles. Their non-polarizable model is a “LJ-3S- q_{\pm} model” (Figure 3.1.d) combining three LJ 12-6 interaction sites with a quadrupole moment (model Be5 LJ-3S- q_{\pm}). The masses are placed on the atomic positions at a distance of 0.742 Å apart. These mass sites carry a charge of $q/e = 0.3732$ but are not the origin of a LJ interaction. The COM has a charge of $-2q$ placed on it and a LJ interaction with parameters $\varepsilon/k_B = 8.8516$ K and $\sigma = 3.2293$ Å. Two other massless sites are placed along the H-H bond at a distance of 0.329 Å from the COM and these are also the origin of a LJ interaction with $\varepsilon/k_B = 4.0659$ K and $\sigma = 2.3406$ Å. It was validated using the second virial coefficients over the 50-500 K range as well as the pressure-density curves at 77 K (for a p range of 0-200 atm) and 298.15 K (for a p range of 0-2000 atm) [245].

3) D. Details of the MD simulations

All MD simulations were carried out on cubic periodic simulation boxes containing typically 512 molecules. The integration time step in the MD algorithm was set to $\Delta t = 1$ fs. The special constraints techniques of Ciccotti *et al.* [246] were used to keep H-H bonds rigid and to handle the dynamics of massless sites. Rigid-body dynamics minimizes problems with equipartition of the kinetic energy and there was no need for intramolecular potentials.

The intermolecular potentials included the Van der Waals LJ 12-6 terms for all models, along with the coulombic terms for the LJ-2S- q_{\pm} and LJ-3S- q_{\pm} models only. As is customary for gas-based systems, the Van der Waals cut-off was set to half the MD box length and long-range corrections to the energy and the pressure were implemented [190]. The long-range nature of the coulombic interactions was accounted for by the Ewald summation technique [209], with the separation parameter, α and the upper bound for the

number of reciprocal space vectors, K_{max} , being optimized for each system [210, 247] (cf. Chapter 2). For the hydrogen systems, at the lowest pressure of 50 bar the half-box length is less than 50 Å.

Tests were carried out under NVT conditions, *i.e.* a constant number of atoms N , a constant volume V and a controlled temperature T . The temperature was maintained close to its required value using the Berendsen loose-coupling technique [211]. Simulations were run for at least 1000 ps with the configurations being stored every 5 ps and the thermodynamic data every 1 ps. Examples of the p vs. time and T vs. time behaviour during these simulations are provided in Figure S3.1 in the Supporting Information. The first 500 ps generally ensured that the systems were decorrelated from their starting configurations and the thermodynamic properties were well equilibrated. The equilibration part was discarded and the averages were taken over the last 500 ps, which constituted the production runs. The atomic structures and trajectories were visualized using the VMD software [248].

Since the interest here is in H₂ on-board storage tanks for use in fuel-cells vehicles, the temperatures and pressures tested were directly linked to values quoted by gas tank manufacturers in the hydrogen field, *i.e.* (i) a range of -50°C to +90°C for T and (ii) a range of 50 to 2000 bars for p , both allowing to deal with all eventualities [46, 62, 71, 233, 234]. The temperatures tested were both extremes (-50°C and 90°C) along with room temperature (20°C). The densities tested were the experimental densities corresponding to H₂ pressures in the range from 50 bar to 100 bar (in steps of 10 bar) and from 100 bar to 2000 bar (in steps of 100 bar). This amounted to 25 different densities for each model at each temperature, and consequently to a total of 600 MD simulations. Figure 3.2 displays examples of three corresponding simulation boxes for different models at 20°C and at pressures of 200 bar, 700 bar and 2000 bar.

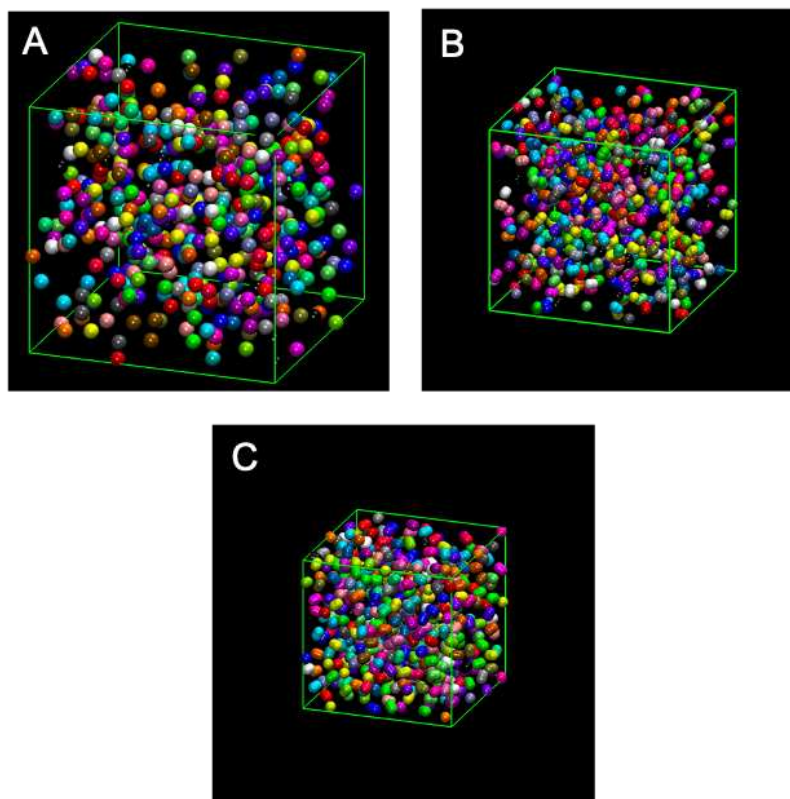


Figure 3.2 MD simulation boxes of (a) the one-site Bu LJ-1S model at 200 bar (box length = 48.46 Å), (b) the two-site YZ LJ-2S model at 700 bar (box length = 35.08 Å) and (c) the five-site Be5 LJ-3S- q_{\pm} model at 2000 bar (box length = 28.67 Å). All of them are at 20°C and colours are used to distinguish the different H₂ molecules.

For each isotherm, the experimental densities corresponding to the test pressures defined previously were obtained from the NIST database [66]. They were used to set the (fixed) volumes of the simulation boxes. Following the MD simulations, the pressures p , energies and actual temperatures T associated to the pre-set densities were averaged over the NVT production runs. The discrepancies between the average pressures obtained from the models and the experimental “target” pressures corresponding to the imposed densities were used to assess the aptitude of the different models to reproduce the equation of state of hydrogen.

The thermal expansion coefficient, α , over the -50°C to 90°C range and at a specific pressure p was evaluated from Equation 3.1 where the volume was interpolated at any pressure between 50 and 2000 bar and at each temperature under study using the calculations and fits mentioned elsewhere [249].

$$\alpha = \frac{1}{V} \left(\frac{\partial V}{\partial T} \right)_p \quad (3.1)$$

In addition to the thermodynamic properties, both the solubilities and the self-diffusion coefficients of the gas molecules in the gas phase were determined. Within the context of H₂ permeation in storage tanks, these properties will have to be determined in *e.g.* barrier coatings. As far as solubility is concerned, the equilibrium uptake in another phase in contact with the pure gas partly depends on the concentration and solubility of H₂ in the gas phase. While simulations of potential barrier materials will be carried out later, the solubility in the gas phase is an important property to compare with experiment, particularly at the highest densities studied. For each *NVT* run, the solubility S of H₂ in its gas phase was calculated using a test particle insertion (*TPI*) technique, which involves performing repeated random virtual insertions of a test particle into the previously stored MD configurations [250]. S is related to the excess chemical potential μ_{ex} and is estimated from *TPI* calculations using the right-hand side of Equation 3.2 [190, 199, 242, 249-252]:

$$S = \exp\left(\frac{-\mu_{ex}}{k_B T}\right) \approx \left\langle \exp\left(-\frac{\Delta\phi}{k_B T}\right) \right\rangle \quad (3.2)$$

where $\Delta\Phi$ is the change in intermolecular potential energy associated with each specific insertion and k_B is the Boltzmann constant. Effectively, the solubility is the average Boltzmann factor for the virtual insertion of test particles at random positions in the system. The *TPI* calculation can be carried out irrespective of what is in the system and what the test particle is. In the present case, the test particle is just a H₂ molecule interacting with the H₂ molecules already present in the system in the same way as they do amongst themselves. At very low densities, the gas molecules are particularly spread out, so $\Delta\Phi \approx 0$ and S approaches 1, which is the solubility of an ideal gas. At higher densities, overlaps become more probable between the randomly-inserted test particle and H₂ molecules in the system: these lead to highly repulsive energies and very low Boltzmann factors, which decrease the solubility. On the other hand, insertions at positions that are close to other molecules (but not overlapping) lead to attractive interactions which are likely to increase the solubility. The solubility is therefore a compromise between these two competing factors.

To compare the model S with experimental data, the relationship between S and the fugacity f was used (Equation 3.3) with n_{mol} being the number of molecules [242, 253].

$$f = \frac{n_{mol} k_B T}{V S} \quad (3.3)$$

In thermodynamics, the fugacity $f(p)$ of a real gas at a pressure p is equal to the pressure that the ideal gas would need to have in order for its chemical potential at T to be the same as the one of the real gas. Fugacity is not directly measurable by an experiment but it can, in principle, be calculated from the

pressure dependence of the molar volume, $V_m(p)$, at constant temperature using the following integral Equation 3.4 where R is the ideal gas constant [254]:

$$\ln\left(\frac{f(p)}{p}\right) = -\frac{1}{RT} \int_0^p \left(\frac{RT}{p} - V_m(p)\right) dp = \frac{1}{RT} \int_0^p (V_m(p) - V_m^{ideal}(p)) dp \quad (3.4)$$

Discrepancies between the isotherm at 20°C predicted by Holley *et al.* using the Beattie-Bridgeman (B-B) equation of state (EOS) [255] which allows the equation above to be integrated analytically [254] and the NIST database were found at high pressures [66]. Other fits also showed discrepancies so a direct numerical integration approach was found to be much more satisfactory. Data of high precision were first extracted from the NIST database: in the interval from 0 to 1 bar a point every 0.001 bar, from 1 to 50 bars, every 0.1 bar and from 50 bar up to 2500 bar, every 5 bars. Using the obtained pressure-density curve and Equations 3.3 and 3.4, the fugacity and the corresponding experimental solubility of H₂ in its gas phase, $S(p)$ were determined.

Finally, the self-diffusion coefficient of each model H₂ in its gas phase was determined from the mean-square displacement (MSD) of the gas atoms as a function of time. The MSD measure the average deviation of the position of an atom as a function of time with respect to an initial reference position. The self-diffusion coefficient D was obtained from Equation 3.5 where $\langle \Delta r^2(t) \rangle$ is the MSD [256].

$$D = \lim_{t \rightarrow \infty} \frac{1}{6t} \langle \Delta r^2(t) \rangle \quad (3.5)$$

When the MSD/6t is plotted as a function of time, the limiting value of its plateau provides an estimation of the D . The corresponding experimental values were taken from the work of Chen *et al.* [257], who measured them for pressures up to 2000 bar and in the temperature range 171–372 K using the spin echo method.

When comparing with target experimental results, visual comparisons of the average model data were first made in order to have an indication of the suitability of the eight models. Standard errors on each average data were estimated using a standard blocking method [190], based on the standard deviation (related to the underlying probability density distribution) combined with the statistical inefficiency (related to the correlation in the data) [194]. In general, the standard errors are not shown in the Figures since they are usually smaller than the size of the symbols. However, they are specifically provided in Tables S3.1, S3.2, S3.3, S3.4, S3.5 and S3.6 in the Supporting Information (SI). Furthermore, to better quantify the differences over the whole pressure range tested, the root-mean-square difference (*RSMD*) of each model vs experimental data was assessed using Equation 3.6:

$$RMSD = \sqrt{\left(\frac{\sum(x_{model} - x_{exp})^2}{25}\right)} \quad (3.6)$$

with x being the property under study at each of the 25 densities used. The relative root-mean-square difference ($\%RMSD$) was also calculated as shown by Equation 3.7:

$$\%RMSD = \sqrt{\left(\frac{\sum\left(\frac{x_{model} - x_{exp}}{x_{exp}}\right)^2}{25}\right)} \times 100 \quad (3.7)$$

Compared to Eqs. 3.6 and 3.7 avoids the results being weighted by absolute differences and ensures that each density simulated contributes in an equal way to the overall comparison between experimental and simulation data. In addition, the percentage differences between the average model and experimental pressures and solubilities are displayed for each density in Figures S3.2 and S3.3. They show whether each model overestimates or underestimates the experimental reference value at a specific density and temperature.

3) E. Results and discussion

3) E. 1. Phase diagram at -50°C, 20°C and 90°C

The phase diagram involves recording the average model isotropic pressure p for each NVT simulation carried out at the requested temperature and at the input experimental density ρ [66]. Figure 3.3 displays the isotherms for $T = -50^\circ\text{C}$, 20°C and 90°C . The details of the average p are also provided in the SI along with their standard errors (Table S3.1 for -50°C , Table S3.2 for 20°C and Table S3.3 for 90°C).

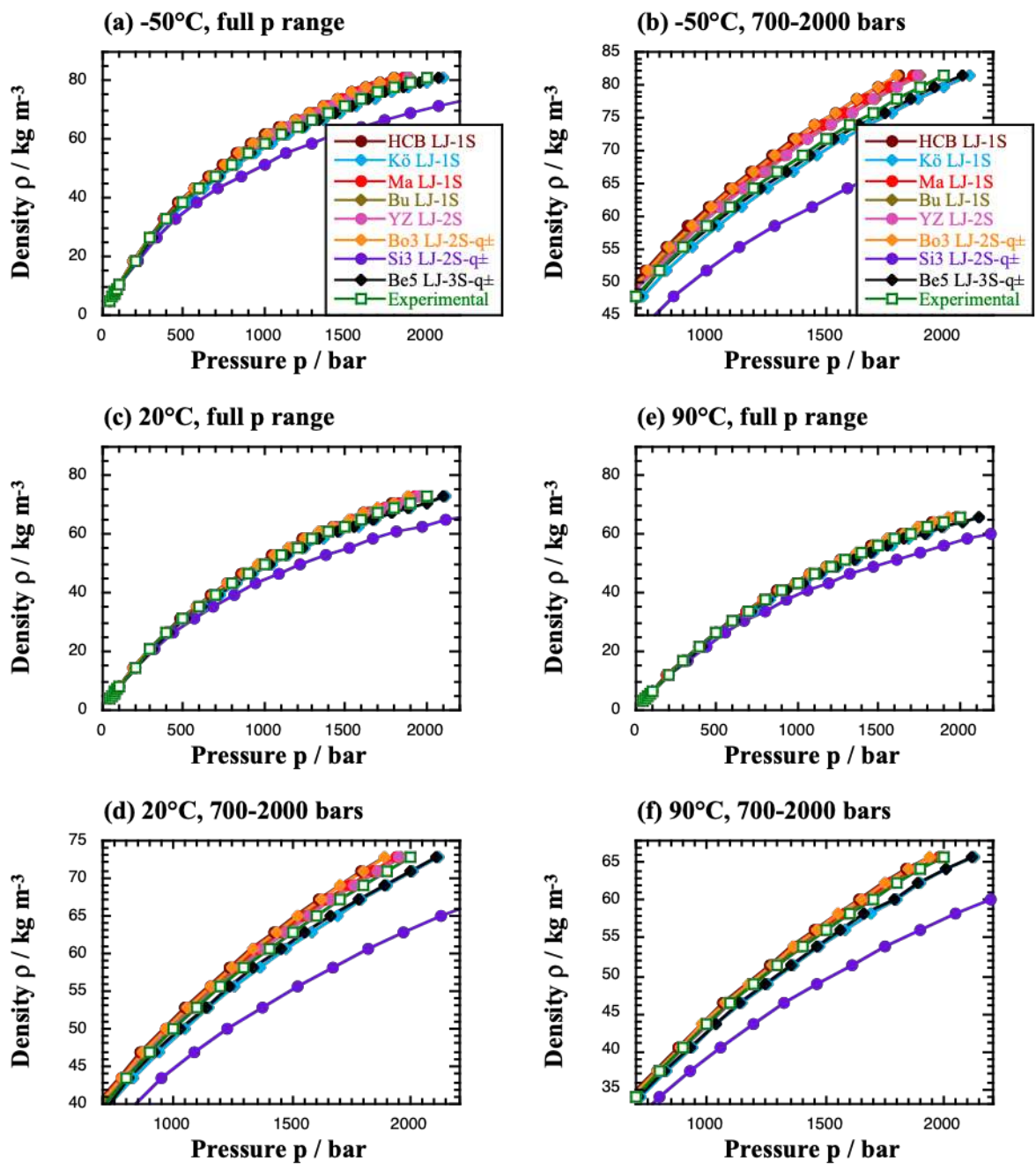


Figure 3.3 H₂ density-pressure isotherms for all eight models (full symbols) compared to experimental data (white squares) at (a-b) -50°C, (c-d) 20°C and (e-f) 90°C. The legend is the same for all graphs. For each temperature, the full 50-2000 bars pressure range is displayed on the left, while the right specifically shows the 700-2000 bars pressure range.

As expected, all models are convergent at the lowest densities and pressures, where a near-ideal gas behaviour is found. The model and experimental pressure-density isotherms overlap quite well up to ≈ 500 bars, at which point deviations become apparent (Figure 3.3). As an example, the model pressures corresponding to the experimental density at 700 bar and 20°C, *i.e.* the typical pressure of H₂ in an on-

board reservoir when fully-fuelled, are reported in Table 3.1 along with their %RMSD (Eq. 7). Under these conditions, the YZ LJ-2S model is the nearest to the experimental reference value, whereas some others, *e.g.* the HCB LJ-1S and Kö LJ-1S models differ by over 3%. The furthest away is Si3 LJ-2S-q_±, which appears to underestimate the gaseous density of H₂ under the conditions tested here (Figure 3.3). It should be remembered that it was parametrized at much lower temperatures, *i.e.* close to the near-critical region [228]. In addition, Siepmann and coauthors had already reported that their H₂ model overpredicted the compressibility factor for gaseous H₂ especially at high pressures, which means that the predicted densities were too low. This is indeed confirmed by our results in Figure 3.3 and Table 3.1.

Table 3.1 Comparison of the average H₂ model pressures p at the experimental density corresponding to 700 bar at 20°C (Figure 3.3 c-d), along with their standard errors and %RMSD.

Models	Exp	HCB LJ-1S	Kö LJ-1S	Ma LJ-1S	Bu LJ-1S	YZ LJ-2S	Bo3 LJ-2S-q _±	Si3 LJ-2S-q _±	Be5 LJ-3S-q _±
p / bar	700	675.9 ± 0.4	726.2 ± 0.4	682.2 ± 0.3	690.0 ± 0.3	698 ± 1	682.9 ± 0.9	821.1 ± 0.9	719 ± 4
%RMSD	0	3.4	3.7	2.5	1.4	0.3	2.4	17.3	2.7

As mentioned before, the target temperature T in each model system is maintained by loose-coupling to a heat bath with a typical value for the relaxation time (0.1 ps) which strongly limits the extent of its fluctuations [211]. The MD simulations output this average temperature T obtained from all degrees of freedom, but it is also possible to record the average translational temperature T_{trans} obtained from just the translational degrees of freedom of the COM of the molecules. Unlike T , T_{trans} is not controlled by loose-coupling and its variations will reflect the exchanges of kinetic energy between the translational and rotational degrees of freedom, which are mostly due to collisions in the gas phase. For the four one-site models, which only have translational degrees of freedom, these two temperatures are rigorously the same. However, for the YZ LJ-2S, Bo3 LJ-2S-q_±, Si3 LJ-2S-q_± and Be5 LJ-3S-q_± models, which contain both translational and rotational degrees of freedom, T and T_{trans} can be different at any particular instant but, within errors, their average should be the same if the systems are sufficiently equilibrated and the kinetic energy is correctly equipartitioned between the degrees of freedom. At low densities, there are relatively infrequent collisions, so the equipartitioning of the kinetic energy is slower and T_{trans} fluctuates quite a lot. This is less of a problem as the density increases as the collision frequency also increases. However, it is important to monitor the equipartition as it directly impacts the reliability of the average pressures obtained.

Equipartition was systematically checked and, as an example, Figure 3.4 presents the averages of the two temperatures as a function of density for the most sophisticated model, *i.e.* the five-site Be5 LJ-3S-q \pm , at 20°C along with their standard errors. The equivalence of T and T_{trans} holds true in the majority of cases and indicates that the simulations are sufficiently long to ensure equipartition. Discrepancies outside of the estimated standard error bars in the odd exceptions are not particularly large, considering the expanded scale of Figure 3.4, and are purely statistical in nature.

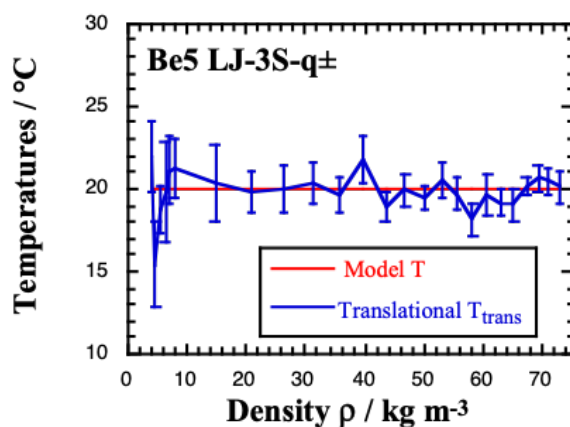


Figure 3.4 Temperatures vs. H₂ density for the Be5 LJ-3S-q \pm model at 20°C showing both the average model temperature T (evaluated from all degrees of freedom) and the average translational temperature T_{trans} (evaluated from just the translational degrees of freedom of the COM). Unlike for T_{trans} , the standard errors for T are all less than 0.002 °C and are thus not visible.

To classify the eight models with respect to the experimental pressure-density data (white squares in Figure 3.3), the $RMSD$ (Eq. 3.6) and $\%RMSD$ (Eq. 3.7) were calculated at the three temperatures under study (Table 3.2). The detailed percentage differences between model and experimental pressures over the whole range of densities tested are provided in Figure S3.2.

Table 3.2 The *RMSD* and *%RMSD* of the model pressures p with respect to the experimental references.

Models	-50°C		20°C		90°C	
	<i>RMSD</i> / bar	<i>%RMSD</i>	<i>RMSD</i> / bar	<i>%RMSD</i>	<i>RMSD</i> / bar	<i>%RMSD</i>
HCB LJ-1S	96.1	6.7	55.6	3.8	32.5	2.2
Kö LJ-1S	51.9	3.8	56.5	3.9	56.3	3.8
Ma LJ-1S	71.1	5.1	34.9	2.5	15.4	1.2
Bu LJ-1S	52.6	3.7	21.9	1.5	5.6	0.4
YZ LJ-2S	51.3	3.2	19.5	1.2	3.0	0.4
Bo3 LJ-2S-q_±	92.2	6.1	49.9	3.2	27.0	1.7
Si3 LJ-2S-q_±	415.3	27.5	343.8	22.5	292.6	19.0
Be5 LJ-3S-q_±	29.4	1.9	46.2	2.9	49.9	3.2

Higher densities lead to increasing discrepancies, and that is reflected both in absolute and in relative terms. As such, it is not surprising that the rankings obtained by using either the *RMSD* or the *%RMSD* are the same. Three models, *i.e.* Kö, Si3 and Be5, tend to overestimate the pressure while the five remaining slightly underestimate it (Figure S3.2). Discrepancies are higher at -50°C and decrease with T . Indeed, at 90°C, the details of the interactions between molecules become less important with respect to the kinetic aspect. At -50°C, the models can be ranked as Be5 > YZ > Bu \approx Kö > Ma > Bo3 > HCB > Si3. At 20°C, the ranking becomes YZ > Bu > Ma > Be5 > Bo3 > HCB \approx Kö > Si3. At 90°C, the ranking is YZ > Bu > Ma > Bo3 > HCB > Be5 > Kö > Si3. While some models such as the Be5 LJ-3S-q_± reproduce well some isotherms but much less others, two models, *i.e.* the two-site model from Yang and Zhong (YZ LJ-2S) and the one-site model derived from Buch (Bu LJ-1S) potential appear to perform very well for all three temperatures considered.

The thermal expansion coefficients α obtained from Eq. 3.1 over the -50°C to 90°C temperature range are shown in Table 3.3 for H₂ pressures of 50 bar (low pressure in reservoir) and 700 bar (fully-fuelled reservoir). At 50 bars, all α are identical as H₂ is close to the ideal gas. At 700 bars, the α are slightly different, but those of the YZ LJ-2S and the Bu LJ-1S remain satisfactorily close to the experimental value.

Table 3.3 The thermal expansion coefficient α calculated over the -50°C to 90°C temperature range at pressures of 50 bar and 700 bar

	Exp.	HCB LJ-1S	Kö LJ-1S	Ma LJ-1S	Bu LJ-1S	YZ LJ-2S	Bo3 LJ-2S-q \pm	Si3 LJ-2S-q \pm	Be5 LJ-3S-q \pm
$\alpha / 10^{-3} \text{ K}$ at 50 bar	3.35	3.36	3.36	3.36	3.36	3.36	3.36	3.38	3.36
$\alpha / 10^{-3} \text{ K}$ at 700 bar	2.54	2.61	2.58	2.61	2.59	2.58	2.60	2.82	2.59 ϵ

3) E. 2. Gas solubilities at -50°C , 20°C and 90°C

Solubility of H_2 in its gas phase is an important parameter for multiphase simulations since the solubility of H_2 in another media (*e.g.* a polymer liner in a gas tank) will be linked to the equilibrium between the gas phase and the other phase. Solubility was calculated from the TPI technique (Eq. 3.2) and compared to the experimental values for S obtained via the fugacities f (Eqs. 3.3 and 3.4). Figure 3.5 displays the solubility isotherms for $T = -50^{\circ}\text{C}$, 20°C and 90°C . The details of the average values for S are also provided in the SI along with their maximum standard errors (see Table S3.4 for -50°C , Table S3.5 for 20°C and Table S3.6 for 90°C).

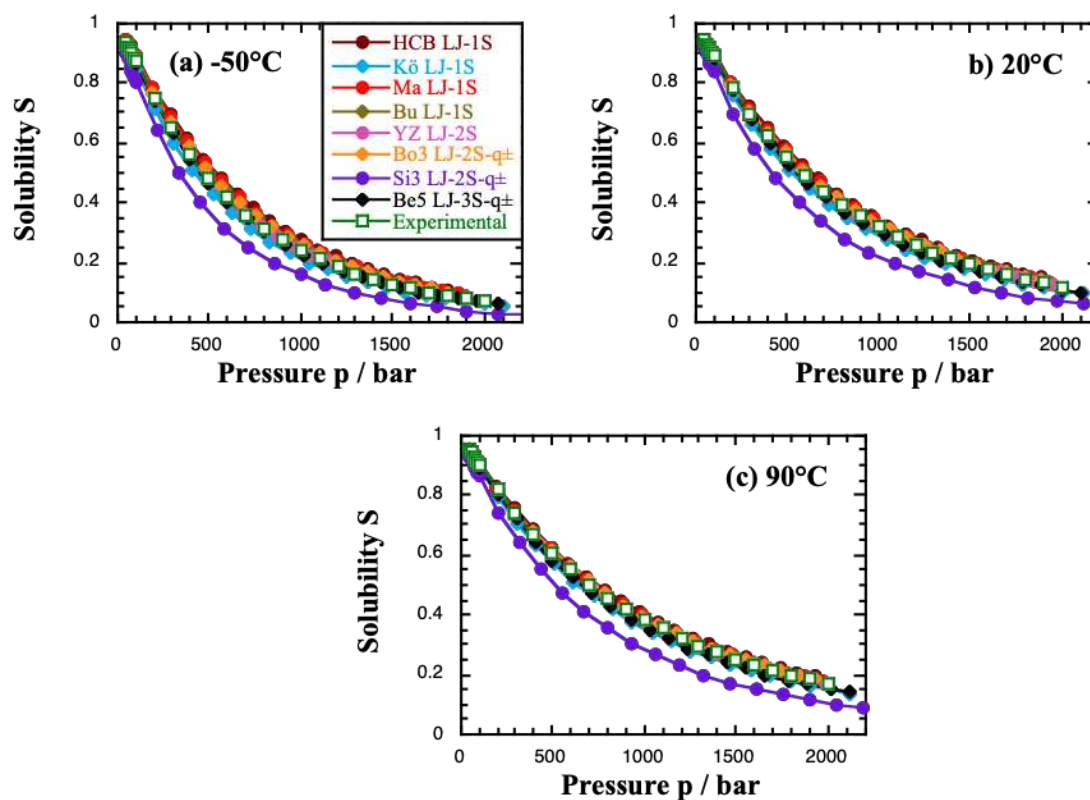


Figure 3.5 H_2 solubility isotherms for all eight models (full symbols) compared to experimental data (white squares) at (a) -50°C , (b) 20°C and (c) 90°C . The legend is the same for all graphs.

Solubility tends to a value of 1 when the gas has a purely ideal behaviour, *i.e.* at the low-pressure limit, and decreases as the density increases. In spite of the possibility of added attractive interactions, S is mostly governed by the increase in overlap probabilities between the inserted test particles and the other H_2 . This is expected from the dominantly repulsive nature of $\text{H}_2\cdots\text{H}_2$ interactions and as such, S decreases (Figure 3.5). At equivalent pressures, solubility is slightly larger at higher temperatures because of the expansion in volume.

All model and experimental S vs p curves overlap for lower densities, *i.e.* up until ~ 100 bars, and tend to slightly diverge afterwards. Differences reflect the fact that the average change in intermolecular potential energy associated with the insertions, $\Delta\Phi$, depends on the model force-field and that discrepancies get more important as the density increases. As expected from its lower densities (Figure 3.3), the Si3 LJ-2S- q_{\pm} model overestimates the repulsions between H_2 , and as such, its S in its own gas phase is lower.

Table 3.4 reports the $RMSD$ (Eq. 3.6) and $\%RMSD$ (Eq. 3.7) for the eight models with respect to the experimental solubility data at the three temperatures under study. It should be noted that, unlike for p (Table 3.2), the S vary only over the fairly narrow 0.1-1 range and there is no tendency for the absolute differences between model and experimental results in the $RMSD$ to increase with density. In relative terms,

the $\%RMSD$ are larger than the ones for p due to the monotonically decreasing value of the solubility. As for the pressures, the detailed percentage differences between model and experimental solubilities over the whole range of densities tested are provided in the SI (Figure S3.3).

Table 3.4 The $RMSD$ and $\%RMSD$ of the model solubility S with respect to the experimental reference values.

Models	-50°C		20°C		90°C	
	$RMSD$	$\%RMSD$	$RMSD$	$\%RMSD$	$RMSD$	$\%RMSD$
HCB LJ-1S	0.05	27.9	0.03	13.2	0.02	6.9
Kö LJ-1S	0.03	14.6	0.03	13.1	0.03	11.5
Ma LJ-1S	0.04	20.5	0.02	8.4	0.01	3.3
Bu LJ-1S	0.02	13.6	0.01	4.6	0.003	0.9
YZ LJ-2S	0.01	8.9	0.01	2.1	0.01	1.5
Bo3 LJ-2S-q_±	0.03	22.3	0.02	9.4	0.01	4.1
Si3 LJ-2S-q_±	0.12	53.6	0.12	45.2	0.12	39.0
Be5 LJ-3S-q_±	0.01	6.9	0.02	9.1	0.03	9.5

It is clear from Table 3.4 that it is easier to distinguish the various models based on the $\%RMSD$ rather than on the $RMSD$, even if both of them vary in the same way. The ranking will thus be given as a function of the $\%RMSD$. As found for the pressure (Figure S3.2), three models (Kö, Si3 and Be5) behave in a different way to the five others, with the former underestimating and the latter slightly overestimating the solubility (Figure S3.3). Based on the $\%RMSD$, at -50°C, the models can be ranked as Be5 > YZ > Bu > Kö > Ma > Bo3 > HCB > Si3. At 20°C, the ranking becomes YZ > Bu > Ma > Be5 > Bo3 > Kö > HCB > Si3. At 90°C, the ranking is Bu > YZ > Ma > Bo3 > HCB > Be5 > Kö > Si3. There again, both models selected from the phase diagram analyses, *i.e.* the two-site YZ LJ-2S and the one-site Bu LJ-1S models, continue to outperform the others for all three temperatures considered.

3) E. 3. Gas diffusion coefficients at -50°C, 20°C and 90°C

The model self-diffusion coefficients of H₂ were obtained from the plots of the MSD/6t (Eq. 3.5). However, the reference experimental data on an extended pressure range are limited, so the closest temperatures for which they were found are -60°C instead of -50°C, 23°C instead of 20°C and 99°C instead

of 90°C [257]. The results are presented on a logarithmic scale in Figure 3.6, with the experimental points being displayed in white squares.

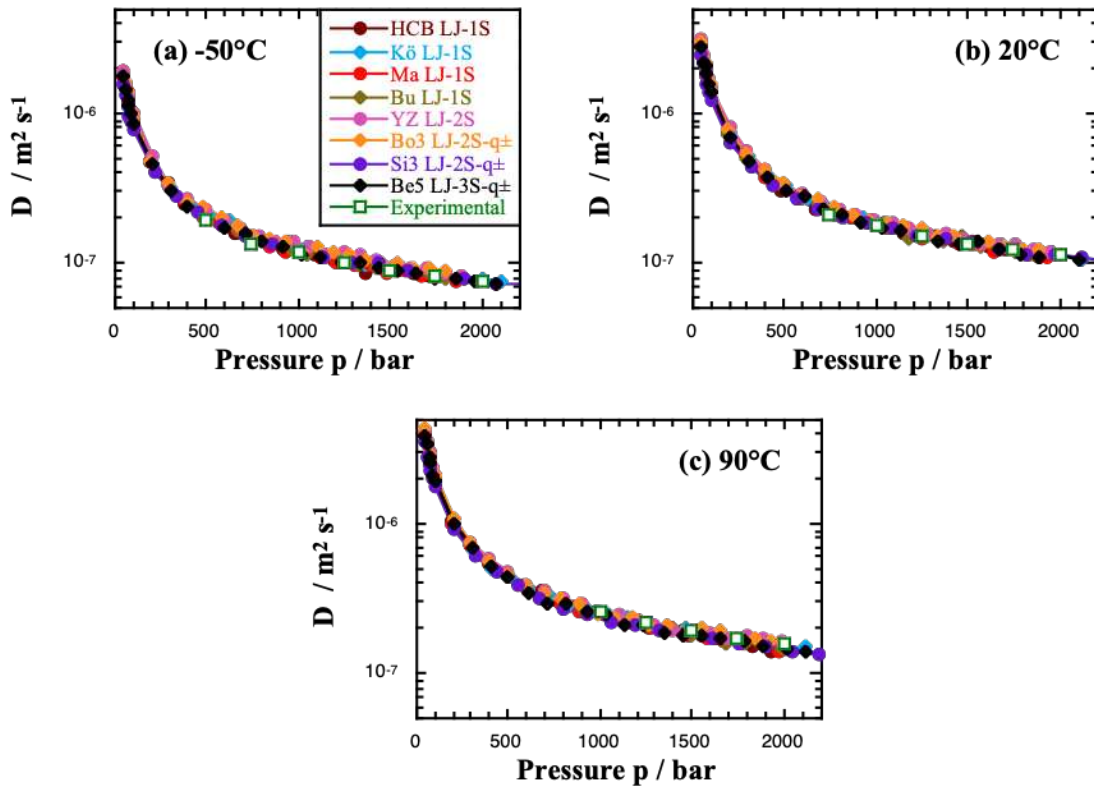


Figure 3.6 H_2 diffusion coefficients for all eight models (full symbols) compared to experimental data (white squares) at (a) -50°C , (b) 20°C and (c) 90°C . The experimental data are those found at the closest temperatures [257] and the legend is the same for all three graphs.

As expected, D decreases with increasing pressure and decreasing temperature since the mobility of H_2 is restricted both with higher densities and with lower temperatures. Figure 3.6 shows that all model curves merge with the experimental data, even if these are at slightly different temperatures [257]. The $RMSD$ (Eq. 3.6) have an order of magnitude of $\approx 10^{-8}$, hence a hierarchy is difficult to establish. It is clear that the eight models cannot be separated based on the diffusion, which appears to be insensitive to the anisotropy of some of the models and kinetically-dominated. Indeed, kinetic theory predicts that D should be inversely proportional to the density ρ at a fixed T (Equation 3.8) [258]:

$$D = \frac{3}{8\sigma_{HS}^2\rho} \sqrt{\frac{mk_B T}{\pi}} \quad (3.8)$$

with σ_{HS} being the T -dependent hard-sphere diameter. As the eight specific model D at a particular ρ and T are very similar (Figure 3.6), they were averaged together and the resulting $\langle D_{8\text{models}} \rangle$ as a function of ρ

and T were fitted to the form of Eq. 3.8. Figure 3.7 shows the $\langle D_{8\text{models}} \rangle$ vs ρ points (symbols) over the range of conditions tested along with the non-linear least-squares regression fits to the kinetic prediction (Eq. 3.8, lines).

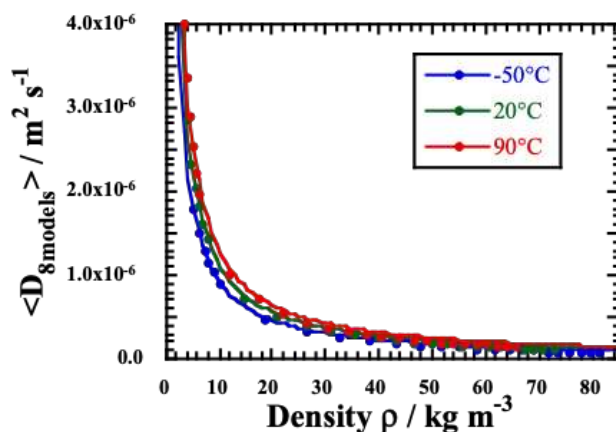


Figure 3.7 The average 8-model diffusion coefficients as a function of density at -50°C , 20°C and 90°C . The full circles are the actual $\langle D_{8\text{models}} \rangle$ obtained from the simulations and the lines are fits to the kinetic theory prediction by non-linear least squares regression.

Figure 3.7 confirms that the diffusion coefficients follow the $1/\rho$ behaviour predicted by the kinetic theory and as such, that they are not sensitive to the details of the interactions between molecules. The best-fit values to Eq. 3.8 for the hard-sphere diameters σ_{HS} are found to be 2.711 \AA , 2.637 \AA and 2.597 \AA at -50°C , 20°C and 90°C , respectively. Related transport properties include the shear viscosity and thermal conductivity [227], but as for diffusion (Figures 3.6 and 3.7), these properties will be dominated by kinetic effects in the range of temperatures and pressures relevant to the on-board storage of hydrogen. As such, they are also unlikely to help to distinguish between the eight models.

3) F. Conclusions

The aim of this study was to select the most appropriate model of hydrogen for the application related to the current work. Eight well-known classical rigid H_2 models based on Lennard-Jones (LJ) 12-6 terms for the van der Waals interactions, and hence easier to transfer to multiphase simulations than potentials based on more sophisticated forms, were pre-selected. In spite of their relative simplicity, they still have to reproduce reasonably well the pVT phase diagram as well as the mobility and solubility of H_2 in its gas phase. The long-term interest being H_2 for fuel-cell-powered electric vehicles, the temperatures and pressures tested were directly linked to those of interest for on-board hydrogen storage tanks, *i.e.* (i) a range of -50°C to $+90^\circ\text{C}$ for T and (ii) a range of 50 to 2000 bars for p .

Most models were found to be quite performant, behaving as expected as a function of pressure and temperature. The diffusion coefficients of the molecules in the gas phase were very similar for all models and, as such, they could not be used as a criterion for the choice of an optimum model. However, differences were detected in the pVT diagram and the solubility, especially at the highest pressures. The $RMSD$ and $\%RMSD$ in Tables 3.2 and 3.4 show that discrepancies decrease at the highest temperatures, where the details of the interactions between molecules are less important with respect to the kinetic aspect.

Among the eight models tested, the HCB LJ-1S, Kö LJ-1S and the Si3 LJ-2S- q_{\pm} were found to be the furthest from experimental data. The latter underestimated the H_2 gas densities more than the others, but this problem had already been identified by the authors [228]. The Ma LJ-1S, Bo3 LJ-2S- q_{\pm} and Be5 LJ-3S- q_{\pm} [215, 217, 245] models had an intermediate behaviour. On the other hand, two models, *i.e.* the two-site model from Yang and Zhong (YZ LJ-2S) [221] and the one-site model derived from Buch (Bu LJ-1S) [218], performed very well for all three temperatures and twenty-five pressures considered. As the latter model was considered without its original weak quadrupole-quadrupole interaction (see previous section), it was chosen to use the YZ LJ-2S model. However, both of them could have been used with confidence, at least for the properties under study. They are clearly a good compromise between realism, simplicity and computational efficiency. These advantages are important for the modelling where they will have to be confronted to the different cross-linked network models (cf. Chapter 5).

3) G. Supporting information

Typical simulation runs, average MD model pressures and solubilities along with their standard errors, differences between average model and experimental pressures and solubilities as a function of densities are presented in the next Figures and Tables.

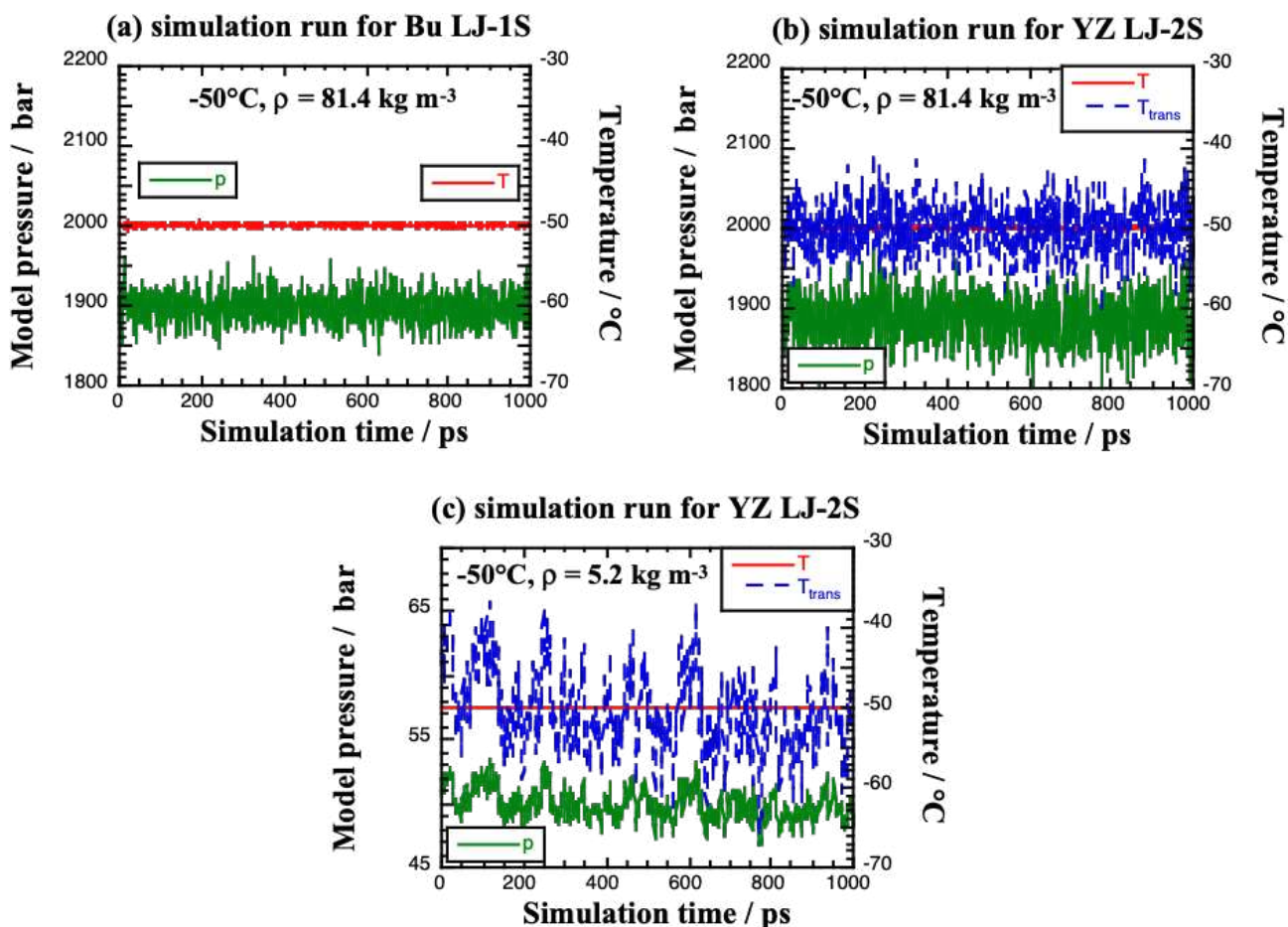


Figure S3.1 Typical 1000-ps simulation runs at -50°C for (a) the one-site Bu model at a high density and (b-c) the two-site YZ model at a high and at a low density, respectively, showing the equilibration of the model pressure p (left axis), temperature T (right axis) and translational temperature T_{trans} (right axis). The latter two, which are identical for the one-site model, will be different for a molecular model, but their average should be the same if the kinetic energy is properly equipartitioned between the translational and rotational degrees of freedom. This is the case here and properties could thus be averaged over the last 500 ps.

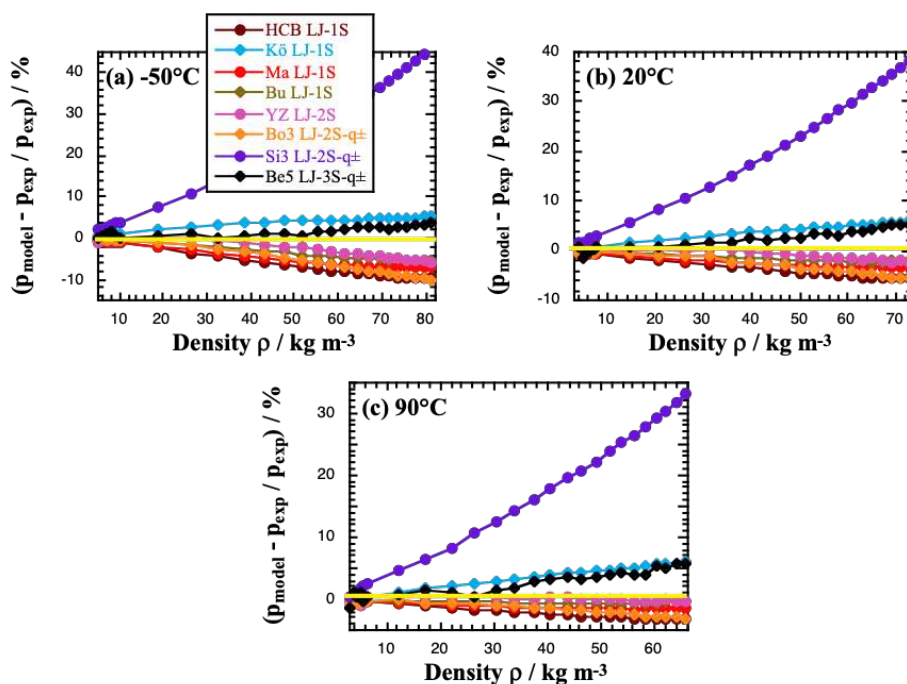


Figure S3.2 Percentage differences between the average model p_{model} and experimental p_{exp} pressures for H_2 (Tables S3.1-S3.2-S3.3) as a function of the fixed densities for all eight models and all temperatures under study. Please note that the scale is different for each plot and that a yellow line at 0% is added as a guide for the eye.

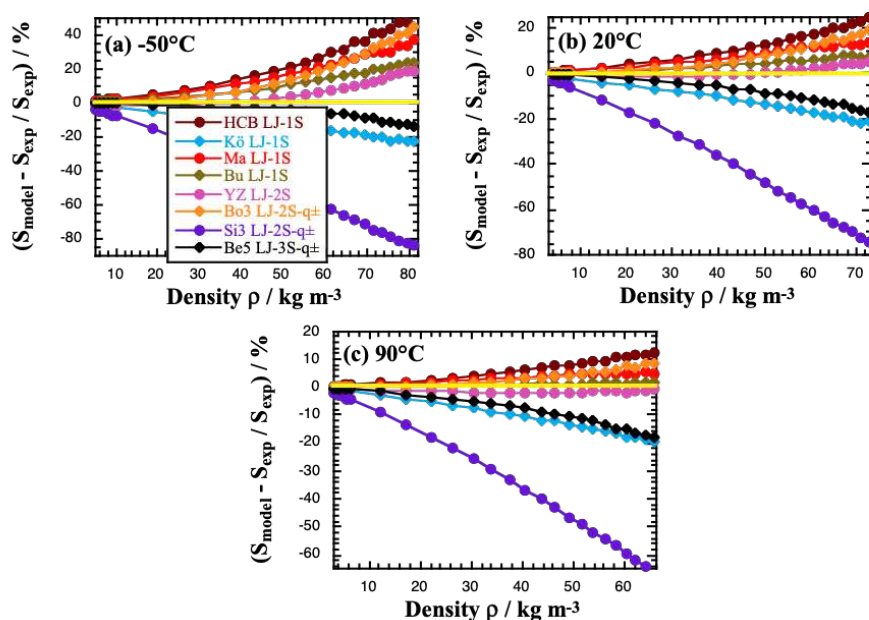


Figure S3.3 Percentage differences between the average model S_{model} and experimental S_{exp} solubilities (Tables S3.4-S3.5-S3.6) as a function of the fixed densities for all eight models and all temperatures under study. Please note that the scale is different for each plot and that a yellow line at 0% is added as a guide for the eye

Table S3.1 The average model pressures p in bars along with their standard errors obtained from the NVT MD simulations at -50°C . The fixed densities are given in the first column.

Exp. density / kg m^{-3}	Exp. Press. / bar	HCB LJ-1S model [212]	Kö LJ-1S model [225]	Ma LJ-1S model [215]	Bu LJ-1S model [218]	YZ LJ-2S model [259]	Bo3 LJ-2S- q_{\pm} model [217]	Si3 LJ-2S- q_{\pm} model [228]	Be5 LJ-3S- q_{\pm} model [245]
5.2521	50	49.63±0.01	50.28±0.01	49.64±0.02	49.80±0.01	49.6±0.2	49.9±0.2	51.2±0.2	50.0±0.3
6.2589	60	59.50±0.01	60.40±0.01	59.54±0.02	59.76±0.01	60.2±0.2	60.1±0.3	61.3±0.2	60.2±0.3
7.2513	70	69.35±0.02	70.57±0.02	69.41±0.03	69.71±0.02	69.8±0.4	69.8±0.3	72.0±0.2	70.6±0.4
8.229	80	79.13±0.02	80.77±0.03	79.27±0.03	79.60±0.03	79.9±0.2	79.9±0.3	82.4±0.3	81.1±0.6
9.1923	90	88.99±0.02	90.99±0.03	89.11±0.03	89.49±0.03	89.7±0.3	89.4±0.3	93.3±0.3	90.5±0.7
10.141	100	98.75±0.03	101.20±0.04	98.91±0.05	99.36±0.04	100.2±0.4	99.7±0.3	103.5±0.3	99.8±0.8
18.864	200	195.4±0.1	204.42±0.06	196.0±0.1	197.65±0.08	200.0±0.5	197.9±0.5	215.0±0.5	201.4±0.8
26.336	300	289.6±0.2	308.7±0.1	291.4±0.2	294.8±0.1	299.7±0.6	294.5±0.6	332.8±0.5	303.7±2.1
32.776	400	382.6±0.2	413.0±0.3	385.7±0.2	391.0±0.3	398.7±0.8	389.8±0.7	454.6±0.8	400.9±1.2
38.384	500	474.3±0.3	518.4±0.3	478.5±0.3	486.5±0.4	494.8±0.8	483.8±0.6	585.6±0.8	503.4±2.3
43.321	600	564.9±0.3	623.5±0.3	571.3±0.4	581.2±0.5	590.8±0.9	576.2±0.6	717.8±1.2	605.1±3.3
47.712	700	654.8±0.4	728.7±0.3	664.1±0.4	676.0±0.4	686.7±0.9	667.0±1.1	857.1±1.2	708.3±2.5
51.658	800	744.0±0.5	834.2±0.4	754.8±0.5	768.0±0.3	782.2±0.7	756.2±1.1	998.8±1.0	803.4±2.8
55.234	900	832.6±0.5	939.0±0.5	847.3±0.7	862.2±0.4	875.6±1.2	845.4±1.0	1139.4±1.2	913.4±3.0
58.503	1000	921.5±0.7	1044.0±0.5	938.2±0.6	956.9±0.5	968.4±1.1	934.9±1.1	1289.4±1.6	1018.2±4.0
61.512	1100	1009.5±0.5	1149.3±0.5	1029.9±0.6	1048.9±0.9	1060.1±0.8	1022.5±1.3	1439.4±1.2	1121.7±3.4
64.299	1200	1097.4±0.7	1254.0±0.7	1121.8±0.9	1143.0±0.6	1154.7±0.9	1109.6±0.9	1594.0±1.5	1230.6±3.1
66.895	1300	1187.1±0.6	1360.9±0.7	1212.7±0.7	1236.4±0.7	1244.4±1.0	1196.3±1.0	1749.0±1.4	1331.7±3.7
69.326	1400	1275.0±0.7	1466.5±0.7	1304.7±0.6	1329.4±0.9	1336.9±1.4	1284.5±1.5	1908.4±1.7	1437.4±3.8
71.611	1500	1362.8±0.6	1572.1±0.8	1398.4±0.6	1423.9±0.9	1426.1±1.5	1370.9±1.9	2070.3±1.9	1534.3±5.3
73.769	1600	1450.7±1.0	1679.1±0.7	1489.3±1.2	1519.4±0.8	1520.7±1.3	1456.9±1.1	2233.5±1.3	1643.8±3.6
75.814	1700	1540.9±1.0	1784.0±0.7	1583.1±0.8	1612.3±0.8	1611.6±1.7	1545.4±1.2	2401.4±1.5	1747.8±3.7
77.757	1800	1629.1±0.9	1890.5±0.8	1675.5±1.0	1707.5±0.9	1703.1±2.0	1629.0±1.4	2570.2±1.4	1855.2±7.0
79.61	1900	1718.5±1.0	1997.5±1.4	1769.3±1.1	1801.8±0.9	1796.3±1.8	1718.8±1.4	2739.9±1.8	1960.6±6.6
81.38	2000	1807.2±0.9	2105.5±1.1	1864.7±1.0	1896.6±1.0	1884.3±1.7	1800.2±1.5	2912.8±2.3	2071.7±5.3

Table S3.2 The average model pressures p in bars along with their standard errors obtained from the NVT MD simulations at 20°C. The fixed densities are given in the first column.

Exp. density / kg m ⁻³	Exp. Press. / bar	HCB LJ-1S model [212]	Kö LJ-1S model [225]	Ma LJ-1S model [215]	Bu LJ-1S model [218]	YZ LJ-2S model [259]	Bo3 LJ-2S-q± model [217]	Si3 LJ-2S-q± model [228]	Be5 LJ-3S-q± model [245]
4.015	50	49.77±0.01	50.15±0.01	49.79±0.01	49.88±0.01	49.9±0.2	49.7±0.3	50.8±0.3	50.3±0.4
4.790	60	59.69±0.01	60.24±0.01	59.71±0.01	59.82±0.02	60.3±0.2	59.8±0.2	61.0±0.3	59.1±0.6
5.555	70	69.61±0.02	70.35±0.01	69.66±0.02	69.80±0.02	69.6±0.2	69.7±0.2	71.2±0.3	69.7±0.4
6.311	80	79.47±0.01	80.51±0.02	79.55±0.02	79.76±0.02	79.8±0.4	80.4±0.3	81.9±0.3	80.0±0.8
7.059	90	89.39±0.02	90.60±0.02	89.51±0.02	89.71±0.02	90.0±0.3	89.5±0.3	91.8±0.3	90.4±0.7
7.797	100	99.25±0.04	100.78±0.02	99.39±0.03	99.63±0.02	100.3±0.3	99.7±0.3	102.8±0.3	100.7±0.6
14.707	200	197.4±0.1	203.1±0.1	197.9±0.1	198.88±0.07	200.1±0.5	198.7±0.5	211.6±0.6	201.4±1.7
20.840	300	294.8±0.2	306.6±0.1	295.7±0.1	297.7±0.1	300.8±0.5	297.2±0.8	324.9±0.7	302.7±1.3
26.309	400	390.7±0.2	410.8±0.2	393.0±0.2	396.2±0.2	399.9±0.6	396.1±0.6	442.6±0.7	404.6±2.0
31.219	500	486.3±0.2	515.2±0.3	489.6±0.2	494.3±0.2	500.5±0.8	493.7±0.7	564.8±0.8	508.0±2.3
35.656	600	581.2±0.2	620.6±0.3	586.3±0.4	592.1±0.3	600.9±0.7	587.0±0.9	691.0±1.0	609.8±2.3
39.693	700	675.9±0.4	726.2±0.4	682.2±0.3	690.0±0.3	697.6±1.2	682.9±0.9	821.1±0.9	719.0±3.5
43.388	800	769.0±0.5	831.7±0.3	778.5±0.5	787.2±0.3	795.0±1.4	777.6±1.2	952.0±1.3	815.2±2.4
46.790	900	863.0±0.3	938.1±0.4	874.1±0.4	884.1±0.4	893.6±1.1	872.6±1.2	1092.6±1.5	923.3±3.1
49.939	1000	955.6±0.6	1044.5±0.5	969.8±0.5	981.7±0.5	990.0±1.3	964.7±1.2	1228.6±1.3	1026.5±2.9
52.868	1100	1049.0±0.6	1150.6±0.7	1065.5±0.5	1079.0±0.8	1089.2±1.7	1059.8±1.2	1373.6±1.4	1136.4±4.1
55.605	1200	1142.6±0.7	1257.4±0.6	1160.3±0.5	1175.6±0.5	1184.3±1.4	1153.3±1.3	1519.5±1.3	1239.1±4.1
58.173	1300	1235.1±0.5	1364.2±0.8	1257.4±0.6	1273.3±0.6	1281.6±1.1	1247.4±1.2	1666.9±1.5	1338.9±4.8
60.592	1400	1328.9±0.6	1472.5±0.9	1353.5±0.7	1369.5±0.7	1378.5±0.9	1338.7±1.0	1817.6±1.5	1451.0±6.3
62.878	1500	1420.4±1.1	1578.4±0.5	1449.4±0.8	1468.0±0.9	1471.4±2.4	1430.1±1.5	1970.1±1.4	1557.0±4.0
65.045	1600	1514.3±1.0	1686.1±0.8	1544.2±0.9	1565.4±0.8	1573.0±2.1	1523.7±1.3	2125.1±1.9	1665.0±5.6
67.105	1700	1608.1±1.0	1794.1±0.8	1642.3±0.6	1663.2±0.8	1665.4±1.7	1616.8±1.6	2283.5±1.9	1780.8±3.4
69.070	1800	1699.4±0.9	1900.8±0.8	1739.7±0.7	1761.4±0.7	1760.7±1.8	1704.6±2.0	2441.2±1.4	1892.3±5.3
70.947	1900	1792.2±1.0	2010.0±1.3	1837.1±0.8	1860.1±1.0	1859.9±1.2	1796.6±2.3	2600.7±1.7	2000.9±5.0
72.744	2000	1886.9±0.9	2118.4±1.2	1933.3±0.9	1958.9±1.0	1952.6±1.8	1893.0±1.5	2766.1±2.2	2107.7±7.8

Table S3.3 The average model pressures p in bars along with their standard errors obtained from the NVT MD simulations at 90°C. The fixed densities are given in the first column.

Exp. density / kg m ⁻³	Exp. Press. / bar	HCB LJ-1S model [212]	Kö LJ-1S model [225]	Ma LJ-1S model [215]	Bu LJ-1S model [218]	YZ LJ-2S model [259]	Bo3 LJ-2S-q± model [217]	Si3 LJ-2S-q± model [228]	Be5 LJ-3S-q± model [245]
3.2544	50	49.82±0.01	50.09±0.01	49.85±0.01	49.90±0.01	49.8±0.3	49.7±0.2	50.2±0.2	49.3±0.4
3.8856	60	59.77±0.01	60.15±0.01	59.81±0.01	59.86±0.01	59.7±0.4	60.2±0.4	60.5±0.3	60.7±0.2
4.5105	70	69.68±0.02	70.23±0.02	69.78±0.01	69.86±0.01	70.1±0.4	69.6±0.3	70.7±0.3	70.3±0.8
5.129	80	79.65±0.02	80.32±0.01	79.73±0.02	79.81±0.01	79.1±0.3	79.5±0.2	81.4±0.3	80.7±0.7
5.7413	90	89.58±0.02	90.38±0.02	89.64±0.02	89.79±0.02	89.7±0.3	89.8±0.2	92.0±0.4	89.6±0.4
6.3475	100	99.53±0.03	100.54±0.02	99.59±0.02	99.79±0.02	100.3±0.2	99.6±0.3	102.5±0.4	100.5±0.4
12.087	200	198.4±0.1	202.3±0.1	199.0±0.1	199.50±0.07	201.1±0.7	200.0±0.6	209.1±0.4	201.3±1.3
17.291	300	296.7±0.1	305.2±0.1	297.8±0.1	299.0±0.1	300.7±0.6	298.0±0.6	319.8±0.6	304.7±1.5
22.029	400	394.5±0.1	408.9±0.1	396.2±0.1	398.5±0.2	401.6±1.0	397.5±0.7	433.2±1.1	403.8±2.5
26.363	500	492.1±0.2	513.0±0.2	494.9±0.2	497.8±0.2	501.8±1.0	496.0±0.7	553.3±0.6	502.5±1.9
30.347	600	589.0±0.3	617.7±0.3	593.3±0.2	597.3±0.3	602.0±1.2	594.6±0.7	674.3±0.9	608.8±3.1
34.027	700	685.6±0.2	723.7±0.4	691.1±0.3	696.4±0.3	700.4±1.2	692.6±1.1	799.1±1.1	713.2±3.5
37.44	800	781.7±0.4	829.3±0.4	789.2±0.4	795.4±0.4	801.6±1.1	788.1±0.8	927.7±1.0	822.0±5.1
40.62	900	878.2±0.4	935.2±0.4	887.1±0.5	895.2±0.3	904.4±1.3	887.4±1.3	1059.4±1.2	930.2±4.9
43.593	1000	975.4±0.3	1041.4±0.5	985.5±0.5	994.9±0.6	1004.2±1.8	982.8±1.5	1195.1±1.5	1034.7±3.5
46.384	1100	1070.1±0.5	1147.3±0.7	1083.1±0.6	1092.7±0.6	1100.0±1.6	1080.5±1.3	1328.4±1.3	1137.3±5.6
49.011	1200	1167.2±0.6	1255.1±0.4	1182.2±0.7	1192.5±0.4	1200.9±1.5	1174.8±1.1	1466.6±1.6	1241.7±5.4
51.493	1300	1261.5±0.6	1362.5±0.7	1280.7±0.5	1292.1±0.6	1299.3±1.5	1271.1±1.4	1609.0±1.2	1350.8±4.3
53.844	1400	1358.6±0.6	1469.5±0.7	1378.5±0.7	1391.8±0.7	1399.2±1.4	1368.9±1.7	1754.1±2.1	1459.3±4.2
56.077	1500	1454.4±0.9	1577.7±0.6	1476.4±0.6	1492.0±0.6	1496.2±1.6	1463.4±1.1	1898.0±2.3	1561.7±7.0
58.203	1600	1549.8±0.6	1686.1±0.7	1577.5±0.6	1591.8±0.9	1597.3±1.3	1557.3±1.7	2044.0±2.2	1663.0±5.2
60.233	1700	1645.3±0.9	1795.0±1.0	1674.6±0.7	1689.8±0.9	1694.9±1.3	1654.8±1.7	2194.8±1.8	1789.8±6.3
62.174	1800	1741.6±1.1	1903.3±0.9	1773.7±0.9	1791.8±0.7	1798.6±1.8	1747.8±1.5	2347.2±1.4	1891.4±5.1
64.034	1900	1837.4±0.8	2011.4±0.7	1874.3±0.6	1891.0±0.6	1891.7±1.9	1844.5±1.5	2500.5±2.1	2011.5±6.7
65.821	2000	1933.2±0.8	2121.7±1.0	1972.9±1.0	1992.0±1.2	1992.6±1.6	1938.9±1.7	2660.6±3.0	2116.1±6.6

Table S3.4 The average model solubilities S obtained from the TPI analyses at -50°C . The maximum standard error is 0.001 and the fixed densities are given in the first column.

Exp. density / kg m^{-3}	Exp. Press. / bar	Exp. solubilities	HCB LJ-1S model [212]	Kö LJ-1S model [225]	Ma LJ-1S model [215]	Bu LJ-1S model [218]	YZ LJ-2S model [259]	Bo3 LJ-2S- q_{\pm} model [217]	Si3 LJ-2S- q_{\pm} model [228]	Be5 LJ-3S- q_{\pm} model [245]
5.2521	50	0.9343	0.9448	0.9201	0.9435	0.9384	0.9291	0.9358	0.8978	0.9311
6.2589	60	0.9214	0.9338	0.9048	0.9323	0.9263	0.9154	0.9233	0.8782	0.9176
7.2513	70	0.9087	0.9229	0.8894	0.9211	0.9140	0.9018	0.9110	0.8588	0.9042
8.229	80	0.8960	0.9121	0.8745	0.9100	0.9022	0.8884	0.8988	0.8400	0.8909
9.1923	90	0.8834	0.9012	0.8598	0.8988	0.8902	0.8752	0.8865	0.8214	0.8779
10.141	100	0.8709	0.8906	0.8452	0.8879	0.8785	0.8623	0.8747	0.8030	0.8648
18.864	200	0.7524	0.7880	0.7121	0.7825	0.7669	0.7421	0.7628	0.6375	0.7432
26.336	300	0.6479	0.6958	0.5997	0.6885	0.6694	0.6396	0.6664	0.5034	0.6365
32.776	400	0.5580	0.6143	0.5066	0.6054	0.5838	0.5544	0.5841	0.3976	0.5451
38.384	500	0.4814	0.5436	0.4312	0.5334	0.5106	0.4819	0.5135	0.3146	0.4675
43.321	600	0.4165	0.4815	0.3677	0.4700	0.4484	0.4203	0.4534	0.2481	0.4035
47.712	700	0.3613	0.4268	0.3139	0.4153	0.3937	0.3680	0.4014	0.1966	0.3473
51.658	800	0.3143	0.3812	0.2714	0.3676	0.3488	0.3252	0.3565	0.1571	0.3009
55.234	900	0.2743	0.3395	0.2328	0.3258	0.3076	0.2872	0.3179	0.1242	0.2609
58.503	1000	0.2400	0.3039	0.2012	0.2908	0.2719	0.2540	0.2829	0.1001	0.2260
61.512	1100	0.2105	0.2733	0.1758	0.2583	0.2424	0.2253	0.2550	0.0794	0.1984
64.299	1200	0.1852	0.2429	0.1528	0.2301	0.2146	0.2018	0.2292	0.0632	0.1727
66.895	1300	0.1632	0.2216	0.1339	0.2064	0.1907	0.1796	0.2056	0.0515	0.1500
69.326	1400	0.1442	0.1964	0.1171	0.1848	0.1700	0.1597	0.1852	0.0409	0.1322
71.611	1500	0.1277	0.1802	0.1026	0.1649	0.1529	0.1441	0.1694	0.0317	0.1169
73.769	1600	0.1133	0.1598	0.0902	0.1471	0.1362	0.1285	0.1528	0.0265	0.1005
75.814	1700	0.1007	0.1449	0.0785	0.1307	0.1217	0.1164	0.1375	0.0212	0.0889
77.757	1800	0.0896	0.1323	0.0707	0.1194	0.1101	0.1049	0.1252	0.0173	0.0781
79.61	1900	0.0799	0.1178	0.0617	0.1065	0.0990	0.0946	0.1130	0.0137	0.0697
81.38	2000	0.0714	0.1075	0.0553	0.0976	0.0882	0.0844	0.1032	0.0114	0.0614

Table S3.5 The average model solubilities S obtained from the TPI analyses at 20°C. The maximum standard error is 0.001 and the fixed densities are given in the first column.

Exp. density / kg m ⁻³	Exp. Press. / bar	Exp. solubilities	HCb LJ-1S model [212]	Kö LJ-1S model [225]	Ma LJ-1S model [215]	Bu LJ-1S model [218]	YZ LJ-2S model [259]	Bo3 LJ-2S-q± model [217]	Si3 LJ-2S-q± model [228]	Be5 LJ-3S-q± model [245]
4.015	50	0.9420	0.9478	0.9326	0.9466	0.9437	0.9386	0.9428	0.9147	0.9382
4.790	60	0.9309	0.9376	0.9197	0.9362	0.9328	0.9268	0.9318	0.8984	0.9263
5.555	70	0.9198	0.9275	0.9069	0.9259	0.9220	0.9152	0.9209	0.8825	0.9145
6.311	80	0.9089	0.9175	0.8944	0.9157	0.9113	0.9038	0.9102	0.8665	0.9029
7.059	90	0.8981	0.9077	0.8819	0.9055	0.9007	0.8925	0.8995	0.8511	0.8913
7.797	100	0.8874	0.8978	0.8698	0.8956	0.8904	0.8811	0.8890	0.8359	0.8799
14.707	200	0.7869	0.8057	0.7574	0.8016	0.7925	0.7775	0.7910	0.6968	0.7737
20.840	300	0.6980	0.7245	0.6607	0.7174	0.7058	0.6883	0.7056	0.5802	0.6809
26.309	400	0.6199	0.6513	0.5775	0.6435	0.6303	0.6117	0.6314	0.4833	0.5997
31.219	500	0.5516	0.5865	0.5067	0.5776	0.5637	0.5441	0.5667	0.4021	0.5293
35.656	600	0.4919	0.5293	0.4463	0.5193	0.5049	0.4861	0.5089	0.3363	0.4673
39.693	700	0.4397	0.4788	0.3945	0.4682	0.4527	0.4357	0.4591	0.2809	0.4154
43.388	800	0.3938	0.4323	0.3488	0.4228	0.4090	0.3910	0.4153	0.2356	0.3680
46.790	900	0.3535	0.3941	0.3088	0.3820	0.3683	0.3515	0.3779	0.1979	0.3275
49.939	1000	0.3180	0.3589	0.2749	0.3464	0.3328	0.3185	0.3423	0.1662	0.2908
52.868	1100	0.2866	0.3258	0.2446	0.3138	0.3013	0.2876	0.3120	0.1392	0.2604
55.605	1200	0.2588	0.2991	0.2185	0.2858	0.2735	0.2614	0.2847	0.1182	0.2337
58.173	1300	0.2341	0.2728	0.1963	0.2605	0.2467	0.2370	0.2601	0.0994	0.2086
60.592	1400	0.2122	0.2488	0.1762	0.2364	0.2260	0.2171	0.2394	0.0842	0.1875
62.878	1500	0.1926	0.2273	0.1577	0.2155	0.2048	0.1975	0.2185	0.0709	0.1676
65.045	1600	0.1750	0.2099	0.1419	0.1959	0.1869	0.1802	0.2014	0.0599	0.1513
67.105	1700	0.1593	0.1918	0.1283	0.1811	0.1714	0.1657	0.1831	0.0512	0.1372
69.070	1800	0.1452	0.1769	0.1146	0.1638	0.1565	0.1510	0.1688	0.0435	0.1224
70.947	1900	0.1326	0.1631	0.1035	0.1493	0.1424	0.1386	0.1556	0.0369	0.1109
72.744	2000	0.1211	0.1507	0.0952	0.1379	0.1301	0.1274	0.1441	0.0311	0.0997

Table S3.6 The average model solubilities S obtained from the TPI analyses at 90°C. The maximum standard error is 0.001 and the fixed densities are given in the first column.

Exp. density / kg m ⁻³	Exp. Press. / bar	Exp. solubilities	HCB LJ-1S model [212]	Kö LJ-1S model [225]	Ma LJ-1S model [215]	Bu LJ-1S model [218]	YZ LJ-2S model [259]	Bo3 LJ-2S-q _± model [217]	Si3 LJ-2S-q _± model [228]	Be5 LJ-3S-q _± model [245]
3.2544	50	0.9497	0.9532	0.9428	0.9521	0.9503	0.9471	0.9500	0.9279	0.9460
3.8856	60	0.9401	0.9441	0.9318	0.9428	0.9407	0.9370	0.9404	0.9141	0.9355
4.5105	70	0.9305	0.9351	0.9209	0.9337	0.9312	0.9270	0.9309	0.9005	0.9252
5.129	80	0.9211	0.9263	0.9102	0.9247	0.9219	0.9170	0.9215	0.8870	0.9150
5.7413	90	0.9118	0.9174	0.8996	0.9157	0.9125	0.9073	0.9122	0.8738	0.9049
6.3475	100	0.9025	0.9088	0.8891	0.9067	0.9033	0.8976	0.9030	0.8608	0.8949
12.087	200	0.8156	0.8267	0.7920	0.8227	0.8170	0.8072	0.8170	0.7409	0.8016
17.291	300	0.7380	0.7529	0.7070	0.7474	0.7399	0.7279	0.7407	0.6374	0.7191
22.029	400	0.6688	0.6873	0.6323	0.6805	0.6713	0.6580	0.6729	0.5492	0.6459
26.363	500	0.6071	0.6280	0.5676	0.6202	0.6097	0.5965	0.6131	0.4737	0.5810
30.347	600	0.5522	0.5747	0.5095	0.5657	0.5559	0.5412	0.5599	0.4090	0.5235
34.027	700	0.5031	0.5274	0.4594	0.5172	0.5067	0.4926	0.5132	0.3539	0.4730
37.44	800	0.4592	0.4833	0.4155	0.4734	0.4631	0.4499	0.4696	0.3062	0.4278
40.62	900	0.4199	0.4459	0.3746	0.4343	0.4232	0.4114	0.4319	0.2656	0.3877
43.593	1000	0.3845	0.4103	0.3395	0.3994	0.3897	0.3766	0.3968	0.2304	0.3514
46.384	1100	0.3527	0.3786	0.3093	0.3664	0.3566	0.3464	0.3665	0.1998	0.3181
49.011	1200	0.3240	0.3492	0.2802	0.3385	0.3266	0.3176	0.3376	0.1734	0.2899
51.493	1300	0.2981	0.3232	0.2553	0.3116	0.3004	0.2925	0.3124	0.1513	0.2638
53.844	1400	0.2746	0.2993	0.2332	0.2875	0.2787	0.2709	0.2896	0.1315	0.2415
56.077	1500	0.2532	0.2774	0.2136	0.2645	0.2568	0.2489	0.2676	0.1149	0.2199
58.203	1600	0.2339	0.2588	0.1947	0.2446	0.2372	0.2306	0.2488	0.1009	0.1997
60.233	1700	0.2162	0.2398	0.1778	0.2261	0.2173	0.2122	0.2323	0.0878	0.1836
62.174	1800	0.2001	0.2233	0.1634	0.2095	0.2029	0.1978	0.2143	0.0761	0.1677
64.034	1900	0.1854	0.2072	0.1500	0.1953	0.1884	0.1832	0.2004	0.0669	0.1539
65.821	2000	0.1720	0.1935	0.1377	0.1803	0.1742	0.1704	0.1859	0.0588	0.1414

3) H. Acknowledgments

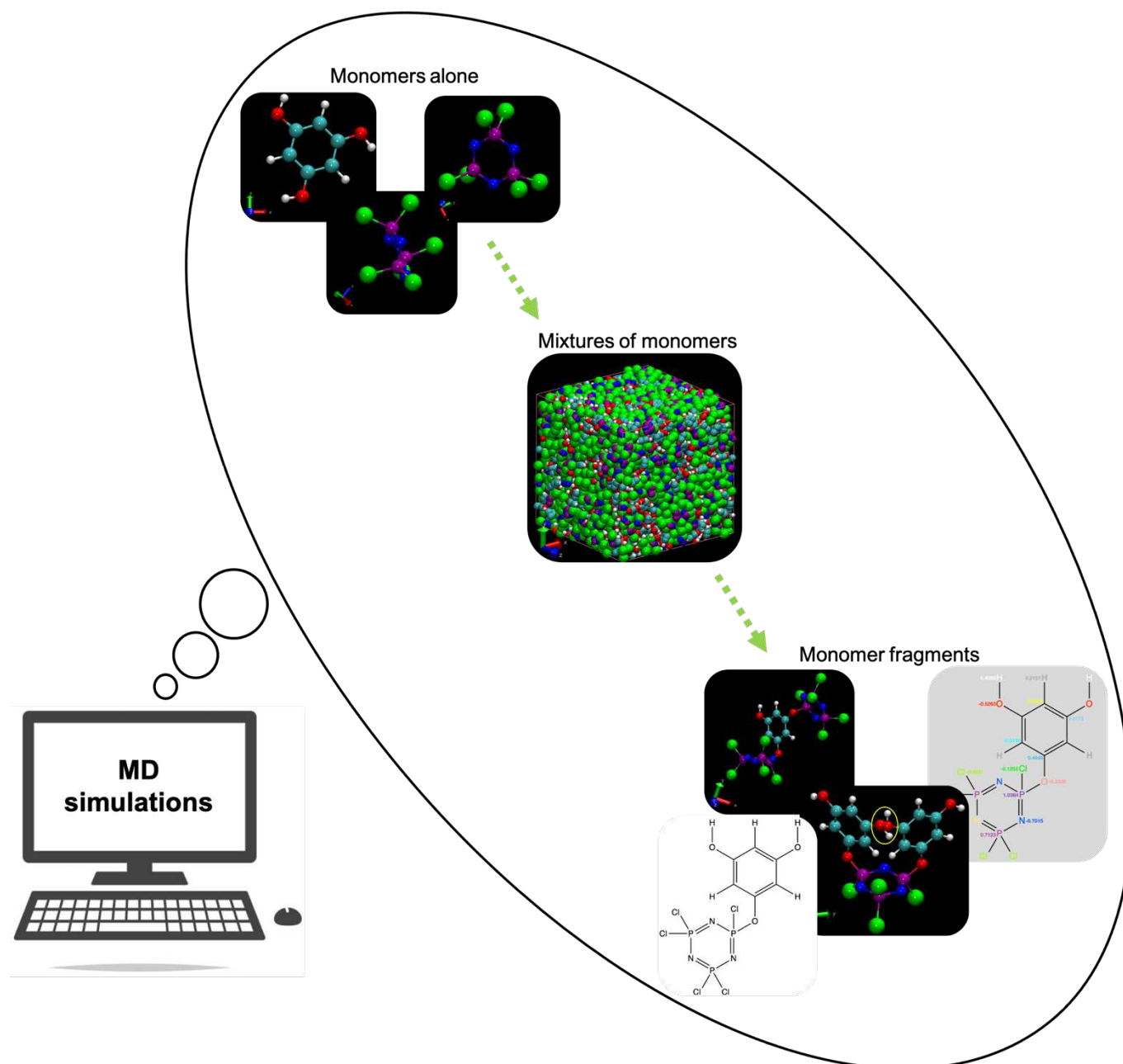
This research forms part of the research programme of DPI, project DINGOES #845. It had access to the HPC resources of TGCC/CINES/IDRIS under the allocations A009-095053 and A011-095053 made by GENCI, France. The MUST computing centre at the University Savoie Mont Blanc, France, is also acknowledged for the provision of computer time. N. Charvin is thanked for his help with the installation and maintenance of the LEPMI local servers.

3) I. Abbreviations list

➤ B-B	Beattie-Bridgeman
➤ COM	Centre-of-mass
➤ EOS	Equation of state
➤ FCEV	Fuel-cell electric vehicles
➤ LJ	Lennard-Jones
➤ MD	Molecular dynamics
➤ MSD	Mean-square displacement
➤ NIST	National Institute of Standards and Technology
➤ PBC	Periodic boundary conditions
➤ RSMD	Root-mean-square difference
➤ TPI	Test particle insertion
➤ VdW	Van der Waals
➤ VMD	Visual Molecular Dynamics

Chapter 4 : Molecular Modelling - Monomer Potentials

4) A. Graphical abstract



Part of this work in this chapter was carried out using the HPC resources of CCRT/CINES/IDRIS under the allocations A011, A013 and A015-095053 made by GENCI, France.

Following the selection of a potential for H₂ and prior to the modelling of a cross-linked layer for H₂ containments, a very thorough investigation first had to be conducted on the monomers. The two monomers concerned were the phosphonitrilic chloride trimer or hexachlorocyclotriphosphazene (HCCP) and 1,2,3-benzenetriol or phloroglucinol (Phg). They were chosen according to a previous work related to gas separation where they were used to synthesize films using IP [133]. Different steps concerning the adaptation of existing force fields or developments from scratch were conducted. Some of these steps were carried out by another member of the team but, as each step is essential for the understanding of the process, they will all be reported in the next Sections (Figure 4.1). In this Chapter, the first two steps in blue will be briefly outlined, whereas the second step in green will be detailed.

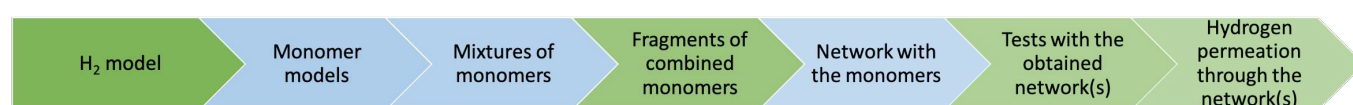


Figure 4.1 Modelling process to obtain hydrogen permeation in a dense polymer network of HCCP and Phg. The first step is detailed in Chapter 3 and the blue steps have been mainly carried out by another member of the project team.

4) B. Pure monomers

As in the previous chapter, the simulations were carried out with the *gmq* package [194], which means that the literature models (if available) had to be adapted to this program.

4) B. 1. General presentation

Phloroglucinol Phg and hexachlorocyclotriphosphazene HCCP were selected according to the previous work of Dr. Radmanesh [260], since they were found to have a surprisingly low permeability coefficient H₂, *i.e.* potentially good barrier properties for hydrogen. Since the aim of the project is to develop a coating film capable of slowing the permeation of this gas out of its container, it was decided to look further into what the corresponding polymer can do in terms of a barrier for this specific application.

4) B. 1. 1. Hexachlorocyclotriphosphazene (HCCP)

Phosphazenes refer to an important class of inorganic cyclic or linear compounds [261] which are formed by the repetition of phosphorus and nitrogen atoms linked by double bonds, *i.e.* (P=N)_n. There are many phosphazene compounds ranging from oligomers to polymers which can also be inorganic-organic

hybrids. Indeed, beside the alternate phosphorus and nitrogen atoms, the P can bond with a large variety of organic or inorganic substituents, as illustrated in Figure 4.2.

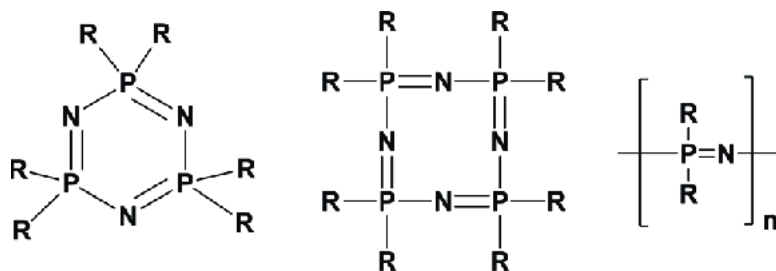


Figure 4.2 Typical phosphazene structures [261].

These materials often display a high flexibility, mechanical strength, durability as well as highly customizable physical and chemical characteristics. They can be tuned according to the substituents bonded to the phosphorus atoms, which will have a significant effect on the final properties of the polymer. Therefore, phosphazenes are used in a variety of fields such as rechargeable batteries, membranes, lubricants, liquid crystals, etc. Among the different phosphazene compounds, derivatives of hexachlorocyclotriphosphazene ($N_3P_3Cl_6$ trimer) and octachlorocyclotetraphosphazene ($N_4P_4Cl_8$ tetramer) are quite interesting as they can give cyclomatrix materials. These are known for their excellent flame-retardant properties but are also used as coatings with biocompatibility or super-hydrophobic properties as well as in sensing and adhesives applications [147, 261]. Moreover, in several previous studies [147, 262], HCCP has been successfully used as a monomer to synthesize cyclomatrix polyphosphazene films *via* interfacial polymerization, demonstrating therefore its ability to be used with this technique. The chemical structure of hexachlorocyclotriphosphazene is given in Figure 4.3, and its main physical and chemical informations are presented in Table 4.1. The experimental characterization techniques used to characterize HCCP were mainly Fourier transform infrared spectroscopy (FTIR) and nuclear magnetic resonance (NMR). Their corresponding spectra for pure HCCP are displayed in Figure 4.4.

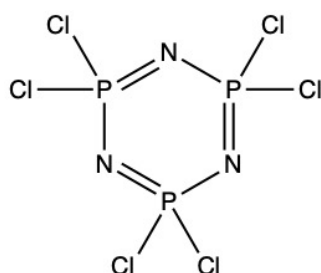



Figure 4.3 Chemical structure of hexachlorocyclotriphosphazene (HCCP) sketched using ChemDraw 20.0 [263].

Table 4.1 Properties and safety data for HCCP [264-266].

Molecular formula	CAS number	Molecular weight	Boiling point	Melting point	Density at 25°C	Refractive index	Safety
Cl ₆ N ₃ P ₃	940-71-6	347.66 g/mol	127°C	110-115°C	2.0 g/ml	1.79	

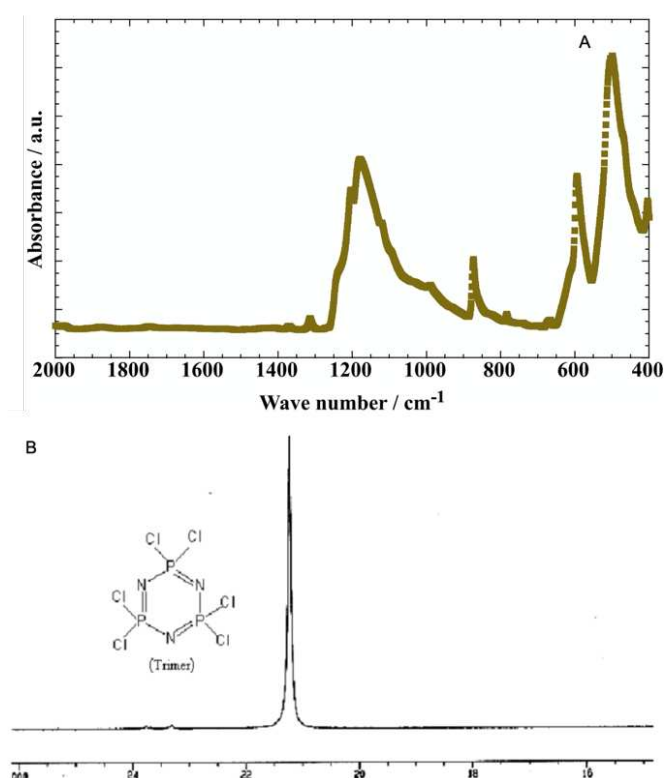


Figure 4.4 FTIR (A) and ³¹P-NMR (B) spectra for pure HCCP. The first was taken *in-situ* and the second from the literature [267].

Concerning its reactivity, cycloliner and cyclomatrix polymers made from HCCP containing six chlorine atoms can be substituted by organic nucleophile compounds such as hydroxyl or amine groups as well as by inorganic groups. If HCCP reacts with di- or trifunctional compounds, it forms a highly cross-linked cyclomatrix polyphosphazene network [268]. Within the IP context, the chlorine atoms can also be substituted by post-functionalization (Chapter 2) [147].

Therefore, its high reactivity associated with a high functionality makes this monomer interesting for the production of hyper-cross-linked networks by IP. In the non-aqueous approach used in this project,

HCCP is dissolved in cyclohexane and reacts with another highly reactive and functional monomer, *i.e.* a compound containing alcohol groups.

4) B. 1. 2. Phloroglucinol (Phg)

Phloroglucinol is a readily available and relatively inexpensive molecule, which is well-known in the pharmaceutical industry [269] since its different properties lead to its use as an antioxidant, antidiabetic, antimicrobial, anti-inflammatory, etc. [270].

Phg is an organic compound from the benzene-triol family and with a high functionality, since it consists of a benzene ring bearing hydroxyl groups at positions 1, 3 and 5 (Figure 4.5) [269]. Its characteristics are provided in Table 4.2.

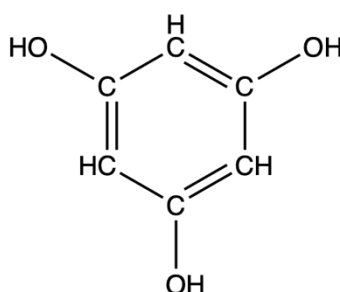


Figure 4.5 Chemical structure of phloroglucinol (Phg) sketched using ChemDraw 20.0 [263].

Table 4.2 Properties and safety data for Phg [271-273].

Molecular formula	CAS number	Molecular weight	Boiling point	Melting point	Density at 25°C	Refractive index	Safety
C ₆ H ₆ O ₃	108-73-6	126.11 g/mol	331.1°C	215-220°C	1.46 g/ml	1.676	

As for HCCP, typical FTIR and NMR spectra are presented for Phg in Figure 4.6.

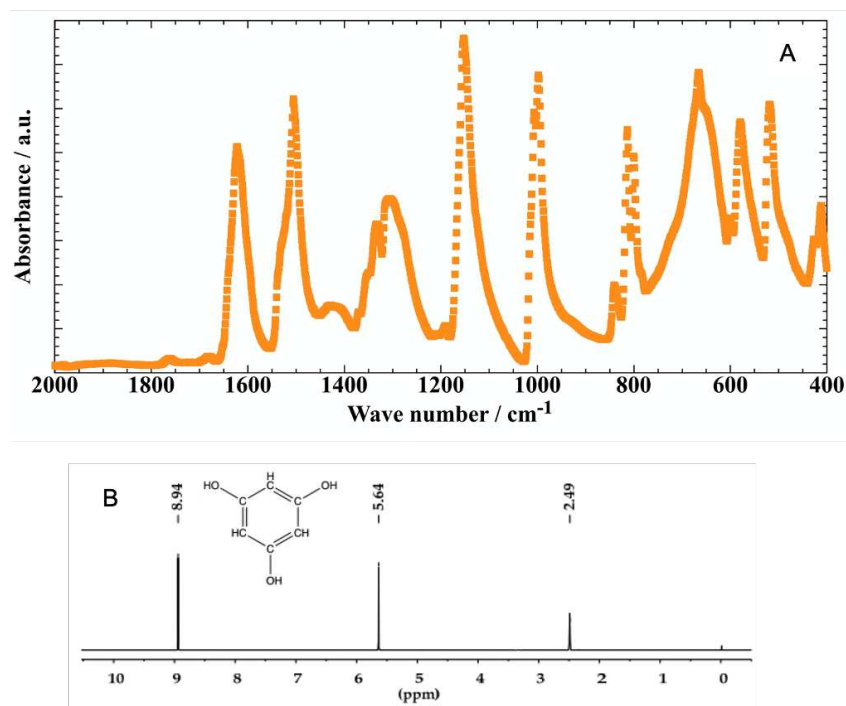


Figure 4.6 FTIR (A) and $^1\text{H-NMR}$ (B) spectra for pure Phg. The first was taken *in-situ* and the second from the literature [274].

Concerning its reactivity, the -OH groups are the ones participating in chemical reactions. Moreover, in an aqueous phase or in an organic solvent, they can be deprotonated into O^- groups when a base is added, which renders them very soluble, nucleophile and therefore very reactive. In IP, Phg is dissolved in dimethylsulfoxide (DMSO) with the presence of KOH to allow for a nucleophilic aromatic substitution.

Both HCCP and Phg monomers are thus well-known for their reactivity and this is the main reason which guided their choice in the IP work of Dr. Radmanesh *et al* [260]. In addition, their other interesting properties lead to their use in numerous fields. Experimental data have already allowed the development of related MD models, which have been used as a basis for the creation of those used in this work [266, 273, 275-278].

4) B. 2. Molecular dynamics models - monomers

A significant amount of work was done in the research group to develop adequate force fields for each monomer. Only a brief summary is given in the following Section so as to understand the coherence of the project as a whole.

4) B. 2. 1. Phloroglucinol

In order to develop a Phg model, the structure of the molecule (Figure 4.5) was first created using *ChemDraw Prime* 20.0 (CDP) [263]. It was converted to the input format required by the *Gaussian09* software [203]. Unlike *gmq* package [194] which is based on a classical force field, the *Gaussian09* software [203] uses the fundamental laws of quantum mechanics to predict *e.g.* energies, molecular structures and partial charges. It is thus widely used in in-depth optimizations of small molecules and the *Gaussian09* results are often used, as is the case here, to feed in some of the parameters of the classical force-field. A geometry optimization of this CDP-generated isolated molecule and the partial charges were extracted. Parallel optimizations were made using geometries taken from the crystal structure. The three approaches are provided in Figures 4.7, 4.8 and Table 4.3, with the molecular structures being displayed using VMD [248]:

- A) Using density functional theory (DFT) at the B3LYP/6-31G** level with *Gaussian09* [203] on the CDP-generated isolated molecule (Figure 4.7 and Table 4.3, column A).

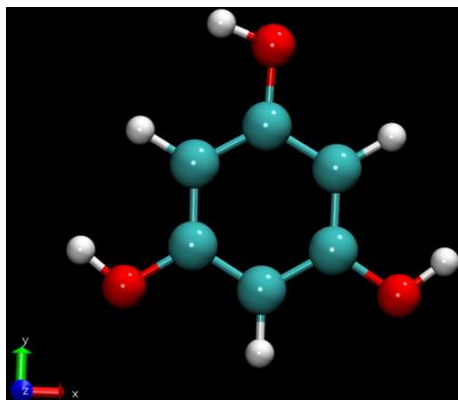


Figure 4.7 The optimized geometry of an isolated Phg molecule generated using CDP. C = cyan, O = red and H = white (same for the next Figures).

Table 4.3 Partial charges calculated from *Gaussian09* using three different approaches for the five atom types in Phg. Car(H) is an aromatic carbon attached to a hydrogen, Car(OH) is an aromatic carbon attached to a hydroxyl group, H(O) is a hydroxyl hydrogen, H(Car) is an aromatic hydrogen.

Symmetrized Partial Charge / e			
Atom Type Name	From <i>Gaussian</i> optimized CDP-generated single molecule (A)	From <i>Gaussian</i> optimized single molecule from crystal structure (B)	From <i>Gaussian</i> calculation on a 2×2×2 supercell of crystal structure (C)
Car(H)	-0.5667	-0.5914	-0.5820
Car(OH)	0.4982	0.5144	0.5170
O	-0.5530	-0.5355	-0.5593
H(O)	0.4135	0.3967	0.4093
H(Car)	0.2080	0.2158	0.2150

The structure in Figure 4.7 is planar with all torsion angles being either 0° (*trans*) or 180° (*cis*). All bond angles with a carbon at the centre are within $\pm 2^\circ$ of the sp^2 -expected value of 120°. The pendant hydroxyl groups have a sp^3 symmetry with the C-O-H bond angles being all within 1° of the tetrahedral value of $\approx 109.5^\circ$.

B) Using DFT and *Gaussian09* [203], but with the starting structure being an isolated molecule taken from the orthorhombic crystal structure with a unit cell containing four molecules [273] [275] (Figure 4.8 and Table 4.3, column B).

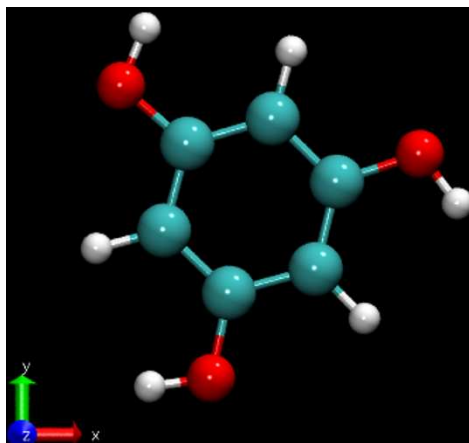


Figure 4.8 The optimized geometry of an isolated Phg molecule taken from the crystal structure.

It is clear from Figures 4.7 and 4.8 that the hydroxyl hydrogens optimized from different starting structures do not point in the same direction. The partial charges also show a certain sensitivity to the orientation of the O-H bond (Table 4.3). This affects as well the stability of the crystal due to the formation of a network of hydrogen bonds [273, 275]. Therefore, a series of MD simulations were carried out to obtain a force field giving a stable crystal structure and a reasonable agreement with the cell lengths, density and molar enthalpy of sublimation of phloroglucinol [273, 275, 276, 279]. The well-known TRIPOS force field [239] was used as a basis for the selection of parameters (when available) for the bond lengths, bending, torsions, out-of-planes and Van der Waals Lennard-Jones 12-6 interactions. The TRIPOS force field was first completed with the partial charges obtained with technique B (Table 4.3).

C) After fine-tuning the various parameters (results not shown), the optimized geometry in Figure 4.8 was used to create a $2 \times 2 \times 2$ crystal supercell containing 32 molecules. Partial charges were re-determined using *Gaussian* (Table 4.3, column C) but no optimization of the structure was performed so as not to perturb the crystal arrangement.

The partial charges obtained from (C) were then transferred to the MD simulations of the crystal structure and the Van der Waals potentials were readjusted so as to bring the density, cell lengths and sublimation energy as close as possible to the experimental values.

The final force field developed for the Phg monomer gave discrepancies of only $\pm 3\%$ for the cell lengths, $< 1\%$ for the density at the different temperatures studied (295 K and 105 K) and a reasonable agreement for the sublimation energy.

4) B. 2. 2. HCCP

As for Phg, the starting structure for HCCP (Figure 4.3) was built with CDP [263] and then converted to the *Gaussian09* input format [194, 203]. The geometry was optimized (Figure 4.9) and the partial charges obtained with DFT were $q_P = 0.7758$ e, $q_N = -0.6456$ e and $q_{Cl} = -0.0651$ e.

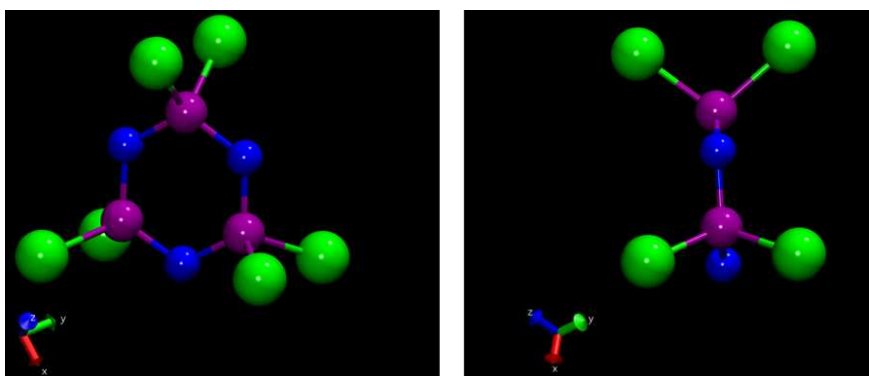


Figure 4.9 Two views of the optimized geometry of an isolated HCCP. The planarity of the ring is clear to see on the right. Cl = green, N = blue, P = purple (same for the next Figures).

The optimized molecule has a planar ring structure for the P and N atoms with all P-N-P-N torsion angles within 0.5° of the *cis* value of $\pm 180^\circ$. The Cl atoms attached to each P are symmetrically placed above and below the plane of the ring with the P-N-P-Cl torsions angles at about $\pm 55^\circ$. This structure is fairly close to what can be found in the studies of Bullen [266] and Bartlett *et al.* [277].

Since the TRIPOS force field [239] does not contain any parameters for the bonds, bends and torsions in HCCP, other published force-fields were exploited to obtain a complete and *gmq*-adapted model [278, 280]. This classical force-field was used to energy-minimize an isolated HCCP molecule (Figure 4.10).

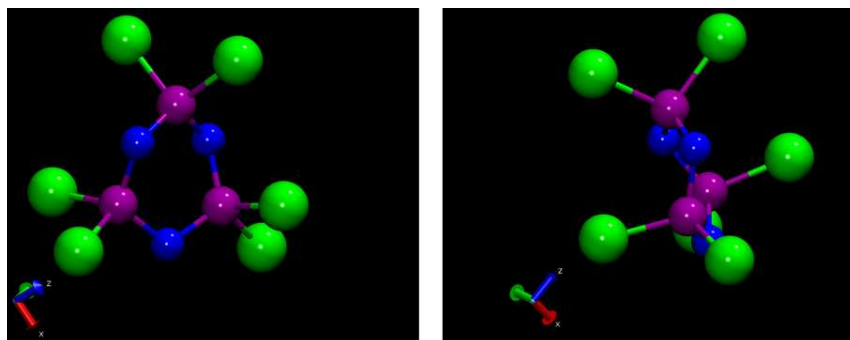


Figure 4.10 The energy-minimized (EM) geometry of an isolated HCCP using a force field with parameters adapted from the literature. The puckering of the ring is clear to see.

Unlike for the previous *Gaussian* DFT-optimized structure, the *gmq* energy-minimized HCCP molecule displayed a clear puckering of the central ring. The reason for the puckering using the classical force field could be traced to the inclusion of 1 \cdots 4 non-bonded interactions in the torsional potential, in particular the Coulombic forces (cf. Chapter 2). As there are no rotatable torsions in the HCCP molecule and the P-N-P-N torsions are kept in the *cis* conformation by the torsional potential alone, it was considered reasonable to switch off the 1 \cdots 4 non-bonded interactions in the classical force field. This in turn led to some slight readjustments to the Phg model in order to make it compatible with this convention and thus with the HCCP model.

As for Phg, attempts were carried out to obtain a stable crystal structure of HCCP with the optimized force field. The starting crystal structures were taken from Bullen [266] and Bartlett *et al.* [277]. The unit cell is also orthorhombic and contains four molecules, the experimental data used for comparison are again the cell dimensions, density and enthalpy of sublimation [281]. As previously, a rather good agreement was found, *i.e.* the density to within $\pm 0.9\%$ or $\pm 0.45\%$ depending on the temperature, along with discrepancies of $< 2.5\%$ for the cell lengths.

A complete force field with “bonded” and “non-bonded” terms encompassing both Phg and HCCP monomers was thus developed and it gave a good agreement with both their crystal structures. More details will be given in a publication. The next stage was to generate dense homogeneous mixtures of the two monomers at different stoichiometric ratios [144, 282]. Again, this part is only a summary and details will be available in future publications.

4) B. 3. Molecular dynamics models - mixture

The creation of a homogeneous mixture mimicks in a very simplified way the situation found in experimental IP, where the monomers dissolved in two immiscible liquids come into contact at the interface

of both liquids. Phg being highly polar, *i.e.* soluble in water or polar solvents, and HCCP being much more apolar, *i.e.* soluble in organic solvents, the model mixtures are likely to have a tendency to phase separate. This has to be avoided as much as possible during the modelling procedure, where there is no attempt to model the different solvents. Indeed, the model system sizes would become far too big if the solvent molecules were included.

The densities of both monomers in a liquid-like disordered dense phase at ambient conditions were obtained by subjecting the two crystal structures developed previously to NPT cycles of heating and cooling, with the density and temperature being monitored as displayed in Figure 4.11.

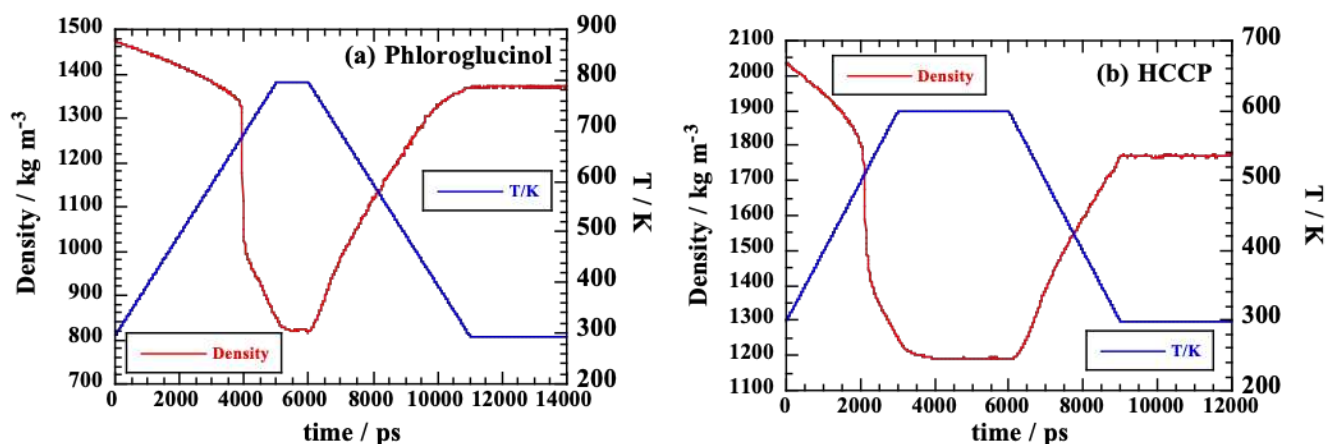


Figure 4.11 The density (red line, left y -axis) and the temperature profiles (blue line, right y -axis) obtained from heating/cooling NPT MD simulations starting from the crystal structure of (a) Phg and (b) HCCP.

The relaxed average densities from the period at ambient temperatures can then be used to estimate the density of an ideal mixture containing N_{HCCP} HCCP molecules and N_{Phg} phloroglucinol molecules by assuming the volume additivity and using (Equation S4.1 detailed in the Supporting Information). The density calculated for an equimolar 1:1 Phg:HCCP mixture was used as target for a simulation starting with one molecule of each type placed in a cubic box at an initially low density. This system was replicated to contain 1024 molecules and driven rapidly to the target density. After NVT relaxation for 1000 ps, it was then allowed to relax further under NpT conditions. The behaviour of the mixture density is monitored in Figure 4.12.

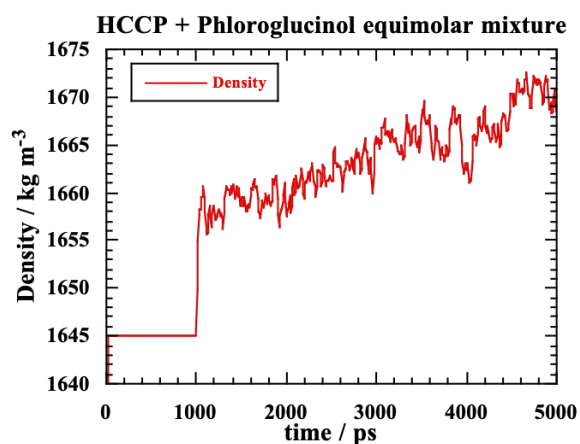


Figure 4.12 Model density as a function of time for an equimolar mixture of Phg and HCCP at ambient temperature.

The rapid initial densification phase is hardly visible on the scale of Figure 4.12 and the first 1000 ps under NVT conditions allow for a relaxation at the target density of the ideal mixture. When switched to NpT conditions, the density rises rapidly to a value higher than the target “ideal mixture” value, then gradually drifts upwards. The structure of this dense system is far from being phase-separated and resembles more a co-continuous interpenetrating network (Figure 4.13).

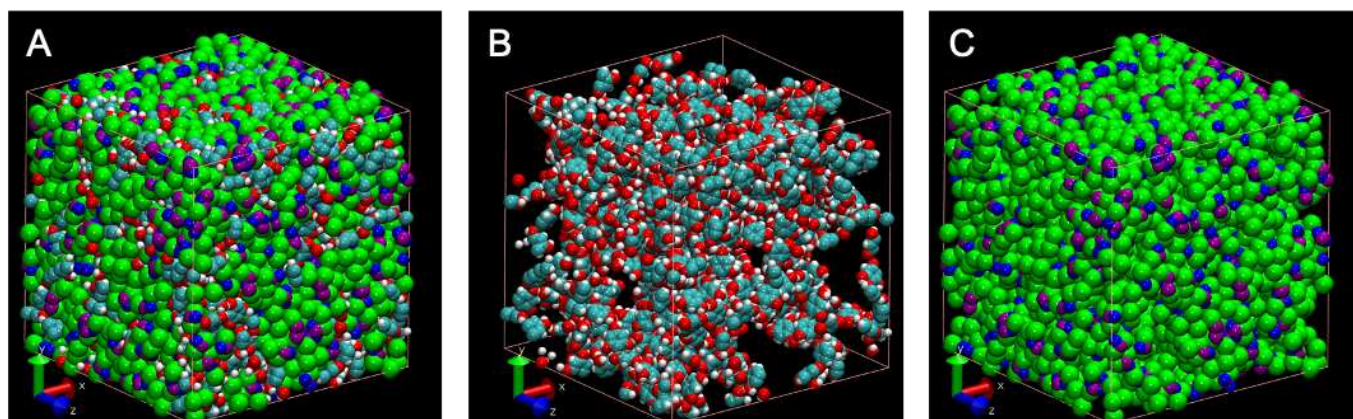


Figure 4.13. Final configuration of a model equimolar mixture of HCCP and Phg containing 512 molecules of each, with all molecules (A), only the Phg molecules (B) and only the HCCP molecules (C).

Therefore, using this procedure, it appears possible to generate starting configurations of mixtures from which the reaction step will be able to be initiated. The next step is the development of a model for different fragments of the *combined* monomers, *i.e.* when the reactions occur between Phg and HCCP and they become bonded together into larger and larger fragments. Indeed, new bonds modify the “chemical

environment” of atoms in the fragments and especially the partial charges q . The force field must thus be adapted to take into account these changes.

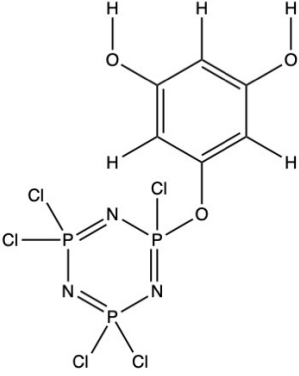
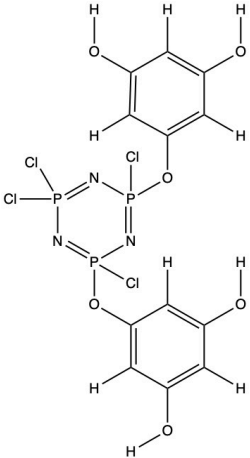
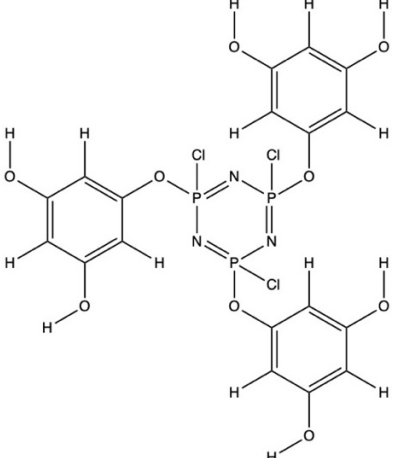
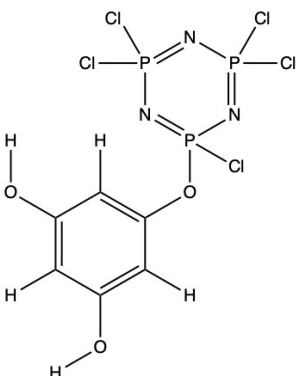
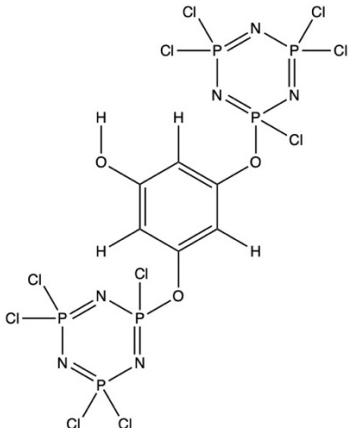
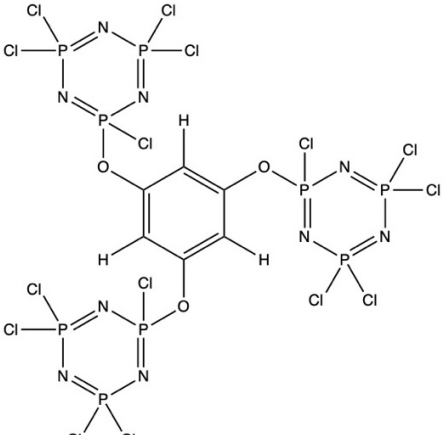
4) C. Fragments of combined monomers

In this Section, a large number of representative molecules were generated and then input to *Gaussian* for optimization. Indeed, optimizing directly the entire network is not feasible, since *Gaussian* calculations [203] become extremely long as the number of atoms rises. Instead, different “fragments” are created and, as for the pure monomers, their geometry is optimized to see how the chemical environment changes the structure and the partial charges on the atoms.

4) C. 1. Definition of a fragment

A “fragment” is referred to here as one type of monomer being linked to one or more monomers of the opposite type. According to their reactivities, HCCP uses its P atoms and Phg uses its O atoms to create P-O bond links. A Phg can be linked to a maximum of three HCCP and conversely, HCCP can in principle be bonded to six Phg. In a first instance, it was considered that each P is link to just one O. This leads to six different fragments (Table 4.4).

Table 4.4 First group of fragments obtained by linking HCCP and Phg. Their names refer to the monomer that is substituted and the number of groups changed.

		
HCCP_1_Cl	HCCP_2_Cl	HCCP_3_Cl
		
Phg_1_OH	Phg_2_OH	Phg_3_OH

Two remarks can be made:

- The HCCP_1_Cl and Phg_1_OH fragments are nominally the same.
- For the HCCP_2_Cl fragment, it is possible to substitute both chlorine atoms attached to the same P (new HCCP_2_Cl_1_P fragment in Table 4.5). Even if this seems complicated due to steric hindrance, there are indications that double substitutions do occur [283-285]. Indeed, it will be shown later that up to four Cl on the same HCCP can react, *i.e.* that means necessarily two substitutions on the same P. However, for the simulations, a maximum of only three substitutions were tested in a first instance.

Table 4.5 gives the numbering of the atoms in each fragment:

Table 4.5 Atom numbers in the first group of Phg-HCCP fragments. The central monomer is linked to a maximum of three others from the opposite type.

HCCP_1_Cl = Phg_1_OH	HCCP_2_Cl	HCCP_3_Cl
Phg_2_OH	Phg_3_OH	HCCP_2_Cl_1_P

As for the pure monomers, the fragment structures were first created with *ChemDraw Prime* [263] and then converted to the *Gaussian09* input format [194, 203]. However, there are two main issues:

- By default, the CDP structures do not contain explicit hydrogens.
- They are only 2D representations of a 3D structure, so all z coordinates are zero.

To solve the first issue, H atoms were explicitly added within CDP. The second issue is more problematic since *Gaussian* cannot optimize the structures correctly if they remain flat. Indeed, there are no out-of-plane forces (cf. Chapter 2) for the atoms. Moreover, these structures are metastable conformations, where the energy is at a maximum stationary point. To workaroud this problem, it is first necessary to assign random velocities to the atoms in order to move them slightly out of the z plane. The lowest local minimum for the energy is found using a basic classical force-field, and the obtained structures are further converted to the *Gaussian* format with the above issues being removed. The force-field optimized on the pure monomers has the ability to represent their intramolecular structure, except for the partial charges. This was found to be enough to produce the “non-flat” structures necessary for the input to the *Gaussian* program.

In practice, the output CT file obtained from the initial CDP structures is first converted into the input format of *gmq* with all the important information, *e.g.* the atom-type number or atom-type name, as shown in Figure 4.14.

```

HCCP_1_Cl.ct
25 26
1.8764 -0.3807 -0.0000 N 2 N_HCCP
3.1954 -1.1422 -0.0000 P 1 P_HCCP
4.5143 -0.3807 -0.0000 N 2 N_HCCP
4.5143 1.1422 -0.0000 P 1 P_HCCP
3.1954 1.9037 -0.0000 N 2 N_HCCP
1.8764 1.1422 -0.0000 P 9 P_OCl
0.5575 1.9037 -0.0000 O 11 O_ether
1.8764 2.6652 -0.0000 Cl 10 Cl_P-Oeth
2.4339 -2.4612 -0.0000 Cl 3 Cl_HCCP
3.9569 -2.4612 -0.0000 Cl 3 Cl_HCCP
6.0373 1.1422 -0.0000 Cl 3 Cl_HCCP
-0.7615 -0.3807 -0.0000 C 4 Car-H
-0.7615 1.1422 -0.0000 C 12 Car-Oeth
-2.0805 1.9037 -0.0000 C 4 Car-H
-3.3994 1.1422 -0.0000 C 5 Car-OH
-3.3994 -0.3807 -0.0000 C 4 Car-H
-2.0805 -1.1422 -0.0000 C 5 Car-OH
-2.0805 -2.6652 -0.0000 O 6 O-H
-4.7184 1.9037 -0.0000 O 6 O-H
5.2758 2.4612 -0.0000 Cl 3 Cl_HCCP
-3.3994 -3.4267 -0.0000 H 7 H-O
-6.0373 1.1422 -0.0000 H 7 H-O
0.5575 -1.1422 -0.0000 H 8 H-Car
-4.7184 -1.1422 -0.0000 H 8 H-Car
-2.0805 3.4267 -0.0000 H 8 H-Car
1 2 2 0
2 3 1 1
3 4 2 0
4 5 1 1
5 6 2 0
6 1 1 1
6 7 1 1
6 8 1 1
2 9 1 1
2 10 1 1
4 11 1 1
12 13 2 0
13 14 1 1
14 15 2 0
15 16 1 1
16 17 2 0
17 12 1 1
13 7 1 1
17 18 1 1
15 19 1 1
4 20 1 1
18 21 1 1
19 22 1 1
12 23 1 1
16 24 1 1
14 25 1 1

```

Figure 4.14 CDP-generated connectivity table file for the HCCP_1_Cl fragment with: in green the atomic coordinates (where all z coordinates are 0 due to the 2D representation); in red the element symbols, atom-type numbers and atom-type names; in blue the connectivity table, which indicates that atom 1 is bonded to atom 2 which is itself also bonded to atom 3, etc.

Following this step, alternating energy-minimization *EM* and constant-energy *NVE* MD simulations are performed until the temperature rise during the latter is less than ≈ 5 K, *i.e.* the structures are close to a local energy minimum. The resulting structures are deemed as being “*gmq*-optimized”. They can then be further optimized using *Gaussian* to give an estimation of the new geometries and partial charges. The “*Gaussian*-optimized structure” is given for HCCP_1_Cl in Figure 4.15. It was used as a starting reference structure to generate all other possible conformations for the fragments based on HCCP.

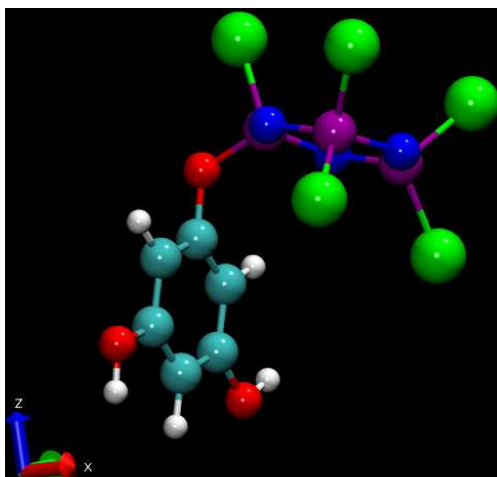


Figure 4.15 *Gaussian*-optimized structure for HCCP_1_Cl. The colour code is the same as previously: cyan = C ; red = O ; white = H ; blue = N ; purple = P and green = Cl.

However, the situation is further complicated by the fact that each fragment can have different structures depending on the values of the torsion angles of the linking bridges. Therefore, these torsions were changed to generate all the possible conformers. Each of them was optimized by *Gaussian* and the results of all the conformers were compared to obtain a global behaviour for each fragment.

4) C. 2. Generation of different conformers

Once a fragment structure has been optimized with *Gaussian* for the first time (as in Figure 4.15 for HCCP_1_Cl), all other conformational possibilities must be generated and optimized. Indeed, a same fragment can have different conformations due to the rotations of the links between HCCP and Phg. The different conformers were considered by changing one or more torsions. To create this new serie of starting structures, the process presented in Figure 4.16 was followed.

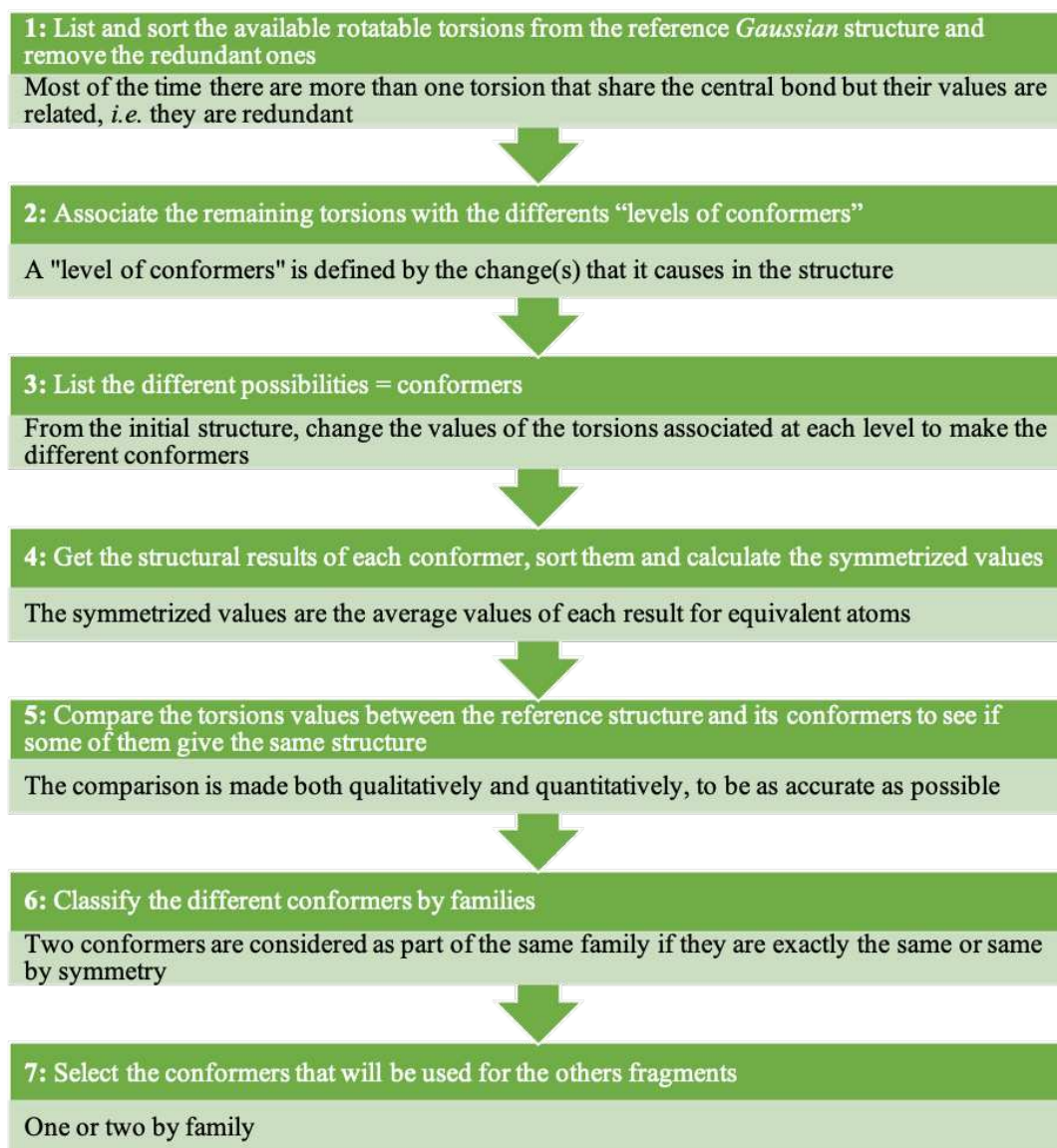


Figure 4.16 Generation process for all possible conformers of a Phg-HCCP fragment.

The process is detailed for clarity for the simplest fragment, *i.e.* HCCP_1_C1. First, all the *rotatable* torsions in the HCCP_1_C1 fragment are listed (Step 1): other torsions exist but they cannot rotate, *e.g.* the ones in the rings. A torsion is defined by 4 atoms and 3 bonds with the central bond being the one around which there will be rotation, *i.e.* the dihedral angle (cf. Chapter 2). If two torsions share the same central bond, their values are related and modifying one will lead to an equivalent change in the other, hence the need to remove the redundancy. Figure 4.17 provides an example of this list, before and after sorting.

13	7	6	1	-114.338	#	Car-Oeth	O_ether	P_OCl	N_HCCP	Type: 3
13	7	6	5	115.012	#	Car-Oeth	O_ether	P_OCl	N_HCCP	Type: 3
12	13	7	6	-92.205	#	Car-H	Car-Oeth	O_ether	P_OCl	Type: 9
14	13	7	6	84.984	#	Car-H	Car-Oeth	O_ether	P_OCl	Type: 9
13	7	6	8	0.443	#	Car-Oeth	O_ether	P_OCl	Cl_P-Oet	Type: 12
12	17	18	21	179.120	#	Car-H	Car-OH	O-H	H-O	Type: 17
14	15	19	22	-0.072	#	Car-H	Car-OH	O-H	H-O	Type: 17
16	15	19	22	179.968	#	Car-H	Car-OH	O-H	H-O	Type: 17
16	17	18	21	-0.784	#	Car-H	Car-OH	O-H	H-O	Type: 17

↓

13	7	6	1	114.338	#	Car	Oeth	O_ether	P_OCl	N_HCCP	Type: 3
13	7	6	5	115.012	#	Car	Oeth	O_ether	P_OCl	N_HCCP	Type: 3
12	13	7	6	-92.205	#	Car-H	Car-Oeth	O_ether	P_OCl	Type: 9	
14	13	7	6	84.984	#	Car-H	Car-Oeth	O_ether	P_OCl	Type: 9	
13	7	6	8	0.443	#	Car-Oeth	O_ether	P_OCl	Cl_P-Oet	Type: 12	
12	17	18	21	179.120	#	Car-H	Car-OH	O-H	H-O	Type: 17	
14	15	19	22	0.072	#	Car-H	Car-OH	O-H	H-O	Type: 17	
16	15	19	22	179.968	#	Car-H	Car-OH	O-H	H-O	Type: 17	
16	17	18	21	0.784	#	Car-H	Car-OH	O-H	H-O	Type: 17	

Figure 4.17 List of the torsions in the HCCP_1_Cl fragment before (above) and after sorting (below), with in blue the atom indices in the torsion, in orange the value of the dihedral angle, in red the corresponding atom types, in black (crossed-out) the torsions eliminated and in green the remaining ones.

Out of nine torsions in the original list, only four are left after sorting. These are then associated to three different “levels of conformers” (Step 2), since each one causes its own change in the structure. Table 4.6 defines each of the three levels.

Table 4.6 Levels of conformers. The first level is not applicable to HCCP_1_Cl and the Phg and HCCP rings are inverted for the Phg_x_OH fragments.

First level of conformers (only for HCCP_2_Cl and 3_Cl)			
Change	How to make it	Concerned torsion(s)/angle(s)	Central bond
Positions of the Phg ring(s) compared the HCCP ring <i>plane</i> (above or below, <i>i.e.</i> either they are on the same side or on different sides)	Change the initial value of the <i>z</i> coordinates in the CT for Cl atoms and O_ethers atoms	No torsion	No central bond
Second level of conformers (for all fragments)			
Positions of the Phg ring(s) compared to the HCCP ring (above; next to; opposite etc...)	Change the corresponding dihedral angle values	C-O-P-N or C-O-P-Cl	O-P
Positions of the Phg ring(s) plane compared to the HCCP ring plane (perpendicular; parallel)	Change the corresponding dihedral angle values	C-C-O-P	C-O
Third level of conformers (for all fragments)			
Positions of the hydroxyl H on the Phg ring(s)	Change the corresponding dihedral angle values	C-C-O-H	C-O

Once these levels have been defined, the remaining torsions of each fragment can be associated. For example, for HCCP_1_Cl, there are two torsions for the second level according to the list of torsions in Figure 4.17: C-O-P-Cl with the atoms numbered 13-7-6-8 and C-C-O-P with the atoms numbered 12-13-7-6. There are also two torsions for the third level as two hydroxyl H are still attached to the ring: numbers 12-17-18-21 and 16-15-19-22. Figure 4.18 highlights the designated torsions in the structure from Table 4.5 to allow for a better visualization.

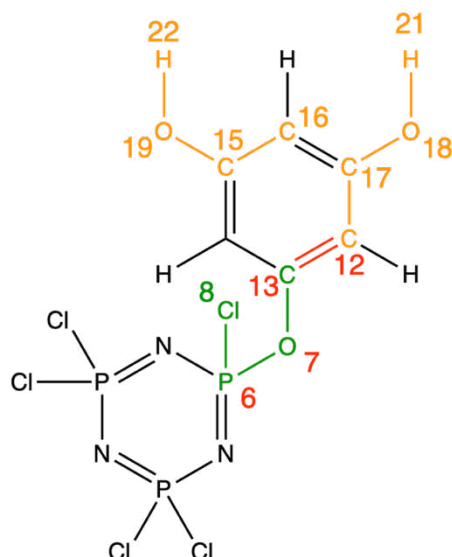


Figure 4.18 Selected torsions from those available in HCCP_1_Cl. When the colour is different between the number and the letter, the atoms are shared by two types of torsion. The green corresponds to C-O-P-Cl, the red to C-C-O-P and the orange to both C-C-O-H.

Once the torsions are sorted and classified by “level”, a list of the different conformers that can be obtained by changing their values is made (Step 3). From the reference structure, *i.e.* the first *Gaussian*-optimized, the values of the torsions C-O-P-Cl and C-C-O-P were changed to 180°, 120°/-120° or 90°/-90° (in different combinations), with only one value modified to see its effect on the entire fragment. The values of the third level, the C-C-O-H torsions, were not changed as testing all permutations and combinations would have led to too many possibilities and it is likely that the H positions have little influence on the charges on the different conformers. Instead, the focus was on the second level, because these torsions correspond to the linking bridge.

Table 4.7 gives the list of the different conformers tested for HCCP_1_Cl and Figure 4.19 shows some of the corresponding input structures, *i.e.* before *Gaussian* optimization.

Table 4.7 Input torsion values in degrees for the different HCCP_1_Cl conformers.

Initial			1	2	3	4	5	6	7	8	9	10	11	12	13
C-C-O-P	12-13-7-6	-92.2	180	0	-92.2	-92.2	-92.2	120	120	-120	-120	120	-92.2	-92.2	180
C-O-P-Cl	13-7-6-8	0.4	180	180	180	120	-120	0.443	120	-120	120	-120	-90	90	0
C-C-O-H	12-17-18-21	179.1													
	16-15-19-22	180.0													

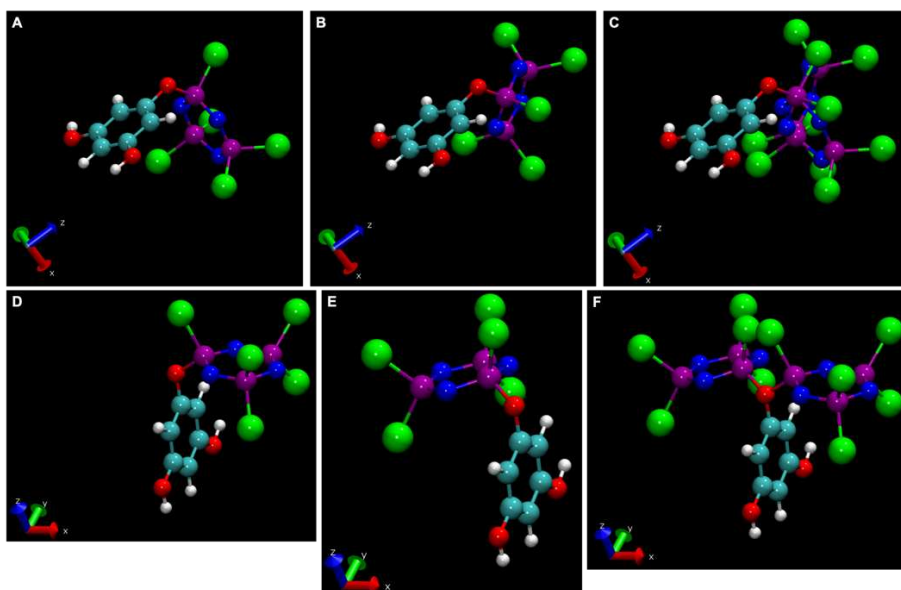


Figure 4.19 Changes in the conformation of HCCP_1_Cl that occur when the input torsion values are set according to Table 4.7 (A) the initial *Gaussian*-optimized structure; (B) conformer 11, in which the C-O-P-Cl value has been changed; (C) a superimposition of both (A) and (B); (D) as (A) viewed from a different angle; (E) conformer 6 where the C-C-O-P torsion has been changed; (F) a superimposition of (D) and (E). N.B. The conformer structures in (B) and (E) are the input ones for *Gaussian*.

By symmetry, some combinations/conformers give the same structure even if the values are different, therefore they were not tested. For example, C-C-O-P = -90° and C-O-P-Cl = 120° (conformer 4) is the same as C-C-O-P = 90° and C-O-P-Cl = 120° . Following their generation, the various conformers of interest were optimized (Step 4) with *Gaussian09*. This gave for each of them their lowest-energy structure, with its bond lengths, its bending and torsion angles as well as with the partial charges on the atoms. It should be noted that *Gaussian* does not provide symmetrized values, *i.e.* the average values for equivalent atoms (same-type and similar chemical environment) had to be obtained manually. Figure 4.20 presents conformer structures before and after optimization.

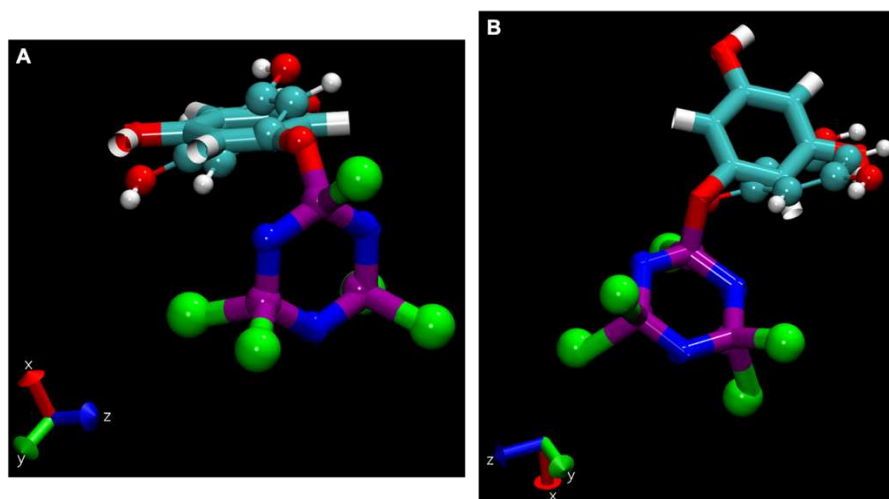


Figure 4.20 Structures before (tubing) and after (thin bonds) *Gaussian*-optimization for conformers 6 (A) and 11 (B) of the HCCP_1_Cl fragment.

Some input conformers converge to the same stable structure after optimization (Step 5). Figure 4.21 compares the optimized torsional values for all the conformers of HCCP_1_Cl using two diagrams: a simple one with all the torsions (Figure 4.21.A) and a Ramachandran plot, where one specific C-O-P-N angle and its corresponding C-C-O-P angle are represented as a point on a two-dimensional angle grid [286] (Figure 4.21.B).

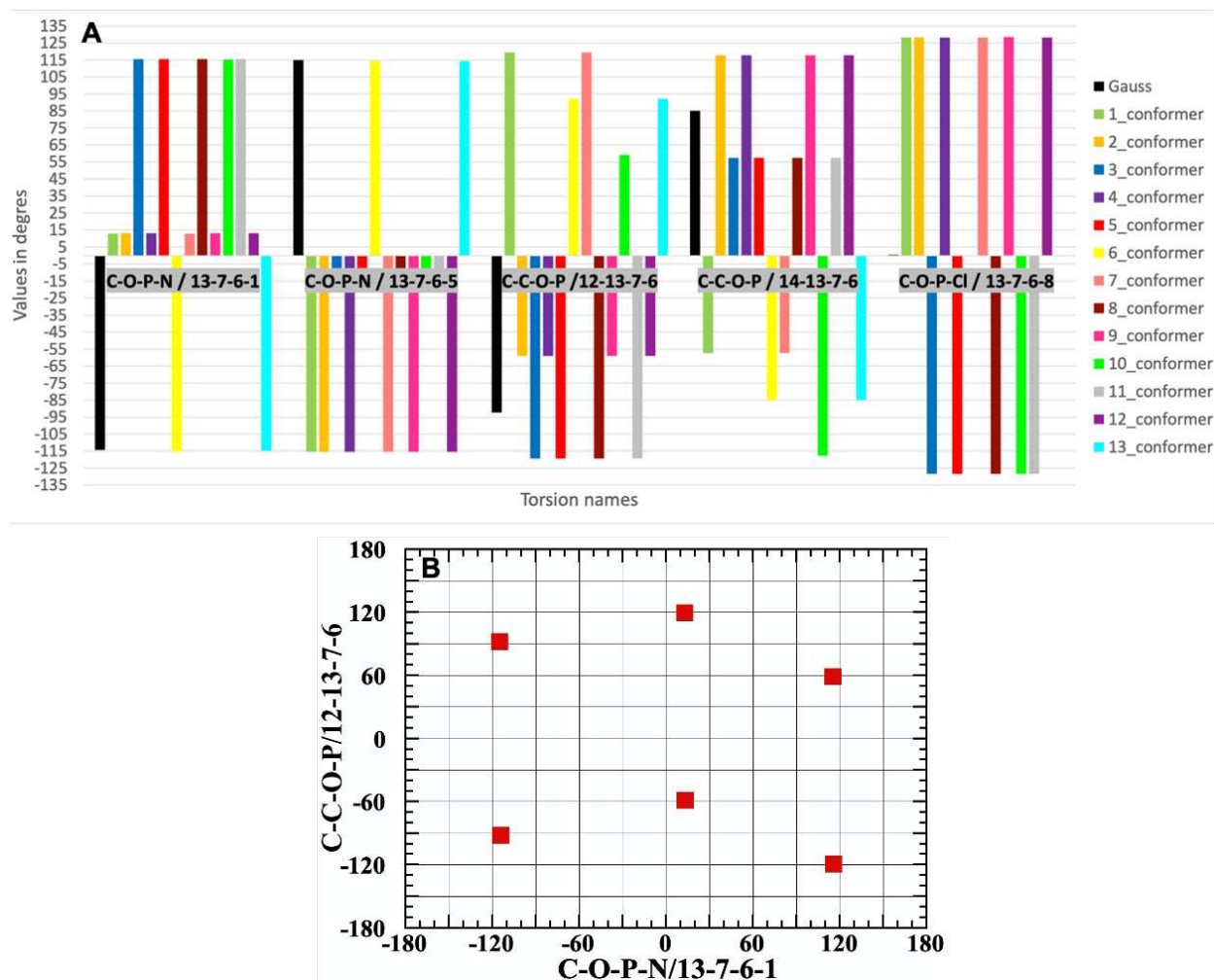


Figure 4.21 *Gaussian*-optimized torsions for the different conformers of HCCP₁_Cl. The C-C-O-H torsions have not been changed and the black columns are from the first *Gaussian*-optimized structures (A). Ramachandran plot of selected C-O-P-N and C-C-O-P angles (B).

As expected, both C-O-P-N angles shown in Figure 4.21.A differ for a same conformer by $\sim 120^\circ$ due to the sp^3 nature of the P atom. They also differ by $\sim 120^\circ$ from the C-O-P-Cl angle for the same reason; all of these torsion angles share the same central O-P bond. Similarly, both C-C-O-P angles for the same conformer must differ by $\sim 180^\circ$ due to the sp^2 nature of the carbon atoms. This inherent symmetry means that, for example, between the *Gaussian*-optimized reference structure (black columns on the chart) and its conformer 6 (yellow columns), the only difference will be the position of the hydroxyl H on the Phg ring. Indeed, when conformer 6 is rotated by $\sim 180^\circ$ around an axis perpendicular to the HCCP plane, it coincides with the reference conformer, except for the hydroxyl H (Figure 4.22):

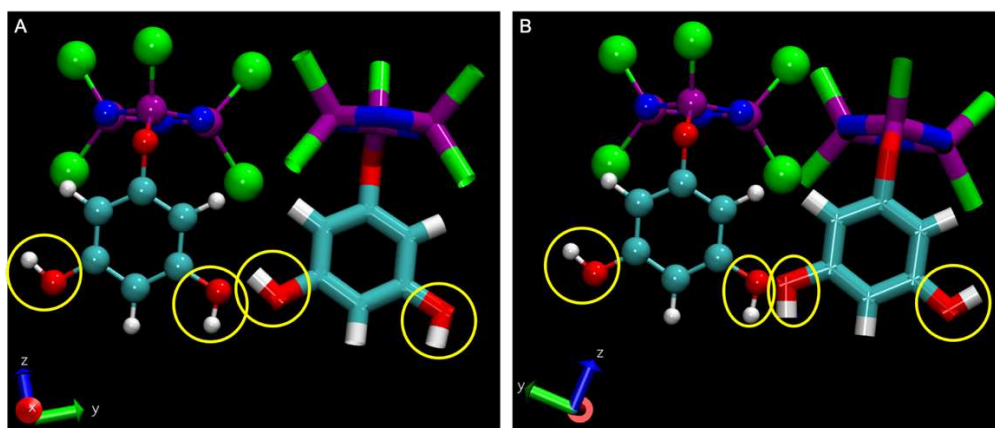


Figure 4.22 Comparison between the *Gaussian*-optimized reference structure for HCCP_1_Cl (tubing) for its conformer 6 (thin bonds), before (A) and after rotation by 180° (B). The positions of the hydroxyl H (yellow circles) are the only differences after rotation.

According to this comparison, the various conformers can be classified by “families” (Step 6). A family is defined as a group of conformers which have essentially the same structure or are symmetrically equivalent. There are 3 different families, A, B and C, which can be described by the dihedral angle obtained for the linking bridge, as shown by Table 4.8.

Table 4.8 Conformer families for the HCCP_1_Cl fragment.

Family	Torsion values for the linking bridge	Conformers	Hydroxyl O ?
A	C-O-P-N $\approx -115^\circ$ or C-O-P-Cl $\approx 0^\circ$ C-C-O-P $\approx \pm 90^\circ$	Gaussian (ref); 13_conformer; 6_conformer	180° difference
			Same
B	C-O-P-N $\approx +15^\circ$ or C-O-P-Cl $\approx +128^\circ$ C-C-O-P $\approx -60^\circ$ and $+120^\circ$	1_conformer; 2_conformer; 4_conformer; 7_conformer; 9_conformer; 12_conformer	180° difference
			Same
			180° difference
			Same as 2 and 4
C	C-O-P-N $\approx -115^\circ$ or C-O-P-Cl $\approx -128^\circ$ C-C-O-P $\approx +60^\circ$ and -120°	3_conformer; 5_conformer; 8_conformer; 10_conformer; 11_conformer	Same
			180° difference
			Same as 3, 5 and 8

One *Gaussian*-optimized conformer from each family of the HCCP_1_Cl fragment was chosen to build a list of permutations for the starting structures of the other fragments having more than one ring attached to the central HCCP/Phg ring (Step 7). Indeed, each attached ring can nominally have a conformation of type A, B or C and this avoids “starting from scratch” when building more complicated fragments. The selected HCCP_1_Cl fragments were conformer 13 for family A, conformer 7 for family B and conformer 10 for family C. To be sure to test all the possibilities, a list of permutations was done according to those HCCP_1_Cl basic fragments. For example, for HCCP_2_Cl (a central HCCP ring attached to two Phg rings, Table 4.5), the list of permutations is:

Phg 1	Phg 2
A	A
A	B
A	C
B	B
B	C
C	C

Both Phg rings are interchangeable so an AB starting conformer is the same as a BA starting conformer. Similar lists of permutations were built for all other fragments and they were processed with the same first four steps described in Figure 4.16.

4) C. 3. Extraction of partial charges for the fragments

The aforementioned TRIPOS force field [239] gives most of the parameters that have to be associated to the occurrence of P-O links and its equilibrium values are very close to those found in the *Gaussian*-optimized structures. This meant using the values of 1.6 Å for the equilibrium P-O bond length and 109.5° for the equilibrium C-O-P bending angle. The other bending angles, *i.e.* O-P-N, O-P-Cl and O-P-O (if both Cl leave) also all have a nominal tetrahedral symmetry of 109.5°. For the extra torsions introduced by the P-O bond, TRIPOS has parameters for the N-P-O-C, P-O-C-C and Cl-P-O-C torsions but not for O-P-N-P. However, there can not be any large rotations around the central P-N bond. As such, it was set to zero and the geometry was maintained by the existing N-P-N-P torsion potential as well as by all the other potentials involving the P atoms bridged to the Phg rings.

The main output of this study is to assess the optimized charges on each atom as a function of the changes in their connectivity in order to complete the force field developed for the monomer fragments. These are very important parameters in a simulation as the quality of the results often depends on the quality of the electrostatic representation.

4) C. 3. 1. HCCP_1_Cl

Results for the torsions of the HCCP_1_Cl conformers have been presented in the former Section but the aim here is to check whether the structures from a same family give rise to similar partial charges on the atoms. When the structures are essentially the same as in family A, the partial charges on a same atom differ by 0.02 e. The gap is slightly bigger (maximum difference of 0.11 e) when the structures differ by 180°, as in families B or C. For example, conformers 1 and 7 are very close but less so with conformers 2, 4, 9 and 12.

Separate charge averages for each conformer family were calculated to be sure that each family had an equal weight in the global average for each atom (Figure 7.23).

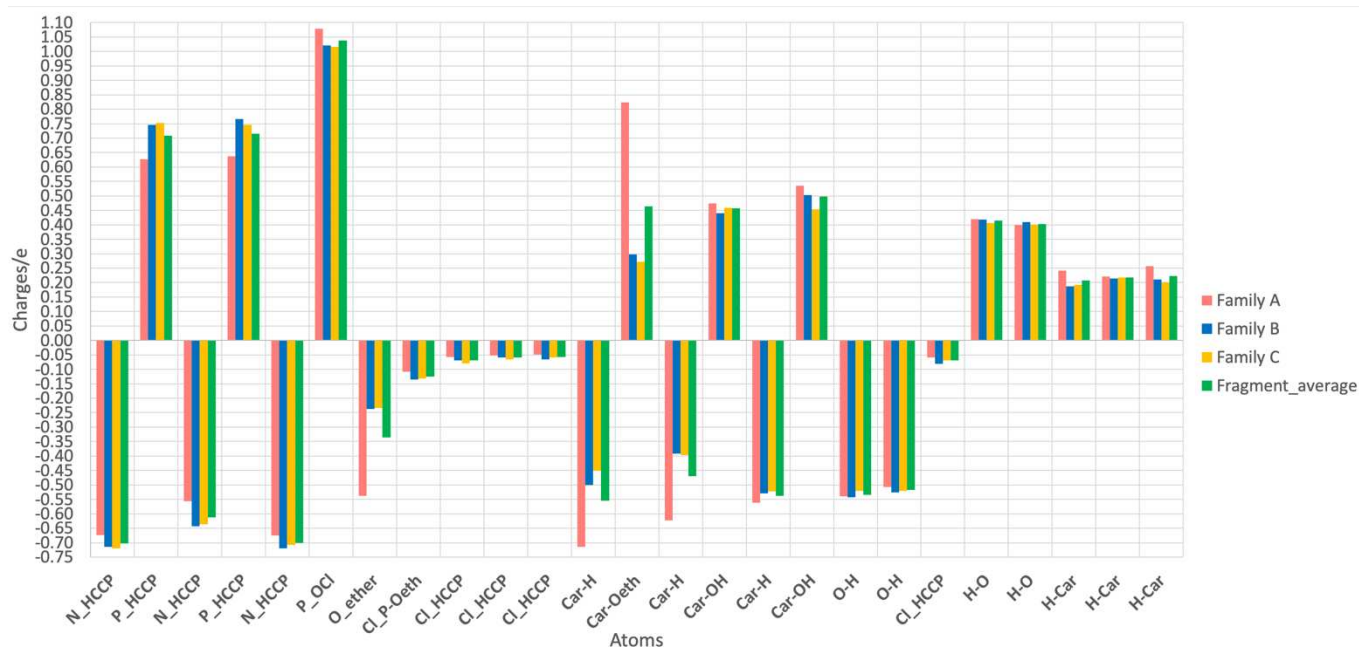


Figure 4.23 Average charges for the HCCP_1_Cl atoms, sorted by conformer families (red for A, blue for B, yellow for C) along with their global average (green). The atoms names come from the CDP connectivity table (Figure 5.14).

From the “fragment average” results (green), the symmetrized partial charges for equivalent atoms, *i.e.* atoms being of the same element and in a similar environment, were calculated for the HCCP_1_Cl fragment. They are provided in Figure 4.24.

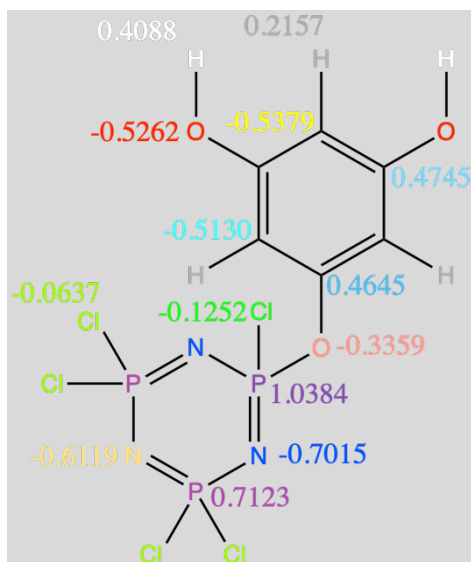


Figure 4.24 Average symmetrized charges q/e for HCCP_1_Cl. Atoms of a same colour are considered as equivalent, hence they have the same partial charge. The Phg carbon labels are not written for clarity, but the two C in *ortho* relative to the bridging oxygen are considered equivalent by symmetry as well as the two C in *meta* (same in the next Figures of this Chapter).

4) C. 3. 2. HCCP_2_Cl

HCCP_2_Cl is a HCCP ring with two Phg rings attached. For this fragment, the “first level of conformers” defined in Table 4.6 is possible. Indeed, the Phg rings are attached to HCCP through the substitution of a Cl by an O, but on each P, there are two Cl that can be involved in the link. Consequently, each Phg ring attached can either be above or below the HCCP plane. As such, there are 6 different conformers (according to the “list of permutations” defined in the previous Section) for the case when both Phg rings are not on the same side of the HCCP plane and 6 others for the case when both rings are on the same side. In order to distinguish these two cases, the conformers are named either “conformer x” (Phg rings on different sides) or “conformer x-x” (Phg rings on same side) with “x” being the conformer number. Figure 4.25 shows the difference between both types of structures.

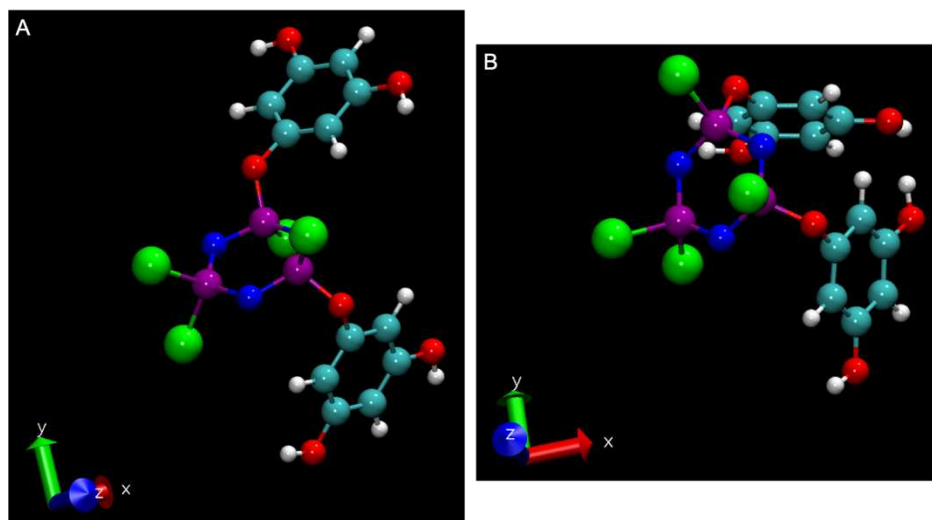


Figure 4.25 Initial *Gaussian*-optimized structure for HCCP_2_Cl with: (A) the Phg rings on different sides of the HCCP plane and (B) the Phg rings on the same side.

Table 4.9 lists the initial values of the remaining torsions after the sorting process and the different conformers which were tested. Here again, the C-C-O-H torsions were left unchanged.

Table 4.9 Input torsion values in degrees for the different HCCP_2_Cl conformers. The first row are the “list of permutations” with the names of the “conformer families” defined from fragment HCCP_1_Cl.

Initial				AA	BB	CC	AB	AC	BC	
				1	2	3	4	5	6	
“ Diff side”	C-C-O-P	4-31-29-28	-98.8	180	120	120	180	180	120	
		6-18-11-12	55.2	180	120	120	120	120	120	
	C-O-P-Cl	7-6-18-11	-126.4	0	120	-120	120	-120	120	
		8-4-31-29	-1.2	0	120	-120	0	0	-120	
	C-C-O-H	12-13-19-24	-179.9							
		14-15-17-23	-0.7							
		26-25-32-38	179.4							
		26-27-33-37	-1.5							
	Initial				1-1	2-2	3-3	4-4	5-5	6-6
	“ Same side”	C-C-O-P	4-31-29-28	-82.3	120	120	120	180	180	120
6-18-11-12			-86.4	120	120	120	120	120	120	
C-O-P-Cl		7-6-18-11	-3.5	0	120	-120	120	-120	120	
		8-4-31-29	15.3	0	120	-120	0	0	-120	
C-C-O-H		12-13-19-24	-6.7							
		14-15-17-23	2.1							
		26-25-32-38	7.4							
		26-27-33-37	-1.0							

Due to the presence of more than one Phg ring, there can be atom overlaps, such as for conformer 1-1 built using conformer 13 from HCCP_1_Cl (Figure 4.26). This situation is an issue because steric overlaps are an indication of unfavourable conformers. Two options are available: either change the values of the torsion by choosing another conformer of the same HCCP_1_Cl family in the construction (Table 4.8) or just eliminate this permutation if no other member of the family avoids these overlaps. The former

case is possible for conformer 1-1, *i.e.* conformer 6 of family A can be used instead of conformer 13 (albeit with values of 120° instead of 180°).

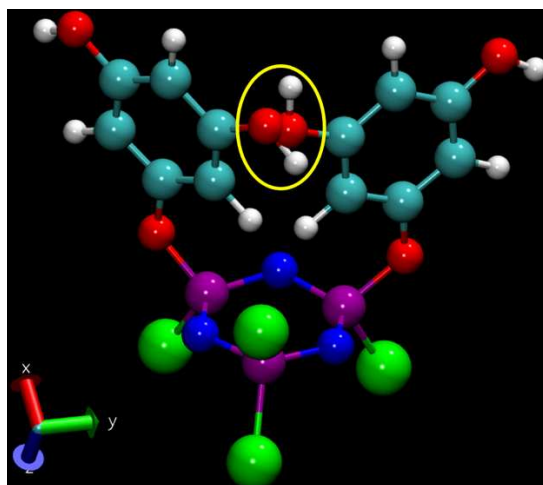


Figure 4.26 Atom overlaps for conformer 1-1 of HCCP_2_Cl when it is built using conformer 13 from HCCP_1_Cl.

For more visibility, only the torsions which have been changed to make the initial configurations of the different conformers (Table 4.9) will be reported. Following *Gaussian* optimization, they are distributed as in Figure 4.27 with one C-C-O-P and its corresponding C-O-P-Cl torsion being shown for each conformer of a given type. The two others as well as the C-C-O-H torsions are provided in Table S4.1.

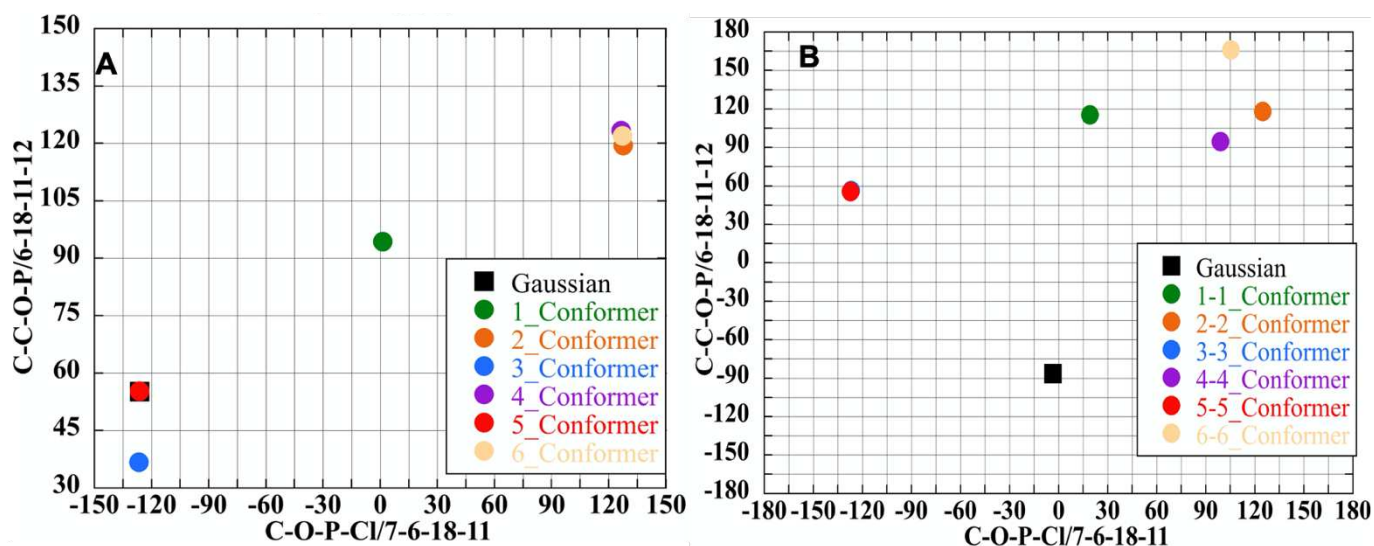


Figure 4.27 *Gaussian*-optimized C-C-O-P vs C-O-P-Cl torsions in degrees for all HCCP_2_Cl conformers with the Phg rings being either “on different sides” (A) or “on the same side” (B). The black squares are the first *Gaussian*-optimized structure.

As for HCCP_1_Cl, the hydroxyl hydrogens of the Phg rings have not really changed their position compared to their initial structures. Whatever the conformer, they stay in the same plane as the ring to which they belong (Table S4.1). Moreover, for some conformers, the entire structure hardly moves as well. For instance, there is no more than 10° difference for conformers 2 and 2-2 before and after their *Gaussian* optimization (Figure 4.28).

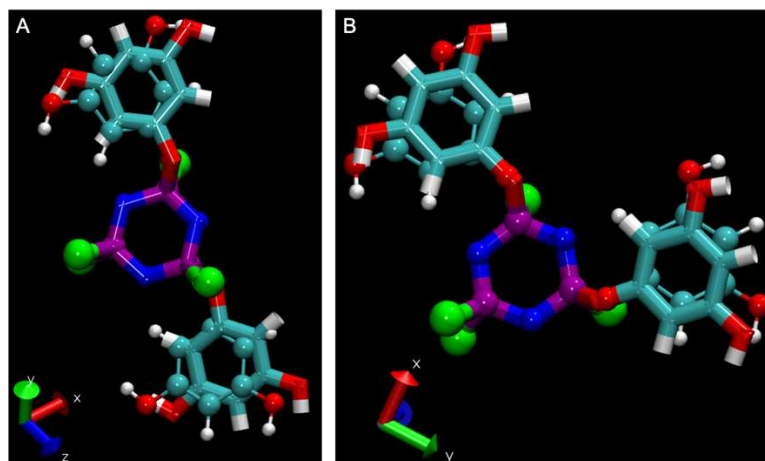


Figure 4.28 Structures before (tubing) and after (thin bonds) *Gaussian* optimization of (A) conformer 2 and (B) conformer 2-2 for HCCP_2_Cl.

The charges were first compared separately within the “on different sides” and “on the same side” conformers in order to see if the relative position of the Phg rings has an effect on the charges. With the symmetrized charges, the difference varied between 0 to 0.0417 e (not presented). This is low enough to conclude that they are the same, even if the main differences are always in the charges of the HCCP ring (N and P atoms). The symmetrized charges for equivalent atoms are shown in Figure 4.29 for the “on different sides” and “on the same side” fragments separately.

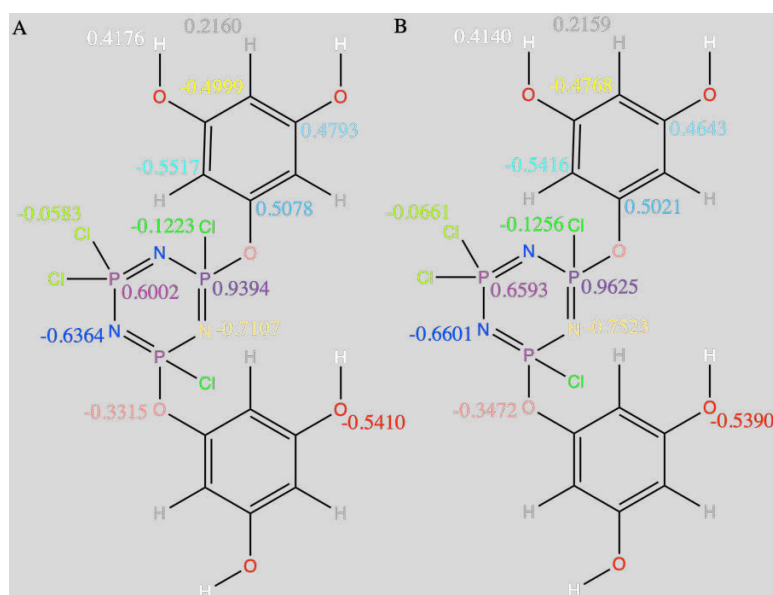


Figure 4.29 Average symmetrized partial charges q/e for HCCP₂Cl fragments with Phg rings being “on different sides” (A) or “on the same side” (B). The atom symbols are in the same colour when they are equivalent.

4) C. 3. 3. HCCP₂Cl₁P

A fragment close to HCCP₂Cl is HCCP₂Cl₁P (Table 4.5). It also has two Phg rings, but they are substituted on the same P instead of two different ones. As such, they are necessarily on either side of the central HCCP ring. However, their main problem is that they are likely to overlap much more. This issue can be seen in permutation AA which, whatever the values used, leads to overlaps of several Phg ring atoms. Consequently, only the permutations presented in Table 4.10 were tested.

Table 4.10 Input torsion values in degrees for the different HCCP₂Cl₁P conformers. The first row corresponds to the “list of permutations”. (same for the following Tables of this Chapter).

Initial		BB	CC	AB	AC	BC	
		2	3	4	5	6	
C-O-P-N	1-6-32-25	116.6	120	-120	0	0	-120
	1-6-19-13	-10.4	120	-120	120	-120	120
C-C-O-P	6-32-25-30	-140.5	120	120	180	180	120
	6-19-13-14	55.1	120	120	120	120	120
C-C-O-H	12-11-18-24	-0.2					
	14-15-17-23	-179.1					
	26-27-33-38	1.1					
	28-29-31-37	1.2					

Another difference concerns the second torsion of the linking bridge. Indeed, for all others fragments, the linking bridge involves two torsions, C-C-O-P and C-O-P-Cl, which are modified to give the different conformers. However, there is no longer a C-O-P-Cl torsion for HCCP_2_Cl_1_P, since both Cl attached to the P are substituted. In this case, an equivalent C-O-P-N torsion is specified instead for the “second level of conformers” (Table 4.6). Figure 4.30 helps to visualize this difference.

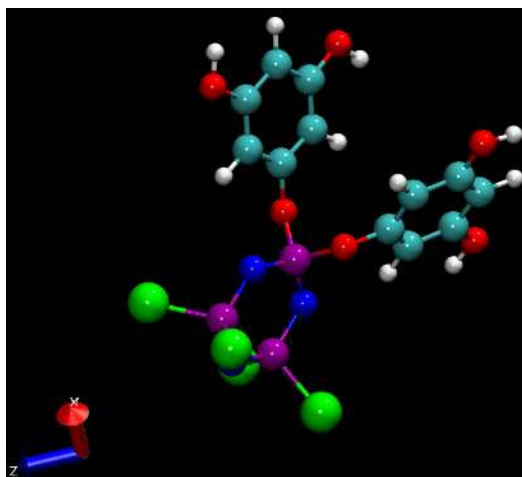


Figure 4.30 First *Gaussian*-optimized structure of HCCP_2_Cl_1_P with both Phg rings attached to the same P.

The results of the optimized HCCP_2_Cl_1_P conformers present several similarities to those for HCCP_2_Cl. As shown by 4.31 some of the conformers keep almost the same structure before and after *Gaussian* optimization. Again, only one C-C-O-P and its corresponding C-O-P-N torsion are shown for each conformer.

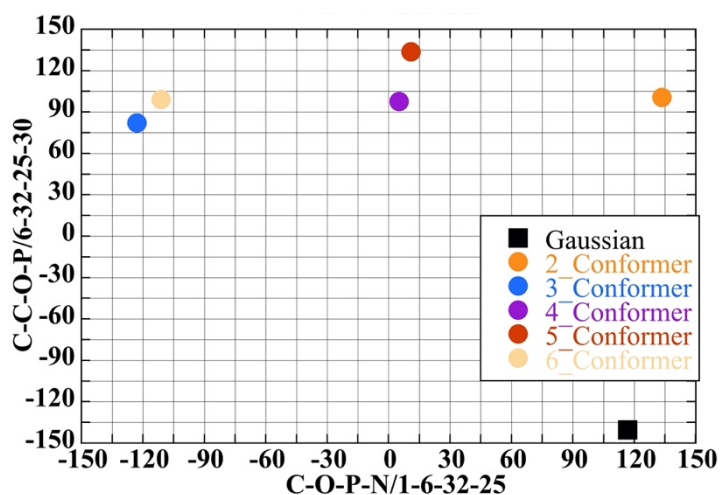


Figure 4.31 *Gaussian-optimized C-C-O-P vs C-O-P-N torsions in degrees for all HCCP_2_Cl_1_P conformers. The black square is the first Gaussian-optimized structure.*

Conformer 2 has similar values between Table 4.10 and Figure 4.31. As for HCCP_2_Cl, it is mostly the C-C-O-P torsions that change: they are initially at -140° and settle around 95° when optimized. The conformers 3, 5 and 6 also present this feature. This means that, except for that specific angle, the initial structures seem to be already in the most stable conformations. However, it has been found that on some particular atoms, the partial charges are quite different between the conformers: the N attached to the P atom involved in the link with the Phg ring, the P, C and O atoms which are part of this link and the C atoms attached to the “C_Oeth” (C of the linking bridge). For the other atoms, the charges are rather similar in all conformers. However, the differences in geometries mean that the charges can be quite different between HCCP_2_Cl_1_P (Figure 4.32) and HCCP_2_Cl (Figure 4. 29).

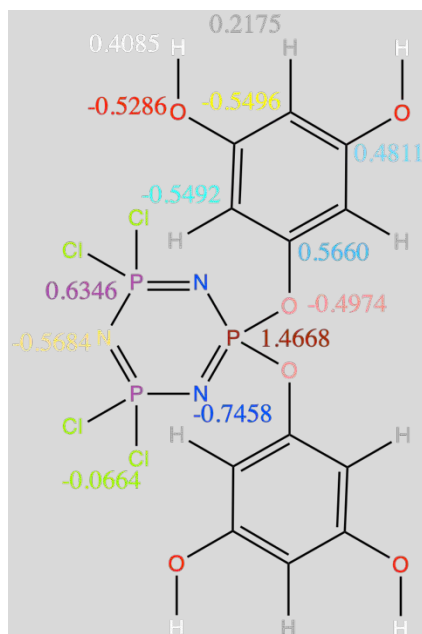


Figure 4.32 Average symmetrized partial charges q/e for HCCP_2_Cl_1_P. The atom symbols are in the same colour when they are equivalent.

4) C. 3. 4. HCCP_3_Cl

The next fragment studied was HCCP_3_Cl, where again two different “groups of conformers” are possible: the three Phg rings can be located on different sides of the plane of the HCCP ring (“on different sides”) or all three can be “on the same side”. As for HCCP_2_Cl, the conformers are named either “conformer x” (Phg rings on different sides) or “conformer x-x” (Phg rings on the same side) with “x” being the conformer number.

Moreover, a third Phg ring leads to a modified “list of permutations”. Indeed, with 3 Phg rings attached, each taking a different or a same configuration, the number of possible permutations increases greatly. However, as for HCCP_2_Cl, the Phg rings are interchangeable, which means that a combination ACC is the same as CCA or even CAC. The AAA combination was not tested either due, as before, to its high probability of overlapping. This significantly decreases the number of possibilities and the new list of permutations as well as the conformers tested are shown in Table 4.11.

Table 4.11 Input torsion values in degrees for the different HCCP_3_Cl conformers. There is a new “list of permutations”.

Initial				BBB	CCC	ABC	ACC	ABB	BBC	BCC	
				1	2	3	4	5	6	7	
“ Diff side”	C-C-O-P	2-46-40-39	-145.5	120	120	120	120	120	120	120	
		4-30-28-27	81.1	120	120	180	180	180	120	120	
		6-17-10-11	108.6	120	120	120	120	120	120	120	
	C-O-P-Cl	7-6-17-10	21.6	120	-120	-120	-120	120	120	-120	
		8-4-30-28	2.7	120	-120	0	0	0	-120	120	
		9-2-46-40	-139.1	120	-120	120	-120	120	120	-120	
	C-C-O-H	11-12-18-23	-2.0								
		13-14-16-22	-176.3								
		25-24-31-37	0.9								
		25-26-32-36	0.9								
		39-38-45-51	-179.9								
		41-42-44-50	179.3								
	Initial				1-1	2-2	3-3	4-4	5-5	6-6	7-7
	“ Same side”	C-C-O-P	2-46-40-39	95.9	120	120	120	120	120	120	120
			4-30-28-27	55.6	120	120	180	180	180	120	120
			6-17-10-11	-96.8	120	120	120	120	120	120	120
		C-O-P-Cl	7-6-17-10	-110.2	120	-120	-120	-120	120	120	-120
			8-4-30-28	-125.8	120	-120	0	0	0	-120	120
9-2-46-40			7.5	120	-120	120	-120	120	120	-120	
C-C-O-H		11-12-18-23	178.7								
		13-14-16-22	1.1								
		25-24-31-37	-179.3								
		25-26-32-36	179.0								
		39-38-45-51	-177.8								
		41-42-44-50	-1.1								

The initial *Gaussian*-optimized structures are displayed in Figure 4.33.

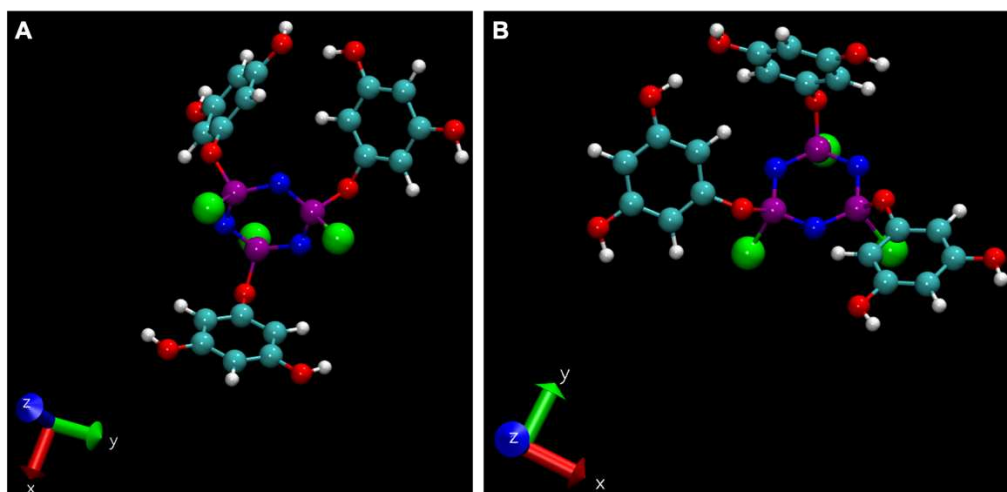


Figure 4.33 Initial *Gaussian*-optimized structure for HCCP_3_Cl with: (A) two Phg rings on one side of the HCCP plane and the third on the other and (B) all three Phg rings on the same side.

Without surprise, some conformers have globally almost the same structures before and after *Gaussian* optimization (Figure 4.34 and Table S4.2). The results of the previous fragments had already shown that some initial structures were stable enough not to change much during the optimization. Moreover, the positions of the hydroxyl H on the Phg rings are always in the same plane as the corresponding phenyl rings, *i.e.* the C-C-O-H torsions are close to $\pm 180^\circ$.

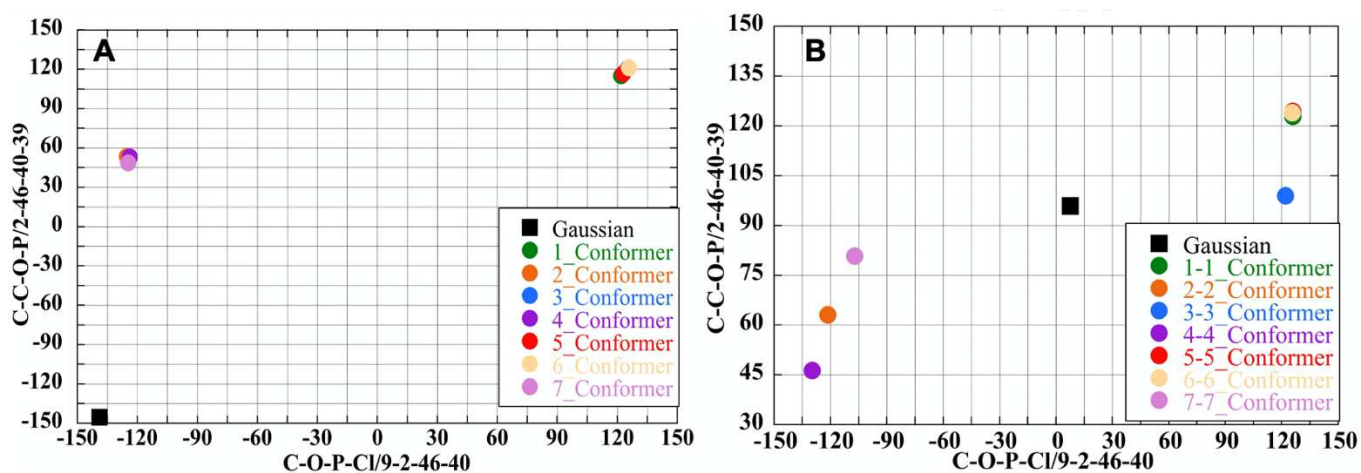


Figure 4.34 *Gaussian*-optimized C-C-O-P vs C-O-P-Cl torsions in degrees for all HCCP_3_Cl conformers with the Phg rings being either “on different sides” (A) or “on the same side” (B). The black squares are the first *Gaussian*-optimized structures.

When comparing the different HCCP_3_Cl conformers, some structures after optimization are close to each other. For example, conformers 3 and 5 (“on different sides”) have quite similar values, as well as conformers 1-1 and 6-6 (“on the same side”). The main differences between the similar conformers are mostly the C-C-O-P torsions: for conformers 3 and 5, the C-C-O-P 6-17-10-11 torsion has a difference of $\sim 70^\circ$, and for the 1-1 and 6-6 conformers, the 4-30-28-27 torsion has a difference of $\sim 40^\circ$. Moreover, conformers which finally end up with the same optimized structure seem to suggest that there are not too many stable structures for HCCP_3_Cl.

In comparison to HCCP_2_Cl, where the charges of the conformers “on different sides” were very close to those “on the same side”, the differences are found to be slightly larger for HCCP_3_Cl. *i.e.* they can change by 0.02 to 0.05 e. The symmetrized charges for equivalent atoms are presented for the “on different sides” and “on the same side” fragments separately in Figure 4.35.

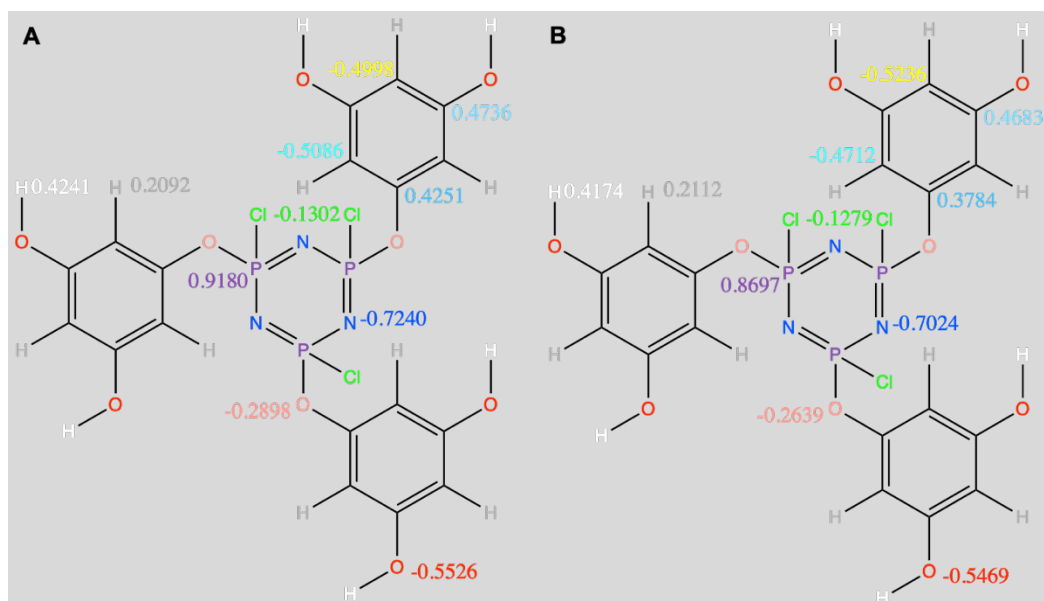


Figure 4.35 Average symmetrized partial charges q/e for HCCP_3_Cl fragments with Phg rings being on “different sides” (A) or “on the same side” (B). The atom symbols are in the same colour when they are equivalent.

4) C. 3. 5. Phg_2_OH

For Phg, all three of its reactive -OH groups can be substituted. Phg_1_OH is the same as HCCP_1_Cl, hence it does not need to be studied. Phg_2_OH has two hydroxyl hydrogens replaced each by a HCCP ring and the same process was applied than for the HCCP-centered fragments. The permutations studied are based as before on the HCCP_1_Cl families and are given in Table 4.12.

Table 4.12 Input torsion values in degrees for the different Phg_2_OH conformers.

Initial			AA	BB	CC	AB	AC	BC	
			1	2	3	4	5	6	
C-C-O-P	2-1-8-30	84.5	120	-90	-90	-90	180	120	
	2-3-9-17	82.8	120	-90	-90	-90	-90	-90	
C-O-P-Cl	1-8-30-31	-1.0	0	90	-120	0	0	120	
	3-9-17-22	-0.1	0	90	-120	120	180	180	
C-C-O-H	4-5-7-13	179.2							

For this fragment, there are only two “levels of conformers”, *i.e.* the second and the third level (Table 4.6). Indeed, there is one *O per carbon*, which means that there is only one possible attachment point for the HCCP monomer. However, this apparent simplification leads to a freedom of movement for the HCCP rings, which unfortunately results in many more possible overlaps than for the other fragments. Although the permutation names have been kept in Table 4.12, the HCCP_1_Cl conformer used to represent the family (Table 4.8) is not obligatorily the same as in the initial selection. The one chosen was simply that which avoided best these overlaps.

The initial *Gaussian*-optimized structure of Phg_2_OH is displayed in Figure 4.36 along with the initial structure of conformer 6 in order to show how HCCP rings can end up on the same side of the Phg plane simply by changing the C-C-O-P torsions. Figure 4.37 presents the *Gaussian*-optimized torsions for all conformers.

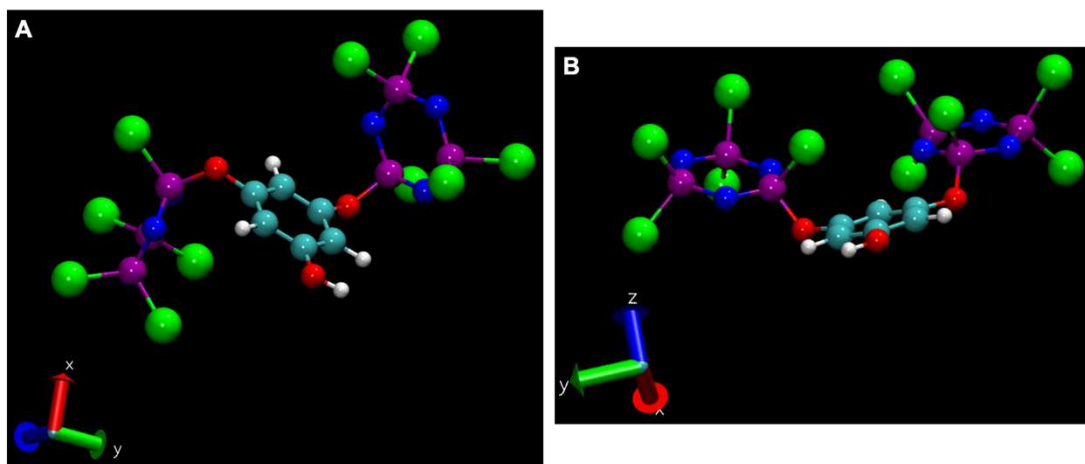


Figure 4.36 Initial *Gaussian*-optimized structure for Phg_2_OH (A) and structure (before optimization) of conformer 6 (B).

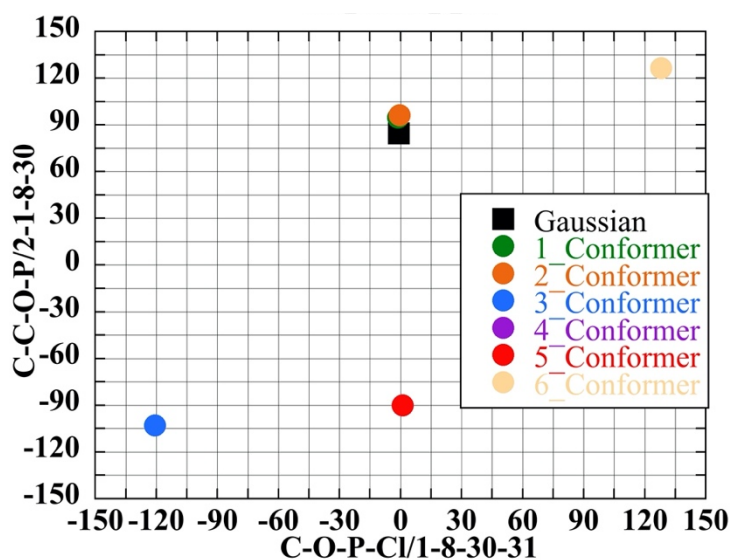


Figure 4.37 *Gaussian*-optimized C-C-O-P vs C-O-P-Cl torsions in degrees for all Phg₂OH conformers. The black square is the first *Gaussian*-optimized structure.

Conformer 1 seems to have the same global structure before and after optimization with a difference of $\sim 30^\circ$ for the C-C-O-P torsions while conformers 4 and 5 have a final structure which has no more than 1° difference on average. The average symmetrized charges are presented in the usual way in Figure 4.38.

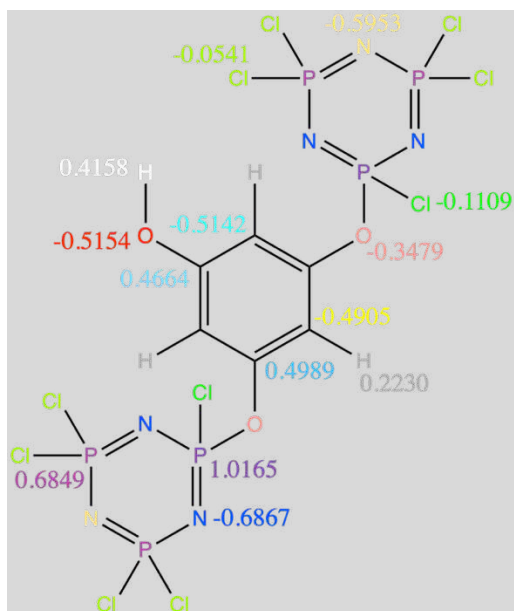


Figure 4.38 Averages symmetrized partial charges q/e for Phg₂OH. The atom symbols are in the same colour when they are equivalent.

4) C. 3. 6. Phg_3_OH

The last fragment studied was Phg_3_OH, *i.e.* all OH groups being substituted by HCCP, and Table 4.13 gives the different conformers tested for this fragment. Only the permutations without overlaps were considered, hence AAA was not tested either. Another particularity of this fragment is the absence of hydroxyl hydrogens (Figure 4.39), since the three -OH are involved in links with HCCP rings. Obviously, the aromatic H cannot rotate, and therefore, there are no torsions including hydrogen atoms in the Table.

Table 4.13 Input torsion values in degrees for the different Phg_3_OH conformers.

Initial			BBB	CCC	ABC	ACC	ABB	BBC	BCC
			1	2	3	4	5	6	7
C-C-O-P	2-1-8-29	79.0	-90	-90	-90	180	-90	-90	-90
	2-3-9-16	-117.2	-90	-90	-90	-90	-90	-90	-90
	4-5-7-38	119.7	-90	-90	-90	-90	-90	-90	-90
C-O-P-Cl	1-8-29-30	0.2	90	-120	0	0	0	90	-90
	3-9-16-21	-125.0	90	-120	120	180	120	90	-90
	5-7-38-43	124.8	90	-120	-120	180	120	180	120

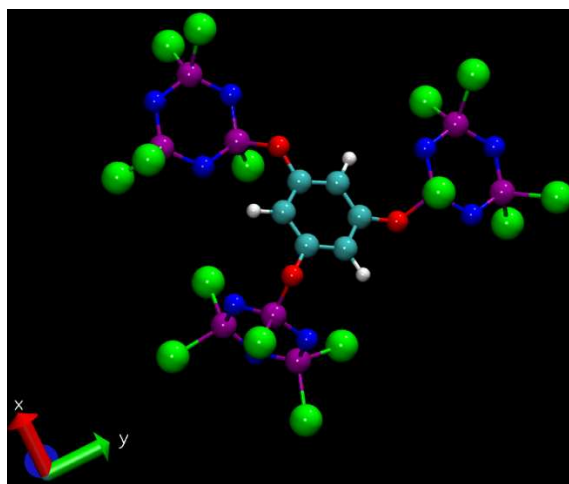


Figure 4.39 First *Gaussian*-optimized structure of Phg_3_OH.

Unlike the previous fragments, no conformers have the same structure before and after optimization. However, the *Gaussian*-optimized structure for conformer 4 is close to that of conformer 5, as shown by Figure 4.40 and Table S4.3.

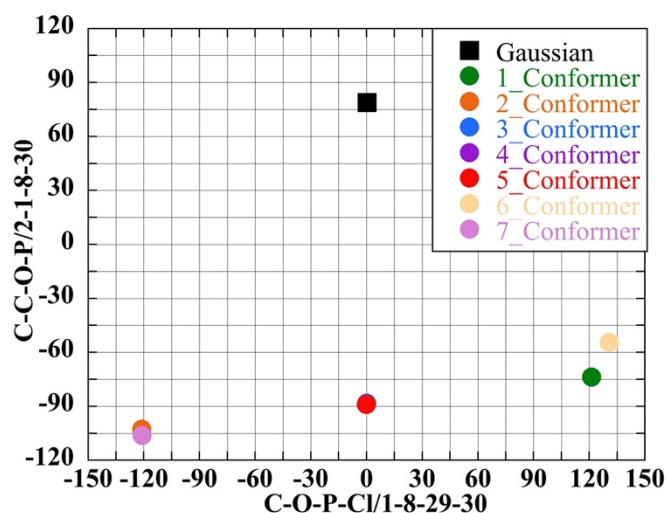


Figure 4.40 *Gaussian*-optimized C-C-O-P vs C-O-P-N torsions in degrees for all Ph₃OH conformers. The black square is the first *Gaussian*-optimized structure.

As expected, the partial charges for the two similar conformers 4 and 5 are very close too. For the other conformers, the partial charges differ a bit more. However, when their average values are compared to those for Phg₂OH, they are quite close except for the charges on the unique Phg ring, *i.e.* its O_{ether}, Car_H and Car_{Oeth} atoms. The final partial charges are presented in Figure 4.41.

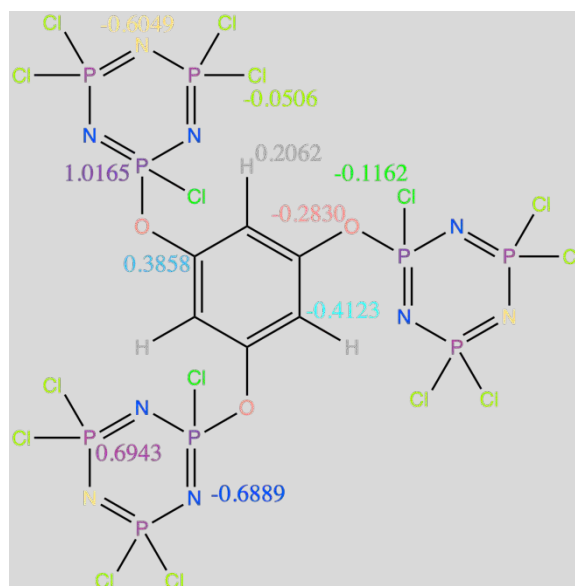


Figure 4.41 Average symmetrized partial charges q/e for Phg₃OH. The atom symbols are in the same colour when they are equivalent.

Now that the average partial charges of atoms have been determined for each fragment, some remarks can be made:

- The charges of the central monomer, *i.e.* the one which is substituted, seem to change more than the charges of the attached monomers.
- The atoms which are away from the linking bridge(s) have much the same charges whatever the fragment studied: Cl-(HCCP), H-(O), H-(Car), O-(H) as well as Car-(OH). On the other hand, the atoms close to the linking bridge(s) show more variations depending on the fragment.
- Two atoms do not follow this trend: (i) the Cl_Oeth which, although close to the linking bridge, does not change too much and (ii) the Car-(H) without an equivalent C, which is as far away as the Car-(OH) or O-(H) atoms, but has a charge that varies a lot between the different fragments. The variability for this particular Car might be explained by the aromaticity, *i.e.* the charge distribution moves easier between carbons than in other types of molecules.

This extended study of the partial charges of atoms (Table 4.5), allowed the force field to be completed by averaging the results over all fragments.

4) C. 4. Set of optimized partial charges

As described in the former Sections, the study of eight different fragments of Phg-HCCP and all their different conformers was carried out using *Gaussian* [203]. *Gaussian* is limited to relatively small fragments so it is not viable as a method to determine the partial charges when the fragments grow in size to form a continuous network. To use a more pragmatic approach, the average partial charges for each atom type in the eight different fragments were thus extracted from all their different conformers and then symmetrized in the case of equivalent atoms.

These values are collected in Table 4.14. They were then averaged over all the fragments studied, when the atom type exists (column “Average for fragments”), and, when possible, the difference with respect to the values in pure HCCP and Phg was assessed (column named “Difference w.r.t. monomer”).

- The charges on the hydroxyl hydrogens H-(O), aromatic hydrogens H-(Car), and Cl atoms are fairly invariant. Their differences with respect to the pure monomers are all less than 0.006 e and therefore these charges were left at the pure monomer values.
- The charges for the Car-(H) and Car-(H)_Oeth, *i.e.* a Car-(H) bonded to an aromatic carbon linked to an ether oxygen Car-(Oeth), are quite close, so it is reasonable to use the same value for both, *i.e.* the average of both their average fragment value.
- The situation is similar for Car-(OH) and Car-(Oeth), so both their fragment average values are averaged together.
- For all the other atoms, the fragment average is used.

The full set of proposed partial charges for all the different atom types that can occur in the Phg-HCCP fragments is highlighted in yellow in Table 4.14. These are the values to be assigned to atoms during the modelling of the polymerization process. However, these values cannot assure an exact electroneutrality for each of the many different possible fragment molecules, consequently Equations S4.2-S4.5 in the SI allow to overcome this issue.

Table 4.14 Partial charges (in units of e) for the different atom types. The average charge extracted from all fragments that contain the atom type are given as well as the difference with that in the pure monomers. The proposed charges to use for the MD simulations are given in the last column highlighted in yellow.

Atom Type	Pure Phg or HCCP	HCCP 1_Cl	HCCP 2_Cl diff.	HCCP 2_Cl same	HCCP 2_Cl_1P	HCCP 3_Cl diff.	HCCP 3_Cl same	Phg 2_O H	Phg 3_OH	Average for fragments	Difference w.r.t. monomer	Propo.
Car(H)	-0.582	-0.5379	-0.4999	-0.4768	-0.5496	-0.4998	-0.5236	-0.5142		-0.5145	0.0675	-0.5097
Car(OH)	0.517	0.4775	0.4793	0.4603	0.4811	0.4736	0.4683	0.4664		0.4724	-0.0446	0.4692
O(H)	-0.5593	-0.5263	-0.541	-0.539	-0.5286	-0.5526	-0.5469	-0.5154		-0.5357	0.0236	-0.5357
H(O)	0.4093	0.4088	0.4176	0.414	0.4085	0.4241	0.4174	0.4158		0.4152	0.0059	0.4093
H(Car)	0.215	0.2157	0.216	0.2159	0.2175	0.2092	0.2112	0.223	0.2062	0.2143	-0.0007	0.2150
P	0.7758	0.7123	0.6002	0.6593	0.6346			0.6849	0.6943	0.6643	-0.1115	0.6643
N	-0.6456	-0.6119	-0.6364	-0.6601	-0.5684			-0.5953	-0.6049	-0.6128	0.0328	-0.6128
Cl	-0.0651	-0.0637	-0.0563	-0.0661	-0.0664			-0.0541	-0.0506	-0.0595	0.0056	-0.0651
P_OCl		1.0384	0.9394	0.9625		0.918	0.8697	1.0165	1.016	0.9658		0.9658
N_(P-OCl)		-0.7015	-0.7107	-0.7523	-0.7458	-0.724	-0.7024	-0.6867	-0.6889	-0.7140		-0.7140
Cl_(P-OCl)		-0.1252	-0.1223	-0.1256		-0.1302	-0.127	-0.1109	-0.1162	-0.1225		-0.1225
O_ether		-0.3359	-0.3315	-0.3472		-0.2898	-0.2639	-0.3479	-0.283	-0.3142		-0.3142
Car(Oeth)		0.4645	0.5078	0.5021	0.566	0.4251	0.3784	0.4989	0.3858	0.4661		0.4692
Car(H)_Oeth		-0.513	-0.5517	-0.5416	-0.5492	-0.5086	-0.4712	-0.4905	-0.4123	-0.5048		-0.5097
P_O2					1.4668					1.4668		1.4668
O_ether_PO					-0.4974					-0.4974		-0.4974

This complex force-field should be now capable of modelling all possible permutations of linked Phg-HCCP molecules along with a mixture of Phg and HCCP monomers. This will allow the creation of a network with the necessary connectivity changes, atom eliminations and partial charge reassignments in order to mimick the reaction of HCCP and Phg.

4) D. Supporting information

The following Equation is used to estimate the density of an ideal mixture containing HCCP and Phg monomers, where the volumes of each can be added.

$$\begin{aligned} V_{mix} = V_{HCCP} + V_{Phg} &\Rightarrow V_{mix} = \frac{N_{HCCP}m_{HCCP}}{\rho_{HCCP}} + \frac{N_{Phg}m_{Phg}}{\rho_{Phg}} \Rightarrow \rho_{mix} \\ &= \frac{N_{HCCP}m_{HCCP} + N_{Phg}m_{Phg}}{V_{mix}} = \frac{N_{HCCP}m_{HCCP} + N_{Phg}m_{Phg}}{\frac{N_{HCCP}m_{HCCP}}{\rho_{HCCP}} + \frac{N_{Phg}m_{Phg}}{\rho_{Phg}}} \end{aligned} \quad (S4.1)$$

For example, for an equimolar (1:1) mixture and densities of 1771 kg m⁻³ for pure HCCP and 1371 kg m⁻³ for pure Phg, the equation above gives an estimated ideal mixing density of ~1643 kg m⁻³.

To ensure electroneutrality for all possible fragments during the reaction phase, a slight adjustment of the partial charge on each atom is carried out for each new Phg-HCCP fragment molecule. The sum of the initial charges, q_i , for each atom, i , in a molecule of N atoms can be written as:

$$Q = \sum_{i=1}^{i=N} q_i \quad (S4.2)$$

If the adjusted charge is defined as:

$$q'_i = q_i - \Delta q \quad (S4.3)$$

and it is required that the sum of these adjusted charges to be zero

$$\sum_{i=1}^{i=N} q'_i = 0 \quad (S4.4)$$

then the slight adjustment that has to be applied can be determined by:

$$\sum_{i=1}^{i=N} (q'_i - \Delta q) = Q - N\Delta q = 0 \Rightarrow \Delta q = \frac{Q}{N} \quad (S4.5)$$

This simple pragmatic approach guarantees that for all possible Phg-HCCP fragments that they respect electroneutrality and the charges are close to the target ones given in Table 4.14.

Table S4.1 Selected *Gaussian*-optimized torsions in degrees for all HCCP_2_Cl conformers “on different sides” (A) and “on the same side” (B). Only non-redundant torsions are shown and the black rows are the first *Gaussian*-optimized structures taken as references.

		P-O-C-C/ 6-18-11-12	Cl-P-O-C/ 8-4-31-29	C-C-O-H/ 12-13-19-24	C-C-O-H/ 14-15-17-23	C-C-O-H/ 26-25-32-38	C-C-O-H/ 26-27-33-37
Diff side	Gaussian	55.2	-1.2	-179.9	-0.7	179.4	-1.5
	Conformer 1	94.4	2.8	-177.6	-1.2	-179.6	2.4
	Conformer 2	119.5	127.1	-178.7	-0.2	-179.8	1.0
	Conformer 3	36.7	-116.3	179.4	-12.0	176.2	0.9
	Conformer 4	123.4	3.7	-178.9	0.5	-179.9	2.4
	Conformer 5	55.3	-1.1	-179.9	-0.7	179.5	-1.5
	Conformer 6	122.0	-127.2	-178.6	-0.3	179.9	0.2
Same side	Gaussian	-86.4	15.348	-6.748	2.119	7.424	-1.0
	Conformer 1-1	115.4	16.1	-29.4	1.3	-1.2	-0.1
	Conformer 2-2	118.0	128.0	0.3	-0.2	-0.5	1.1
	Conformer 3-3	56.5	-124.9	-0.7	-1.1	-1.2	0.3
	Conformer 4-4	94.7	3.7	0.8	-1.0	-1.8	11.2
	Conformer 5-5	55.8	5.2	-0.6	-1.1	1.8	-0.6
	Conformer 6-6	166.3	-122.8	-2.7	0.6	-9.9	0.8

Table S4.2 Selected *Gaussian*-optimized torsions in degrees for all HCCP_3_Cl conformers “on different sides” (A) and “on the same side” (B). Only non-redundant torsions are shown and some C-C-O-H are removed for the sake of clarity. The black rows are the first *Gaussian*-optimized structures.

		P-O-C-C/ 4-30-28-27	P-O-C-C/ 6-17-10-11	Cl-P-O-C/ 7-6-17-10	Cl-P-O-C/ 8-4-30-28	C-C-O-H/ 11-12-18-23	C-C-O-H/ 13-14-16-22	C-C-O-H/ 25-26-32-36	C-C-O-H/ 39-38-45-51
Diff side	Gaussian	81.1	108.6	21.6	2.7	-1.9	-176.3	0.9	-179.9
	Conformer 1	114.0	119.3	125.4	120.9	0.2	-179.7	-0.5	179.9
	Conformer 2	34.8	59.3	-116.6	-125.8	-1.0	175.8	0.6	-179.9
	Conformer 3	-103.9	54.4	-127.7	-5.7	-0.4	179.1	-3.2	-179.8
	Conformer 4	-96.1	56.5	-124.2	-2.8	-0.2	179.2	-2.7	179.9
	Conformer 5	-98.1	122.9	125.7	-3.5	0.3	-179.7	-2.8	-179.6
	Conformer 6	50.0	120.2	123.5	-125.0	0.3	-179.8	-0.0	-179.0
Conformer 7	123.3	56.0	-125.2	125.4	-0.6	-179.8	0.6	179.7	
Same side	Gaussian	55.6	-96.8	-110.2	-125.8	178.7	1.1	179.0	-177.8
	Conformer 1-1	117.1	116.7	121.2	124.0	-178.0	-1.0	179.4	-178.6
	Conformer 2-2	57.3	54.7	-125.2	-125.6	-179.7	-1.0	179.4	-179.1
	Conformer 3-3	-119.7	81.8	-34.4	-30.2	165.8	-11.6	170.4	176.8
	Conformer 4-4	-126.7	62.2	-35.7	-18.8	-179.9	-6.6	173.1	179.9
	Conformer 5-5	-93.1	97.5	110.7	-8.6	-178.1	-1.7	-179.9	-178.0
	Conformer 6-6	78.8	113.2	119.8	-108.8	175.4	-1.0	179.7	-178.5
Conformer 7-7	125.9	55.4	-124.1	129.7	-179.9	-1.2	179.0	-178.5	

Table S4.3 Selected *Gaussian*-optimized torsions in degrees for all Phg₃_OH conformers “on different sides” (A) and “on the same side” (B). Only non-redundant torsions are shown and the black row is the first *Gaussian*-optimized structure.

	C-C-O-P/2-3-9-16	C-C-O-P/4-5-7-38	C-O-P-Cl/3-9-16-21	C-O-P-Cl/5-7-38-43
Gaussian	-117.2	119.7	-125.0	124.8
Conformer 1	-55.3	-74.6	125.5	118.6
Conformer 2	-101.6	-121.2	-118.6	-125.5
Conformer 3	-54.9	-121.8	131.7	-131.8
Conformer 4	-50.7	-56.8	127.6	125.3
Conformer 5	-50.7	-56.8	127.6	125.3
Conformer 6	-50.3	-53.4	126.3	128.8
Conformer 7	-98.8	-54.7	-115.1	126.3

4) E. Acknowledgments

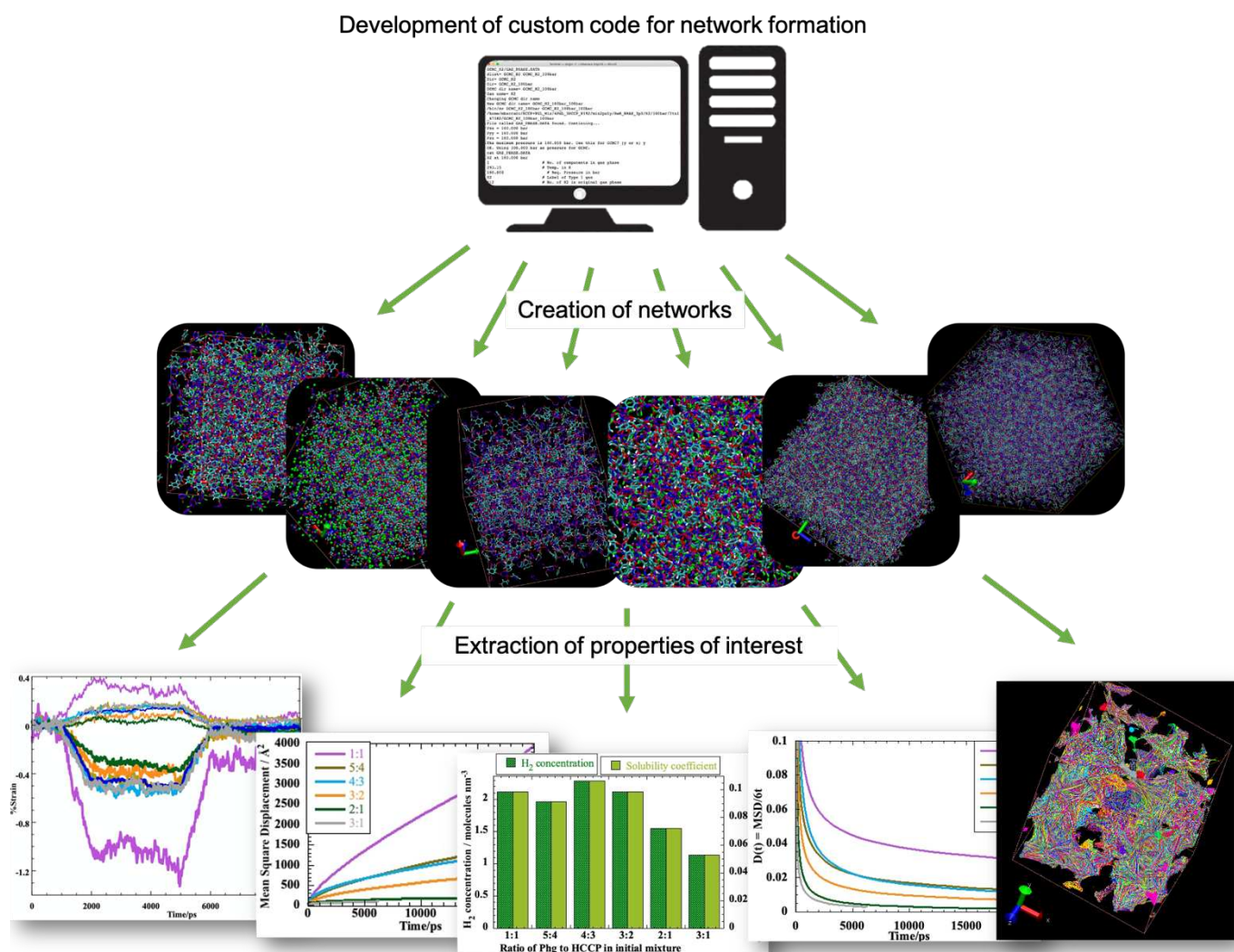
This research forms part of the research programme of DPI, project DINGOES #845. It had access to the HPC resources of TGCC/CINES/IDRIS under the allocations A009-095053 and A011-095053 made by GENCI, France. N. Charvin is thanked for his help with the installation and maintenance of the LEPMI local servers.

4) F. Abbreviations list

➤ CDP	ChemDraw Prime
➤ CT	Connectivity Table
➤ DFT	Density functional theory
➤ DMSO	Dimethyl sulfoxide
➤ EM	Energy minimization
➤ FTIR	Fourier transform infrared
➤ HCCP	Phosphonitrilic chloride trimer
➤ IP	Interfacial polymerization
➤ LJ	Lennard-Jones
➤ MD	Molecular dynamics
➤ NMR	Nuclear magnetic resonance
➤ Phg	1,2,3-Benzenetriol
➤ VMD	Visual Molecular Dynamics

Chapter 5 : Molecular Modelling - Cross-linked Polyphosphazene Networks

5) A. Graphical abstract



Part of this work in this chapter was carried out using the HPC resources of CCRT/CINES/IDRIS under the allocations A011, A013 and A015-095053 made by GENCI, France.

Figure 5.1 recalls the modelling process carried out to eventually characterize the permeation of hydrogen in models of cross-linked phloroglucinol-hexachlorocyclotriphosphazene (Phg-HCCP) polymer. Even if the former experimental work suggested that this network polymer has promising hydrogen barrier properties [260], there remain a large number of unanswered questions. Indeed, it is not clear if the network polymer is solely responsible for the barrier effect or whether the excess reactants, the solvents and the by-products of the reaction trapped within the network are also part of it. The exact composition of the network polymer is difficult to ascertain by standard elemental analyses due in part to the presence of these contaminants. It is also possible that there is an optimal stoichiometry of the monomers to obtain the best barrier behaviour. As such, an extensive study of the effect of this parameter was undertaken *in silico* to assess which Phg:HCCP ratio gave the best results, *i.e.* the lowest permeability coefficient for H₂. It is much easier to control the monomer ratio at the interface in a simulation than experimentally. Moreover, it is also relatively straightforward to determine hydrogen permeation at high pressures in a dense polymer model. Experimentally, this is a task that is not without risk and which requires specialist equipment. To obtain a model polymer network, the modelling part was separated into several step (Figure 5.1).

As for the previous Chapter, some parts were conducted by another member of team but they will be summarized in the next Sections. Manuscripts with more details are under preparation.

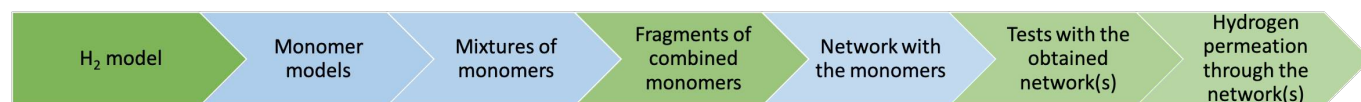


Figure 5.1 Modelling process to obtain hydrogen permeation in a dense polymer network of HCCP and Phg. Step 1 is detailed in Chapter 3, Steps 2-4 in Chapter 4 and the present Chapter concentrates on Steps 5-7. The blue steps have been mainly carried out by another member of the project team.

In Chapter 4, mixtures of the monomers were prepared and a force field capable of modelling all possible fragments constructed by reactions was optimized. This Chapter focuses on the reactions between the monomers *in-silico* in order to obtain a series of cross-linked Phg-HCCP structures, which are then used to make different tests.

5) B. The algorithm to mimick polymerization

An homogeneous Phg:HCCP 1:1 mixture of 1024 molecules was prepared at room temperature, *i.e.* 20°C (cf. Chapter 4). This equimolar mixture served as a basic test system for the protocol to create the

network polymers. To perform the reaction between the model monomers, *i.e.* bonding them together by linking the P atom in HCCP to the hydroxyl O in Phg, different criteria are necessary to define if a reaction should occur or not in the mixture.

5) B. 1. Definition of the main “reaction” criterion

A simple distance criterion was used for the reactions between the OH groups on Phg and the P-Cl groups on HCCP. To determine the typical distances between the atoms involved in the reaction, radial distribution functions $g(r)$ were calculated for the Phg:HCCP 1:1 mixture. The average $g(r)$ functions for the O \cdots P, O \cdots Cl and (O)-H \cdots Cl distances are provided in Figure 5.2. They show that the closest distance between the hydroxyl H in Phg and the Cl in HCCP is ~ 2.5 Å. The $g(r)$ for O \cdots Cl is inevitably close to that of the (O)-H \cdots Cl. The $g(r)$ for O \cdots P shows that, when the connectivity will be changed to an O-P covalent bond, the latter is expected to be considerably stretched at the start since the minimum O \cdots P distances are at least 3 Å, compared to the equilibrium length of 1.6 Å for the new O-P bond.

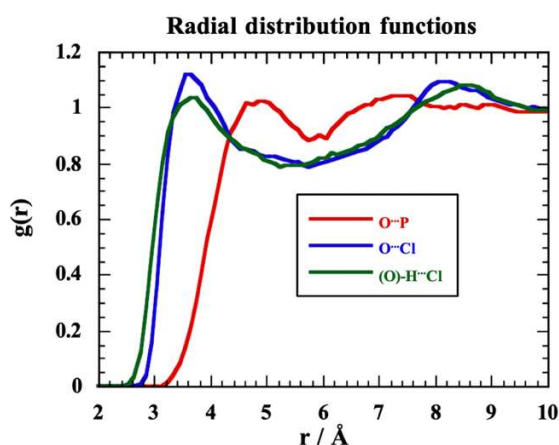


Figure 5.2 Radial distribution functions $g(r)$ for the different atom types of a mixture involved in the reactions between HCCP and Phg.

To perform the reactions, the distance criterion R_{\max} , which defined the upper limit for a reaction to occur, was based on the lowest (O)-H \cdots Cl distances observed in the radial distribution functions. The reaction algorithm can be described as follows:

- 1) Read-in a configuration containing a mixture of Phg and HCCP monomers, as well as any existing Phg-HCCP fragment molecules from previous reaction steps.
- 2) For each Cl atom on a HCCP moiety, search all the hydroxyl H on the Phg moieties and calculate the (O)-H \cdots Cl distance. If the distance is $\leq R_{\max}$, store the distance and the identity of the hydroxyl H. Once the search is finished, reorder the list in terms of increasing (O)-H \cdots Cl distances.
- 3) Search the stored list of (O)-H \cdots Cl distances for the minimum distance R_{\min} between each Cl and a hydroxyl H. Go to Step 4
- 4) The H and Cl atoms concerned are flagged as reacting and are to be removed from the system (including from the list), while the O and P atoms are bonded together and their connectivities are updated to account for the elimination of the H and Cl atoms. Go back to Step 3 to redo a search for minimum (O)-H \cdots Cl distances.
- 5) The reaction step is terminated when no (O)-H \cdots Cl distances are found $\leq R_{\max}$.
- 6) Search the connectivity table to identify individual molecules and reorder atoms into a molecule-by-molecule sequence.
- 7) For all molecules that have undergone reactions, reassign the basic charges found in the previous Chapter (Table 4.14) according to their atom types. Set the net charge on these molecules to zero (cf. SI of the previous Chapter).
- 8) Write out the final configuration, connectivity table and charges etc. following the reactions.

Some remarks are in order concerning the simplified approach to polymerization used in the simulations compared to the experimental procedure:

- No explicit all-atom simulation is made of the interface between the two immiscible solvent. This would require significantly greater resources than is currently possible. Only the monomers are simulated explicitly and standard 3D periodic boundary conditions are used to minimize system size effects (cf. Chapter 2). At the molecular scale, the monomers are assumed to form a relatively homogeneous mixture at the interface with a specific stoichiometric molar ratio. This *local* stoichiometric molar ratio can be simply controlled by varying the numbers of each monomer when initially preparing the dense model mixture. In reality, the link between this local ratio at the interface and the bulk molar ratios in the macroscopic solutions is clearly much more complicated, as will be seen later. Nevertheless, experimentally, the absolute molar concentrations of both *bulk* solutions can be controlled and can probably be optimized to promote the best properties for the barrier film.

- No attempt is made to explicitly simulate the deprotonation of the Phg hydroxyl groups using KOH to render them reactive as in the experimental process. It is assumed that all OH groups can potentially react since it is very likely that the deprotonation kinetics is a dynamic equilibrium *i.e.* the deprotonation is an ongoing dynamic process throughout the reaction phase.
- The probability of a reaction occurring is only dependent on the distance between the Cl atoms and the hydroxyl groups.
- It is assumed that the H^+ and Cl^- produced by the reaction are eliminated from the polymer when a new bond is formed. Experimentally, there is evidence that KCl is present as a contaminant in the films.
- All unreacted monomers or partially-reacted fragments are assumed to be trapped in the network polymer that is formed. Indeed, they are only found in minimal amounts.

Initial tests with various R_{max} were made on a single configuration of the Phg:HCCP 1:1 mixture (1024 molecules, *i.e.* 512 Phg and 512 HCCP) at 20°C. The numbers of reacted chlorines as a function of R_{max} are presented in Figure 5.3 and their percentage is shown in Figure S5.1.

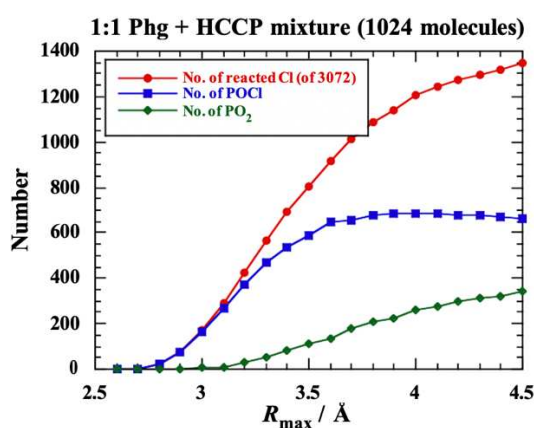


Figure 5.3 Numbers of reacted Cl as a function of the R_{max} parameter, *i.e.* the distance below which the H-(O) and Cl atoms are deemed to “react”. Also shown are the numbers of POCl (only one Cl reacted on a P) and PO₂ (both Cl reacted on a P) groups created by the reactions.

The number of possible reactions increases rapidly above $R_{max} \sim 3.0 \text{ Å}$, in coherence with the radial distribution functions (Fig. 5.2). To limit the steric strain on the system when the long P-O bonds formed are reduced down towards their equilibrium value of 1.6 Å , it was found necessary to limit the number of simultaneous reactions by introducing a progressive procedure with consecutive reaction phases. This allows the system to relax between reaction phases and this will in turn affect the reactions that occur in the

following reaction phase. A compromise for R_{\max} will have to be found as very low values will lead to extremely long simulations in order to get to completion, *i.e.* when no more reactions occur.

Moreover, Figure 5.3 showed that both Cl attached to one P atom can react at the same instant to form PO₂ groups above $R_{\max} \sim 2.8$ Å. The number of POCl groups formed passes through a maximum at $R_{\max} \sim 3.9$ Å before tailing off as larger values of R_{\max} favour the formation of PO₂ groups. On the other hand, smaller values of R_{\max} could create a network without sufficient links to have a robust membrane. As it is not obvious whether the reaction of one Cl attached to a P has an influence on whether the second Cl can react, it was decided to prevent a P from having simultaneous reactions on each of its attached Cl atoms. Once one of its Cl has reacted, the other one can react, but only after the system has been relaxed. The effect of this modification is shown in Figure 5.4.

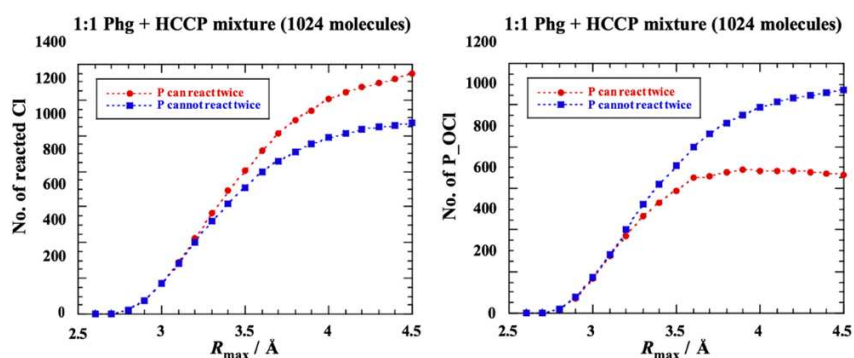


Figure 5.4 Numbers of reacted Cl as a function of R_{\max} when the P atoms are either allowed to (in red) or prevented from (in blue) having simultaneous reactions on both their attached Cl atoms (A). The same with the numbers of POCl groups (B).

Preventing the P from undergoing two reactions at the same step lowers the number of Cl that react and increases the number of P-(OCI) formed, but the effect is not too significant at the low values of R_{\max} used to generate the polymer networks.

5) B. 2. The iterative reaction/relaxation procedure

To generate the network polymer structures, an iterative process of successive reaction and relaxation steps was followed, as done elsewhere for polyPOSS-imide networks [144, 282]. The starting point is a relaxed configuration of a dense Phg:HCCP mixture, which first undergoes a static reaction phase as described in the previous Section with a specified value for R_{\max} . The output configuration thus contains a set of fragment molecules with links between their Phg and HCCP moieties as well as unreacted monomers. In the fragment molecules, the newly-formed P-O bonds are inevitably severely stretched (typically around 3 Å) and have first to be brought back down to their equilibrium value of 1.6 Å. This is

carried out by using a flexible harmonic P-O bond potential with a force constant of 500 kg s^{-2} . All other bonds are kept rigid. The following optimized procedure was generally sufficient to ensure the *in-silico* polymerization process:

- 1) Carry out a reaction phase. If reactions do occur, go to Step 2. If no reactions occur, go to Step 6.
- 2) Perform an energy minimization (EM) of 18000 steps in order to reduce the length of the newly-created P-O bonds closer to the equilibrium value.
- 3) Carry out a 2 ps constant-energy *NVE* (cf. Chapter 2) simulation with MD to check whether the steric strain has been sufficiently relaxed and to partially re-thermalize the system. Under *NVE* conditions, large forces rapidly lead to algorithmic breakdowns.
- 4) Randomly reset the velocities of the atoms at the desired temperature and then perform a constant-volume controlled-temperature *NVT* (cf. Chapter 2) MD simulation for 30 ps.
- 5) Continue the MD simulation for 50 ps under controlled-pressure-tensor *NPT* conditions (cf. Chapter 2), with the on-diagonal elements of the required pressure tensor being set to 1 bar and the off-diagonal components being set to zero. This phase allows for the volume and shape of the MD box to adjust to the reactions creating more and more bonds whilst eliminating H^+ and Cl^- . The use of *NPT* conditions is also important as the system is gradually transformed from a liquid to an elastic solid. Allowing the box size *and* shape to respond prevents the build-up of inequalities between the on-diagonal components and non-zero off-diagonal components of the pressure tensor, *i.e.* shear stresses. Once the system is thermalized and relaxed, go back to Step 1 to attempt further reactions (unless the preset time limit for the simulation has been reached, in which case exit).
- 6) If no reactions have occurred, perform an additional 10 ps of *NPT* MD. Go back to Step 1 to attempt further reactions.

When no further reactions take place in spite of repeatedly applying Step 1, the polymerisation is judged to be at completion. At that stage, the P-O bonds are made rigid, an EM run of 10000 steps is performed, a 10 ps *NVE* MD phase follows, the velocities are reset to the required temperature, a 30 ps of *NVT* MD phase follows and the relaxation is continued for a further 950 ps using *NPT* MD. Properties were averaged over the final 500 ps.

Tests were carried out using this iterative approach on the Phg:HCCP 1:1 mixture containing 1024 monomers at 20°C with a series of 5 R_{max} values, *i.e.* 2.7, 2.8, 2.9, 3.0 and 3.1 Å. The aim was to assess the effect of this parameter on the number of reactions that occur, the time required to attain completion as well as the composition and connectivity of the resulting network. Selected results are given in Table 5.1 and a more complete set in the SI Table S5.1.

Table 5.1 Selected results using the iterative polymerization procedure on an equimolar Phg:HCCP mixture containing 512 monomers of each type at 20°C. Different values of the R_{max} parameter were tested.

$R_{max} / \text{Å}$	2.7	2.8	2.9	3.0	3.1
Time of last reaction / ps	58390	18220	9840	6310	2740
Total No. of reactions	1501	1506	1506	1506	1506
No. C-H in final configuration	1536	1536	1536	1536	1536
No. C-OH in final configuration	35	30	30	30	30
No. P-Cl ₂ in final configuration	392	401	390	384	368
No. Cl-PCl in final configuration	784	802	780	768	736
No. P-OCl & Cl-PO in final configuration	787	764	786	798	830
No. Oether & C-Oether in final configuration	1501	1506	1506	1506	1506
No. P-O ₂ in final configuration	357	371	360	354	338
Total No. of reacted P (out of 1536)	1144	1135	1146	1152	1168
%P-O ₂ of P bonded to an O	31.2%	32.7%	31.4%	30.7%	28.9%
%P-O ₂ of all P	23.2%	24.2%	23.4%	23.0%	22.0%
Average No. of Cl reacted <i>per</i> HCCP ring	3.088	3.067	3.061	3.092	3.042
P/Cl ratio	0.978	0.981	0.981	0.981	0.981
Avg. No. of Cl reacted <i>per</i> HCCP ring from P/Cl ratio (Chapter 6, Eq. 6.5)	2.932	2.941	2.941	2.941	2.941
C/N ratio	2.000	2.000	2.000	2.000	2.000
Avg. No. of Cl reacted <i>per</i> HCCP ring from C/N ratio (Chapter 6, Eq. 6.3)	3.000	3.000	3.000	3.000	3.000
No. of reacted O <i>per</i> Phg ring (out of 3)	2.932	2.941	2.941	2.941	2.941
No. of unreacted HCCP	26	21	20	25	17
No. of unreacted Phg	0	0	0	0	0
No. of atoms in largest molecule	10510	10560	10572	10512	10608
Total simulation time / ps	62000	20000	12000	9000	4000
Avg. density / kg m ⁻³ (from last 500 ps)	1685.3	1703.6	1686.9	1734.4	1700.0

Table 5.1 shows that the total number of reactions taking place (third row) is not particularly sensitive to the value of R_{\max} . In all cases, there are ~ 1500 reactions. There is sufficient mobility in the system to allow the H-(O) \cdots Cl distances to explore the range of values in the first peak of its $g(r)$ (Fig. 5.2). On the other hand, the value of R_{\max} considerably influences the total simulation time, *i.e.* the time taken to achieve completion (second row starting from the end). This is particularly marked when R_{\max} is reduced from 2.8 Å to 2.7 Å, as it leads to a threefold increase in the time required for completion. The cumulative number of reactions as a function of the simulation time is displayed in Figure 5.5 and in Figure S5.2 for all the values of R_{\max} tested.

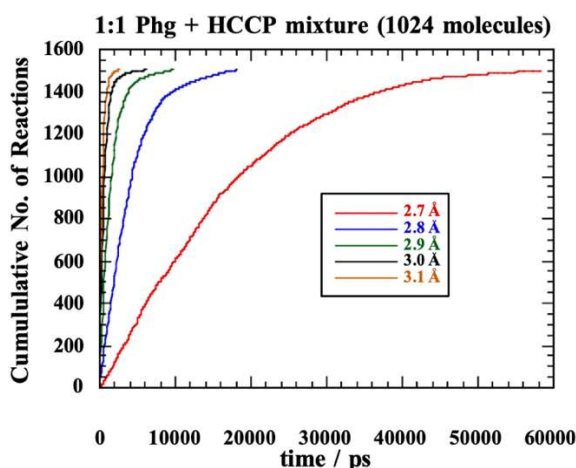


Figure 5.5 Cumulative number of reactions during the iterative procedure to form the network polymers from the Phg:HCCP 1:1 mixture containing 1024 monomers at 20°C as a function of the simulation time. The different colours are the different R_{\max} used.

The final network compositions after completion are very similar. There is essentially one large percolating network polymer molecule, which contains ~ 10500 to ~ 10600 atoms. A snapshot with $R_{\max} = 2.8$ Å is provided in Figure 5.6. In addition, there are ~ 20 or so unreacted excess HCCP monomers remaining in the system. There are no unreacted Phg monomers since all are incorporated in the large network molecule. This suggests that a Phg:HCCP 1:1 ratio is probably slightly too rich in HCCP, which is consistent with the experimental results presented later.

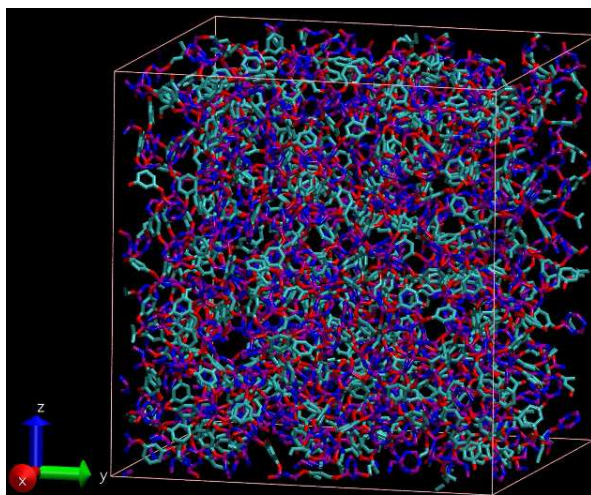


Figure 5.6 The network polymer formed after the application of the iterative polymerization procedure to a Phg:HCCP 1:1 mixture containing 1024 monomers at 20°C and using a R_{\max} value of 2.8 Å. For clarity, the H and the Cl are omitted. The colour code is: C = cyan, N = blue, P = purple, O = red and the image was created using VMD [248]. Same for the next Figures.

For Phg, the average number of reacted C-OH groups is ~ 2.94 out of 3 so there are only a very slight number of residual unreacted -OH groups. For HCCP, the number of reacted Cl *per* ring is just slightly over 3. The estimate of this number using the P/Cl ratio and Eq. 6.4 (Chapter 6) is slightly lower at ~ 2.94 due to the presence of unreacted HCCP. The estimate based on the C/N ratio and Eq. 6.3 (also Chapter 6) gives an exact value of 3, due to the stoichiometry of the mixture.

The tests also suggest that the formation of two links on the same P atom is relatively common, since almost 1/3 of the P atoms linked to *at least* an ether O are actually linked to two. If one takes into account all the P in the final system (including the P-Cl₂), $\sim 23\%$ are P-O₂. Lower values of R_{\max} tend to favour the formation of P-O₂, but the differences are marginal on these relatively small systems.

The behaviour of the simulation box volume is shown in Figure S5.3 for all the R_{\max} tested. Since each reaction eliminates one H⁺ and one Cl⁻ ion, the systems tend to contract under *NPT* conditions as the polymerization advances. Indeed, the final volumes are $\sim 24\%$ lower than the initial ones, which is consistent with the systems losing ~ 1500 H⁺ and Cl⁻ ions, *i.e.* $\sim 22\%$ of the atoms. There is also an effect due to the gradual formation of the network as more and more atoms become bonded together into a single macromolecule. The average densities for the relaxed systems are given in Table 5.1, and as expected, they are all higher than that of the initial starting mixture (~ 1670 kg m⁻³). There is a variation in the final densities obtained for different R_{\max} , but it remains within a limited range. It should be noted that volume changes can lead to the Ewald sum not converging as well unless the parameters are reoptimized (cf. Chapter 2).

A more problematic issue is that these initial tests revealed an intermittent instability in the solution of the equations of motion during the MD simulations. It was traced to a problem with the newly formed C-O-P bending angle.

5) B. 3. Algorithmic instability and change of C-O-P potential

Even if the TRIPOS force field [239] gives parameters for the linking bridges, the C-O-P angles became close to linear, causing the associated C-C-O-P, C-O-P-Cl and C-O-P-N torsion angles to become ill-defined with a concomitant divergence of the forces and hence an algorithmic breakdown. The origin of the strain in the nominally tetrahedral C-O-P angle was traced back to the interaction between the Cl atom attached to P in HCCP and the Phg ring. This was already noticed in the *Gaussian* [203] optimization of Phg-HCCP fragments, where the C-O-P angle was typically found to be $\sim 126^\circ$ (cf. Chapter 4). Figure 5.7 shows an illustration of the problem for the fragment linking one Phg and one HCCP (referred to as fragment HCCP_1_Cl in Chapter 4).

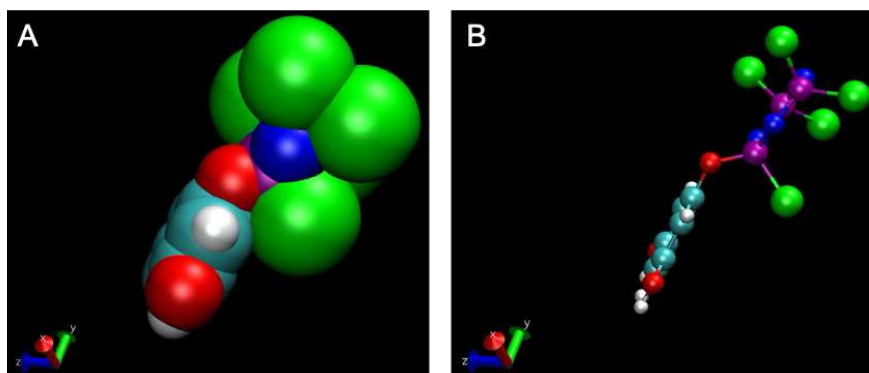


Figure 5.7 A *Gaussian*-optimized structure for a fragment made from one Phg molecule and one HCCP molecule. The “Van der Waals” representation (A) illustrates how the Cl atom impinges on the Phg atoms causing the C-O-P linking bend to be stretched. The stretching in the C-O-P angle is clearer to see in the “ball-and-stick” representation (B).

The strain in this specific C-O-P angle is particularly important since the O-P distances are considerably stretched when the bond is initially created and subsequently energy-minimized. The problem is exacerbated by the form used for the bending potential in *gmq* (cf. Chapter 2 and Equation S5.1 in SI) [194]. Although computationally more efficient than the form used in TRIPOS [239] (Equation S5.2 in SI), it has a known weakness when the angle becomes close to 180° : the potential passes through a maximum and the restoring forces go to zero. Figure S5.4 compares the *gmq* and TRIPOS forms both in the region of the equilibrium angle $\theta_0 = 109.5^\circ$ (Fig. S5.4.A), and over a wider region out to 180° (Fig. S5.4.B). To maintain the computational advantage of a formulation in terms of the *cosine* of the angle, an alternative

form of the bending potential proposed by Bulacu *et al.* [287] was implemented in *gmq*. This Restricted Bending Potential is similar to the initial form in *gmq*, except for a division by $\sin^2\theta$ (Equation S5.3 in the SI). This causes the potential to stiffen significantly as θ approaches 180° due to the fact that $\sin^2\theta$ tends to zero. The bending potential for the C-O-P bends was thus replaced by this ReB potential with $k_\theta^{\text{ReB}} = 549.41$ kJ/mole (Figure S5.4).

5) C. Effect of the monomer ratio on the polymer networks

Since the Phg:HCCP ratios at the reaction site, *i.e.* the interface, are easier to control *in silico* than in experiments, molecular modelling was used to see how the properties of the resulting network depend on this parameter. Ultimately, this can give indications as to how to optimize the synthesis in order to get a material with the best possible hydrogen barrier characteristics.

5) C. 1. Network formation with different monomer ratios in the mixture and variable R_{max}

Since the preliminary tests had shown that setting R_{max} to 2.7 \AA led to excessive simulation times (Table 5.1), this value was excluded and further tests were performed using R_{max} values of 2.8, 2.9, 3.0 and 3.1 \AA . In addition to the equimolar 1:1 mixture, the Phg:HCCP monomer ratios in the other starting mixtures were varied in favour of Phg, starting from 5:4 to 4:3 (two different system sizes), 3:2, 2:1, 3:1, 4:1, 5:1 and finally 8:1. In the experimental IP, the bulk ratio is usually 8:1, but 4:1 and 2:1 were also tested. Table 5.2 presents the combinations tested by molecular modelling.

Table 5.2 Combinations of the R_{max} parameter and Phg:HCCP monomer ratios in the mixture tested.

Ratio	R_{max}		R_{max}	Ratio
1:1	2.8	Selection of two preferential R_{max}	2.8	5:4 (= 1.25)
				4:3 ($\times 2$ for $R_{max} = 3.0$) (≈ 1.33)
	2.9			3:2 (= 1.5)
				2:1
	3.0			3:1
				4:1
	3.1			5:1
				8:1

5) C. 1. 1. Phg:HCCP 1:1 ratio and variable R_{max}

These tests were mostly aimed at checking the replacement of the C-O-P bend potential. They were carried out in the same way and on the same initial 1:1 mixture than in the former Section, albeit by

excluding $R_{max} = 2.7 \text{ \AA}$. Selected results are provided in Table 5.3 and a more complete set can be found in Table S5.2.

Table 5.3 Selected results using the iterative polymerization procedure on an equimolar Phg:HCCP mixture containing 512 monomers of each type at 20°C. The ReB potential was used for C-O-P bends and different values of R_{max} parameter were tested.

$R_{max} / \text{\AA}$	2.8	2.9	3.0	3.1
Time of last reaction / ps	19750	8830	4430	5820
Total No. of reactions	1498	1507	1506	1507
No. C-H in final configuration	1536	1536	1536	1536
No. C-OH in final configuration	38	29	30	29
No. P-Cl ₂ in final configuration	407	397	379	365
No. Cl-PCl in final configuration	814	794	758	730
No. P-OCl & Cl-PO in final configuration	760	771	808	835
No. Oether & C-Oether in final configuration	1498	1507	1506	1507
No. P-O ₂ in final configuration	369	368	349	336
Total No. of reacted P (out of 1536)	1129	1139	1157	1171
%P-O ₂ of P bonded to an O	32.7%	32.3%	30.2%	28.7%
%P-O ₂ of all P	24.0%	24.0%	22.7%	21.9%
Average No. of Cl reacted <i>per</i> HCCP ring	3.076	3.057	3.042	3.026
P/Cl ratio	0.976	0.981	0.981	0.981
Avg. No. of Cl reacted <i>per</i> HCCP ring from P/Cl ratio (Chapter 6, Eq. 6.5)	2.926	2.943	2.941	2.943
C/N ratio	2.000	2.000	2.000	2.000
Avg. No. of Cl reacted <i>per</i> HCCP ring from C/N ratio (Chapter 6, Eq. 6.3)	3.000	3.000	3.000	3.000
No. of reacted O <i>per</i> Phg ring (out of 3)	2.926	2.943	2.941	2.943
No. of unreacted HCCP	25	19	17	14
No. of unreacted Phg	0	0	0	0
No. of atoms in largest molecule	10528	10582	10608	10642
Total simulation time / ps	23000	13000	7000	7000
Avg. Density / kg m ⁻³ (from last 500 ps)	1700.6	1704.2	1679.2	1743.9
Avg. C-O-P angle / deg. (from last 500 ps)	122.8	122.7	122.6	122.7

The influence of the new ReB potential for the C-O-P angles can be seen in the average values of these angles (last row), which is reduced by $\sim 6^\circ$ compared to the form used in the initial series (last row in Table 5.3). Despite the stiffer C-O-P angles, there is no evidence to suggest that this prevents the reactions from happening.

The total number of reactions is still around 1500, the number of atoms in the percolating network, the numbers of excess HCCP molecules, the proportion of P-O₂ as well as the density are also very similar to those obtained before. The stiffer C-O-P angles do lead to a reduction in the average bending energy with a concomitant increase in the torsion and out-of-plane energies, since these other intramolecular modes take up the strain. There is also a change in the Van der Waals energy, which becomes slightly less negative (end of Tables S5.1 and S5.2).

As a whole, the use of the ReB potential for the C-O-P angles does not have a significant influence on the results, but its main advantage is that it does avoid instability problems in the procedure. For this reason, it was used systematically from here on.

In the next stage, two values of R_{max} (2.8 Å and 3.0 Å) were selected for further tests with variable Phg:HCCP ratios in order to compare a slower (2.8 Å) and a faster (3.0 Å) rate of reaction.

5) C. 1. 2. Variable Phg:HCCP ratios and $R_{max} = 2.8 \text{ \AA}$

As shown in Table 5.1 and Table 5.3, the 1:1 mixture does give a percolating polymer network structure but with a slight excess of unreacted HCCP molecules. A simple way to create other mixtures in favour of Phg and with different Phg:HCCP ratios was the following:

- 1) Start from the relaxed 1:1 mixture containing 512 monomers of each type.
- 2) Scale-up this system by 8 to form a 2×2×2 supercell containing 4096 monomers of each type.
- 3) Remove randomly a certain number of monomers of each type to obtain the required ratio.
- 4) Set the volume of the simulation box back to that expected for an ideal mixture.
- 5) Relax the system first under NVT conditions and then under NpT conditions.

A series of mixtures were obtained for Phg:HCCP ratios of 2:1, 3:1, 4:1, 5:1 and 8:1, each containing 512 monomers of HCCP. Further mixtures (5:4, 4:3 and 3:2) were then obtained in a similar fashion by using the relaxed 2:1 system. Since there were many mixtures, only those which have gone to completion will be included in the present Chapter.

It was expected that there would be too much Phg to form a percolating polymer network when starting from the 8:1 mixture, but this is the typical molar ratio used in the bulk experimental solutions. However, there is no certainty that the bulk concentration is the *local* concentration at the interface. In the simulations, no explicit solvent is simulated and, as such, the effect of the monomer ratio in the initial mixture is easier to test.

Six ratios were tested with $R_{max} = 2.8 \text{ \AA}$ (Table 5.4, where the last column corresponds to 8:1).

Table 5.4 Selected results with a R_{max} parameter of 2.8 \AA and the starting configurations being Phg:HCCP mixtures with different ratios sorted from the lowest to the highest proportion of Phg.

<i>Ratio Phg to HCCP in initial mixture</i>	1:1	5:4	4:3	3:2	2:1	8:1
Total simulation time / ps	23000	33000	27000	32000	36000	45000
Time of last reaction / ps	19750	31290	24640	30390	33540	40800
Total No. of reactions	1498	1820	1905	2045	2520	3002
Initial No. of HCCP rings	512	512	512	512	512	512
Initial No. of Phg rings	512	640	683	768	1024	4096
Total No. of reacted P (out of 1536)	1129	1278	1307	1332	1485	1536
%P-O ₂ of P bonded to an O	32.7%	42.4%	45.8%	53.5%	69.7%	95.4%
%P-O ₂ of all P	24.0%	35.3%	38.9%	46.4%	67.4%	95.4%
Avg. No. of Cl reacted <i>per</i> HCCP ring (out of 6)	3.076	3.647	3.772	4.066	4.922	5.863
P/Cl ratio	0.976	1.227	1.316	1.496	2.783	21.943
Avg. No. of Cl reacted <i>per</i> HCCP ring from P/Cl ratio (Chapter 6, Eq. 6.5)	2.926	3.555	3.721	3.994	4.922	5.863
C/N ratio	2.000	2.500	2.668	3.000	4.000	16.000
Avg. No. of Cl reacted <i>per</i> HCCP ring from C/N ratio (Chapter 6, Eq. 6.3)	3.000	3.750	4.002	4.500	6.000	24.000
Avg. No. of O reacted <i>per</i> Phg ring that reacts	2.926	2.844	2.793	2.677	2.475	1.320
No. of HCCP rings undergoing reactions	487	499	505	503	512	512
No. of Phg rings undergoing reactions	512	640	682	764	1018	2274
Ratio of <i>ALL</i> Phg rings to HCCP rings in network	1.051	1.283	1.352	1.527	2.000	8.000
Total No. of HCCP+Phg rings that react	999	1139	1187	1267	1530	2786
Avg. ring connectivity	2.999	3.196	3.210	3.228	3.294	2.155
No. of molecules in final config.	26	14	9	14	7	1861
No. of unreacted HCCP in final config.	25	13	7	9	0	0
No. of unreacted Phg in final config.	0	0	1	4	6	1822
No. of atoms in largest molecule	10528	11948	12480	13406	16374	28048
No. of HCCP rings in largest molecule	487	499	505	503	512	431
No. of Phg rings in largest molecule	512	640	682	764	1018	1862
Ratio of Phg to HCCP in initial mixture	1.000	1.250	1.333	1.500	2.000	8.000
Ratio of Phg to HCCP rings in the largest molecule	1.051	1.283	1.350	1.519	1.988	4.320
No. of reactions in largest molecule	1498	1820	1905	2045	2520	2527
Avg. ring connectivity in largest molecule	2.999	3.196	3.21	3.228	3.294	2.204
Avg. density / kg m ⁻³ (from last 500 ps)	1700.6	1727.9	1711.2	1741.2	1710.4	1455.8

When the initial Phg:HCCP mixture ratio is 8:1, there is a large number (1822) of unreacted Phg monomers and no unreacted HCCP. The system does contain a network of 28048 atoms, as well as a number of smaller fragments. As a result of this excess of Phg, the Phg/HCCP ratio of both monomers in the network molecule is ~ 4.3 , *i.e.* much lower than the ratio of 8 in the mixture.

On the other hand, for the lower initial ratios, there are relatively few unreacted monomers and one large percolating network polymer molecule. The size of the latter increases with the number of Phg monomers in the initial mixtures. In all these cases, the Phg/HCCP ratio in the network molecule end up being close to that in the initial mixtures, *i.e.* with less than 2% of difference between both these ratios. Given the numbers of unreacted monomers, an optimal ratio would appear to be somewhere between 3:2 and 2:1.

Out of the three available hydroxyl O *per* Phg ring, the number that react decreases when the initial ratio increases but, except for 8:1, there are still more than two which react. Inversely, the number of reacted Cl *per* HCCP ring increases as expected with higher Phg:HCCP ratios, since there are more Phg to react with. This is also the case for the number of P-O₂ groups (both Cl having reacted), which account for ~ 30 to $\sim 70\%$ of all the P atoms linked to at least an ether O.

The cross-linking degree is characterized by the average (indiscriminate) ring connectivity, which is defined as twice the number of reactions that undergo a network molecule (number of O-P bonds) divided by the total number of Phg and HCCP rings in the network. The factor two comes from the fact that each O-P bond creates two links, one to each ring. In other words, the average ring connectivity is the average number of links a ring has to other rings. It is highest for the 2:1 system, hence this is, amongst the systems simulated, the system with the highest cross-linking degree.

Concerning the density, the volume decreases throughout the polymerization phase due to the elimination of H⁺ and Cl⁻ ions and the density ultimately increases.

5) C. 1. 3. Variable Phg:HCCP ratios and $R_{max} = 3.0 \text{ \AA}$

In this Section, R_{max} was changed to 3.0 Å and the full set of results, which include more ratios than for $R_{max} = 2.8 \text{ \AA}$ (Table 5.4), are provided in Table S5.3. For clarity, they will be detailed in the following Figures. A repeat calculation on a different 1:1 system was carried out to compare with the former results (Table 5.3). Moreover, for the 4:3 ratio, which corresponds to the best experimental Phg/HCCP estimate in the network, a larger mixture with 3510 monomers of HCCP (instead of 512) and 4682 monomers of Phg (instead of 683) was prepared in order to improve the statistics.

The fact that there is always one large molecule corresponding to the network and some remaining monomers is highlighted in Figure 5.8 by comparing the number of molecules in the final system with the number of unreacted HCCP and Phg. For example, for both 1:1 systems, there are 18 and 21 molecules in the final configuration, respectively, out of which 17 and 20 are unreacted HCCP and 0 are unreacted Phg. This means that there is one large network with all Phg rings incorporated into it. It is the opposite situation for the 2:1 and 3:1 systems: all the HCCP are in the network and there are a few excess Phg. In all cases, the mixture is slightly too rich either in one or in the other monomer.

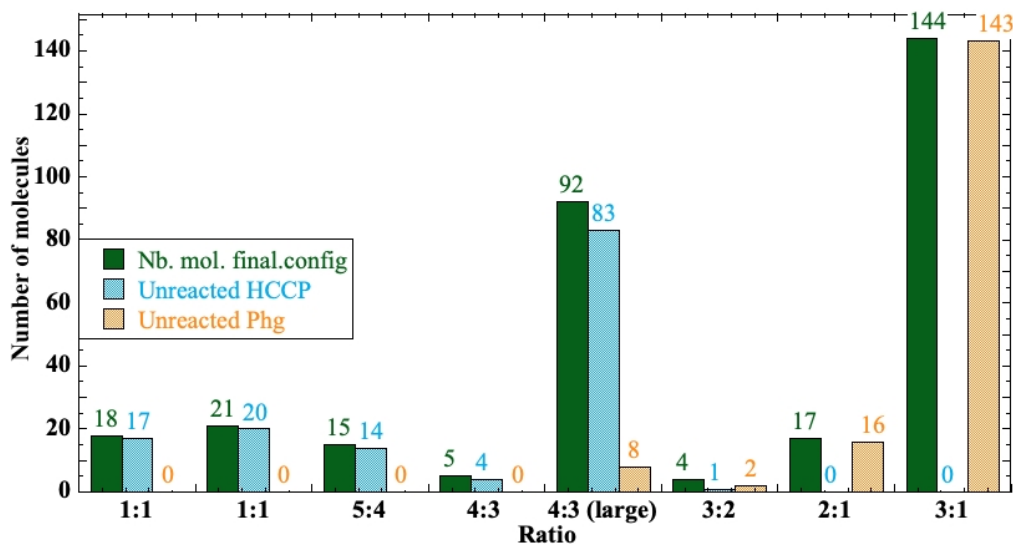


Figure 5.8 Numbers of molecules in the final configurations generated from mixtures with different Phg:HCCP ratios and using a R_{\max} parameter of 3.0 Å.

Despite these unreacted monomers, the Phg/HCCP ratios in the final networks (Table S5.3) are again almost the same as those of the initial mixtures up to a ratio of $\sim 3:1$. Above that, the correspondence becomes non-linear, as shown for the 8:1 system in Table 5.4.

When there are two separate simulations for the same ratio (1:1 and 4:3), the results are very similar. This suggests that the statistics obtained from the standard size (512 HCCP monomers and various numbers of Phg monomers) are satisfactory. Figure 5.9 and S5.5 confirm that the number of reacted Cl *per* HCCP ring and O *per* Phg ring is the same when the initial ratio in the mixture is the same. As far as the various ratios are concerned, they follow the trend seen with $R_{\max} = 2.8$ Å, *i.e.* the number of reacted Cl *per* HCCP ring increases, whereas the number of reacted O *per* Phg ring decreases with increasing ratios. It will be shown later that estimations of the number of reacted Cl *per* HCCP ring can be obtained from the experimental P/Cl elemental analyses. These estimations are provided in Table S5.3 from the total number of P and Cl atoms in the simulations, *i.e.* including any excess HCCP molecules as would happen with an

experimental analysis. They are in reasonably good agreement with the exact values for network molecules. As far as the P-O₂ groups are concerned, they are still very common (from ~30% to ~85% of all the P atoms linked to at least an ether O) and increase with higher Phg:HCCP ratios (Table S5.3).

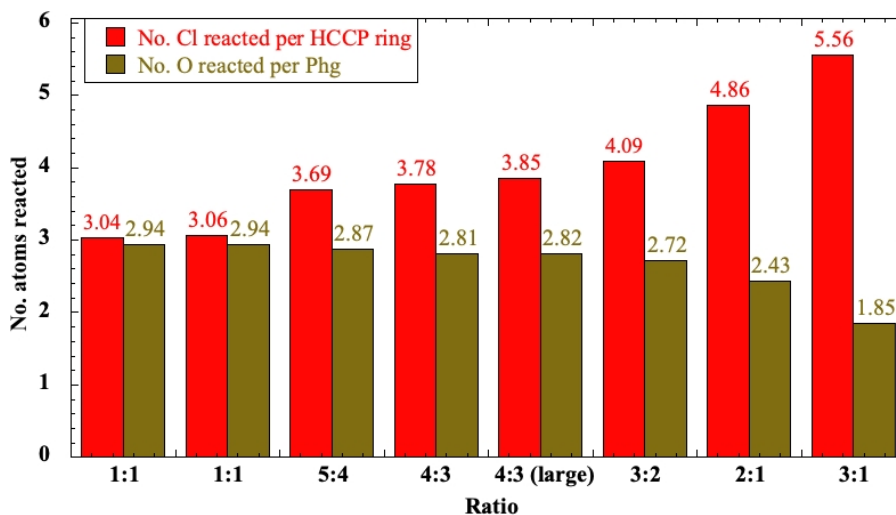


Figure 5.9 The average number of reacted Cl *per* HCCP ring and O *per* Phg ring in the network molecules generated from mixtures with different Phg:HCCP ratios and using a R_{\max} parameter of 3.0 Å.

The network connectivities are analysed in Figures 5.10 and S5.5. In Figures 5.10, the average ring connectivity, *i.e.* the cross-linking degree, is given as a function of the Phg:HCCP ratio in the mixture. There is clearly an optimal Phg:HCCP ratio that maximizes the cross-linking degree. Of the ratios tested, the maximum of 3.274 links *per* ring occurs again for the 2:1 system, the actual Phg/HCCP ratio in the network being 2.721 (Table S5.3). This cross-linking degree is only slightly higher than the values for the 4:3 and 3:2 ratios (Table S5.3). There thus appears to be a rather broad plateau of near-optimal values, which may extend further but would require simulating an extra 5:2 ratio. This is a very interesting result and it will be useful to see if the other properties show a correlation with the cross-linking degree.

More detailed information concerning the connectivity of the rings in the network are given in Figure S5.5. It shows the probability distributions for the number of reacted Cl *per* HCCP ring and number of reacted O *per* Phg ring. For all ratios, except for the higher 3:1, more than 50% of the Phg rings in the network have three links to HCCP rings, *i.e.* all their OH groups have reacted. As the Phg:HCCP ratio is increased, the distributions shift to lower values since Phg is more in excess. For the number of reacted Cl *per* HCCP, the distributions are fairly broad and are skewed to higher values as the Phg ratio is increased.

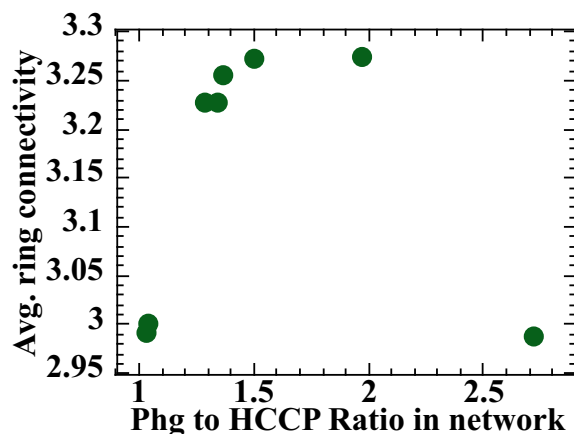


Figure 5.10. The average (indiscriminate) ring connectivity, *i.e.* the cross-linking degree, in the network molecules generated from mixtures with different Phg:HCCP ratios and using a R_{\max} parameter of 3.0 Å.

During the formation of the network, each reaction leads to the elimination of a H^+ and a Cl^- ion and this leads to the volume gradually decreasing with time, as illustrated by Figure 5.11.A. The behaviour of the density is less obvious, due to the decrease in both the mass and the volume. However, as shown by Figure 5.11.B, all systems ultimately undergo a net densification compared to the initial mixtures. The variations in both properties seem to be similar for all the ratios with a diminution of 25% to 32% for the volume and an augmentation of 6% to 11% for the density.

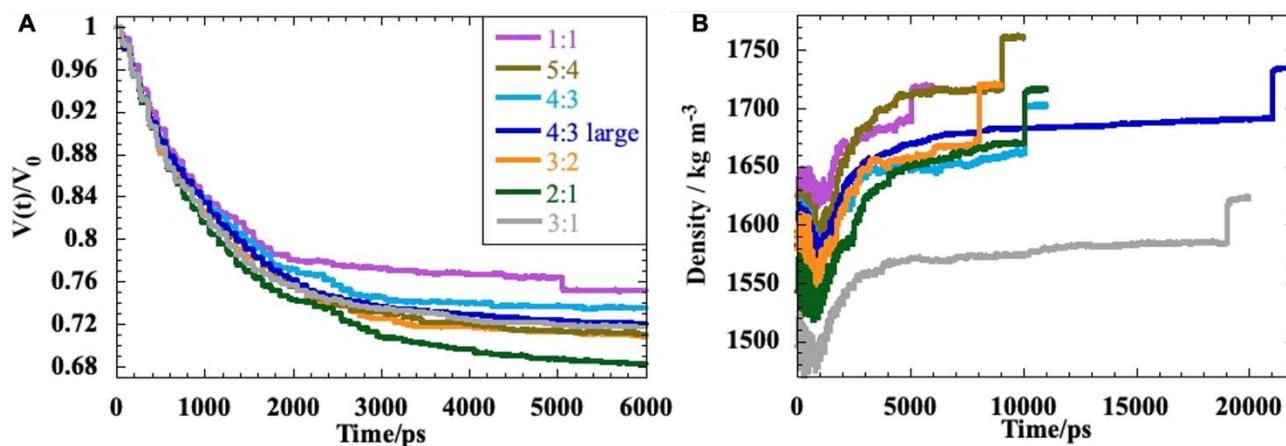


Figure 5.11 The behaviour of the relative volume, $V(t)/V_0$ where V_0 is the initial volume of the MD box, over the first 6000 ps of the reaction phase (A). The density of the systems as a function of time during the complete reaction phase (B). The different colours indicate the different Phg:HCCP ratios in the mixtures. The abrupt increases in density towards the end of the relaxation phase corresponds to the rigidification of the O-P bonds once all the reactions have finished.

To conclude, the iterative procedure, allowed for the formation of a series of networks with different connectivities and cross-linking degrees, starting from mixtures with different Phg:HCCP monomer ratios. Characterization tests were made on these virtual films in order to determine their performances.

5) C. 2. Mechanical tests

To ascertain the resistance of the networks to the pressure that they are likely to encounter within a storage tank and their capacity to recover elastically between cycles of compression/decompression (cf. Chapter 1), some mechanical tests were carried out on the polymer networks originating from mixtures with different Phg:HCCP ratios and several values of R_{\max} (Tables 5.3 and 5.4 and Figures 5.8 and 5.9). Uniaxial compression tests were considered the most appropriate as they mimick best the situation within the storage tanks. The biaxial stretching induced in the transverse direction by this compression is important with regard to the tendency to delaminate if it is very different to that of the reinforced outer casing.

To perform these tests, each of the network systems was first relaxed under *NPT* conditions for 1000 ps at an isotropic pressure of 1 bar, in order to establish a baseline for the dimensions of the trigonal MD box. The required pressure in the y direction was then increased by 1000 bar at a rate of 1 bar/ps, whilst keeping those in the x and z directions at 1 bar. The system was allowed to adjust to the increased pressure for 3000 ps before reducing the required pressure in the y direction by 1000 bar at a rate of -1 bar/ps. Finally, the system was simulated for a further 3000 ps under the isotropic pressure of 1 bar to assess whether the system undergoes any permanent deformation.

The longitudinal ε_l and transverse ε_t engineering strains were determined using Equations 5.1 and 5.2, where l is the length and A is the cross-sectional area of the MD box, have been determined, as a function of time, for these mechanical tests. l_0 is the reference MD box length and A_0 the cross-sectional area as determined from the initial baseline simulation of 1000 ps.

$$\varepsilon_l = \frac{l - l_0}{l_0} \quad (5.1)$$

$$\varepsilon_t = \frac{A^{1/2} - A_0^{1/2}}{A_0^{1/2}} \quad (5.2)$$

If the measured tension in the y direction, $-P_{yy}$, is plotted against the measured longitudinal strain ε_l , the slope gives an estimation of the Young's modulus E . It is also possible to make estimates of the

Poisson's ratio ν from the negative ratio of the transversal to longitudinal strains. Formally, ν is defined in the limit of vanishing longitudinal strain as (Equation 5.3):

$$\nu = \lim_{\varepsilon_l \rightarrow 0} \frac{-\varepsilon_t}{\varepsilon_l} \quad (5.3)$$

All the mechanical tests were made on the samples described in the previous Sections.

5) C. 2. 1. Phg:HCCP 1:1 ratio and variable R_{max}

Figure 5.12 presents the longitudinal and transversal strains as function of time for the four R_{max} tested with the initial Phg:HCCP 1:1 mixture.

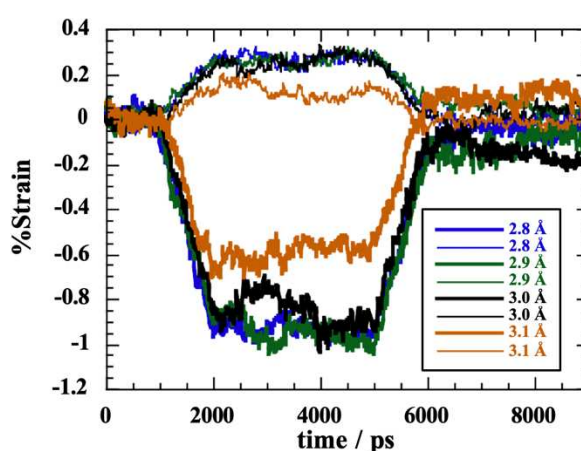


Figure 5.12 The longitudinal strains ε_l (thicker lines) and transverse strains ε_t (thinner lines) as a function of time for the uniaxial compression tests on the network systems created from an equimolar mixture of Phg and HCCP. Colours refer to the different values of R_{max} used.

In these uniaxial compression tests, the longitudinal strains decrease and a change in pressure of 1000 bar induces strains up to about -1%. Transversal strains increase up to $\sim 0.3\%$ due to the flattening effect of the compression. Within the statistical fluctuations, the systems generated with the R_{max} of 2.8, 2.9 and 3.0 Å show a quite similar behaviour. The $R_{max} = 3.1$ Å system deforms less in general. Whether this is a statistical problem or an inherent stiffer network structure is difficult to say without doing further tests. In all cases, however, the response of the systems is fairly elastic. The strains tend to remain constant once the pressure in the y direction has reached its plateau value and, once the pressure is returned to its initial value, the systems more or less return to their starting dimensions, *i.e.* they all show an elastic recovery.

For the Young's modulus, an illustration for the $R_{max} = 2.8$ Å system is provided in Figure 5.13. The data have been fitted to a linear function and estimates of the Young's modulus of 11.1, 11.4, 12.7 and 14.4

GPa were found for the $R_{\max} = 2.8, 2.9, 3.0$ and 3.1 \AA systems, respectively. As expected for these network polymers, the values of E are higher than for most common linear polymers.

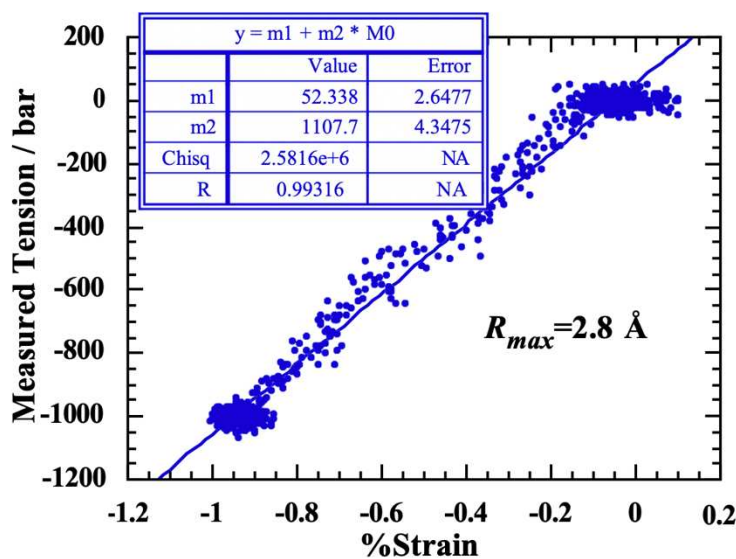


Figure 5.13 The measured tension in the y direction $-P_{yy}$ as a function of the longitudinal strain ε for the network system created with $R_{\max} = 2.8 \text{ \AA}$ and an initial Phg:HCCP ratio of 1:1. The linear least squares fit to the data points is shown as a straight line and the coefficients are given in the inset. The slope of the linear fit corresponds to a Young's modulus of $\sim 11.1 \text{ GPa}$.

For the Poisson's ratio, the MD box under NPT conditions fluctuates continuously in size and shape in response to the difference between the measured and required pressure tensor. As such, the ratio in Eq. 5.3 is subject to quite large statistical errors in the limit of low longitudinal strains. For this reason, estimates of ν have instead been made by averaging Poisson's ratio in a certain period of time where the required value of P_{yy} is constant at a value of 1001 bar. The strains in this region remain relatively modest (Figs. 5.12 and 5.13), so this is not an unreasonable approximation. The values obtained for Poisson's ratio were 0.29, 0.28, 0.30 and 0.21 for the $R_{\max} = 2.8, 2.9, 3.0$ and 3.1 \AA systems, respectively. These are at the lower end of the scale compared to common linear polymers and quite different to the limit of 0.5 for rubbery materials.

These three mechanical parameters were also determined for the systems with variable monomer ratios in the mixtures and two preferential R_{\max} values.

5) C. 2. 2. Variable Phg:HCCP ratios and $R_{\max} = 2.8$ or 3.0 \AA

The behaviour during uniaxial compression tests of the different systems obtained using a $R_{\max} = 3.0 \text{ \AA}$ is presented in Figure 5.14.

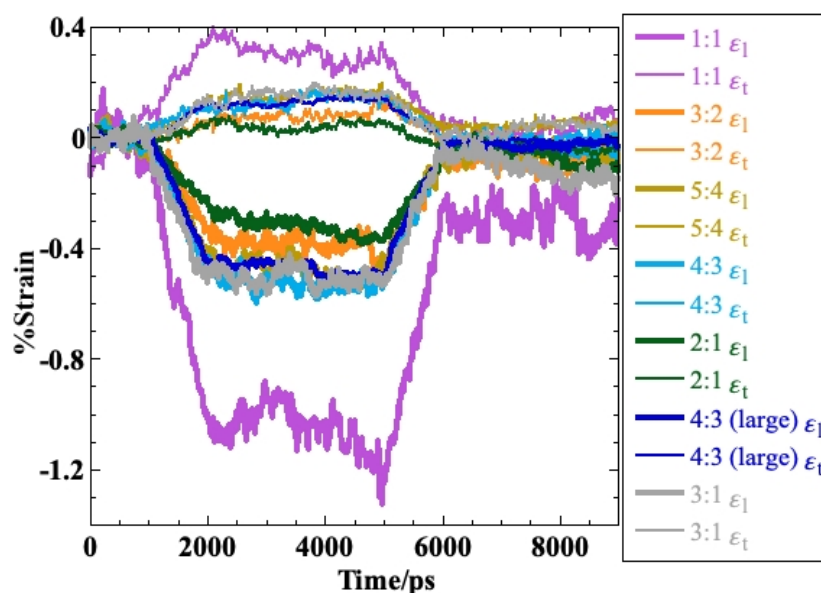


Figure 5.14 The longitudinal ε_l (thicker lines) and transverse strains ε_t (thinner lines) as a function of time for the uniaxial compression tests on the network systems created from mixtures with various Phg:HCCP ratios and a $R_{max} = 3.0 \text{ \AA}$. The colours refer to the different ratios.

The longitudinal strains ε_l vary by -0.5% to -0.3% when the compression is applied, except for the 1:1 ratio where the induced strains are up to -1.2% . In general, there does not seem to be any particular trend regarding the initial mixture monomer ratio nor the size of the network. For the transversal strain ε_t , the 1:1 system goes up to 0.3% whereas the others stay around 0.1% . Within the statistical fluctuations, the non-equimolar systems have a similar behaviour and deform less than the 1:1 mixture. Indeed, if all the networks are more or less back to their initial dimensions at the end of the test, *i.e.* they show elastic recovery, the 1:1 system deforms more than the others. Knowing that it has the lowest number of reacted Cl (Figure 5.9) and the lowest cross-linking degree (Figure 5.10 and Table S5.3), this tends to suggest that the more interconnected the system is, the stiffer it is.

This trend is confirmed by the Young's modulus E . Indeed, Figure 5.15 shows the results obtained with $R_{max} = 3.0 \text{ \AA}$ and Table S5.4 those for $R_{max} = 2.8 \text{ \AA}$. As the monomer ratio increases in the mixture, E tends to increase before passing through a maximum for a ratio of 2:1. As already found, the values of E are higher than for most linear polymers. More interestingly, there does seem to be a correlation with the cross-linking degree. Indeed, the highest average ring connectivity also occurs for a ratio of 2:1 (Figure 5.10 and Table S5.3).

The size of the system does not really have an effect, as shown by both 4:3 networks. There is a slightly higher difference in E between both 1:1 networks, but this is not unusual for a property measured from the slope of a stress vs. strain plot.

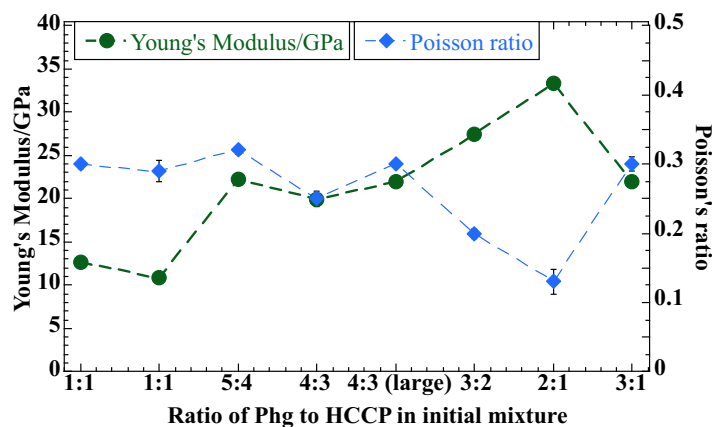


Figure 5.15 Young's modulus (y-axis on the left) and Poisson's ratio (y-axis on the right) for the network systems created from mixtures with various Phg:HCCP ratios and a $R_{max} = 3.0 \text{ \AA}$. Errors are displayed but are sometimes smaller than the symbols. The dashed lines are just a guide for the eye.

Figure 5.15 and Table S5.4 also give the Poisson's ratio for the different systems and there is no consistent trend with the different monomer ratios. This is not so surprising given the difficulties of measuring this property in relatively modest sized systems. Values vary between 0.13 to 0.35 which is, as previously stated, quite low for polymeric materials and far from the 0.5 of the rubbery materials. Both 1:1 systems almost have the same value, while both 4:3 systems give slightly different values but within the range of the other systems. However, it is interesting to note that the lowest value of ν measured corresponds again to the 2:1 ratio, that also has the highest value of E and the highest average ring connectivity (Figure 5.10 and Table S5.3).

These mechanical tests show that the polymer obtained from the reaction between Phg and HCCP appears to be mechanically resistant and elastic in a range up to 1000 bar, which is a good property for the application in storage tanks subject to significant pressure variations (cf. Chapter 1).

5) C. 3. Hydrogen uptake

The different networks were also tested for their hydrogen permeation properties. Only results with $R_{max} = 3.0 \text{ \AA}$ will be presented here.

5) C. 3. 1. Methods and models

In Chapter 3, the solubilities of H₂ in its gas phase were obtained using a test particle insertion (TPI) method [250]. While this is valid for the gas phase, it gets more complicated when the matrix is a higher-density polymer network.

TPI was still used to determine the infinite-dilution solubilities in a given network matrix, *i.e.* in the absence of any other penetrant. However the equilibrium uptake of H₂ in the same matrix for different applied external pressures was determined using the Grand Canonical Monte Carlo (GCMC)-MD method [194, 249]. In this iterative method, which will be detailed hereafter, GCMC (also based on particle insertions, as well as deletions) is used to predict the number of sorbed molecules whereas MD is used to relax the system following the GCMC sorption phase. Once the equilibrium gas uptake is established, the MD simulation can then be extended to longer times in order to estimate the diffusion coefficient of H₂ in the different polymer matrix.

Before providing more details, it should be noted that either TPI or GCMC with purely random particle insertions lead to very inefficient sampling in such dense polymer systems. For this reason, a third technique, the excluded-volume map sampling (EVMS) method was added to both of them [288-290]. EVMS pre-excludes a large part of the volume and limits insertions to those regions where favourable insertions are more likely, *i.e.* the low-energy sites. Indeed, purely random particle insertions in dense systems lead to a high percentage of insertions which overlap with the atoms already present and, therefore, have highly positive (repulsive) interaction energies. This is tantamount to having very low insertion probabilities (\approx solubility, cf. Chapter 3). In EVMS, a fine virtual 3D grid is placed over the system and cells in this grid are excluded when they already contain atoms. The non-excluded cells thus make up the space where the insertion of test particles can be made [194, 199, 249]. This leads to a large reduction of the computing time.

For TPI, the virtual insertions into specific configurations were made with the pre-selected (Chapter 3) YZ LJ-2S H₂ model as the test particle [221]. The configurations to be sampled were the different networks at 293.15 K (20°C) created previously at the end of their relaxation phase. These EVMS-TPI tests gave the infinite-dilution solubilities.

For GCMC-MD, the pressure range of interest varied from 50 bar to 800 bar. The prerequisite to any GCMC phase is the concentration and solubility of the gas, here the same YZ LJ-2S H₂ model, in its pure gas phase at the defined temperature and pressure. Indeed, the external gas pressure and the number of penetrant molecules absorbed by the polymer system are linked. Briefly, GCMC tries to find how many

penetrants molecules enter the polymer system when a certain pressure of gas is applied, whilst maintaining the equality of the chemical potentials for the penetrant molecule in the gas phase, $\mu_{Gas}(p)$, and the penetrant molecule in the polymer phase, $\mu_{Pol}(p)$. In the case of gas molecules modelled as rigid bodies (cf. Chapter 3), the equality of the chemical potential in both phases gives rise to Equation 5.4:

$$\mu_{Pol}(p) = \mu_{Gas}(p) \Rightarrow \frac{\rho_{Pol}(p)}{\rho_{Gas}(p)} = \frac{S_{Pol}(p)}{S_{Gas}(p)} \text{ or } \frac{C_{Pol}(p)}{C_{Gas}(p)} = \frac{S_{Pol}(p)}{S_{Gas}(p)} \quad (5.4)$$

with, $S_{Gas}(p)$ being the solubility of the gas in the gas phase, $C_{Gas}(p)$ its concentration in the gas phase, $S_{Pol}(p)$ the solubility of the gas in the polymer, and $C_{Pol}(p)$ its concentration in the polymer.

The gas phase solubilities and concentrations were obtained from the *NVT* MD simulations of the YZ LJ-2S model in its pure gas phase at pressures ranging from 50 to 2000 bar (cf. Chapter 3). The solubility vs. pressure and inverse volume vs. pressure curves were fitted to analytical functions having the ideal-gas limit at low pressures [194]. The $S_{Gas}(p)$ and $C_{Gas}(p)$ could then be interpolated at any pressure p in the range of validity (Table 5.5). Since they characterize the gas phase, they are the same for each monomer ratio system.

Table 5.5 Gas phase properties of the YZ model of H₂ at 20°C and various pressures. The typical errors are ±0.002 for the concentration and ±0.001 for the solubility.

Pressures	50 bar	100 bar	200 bar	400 bar	600 bar	800 bar
Gas phase concentration - Molecules/nm ³	1.205	2.349	4.467	8.076	10.965	13.270
Gas phase solubility	0.942	0.887	0.785	0.615	0.484	0.384

An important point with the GCMC method [249] is that it performs trial insertions and deletions in a *static* polymer configuration and adjusts the number of penetrant molecules N_p so that the equality of Eq. 5.4 is ensured. As it is performed at constant volume, an *NPT* MD phase has to be done to allow the polymer + gas system to relax to its new volume. This often results in Eq. 5.4 not being obeyed anymore. For this reason, successive iterations of GCMC and *NPT* MD phases have to be repeated, until the number of penetrants converges to a stable value. This iterative method is schematized in Figure 5.16.

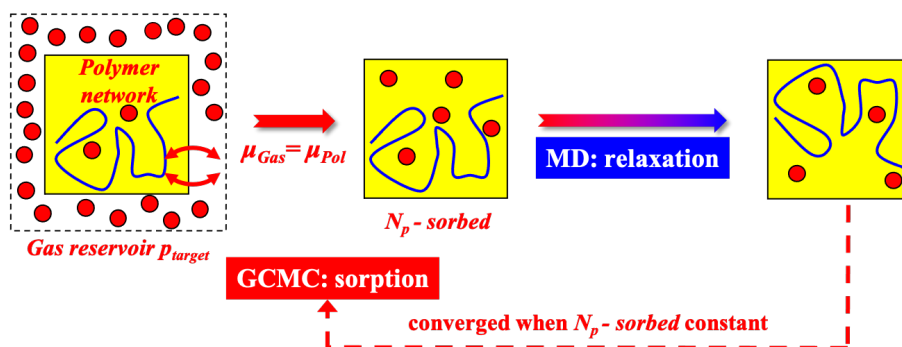


Figure 5.16 Schematic representation of the iterative GCMC-MD method.

Once the number of H₂ in the network system has converged, the last MD simulation can be extended to obtain a longer trajectory. The mean-square displacements (MSD) of the H₂ molecules lead to the H₂ self-diffusion coefficient (Chapter 3).

In practice, GCMC calculations were averaged over the last 20 stored configurations, separated by 5 ps, taken from a 1000 ps MD simulation of the network polymer system. At the start of the initial GCMC phase, the system contains no H₂. Then its uptake rises rapidly before stabilizing, as shown in Figure 5.17 for two network systems at 800 bar. A total of 10 million GCMC steps at each iteration was considered sufficient to converge the number of H₂ molecules sorbed by the system. For each MD phase, 100 ps under *NVT* conditions allowed the system to rethermalize, followed by 900 ps under *NPT* conditions, which were long enough for the system to relax.

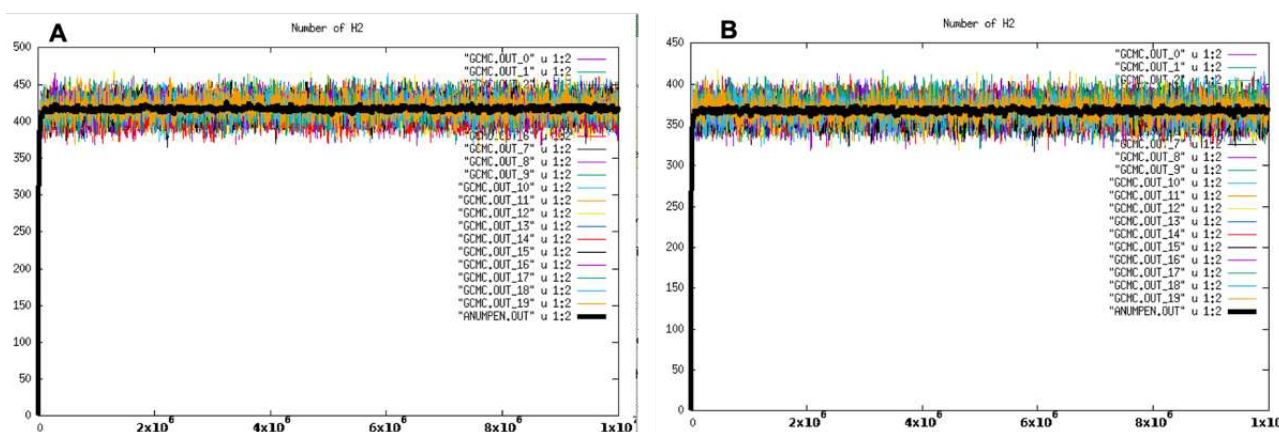


Figure 5.17 Uptake of the YZ model of H₂ in a Phg-HCCP network generated from a mixture with a Phg:HCCP ratio of 4:3 (A) and of 1:1 (B), at 20°C and for a pressure of 800 bar. The number of H₂ molecules in the matrix is shown as a function of the number of attempted GCMC moves. The thin lines of different colours represent the 20 different polymer network configurations used. The average uptake is highlighted as a thick black line.

Due to the EVMS technique, the low solubility of H₂ and a low swelling of the Phg-HCCP network, these GCMC-MD simulations converge within a relatively limited number of iterations. Indeed, for the different systems tested, the maximum number of iterations was nine for the highest pressure of 800 bar and four for the lowest of 50 bar. This remains quite reasonable.

5) C. 3. 2. H₂ solubility, diffusion and permeability as a function of the Phg:HCCP ratio

The infinite-dilution solubilities for H₂ obtained from TPI are reported in Figure 5.18. In general, they are significantly lower in the Phg+HCCP mixtures (white squares) than in the corresponding Phg-HCCP networks (black circles). The differences are due to the Phg and HCCP molecules being better packed together when not bonded. The introduction of bonds between the rings inevitably causes steric hindrance, which leads to the formation of additional free volume.

The effect seems to diminish as the Phg:HCCP ratio in the initial mixture increases. For the higher ratios, *i.e.* 2:1 and 3:1, this can be correlated with the cross-linking degree, which decreases as Phg:HCCP enters into a regime of excess Phg. The steric hindrance of the network is thus gradually lessened. This is confirmed by preliminary results on the 4:1, 5:1 and 8:1 systems (not shown). The behaviour at the lower ratios is more difficult to explain since they have cross-linking degrees just slightly below that of the 2:1 system (Figures 5.10). However, it should be remembered that they are further away from the 2:1 system in terms of the average number of reacted Cl *per* HCCP ring and O *per* Phg ring in the network molecules (Figure 5.9). This effect of the cross-linking morphology on the results probably warrants future investigations.

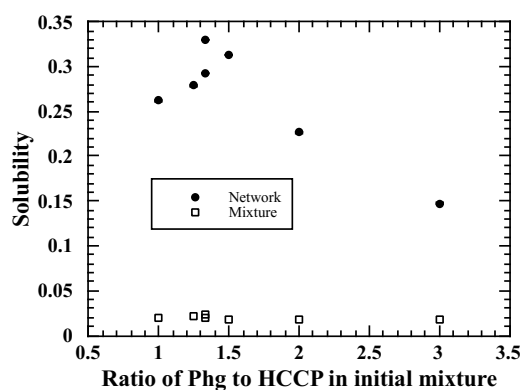


Figure 5.18. The infinite dilution solubilities of H₂ in the Phg:HCCP mixtures with different monomer ratios (squares) and their corresponding Phg-HCCP networks obtained using $R_{max} = 3.0 \text{ \AA}$ (circles). The error bars are smaller than the size of the symbols.

The significant available volume (SAV) in a system was also extracted from the results of the TPI calculations. The SAV is defined as the proportion of the volume of the system that contributes to 99.9% of the solubility of the test-particle [194]. The %SAV are given in Figure 5.19 for both the initial Phg:HCCP mixtures and their corresponding Phg-HCCP networks. As found for dense matrices, the actual percentages are quite small since most of the volume is occupied by the polymer network atoms and the few unreacted monomers. However, the difference between the %SAV for a mixture and its network clearly quantifies the tendency of the network formation to introduce extra space into the system, and thus the concomitant increase in H₂ solubility. Indeed, there is a good correlation with the behaviour of the infinite dilution solubility (Figure 5.18). Again, the lessening of the steric hindrance is responsible for the diminution in the %SAV at the higher ratios.

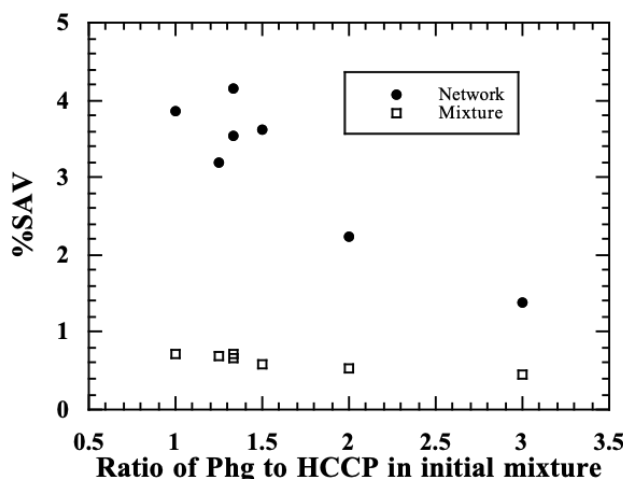


Figure 5.19 The %SAV for H₂ in the Phg:HCCP mixtures with different monomer ratios (squares) as well as in their corresponding Phg-HCCP networks (circles).

The sorption isotherms for the uptake of H₂ in the Phg-HCCP networks were obtained from the GCMC-MD calculations. The sorption isotherms for the 1:1 and 2:1 systems are provided in Figure 5.20 and the isotherms for the other ratios (not shown) have a similar shape. There is some typical non-linearity since, at very high pressures, the systems are no longer in the domain of Henry's law. Nevertheless, the non-linearity remains relatively modest with H₂ and simply follows from a diminishing solubility as the free-volume is gradually filled in the network.

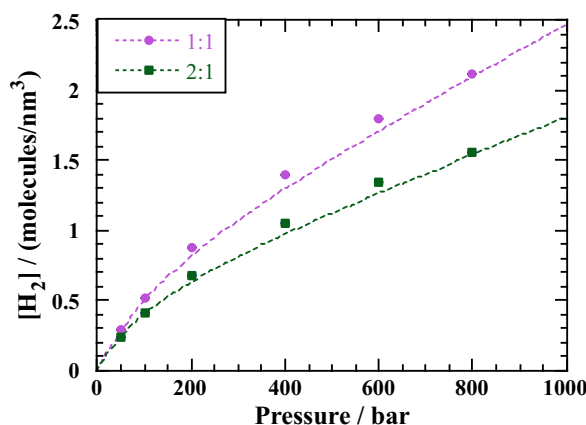


Figure 5.20 The uptake curves for H₂ in two different Phg-HCCP networks obtained using the iterative GCMC-MD method. The converged H₂ concentrations are shown at each of the pressures applied. The error bars on the concentrations are smaller than the symbols. The dotted lines are just guides for the eye.

The actual sorbed H₂ concentrations at the highest pressure of 800 bar are reported in Figure 5.21 for six different ratios. The high-pressure uptakes correlate in fact very well with the infinite dilution solubilities (Figure 5.18) and follow from the behaviour of the uptake curves Figure 5.20. However, the differences in concentration and, hence solubility coefficient, $S_c(p) = C(p)/p$, are no more than a factor of two. It is thus unlikely to be the driving force behind any possible significant differences in permeabilities. However, the permeability coefficient is the product of the solubility coefficient *and* the diffusion coefficient.

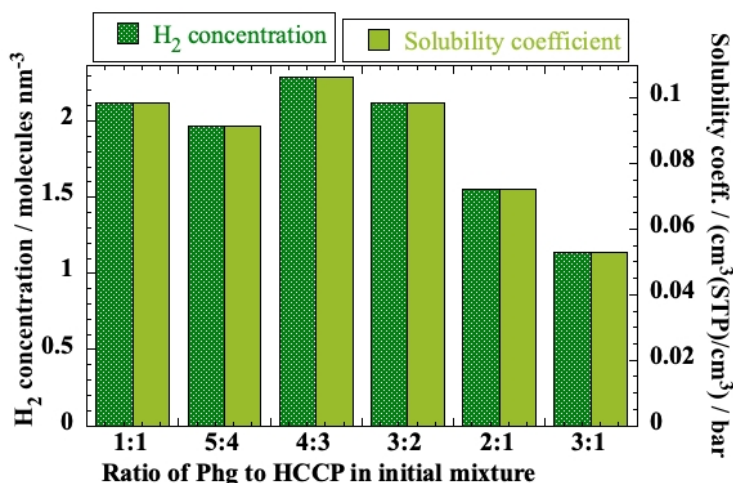


Figure 5.21 Concentration of H₂ sorbed (y-axis on the left) and solubility coefficient (y-axis on the right) in the Phg-HCCP networks produced from different mixtures at 20°C. The pressure is 800 bar.

The behaviour of the significant available volume (SAV) in the networks was monitored during the progressive loading of H₂ (Figure 5.22). Due to the non-linear behaviour of the H₂ concentration with pressure (Figure 5.21), the %SAV have been displayed as a function of the H₂ concentration. The results show a well-known hole-filling behaviour: the more sorbed penetrants in the network polymer, the less space available for the next penetrant molecules, and consequently a progressive decrease of the SAV as the H₂ concentration increases with the greater applied pressure.

The %SAV at 800 bar are shown for six Phg-HCCP network systems in Figure 5.23 as a function of the average H₂ concentration obtained. The systems having the lowest SAV have also the lowest solubilities and, thus, the lowest uptakes. These systems coincide with the higher Phg:HCCP ratios. This is useful to bear in mind for the discussion of the diffusive behaviour of H₂.

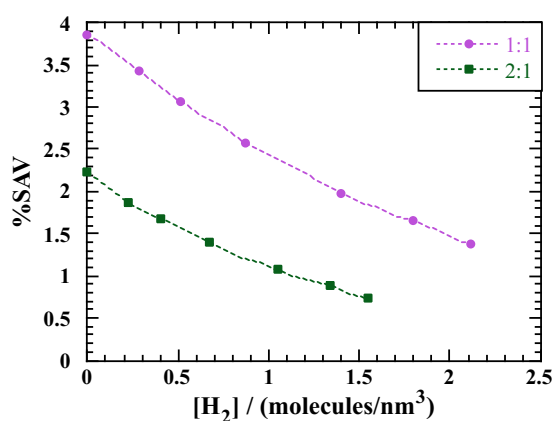


Figure 5.22 The behaviour of the %SAV as a function of the converged H₂ concentration at each of the pressures applied during the loading of H₂ in two different Phg-HCCP networks. The dotted lines are just guides for the eye.

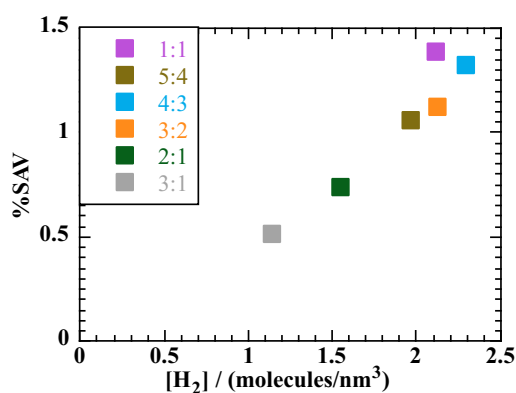


Figure 5.23 %SAV for six different Phg-HCCP polymer networks as a function of the H₂ concentration at 800 bar and 20°C.

Finally, the volume changes of the networks were monitored and they confirmed that the swelling of the polymer induced by the H₂ molecules is negligible. At 800 bar, it is less than 0.2% in spite of hundreds of H₂ molecules sorbed.

The infinite dilution solubilities and the sorption isotherms suggest that the initial Phg:HCCP ratio in the mixture, and therefore the Phg/HCCP ratio in the network, influences the uptake of H₂. It will now be seen whether this also affects the diffusive behaviour of the H₂ molecules in the network systems. Furthermore, the networks contain also a small, but ratio-dependent, number of trapped unreacted monomers. These relatively bulky molecules could block some of the diffusion paths for H₂.

The mean square displacements (MSD) were evaluated from the MD simulations of the H₂-containing network systems at 800 bar. Following the GCMC-MD sorption/relaxation phases, the MD simulations were extended up to a maximum of 20000 ps. The MSDs for the H₂ molecules are shown as a function of time in Figure 5.24.

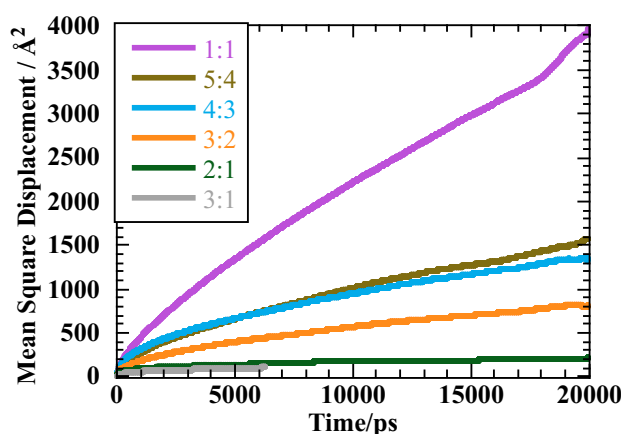


Figure 5.24 Average MSD as a function of time for H₂ molecules in different Phg-HCCP networks.

The MSDs for H₂ in Figure 5.24 attain values of at least $\sim 200 \text{ \AA}^2$ for the systems that have been simulated up to 20000 ps. This implies a root mean square displacement of $\sim 14 \text{ \AA}$, which is sufficient to show that hydrogen diffusion is occurring. However, it is very clear that the MSDs are extremely sensitive to the Phg:HCCP ratio in the initial mixtures. There is a gradual trend towards lower diffusion rates with increasing Phg:HCCP ratio. As seen in Figure 5.23, the higher Phg:HCCP ratios are correlated with smaller values of the significant available volume SAV. Indeed, a lower SAV in a network system inevitably reduces the possible pathways available for H₂ to pass through the matrix, which could explain the notable decrease in the diffusion rate.

In contrast to the MSDs for H₂, those of the atoms in the networks and the excess monomers (not shown) never exceed $\sim 1 \text{ \AA}^2$. This indicates that they are only undergoing reactions in the potential wells on the time scale of these simulations and that there is no measurable diffusion. For the unreacted monomers, this is consistent with the assumption that they are effectively trapped in the network system, even if they are not bonded to it. It is very unlikely that any amount of washing can eliminate them entirely.

Estimates of the diffusion coefficients were obtained by plotting the $D(t) = \text{MSD}/6t$ as a function of time and taking the limiting plateau value (Figure 5.25). The values obtained for each ratio are given in Table 5.6.

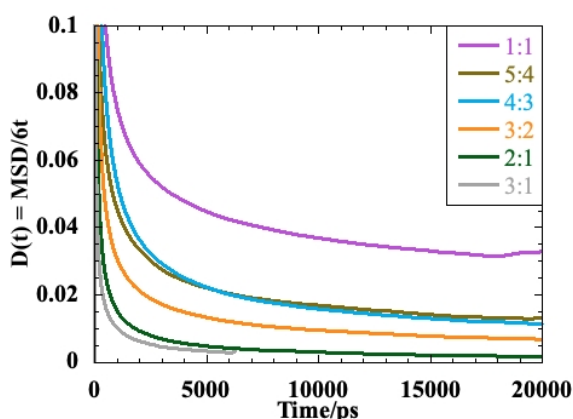


Figure 5.25 Diffusion behaviour of the YZ model for H₂ in different Phg-HCCP polymer systems at 20°C and 800 bar. The long-time limiting diffusion coefficients were estimated from the plateau values of the MSD/6t.

Table 5.6 Estimates of the limiting long-time diffusion coefficients of H₂ determined from the $D(t) = \text{MSD}/6t$ plots (Figure 5.25). These were all obtained for an applied pressure of 800 bar in polymer networks of different stoichiometries. Values are shown just for those systems where the MD simulations were extended to 20000 ps.

	1:1	5:4	4:3	3:2	2:1
$D / \text{\AA}^2/\text{ps}$	0.032 ± 0.002	0.013 ± 0.002	0.012 ± 0.002	0.008 ± 0.002	0.002 ± 0.001
$D / 10^{-10} \text{ cm}^2/\text{s}$	32300 ± 1500	14000 ± 1500	12000 ± 2000	8000 ± 2000	2000 ± 1000

The estimates of D given in Table 5.6 give a quantitative idea of the effect of the network stoichiometry. The diffusion coefficient is reduced by over a factor of 16 when going from a 1:1 system to the 2:1 system.

The actual trajectories of H_2 molecules over the entire 20000 ps NPT simulation at 20°C and 800 bar in the 4:3 system are schematically presented in Figure 5.26. Although not so evident in a static image, such representations show that there are regions impermeable to the penetrant molecules, but also that there is an interconnecting percolating diffusion pathway which is accessible even within the limited time scale of the MD simulations.

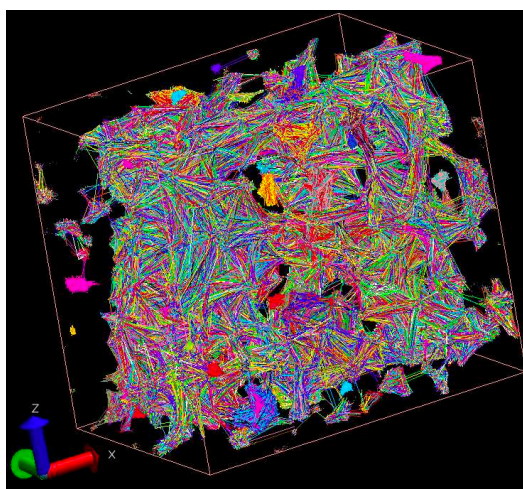


Figure 5.26 Trajectories of the YZ model H_2 molecules in the 4:3 Phg-HCCP system at 20°C and for a pressure of 800 bar. Each trajectory is constructed from positions stored every 5 ps. Different colours are used to distinguish different molecules. The image was created using the VMD software [248].

From the product of the solubility and diffusion coefficients, it is then possible to estimate the permeability coefficient, $P_c = S_c \times D$. Table 5.7 provides these results for each system fully studied.

Table 5.7 Permeability coefficients of the YZ model of H₂ as calculated from the product of the solubility coefficients and diffusion coefficients at 800 bars and 20°C in different polymer networks. Values are shown just for those systems having been simulated for 20000 ps.

	1:1	5:4	4:3	3:2	2:1
Permeability coeff. / 10^{-15} cm ³ (STP) cm cm ⁻² s ⁻¹ Pa ⁻¹	3210 ± 197	1281 ± 183	1283 ± 213	802 ± 99	166 ± 72
Permeability coeff. / Barrer	42.3 ± 2.0	16.3 ± 1.8	17.2 ± 2.8	10.5 ± 2.6	2.1 ± 1.0

As both the solubility and diffusion coefficients decrease when the initial Phg:HCCP ratio in the mixture increases, there is an even greater difference in permeability coefficients. Indeed, there is now almost a factor of 20 between the highest and the lowest permeability coefficient (Table 5.7).

The best result up to now is obtained for the 2:1 ratio (highest cross-linking degree, Figure 5.10), but the constant tendency for *both* the solubility and diffusion to diminish with the initial Phg:HCCP ratio suggest that an even better barrier could be obtained with a higher ratio, *i.e.* potentially with a system having a lower cross-linking degree than the 2:1 ratio. Indeed, there are two sides to the cross-linking degree. On one hand, it leads to a resistant well-connected system, but on the other side, higher cross-linking leads to more steric hindrance and a larger SAV.

Both solubility and diffusion rate are clearly quite sensitive to this balance. How much lower the diffusion coefficient and solubility can go, as the Phg:HCCP ratio is increased, remains to be seen. Simulations are underway. Ultimately, at high Phg:HCCP ratios, the initial mixture will become too dilute in terms of HCCP to have a percolating network. There will only be fragments of different sizes formed but they will probably not be linked together into one large molecule.

Even if a network is formed, it may also be too open to immobilize or retain the excess monomers and this could lead to an increase in the H₂ diffusion rate. With regard to their role, there are relatively few excess monomers trapped in the systems (Table S5.3), and as such, it is unlikely that this is the sole reason for the variations in the diffusion. Comparisons can easily be made between systems with and without excess monomers in them and this is already being investigated. However, the barrier properties are more likely to originate from the intrinsic characteristics of the networks.

5) D. Supporting information

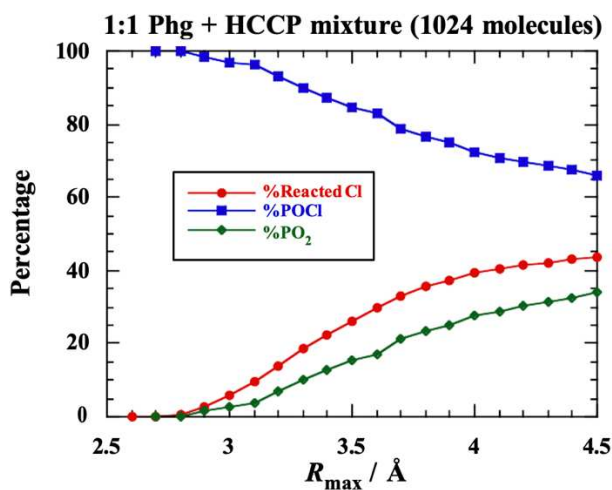


Figure S5.1 Variation of the % of reacted Cl as a function of the R_{\max} parameter, *i.e.* the distance below which the H-(O) and Cl atoms are deemed to “react”, when the initial structure is the Phg:HCCP 1:1 mixture containing 1024 monomers in total. Also shown are the % of POCl and PO₂ groups created by the reactions.

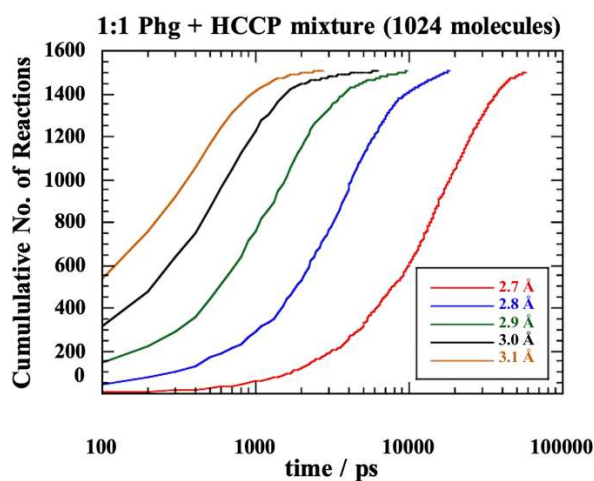


Figure S5.2 The cumulative number of reactions that occur during the iterative procedure to form the network polymers as a function of the logarithm of time. The results shown are for the Phg:HCCP 1:1 mixture. The different colours indicate the different values of R_{\max} used.

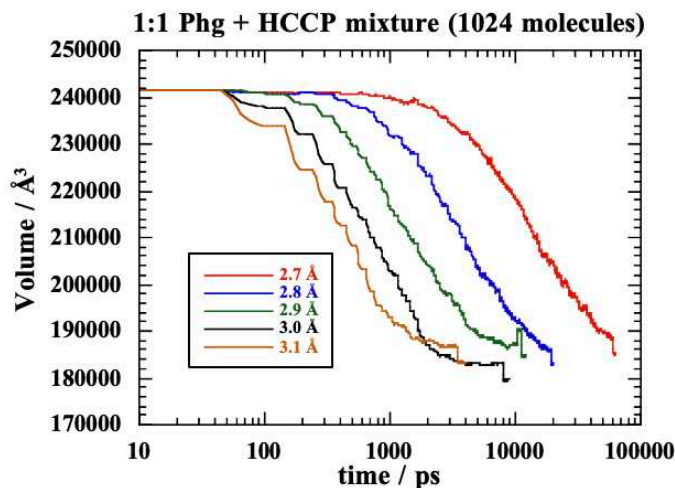


Figure S5.3 Evolution of the volumes of the MD boxes as a function of time (logarithmic scale) during the reaction phase for the Phg:HCCP 1:1 mixture. The different colours indicate the different values of R_{\max} used. The slightly abrupt changes at the ends of the simulations correspond to the final stage where the flexible P-O bonds are converted to rigid bonds.

The following equations are used to define the bending potential in the case of the network creation, with Eq. S5.1 corresponding to what is generally used with the *gmq* package [194], Eq. S5.2 that used in TRIPOS [239] and Eq. S5.3 the restricted bending (ReB) potential of Bulacu *et al.* [287]. Eq. S5.4 gives the correspondence between the different force constants when the curvature at the minimum in these potentials are matched.

$$\Phi(\theta) = \frac{1}{2}k_{\theta}(\cos \theta - \cos \theta_0)^2 \quad (\text{S5.1})$$

$$\Phi'(\theta) = \frac{1}{2}k'_{\theta}(\theta - \theta_0)^2 \quad (\text{S5.2})$$

$$\Phi^{\text{ReB}}(\theta) = \frac{1}{2}k_{\theta}^{\text{ReB}} \frac{(\cos \theta - \cos \theta_0)^2}{\sin^2 \theta} \quad (\text{S5.3})$$

$$\frac{d^2\Phi_{\text{ReB}}(\theta_0)}{d\theta^2} = \frac{d^2\Phi(\theta_0)}{d\theta^2} = \frac{d^2\Phi'(\theta_0)}{d\theta^2} \Rightarrow k_{\theta}^{\text{ReB}} = k_{\theta} \sin^2 \theta_0 = k'_{\theta} \quad (\text{S5.4})$$

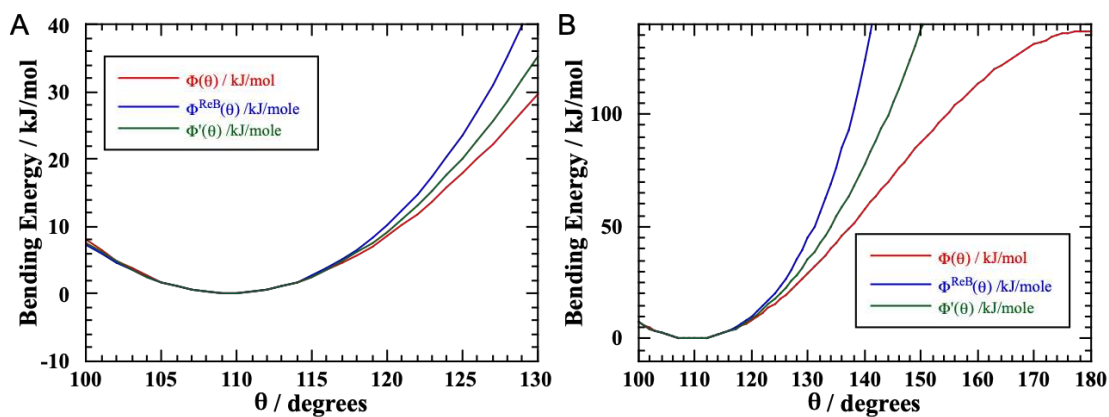


Figure S5.4 Three forms of the bending potential for the C-O-P angle. The harmonic in the angle form used in TRIPOS (Φ' in green) is compared to the standard harmonic in the *cosine* of the angle form of *gmq* (Φ in red) as well as the Restricted Bending Potential (ReB) form of Bulacu *et al.* (Φ^{ReB} in blue). The equilibrium angle is $\theta_0 = 109.5^\circ$ and the force constant, k_θ' , of the Φ form is adjusted so that the curvature at the minimum is the same as that for the original TRIPOS potential and the ReB potential (Eq. S5.4). The different behaviours are presented in the region of the equilibrium angle (A) and over a wider region out to 180° (B).

Table S5.1 Tests of the iterative polymerization procedure starting from the same equimolar Phg:HCCP 1:1 mixture containing 512 monomers of each type at 20°C.

$R_{\max} / \text{Å}$	2.7	2.8	2.9	3.0	3.1
Time of last reaction / ps	58390	18220	9840	6310	2740
Total No. of reactions	1501	1506	1506	1506	1506
No. C-H in final configuration	1536	1536	1536	1536	1536
No. C-OH in final configuration	35	30	30	30	30
No. P-Cl ₂ in final configuration	392	401	390	384	368
No. Cl-PCl in final configuration	784	802	780	768	736
No. P-OCl & Cl-PO in final configuration	787	764	786	798	830
No. Oether & C-Oether in final configuration	1501	1506	1506	1506	1506
No. P-O ₂ in final configuration	357	371	360	354	338
Total No. of reacted P (out of 1536)	1144	1135	1146	1152	1168
%P-O ₂ of P bonded to an O	31.2%	32.7%	31.4%	30.7%	28.9%
%P-O ₂ of all P	23.2%	24.2%	23.4%	23.0%	22.0%
Total No. of Cl remaining (out of 3072)	1571	1566	1566	1566	1566
No. of HCCP rings that react (out of 512)	486	491	492	487	495
Average No. of Cl reacted <i>per</i> HCCP ring	3.088	3.067	3.061	3.092	3.042
P/Cl ratio	0.978	0.981	0.981	0.981	0.981
Avg. No. of Cl reacted <i>per</i> HCCP ring from P/Cl ratio (Chapter 6, Eq. 6.5)	2.932	2.941	2.941	2.941	2.941
C/N ratio	2.000	2.000	2.000	2.000	2.000
Avg. No. of Cl reacted <i>per</i> HCCP ring from C/N ratio (Chapter 6, Eq. 6.3)	3.000	3.000	3.000	3.000	3.000
No. of reacted O <i>per</i> Phg ring (out of 3)	2.932	2.941	2.941	2.941	2.941
Ratio of Phg rings to HCCP rings in network	1.053	1.043	1.041	1.051	1.034
No. of molecules in final config.	27	22	21	26	18
No. of unreacted HCCP	26	21	20	25	17
No. of unreacted Phg	0	0	0	0	0
No. of atoms in largest molecule	10510	10560	10572	10512	10608
Total simulation time / ps	62000	20000	12000	9000	4000
Avg. density / kg m ⁻³ (last 500 ps)	1685.3	1703.6	1686.9	1734.4	1700.0
Avg. C-O-P angle / deg.	128.6	129.0	128.6	128.5	128.3

Table S5.2 Tests of the iterative polymerization procedure starting from the same equimolar Phg:HCCP 1:1 mixture containing 512 monomers of each type at 20°C, but with the ReB potential used for C-O-P bend.

$R_{\max} / \text{Å}$	2.8	2.9	3.0	3.1
Time of last reaction / ps	19750	8830	4430	5820
Total No. of reactions	1498	1507	1506	1507
No. Car-H in the final configuration	1536	1536	1536	1536
No. Car-OH & O-H & H-O in the final configuration	38	29	30	29
No. P-Cl ₂ in final configuration	407	397	379	365
No. Cl-PCl in final configuration	814	794	758	730
No. P_OCl & Cl_POeth in final configuration	760	771	808	835
No. O_ether & C-Oether in the final configuration	1498	1507	1506	1507
No. P-O ₂ in final configuration	369	368	349	336
Total No. of reacted P (out of 1536)	1129	1139	1157	1171
%P-O ₂ of P bonded to an O	32.7%	32.3%	30.2%	28.7%
%P-O ₂ of all P	24.0%	24.0%	22.7%	21.9%
Total No. of Cl remaining (out of 3072)	1574	1565	1566	1565
No. of HCCP rings that react (out of 512)	487	493	495	498
Average No. of Cl reacted <i>per</i> HCCP ring	3.076	3.057	3.042	3.026
P/Cl ratio	0.976	0.981	0.981	0.981
Avg. No. of Cl reacted <i>per</i> HCCP ring from P/Cl ratio (Chapter 6, Eq. 6.5)	2.926	2.943	2.941	2.943
C/N ratio	2.000	2.000	2.000	2.000
Avg. No. of Cl reacted <i>per</i> HCCP ring from C/N ratio (Chapter 6, Eq. 6.3)	3.000	3.000	3.000	3.000
No. of reacted O <i>per</i> Phg ring (out of 3)	2.926	2.943	2.941	2.943
Ratio of Phg rings to HCCP rings in network	1.051	1.039	1.034	1.028
No. of molecules in final config.	26	20	18	15
No. of unreacted HCCP	25	19	17	14
No. of unreacted Phg	0	0	0	0
No. of atoms in largest molecule	10528	10582	10608	10642
Total simulation time / ps	23000	13000	7000	7000
Avg. density / kg m ⁻³ (last 500 ps)	1700.6	1704.2	1679.2	1743.9
Avg. C-O-P angle / deg.	122.8	122.7	122.6	122.7

Table S5.3. Tests of the iterative polymerization procedure with a R_{\max} parameter of 3.0 Å and starting configurations from mixtures with various Phg:HCCP ratios. The two 1:1 columns are repeated calculations starting from the same initial configuration. Divergence occurs due to the assignment of random velocities after the *NVE* phase of the MD relaxation.

<i>Ratio Phg to HCCP in initial mixture</i>	1:1	1:1	5:4	4:3	4:3	3:2	2:1	3:1
Total simulation time / ps	7000	5000	9000	10000	21000	8000	10000	19000
Time of last reaction / ps	4430	4330	8260	9850	20860	7830	9690	18610
Total No. of reactions	1506	1506	1837	1922	13183	2089	2488	2845
Initial No. of HCCP rings	512	512	512	512	3510	512	512	512
Initial No. of Phg rings	512	512	640	683	4682	768	1024	1536
No. Car-H in the final configuration	1536	1536	1920	2049	14046	2304	3072	4608
No. Car-OH & O-H & H-O in the final configuration	30	30	83	127	863	215	584	1763
No. H-Car in the final configuration	1536	1536	1920	2049	14046	2304	3072	4608
No. P_HCCP in the final configuration	379	396	250	231	1541	149	45	7
No. N_HCCP in the final configuration	1536	1536	1536	1536	10530	1536	1536	1536
No. Cl_HCCP in the final configuration	758	792	500	462	3082	298	90	14
No. P_OCl & Cl_P-Oeth in the final configuration	808	774	735	688	4795	685	494	213
No. O_ether & C-Oether in the final configuration	1506	1506	1837	1922	13183	2089	2488	2845
No. P_O2 in the final configuration	349	366	551	617	4194	702	997	1316
Total No. of P	1536	1536	1536	1536	10530	1536	1536	1536
Total No. of reacted P	1157	1140	1286	1305	8989	1387	1491	1529
%P-O ₂ of P bonded to an O	30.2%	32.1%	42.8%	47.3%	46.7%	50.6%	66.9%	86.1%
%P-O ₂ of all P	22.7%	23.8%	35.9%	40.2%	39.8%	45.7%	64.9%	85.7%
Total No. of Cl	1566	1566	1235	1150	7877	983	584	227
Average No. of Cl reacted <i>per</i> HCCP ring	3.042	3.061	3.689	3.783	3.847	4.088	4.859	5.557
P/Cl ratio	0.981	0.981	1.244	1.336	1.337	1.563	2.630	6.767
Avg. No. Cl reacted <i>per</i> HCCP ring from P/Cl ratio (Chapter 6, Eq. 6.5)	2.941	2.941	3.588	3.754	3.756	4.080	4.859	5.557
C/N ratio	2.000	2.000	2.500	2.668	2.668	3.000	4.000	6.000
Avg. No. Cl reacted <i>per</i> HCCP ring from C/N ratio (Chapter 6, Eq. 6.3)	3.000	3.000	3.750	4.002	4.002	4.500	6.000	9.000
Avg. No. of O reacted <i>per</i> Phg ring that reacts	2.941	2.941	2.870	2.814	2.820	2.727	2.468	2.042
No. of HCCP rings undergoing reactions	495	492	498	508	3427	511	512	512
No. of Phg rings undergoing reactions	512	512	640	683	4674	766	1008	1393
Total No. of HCCP+Phg rings that react	1007	1004	1138	1191	8101	1277	1520	1905
Avg. ring connectivity	2.991	3.000	3.228	3.228	3.255	3.272	3.274	2.987
No. of molecules in final config.	18	21	15	5	92	4	17	144
No. of unreacted HCCP in final config.	17	20	14	4	83	1	0	0
No. of unreacted Phg in final config.	0	0	0	0	8	2	16	143
No. of atoms in largest molecule	10608	10572	11902	12497	84868	13444	16288	21349
No. of HCCP rings in largest molecule	495	492	498	508	3427	511	512	512

No. of Phg rings in largest molecule	512	512	640	683	4674	766	1008	1393
Ratio of Phg to HCCP in initial mixture	1.000	1.000	1.250	1.333	1.333	1.500	2.000	3.000
Ratio of Phg to HCCP in the largest molecule	1.034	1.041	1.285	1.344	1.364	1.499	1.969	2.721
No. of reactions in largest molecule	1506	1506	1837	1922	13183	2089	2488	2845
Avg. ring connectivity in largest molecule	2.991	3.000	3.228	3.228	3.255	3.272	3.274	2.987
Avg. density / kg m ⁻³ (last 500 ps)	1679.2	1717.3	1760.9	1702.6	1734.3	1720.0	1716.0	1623
T/K	293.10	293.10	293.10	293.10	293.15	293.10	293.10	293
P/bar	2.1	0.4	1.0	0.8	0.6	1.2	1.1	1
Ttrans/K	291.23	294.22	296.32	297.60	292.05	289.01	295.05	294
Avg. C-O-P angle / deg.	122.6	122.7	123.3	123.1	123.2	123.3	123.8	123.8404

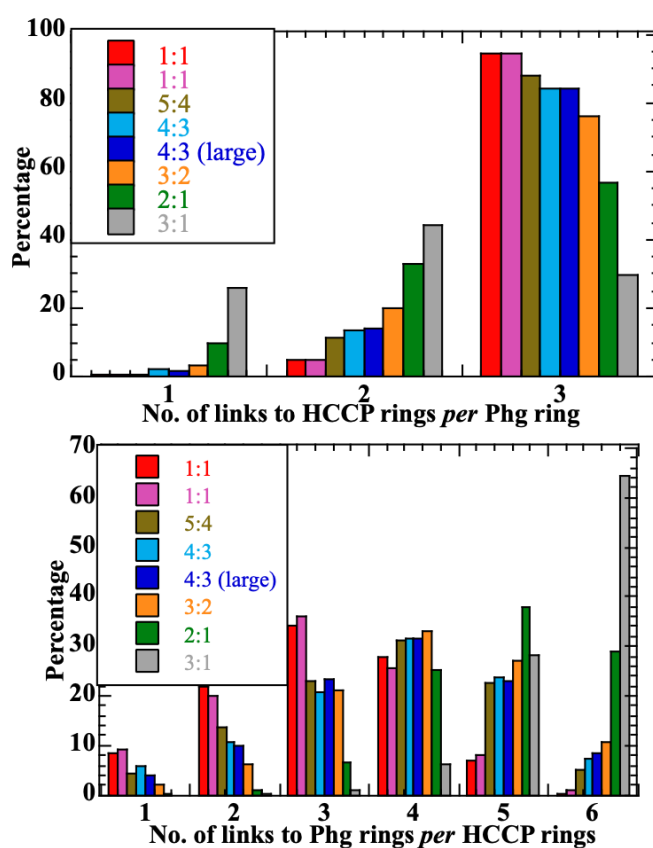


Figure S5.5 Connectivity of HCCP and Phg rings in different networks formed from mixtures with various initial Phg:HCCP ratios. Top panel: distribution of the number of links to HCCP *per* Phg ring in the largest molecule. Bottom panel: the number of links to Phg *per* HCCP ring.

Table S5.4 Young's modulus and Poisson's ratio for network polymer systems created from Phg:HCCP mixtures with different initial ratios and a $R_{max} = 2.8 \text{ \AA}$.

R_{max}	2.8 Å					
Monomer ratio	1:1	5:4	4:3	3:2	2:1	8:1
Young's Modulus (GPa)	11.08±0.04	24.1±0.1	20.0±0.1	22.3±0.2	34.0±0.2	7.1±0.1
Poisson's ratio	0.291±0.004	0.298±0.008	0.316±0.009	0.252±0.005	0.204±0.009	0.352±0.002

5) E. Acknowledgments

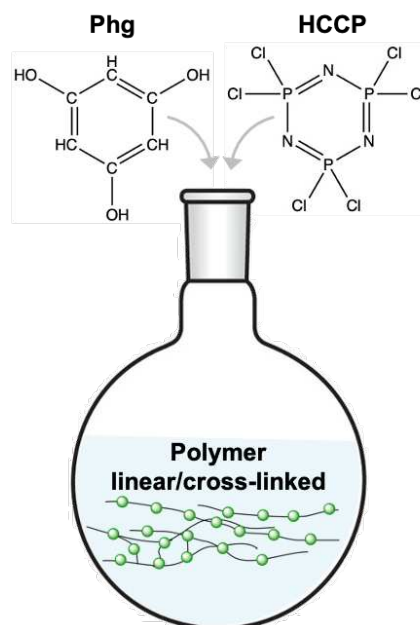
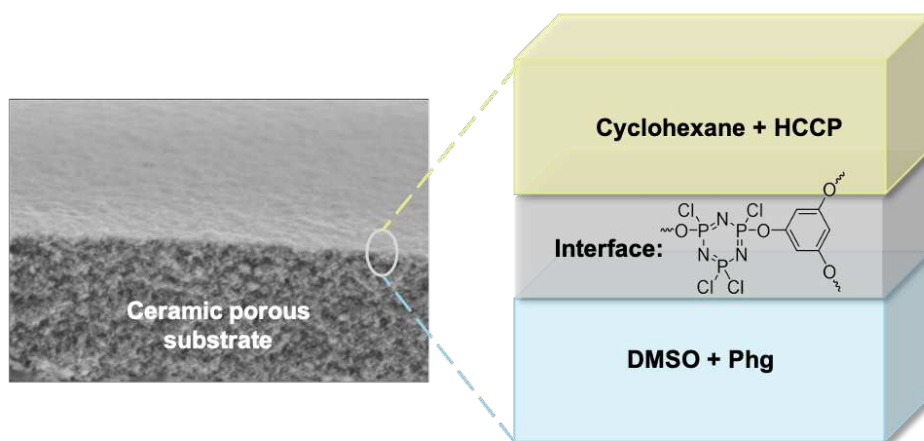
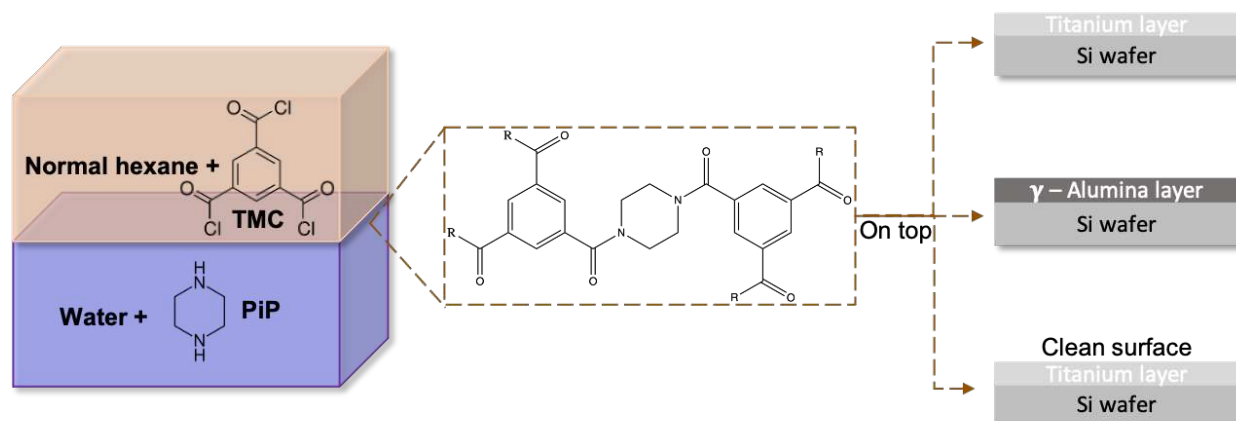
This research forms part of the research programme of DPI, project DINGOES #845. It had access to the HPC resources of TGCC/CINES/IDRIS under the allocations A009-095053, A011-095053 and A013-095053 made by GENCI, France. N. Charvin is thanked for his help with the installation and maintenance of the LEPMI local servers.

5) F. Abbreviations list

➤ CT	Connectivity Table
➤ EM	Energy minimization
➤ EVMS	Excluded volume map sampling
➤ GCMC	Grand-Canonical Monte Carlo
➤ HCCP	Hexachlorocyclotriphosphazene
➤ IP	Interfacial polymerization
➤ LJ	Lennard-Jones
➤ MD	Molecular dynamics
➤ MSD	Mean-square displacement
➤ PBC	Periodic boundary conditions
➤ Phg	Phloroglucinol
➤ SAV	Significant available volume
➤ TPI	Test particle insertion
➤ VdW	Van der Waals
➤ VMD	Visual Molecular Dynamics

Chapter 6 : Experimental - Interfacial Polymerization

6) A. Graphical abstract



The work in this chapter was carried at the University of Twente in collaboration with the team of Prof. Nieck Benes (“Films in fluids” group) and especially Dr. Farzaneh Radmanesh.

Creating a network using molecular dynamics simulation was not an easy task but was finally a success. Since this modelling part was there to guide the synthesis technique, it is now time to discuss the experimental approach using interfacial polymerization. Chapter 2 of this present work already introduced this technique. However, as this approach is rich and complex in terms of its range of uses, parameters and processing, it requires training before being used for the application of interest. As such, a first test study was carried out with well-known monomers for interfacial polymerization, in order to learn how to use it with safe working chemistry. Consequently, the following part will provide the information needed to understand its operation, advantages and difficulties of implementation.

6) B. Test monomers

As introduced in Chapter 2, interfacial polymerization (IP) consists of a localized polymer formation at the interface of two immiscible phases, which are here solvents (Figure 6.1).

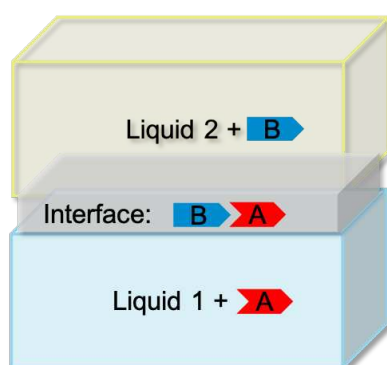


Figure 6.1 A schematic illustration of polymerization occurring at the interface between a first solvent containing the dissolved monomer A, and a second solvent with monomer B.

This technique can be used to make films (Figure 6.1), either as “free-standing film”, or on top of a support, referred to in the following as “IP or film on support”. This latter possibility is used to give mechanical strength as well as facilitating the characterization of the formed film (detailed later). As the aim of this project is to coat a barrier film on another material, both approaches were studied, first with the reactants used for familiarization with this kind of polymerization (piperazine and trimesoyl chlorine), and then with the selected monomers for polyphosphazene networks (Chapter 4).

6) B. 1. Piperazine and trimesoyl chlorine

These two organic compounds are widely used to produce polyamide thin film composites via IP, as membranes for nanofiltration and reverse osmosis for desalination, for example [291]. The reaction

occurs at the interface between the organic phase containing the trimesoyl chloride (TMC) and the aqueous solution with the piperazine (PiP) and results in the formation of a poly(piperazine-amide) (Figure 6.2) [146].

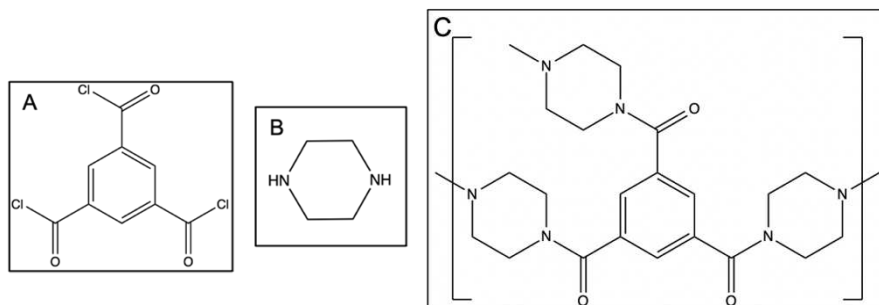




Figure 6.2 Structures of the trimesoyl chloride (A), piperazine (B) and poly(piperazine-amide) (C) structures (images created using *ChemDraw 20.0* [263]) [292].

TMC contains three acyl chloride groups which are converted into carboxylic acid groups to react with the PiP amine groups and form amide linkages. If some of them remain unreacted, they can again be hydrolysed to react subsequently [132, 293]. Both these monomers are quite reactive and are used in different fields.

For example, the piperazine PiP, also named diethylenediamine, is a relatively low-cost product and one of the most common N-heterocycles appearing in pharmaceuticals [132, 294, 295]. Indeed, its six-membered heterocyclic ring structure with two opposing nitrogen atoms is very rigid and offers a large polar surface area and the possibility of hydrogen bonding. This reactivity allows for it to form polymers with antimicrobial or water-solubility enhanced properties. Furthermore, this molecule is freely soluble in water as well as in ethylene glycol. This means that it can be used both in an aqueous or an organic phase if this last is for example ethylene glycol [295].

On the other hand, trimesoyl chloride TMC or 1,3,5-benzenetricarboxylic acid chloride, has a more complex structure consisting of an aromatic ring branched with three acid chloride groups. Due to its antioxidative properties, i.e. it can break down organic compounds, and high water permeability, it shows good effectiveness in the treatment of wastewater, hence its use in nanofiltration (usually corresponding to water purification). In membrane applications, it can also transport ionic species across a layer and has a good chemical stability in harsh conditions such as an acidic or a saline environment. Finally, in addition to its interesting reactivity, TMC is not soluble in water, which is a great advantage in an IP reaction where it is dissolved in the organic phase and is insoluble in the aqueous phase [296]. Table 6.1 gives the main physical and chemical information for both monomers.

Table 6.1 Identification, properties and safety data of for the PiP and TMC molecules [297-300].

Monomers	Molecular formula	CAS number	Molecular weight	Boiling point	Melting point	Density at 20 or 25°C	Refractive index	Safety
Piperazine	C ₄ H ₁₀ N ₂	110-85-0	86.14 g/mol	146°C	106°C	1.1 g/ml	1.424	
Trimesoyl chloride	C ₉ H ₃ Cl ₃ O ₃	4422-95-1	265.48 g/mol	180°C	32-38°C	1.487 g/ml	1.595	

To conclude, the two monomers above are two well-known compounds in chemistry and their reactivity allows them to be used in different fields, including the interfacial polymerization of a polyamide layer. Studies on this subject already exist [142, 160, 163, 169, 301] and this has facilitated the familiarization with the method step. However, the IP method has a lot of different interdependent parameters (cf. Chapter 2, Figure 2.10) which can easily complicate its use and understanding. Consequently, to simplify the first experiments, many of these conditions were defined and fixed with respect to previous works and the products used [132, 146, 260, 302]. Table 6.2 lists the main parameters (based on Figure 2.10, Chapter 2) that were fixed during the study and those that were variable.

Table 6.2 The main interfacial polymerization parameters for different reactions between piperazine and trimesoyl chloride. The top panel shows the parameters which were varied and the bottom, those that were fixed.

Variable parameters			
Reaction	Reaction time		
Supports	Soaking time; Cleanliness		
Process	Preparation of the solutions; drying step(s)		
Fixed parameters			
Monomers	Concentration; Stoichiometry/ Ratio; Diffusivity; Solubility in the opposite phase; Purity; Reactivity	Process	Temperature; Pressure
Reaction	Stirring; No side product	Solvents	pH; Viscosity; Miscibility
Supports	Pore size; Hydrophobicity/Surface tension	No surfactant	No additional product(s)

The plan followed was aimed at finding the “best protocol”, *i.e.* that giving a defect-free layer with a good continuity and homogeneity on the selected substrate (little studied before these tests). Therefore, the experimentations were separated into different batches, made one after the other, with the conditions being changed as a function of the results of the previous batch. For each of them, the process was the same:

- First, a free-standing film is produced to ensure that a reaction can occur with the parameters defined.
- Then, an attempt of growing the layer on top of a support is made in order to characterize the obtained film.

For this last part, different substrates, all of which from previous studies, were used depending on availability. The first was a silicon wafer with a titanium layer on top.

6) B. 2. Silicon wafer with titanium layer

A first batch (Batch 1) was made with a 2w/v% solution of piperazine, as obtained from Sigma-Aldrich, in water and 0.2w/v% trimesoyl chloride, also from Sigma-Aldrich, dissolved in n-hexane, from VWR Chemicals. Note that the solutions are prepared in the laboratory using concentration units expressed as the weight of the solute in grammes versus the percent of the solvent volume in millilitres (wt/vol%). For example, for a solution of 25 ml of water and a required concentration of PiP of 2 wt/vol%, the mass of PiP to dissolve is $2 \times 25 / 100 = 0.5$ g. A silicon wafer with a titanium (Si-Ti) layer on top with a very small pore size (< 5 nm), is used as support, as supplied by Siltronic. The support is first cleaned with ethanol and then dried with nitrogen before use. Concerning the time during which the support is soaked in the first solution (soaking time) and the time for the contact of the two phases (reaction time), they differ as a function of the sample. This is also the case for the way the excess of the first solution is removed (drying step). For each test, a well-defined interface was obtained as well as a free-standing film instantly after contact of the solutions (Figure 6.3).

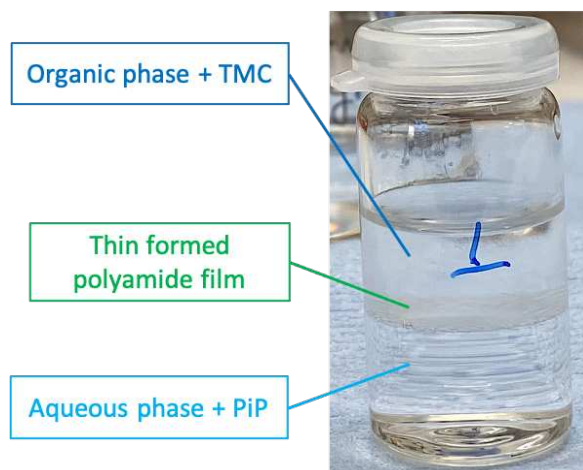


Figure 6.3 Film formed after the reaction between piperazine (PiP) and trimesoyl chloride (TMC) at the interface of an aqueous and organic phase. The first solution put in the reaction bottle is the denser one (water), to avoid mixing when adding the second solution (hexane). The order is the same when a substrate is involved.

The reaction is very fast and automatically stops once a certain film thickness is attained. When the formed layer is removed, another one is instantly formed at the same interface. It shows that this reaction is a self-limited process controlled by the monomer diffusion: it stops when the monomers can no longer come into contact due to thickness of the film [132].

Once the formation of the layer with the selected parameters is confirmed using a free-standing film as in Figure 6.3, it can then be attempted on a support. The selection of the support depends mostly on the characterization techniques to be used; all the details of the devices used as well as their parameters can be found in Table S1.1 of the SI. Ellipsometry spectroscopy is an interesting method with the advantages of being fast, non-intrusive, non-destructive, precise and accurate, giving optical information, such as the refractive index or light absorption, as well as the film thickness or roughness [303]. However, this technique requires that the substrate reflects the light, which is the case for a silicon wafer. As introduced in Chapter 2, another very important property of the support is the presence of pores and their size. Indeed, the two different types of monomers have to come into contact to have a reaction. Chronologically, the support is first soaked with the aqueous phase containing the piperazine and then the excess is removed during a drying step. However, if the substrate does not retain a part of this solution, nothing happens when the second TMC-based solution is added because there is ultimately only the TMC monomer on the surface. The role of the pores is therefore to ensure this contact between the monomers. The silicon wafer being dense (no pores), the titanium layer added on top of it is there specifically to supply these pores and provide some kind of reservoir for the solutions. Moreover, the negative charges on its surface help to adsorb the

first solution. If the monomers come into contact inside the pores, the polymerization starts from inside the pores and then grows to the surface of the support (Figure 6.4). This is also the reason why the pore size affects the formation of the layer and eventually its properties.

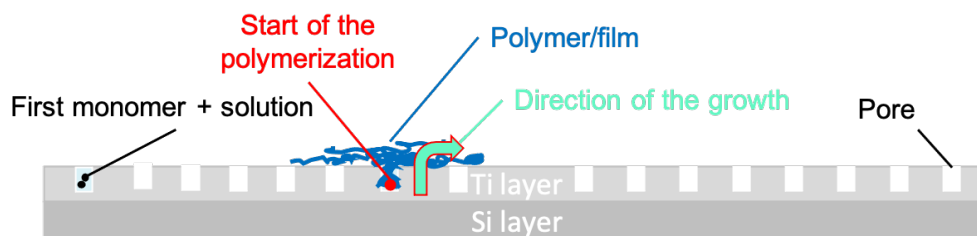


Figure 6.4 Illustration of the growth mechanism of an IP film on top of a Si-Ti substrate.

For the first batch of PiP-TMC films, four different samples were made on this Si-Ti support and the soaking and reaction times were as follows:

- 5 and 10 min for Samples 1, 3 and 4
- 15 and 30 min for Sample 2

The main difference between Sample 1 and Samples 3 and 4 is the drying step which, for the first was carried out using a tissue and nitrogen (in the same way as for Sample 2), and for the last two, by using only nitrogen.

Figure 6.5 shows Samples 1 and 2, where a layer seems to have grown. This layer is non-continuous and inhomogeneous in term of chemical composition and thickness. This observation is also applicable to Samples 3 and 4 which are similar (not shown), albeit more continuous.

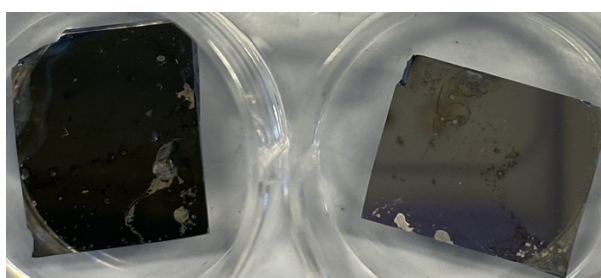


Figure 6.5 Sample 1 (left) and Sample 2 (right) from the first batch, obtained by IP of piperazine and trimesoyl chloride on a Si wafer with a Ti layer on top.

This purely visual impression must be confirmed as well as the continuity and homogeneity. This information can be obtained by ellipsometry measurements on different points of the surface. As for other

spectroscopic techniques, this method uses radiated energy to analyse material properties. In the case of ellipsometry, this energy comes from a basic configuration where a source provides a light, which passes through a polarized unit that sets the incident polarization state, which is subsequently changed upon reflection from the sample. This change, which can be described as two different angles (Ψ and Δ), is measured by a second polarizer coupled with a detector. These angles are then fitted with an optical model and transformed into useful results such as thicknesses, refractive indices, etc. [303, 304].

For the four samples of Batch 1, the ellipsometry confirmed the presence of a layer on top on the support with a thickness from 30 to 60 nm. However, several informations were also revealed by these measurements:

- The layer is not uniform in terms of thickness: several points were analyzed on each sample and the thickness was not the same for all of them.
- There was dust on the surface before the formation of the film: besides giving visual defects, the thickness was much higher than elsewhere and the refractive index, which to some extent allows the identification of the material, was varying too much between the different points on the same sample, *i.e.* it took into account not only the layer but also the dust.
- The layer grown did not agree with what was supposed to be formed when PiP and TMC react together, *i.e.* a polyamide whose refractive index is around 1.5. Indeed, the refractive indices found on the different samples of Batch 1 were closer to the one of the monomers alone rather than the one of polyamide. They were sometimes ~ 1.4 like for piperazine and sometimes around ~ 1.6 like for TMC.

According to these results, it was assumed that there might be just unreacted monomers instead of a polymer on the support. Therefore, Fourier transform infrared spectroscopy (FTIR) measurements were carried out on the same samples to try to determine the exact nature of the material present on the support. They confirmed the presence of a layer on the substrate, but it was probably too thin to be correctly detected with FTIR and determine its nature. As such Scanning electron microscopy – energy dispersive spectroscopy (SEM-EDS) analyses were attempted. Figure 6.6 shows two SEM pictures, one of the Si-Ti support alone and one of Sample 4 of Batch 1 with the EDS results of two different areas on the surface of this sample.

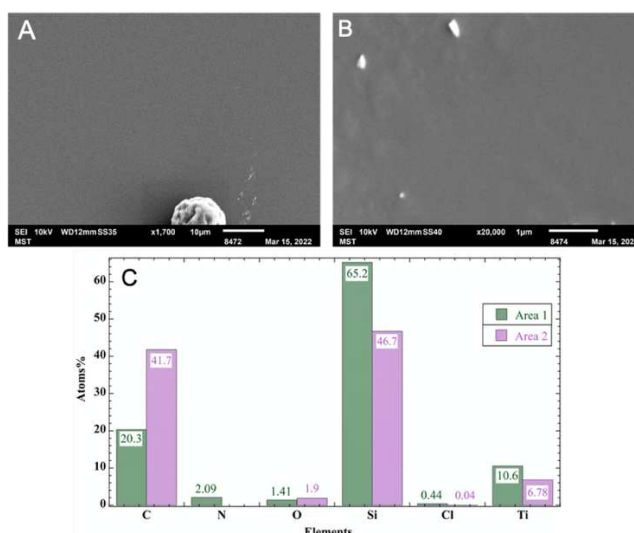


Figure 6.6 SEM pictures of the surface of the Si-Ti support alone (A) and Sample 4 of Batch 1 (B) with the EDS analysis of two different areas (C) of the interfacial polymerization between piperazine and trimesoyl chloride. The white particles are dust.

The comparison of these two pictures confirmed again that there is a layer on the surface (not the same aspect). As for the ellipsometry, several points on each sample were analysed and they suggested that the layer formed was neither continuous nor homogeneous. Finally, the EDS results on two different samples, brought two useful pieces of information:

- The layer formed is a polymer but it is not continuous (island repartition) and contains unreacted TMC: in one area (Figure 6.6.C), carbon, nitrogen, oxygen and chlorine are detected. As all of these elements can only come from the monomers, this confirms their presence on the surface. The relatively low quantity of Cl in the area 1 could indicate that there are unconverted acyl chloride groups. Since they are supposed to be transformed into carboxylic acid groups to react with the amine groups of the piperazine, it could be due to the presence of TMC monomers with unreacted groups.
- The EDS results of area 2 show that there are also partly reacted TMC but no PiP, since C and O are detected but no N or Cl. Besides the absence of the piperazine, it means that the functional groups of the trimesoyl were converted during a first step, but did not react during the following polymerization step.

These two comments suggest that the reaction starts, the hydrolysis of the chloride groups is done, but it stops before the formation of the membrane. It can be explained by problems related to the soaking and/or diffusion of the PiP on the substrate. Indeed, the TMC is dissolved in the organic phase and the conversion should be initiated by the contact with water and PiP, which is the first solution added. The lack

of polymerization is due to the absence of contact between the two monomers, which means that some of the PiP is not present on the support when TMC is added.

Consequently, this first batch shows that, with the experimental conditions chosen, the piperazine did not diffuse properly on the support during the soaking in the first solution. This led to the formation of a polymer with a patchy distribution and to the presence of unreacted monomers. Two probable reasons were evoked for the incomplete diffusion of PiP, based on the parameters related to the substrate in Table 6.2:

- Due to the nature of the Ti layer, there were impurities on the support, apart from dust, which inhibited diffusion.
- The results being similar between Sample 2 and all the others implies that the soaking time is not responsible. However, the porosity of the support could affect the diffusion of the monomers.

For the above reasons, it was decided to change the support and its porosity.

6) B. 3. Silicon wafer with alumina layer

For the second batch (Batch 2), the support was still a silicon wafer but with a gamma (γ)-alumina (Al_2O_3) layer on top (Si-Alu support). Unlike the Ti layer on top of the Si wafer substrate used for Batch 1, which was purchased in its final form, the alumina layer used here was made *in-situ* using a process similar to two previous studies [305, 306]. The support was characterized before being used to check if it was correctly formed and with the right pore size (supposedly more than 5 nm) and thickness. Consequently, the support itself was also analysed by ellipsometry and SEM in addition to the samples. As the main factor to check was the influence of the pore size on the diffusion of the monomers, the same kind of solutions of piperazine and trimesoyl chloride in water and n-hexane, respectively, were used. The protocol and fixed parameters were also the same as for the first batch (Table 6.2). The soaking, reaction times and drying step for the four samples of this second batch, are presented in Table 6.3.

Table 6.3 The variable IP parameters for piperazine and trimesoyl chloride on top of a silicon wafer with γ -alumina layer.

Parameters	Sample 5	Sample 6	Sample 7	Sample 8
Time of soaking	5 min	15 min		
Time of reaction	10 min	10 min	30 min	
Drying step	Nitrogen			Rubber roller

The substrate is again cleaned with ethanol and dried with nitrogen, if necessary, and, as for the first batch, it is kept in a dust-free box when it is not used so as to limit the contamination and to avoid damaging the surface. At the end of the reaction, the samples shown in Figure 6.7 are obtained and, despite the different lighting conditions of the pictures, no layers seems to have grown on the supports.

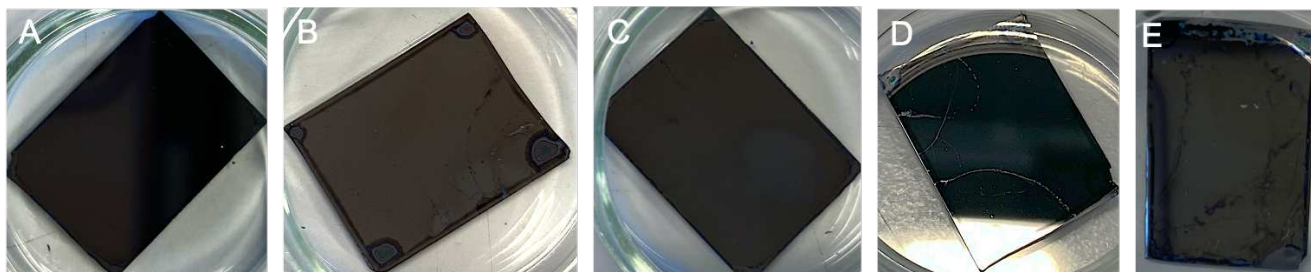


Figure 6.7 Si-Alumina support (A), sample 5 (B), sample 6 (C), sample 7 (D) and sample 8 (E) from the Batch 2 obtained by IP on a Si wafer with a γ -alumina layer on top.

Visually, there are not many differences between the raw support (Figure 6.7.A) and the samples (Figure 6.7.B-E). It is likely that there is nothing deposited on them.

They were first checked again by ellipsometry. The analysis of the raw substrate confirmed the presence of the alumina coating on top with a thickness of ≈ 30 nm. For all the samples, the results indicated that there was either nothing on top of this alumina layer or possibly something very thin (~ 3 nm).

SEM-EDS measurements were done to try to understand why. They confirmed the presence of the alumina layer on top of the substrate, but not correctly formed, and the absence of any other material. This suggested that:

- The alumina layer was not formed correctly which was maybe due to an issue with the procedure or growing steps.
- No polymer layer grew, either because of the poor-quality alumina layer or because this type of support is not suitable for a reaction with these two monomers.

As such, this second batch did not give any indications as to the effect of the pore size on the diffusion of the piperazine on the substrate. Since the problem most likely comes from the alumina layer, the easiest way to investigate this possibility would be to change the method of depositing the alumina on the silica support so as to have something more homogeneous. However, its fabrication would require more resources and a relatively long time. Given the limited time available, further studies with this support were not carried out.

Nevertheless, to investigate further the effect of the porosity of the support, a third and final batch was tested. As the Si-Ti support ultimately showed better results than the silicon wafer with γ -alumina, it was decided to make another try with the first support. However, in order to improve the layer, its preparation was modified.

6) B. 4. Silicon wafer with clean titanium layer

For the third batch (Batch 3), the substrate was purchased from Siltronic with the titanium layer already deposited on top. As such, besides the cutting part, its preparation for the reaction should only consist only in a cleaning step with ethanol and nitrogen to dry, if necessary. However, due to the presence of dust and probably other impurities observed with Batch 1, this preparation is not sufficient to have a surface clean enough for the interfacial polymerization. Therefore, the cleaning step was improved with the following protocol:

1. Clean the surface with ethanol.
2. Place 1 hour in a vacuum oven, or less if the surface dries sooner (no nitrogen).
3. Place 20 min in a UV ozone cleaner, which should clean any organic contaminants that may have grown on the surface. This is often the case with a titanium layer [307-310].

If an interruption follows this last step, keep the substrate in a closed box filled with dust-free tissue.

Apart from this improved support preparation, the step after soaking in the first solution and before the second (drying step) was changed as well. Until now, only nitrogen was used to remove the excess aqueous solution. Seemingly, this could lead to contamination by impurities. Then, for this batch, the samples were put on a dust-free tissue and placed in an oven for a few minutes, either at 45°C or 100°C. The rest of the process was based on that used for Batch 1, with the 2w/v% piperazine in water and 0.2w/v% TMC in n-hexane solutions. The reaction time was increased to 60 min and the soaking time was kept at 15 min in all cases.

Only two samples were made and they are presented in Figure 6.8. It shows that one of them is covered with particles and a layer with different thicknesses at different places while the other displays a smooth, continuous and homogeneous surface.

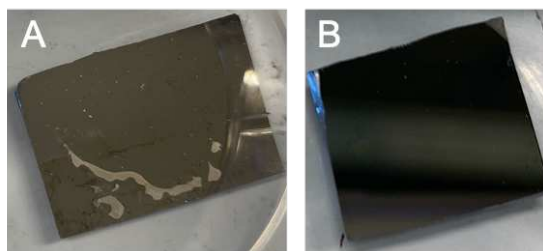


Figure 6.8 Sample 9 (A) and Sample 10 (B) from the third batch of IP with PiP and TMC on a silicon wafer with a titanium layer on top cleaned by UV irradiation before being used.

The visual aspect for Sample 9 can be explained by a small difference in the protocol between both samples. As the different batches were made in quick succession, the solutions prepared for Batch 2 could be used for the beginning of Batch 3, *i.e.* for Sample 9. However, there were particles in the PiP/water solution which, according to the surface aspect, ended up on the sample. Therefore, new solutions were made for the other sample and a filtration step for the solutions was added before they were used.

Judging by the visual inspection of Sample 10, these changes in the process were beneficial. As for the other batches, ellipsometry (results not shown) and SEM-EDS analyses were carried out and, despite the particles, they suggest a polymer layer is formed in both Samples 9 and 10 (Figure 6.9).

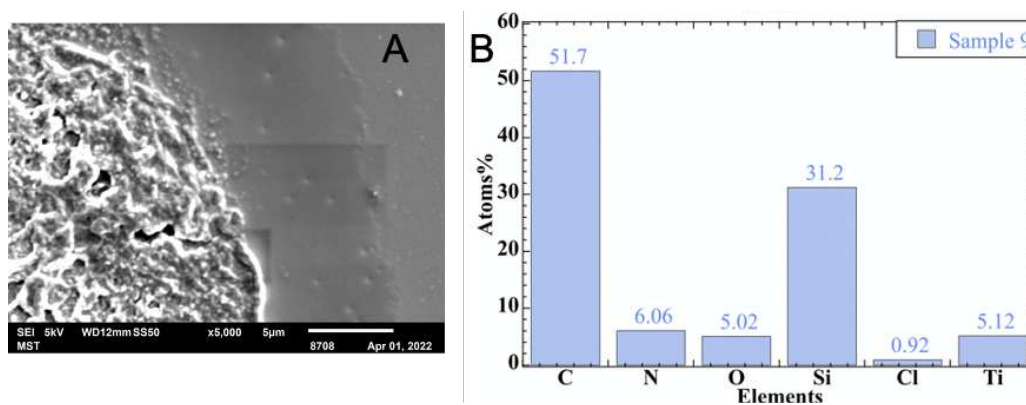


Figure 6.9 SEM picture of Sample 9 (A) and its EDS analysis of the whole area (B), obtained by interfacial polymerization of piperazine and trimesoyl chloride on top of a silicon-titanium cleaned substrate.

Indeed, with ellipsometry, a layer (with a thickness between 30 and 40 nm) was detected on both samples and, with SEM-EDS, the presence of carbon, nitrogen, oxygen and chlorine suggest that both agglomerated and smooth parts on Figure 6.9.A, are part of a polymer.

From these preliminary results, it seems reasonable to say that a properly-cleaned Si-Ti support could be a good substrate to grow a layer with piperazine and trimesoyl chlorine, using the conditions defined for the samples of the Batch 3, including fresh and filtered solutions. It can be noted that solutions of the dissolved monomers are more or less stable over time, *i.e.* particles appear only after several days.

It is clear that further analyses would be interesting to do but these three different batches of IP samples have already underlined that even a small change can make a huge difference for the formation of the layer. For example, the use of a tissue or not (in addition to nitrogen) to remove the excess of the first solution (drying step) has shown how much this step can be critical. The preparation of the support, *i.e.* its cleanliness, and the characteristics of the support itself, *i.e.* its pore sizes and *in-situ* modifications, are of course crucial. The monomer solutions must be prepared at the last moment and as homogeneous as possible, even if it means filtering them before use.

These different examples demonstrate the very high sensitivity of the technique, which confirms that its use requires training in order to be correctly operated. Since the formation and properties of an IP film are also dependant of the monomers, the next set of experiments were carried out this time with both monomers of interest: hexachlorocyclotriphosphazene or phosphonitrilic chloride trimer (HCCP) and phloroglucinol or 1,2,3-benzenetriol (Phg or PGL).

6) C. Monomers for polyphosphazene networks

A general presentation of these two monomers chosen for this project, phloroglucinol (Phg) and hexachlorocyclotriphosphazene (HCCP), already appeared in Chapter 4. However, in the next sections, the characteristics of the two reactants are recalled as well as the interest of using them in IP to make network polymers for barrier applications. In order to improve the knowledge about these monomers, both IP and bulk polymerization will be considered.

6) C. 1. Hexachlorocyclotriphosphazene (HCCP) and phloroglucinol (Phg)

As seen in the molecular modelling part, the organic molecule phloroglucinol (Phg) of chemical formula $C_6H_6O_3$, is a member of the benzenetriol family, with a high functionality as its benzene ring bears hydroxyl groups at positions 1, 3 and 5 (Figure 6.10.).

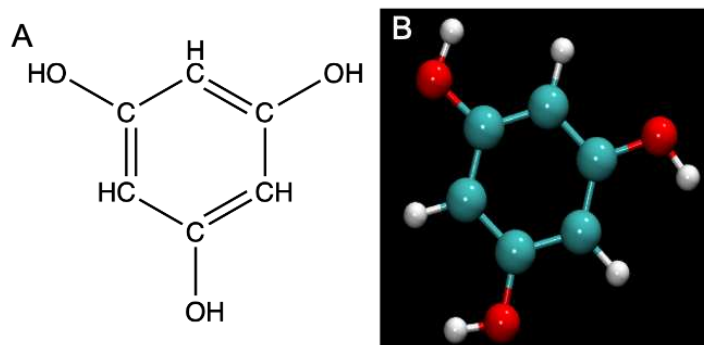


Figure 6.10 The phloroglucinol molecule sketched using *ChemDraw* 20.0 [263] (A) and its ball-and-stick representation of the same molecule rendered using *VMD* 1.9 Catalina Rev7 [248] (B) with the colour code C = cyan, O = red, H = white.

In general, the reactants are the hydroxyl groups. In an aqueous phase or in an organic phase containing a base, and depending on the pH, they can become deprotonated to form O^- groups which are very soluble, nucleophile and therefore very reactive. In the case of non-aqueous interfacial polymerization, phloroglucinol can be dissolved in one of the organic phases such as DMSO [131].

This other reactant is hexachlorocyclotriphosphazene (HCCP), whose its structure is reminded in the Figure 6.11.

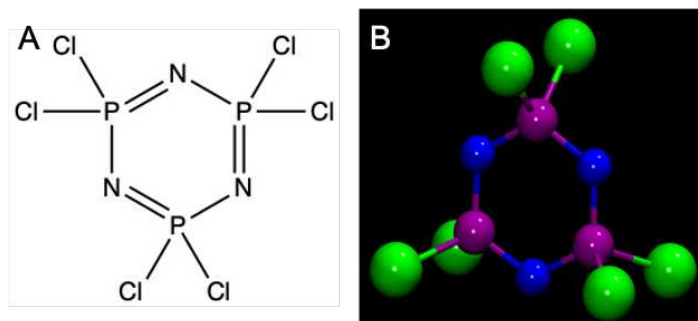


Figure 6.11 The HCCP molecule sketched using *ChemDraw* 20.0 [263] (A) and its ball-and-stick representation of the same molecule rendered using *VMD* 1.9 Catalina Rev7 [248] (B) with the colour code C = cyan, O = red, H = white.

The chlorine atoms can be substituted in reactions with a wide range of small organic molecules or polymer/monomer bearing hydroxyl or amine groups [283], or in post-functionalization [147]. This gives HCCP a high functionality since all six chlorine atoms have the possibility to be substituted. As HCCP is soluble in a number of organic solvents such as cyclohexane, it can react with Phg in DMSO using interfacial polymerization. It should be noted that, although HCCP can in principle be soluble in DMSO, it

is quite difficult to dissolve it and the immediate formation of the interface when both Phg/DMSO and HCCP/cyclohexane are mixed prevents too much diffusion of HCCP into the Phg-containing DMSO phase.

If their reactivity seems to make these two monomers very good candidates for IP, this was confirmed by the previous study of Radmanesh *et al.* which inspired this current work [260]. Indeed, this first work showed that they had promising performances for barrier applications. It was thus attempted to reproduce and improve the results obtained by Radmanesh *et al.*, grow a continuous, homogeneous layer on top of a porous substrate and with a low hydrogen gas permeability.

6) C. 2. Fabrication procedure via IP

In the work concerning gas separation [133], the membrane synthesized from Phg and HCCP showed surprisingly good barrier properties, which was the opposite of what was initially sought. However, it could give a good layer for this project if the results could be reproduced, improved and adapted for inclusion in hydrogen tanks. Furthermore, the advantage of starting an IP experimentation based on previous work is to reduce and set most of the parameters of the IP. As seen before, there are a lot of interconnected parameters which can affect the membrane formation and properties (cf. Chapter 2). Indeed, the tests with the test monomers suggested that even a small change in the process could have a huge effect on the final product. Therefore, before trying to improve its properties, it is important to check if the same process gives the same results.

6) C. 2. 1. Material fabrication

Both “free-standing” and “films on support” films are complementary and give different information about the product. As for PiP-TMC, analyses of free-standing films are usually carried out before to provide information about the elemental composition, type of reaction and properties such as the thermal stability or the degree of cross-linking in the network polymer. The process to synthesize a free-standing film from HCCP and Phg is schematised in Figure 6.12.

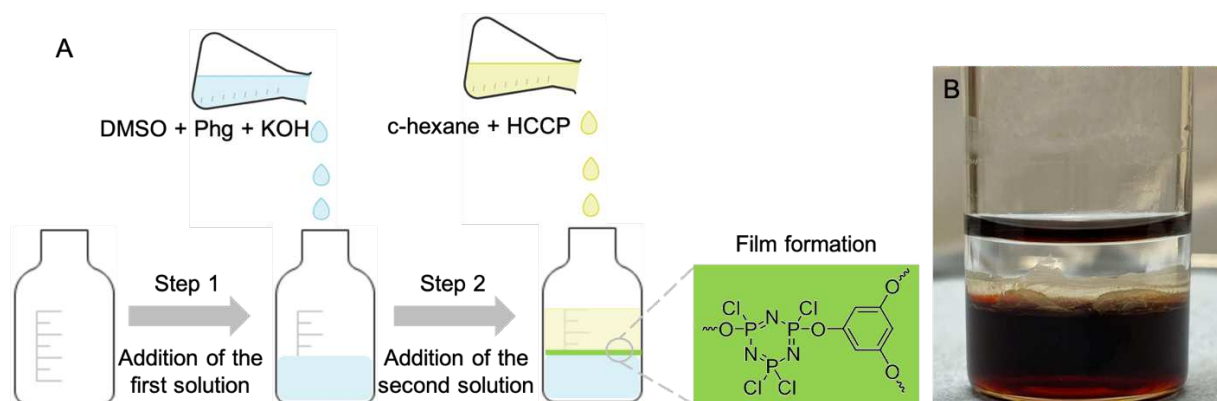


Figure 6.12 Schematic illustration of the different steps involved in the formation of a free-standing Phg-HCCP film via interfacial polymerization (A) and photograph of the sample S2 made following this protocol (B).

It allows a stable and well-defined interface to be formed between the two solutions.

For the “films on support”, their added strength allows more robust characterization techniques, such as microscopic imaging or gas permeation measurement, to be used. Although the principle of the reaction is the same, the process is obviously more complicated (Figure 6.13).

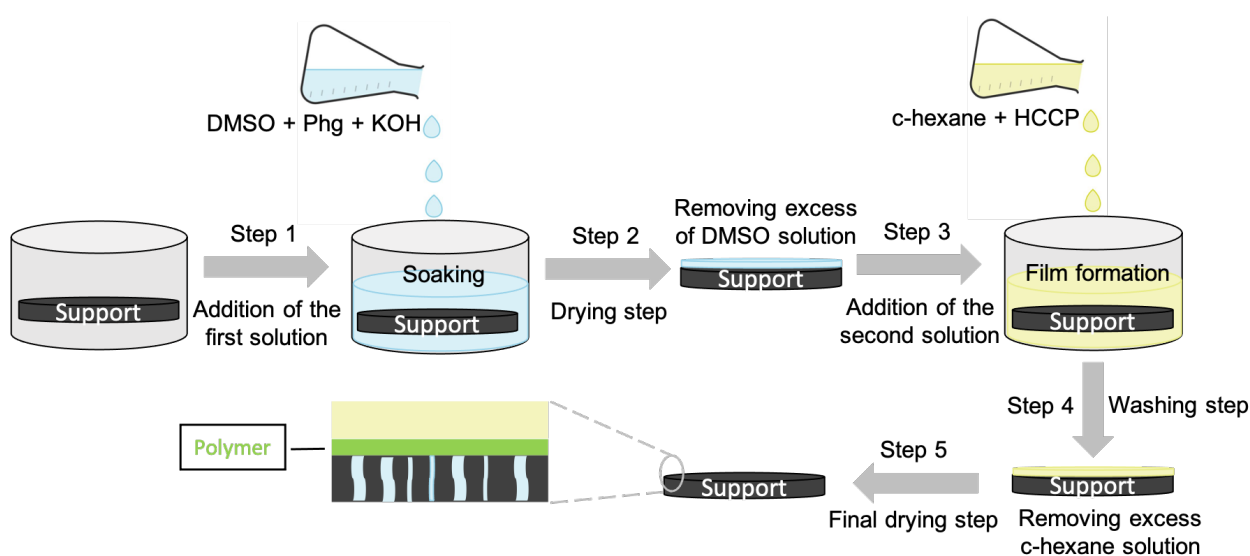


Figure 6.13 Schematic illustration of the different steps involved in the formation of a Phg-HCCP film on a substrate using interfacial polymerization.

For both approaches, the preparation of the solutions is the same and involves a first organic phase of 10w/v% of Phg dissolved in a mixture solution of dimethyl sulfoxide and potassium hydroxide

(DMSO/KOH). This solution is then contacted with the second organic phase, which contains 3.5w/v% of HCCP in cyclohexane.

In the case of Phg, a deprotonation step is necessary in addition to the dissolution step. Indeed, the hydroxyl groups on the Phg monomer need to be transformed into O⁻ groups capable of reacting in a nucleophilic reaction in order to have a good polymerization with HCCP. Phg is thus dissolved at 80°C in a mixture of DMSO and KOH, both having a role in this preliminary step, which is associated to the additional parameter “conversion time”:

- The potassium hydroxide is a strong base which increases the pH and leads to the deprotonation of the OH groups, *i.e.* the conversion of hydroxyl groups into reactive phenolate anions O⁻K⁺ which are both hydrophilic and nucleophilic.
- DMSO is a polar aprotic solvent that is immiscible with organic solvents such as cyclohexane, and facilitates the attack of the Phg O⁻ on the HCCP P⁽⁺⁾, with as leaving atom(s) one or more chlorine atoms carried by the HCCP ring.

The substrate used was the same as in the previous work [260], *i.e.* the microporous α -alumina (Al₂O₃) discs with a diameter of 39 mm, a thickness of 2 mm and a pore size of 80 nm with on top a prepared mesoporous γ -Al₂O₃ layer (procedure described in [305, 306]) with a thickness of 4-5 μ m and a pore size of 5 nm. It will be referred to as a “ceramic support”, as obtained from COBRA Technologies BV.

The other IP parameters are similar for free-standing and supported films, except for the reaction time which is a bit longer for the substrate since the interface is not exactly the same as for the free-standing type. The concentration in both wt/vol% and moles/litre (M) are recalled with the other significant parameters in Table 6.4.

Table 6.4 Interfacial polymerization parameters for Phg-HCCP films based on the former work of Radmanesh *et al.* [260].

Molar ratio of hydroxyl groups Phg/KOH	Conversion time	HCCP concentration	Phg concentration	Reaction time	Soaking time	Volume of	
						DMSO	c-hexane
2.2:1	2.5 h	3.5 wt/vol% 0.101 M	10 wt/vol% 0.793 M	10 min (15 min for support)	10 min	5 ml	

The pressure and temperature are also very important for the reaction. All steps were carried out at the ambient atmospheric pressure. For the temperature, the solution containing phloroglucinol was prepared at 80°C, due to the limited solubility of KOH in DMSO, whereas the solution of HCCP in cyclo-hexane was prepared at ambient temperature. The support was held at 80°C for 30 min prior to soaking in the Phg-containing saturated solution of KOH in DMSO. All other steps were carried out without control of the temperature but as close as possible to ambient.

6) C. 2. 2. Results and discussion

The results presented in this Section are compared to the previous work [260] in order to check their reproducibility. Four free-standing films and one film on top of a substrate were prepared.

Following a similar procedure with the same parameters (Figures 6.12 and 6.13 and Table 6.4) results in a well-formed free-standing film at the interface of the DMSO and cyclohexane solutions. After the reaction, the film was collected, ground, washed and filtered with acetone, then with ethanol and finally with water. The obtained powder is used for characterizations. This final washing step allows to remove the excess of cyclohexane solution and, therefore, any unreacted HCCP monomers because ethanol is a good solvent for HCCP (Step 4, Figure 6.13). The excess of DMSO solution is removed during the first drying step (Step 2 in Figure 6.13). Then, the resulting powder was dried and analysed using FTIR and classic elemental analyses, *i.e.* organic carbon and nitrogen (CN) analysis and X-Ray Fluorescence (XRF). Figure 6.14 shows the separate FTIR spectra of the monomers, the previous Phg-HCCP film and a sample made during this step (S4).

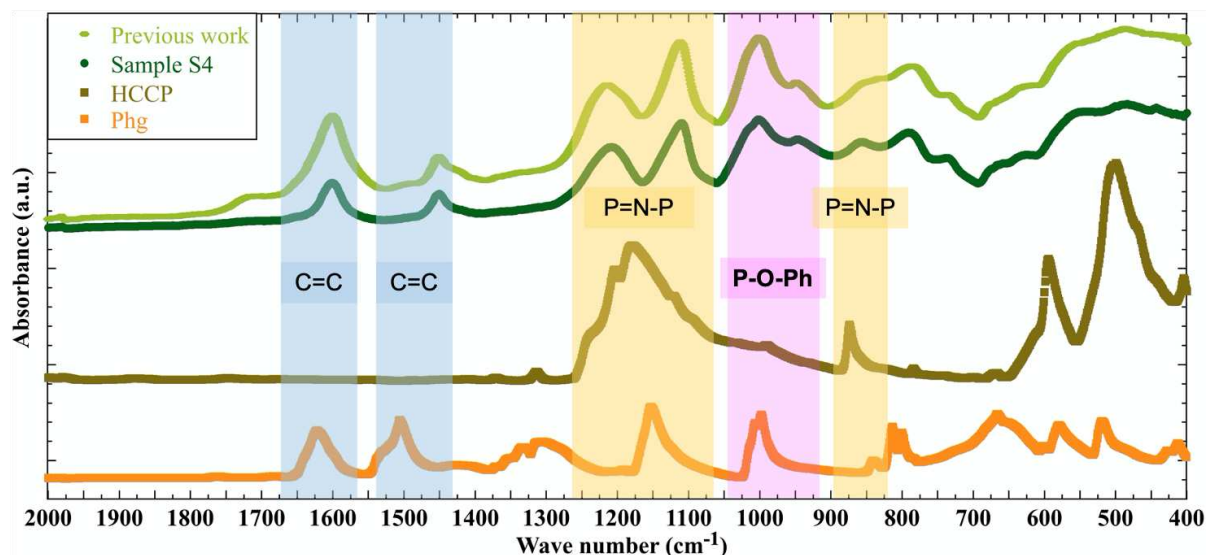


Figure 6.14 FTIR spectra of the HCCP and Phg monomers compared to that of the polyphosphazene film formed at the the interface of the DMSO and cyclo-hexane solutions. “Sample S4” indicates the results for a film obtained in this work. “Previous work” indicates the results taken for reference from [260].

Both green curves correspond to a Phg-HCCP network polymer and they can be superimposed, indicating that a very similar product has been formed. In both spectra, the presence of the benzene-triol Phg monomer is confirmed by the peaks around 1480 and 1600 cm^{-1} corresponding to the phenyl ring bonds (C=C) [311]. The presence of phosphazene compounds is displayed by the peaks corresponding to the two vibration types of the P=N bonds: from 1100 to 1250 cm^{-1} for the asymmetric stretching (matching with the large peak between these same values in the HCCP spectra) and around 870 cm^{-1} for the symmetric stretching [312]. Finally, the link between the two monomers, *i.e.* the confirmation that the reaction happened, is apparent from the two peaks due to the stretching vibrations of P-O-Phenyl around 1003 and 950 cm^{-1} [313].

Despite this product identification, the powder was visually inhomogeneous, therefore its composition needed to be completed. Tables 6.5 and 6.6 present the CN and XRF elemental results of the previously generated film and Sample S4, which were analysed by FTIR (Figure 6.14).

Table 6.5 CN analysis data for two free-standing Phg-HCCP films. The previous results are the average two measurements and the errors displayed correspond to their standard deviation. For S4, results of both measurements are given. Estimates of the molar ratio of Phg to HCCP rings in the resulting network polymer and the upper and lower estimates of the number of reacted Cl groups per HCCP ring are based on Eqns. 6.1- 6.3, as explained in the text.

Samples	Molar Ratio C/N	Estimated Molar Ratio Phg/HCCP in the network (Eq. 6.1)	No. of reacted Cl per HCCP	
			Lower estimate (Eq. 6.2)	Upper estimate (Eq. 6.3)
Previous work [260]	2.58 ± 0.09	1.29 ± 0.04	2.58 ± 0.09	3.88 ± 0.13
This work S4	2.70	1.35	2.70	4.04
	2.75	1.38	2.75	4.13

Table 6.6 Molar ratios of P, K and S atoms compared to Cl as obtained from the XRF data for two free-standing Phg-HCCP films. For S4, two measurements have been made. Estimates of the number of reacted Cl groups per HCCP ring are based on Eqns. 6.5 and 6.8, as explained in the text. The presence of potassium and sulphur are probably due to salt formation (KCl) and residual DMSO.

Samples	Molar Ratios			Number of reacted Cl per HCCP (Eq. 6.5)	Number of reacted Cl per HCCP (Eq. 6.8)
	P/Cl	K/Cl	S/Cl		
Previous work [260]	0.86	0.16	0.11	2.5	3.1
This work S4	1.63	0.15	0.14	4.2	4.4
	1.48	0.18	0.15	4.0	4.3

The elemental analyses provide some estimates of the stoichiometry of the films in terms of the proportion of HCCP and Phg rings linked together and the degree of cross-linking. If the first assumption is that all the carbon and nitrogen atoms present in the samples are in the network, *i.e.* there are no unreacted monomers nor residual solvent molecules, then the number of Phg rings is $N_c/6$ (with N being a number of

atoms and, therefore, N_C being the number of carbons) and the number of HCCP rings is $N_N/3$ (with N_N being the number of nitrogens). The ratio of Phg to HCCP in the network is then:

$$(N_C/6)/(N_N/3) = N_C/(2N_N) \quad (6.1)$$

i.e. a half of the C/N ratio given in Table 6.5. The estimates from both the previous work [260] and the current study suggest that the Phg rings are $\sim 1/3$ more present than the HCCP rings in the network structure, *i.e.* the Phg to HCCP stoichiometry is about 4:3.

Although there is no direct information in the C/N ratio does not provide directly the number N_{Cl_reac} of reacted Cl atoms *per* HCCP ring, it is possible to make some lower and upper estimates by assuming that at least two -OH groups on Phg must react so as to ensure a network structure, *i.e.* a lower estimate is $2*(N_C/6)$ reacted Cl, and that all three -OH groups could react, *i.e.* an upper estimate is $3*(N_C/6)$ reacted Cl. These two extremes give the following estimates for the number of reacted Cl *per* HCCP ring:

$$\text{lower estimate:} \quad 2 \times (N_C/6)/(N_N/3) = N_C/N_N \quad (6.2)$$

$$\text{upper estimate:} \quad 3 \times (N_C/6)/(N_N/3) = 1.5 \times N_C/N_N \quad (6.3)$$

These lower and upper estimates of the number N_{Cl_reac} of reacted Cl atoms *per* HCCP ring are also given in Table 6.5.

The P/Cl ratios given in Table 6.6, also allow to estimate N_{Cl_reac} . If the number of initial Cl atoms N_{Cl_init} is assumed to be just twice the number of P atoms, *i.e.* $N_{Cl_init} = 2N_P$, then the number of reacted Cl atoms is:

$$N_{Cl_reac} = N_{Cl_init} - N_{Cl} = 2N_P - N_{Cl} \quad (6.4)$$

where it is assumed all the Cl atoms detected by XRF, N_{Cl} , are in the network polymer. The number of HCCP rings is just $N_P/3$ so the average number of reacted Cl *per* HCCP ring is:

$$N_{Cl_reac}/(N_P/3) = (2N_P - N_{Cl})/(N_P/3) = 3(2 - (N_{Cl}/N_P)) = 3(2 - (N_P/N_{Cl})^{-1}) \quad (6.5)$$

A second estimate can be made as the XRF data suggest a significant proportion of potassium ions present in the film. If each K^+ ion is associated with a Cl^- ion, *i.e.* that not all Cl atoms are in the network polymer, then the number of chlorine atoms detected by the XRF analysis can be written as:

$$N_{Cl} = N_{Cl_network} + N_{Cl^-} = N_{Cl_network} + N_{K^+} \quad (6.6)$$

The number of reacted Cl atoms N_{Cl_reac} then becomes:

$$N_{Cl_reac} = N_{Cl_init} - N_{Cl_network} = 2N_P - (N_{Cl} - N_{K+}) = 2N_P - N_{Cl} + N_{K+} \quad (6.7)$$

and so the average number of reacted Cl *per* HCCP ring is:

$$\begin{aligned} N_{Cl_reac}/(N_P/3) &= (2N_P - N_{Cl} + N_{K+})/(N_P/3) = 3(2 - (N_{Cl}/N_P) + (N_{K+}/N_P)) = \\ &3(2 - (N_P/N_{Cl})^{-1} + (N_{K+}/N_P)) = 3(2 - (N_P/N_{Cl})^{-1} + ((N_{K+}/N_{Cl})/(N_P/N_{Cl}))) \end{aligned} \quad (6.8)$$

Estimations from Eqns. 6.5 and 6.8 are also given in Table 6.6

The C/N and XRF results confirm that the product contains both monomers, as seen previously [260], *i.e.* the reaction happened. The C/N analysis seems to indicate that in both studies a product is formed with a similar ratio of Phg to HCCP rings of ~4:3. However, the XRF results (Table 6.6) for the P/Cl ratio differ significantly between the former work and the current study. The former work suggests a number N_{Cl_reac} of reacted Cl *per* HCCP in the range from 2.5 to 3.1 using Eqns. 6.5 and 6.8. These values are reasonably consistent with the lower estimates (Eq. 6.2) from the C/N analysis of two reacted -OH groups *per* Phg ring. The current study, however, gives higher values for N_{Cl_reac} in the range of 4.0 to 4.4, which are more consistent with an upper estimate (Eq. 6.3) of three reacted -OH groups *per* Phg.

These discrepancies could be explained by the inhomogeneity of the powder, *i.e.* an inhomogeneity in composition: the difference between the two separate XRF measurements of the current study supports this possibility. Results from both elemental analyses suggest an incomplete substitution of the Cl groups, *i.e.* between 2 to 4 out of the total possible of 6. This indicates that the networks formed from HCCP and Phg have an intermediate degree of cross-linking, albeit with a higher degree for the samples studied here. The fact that the materials are not easily dissolved in a variety of solvents does suggest a certain degree of cross-linking.

This uncertainty about the extent of the crosslinking density can be clarified by analyzing the thermal stability of the film. Indeed, it was shown in the previous work [260] that from the deprotonation of the phloroglucinol to its thermal stability, the main link was the cross-linking degree: the greater the extent of deprotonation, the greater the degree of crosslinking, the less likely the opening of HCCP rings, and therefore the higher the thermal stability. Figure 6.15 displays the mass loss of a Phg-HCCP sample (S3) measured using thermogravimetric analysis (TGA) coupled with a mass spectrometer (MS) upon heating under N₂.

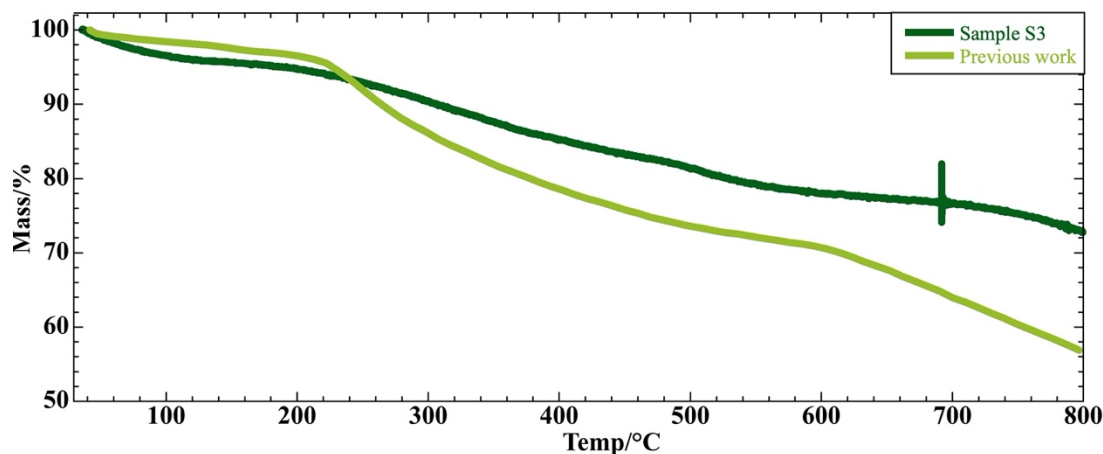


Figure 6.15 TGA curves of the free-standing films formed by Phg and HCCP.

Both samples show a similar progressive decrease in weight with a potential onset temperature of around 200 to 250°C. This first part of the mass loss, between 30 to 300°C, can be attributed to the removal of residual solvents, such as DMSO or absorbed water as well as side products of the reaction between unreacted Cl and OH groups. It can also be the gradual release of trapped unreacted monomers and all these interpretations are supported by the release of H₂O, CH₃S and Cl, as detected by the mass spectrometer in the previous work [260]. For the samples studied here, no MS could be used due to technical issues.

For the second part until 800°C, even if they are still in the same range, there is more discrepancy between the results. As explained before, a good substitution of the Cl groups, *i.e.* a high cross-linking degree, prevents better the opening of the HCCP rings than a lower one. Indeed, it is well-known that HCCP rings can be opened at a temperature exceeding 250°C [314]. So the thermal stability after 300°C is better for the current sample, which has a higher cross-linking degree, and in which the HCCP opening is less probable.

Once the product was identified as being similar to the previous work, a film was made on top of a ceramic substrate was made by following again the same process and parameters (Figure 6.13 and Table 6.4) and using a specific setup shown in Figure S6.1 of the SI. The film was washed with ethanol not only to remove the excess of cyclohexane and the dissolved HCCP monomers but also to check if the film was well attached to the surface: if after the final washing and drying step, nothing remains on the surface, this means that the film was formed but not on the support. In this case, it remained on the surface and the morphology of the sample was studied using field emission scanning electron microscopy (FE-SEM), as shown in Figure 6.16.

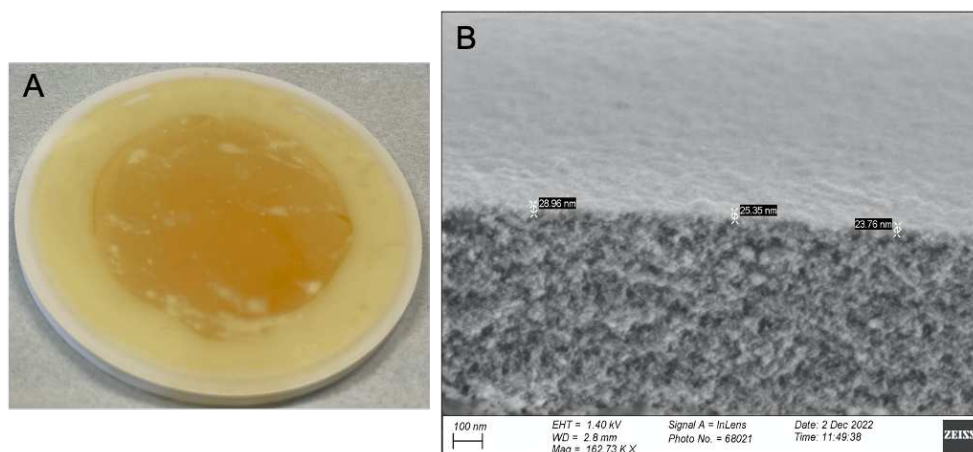


Figure 6.16 Phg-HCCP film prepared on top of a ceramic support via IP (A) and cross-section seen by FE-SEM of the same sample (B).

Both pictures of Figure 6.16, show a continuous and corrugated film all along the substrate, albeit with some defects. Probably due to these imperfections, the thickness is not uniform but has an average value around 25 nm. This corresponds to the range found previously [260].

Another property which can be compared is the hydrogen gas permeation. This measurement allows to find the permeance and permeability coefficient of the sample. This defines the “barrier property”, *i.e.* the lower the permeance, the better barrier for the gas studied. Figure 6.17 compares the hydrogen permeability coefficient of both types of polyphosphazene films (current and previous work) along with those for some published barrier materials for hydrogen. However, caution has to be applied as this comparison is made with the permeability coefficient data. Consequently, it is important to note that measurement methods and thicknesses can be different, except for the ones related to this and the previous work [260]. Moreover, if the interfacial polymerization used here is relatively easy to scale up to industrial fabrication, this is much more difficult for complex techniques, *e.g.* those using graphene oxide.

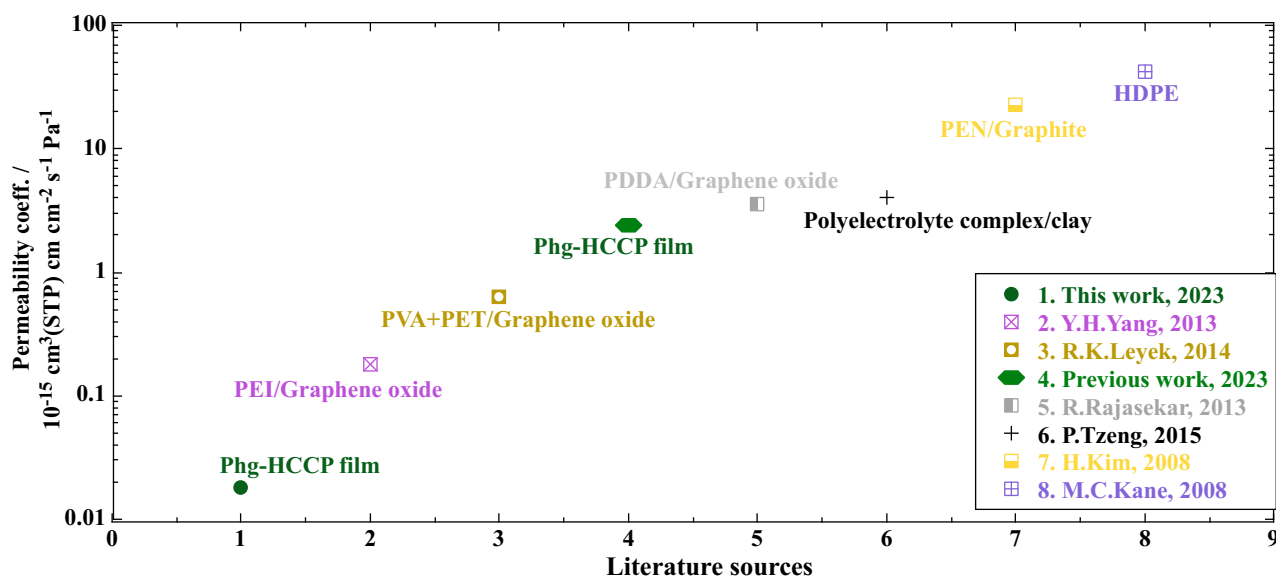


Figure 6.17 Hydrogen permeability coefficient of different barrier materials. The current and previous Phg-HCCP films are in green and have permeability coefficient values of 0.0182×10^{-15} and $2.5 \times 10^{-15} \text{ cm}^3(\text{STP}) \text{ cm cm}^{-2} \text{ s}^{-1} \text{ Pa}^{-1}$, respectively [76, 94, 98, 315-317].

Figure 6.17 shows that, despite a similar composition, the small differences in morphology, defects, and most likely in cross-linking degree lead to a different permeation behaviour between the two Phg-HCCP materials, and especially to the better H₂ barrier properties of the current work. Indeed, it seems very promising with respect to other materials reported in the literature.

As for the study with piperazine and trimesoyl chloride, this demonstrates the sensitivity of the interfacial polymerization: any changes in the process have to be well studied and tested before being set up. To improve the knowledge about both monomers, their reaction was carried out in one solution like any other common polymerization.

6) C. 3. Bulk polymerization

Due to the difficulties encountered using IP and its high sensitivity, a simple system, such as a reaction in only one solvent, *i.e.* a bulk polymerization, could help casting a light on what is formed exactly when these two monomers react together. The first aim was to further investigate the reactivity of the monomers, such as how many groups on each monomer are involved in the reaction or what is the best way to increase this number. Indeed, as Tables 6.5 and 6.6 indicate, the substitution of -Cl or -OH groups is not complete and not precisely known with IP. Indeed, the number of reacted Cl atoms *per* HCCP ring has been found to vary between 2 to 4 out of 6 and it defines the cross-linking degree. It is an essential polymer property; but it is difficult to obtain with precision from the experimental results on the Phg-HCCP films.

A secondary aim of the bulk polymerization was to produce a thicker layer, which is easier to analyse than a thinner one, has supposedly better barrier properties, and could be applied by spin coating on a substrate (cf. Chapter 1).

6) C. 3. 1. Procedure

The procedure and parameters were based on the previous work of Zhang *et al.* [133, 312]. First, a common solvent had to be selected, and it must be able to dissolve both HCCP and Phg. This is the case for dimethyl sulfoxide (DMSO).

Although the precise pathway of the reaction is not known, the one involving these two monomers is a nucleophilic substitution like in most IP [133, 146]: it was reported elsewhere that DMSO enhances the nucleophilicity of phenols as compared to alcohols or water [318, 319]. Therefore, the use of this solvent seemed a good option. However, to be involved in the reaction, the hydroxyl groups of phloroglucinol must be transformed into activated anions, *i.e.* they have to change from -OH to -O⁽⁻⁾. This is the role of potassium hydroxide (KOH), which is added to a solution of 5 ml of DMSO with 0.5g of Phg and then heated up to 80°C during a certain time. This conversion step is very important for the formation and properties of the polymer, therefore its “time of conversion” and the concentration of KOH are essential. For the time, different works [133, 312] suggest that around 2 h should be enough to have a good conversion, which can be followed by the colour change of the solution. The concentration is chosen with respect to the ratio of the -OH groups of Phg with respect to the -OH groups of KOH. Here, it was set to a ratio of 1:1 according to the same studies.

The experiment itself proceeded as follows, with the conditions defined in Table 6.7:

1. In an assembly of a three-neck flask with oil bath, refrigerant and set up for nitrogen atmosphere (anhydrous atmosphere), put in order: Phg monomers, KOH and DMSO.
2. Add stirring and heat up to 80°C for 2 h: conversion step.
3. Over 1 h, add progressively 0.85 g of HCCP monomers but keep the time of addition as short as possible (keep the system water free).
4. Keep the stirring and temperature for the time of reaction
5. At the end, wash and filter the obtained product with water, acetone and ethanol.

During all the process, different samples were collected in order to make NMR analyses.

Table 6.7 Experimental conditions of the bulk polymerization of Phg and HCCP monomers, in DMSO including a Phg deprotonation step with KOH.

Under nitrogen atmosphere	Temperature	Pressure	Phg mass	Solution volume	Ratio -OH Phg/ -OH KOH	Conversion time	Reaction time	HCCP mass
	80°C	Ambient	0.5 g	5 ml	1:1	2 h	Overnight	0.85 g

6) C. 3. 2. Results and discussion

After the reaction, Figure 6.18 presents what was obtained in the flask before and after washing. In contrast with interfacial polymerization, the product was an homogeneous powder.

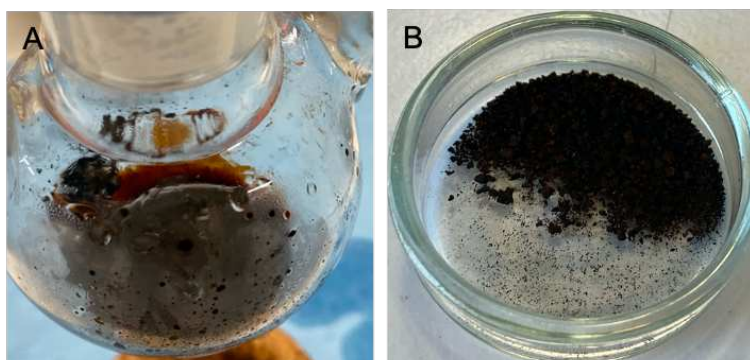


Figure 6.18 Powder obtained after bulk polymerization of Phg and HCCP monomers in DMSO solvent with a conversion step using KOH. The product before washing (A) and after washing (B) are shown.

Due to the complexity of the obtained material, FTIR measurements (not shown) were inconclusive but they suggest that the product is indeed a Phg-HCCP polymer as what obtained by IP. It can thus be expected that, whatever this product, its characteristics and properties are similar. Furthermore, if a better polymer is produced by the easier bulk polymerization approach, the same conditions could be applied to IP in order to obtain this desired product. However, to be able to use this way to improve the Phg-HCCP film, a formal identification of the bulk product is first necessary. NMR measurements were thus carried out on the different samples collected during the process and on the final powder, before and after the washing step. The list of the different samples as well as the type of NMR are presented in Table 6.8.

Table 6.8 Samples for NMR analyses collected during the whole bulk polymerization process of the Phg and HCCP monomers. If it was not already the case, the product was dissolved in DMSO-D6 to allow the analysis.

Name	Content	Type of analysis		
		H-NMR	C-NMR	P-NMR
Sample 1	Solution of Phg in DMSO-D6 (no KOH)	YES	YES	NO
Sample 1 ^{bis}	Solution of HCCP in DMSO-D6	YES	YES	NO
Sample 2	Product of the bulk polymerization before washing step	YES	YES	YES
Sample 3	Product of the bulk polymerization after washing step	YES	YES	YES

For the interpretation of the results, some literature spectra were extracted from the ChemicalBook website [66, 320] or from the work of Sun *et al.* [274] and Yildiz *et al.* [267] to be used as references. Moreover, the book of Pavia *et al.* [321] helped to analyze the results and the article of Fulmer *et al.* was used to detect the signature of usual NMR impurities [322]. As many results were obtained, Figures 6.19, 6.20 and 6.21 only present the most interesting ones and the main conclusions.

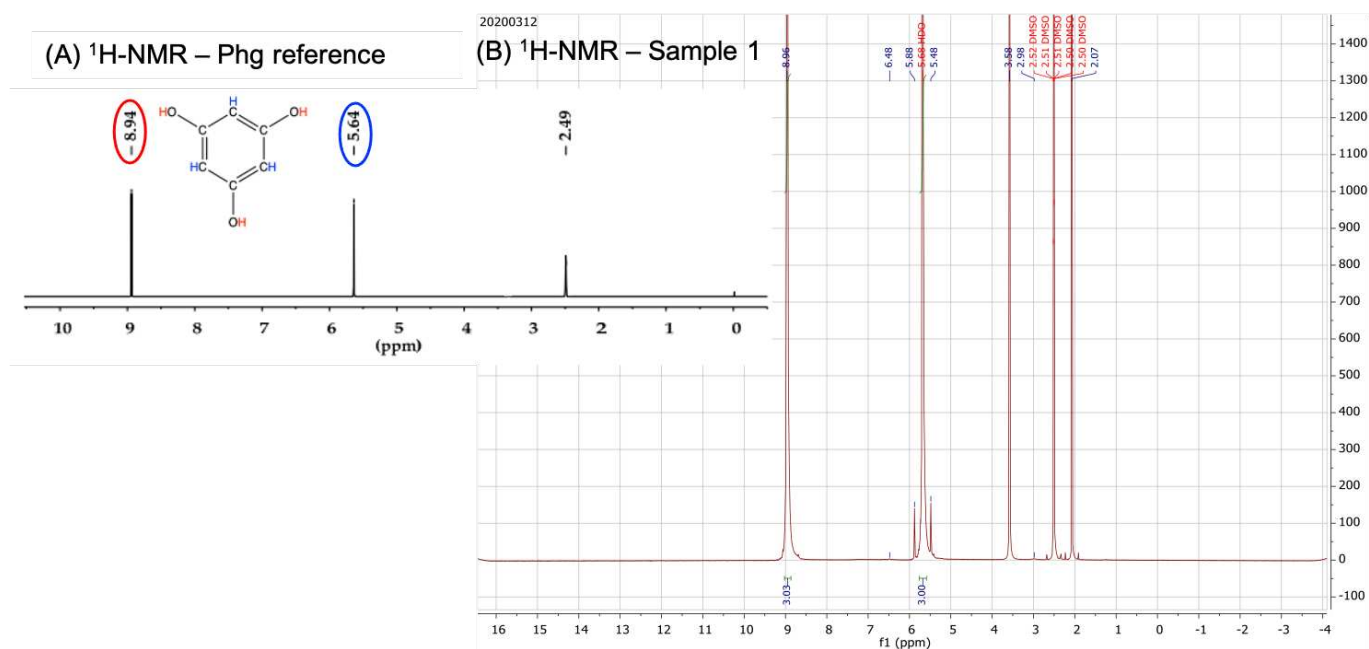


Figure 6.19 $^1\text{H-NMR}$ spectrum of phloroglucinol from a reference [274] (A) and from sample 1 (B). Both have been analysed in DMSO-D6 whose signal appears around 2.49 ppm.

In Figure 6.19, the two peaks at ~ 9 and ~ 5.6 ppm correspond to the two different groups of equivalent H, in phloroglucinol, whereas the peaks between 4 to 2 ppm correspond to DMSO and probably some impurities such as acetone or ethanol. The Phg monomers are well detected by NMR, *i.e.* their concentration is sufficient. This is also confirmed by the $^{13}\text{C-NMR}$ (not shown).

The $^1\text{H-NMR}$ of Samples 2 and 3 (Figures 6.20.C and 6.21.E) are different to those of the Phg alone: the product is more than just Phg monomers. Several additional peaks mean that there are more than just two groups of equivalent H. Moreover, according to the chemical shift of these peaks, their chemical environment changed, which is most likely due to new bonds with other atoms. Therefore, it was supposed that, in the signals between 9 to 7 ppm of Figure 6.20.C, one of the peaks could be the protons of the hydroxyl function originating from Phg (the wide peak at 9 ppm comes from KOH), whereas among the peaks between 4 and 2 ppm, one would be the second kind of hydrogen group. This assumption is consistent with the fact that the only source of H is the Phg, as such that any peaks in $^1\text{H-NMR}$ spectrum come necessarily from this compound. To conclude, the $^1\text{H-NMR}$ seems to indicate that bonds are modified or created, *i.e.* that a reaction has occurred.

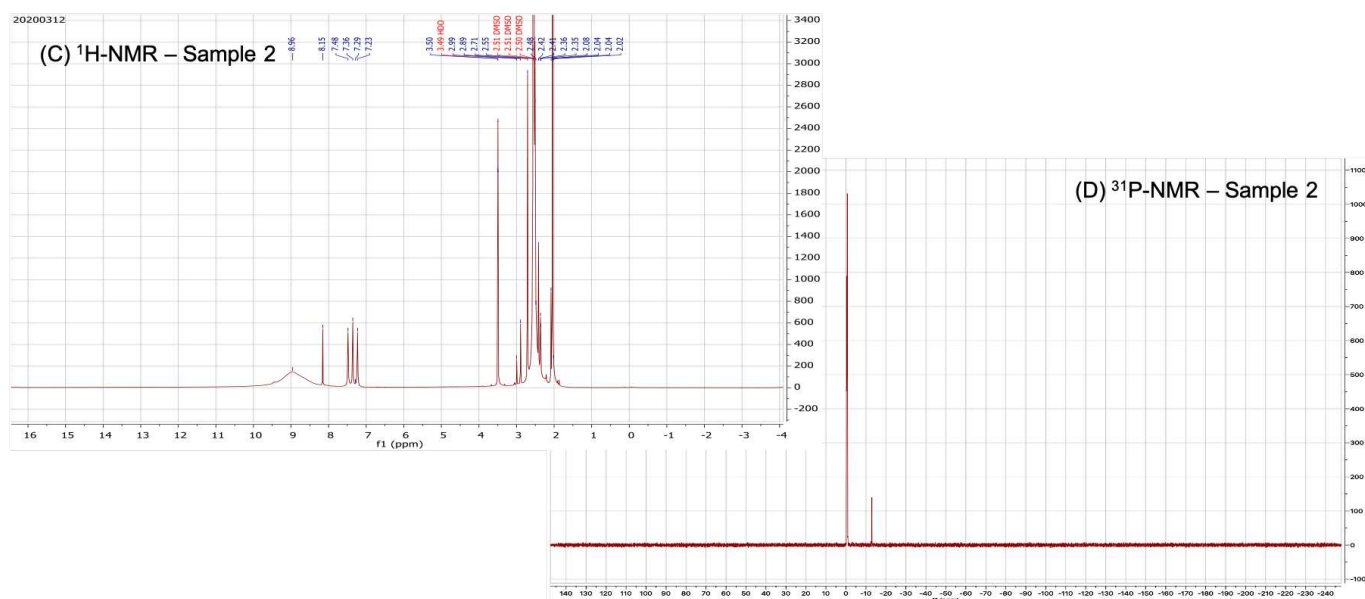


Figure 6.20 $^1\text{H-NMR}$ (C) and $^{31}\text{P-NMR}$ (D) spectra of Sample 2. Both have been analysed in DMSO-D_6 .

This inference that the reaction took place is also supported by the analysis of the $^{31}\text{P-NMR}$ spectrum of Sample 2 (Figure 6.20.D). Indeed, the reference spectrum (Figure 6.21.G) shows one signal, which makes sense as all the P in the pure HCCP monomer are equivalent. However, the spectrum of Sample 2 has two different signals instead of one, as well as a chemical shift. Since the peak of HCCP is around 20-22 ppm whereas they are between 0 and 12 ppm in the Sample 2, this means there are two different groups of P atoms. As found with the study of H groups, a reaction occurred and changed the chemical environment of the phosphorus atoms compared to the pure HCCP. Nonetheless, neither $^1\text{H-NMR}$ nor $^{31}\text{P-NMR}$ for Sample 2 allow to be sure of the exact nature of this reaction, *i.e.* whether a polymer has been created or whether there are simply been a change of the functional groups of each monomer.

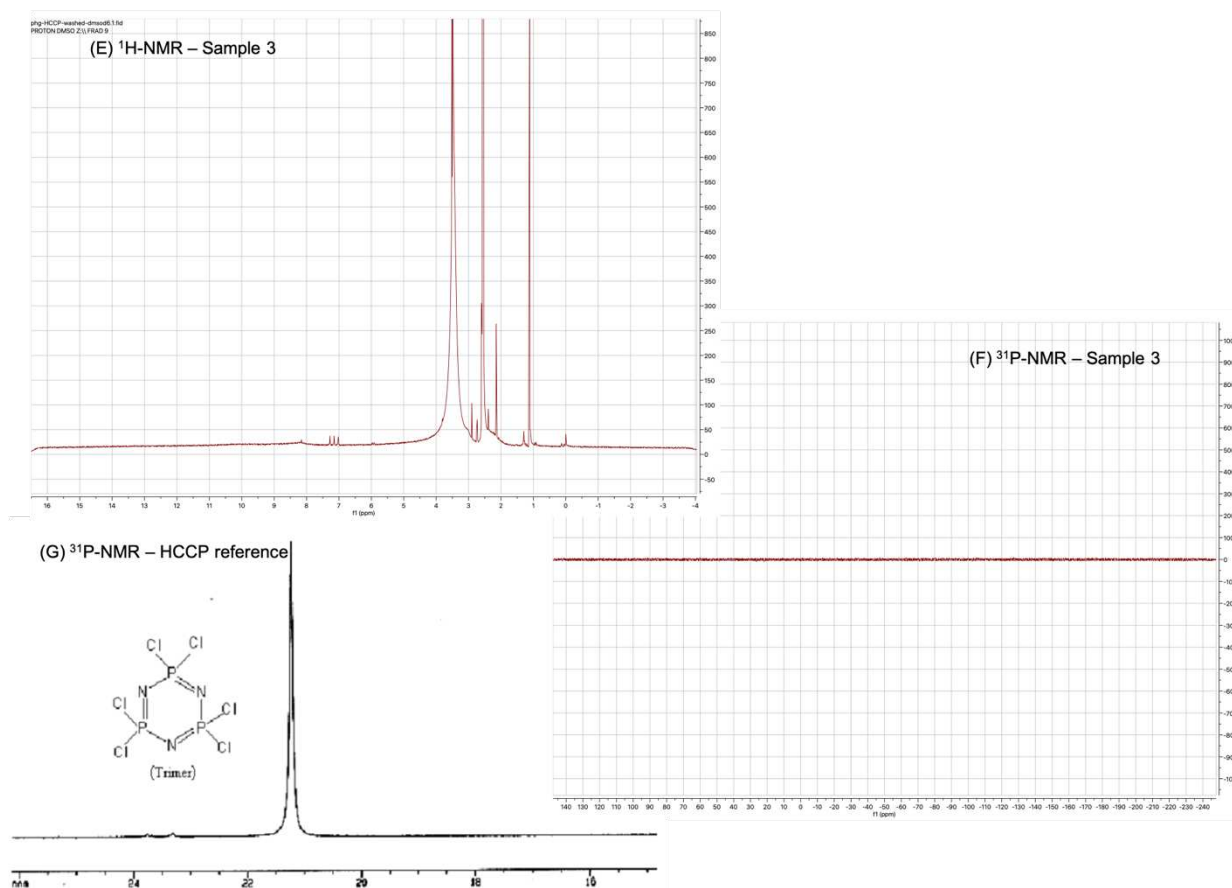


Figure 6.21 $^1\text{H-NMR}$ (E) and $^{31}\text{P-NMR}$ (F) results for Sample 3 as well as the spectrum of the HCCP taken as reference (G) [267].

Finally, the $^{31}\text{P-NMR}$ analysis of the powder obtained after washing step (Figure 6.21.F) seems to indicate that this step eliminated the phosphazene from the product. Indeed, as mentioned above, P atoms only come from the HCCP monomers but there are no peaks on the spectrum of Sample 3. This lack of detection suggests an absence of HCCP molecules. However, it is not possible to determine if this could be due to a concentration too small to be detected, *i.e.* there is still HCCP in the product but in too small a quantity to be seen, or if there is really no more HCCP.

At this point, it can be noted that a reaction has taken place and a polymer was formed as indicated by IR, but it has been modified by the washing step. More precisely, the HCCP molecules seem to disappear, partly or totally, when solvents are used to clean the sample. This suggests that the bonds established with the Phg monomers during the reaction were too weak to resist to the solvent or simply not numerous enough: the polymer formed may be partly linear and partly a network, which is normally much more resistant to solvents.

A study of the powder solubility as well as gel permeation chromatography (GPC) results (not shown), seems to support this nature of the polymer formed. Of course, the solubility of a polymer depends on other parameters than the degree of branching but it is still a good indicator of the presence of cross-linked parts. In order to determine its molecular mass distribution via GPC, attempts were made to dissolve the powder in pure tetrahydrofuran (THF) solvent. This was quite unsuccessful so a mixture of DMSO and THF was used instead. However, the concentration of the resulting solution was quite low and the GPC results were inconclusive. Nevertheless, this dissolution issue during the sample preparation has led to further investigations of the solubility behaviour of the powder by simply trying to dissolve it in different solvents. First, as shown by the washing step, a part of the obtained polymer is not soluble in water, acetone, ethanol as well as in pure THF. Second, three other solvents, with different polarities, were tested and Figure 6.22 presents the results:

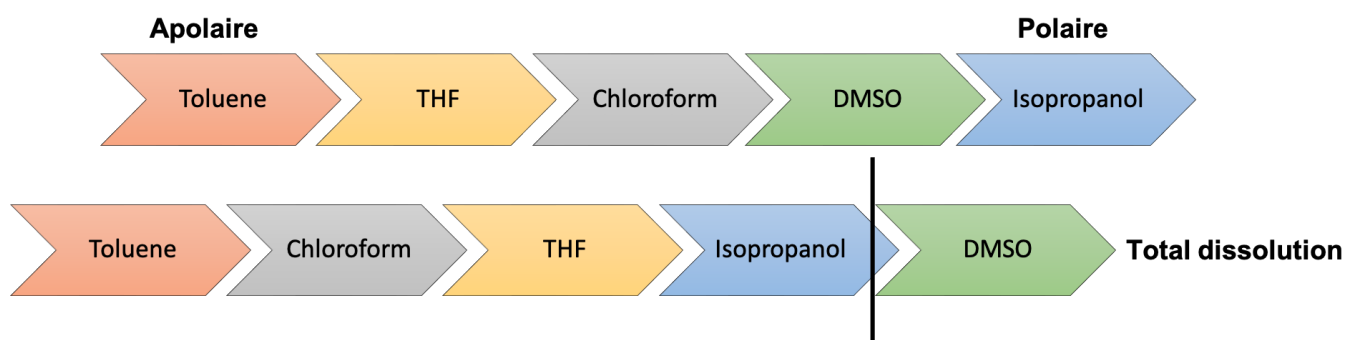


Figure 6.22 Solubility trends of the product obtained by bulk polymerization of the Phg and HCCP. Top panel: solvents are ranked from least to the most polar. Bottom panel: solvents are ranked by their ability (lowest to highest) to dissolve the product. The thick black line indicates from where the dissolution is complete.

This test shows an absence of trend since the solubility of the sample does not seem to match with the increasing polarity of the solvents. If the DMSO succeeds in dissolving the polymer, it is not only because it is a polar solvent. If this information is not particularly useful here and was not further examined, the fact that the polymer seems to have lost a part of itself during the washing step and is hard to dissolve supports the NMR conclusions: the polymer formed is both linear, *i.e.* more easily dissolvable with, *e.g.* rinsing solvents, and networked with an intermediate degree of cross-linking, *i.e.* more resistant to solvents.

This incomplete network is consistent with the results found with IP. If the partial substitution of the Cl atoms was based on elemental analysis results for the Phg-HCCP IP films (Tables 6.5 and 6.6), the product of this simpler polymerization seems to confirm this incomplete reaction of the chlorine. Indeed, the number of reacted Cl was found ranging from 2 to 4 out of the 6 available on HCCP monomers, which

corresponds also to a more or less cross-linked polymer. Whether with interfacial or bulk polymerization, it is not a highly cross-linked network which is formed right after the reaction but something with enough cohesion and branching to resist certain solvents, have quite a good thermal stability and even a low permeability coefficient for H₂. Moreover, another study of Dr. Radmanesh shows that this incomplete cross-linked network formed just after the reaction can become a highly cross-linked polymer after heating it up to 200°C, where the further densification of the network can originate from reactions between unreacted functional groups [323, 324].

Concerning the secondary purpose of this bulk polymerization study, try to produce a polymer that could be spin coated on a substrate, a short test quickly showed that the product was too viscous and insoluble to be used by this method. As this technique is not the one studied in this project, no further attempts were carried out on it but finding a better solvent could improve this approach.

6) C. 4. Conclusion of the studies on Phg-HCCP monomers

Apart from the contribution concerning the use of these products in interfacial polymerization and, therefore, an improvement in the practice of this technique, more specific information related to the reaction itself have been provided. Indeed, if the reaction was sufficiently known to reproduce the previous results by IP [260] and carry out bulk polymerization, there were always uncertainties regarding its progress. For example, it was confirmed that not all of the reactive groups, neither from Phg nor from HCCP monomers, react. There are still a certain number of unknowns but a slightly more complete process can already be deduced.

Like most interfacial polymerizations, the reaction between HCCP and Phg is a nucleophilic substitution and more precisely, due to the aromatic compounds (Figures 6.10 and 6.11), a nucleophilic aromatic substitution. In this kind of reaction, similar to aliphatic nucleophilic S_N2 substitutions, an electron-poor aromatic ring (here HCCP) is attacked by a nucleophile (Phg after conversion), resulting in a substitution reaction or polycondensation. Usually, a certain assembly is necessary to remove the inevitable by-products and to favour high molecular-weight polymer production (cf. Chapter 2) [325, 326]. Moreover, the use of HCCP and Phg, which require “specific conditions” for their reaction, led to the establishment of a complex setup to carry out the bulk polymerization, which consisted of a three-neck flask along with the necessities to heat up to 80°C and provide a nitrogen-rich atmosphere (Figure S6.2 in SI). This last is related to the monomers, more precisely to the chlorine groups of the HCCP, which are sensitive to water. Therefore, the system must be anhydrous to avoid the reaction of Cl before its involvement in the polymerization. It was even more important for the one-solvent reaction as the aim was

to study the reactivity of the monomers together only, *i.e.* with as few side reactions as possible. This assembly was thus used only for bulk and not for interfacial polymerization, whose aim is not to investigate the reactivity but to form the best layer possible. From a more practical point-of-view, the different times are shorter in IP and there is much more handling, which means that the use of this equipment would not be convenient. However, to limit as much as possible the exposure to water, all possible preparations were made under an anhydrous atmosphere and the products were stored in a dry environment.

Another “specific condition” required by the monomers is the conversion step. Indeed, a nucleophilic reaction implies anions. Here, the anions come from the Phg compound after the conversion of their hydroxyl groups into hydroxide -O^{\ominus} . For both IP and bulk polymerization, this conversion step, which is essential for the properties of the layer, is performed in DMSO in the presence of KOH. The solvent is chosen with respect to the following IP and all its requirements (cf. Chapter 2), but also in this particular case, because it is known that DMSO helps the nucleophilic reaction by enhancing this property of the phenolates [318, 319]. KOH is the most important element in this step, which means that its quantity has to be chosen carefully. Indeed, by changing the pH, this strong base allows the deprotonation of the Phg hydroxyl groups. Its concentration is therefore related to the concentration of Phg and more precisely, to the ratio of the hydroxyl groups of both compounds. However, depending on the bulk or IP reaction and on the conditions, this ratio varies: for the bulk study, it was set to 1:1 in accordance with the literature used to set up the reaction, which means as much -OH from Phg than from KOH. On the other hand, during the IP study, it was defined at 2.2:1 from the previous work, *i.e.* 2.2 times more Phg than KOH. This ratio is a tuneable parameter of the reaction: for example, after free-standing film tests, values above 4 do not lead to the formation of a layer. Moreover, due to a limited solubility of KOH in DMSO, the conversion step must take place at 80°C and during at least 2 to 2.5 hours depending on the type of reaction in order to have the best possible degree of deprotonation of Phg. The state of deprotonation of Phg can be followed by the change in colour of the solution, which varies from transparent to brown/dark brown at the end of the conversion (Figure 6.23).

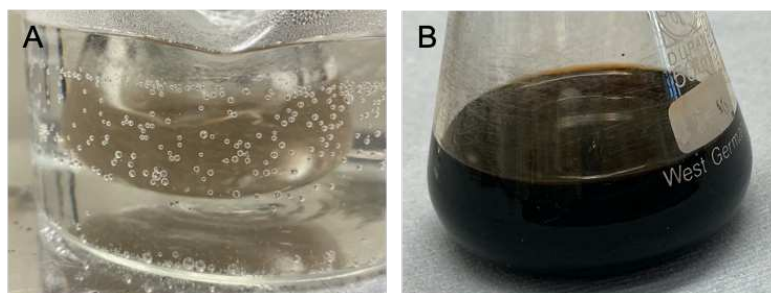


Figure 6.23 Solution of phloroglucinol in DMSO right after the addition of KOH (A) and 2.5 h at 80°C later: conversion step of the Phg.

Once the phenols are deprotonated into phenolate anions ($R-O^-$), they can react with the P^+ atoms of the HCCP rings, displacing the chlorine and creating a P-O bond between both monomers, as shown in Figure 6.24.

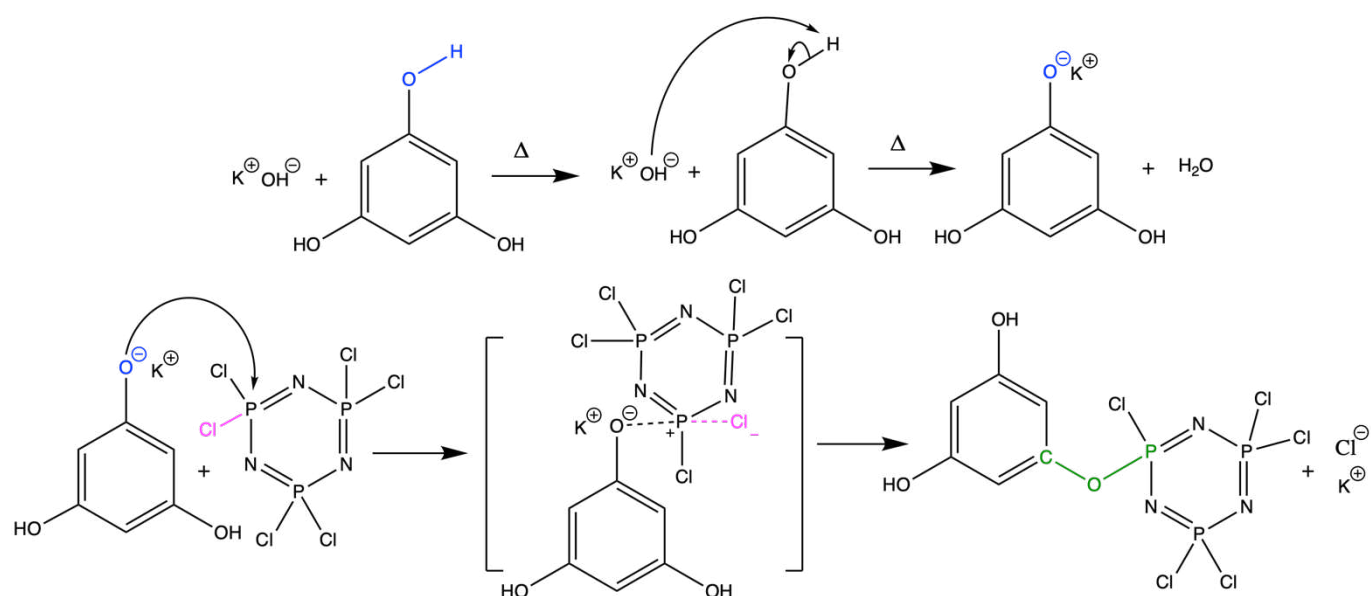


Figure 6.24 Illustration of the reaction between Phg and HCCP with two different steps: conversion of Phg functional groups (top panel) and polymerization with HCCP (bottom panel). As the exact process is not completely known, intermediates and by-products might be missing.

Most of the hydroxyl groups are deprotonated during the first part. However, the possibility of more conversion during the polymerization is not excluded. Furthermore, according to the visual appreciation of the products, there is a difference between bulk and interfacial polymerization concerning the KCl salts. In the bulk polymerization, they are not in the final product and the powder is quite homogeneous (Figure 6.18.B): the KCl is most likely removed during the final washing step. As for the IP, the powders obtained from free-standing films are more inhomogeneous and it could be due to these salts. In the XRF results

(Tables 6.5 and 6.6) it was assumed that *all* of the chlorine detected belong to the network. However, as it will be confirmed in the next studies, salts such as KCl, remain in the product. They were detected on the surface of the “film on support” samples, which means that they are probably also present in the powder coming from the free-standing films. This is supported by the XRF detection of potassium and this presence in the final product means that they are not removed by the final washing step in the IP process.

Finally, if a similar product seems to be obtained whether by bulk or interfacial polymerization *i.e.* a Phg-HCCP polymer, this leads to the formation of a network with an intermediate cross-linking degree. However, after a thermal treatment, this cross-linking degree can be increased and, therefore, this number as well [323]. This means that a complete substitution of the active groups on the HCCP ring might be possible by modifying the IP process. This will be one of the guiding lines of the next chapter.

6) D. Supporting information

The detailed information on the characterization devices is given in Table S6.1.

Table S6.1 Details of the characterization devices used to analyze the IP and bulk samples.

Analysis	Device	Information	Parameters
Ellipsometry measurements	M-2000 Ellipsometer, J.A.Woollam, USA	Ellipsometry spectroscopy	Optical models with 4 layers: substrate – layer #1 interface – layer #2 Ti layer – layer #3 film
FTIR-ATR	PerkinElmer Spectrum Two, USA	Fourier transform infrared spectroscopy in attenuated total reflectance mode	Spectrum averaged over 16 scans with a resolution of 4 cm ⁻¹ over a range of 400 - 4000 cm ⁻¹
SEM-EDS	JSM-6010LA, JEOL, France	Scanning electron microscope with Energy dispersive X-ray spectra	Depends on the picture but EDS at 10 kV with >1000 counts/s
UV Ozone-cleaner	Procleaner Plus, Bioforce nanosciences, USA	Surface cleaning of the silicon wafer with titanium layer on top	20 min (no other parameters)
CN elemental analysis	FLASH 2000 series analyzer, Thermo Scientific, USA	Carbon and Nitrogen elemental composition	
X-Ray Fluorescence (XRF)	S8 Tiger, Bruker, USA	Chlorine, phosphorus, potassium and sulphur elemental composition	Mesurement mode: He, 8 mm, oxides
Thermo Gravimetric Analysis (TGA)	STA 449 F3 Jupiter®, Netzsch, Germany	The thermal stability	Heating a fixed amount of sample (10 mg) on a heating stage under an inert nitrogen atmosphere at a heating rate of 10°C min ⁻¹
Mass spectrometry (MS)	QMS 403 D Aeolos MS, Netzsch, Germany	Coupled with TGA to identify thermally degraded materials	
FE-SEM	JSM-7610F, JEOL, France	Field emission scanning electron microscope	Samples were prepared by immersing in liquid nitrogen for 5 min and carefully fractured to reveal the complete cross-section. Subsequently, all samples were mounted on an FE-SEM holder using double-sided carbon tape.
NMR	Agilent 400-MR DD2, USA	Fourier Transform, Nuclear magnetic resonance spectroscopy	Deuterated DMSO (DMSO-d ₆). ¹ H (400 MHz), ³¹ P (162 MHz)
GPC	Agilent Technologies 1200/1260 Infinity GPC/SEC series, USA	Gel permeation chromatography to determine the molecular mass distribution	Try to reach 0.01g/ml

Figure S6.1 displays the specific setup used for the interfacial polymerization of HCCP with Phg on top of a ceramic substrate.



Figure S6.1 Ceramic interfacial polymerization setup, unassembled on the left and assembled on the right.

Figure S6.2 shows the assembly used for the bulk polymerization of HCCP with Phg. It is built up with a three-neck flask, a refrigerant and the equipment necessary to raise the temperature and create a nitrogen atmosphere (water-free).

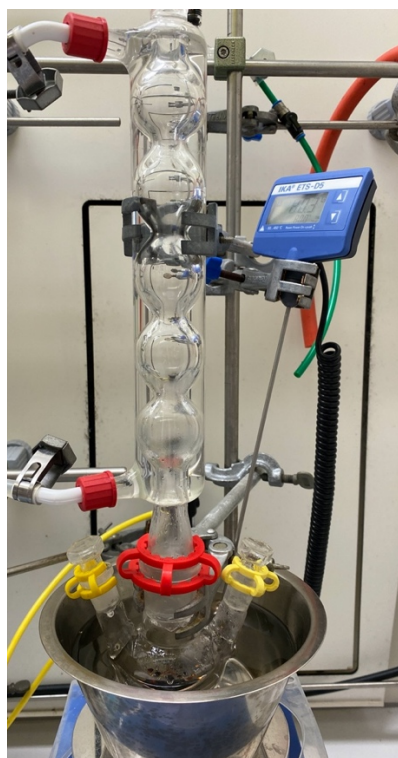


Figure S6.2 Bulk polymerization assembly, for the reaction of HCCP and Phg monomers at 80°C and under an anhydrous atmosphere.

6) E. Acknowledgments

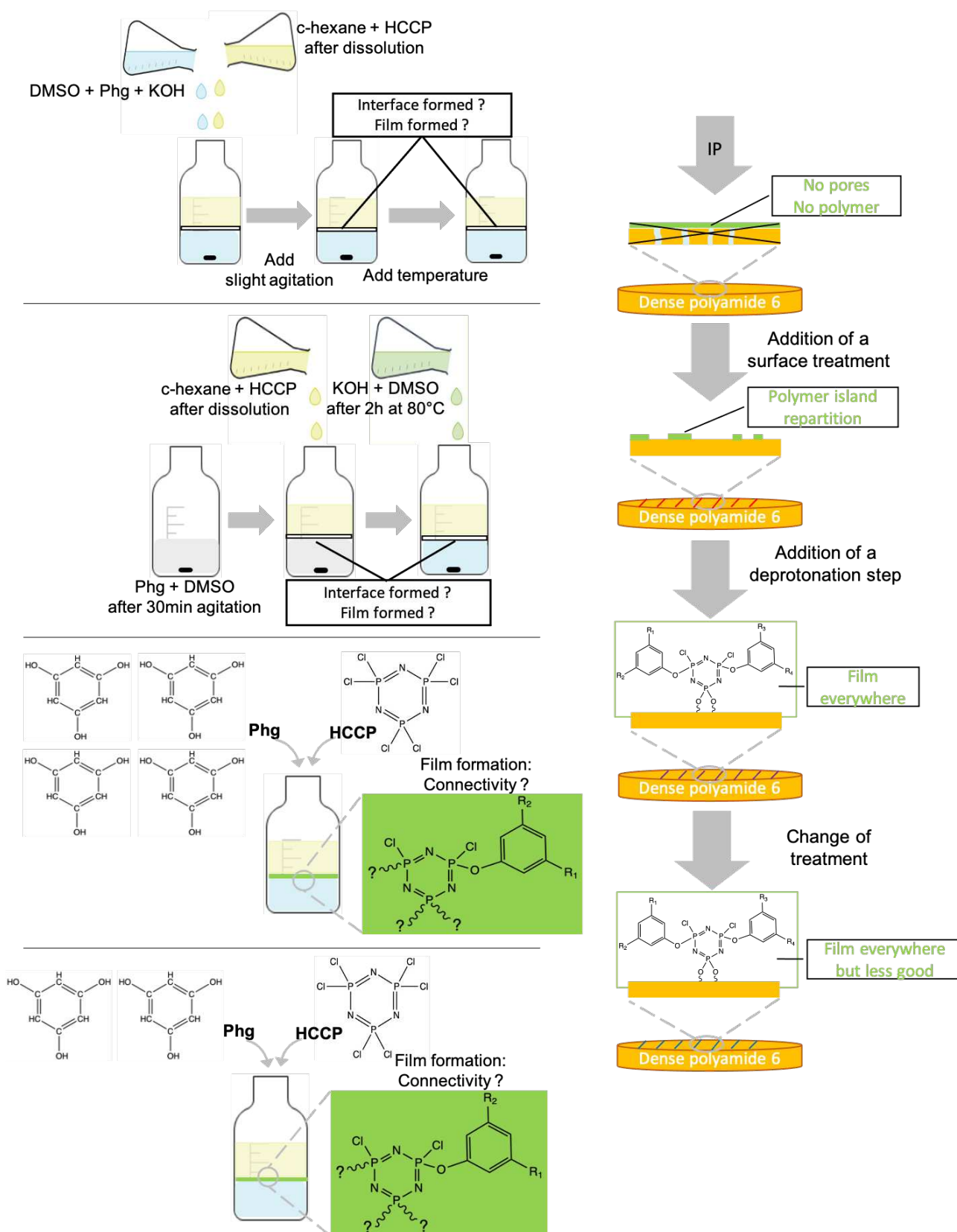
This research forms part of the research programme of Dutch Polymer Institute (DPI), project DINGOES #845. It had access to the resources of the University of Twente, faculty of Science and Technology (TNW), The Netherlands.

6) F. Abbreviations list

➤ C/N	Carbon and Nitrogen (elemental analysis)
➤ DMSO	Dimethyl sulfoxide
➤ EDS	Energy dispersive X-ray spectra
➤ FTIR	Fourier transform infrared
➤ GPC	Gel permeation chromatography
➤ HCCP	Hexachlorocyclotriphosphazene
➤ IP	Interfacial polymerization
➤ KOH	Potassium hydroxide
➤ MS	Mass spectrometer
➤ NMR	Nuclear magnetic resonance
➤ Phg	Phloroglucinol
➤ PiP	Piperazine
➤ SEM	Scanning electron microscope
➤ Si-Alu	Silicon wafer with alumina layer on top
➤ Si-Ti	Silicon wafer with titanium layer on top
➤ TGA	Thermo Gravimetric Analysis
➤ THF	Tetrahydrofuran
➤ TMC	Trimesoyl chloride
➤ UV	Ultra-violet
➤ XRF	X-Ray Fluorescence

Chapter 7 : Experimental - Interfacial
Polymerization on Hydrogen Tank
Substrates

7) A. Graphical abstract



The work in this chapter was mostly carried out at the University of Twente in collaboration with the team of Prof. Nieck Benes ("Films in fluids") and especially Dr. Farzaneh Radmanesh.

The interfacial polymerization IP of hexachlorocyclotriphosphazene HCCP and phloroglucinol Phg was found to synthesize a film with good hydrogen barrier properties (cf. Chapter 6). A layer was formed both as a free-standing film as well as on top of a porous ceramic support. However, the parameters and conditions defined up to now produce a film with an intermediate cross-linking degree. Although this partially branched network already shows a very low permeability coefficient to hydrogen (Figure 6.17), it is assumed, as suggested by molecular modelling (cf. Chapter 5), that a higher cross-linking degree would mean a better barrier with a better morphology. Moreover, if porous substrates are perfect for IP, the H₂ storage tank walls are unfortunately dense. Growing a layer on this kind of support is therefore a daunting challenge in itself. The work described in this Chapter also attempts to provide answers on this specific problem. Indeed, it can widen the IP application field with the assumption that, if a layer can grow on a dense substrate, it can grow on any porous support which is easier to process.

Consequently, the goal of “film improvement” is separated into three parts: (1) produce a layer on top of a dense support (2) the layer should be as continuous and homogeneous as possible and (3) the network polymer should have a higher cross-linking degree. The branching can possibly be increased by post-treatment, *e.g.* by the thermal treatment already reported [323], but attempting to modify the conditions should be a more direct way to achieve this. Therefore, before trying to grow this layer on a dense substrate, the third axis was first investigated on free-standing films. This reduces the large number of parameters, especially those related to the support. Certain parts of the process were also simplified, *e.g.* no drying step (cf. Chapter 2, Figure 1.10 and Chapter 6, Figure 6.13).

7) B. Free-standing films

As already mentioned, the interfacial polymerization of HCCP and Phg is in reality a two-step reaction: a preliminary conversion step of the phenols into phenolates in a superbasic solution of potassium hydroxide (KOH) in dimethyl sulfoxide (DMSO), and the reaction itself by contact with the HCCP dissolved in cyclohexane. Although it is the first step in quite a long process, the deprotonation of hydroxyl groups is essential both for the formation of the layer and for its properties, *e.g.* its cross-linking degree. However, not all the available active groups react and it can be because they are not converted during the first deprotonation step. A greater extent of deprotonation should mean a greater degree of crosslinking. Up to now, the monomer molar ratio in the solutions was 8:1 in favour of phloroglucinol and the quantity of Phg was therefore always higher than that of HCCP in order to promote the substitution of chlorine as much as possible. Two different approaches were attempted to increase the cross-linking degree: change the monomer ratio and change the deprotonation step.

Many other factors could have been changed too, but these two seemed worth investigating in a first place. As a reminder, molecular modelling showed that the number of reacted chlorines *per* HCCP ring increases with the increase of the Phg:HCCP ratio in the mixture so as its barrier property (cf. Chapter 5).

7) B. 1. Testing the changes in the procedure

For both approaches, two samples were made in each case by following the IP process presented in Figure 6.12. For the first pair of samples (Samples S5 and S6), the monomer ratio was changed and for the second pair (Samples S7 and S8), the conversion step process was modified. Almost all the remaining settings were fixed, *e.g.* the solvent viscosity or the monomer diffusivities. Table 7.1 summarizes the important parameters among those that are fixed.

Table 7.1 Main interfacial polymerization conditions for Phg-HCCP free-standing films. The conversion step is conducted at 80°C, and the solution is filtered before use. Concentration units are the weight of the solute in grammes as a percentage of the solvent volume in ml.

Ratio -OH Phg/ -OH KOH	Conversion time	Reaction time	Phg concentration	HCCP concentration	Temperature	Pressure
3.5:1	2 h (for S5 and S6)	10 min (for S5 and S6)	10 w/v% (for S7 and S8)	3.5 w/v% (for S7 and S8)	Ambient	

The conversion and reaction times are specified for samples S5 and S6 because they follow a “traditional” conversion process while S7 and S8 have different values. This is the same for the monomer concentrations, which do not vary for S7 and S8 but are changed for S5 and S6.

In the previous work [260], the nominal molar Phg:HCCP ratio was ~8:1. Therefore, a different Phg:HCCP ratio of ~4:1 was chosen for sample S5 and a ratio of ~2:1 for sample S6. In practice, the concentration of Phg in DMSO was kept fixed due to the presence of KOH with a specific ratio (Table 7.1), and the concentration of HCCP in cyclohexane was increased. This gave the following solutions:

- 20ml of DMSO with 10w/v% of Phg and 0.76g of KOH
- 20ml of c-hexane with 7w/v% (for S5) or 14w/v% (for S6) of HCCP

The same reaction bottle was used for each pair of samples (S5 with S6 and S7 with S8) in order to generate an interface as similar as possible, *i.e.* with the same glass surface. Indeed, the morphology of the reaction bottle itself can influence the formation and properties of the layer (cf. Chapter 2).

For samples S7 and S8, each phase had the same volume of 10 ml with the quantities given in Table 7.1. For S7, a check was made to see if the reaction happens in the absence of KOH, *i.e.* there is no deprotonation step at the start but KOH can be added later if the film does not form. For S8, it was checked whether putting everything at the same time, *i.e.* Phg with KOH in DMSO and then HCCP in c-hexane, but without the heating phase of the deprotonation step, will produce a film, even at a slower rate. Both processes are summarized in Figure 7.1:

S7	S8
<input type="checkbox"/>	<input type="checkbox"/>
<input type="checkbox"/> Make a solution (1) of KOH in DMSO and dissolve during 2h at 80°C	<input type="checkbox"/> Make a solution (4) of Phg and KOH in DMSO
<input type="checkbox"/> Make a solution (2) of Phg in DMSO and dissolve for around 30 min	<input type="checkbox"/> Make a solution (5) of HCCP in c-hexane for a total of 10ml
<input type="checkbox"/> Make a solution (3) of HCCP in c-hexane	<input type="checkbox"/> In a reaction bottle, add the solution 4 and right after the solution 5
<input type="checkbox"/> In a reaction bottle, put the solution 2 and solution 3	<input type="checkbox"/> Check if there is the interface and if a film is instantaneously formed
<input type="checkbox"/> Check if there is the interface and if a film is instantaneously formed	<input type="checkbox"/> Add slight agitation and check regularly for any change
<input type="checkbox"/> If not, add the solution 1	<input type="checkbox"/> Add temperature (to help for the KOH dissolution)
<input type="checkbox"/> Check again if there is the interface and a film	
<input type="checkbox"/> Add slight agitation and check regularly for any change	

Figure 7.1 Free-standing film process for samples S7 and S8, where the influence of the deprotonation step is investigated. Solution 1 for S7 is cooled to room temperature and filtered before use.

7) B. 2. Test results

For both samples S5 and S6, a film was well formed at the interface of the immiscible solutions. After collecting the film from the reaction bottle and washing with acetone, ethanol and water, an inhomogeneous powder with different colours and textures was obtained. Despite following strictly the same protocol between both samples (same volume of solution, same reaction bottle, same times...), there

was visually less powder collected for the second than for the first. This could be due to the product being partly dissolved in one of the solvents of the washing step and accordingly, less is retrieved afterwards. This could indicate that the polymerization degree is smaller for the ratio 2:1 than for 4:1, as the more the polymer is cross-linked, the more resistant it is to solvents. To investigate this further, samples S5 and S6 were first analysed using FTIR to confirm whether the Phg-HCCP polymer was formed or not. Then CN and XRF elemental analyses were performed to study the compositions. All the results are given in Figure 7.2 and in Tables 7.2 and 7.3.

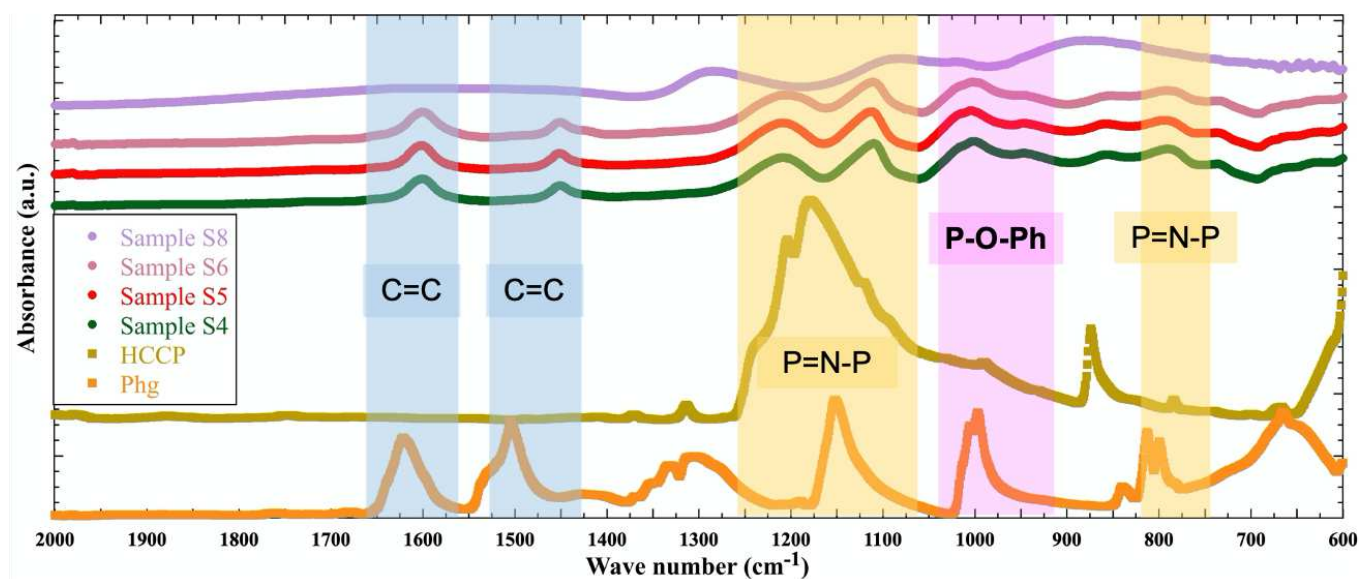


Figure 7.2 FTIR results of samples S5, S6 and S8 as well as sample S4 from Chapter 6 to compare with a known Phg-HCCP polymer obtained by IP.

The spectrum of sample S8 is displayed here but will be analyzed later and the sample S4 (Chapter 6) is used here as a reference for the Phg-HCCP polymer. In the next Tables, this same sample, which is representative of a Phg:HCCP ratio of $\sim 8:1$, is used to compare the different ratios.

Table 7.2 CN analyses for three different free-standing Phg-HCCP films, S4, S5 and S6, with Phg:HCCP molar ratios in the bulk solutions of $\sim 8:1$, $\sim 4:1$ and $\sim 2:1$, respectively. The exact values for the ratio are given in the Table. For S4 and S5, two measurements were made. Estimates of the molar ratio of Phg to HCCP rings in the resulting network polymer and the upper and lower estimates of the number of reacted Cl groups *per* HCCP ring are based on Eqns. 6.1-6.3 (Chapter 6).

Samples	Molar Ratio Phg:HCCP of bulk solutions	Molar Ratio C/N in network polymer	Estimated Molar Ratio Phg/HCCP in network polymer (Eq. 6.1)	No. of reacted Cl <i>per</i> HCCP	
				Lower estimate (Eq. 6.2)	Upper estimate (Eq. 2.3)
S4	7.88 : 1	2.70	1.35	2.70	4.04
		2.75	1.38	2.75	4.13
S5	3.94 : 1	2.67	1.34	2.67	4.01
		2.57	1.28	2.57	3.85
S6	1.97 : 1	3.19	1.59	3.19	4.78

Table 7.3 The molar ratios of P, K and S atoms compared to Cl as obtained from the XRF for S4, S5 and S6, with Phg:HCCP molar ratios in the bulk solutions of $\sim 8:1$, $\sim 4:1$ and $\sim 2:1$, respectively. Two measurements were made in each case. Estimates of the number of reacted Cl groups *per* HCCP ring are based on Eqns. 6.5 and 6.8 (Chapter 6). The presence of potassium and sulphur are probably due to salt formation (KCl) and residual DMSO.

Samples	Molar Ratios			Number of reacted Cl <i>per</i> HCCP (Eq. 6.5)	Number of reacted Cl <i>per</i> HCCP (Eq. 6.8)
	P/Cl	K/Cl	S/Cl		
S4	1.63	0.15	0.14	4.0	4.3
	1.48	0.18	0.15	3.7	4.3
S5	1.33	0.24	0.19	3.7	4.2
	1.31	0.21	0.19	3.5	4.2
S6	1.22	0.29	0.11	3.6	4.3
	1.26	0.29	0.12	4.0	4.3

The CN analysis of sample S5 suggests a same molar ratio of Phg to HCCP rings in the network of the order of 4:3 (or 1.33:1) for than S4, regardless of the monomer ratio in the bulk solutions. On the other hand, sample S6 has an estimated molar ratio of Phg to HCCP in the network, which is somewhat higher at 1.59. It is difficult to determine what the contributions of the residual solvent molecules (DMSO and cyclohexane) and the unreacted monomers of Phg and HCCP are on these estimations of the polymer stoichiometry. Indeed, the elemental CN analysis cannot distinguish between atoms in the polymer and those in the solvent or monomer molecules, and the XRF analysis clearly shows the presence of sulphur, *i.e.* DMSO. All the bulk solution Phg:HCCP ratios tested correspond to an excess of Phg compared to the ratio found in the actual polymer films. But there are probably other factors that influence the *local* concentrations of the monomers at the interface between the two immiscible solvents (cf. Chapter 2).

The estimations from the XRF results for the number of reacted Cl *per* HCCP uncorrected for the presence of KCl (using Eq. 6.5), show a slightly decreasing trend when the Phg:HCCP ratio in the bulk solutions is diminished. However, estimations corrected for the presence of Cl⁻ ions (Eq. 6.8) show an almost constant number of just over four (out of six) reacted Cl atoms *per* HCCP ring. Upper estimates from the CN analyses (Eq. 6.3) are also close to four for samples S4 and S5 but increase to nearly 4.8 for S6, which has the highest estimated Phg/HCCP ratio in the polymer. These results are difficult to reconcile with the experimental observation of a lower yield for S6. However, the manipulation to collect the free-standing film has a quite a large margin of error so that the difference in quantity of powder could simply be due to the handling. Differences are not due to the film being dissolved in the rinsing solvents. As for the ratio of rings, there is an absence of a trend in the number of reacted Cl, which basically gives in all cases a film with intermediate cross-linking degree.

It does appear that the Phg:HCCP ratio of the bulk solution has much less of an impact than one would expect. Whether this is due to the *local* concentrations at the interface being different from those in the bulk or the reaction mechanism having more of an influence remains to be seen. To try to investigate this uncertainty, it was studied by molecular modelling what happens in terms of interconnectivity when the *local* ratio is actually 8:1, 4:1 or 2:1 along with some others not tested experimentally. It showed that the Phg:HCCP rings ratio in the network as well as the number of reacted Cl does increase with the initial local ratio (cf. Chapter 5). However, in the simulations, there are no other factors than the initial local ratio, and it is easier for it to be linked directly to the cross-linking degree.

This conclusion about the absence of a direct impact of the bulk monomer concentration in the solutions on the Phg-HCCP ratio in the polymer or the number of reacted Cl is not so surprising, because it is mostly the interdependence of IP factors which is important (cf. Chapter 2). Therefore, changing the

relative molar ratio of the initial solutions does not seem to be the best way to increase the degree of cross-linking of the network polymer film.

For samples S7 and S8, the modifications of the conversion step led to no (or almost no) film formed. Therefore, elemental analyses or other characterization techniques were not possible. However, some observations were still noted as the deprotonation of phloroglucinol gives rise to certain colour changes in the solution as the reaction progresses (Chapter 6).

For sample S7, both solutions 1 and 2, *i.e.* KOH in DMSO and Phg in DMSO (Figure 7.1), are coloured but not as much as the classic solution of Phg after the deprotonation step (cf. Chapter 6, Figure 6.23). Under the same conditions, DMSO alone shows no colour change. When the HCCP solution is added to solution 2, an interface is well present but no film is instantaneously formed. Therefore, solution 1 (DMSO/KOH) is added and it passes through the less dense c-hexane/HCCP phase on top to mix with the DMSO/Phg solution below. There is no immediate formation of a layer at the DMSO/c-hexane interface either. However, the colour of the phase containing Phg/KOH/DMSO becomes pinkish and after around 30 min, it gets shadier while the HCCP solution becomes cloudy. There is still no film formed at the interface. After 4 or 5 h of slight agitation, the colour of the phloroglucinol solution becomes more and more pink and the upper phase gradually clears. Finally, after a night of contacting and with agitation, no obvious layer forms at the interface, the colour stabilises and the HCCP solution is ultimately limpid. All the different colours can be seen in Figure 7.3.

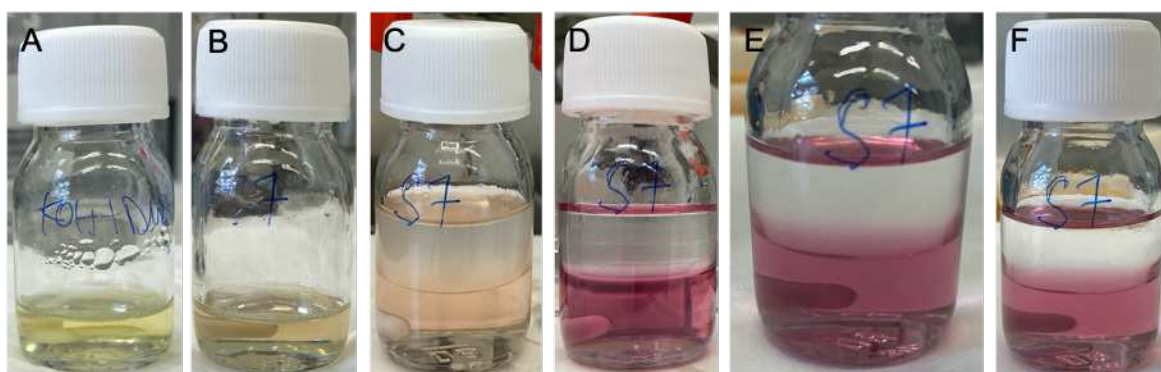


Figure 7.3 Changes in colour of the different solutions and of the IP reaction system for sample S7 with KOH in DMSO after 2 h at 80°C (A), Phg in DMSO (B), HCCP/c-hexane on top and newly-mixed Phg/KOH/DMSO below after about 30 min (C), 4 h (D), 5 h (E) and overnight (F).

It can be concluded with sample S7 that no reaction occurs:

- Without the presence of KOH.
- Without the full deprotonation step at 80°C.
- When KOH is added separately but already dissolved in DMSO.
- When an agitation is added to a system with Phg without the full deprotonation step at 80°C and KOH already dissolved.

According to the changes in colour, there are reactions but there is no clear film formation.

For sample S8, solution 4, *i.e.* Phg/KOH in DMSO, acquires a colour after 20 min of agitation, which looks like the usual solution before the conversion step (Figure 6.23.A). After the addition of HCCP/c-hexane, an interface is created and a very thin film seems to be formed. However, if after 30 min of slight agitation, the colour changes into something similar to a classic Phg/KOH/DMSO solution, the film seems to disappear and as for sample S7, the c-hexane phase becomes cloudy. The temperature was then increased to 30°C for around 1 h without any change apart from the shade of the colour in the DMSO phase. It was further increased to 45°C for around 2 h and if the top solution became clear, the Phg phase continued its colour change towards the characteristic orange of the conversion step but there was still no film being formed. Finally, everything was heated up to 60°C and after 1 h 20, no real changes could be noticed except that the HCCP solution was now clear again so, as for sample S7, the reaction system was left with these conditions overnight. This time, the interface collapsed and only one viscous solution was left in the reaction bottle. If the colour is brown like the Phg/KOH/DMSO solution after deprotonation step (Figure 6.23.B) and the aspect is like the product of bulk polymerization with these two monomers before washing (Figure 6.18.A), FTIR reveals that what is obtained is not a Phg-HCCP film (Figure 7.2), since it does not correspond at all to sample S4. If the disappearance of the interface could be explained by a heating problem during the night, the absence of a film seems to indicate that without a proper deprotonation step, *i.e.* a mixture of Phg and KOH in DMSO prepared separately and heated at 80°C for a certain time, no reaction occurs even when the temperature is increased. Figure 7.4 displays the different aspects of sample S8.

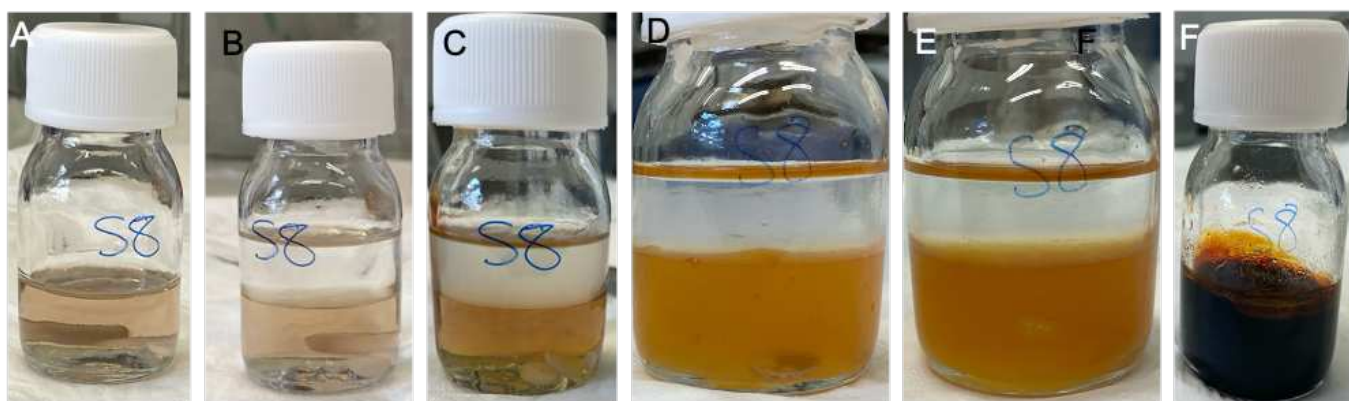


Figure 7.4 Aspect changes of sample S8 when Phg with KOH are dissolved in DMSO for around 20min (A) and then contacted with HCCP dissolved in *c*-hexane (B), after 30 min of agitation at ambient temperature (C), after 1 h at 30°C and 2 h at 45°C (D), after 1 h at 30°C, 2 h at 45°C and 1 h 20 at 60°C (E) or after a night at 60°C (F).

Sample S8 thus confirms the importance of the separate preliminary deprotonation of Phg by KOH in DMSO. As no film was formed, nothing can be concluded about the effect of a change in the conversion step process on the cross-linking degree of the network. Another way to modify the degree of deprotonation of Phg would have been to change the concentration of KOH. However, this had already been investigated in the previous work [260], and the results had showed that increasing the quantity of KOH added does increase the concentration of phenolate anions (mono, di or tri), and that a maximum of 45-50% of all the hydroxyl groups are converted [260]. Nevertheless, whatever the concentration of KOH, the presence of anions means that converting all the hydroxyl groups is not controlled [260, 327] which means that converting all the hydroxyl groups is not controlled. This could explain why the interconnectivity results are different with the same process (cf. Chapter 6, Tables 6.5 and 6.6) and why the results are quite similar when solutions with different ratio of monomers are involved (Tables 7.2 and 7.3).

To conclude, changing the deprotonation step process, KOH concentration or monomer ratios does not seem to increase the number of reacted Cl, at least experimentally. However, since interfacial polymerization is a multiple-parameter reaction, many other factors could be changed for future work. If in the next Section, the aim is mainly to grow a layer on top of a dense organic substrate, the intent to increase the cross-linking degree being is still present as a secondary purpose.



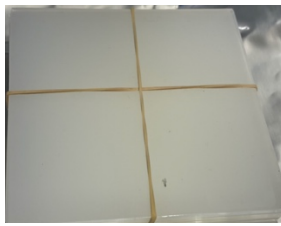

7) C. Hydrogen tank substrates

Two of the partner companies associated to the project, DSM and Teijin Aramid, have generously provided supports similar to the materials used in the liners of hydrogen storage tanks. Before trying to

grow the Phg-HCCP layer on top of these supports, it is important to know more about the substrate and its properties as they are part of the IP parameters that can affect the film properties (cf. Chapter 2, Figure 2.10).

Each company provided two different supports and their basic characteristics are given in Table 7.4, along with an assessment about the feasibility of growing a layer on them using IP.

Table 7.4 Basic characteristics and observations of the supports provided by Teijin and DSM. The materials are similar to those used for the inner liners of hydrogen tanks and, as such, can be considered for as potential substrates for the IP of Phg with HCCP.

Teijin aramid			
	Polyester "tape" (PE tape)		Polyester "band" (PE band)
	<ul style="list-style-type: none"> ➤ Thin ~0.11 mm ➤ Seems non-porous ➤ Surface not smooth ➤ Ductile 		<ul style="list-style-type: none"> ➤ Thick ~1.09 mm ➤ "Open" structure ➤ Rough surface ➤ Soft and flexible
	Surface not flat and smooth enough to grow the layer		Surface too open to grow the layer with solution absorption
DSM			
	Polyamide 6 (F136)		Polyamide 6 (FLE40)
	<ul style="list-style-type: none"> ➤ Thick ~2 mm ➤ Seems non-porous ➤ Surface non-homogeneous + fragile ➤ Rigid 		<ul style="list-style-type: none"> ➤ Thick ~2 mm ➤ Seems non-porous ➤ Surface more homogeneous + fragile ➤ Rigid
	Surface inhomogeneous but maybe possible to grow the layer		Surface homogeneous enough to grow the layer

Information concerning the support is not only important for the film properties but also for the process itself. Indeed, the experimental conditions for this kind of IP are quite severe: high pH, high

temperature, harsh solvent, etc. which means that the substrate has to be resistant enough. Along the process, the exposures to DMSO and to DMSO+KOH+80°C are the hardest conditions that the substrate can face. Therefore, a preliminary DMSO resistance test was made to check the behaviour of the supports. A piece of each support was first cleaned with ethanol and then dried with a nitrogen gun. It was weighed on a precision scale before being exposed to different conditions (DMSO + ambient temperature; DMSO + 80°C; and DMSO + KOH + 80°C) during different times (30 min and 1 h). Afterwards, the samples were dried and weighed again for any difference in weight, which could identify a degradation by the treatments (= mass loss) or the absorption of DMSO (= mass gain).

These tests showed that no mass loss occurred and there were no obvious modifications of the materials following exposition. The substrates seem to be resistant to DMSO, even under harsh conditions. However, several remarks could be made:

- The “PE tape” is not damaged by DMSO or ethanol but it absorbs some of the solvents.
- The “PE band” is also resistant to the solvents but it definitely absorbs them on a larger scale.
- The two polyamides are resistant to DMSO but their surfaces seem to be damaged by ethanol. There was no evidence of solvent absorption.

These simple tests highlighted problems with some of the supports. Due to a limited amount of time, a more in-depth investigation of all substrates could not be done, but a selection had to be made. Following the solvent tests and a first try of IP on the supports, it was decided to not go further with both polyester substrates due to their solvent absorption and relatively rough surfaces. Further work thus concentrated on the DSM-provided polyamide supports.

7) C. 1. Polyamide supports and first tests

Additional properties were characterized for the PA substrates and these are presented in Table 7.5 and Figures 7.5 and S7.1. If PA6 F136 is “only” similar to the materials used in hydrogen tanks, PA6 FLE40 is actually already used in them.

Table 7.5 Properties of the DSM-provided PA substrates to be used as supports for the IP of Phg and HCCP.

	<i>PA6 F136</i>	<i>PA6 FLE40</i>
<i>Density</i>	1.14 g/cm ³	1.06 g/cm ³
<i>Water contact angle</i>	72.9 ± 0.2 °	103.5 ± 1.7 °
<i>Hardness</i>	72 ± 1 Shore D	67 ± 1 Shore D

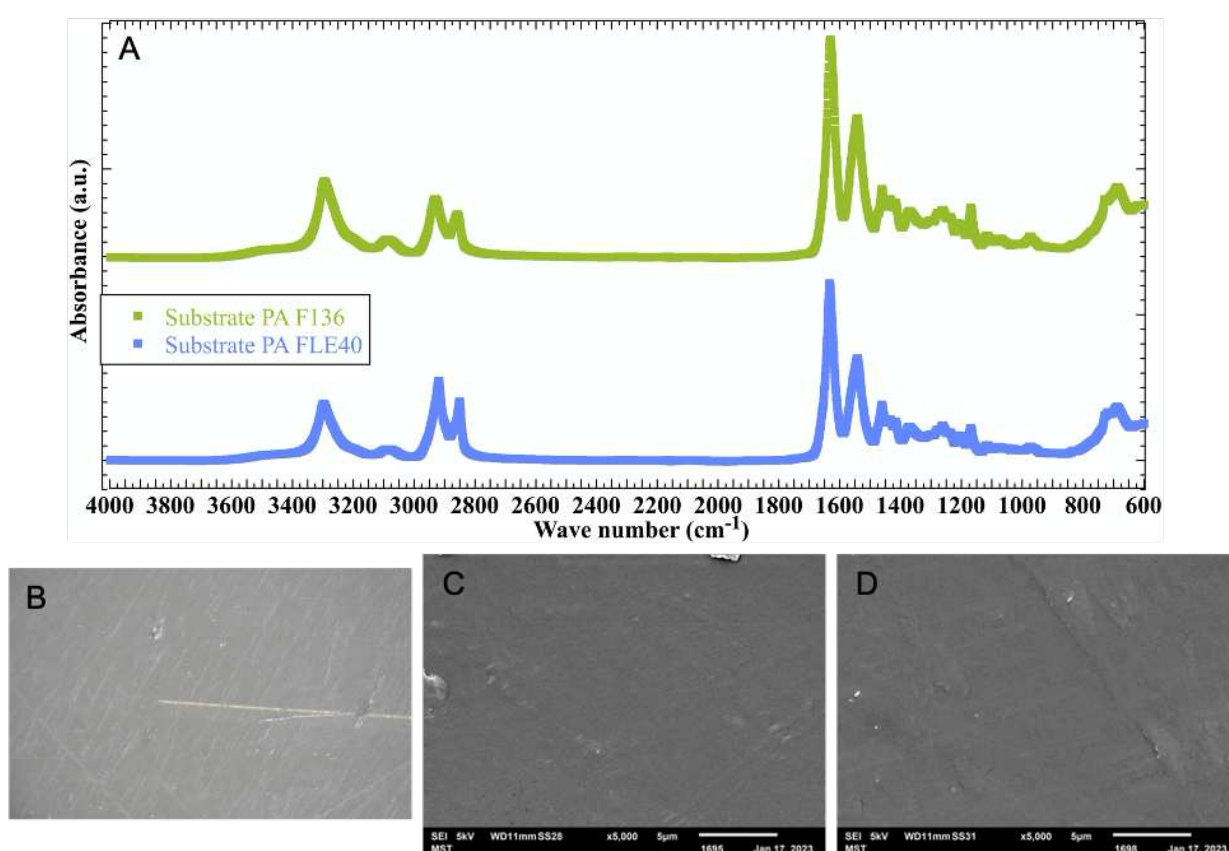


Figure 7.5 FTIR spectra of PA6 substrates F136 and FLE40 (A), optical microscopy for F136 (B) and SEM for F136 (C) and FLE40 (D). The optical view of the surface is similar for both supports.

The pictures obtained by microscopy, both optical or SEM, show that there are defects on the surfaces with scratches and holes. However, they also confirm that the substrate is dense, *i.e.* no pores.

7) C. 1. 1. IP on supports using previous protocol

Unlike the ceramic substrates used so far (Chapter 6), the supports provided by the companies are non-porous. A reminder of the Phg-HCCP process for porous supports is provided in Figure 7.6. Even if the IP principle is the same, it is expected that this protocol might not work as well for non-porous substrates.

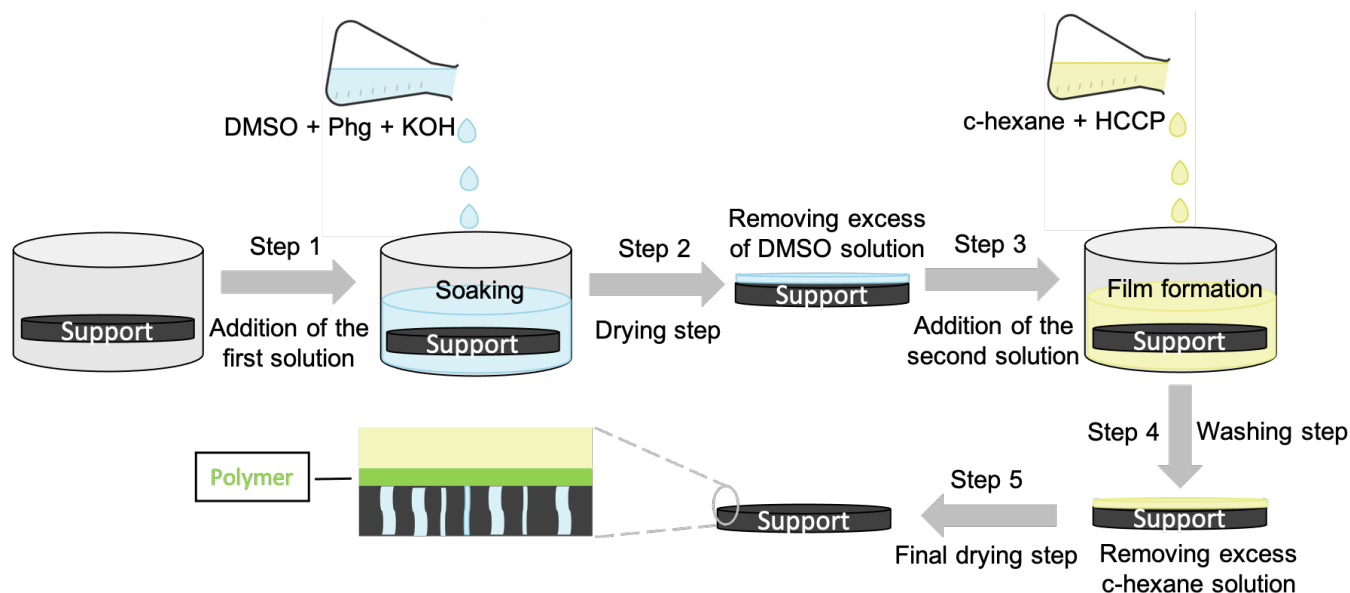


Figure 7.6 The interfacial polymerization process for a Phg-HCCP film on a porous substrate.

The parameters and conditions defined in Table 7.6 were chosen for the first tests on the PA6 supports. They were consistent with the work carried out before (Table 7.1).

Table 7.6 IP conditions for a Phg-HCCP film on top of a polyamide 6 substrate.

Ratio -OH Phg/ -OH KOH	Conversion time	Soaking time	Reaction time	Drying step	Temperature	Pressure
3.5:1	2 h	15 or 25 min	10 or 20 min	Twice rubber roller	Ambient or 80°C*	Ambient

Several explanations are in order to better understand Table 7.6:

- The ratio of hydroxyl groups is used to set the KOH concentration according to the calculations given in Table S7.1 in the SI.
- Up to now, the conversion time varied between 2 and 2.5 h due to the limited solubility of KOH in DMSO. It was set to 2 h because of the use of a KOH powder rather than pellets. It was assumed that a powder will be easier to dissolve.
- The soaking time is longer than with the ceramic substrate (10 min), because the pore sizes are smaller. With a dense support, it obviously has to be increased [131].
- The reaction time is also increased for the same reason.
- The drying step is the same as for the ceramic substrate.
- For the temperature, two conditions are defined as follows: “ambient” means that the Phg/KOH/DMSO solution at 80°C is cooled until at ambient T, filtered and then used on the support at room temperature. “80°C” means that the solution is kept at its previous temperature, the support is heated to 80°C and the soaking takes place at 80°C. However, the reaction with HCCP in cyclohexane is carried out at ambient T.

As previously, the solutions were prepared with the concentration units in weight of solute (g) as a percentage of the volume (ml), and still with 10w/v% of Phg in DMSO and 3.5w/v% of HCCP in cyclohexane.

7) C. 1. 2. First tests

One sample (out of the six made) is presented in Figure 7.7. It is referred to as “S10-10” because it is the tenth sample of IP made on support and the same nomenclature will be used afterwards. The samples confirm the suspicion that the IP process used until now is not suitable for the PA6 dense substrates. Apart from practical issues, such as poor cleaning of the support, poor soaking because of a flotation problem or not enough solution, some information can be extracted, even if no proper films were formed:

- After the drying step (Step 2, Figure 7.6), there was visually nothing left of the first solution on the surface and just a little on the edges.
- After the reaction (Step 3), a product formed on the surface but it was inhomogeneous and not continuous (Figure 7.7.A).
- After the final rinsing and drying (Steps 4 and 5), almost nothing was left on the surface. Some product remained on the edges but in negligible amounts (Figure 7.7.B).

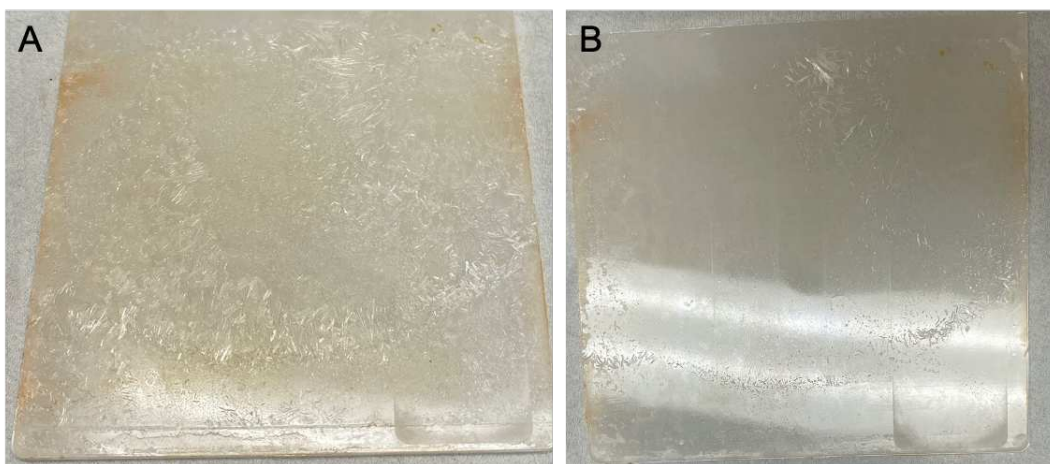


Figure 7.7 Sample S10-10 after the IP of HCCP and Phg in cyclohexane and DMSO on top of a PA6 F136 substrate. On the left, before the final washing step (A) and on the right, after the washing and drying steps (B).

The aspect of sample S10-10 is different before and after the final washing and drying steps of the process. Similar results were found for the other samples of this first set. If the orange parts on the edges could be the film, the crystal-looking parts are most likely unreacted HCCP monomers. This was confirmed by FTIR, which showed that the spectrum obtained is characteristic of pure HCCP (Figure S7.2 in SI).

The fact that there is almost nothing left after the drying step associated to the presence of unreacted HCCP suggest that, when HCCP was added, there were probably not many Phg monomers left on the surface to react with. The Phg solution was entirely removed instead of just the excess, except on the edges. According to the FTIR results in Figure 7.8, the product on the edges could indeed be a Phg-HCCP film. Most of the peaks correspond to the PA6 substrate (Figure 7.5) but the small double peaks between 1025 to 975 cm^{-1} associated to P-O-C bonds indicate a reaction between the monomers [313].

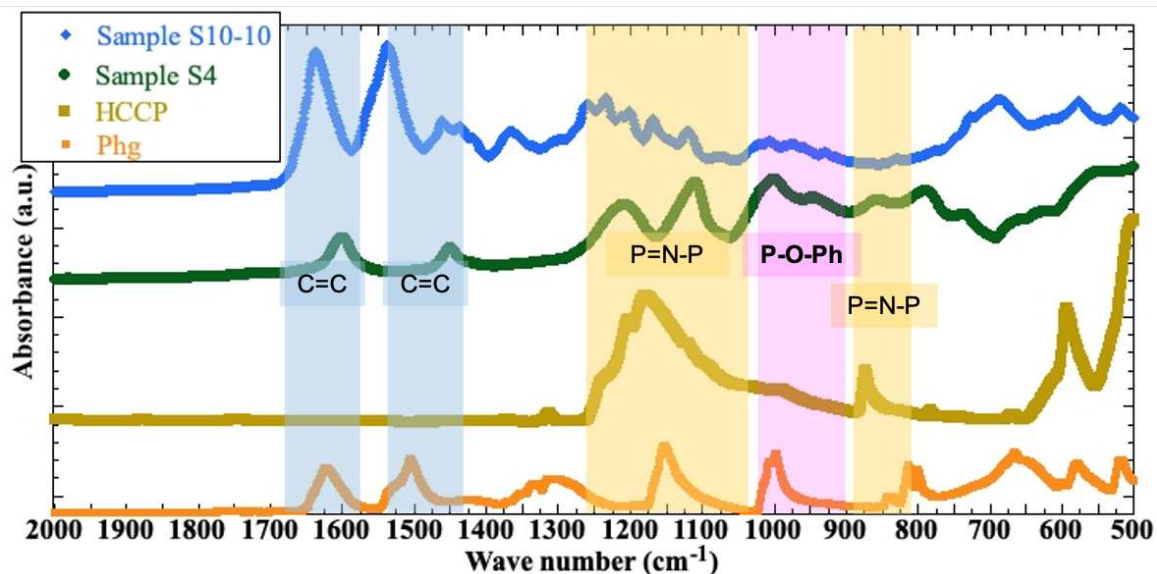


Figure 7.8 FTIR spectra for the edges (orange part) of sample S10-10 and for the pure monomers. Sample S4 shows a Phg-HCCP film spectrum.

Therefore, growing a product on the support seems possible but, as expected, the process has to be changed. Unlike for a porous support, the soaking is the most difficult part for a dense substrate. The absence of pores means no reservoirs and, as such, it is difficult to keep enough of the Phg solution on the surface during the drying step (Figure 6.4) In conclusion, it is definitely necessary to attach the first monomers, *i.e.* up to now Phg, to the surface. Consequently, it was decided to add a surface treatment of the support before soaking.

7) C. 2. Addition of a surface treatment

To coat any support with paint, glue, varnish or any other coating, the substrate must be prepared in order to obtain a good adhesion. This ensures that the coating is well-attached to the surface, with a good thickness and the required properties. The preparation requires a surface tension of the support, which is superior to the surface tension of the coating. Surface tension is a force which exists at the level of any interface between two different phases (liquid; solid; gas) and which causes the liquid on the solid, for example, to spread more or less well [328]. Most of the time, solid substrates have a low surface tension compared to liquids. Typically, it varies between 30 mN/m to 40 mN/m for PA compared to 73 mN/m for water [329, 330]. Therefore, the role of the surface treatment is to increase the surface tension of the substrate, so as to allow a good coating.

Two main categories of surface treatments exist: chemical and mechanical. The chemical treatments affect the surface by breaking bonds or introducing functions which allow new bonding, whereas the

mechanical treatments modify the surface by creating asperities which can then be filled by the coating. Since the response of the PA supports to such treatments was unknown, it was decided to try one in each category. A UV/Ozone cleaner was first used for the chemical treatment (Table S6.1) and a common polishing machine for the mechanical treatment (Tegramin 30, details in Table S7.1). These treatments were carried out on the supports alone, before trying an incorporation into the IP process.

7) C. 2. 1. Mechanical treatment

The first aim of a mechanical treatment is to improve the quality of the surface by removing scratches and other defects from the substrate. The second aim is to obtain the most homogeneous and smoothest surface possible, while still being able to grip the Phg solution applied. However, the surface cannot be too rough either. The polishing machine offers a number of parameters that can be tuned, such as the grit size (the higher the grade, the less abrasive the paper), the force applied, the rotation speed, the time and the use of water to lubricate and clean the residues during the process. The surface conditions after polishing were checked with a stereo-microscope. Different tests were conducted according to Table 7.7 and, from the start, it became clear that both polyamide F136 and FLE40 supports do not behave in the same way.

Table 7.7 Parameters of the polishing machine tested to improve mechanically the surface of PA6 substrates for the IP of HCCP and Phg. The sample used in tests 4 and 5 is the same.

Test number	Support	Grit size	Force / N	Disc rotation speed / rpm	Sample holder rotation speed / rpm	Direction	Time / sec	Water
1	F136	320	100	150	150	Same direction	60	Yes
2	F136	320	150	150	150		60	Yes
3	F136	800	50	150	150		15	Yes
4	FLE40	800	50	150	150		5	Yes
5	FLE40	800	50	150	150	Counter-rotation	5	Yes
6	FLE40	1200	50	150	150		5	Yes
7	FLE40	2000	65	150	150		5	Yes
8	FLE40	1200	65	150	150		5	Yes

Indeed, although the parameters were quite similar for both supports, Figure 7.9 shows that their surfaces are not the same after polishing.



Figure 7.9 Stereo-microscopy for three different samples of the PA6 substrates after polishing according to Table 7.7 From left to right, Test 3 for F136 (A), Test 5 for FLE40 (B) and Test 7 for FLE40 (C).

These different aspects could be due to the different hardnesses (Table 7.5). Indeed, FLE40 is less hard than F136 and this seems to improve the quality of its surface, *i.e.* it is less rough and more homogeneous. The mechanical treatment was thus considered more satisfactory for the FLE40 than for the F136 substrate.

7) C. 2. 2. Chemical treatment

In general, the UV/Ozone cleaner device is used to remove organic contaminants from a substrate [331]. For example, it was used in the previous chapter to pre-clean the silicon-alumina support. However, the silicon wafer is not organic so the effect of its exposure is just the removal of any organic matter from its surface. On the other hand, for an organic substrate such as a PA, this treatment can also modify the surface chemistry. Its use as a treatment to improve the wettability of a surface is not new [332]. Hydroxide radicals are formed during the process and they can react with bonds on the surface of substrates. This results in the formation of hydroxide groups which in turn affect the affinity with water [333, 334]. This difference in hydrophobicity, which is also linked to the surface tension, can be checked with the water contact angle (WCA) measurement. This is the best way to monitor the surface modification as any change in the WCA implies that the surface has been modified. Moreover, if the WCA decreases, it means that the wettability and the surface tension are increased. This is the expected effect of such a surface treatment [335].

Only the exposure time can be changed on the device available, consequently it was varied between 10 to 30 min. The WCA was checked before exposure (Table 7.5) and after 10, 15 and 30 min for FLE40

and after 10 and 25 min for F136. Averages of the WCA were taken over six measurements for each support. Figure 7.10 gives an example of the water droplet and contact angle measurement on both substrates.

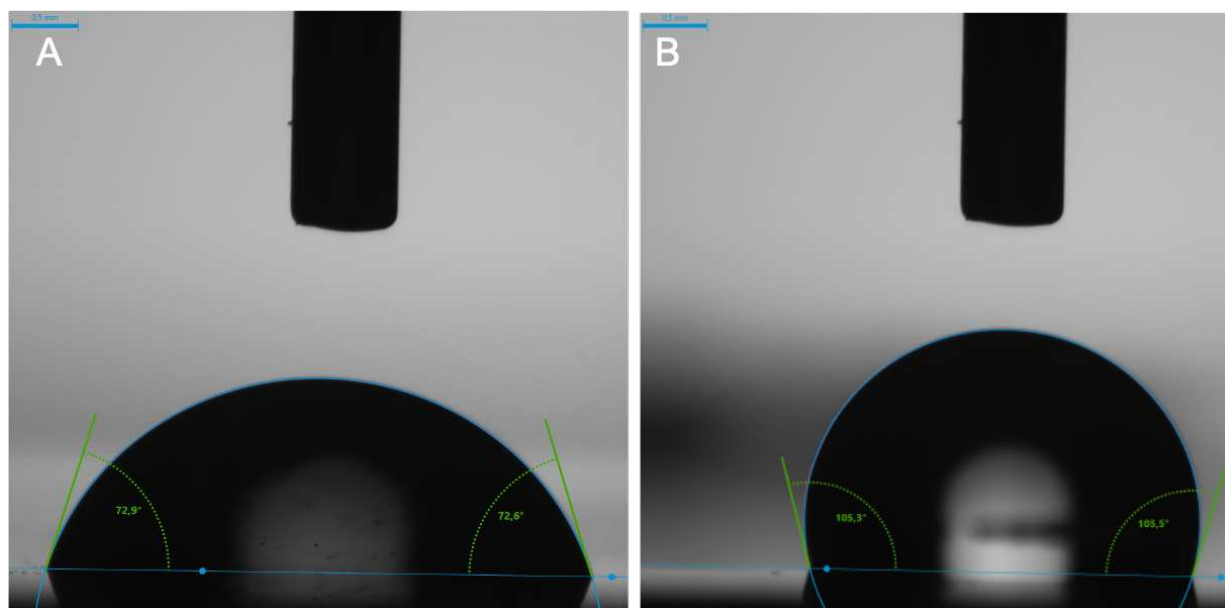


Figure 7.10 A water droplet and its corresponding contact angle on the F136 substrate for the lowest angle obtained (A) and on the FLE40 for the largest obtained (B), after different times of exposure to a UV/Ozone cleaner device.

For the PA6 FLE40 substrate (Figure 7.10.B), the average WCA changes with the different exposure times. The largest change, from 98.1° to 50.5° , occurred after only 10 min. Extending the exposure time caused the WCA to start rising again to 54.6° after 15 min and 86.1° after 30 min. The angles are still lower than the before-exposure reference value of 103.5° (Table 7.5), but they are larger than the optimum at 10 min. This tendency for the WCA to increase again for exposure times beyond the optimum indicates that too much exposure decreases the surface tension instead of increasing it.

For the PA6 F136 substrate, the average starting WCA of 72.9° is already lower than for FLE40 and it falls to 31.1° after 10 min of exposure. Subsequently, the angle continues to decrease with the exposure time and, after 25 min, it is difficult to measure it as the water completely spreads out ($\approx 9^\circ$).

To conclude for both substrates, an exposure of 10 min to the UV/Ozone cleaner seems to increase their wettability and their surface tension. However, only the F136 continues to respond favourably beyond 10 minutes of exposure. The chemical treatment was thus considered more satisfactory for the F136 than for the FLE40. However, whereas both types of treatments will be considered in the first steps, the chemical treatment will mostly be used afterwards.

7) C. 2. 3. First tests with surface treatment

Following the tests of the selected surface treatments on the substrates, a first set of IP samples on surface-treated PA6 were prepared with the parameters provided in Table 7.8. The conditions not mentioned are the same than for the previous samples.

Table 7.8 IP conditions for the first samples of Phg-HCCP films prepared on PA6 substrates with a surface pre-treatment is included in the protocol. All the substrates are cleaned with isopropanol and dried with nitrogen before use. The temperature is 80°C for the soaking and ambient for the reaction, as before.

Samples names	Ratio -OH Phg/ -OH KOH	Reaction time (min)	Conversion time (h)	Time of soaking (min)	Temperature	Drying step	Surface treatment
S13-13 (FLE40)	3.5:1	20	2	15	80°C*	Rubber roller ×2	10 min in the UV/Ozone cleaner
S14-14 (F136)						Rubber roller ×1	15 min in the UV/Ozone cleaner
S15-15 (FLE40)						Rubber roller ×2	Polishing 10 sec at 65 N and grit size of 2000 (test 7, Table 7.7)

As for the first trials on PA6 substrates, no complete layer was formed on the three samples tested. Indeed, after the drying step, there was little left on the surfaces, except for the presence of unreacted HCCP. At the end, there were only traces on the edges for S13-13 (Figure S7.3.A), on the side for S14-14 (Figure S7.3.B) and different small spots for S15-15 (Figure S7.3.C). Even if the FTIR indicated that the small traces/spots on each sample were probably Phg-HCCP films (Figure S7.3), this is obviously not what is expected. The fact that the drying step removes most of the solution from the substrate shows that the rubber roller is inadapted for a dense support without reservoirs. Indeed, this is probably one of the most critical steps of the process.

On the other hand, traces of films can be formed on the small parts where the Phg/DMSO solution remains, which means that it can be attached sufficiently well to the surface to resist up to the end of the process. Since unreacted HCCP also remains after the reaction, the Phg monomers are either not

sufficiently present on the support after the drying step or there are not enough active groups to react both with the activated substrate and with the limiting HCCP. Indeed, the UV/Ozone treatment allows bonds to be formed between the support and the “coating” which, here, corresponds to the Phg/DMSO solution. As Phg is partially deprotonated by KOH during the conversion step, these bonds are most likely due to the reactive deprotonated hydroxyl groups, *i.e.* they are the same than those involved in the formation of O-P bridges. Therefore, if there is a lack of active groups, this is due to a too low Phg conversion rate.

To try to overcome these problems which may come from a poor soaking, an inadapted drying step or not enough Phg deprotonation, several changes were made to the IP parameters (Table 7.9) and the surface treatment, before being applied to a second set of samples.

Table 7.9 Changes in IP conditions for a new batch of Phg-HCCP films prepared on PA6 substrates with a surface pre-treatment. All the samples are cleaned with isopropanol and dried with nitrogen before use.

S16-16 (F136)	S17-17 (FLE40)	S18-18 (FLE40)	S19-19 (F136)
<ul style="list-style-type: none"> ➤ Soaking and reaction times increase, respectively, to 25 and 30 min. ➤ Only ×1 rubber roller during the drying step, except for S19-19 where this step was left out. ➤ KOH concentration increases (-OH ratio from 3.5 to 2.2) and a reversion to using KOH in pellet form. 			
<ul style="list-style-type: none"> ➤ Soaking at ambient T ➤ Reaction at 70°C 	<ul style="list-style-type: none"> ➤ Soaking at ambient T ➤ Reaction at 70°C 	<ul style="list-style-type: none"> ➤ Soaking at 80°C ➤ Reaction at ambient T 	<ul style="list-style-type: none"> ➤ Soaking at 80°C ➤ Reaction at ambient T

For the surface treatment, sample S17-17 was polished with a grit size of 1200 and a force of 50 N. All the other samples were chemically modified but with a new low-pressure O₂ plasma cleaner (Femto model 1A) instead of the UV/Ozone cleaner. A plasma treatment is already known to be able to modify polymers [336-339], with an action is quite similar to the UV treatment. The advantage of the plasma approach is that more settings can be changed: time, power, gas flow, etc. After preliminary tests, the chosen parameters were 5 min at 70 W with the oxygen pressure always kept between 0.2 and 0.5 bar.

The results of the second batch of samples were still not what was expected, since no continuous layers were formed over the entire surfaces. However, there were some improvements:

- On samples S16-16 and S17-17, there are larger areas with a film according to the FTIR spectra (Figure 7.11).

- Sample S18-18 is more similar to the previous FLE40 sample with a chemical treatment (S13-13, Table 7.8), *i.e.* almost nothing is formed.
- Sample S19-19 without a drying step shows that, when the excess of the first solution is not removed, a film is formed when the second solution is added. However, the film is not attached to the surface of the substrate, *i.e.* it is more like a free-standing film.

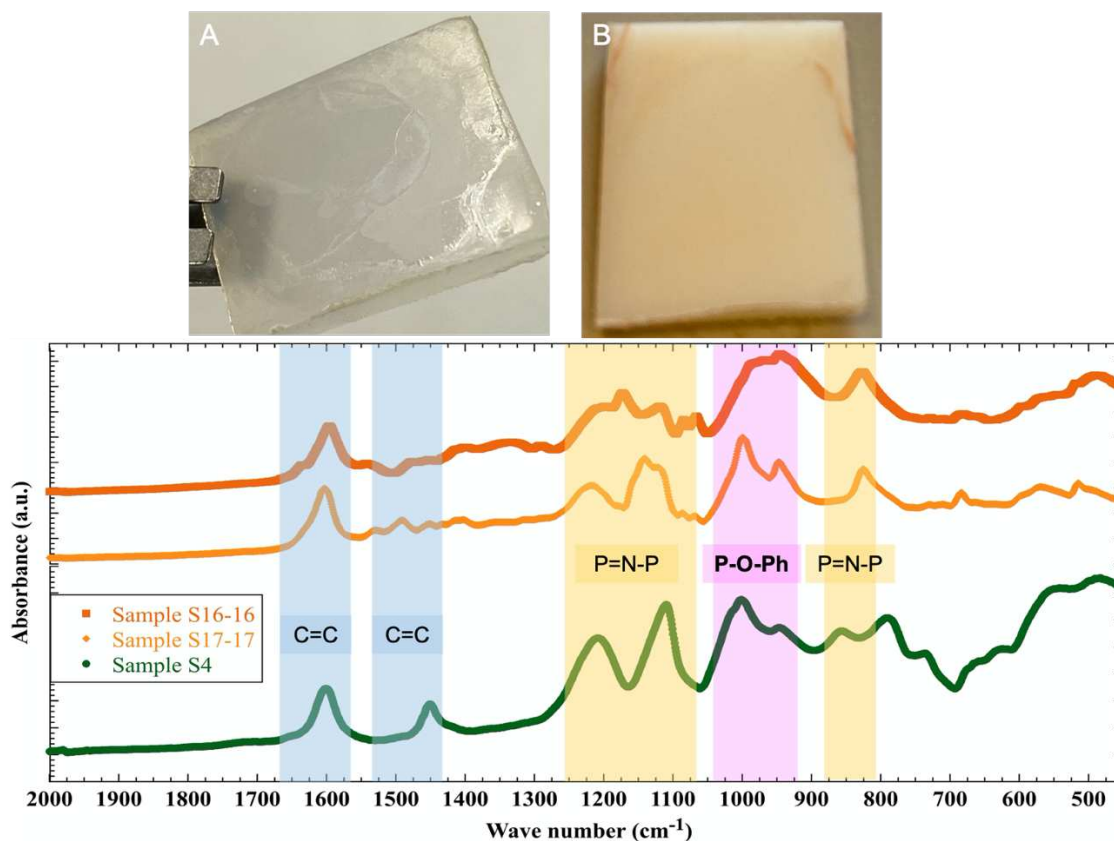


Figure 7.11 FTIR spectra for samples S16-16 (A) and S17-17 (B). Sample S4 shows a Phg-HCCP film spectrum.

The addition of a surface treatment does seem to compensate for the lack of pores but a film is only formed in patches. Both chemical and mechanical treatments need to be improved and, as already suggested, polishing seems more appropriate for FLE40 while O_2 plasma (or UV/Ozone) is more satisfactory for F136. The drying step (Step 2, Figure 7.6) is the most critical step: the rubber roller appears to be too harsh and conversely, leaving out this step is not satisfactory either.

To conclude, the addition of a surface treatment does seem to improve the “usual” IP on support process. Therefore, a new process for organic dense substrates, which includes this novel step, was defined on the basis of the information provided by the preliminary tests.

7) C. 3. Definition of a new process

The new process designed for film formation on PA substrates is presented in Figure 7.12. It includes, in particular, an additional substrate deprotonation step carried out just after the surface plasma treatment. The new process also reverses the order in which the solutions are added: HCCP in cyclohexane now becomes the first to be added instead of Phg+KOH in DMSO. Note that in the previous Section, a mechanical surface treatment was studied but its optimization was not possible due to limited time. This remains an area of improvement for future work.

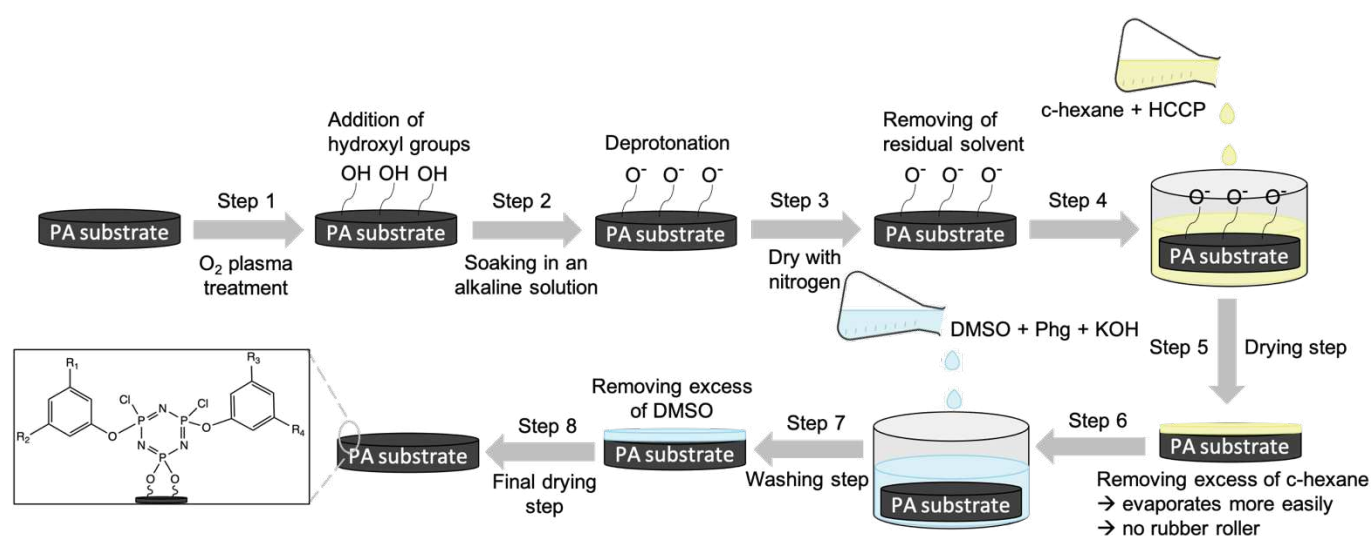


Figure 7.12 Schematic illustration of the new process for the interfacial polymerization of a Phg-HCCP film on a PA dense substrate. Deprotonation can involve other groups than the OH only.

According to the literature [340-343], the O_2 plasma treatment adds hydroxyl and carboxylic groups to the PA surface. It is also possible that the plasma affects the NH_2 end-groups of the PA chains close to the surface. All these new groups need to be deprotonated in order to react with the HCCP monomers, that are now added first. Effectively, the deprotonated groups on the surface of the substrate will form the required grafting points for the rest of the process. This time, a stronger base than KOH is probably necessary for the groups added on the surface. The pKa values of Phg are between 8 to 14 and it is a highly reactive product [327, 344]. It is likely that the pKa values of the groups added to the surface are higher, *i.e.* there are less reactive, and that KOH with a pKa of 13.5 is not basic enough to deprotonate them. For this reason, potassium *tert*-butoxide *t*-BuOK with a chemical formula $(CH_3)_3COK$ and a pKa of ≈ 17 , was used as a replacement for KOH.

Since the drying step had been identified as very critical, the order of the solutions for the wetting is now inverted: the HCCP solution is applied first followed by Phg dissolved in DMSO. As cyclohexane

evaporates more easily, it avoids using the rubber roller. Indeed, the excess solvent can simply be absorbed by a tissue which should leave enough of the first solution on the surface for the reaction to take place. There are no pores on a dense substrate, so the drying step must only remove the excess of solution and not all of it.

7) C. 3. 1. Vacuum plasma

As indicated in Figure 7.12, the surface treatment is provided by a low-pressure or vacuum O₂ plasma. For testing this new protocol, four samples (two F136 and two FLE40) were prepared with changing the time in the plasma device and the soaking time in the *t*-BuOK/DMSO solution. The new IP conditions are listed in Table 7.10.

Table 7.10 IP conditions for IP of Phg-HCCP films with the new process and a plasma surface treatment of the PA6 substrates. The Phg conversion step is still at 80°C. All the substrates are cleaned with isopropanol and dried with nitrogen before use.

Samples names	S20-20 (F136)	S21-21 (F136)	S22-22 (FLE40)	S23-23 (FLE40)
Temperature	70°C (for soaking in HCCP and reaction)			
Plasma parameters	7.5 min/80W	10 min/80W	7.5 min/80W	10 min/80W
Time in <i>t</i> -BuOK solution	1 h	1 h 30	1 h	1 h 30
Concentration of <i>t</i> -BuOK solution	0.1 mol/l			
Ratio -OH Phg/ -OH KOH	3.5:1			
Conversion time	2 h 30			
Time of soaking	25 min			
Reaction time	30 min			
HCCP concentration	3.5 w/v%			
Phg concentration	10 w/v%			

The concentration of the alkaline solution was set after discussion with specialists. The KOH concentration in Phg/DMSO solution has been kept the same for all the following samples. The KOH dissolution time in DMSO was increased because of the use of pellets. The temperature was set to 70°C instead of 80°C, because of the lower boiling point of cyclohexane at 80.7°C [345]. Finally, after their soaking in *t*-BuOK solution, the supports were washed with acetone, which allows rinsing without risk of re-protonating the surface. They were then dried with nitrogen before carrying out the rest of the process. Figure 7.13 shows the four samples obtained.

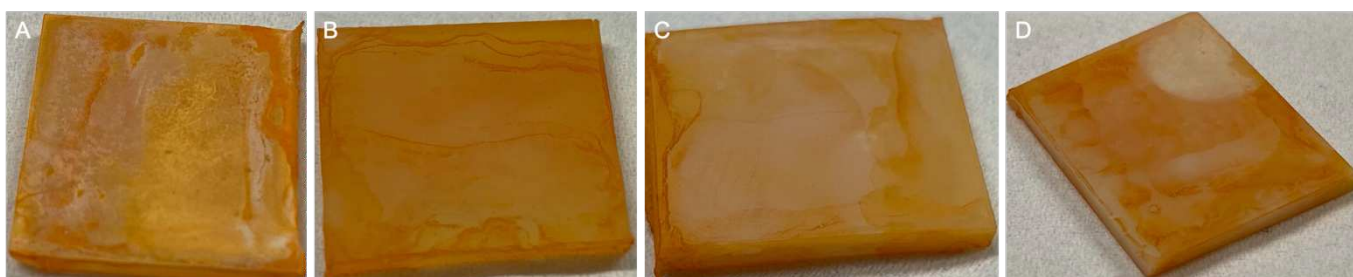


Figure 7.13 Samples S20-20 (A), S21-21 (B), S22-22 (C) and S23-23 (D) after the IP of HCCP and Phg on top of the plasma-treated and *t*-BuOK-soaked PA6 substrates: A and B are F136, and C and D are FLE40 supports.

The results are clearly much more satisfactory. All the samples show a layer wrapped around the substrate. However, the layers have defects and do not seem homogeneous in terms of composition and thickness. The FTIR measurements (Figure 7.14.A), as well as the SEM pictures (Figure 7.14.B-E), taken on different areas confirm this visual impression.

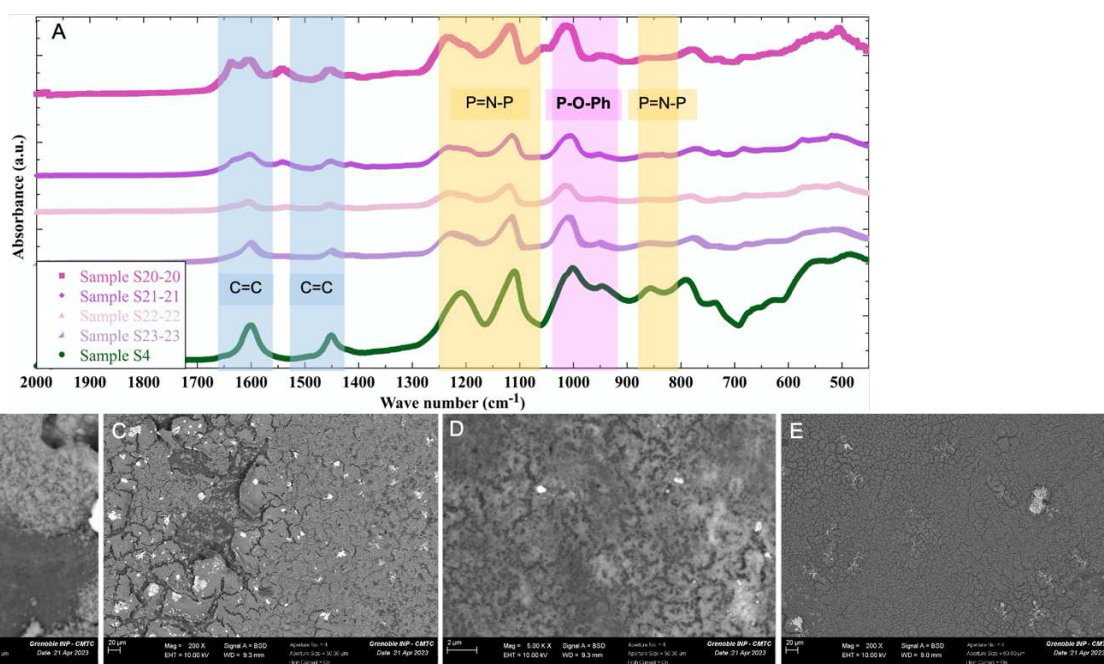


Figure 7.14 FTIR spectra for the four S20-20, S21-21, S22-22, S23-23 samples on top of a plasma and *t*-BuOK-treated PA6 substrate along with S4 for comparison (A). SEM pictures generated using backscattered electrons (BSE) for the surface of S20-20 (B), S21-21 (C), S22-22 (D) and S23-23 (E). The different shades of grey correspond to different chemical compositions.

The FTIR spectra of these new samples all resemble that of sample S4, *i.e.* the layer formed everywhere is a Phg-HCCP film but with different thicknesses and different compositions. EDS analyses

(not shown) detect Cl and K with traces of S on some parts of the samples. This suggests that the rinsing steps were not enough to remove DMSO the solutions properly.

Both the SEM and EDS analyses provide information about these films:

- All the samples have a surface with lots of defects (pin holes, cracks) and also sometimes a clear delamination of the film from the substrate (Figure 7.14.C and E).
- The films seem to be a pile of grains more or less coalesced (Figures S7.4), with diameters ranging from 80 to 120 nm.
- Even if the thickness is not uniform everywhere, it is between 1 to 3 μm . This is thicker than all previous samples on porous supports [260]. Furthermore, the cross-sections show that, when the layer has grown on the underside (not exposed directly to the plasma), it is less homogeneous and less attached to the surface than the one on the side exposed to the plasma.
- The different shades displayed by Figure 7.14.B-E that the white spots on the surfaces are the salts, while the darker parts are the films: carbon, oxygen, potassium, nitrogen, phosphorus and chlorine are detected. If C, O and N cannot be attributed to the films for sure (carbon metallization for SEM measurements, plus the atoms present in PA), the P and Cl necessarily originate from HCCP-based compounds. The amounts of P and Cl vary even over a same sample. For example, S20-20 has darker parts which contain more Cl than P, as well as light grey parts (present on all samples) which contain more P than Cl.

According to these results, the addition of a deprotonation step after the surface treatment leads to the formation of a more continuous and thicker layer than before, albeit with a different quality depending on the location on the substrate. Surprisingly, there is a layer of lower quality on the underside, which means that the HCCP monomers were also attached there, even if it was not directly exposed to the plasma treatment. This could be explained by two hypotheses.

- The plasma treatment could reach underneath the support, but this is not expected with the device used.
- It could come from the deprotonation step with *t*-BuOK. Indeed, the end groups of the PA are NH₂ primary amines with a pK_a between 4 to 10, which is low compared to that of the base [346, 347]. They can easily be deprotonated and this promotes the links with HCCP. This is consistent with DSM, which used these groups to modify their PA. However, the notion of “end groups” means that there should not be many (and their distribution on the surface is not known), therefore, it is unclear whether they can make a sufficient level of grafting.

For the film on the top plasma-treated side, the cross-linking degree needs to be characterized but there are several questions related to the differences in chemical composition:

- When more chlorine than phosphorus is detected, is it due to unreacted HCCP (6 Cl for 3 P) and/or to residual KCl? Or is it a polymer film with a low cross-linking degree? Indeed, chlorine is the leaving group involved in the nucleophile substitution reaction between HCCP and Phg (Figure 6.24).
- Inversely, when there is more phosphorus than chlorine, is it a film with a high cross-linking degree?

The thickness seems to support the idea of a low cross-linking degree of the film. In IP, the film formation is self-controlled by the monomer diffusion, *i.e.* it stops when the monomers cannot pass through the formed layer anymore (no more contact) [143]. The thicker the layer, the longer the two monomers came into contact. This suggests that, despite the formation of a network, its cross-linking degree is low enough to still allow the monomers to diffuse through the layer, eventually leading to thicker samples than before.

These four samples thus raised a number of questions but they also showed quite promising results as 1-3 μm -thick layers of Phg-HCCP could grow on the PA6 dense substrates provided by DSM. Even if the layers still had defects and delamination issues, they were quite continuous and homogeneous on the surfaces and this is a clear step forward in the film synthesis process on top of non-porous substrates. This new process is beneficial but further developments are necessary to improve the following aspects: more homogeneity in thickness and composition, less defects, less salt deposits, sufficient cohesion with the surface of the support to avoid delamination and a good cross-linking degree to achieve good barrier property. The next studies were conducted along these lines, albeit with a different plasma device due to a change of location.

7) C. 3. 2. Atmospheric plasma

Following the previous work at the University of Twente, the next tests were carried out at the University Savoie Mont Blanc. A different plasma device, *i.e.* a high-density plasma with a low heating effect (Atmospheric plasma, MTP2) had to be used. However, its main effect is expected to be the same. It should improve the surface tension by breaking bonds or introducing new functions on the PA surface [340-343].

Tests were made to check if an increase in surface tension is indeed obtained after exposure to the new plasma. Unlike the oxygen low-pressure plasma, the relatively easy-to-use MTP2 only has an on/off button and no other settings that can be changed (Figure 7.15). However, for a very sensitive technique such as IP, more precision is needed. The device thus was mounted on a support in order to control the distance between the nozzle of the plasma and the surface of the samples, as well as the speed of movement.



Figure 7.15 MTP2 atmospheric plasma from STTS [348].

As for the other chemical treatments, the F136 seemed to react better than the FLE40 support. As such, better samples were obtained in general with F136 rather than with FLE40. Tests with the MTP2 atmospheric plasma showed that the water contact angle WCA decreased whatever the substrate, *i.e.* the surface was affected by the treatment in the right direction towards an increase of the wettability. The parameters in Table 7.11 gave the smallest WCA and therefore the best surfaces for the rest of the process.

Table 7.11 Parameters for the MTP2 atmospheric plasma treatment of both PA6 substrates used in the new IP Phg-HCCP process.

Distance between pen and sample (mm)	Speed (mm/min)	Number of passes
4	1000	2

A first set of 4 samples (two on each support) were prepared with the IP parameters of Table 7.10, except for the time of soaking in the alkaline solution, which was set to 1 h 30 for the F136 samples and to 1 h for the FLE40 samples. One sample for each type of substrate was made by deliberately omitting the plasma treatment and going directly to the soaking phase in the alkaline solution. This was aimed at checking the hypotheses related to the underside layer of the initial samples prepared with the new process, *i.e.* whether the deprotonation of the PA -NH₂ end groups could be sufficient for the IP layer to attach itself to the substrate.

As seen in Figure 7.16, the samples appear visually less good than the first batch made with the new process and the other plasma device. However, they are still better than the samples made without the new process. Indeed, there is a fairly continuous layer on all of the samples, albeit still inhomogeneous.

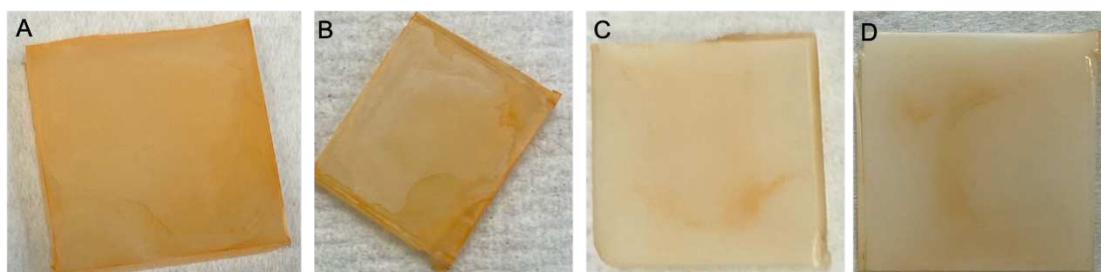


Figure 7.16 Samples S24-24 (A), S29-29 (B), S26-26 (C) and S27-27 (D) obtained using the new IP process to deposit a Phg-HCCP film on top of the F136 (A and B) and FLE40 (C and D) PA6 substrates. Note that the MTP2 plasma treatment was used for samples S24-24 (A) and S26-6 (C), whereas it was omitted for samples S29-29 (B) and S27-27 (D).

Clearly, omitting the MTP2 plasma treatment did not give good results. The layers formed in samples S29-29 and S27-27 showed a poor continuity and/or a poor adhesion to the surface. The visual observation is confirmed by FTIR (Figure 7.17), which suggest very thin films, some parts even disappearing after the final drying (Figure 7.18).

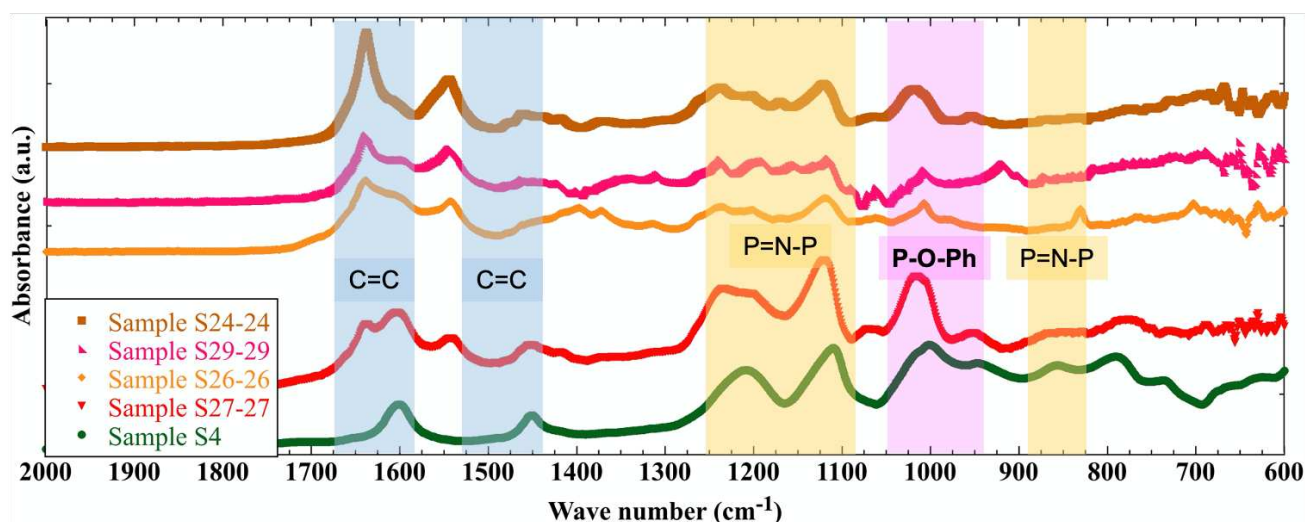


Figure 7.17 FTIR spectra for samples S24-24, S29-29, S26-26 and S27-27 obtained with the new IP process on the PA6 substrates. Sample S4 shows a Phg-HCCP film spectrum.

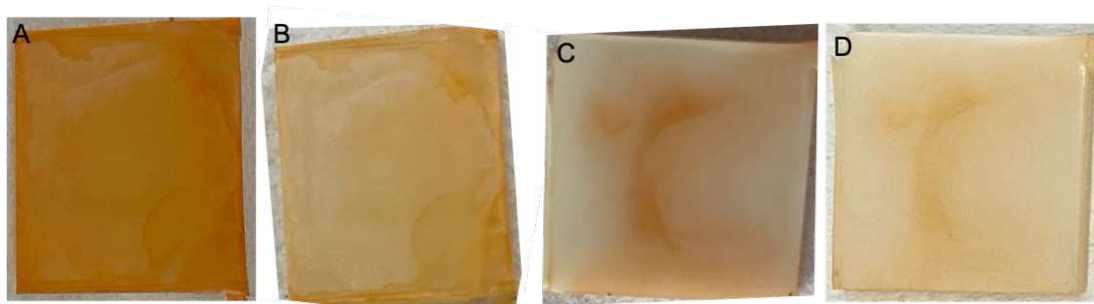


Figure 7.18 Sample S29-29 (F136) before (A) and after drying (B), and sample S27-27 (FLE40) before (C) and after drying (D). Neither of them underwent the plasma treatment.

Besides the solvent evaporation that inevitably occurs and the changes in the colour of the surface (Phg/KOH/DMSO stains all the samples where the film is formed), the drying step is not supposed to remove any film that is formed. However, at some places on sample S27-27, the very thin film detected by FTIR before the drying disappears after 24 h in a vacuum oven. Moreover, for both these non-plasma-treated samples, no layer grew on the underside. This low thickness and non-continuity of the film are confirmed by SEM analyses. The cross-section of sample S27-27 gave thicknesses ranging from 200 to 300 nm, which are the lowest found as yet for the new process. The surface also shows multiple defects (Figure 7.19.A). C and O are detected over almost all the surface. This could come from Phg but it could also be due to the substrate (Figure 7.19.C). However, the aspect is not exactly the same as the uncoated substrate (Figure 7.19.B) Indeed the white particles in Figure 7.19.A contain P and K with relatively small amounts

of Cl (Figure 7.19.D). As P can come only from HCCP, this suggests that there is a film present on the substrate but not everywhere and in small quantities.

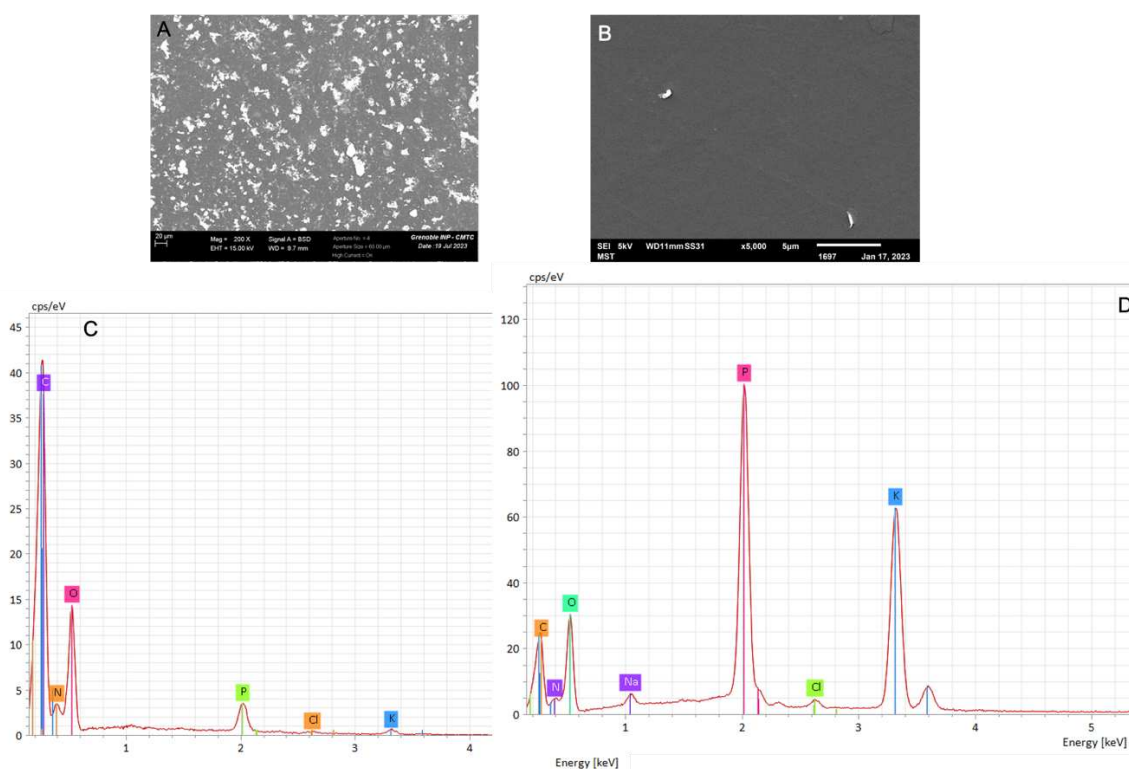


Figure 7.19 SEM pictures of the S27-27 surface (A) compared to that of the PA substrate alone (B). Also shown are EDS results of the S27-27 global surface (C) and of one of the white particles on this surface (D).

EDS elemental analysis cannot determine the exact composition of a layer but it is sufficient to give an indication of the elements present. For example, for sample S27-27, the fact that more P and K are detected than Cl suggests that the layer is present as well as salts. For the former, either the film has a high cross-linking degree or the HCCP monomers have reacted with PA before reacting with Phg. Indeed, both cases lead to the departure of many Cl and therefore to much more remaining P. As mentioned in the previous Section, these assumptions need to be clarified by an analysis allowing *e.g.* the determination of the cross-linking degree.

Compared to the plasma-treated samples, the results for the non-plasma-treated samples suggest that the plasma is largely responsible for the extent of the layer, albeit not the only cause. If this does not explain why the layer could grow on the underside, it was noticed during the treatment of samples S24-24 and S26-26 with the MTP2, that the arc form of the new plasma conforms to the shape of the sample and

also goes to the edges. This could explain why the layer grew on the upper face and on the sides for these two samples. However, this still does not explain the presence of the film on the underside.

If both samples S24-24 and S26-26 are better than those without plasma treatment, only the S24-24 coated on the PA6 F136 substrate presents a sufficiently continuous and homogeneous layer to warrant pursuing further studies. This shows once again that F136 reacts better than FLE40 to chemical treatment. Due to the almost transparent nature of the F136 substrate, it is easy to see on Figure 7.16.A that there is a layer everywhere. This confirms that the underside is affected by the plasma treatment allowing the film to form, even if the precise mechanism remains unclear.

Figure 7.17 shows that the S24-24 FTIR spectrum corresponds mostly to the reference Phg-HCCP film illustrated by sample S4. However, the presence of a peak around 1540 cm^{-1} and the apparent shift of the C=C peak from 1600 cm^{-1} (S4 sample) to 1635 cm^{-1} (S24-24 sample) could be due to the PA substrate. This suggests that the film is probably too thin to prevent the FTIR detecting the PA substrate. It is confirmed by the SEM analyses of the cross-section, which give a non-uniform thickness between 220 to 300 nm, *i.e.* a much lower thickness than for the first samples with the new process. This is not necessarily a drawback if the film is defect-free, presents a good connection between the layer and the substrate and a good barrier performance. In Chapter 6 and previous work [260], layers around 30 nm thick were obtained by IP on porous ceramic supports and their permeability coefficients ranged from 1.82×10^{-17} to $240 \times 10^{-17}\text{ cm}^3\text{ cm cm}^{-2}\text{ s}^{-1}\text{ Pa}^{-1}$.

The morphology of sample S24-24 and its link with the substrate were further studied by SEM and EDS. Unlike the samples S20-20 to S23-23 considered the best so far, there is no delamination here. Nevertheless, there are many defects such as hollows (Figure 7.20.A and B), which could eventually cause delamination.

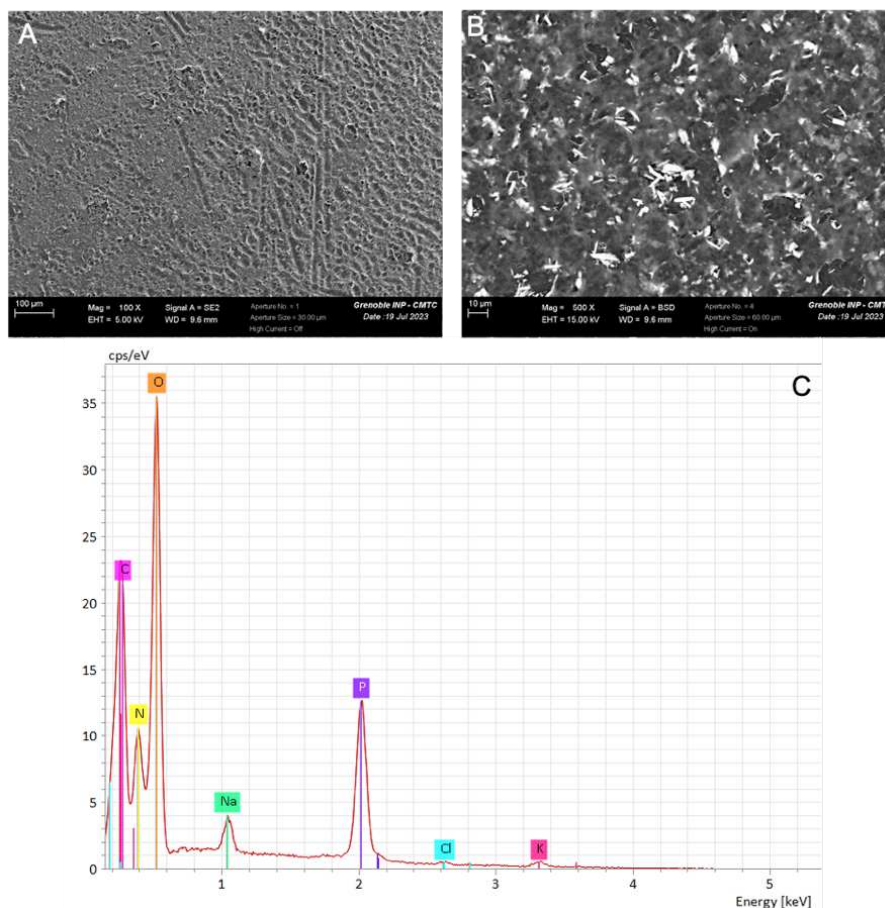


Figure 7.20 The S24-24 surface characterized with SEM (A) and with BSE (B). The different shades in (B) correspond to different chemical compositions. Also shown is the EDS result of the global surface (C).

According to EDS (Figure 7.20.C), there is again more P than Cl and surprisingly little K. As the sample does not show any delamination, the absence of Cl was attributed to a double reaction of HCCP with the substrate and Phg rather than to a high cross-linking degree. This needs to be checked. Moreover, to explain the low amount of K, the aspect of the surface suggests that salt crystals, *e.g.* KCl, are formed and adhere to the surface before or during the film formation. The film covers them but, at some point, these crystals are removed and leave holes/hollows at their previous location. It could also be residues of *t*-BuOK particles in powder form which persist on the surface when the film is formed. If part of the layer covers any of these particles on the surface, this could explain why the BSE image (Figure 7.20.B) shows crystals (either salts or *t*-BuOK particles), whereas there is not much K. On the other hand, there is a lot of P, *i.e.* the film is preferentially detected over any particles. Sample S24-24 also exhibits a relatively good chemical homogeneity as only two different colours appear.

If the morphology and elemental composition could be explained with these assumptions, it does raise some questions:

- If salts are formed or *t*-BuOK particles remain on the surface, how and at which step are they removed?
- In addition, why are they eliminated to a certain extent on samples S24-24 and S27-27, and not on others samples such as S20-20 to S23-23?

According to the samples studied in this Section, the new process with the MTP2 plasma treatment thus seems to give promising results as well. However, the layer can still be improved, especially on the FLE40 substrate. Consequently, additional changes in the conditions were again attempted in order to allow for an identification of the key parameters for IP on a dense organic substrate such as PA6.

7) C. 4. Treatment parameters for IP on dense organic substrates

As the IP parameters are too numerous and too interdependent, it was not possible to change all of them. Obviously, further studies have to be done to determine the optimal protocol, *i.e.* a procedure which is reproducible, repeatable and gives the most homogeneous, continuous and high-barrier film possible. Ideally, this will not only be suitable for PA substrates but also be applicable more widely to other dense organic supports.

The changes in the previous parts of this work have mostly focused on changes to the parameters of the IP itself, *e.g.* the reaction and soaking times, the temperature and the drying step, etc. Here, the idea is to consolidate the new process and, therefore, the changes focused mostly on the new steps related to the support, *i.e.* its surface treatment *via* plasma and its deprotonation *via* soaking in *t*-BuOK.

7) C. 4. 1. Polyamide FLE40 substrate

As explained before, the FLE40 has been found to be less receptive to the so-called “chemical treatments” than the other PA6 support. The first stage was to identify the parameters related to the process that can be changed (Table 7.12).

Table 7.12 Parameters for the MTP2 atmospheric plasma and the alkaline solution of *t*-BuOK in DMSO that could be changed in the new IP process for Phg-HCCP film formation.

	Plasma	<i>t</i> -BuOK solution
Intrinsic parameters	Distance between sample and pen	Soaking time of the sample
	Speed	Concentration
	Number of passes	Dissolution time
Protocol parameters	Time between plasma initiation and start of treatment	Extent of washing off the excess

Unless stated otherwise, the basic IP parameters were the same as in Table 7.10. In a first instance the following parameters were changed:

- The distance between the sample and the plasma was changed from 4 mm to 3 mm. It is based on studies by Károly *et al.*, Hanusová *et al.* or Štěpánová *et al.* about plasma treatments for PA [340, 349, 350], who all suggest a smaller distance between the surface and the pen.
- The soaking time in *t*-BuOK was increased from 1 h to 1 h 30.
- The washing of the surface after the deprotonation step was reduced.
- The dipping time in the monomer solutions (first HCCP/cyclohexane then Phg/DMSO) was increased.

The effects of these first changes were not too significant. Indeed, there were no layers formed, except for low thickness traces. There was nothing either on the underside (Figure 7.21).

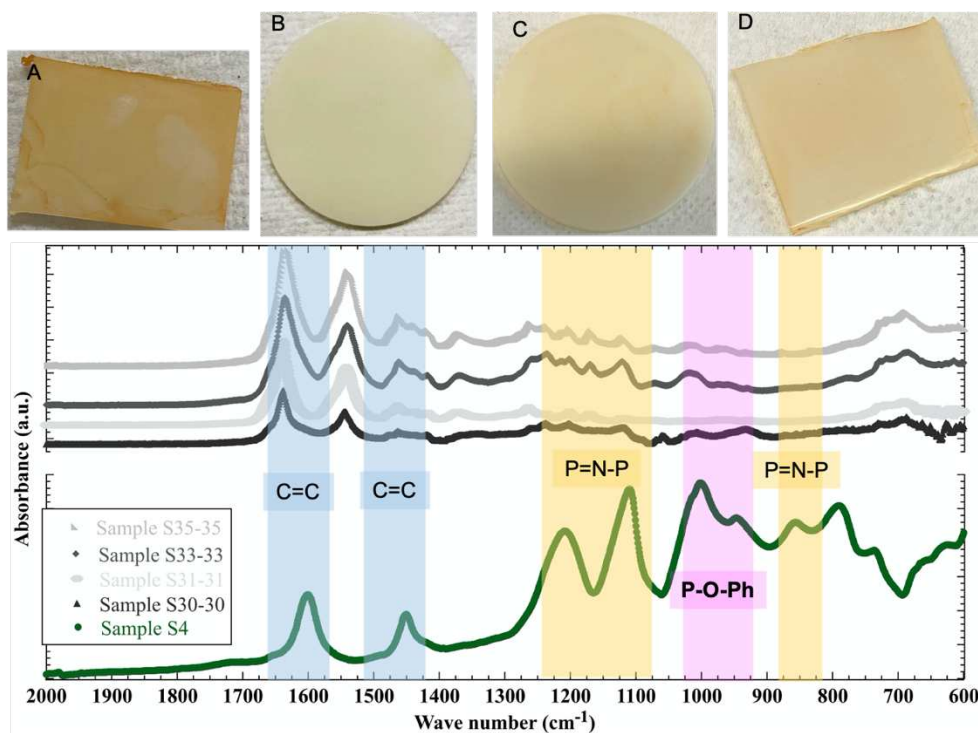


Figure 7.21 Samples S30-30 (A), S31-31 (B), S33-33 (C) and S35-35 (D) where attempts to deposit a Phg-HCCP film on the FLE40 substrate were made. Also shown are the corresponding FTIR results (lower panel). Sample S4 shows a Phg-HCCP film spectrum.

Samples S30-30 and S31-31 differ by an increase of the soaking time in cyclohexane and the reaction time for the latter. It does not lead to the formation of a layer. Nevertheless, for both samples, the surface looked different before and after the deprotonation step, including the washing step.

Figure 7.22 displays for comparison the different aspects of the S20-20 surface over the whole process. These photos can be considered as “references” since they are consistent with the formation of a Phg-HCCP film on the PA substrate.

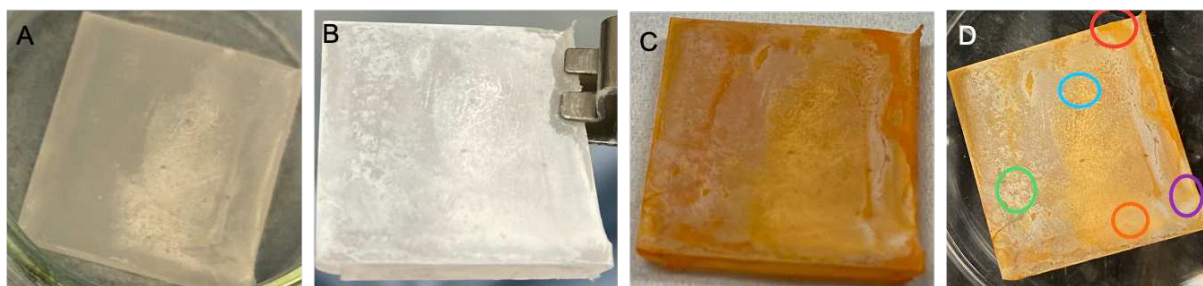


Figure 7.22 Sample S20-20 after soaking in the *t*-BuOK solution (A), after soaking in the HCCP solution (B), after the soaking/reaction in the Phg solution (C) and after the final drying step (D). The coloured circles on (D) indicate the locations of the FTIR measurements and the white area on (A) is most likely a residue of *t*-BuOK.

For both samples S30-30 and S31-31, no HCCP crystals are detected after the soaking in the HCCP solution, hence no layer is formed afterwards. However, both surfaces already did not have the appearance of sample S20-20 after the deprotonation step (Figure 7.22). The simplest modification was to reduce the intensity of the washing step after soaking with *t*-BuOK in terms of time and quantity of solvent. The soaking time in HCCP and the reaction time were also reset back to their original values, *i.e.* 25 min and 30 min, respectively. In addition, an IP specific setup (cf. Chapter 6, Figure S6.1) was introduced into the protocol. This allows the sample to be properly held during the process, which avoids flotation. Indeed, the FLE40 substrate floats in DMSO because of its slightly lower density (Table 7.5).

After these modifications, the results were better in terms of surface aspect after deprotonation and drying. Samples S33-33 and S35-35 (Figure 7.21) now looked more like samples S20-20 (Figure 7.22.A) or S21-21 to S24-24. However, despite this improvement, only a really thin layer could grow. Less washing after soaking in the *t*-BuOK solution and using the specific setup improved the aspect of the surface, but they were still not enough to grow a continuous layer.

Another aspect that can impact the formation of the layer was observed during the preparation of the last samples: when the plasma is ignited, the arc sparks just after ignition then stabilizes and retains a roughly constant shape and intensity (Figure 7.23).

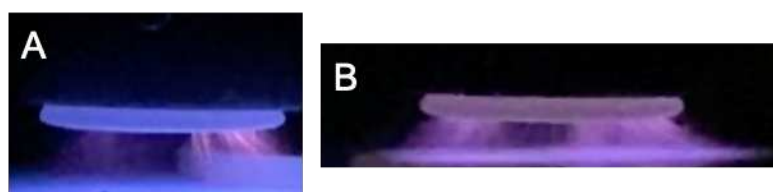


Figure 7.23 Arc of the atmospheric plasma immediately after its ignition (A) and about 1 min later (B).

This might be because the plasma needs some time to stabilize in an atmospheric environment which is not controlled. Consequently, the time between the plasma initiation and the start of the treatment was increased until the sparks stopped and the shape of the arc became stable. Moreover, it was speculated that the non-continuous layer could be due to a too long interval between the plasma treatment and the soaking in alkaline solution, *i.e.* a time-limited treatment effect [349]. This should be most critical for the largest samples, where the first part is treated a few seconds before the last. Figure 7.24 shows the most likely pathway of the plasma treatment on the sample, according to the nozzle diameter, and, therefore, which area is treated first and will relax the most before being wetted by the *t*-BuOK solution.

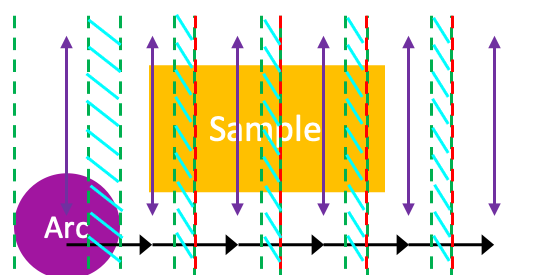


Figure 7.24 The (likely) plasma treatment path on a rectangular sample with the purple arrows corresponding to the vertical displacements, the black arrows to the horizontal displacements and the green/red dashes to the “limits” of the treatment. As the shape of the arc plasma is not stable, neither are its limits. The blue oblique dashes indicate potential overlappings.

As the treatment starts from the left and moves to the right, there is a delay of a few seconds between the first and last area treated. To try to reduce this time difference, the speed was increased to 1500 mm/min and the number of passes was doubled.

Besides the changes in the plasma protocol, the concentration of the *t*-BuOK solution was increased and its soaking time reset to 1 h. In addition, the substrate was turned over in the *t*-BuOK solution, *i.e.* with the plasma-treated side facing downwards. Consequently, even if the substrate floats, its working face is bound to be submerged (Figure 7.25).

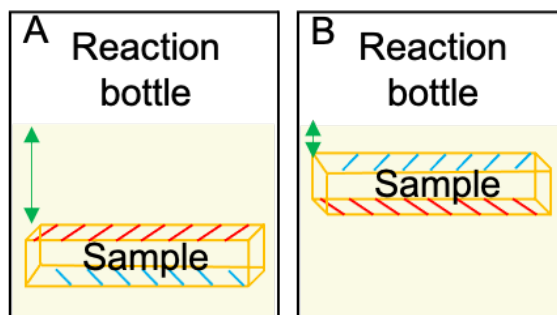


Figure 7.25 The different sample positions in the IP reaction bottle with the plasma-treated (or working) face in red facing upwards (A) and downwards when the sample is turned over (B). The immersion proportions (green arrows) are realistic.

As shown by Figure 7.26, the samples made with all the above changes are better than before, but still not as good as the first set with the new plasma (Figure 7.16) and the first set with the new process (Figure 7.13).

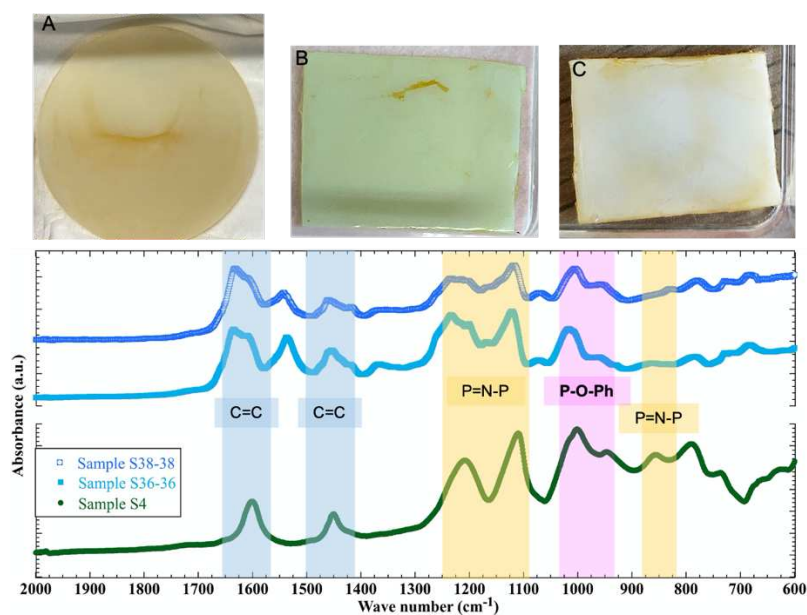


Figure 7.26 Sample S36-36 (A), the working face of S38-38 (B) and the underside of S38-38 (C). Also shown are the corresponding FTIR spectra (lower panel). Sample S4 shows a Phg-HCCP film spectrum.

The IR spectra in Figure 7.26 show that a Phg-HCCP film is detected but it is thin because the majority of the peaks belong to the PA6 substrate. However, characteristic monomer peaks as well as the double peak between 1000 to 920 cm^{-1} (P-O-C link between the reactants), can be found. Naturally, this layer is again not continuous and probably not uniform in terms of thickness: the parts that are more orange

(Figure 7.26), are probably the thickest. Figure 7.27 summarizes the main observations during these experiments.

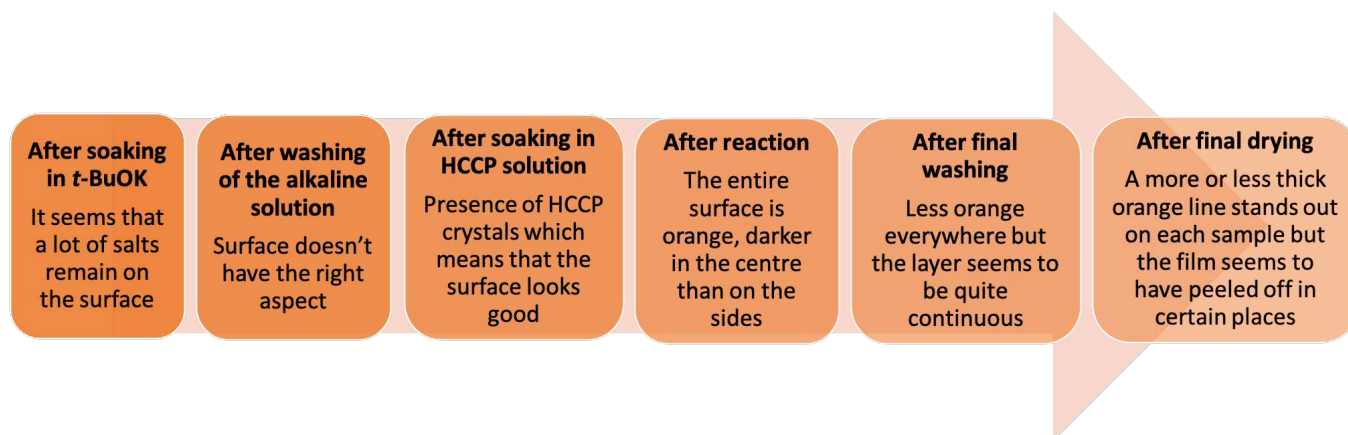


Figure 7.27 Chronological description of the surfaces for S36-36 and S38-38 after the main IP steps between Phg and HCCP monomers.

Due to the higher concentration of *t*-BuOK, the samples probably needed more washing to remove the residue of salts. This resulted in a poor aspect after the deprotonation step compared to sample S20-20 Figure 7.22. However, the aspect improved after being wetted by HCCP/cyclohexane and remained satisfactory until the end of the process. This suggests that a poor surface appearance after the soaking in *t*-BuOK is not necessarily synonymous with a poor-quality film. Inversely, a good appearance does not necessarily guarantee a good-quality film (see samples S33-33 and S35-35). Nevertheless, the change in aspect is a good indication of a reaction during a step, *e.g.* a deprotonation, grafting or polymerization.

Surprisingly, for the sample S38-38 that was turned over in the solution, a growth occurred on both sides (Figure 7.26.B and C) and a better layer was even observed on the underside (Figure 7.25.B). This could mean that a slight immersion (green arrow, Figure 7.25.B) is sufficient to have enough HCCP monomers on the surface for the reaction to take place. However, it does not explain why the best layer did not grow on the most submerged face, *i.e.* the plasma-treated one.

The combination of parameters applied to samples S36-36 and S38-38 are the best so far. Table 7.13 summarizes these optimized experimental conditions.

Table 7.13 Optimized parameters for the MTP2 atmospheric plasma and the alkaline solution of *t*-BuOK dissolved in DMSO. They were used for samples S36-36 and S38-38 with PA6 FLE40 as the substrate.

Plasma		<i>t</i> -BuOK solution	
Distance between sample and pen	4 mm	Soaking time of the sample	1 h
Speed	1500 mm/min	Concentration	0.2 M
Number of passes	2	Dissolution time	2 h 30
Time between plasma initiation and start of treatment	1 min	Extent of washing of the excess	Limited

These results for the FLE40 substrate were better than all previous samples made with the MTP2 plasma (Figure 7.16 and Figure 7.21). However, they were not as good as samples S22-22 and S23-23 (Figure 7.13), which means that they could still be improved.

The last two samples on the FLE40 substrate were made with the same parameters and two more changes: the same concentration of *t*-BuOK solution but a smaller volume for S40-40 and KOH dissolved in DMSO (0.4 M) as an alkaline solution instead of *t*-BuOK for S41-41. The results are provided in Figure 7.28.

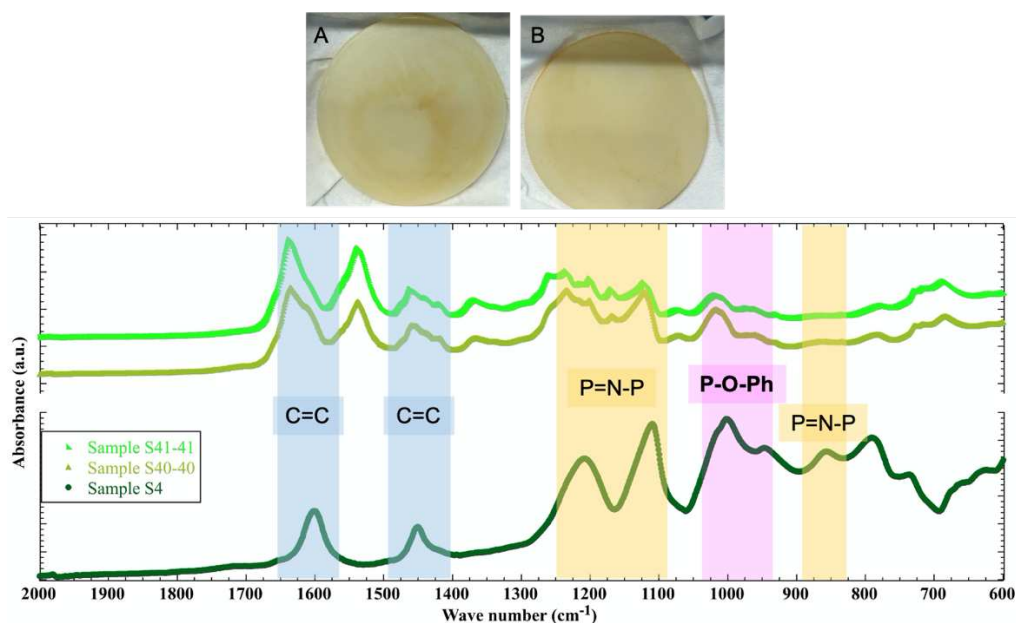


Figure 7.28 Samples S40-40 (A) and S41-41 (B) on FLE40 supports. Also shown are the corresponding FTIR spectra (lower panel). Sample S4 shows a Phg-HCCP film spectrum.

Visually, a layer is formed and remains on the surface of both samples after the entire process. However, it is again not continuous and really thin according to the FTIR results, which show both the presence of peaks belonging to the PA substrate, *e.g.* around 1550 cm^{-1} or 1350 cm^{-1} (Figure 7.5), and to the film, *e.g.* between 1000 and 930 cm^{-1} .

After soaking in KOH/DMSO, the surface aspect of sample S41-41 is hardly changed. This suggests that not much happened. Indeed, it was anticipated that a stronger base than KOH would be necessary to deprotonate the groups added on the surface by the plasma treatment, hence the switch to *t*-BuOK. Nevertheless, the aspect is not so bad after soaking in HCCP/cyclohexane and moreover, a layer grows on some areas. Despite an inadequate deprotonation step, the formation of the film is still possible. This confirms the observation that a film grows on the samples with a plasma treatment only, albeit with a patchy distribution (samples S16-16 or S17-17, Figure 7.11).

For sample S40-40 with less *t*-BuOK solution, the behaviour was similar. Again, not much seemed to happen during the first step. This suggests that the volume of alkaline solution does affect somehow the extent of deprotonation of the surface and therefore the formation of the layer.

To conclude, if the use of a new plasma in the new IP process also allows the production of a layer on a dense substrate such as PA6 FLE40, the first two steps are indeed quite critical and should be optimized before starting the reaction.

7) C. 4. 2. Polyamide F136 substrate

Both PA6 substrates do not behave in exactly the same way. Nevertheless, similar tests to those for FLE40 (Table 7.12) were carried out for F136. Almost all the parameters were varied in the same way.

For samples S28-28 and S32-32, the distance between the nozzle and the surface was decreased from 4 mm to 3 mm. For samples S32-32, the soaking time in HCCP/cyclohexane was increased from 25 to 30 min and the reaction time from 30 to 35 min. In sample S34-34, the extent of washing of the alkaline solution was reduced. Results are displayed in Figure 7.29. Without surprise, the films are better than the ones made on the FLE40 substrate with the same parameters and process.

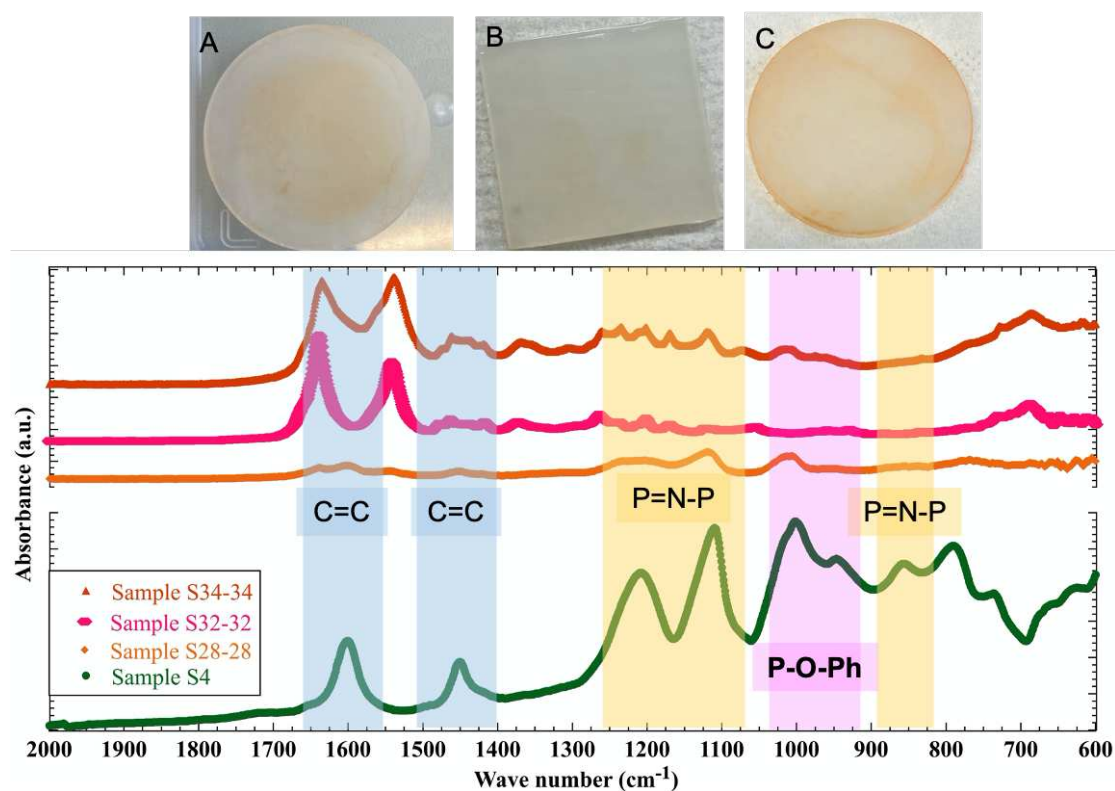


Figure 7.29 Samples S28-28 (A), S32-32 (B) and S34-34 (C) obtained after IP of Phg and HCCP on the surface of the F136 substrate. Also given are the corresponding FTIR spectra. Sample S4 shows a Phg-HCCP film spectrum.

From sample S32-32, it can be seen again that increasing the wetting time of HCCP/cyclohexane and the reaction time does not help. Basically, the FTIR spectrum of sample S32-32 corresponds to that of the substrate (Figure 7.5). Inversely, there is clearly a rather continuous film in the centre of sample S28-28, but it is quite thin and even thinner towards the edges until nothing is left. FTIR shows that the thickest part is indeed a Phg-HCCP film. For sample S34-34, the washing of the *t*-BuOK solution was modified (and the plasma to surface distance was reset to 4 mm for practical reasons). If the surface looks better, only a thin film grew on some parts.

As for the FLE40 substrate, it was assumed that the plasma treatment and the deprotonation steps had to be changed more radically. The following modifications were made for the next batch:

- The concentration of the *t*-BuOK solution was increased from 0.1 mol/l to 0.2 mol/l but the dissolution time was maintained at 1 h 30 min.
- The treatment started 2 min after plasma ignition and two passes were made instead of one.
- The specific setup for IP was used.

The S37-37 sample produced with the above settings was definitely the best among all the ones produced with the F136 support, and hence all the samples treated with the MTP2 plasma. Figure 7.30 presents its visual appearance, its FTIR spectrum and its UV-visible spectrum.

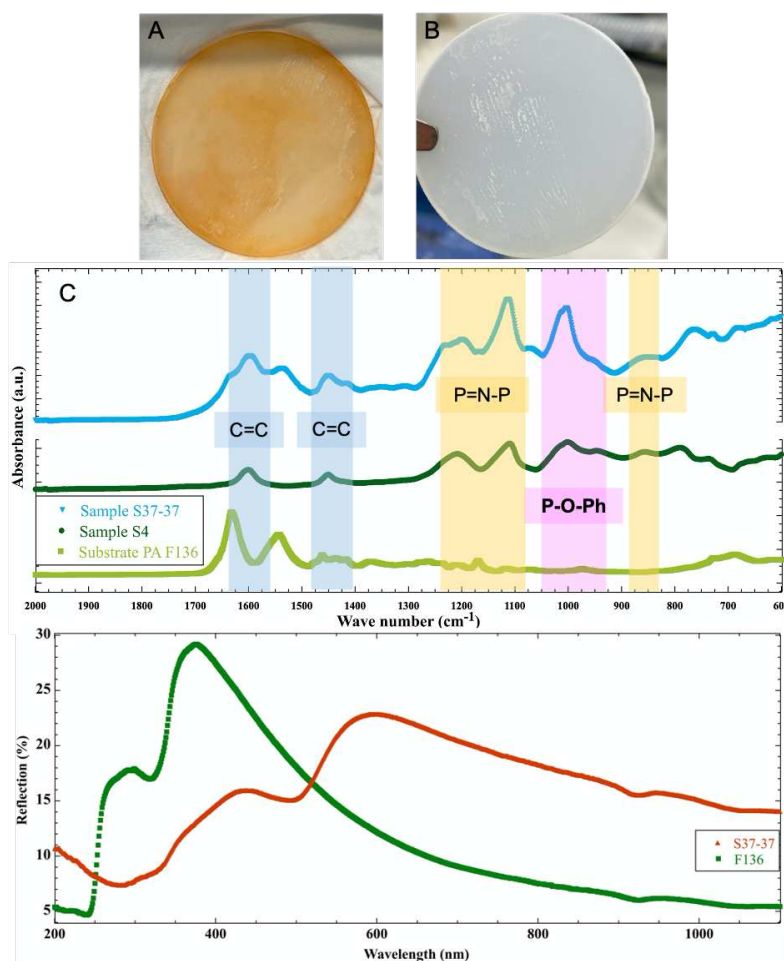


Figure 7.30 Sample S37-37 after the optimized IP process for Phg and HCCP on a PA6 F136 support (A), the same sample after its deprotonation step (B). FTIR spectrum for sample S37-37 along with those for sample S4 for a known Phg-HCCP film and F136 for a comparison with the raw PA6 substrate (C). UV-visible spectra for sample S37-37 and the raw PA6 substrate (D).

The few white marks on 7.30.B are probably due to not enough dissolution of *t*-BuOK. Except for these, the appearance is quite satisfactory after the deprotonation step as well as after soaking in

HCCP/cyclohexane. It is easy to see that a continuous and homogeneous layer grew on the surface of sample S37-37 (Figure 7.30.A) along with the edges of its underside. Its FTIR spectrum presents both the characteristic peaks of a Phg-HCCP film and those of the PA6 substrate (Figure 7.30.C). The UV-visible spectra of sample S37-37 and the raw substrate confirm that the support is coated (Figure 7.30.D). Furthermore, the SEM and EDS analyses of the surface and cross-section also confirm that the layer is a Phg-HCCP film with a thickness between 1 to 2 μm (Figure 7.31). Although this is less than the samples with the initial plasma, it is still greater than all the samples made with the MTP2 plasma.

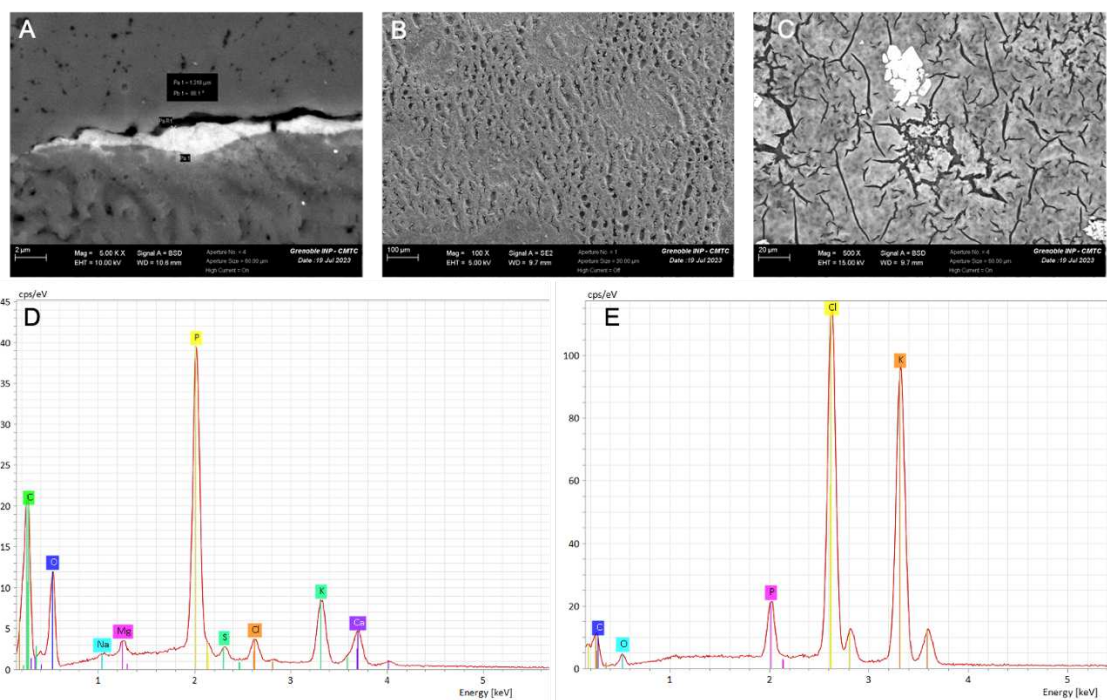


Figure 7.31 SEM pictures of the cross-section of sample S37-37 (A), of its surface with a secondary electron detector (SE2) (B) and with a backscattered detector (BSD) (C). EDS analyses of the global surface (D) and of the white particles apparent in (C) above, (E).

Besides providing the thickness, the cross-section (Figure 7.31.A) shows that the S37-37 layer is non-uniform in thickness but more continuous than for sample S24-24 (first sample with the MTP2 plasma, Figure 7.20). The black-line layer peeled off from the substrate in Figure 7.31.A is due to the preparation for SEM measurements. The film itself is well-attached to the substrate as no delamination occurs. The continuity of the film is also visible on the pictures of the surface, Figures 7.31.B and C, which have a similar appearance to sample S24-24: no delamination, holes instead of hollows and a relatively good homogeneity according to BSD (Figure 7.31.C). Indeed, except for the salt in white, there is only one colour, *i.e.* one chemical composition.

As for the holes which at some point make cracks, the hypotheses made for sample S24-24 should be valid here. Salts are formed and/or *t*-BuOK particles and some DMSO remain and persist on the surface. After formation of the film, they are removed by washing and, due to the greater thickness of these particles, they make holes and cracks rather than just hollows. This is again supported by EDS (Figure 7.31.D). P is detected on the entire surface, which means that the film is formed. Cl and K are also present in smaller quantities but, this time, traces of S are also found (Ca, Na and Mg detected are usual contaminants detected by EDS). Sulphur can only originate from DMSO. According to the amount of Cl, K and S, it can be deduced that *t*-BuOK particles remain indeed after the deprotonation step and that some DMSO solvent is trapped in the film. These “contaminants” are not entirely eliminated by the post-deprotonation washing step, as suggested by the white marks on Figure 7.30.B and are still there when the film is formed. The final washing step removes a large part of those particles and leaves the holes. Unfortunately, the drying step accentuates the holes into cracks. As far as the white particle in Figure 7.31.C is concerned, EDS reveals that it has a large amount of Cl and K, hence it is KCl salt (Figure 7.31.E).

A rapid ^{31}P -NMR measurement (not shown) proved that the layer present on the sample displays a difference in chemical environment for P between the monomers alone (HCCP spectrum, Figure 6.21.G) and sample S37-37, which confirms again that a reaction did take place.

Finally, as for FLE40, a last sample S39-39 with another type of alkaline solution, *i.e.* KOH instead of *t*-BuOK, was prepared (Figure 7.32).

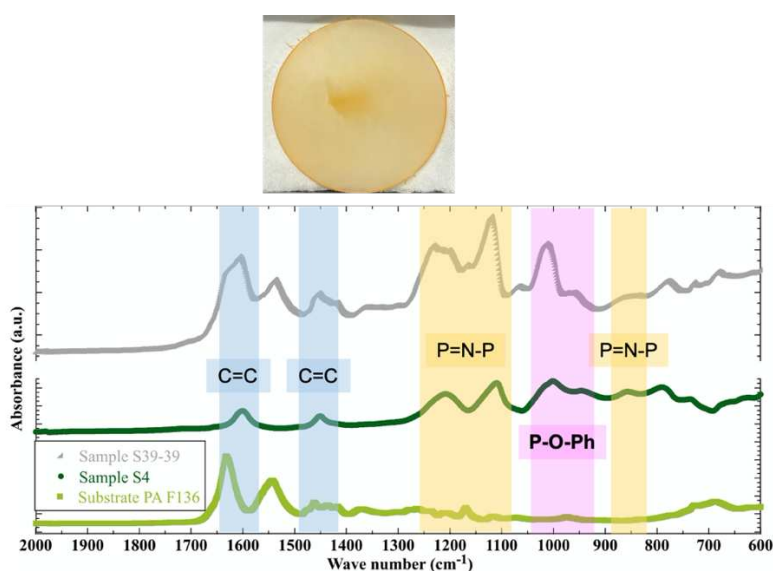


Figure 7.32 Sample S39-39 and its corresponding FTIR spectrum. Also given for comparison are the spectra for sample S4, which shows a Phg-HCCP film spectrum, and for the raw substrate F136.

Without surprise, S39-39 is really similar to S41-41, which was the equivalent sample for FLE40. A film is on formed on some parts of the surface, but it is so thin that it is not well detected by FTIR. This confirms that the MTP2 plasma treatment does allow for the formation of the film even when the deprotonation step is not very efficient.

This Section highlights again that the plasma treatment and deprotonation steps are the key part of the new process. As expected, the parameters giving the best layer for substrate F136 with the MTP2 plasma are the same than those for FLE40 (Table 7.14).

Table 7.14 Parameters for the MTP2 atmospheric plasma and the alkaline solution of *t*-BuOK dissolved in DMSO, for which the best Phg-HCCP film was obtained with the new IP process and new plasma. The support is PA6 F136.

Plasma		<i>t</i> -BuOK solution	
Distance between sample and pen	4 mm	Soaking time of the sample	1 h 30 min
Speed	1500 mm/min	Concentration	0.2 M
Number of passes	2	Dissolution time	2 h 30
Time between plasma initiation and start of treatment	1 min	Extent of washing off the excess	Limited

Although the results of samples S36-36 for FLE40 and S37-37 for F136 are interesting, they are still less good than the first samples made with the new process (samples S20-20 to S23-23, Figure 7.13). This indicates that the vacuum plasma initially used in Twente is more efficient than the atmospheric plasma used later at USMB.

Therefore, it is reasonable to say that, if further studies are still necessary to determine a more optimal protocol, the work done so far allowed the identification of very critical steps and key parameters in the interfacial polymerization of a polyphosphazene film on the surface of an organic dense support. Several additional remarks can be done:

- First, it was observed with the use of the usual process that the drying step between the soaking in each solution is quite critical, whatever the order (Figure 7.6 - step 2 or Figure 7.12 - step 5).
- Then, with the addition of a surface treatment consisting of an exposure to plasma and a deprotonation step, new potential sources of problems appeared. This includes the washing of the surface after the alkaline soaking, which is a key point for the presence of particles on the surface.
- The type of plasma used is also important for the quality of the layer. A vacuum device is better than an atmospheric one but the time of exposure as well as the distance between the nozzle and the surface, seem to be good levers for improvement.

Moreover, a quick study of the water contact angle on a polyamide substrate showed that the effect of the plasma is limited in time, at least for the MTP2 atmospheric type. This was also noticed by Karoly *et al.* [349].

7) C. 4. 3. Estimation of the film/substrate hydrogen permeability

It would be incomplete not to mention the most interesting target property of this project, *i.e.* hydrogen permeation. A measure of hydrogen permeation on the raw PA6 FLE40 support was made. Then, the intention was to make further measures on these supports after coating with a layer of the Phg-HCCP polymer. However, the deposition of a completely satisfactory film was not obtained on the supports and there were issues with the permeation analyses.

Nonetheless, using the hydrogen permeability coefficient of the substrate and, by making the assumption that the hydrogen permeability coefficient found for the film on the surface of a porous substrate (cf. Chapter 6) is the intrinsic value of this film, a “theoretical” result can be estimated for the value for the combined Phg-HCCP film/substrate. The estimations are based on Figure S7.5 and Tables S7.2, S7.3 and S7.4 of the SI and they are also presented in Chapter 1.

The hydrogen permeability coefficient communicated by DSM for a 2 mm thick sample of the PA6 FLE substrate was $76.8 \times 10^{-15} \text{ cm}^3(\text{STP}) \text{ cm cm}^{-2} \text{ s}^{-1} \text{ Pa}^{-1}$. The corresponding estimated value for the combined substrate with a 25 nm thick Phg-HCCP layer was $73.0 \times 10^{-15} \text{ cm}^3(\text{STP}) \text{ cm cm}^{-2} \text{ s}^{-1} \text{ Pa}^{-1}$ (named “Phg-HCCP film 25 nm on PA6”). This estimated value suggest that the benefit of adding a layer on top of this PA substrate is not that significant. However, it still represents a slight improvement in terms of barrier properties and the combined permeability coefficient depends a lot on the thickness of the Phg-HCCP layer. A 25 nm layer is extremely thin compared to 2 mm. If the same estimation is used to extrapolate the value for a barrier material with a modest thickness of 500 nm it would give a permeability coefficient of

$37.3 \times 10^{-15} \text{ cm}^3(\text{STP}) \text{ cm cm}^{-2} \text{ s}^{-1} \text{ Pa}^{-1}$ for the combined system. This represents already half of the permeability coefficient of the support alone.

It is important to recall that the main point of the above study was to obtain defect-free films and, therefore, a real barrier to hydrogen. Indeed, defects present in the films provide many paths allowing hydrogen to pass through and, consequently, increase its permeability coefficient. An example of the influence of the film quality on this permeability is the difference between the value for Phg-HCCP on a porous support in the previous work [260] and in the current study (Chapter 6). There is already a difference of a factor of 100, which underlines the extreme sensitivity of the permeability to the quality of the film. This is why the improvement of Phg-HCCP films is an interesting direction of research for gas storage containment, especially now that its coating on a dense substrate seems possible.

To conclude, Figure 7.33 presents again the published values for the permeability coefficients of some barrier materials for hydrogen, already shown in Figure 6.17 of the previous Chapter, but now includes the value for the raw PA6 support as well as the estimated value for a combined PA6 support with a 25 nm thick Phg-HCCP layer. Again, it is important to note that the measurement methods and thicknesses are different for all points.

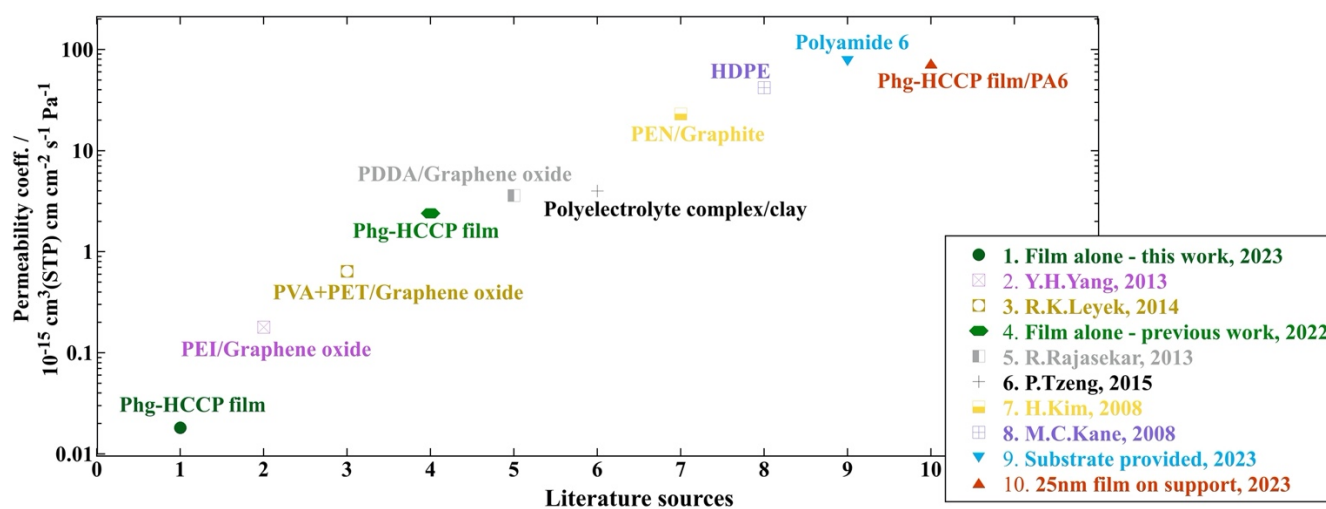


Figure 7.33 Hydrogen permeability coefficients for different barrier materials [76, 94, 98, 315-317]. Phg-HCCP films alone from the current and previous work [133, 260] are in green, the PA6 DSM-provided substrate FLE40 is in blue and the estimated value of this support combined with a 25 nm thick Phg-HCCP film is in red: “25 nm film on support, 2023”.

In Chapter 6, polyphosphazene film synthesized by IP from hexachlorocyclotriphosphazene (HCCP) and phloroglucinol (Phg) were successfully produced on top of a ceramic substrate. However, the

current hydrogen tanks of type IV (cf. Chapter 1, Figure 1.19) are made of three layers whose dense inner liner could be coated with a hydrogen barrier film if this can be grown on a dense support. Therefore, this Chapter tried to improve the existing Phg-HCCP layer by three different ways: deposit it on top of a dense support (1) ensure that it is as continuous and homogeneous as possible (2) and try to obtain a higher cross-linking degree (3). Indeed, despite a good barrier property, such a polyphosphazene film tends to have an intermediate cross-linking under the current conditions. With the assumption that if this cross-linking degree is higher, the permeability coefficient would be lower, different tests were made to increase this cross-linking degree. However, no significant results for aim (3) could be obtained within the time available. However, both aims (1) and (2) were achieved since a quite continuous and homogeneous Phg-HCCP layer could grow on dense supports after the definition of a new IP process including a plasma treatment and a deprotonation step to activate the surface. If there is still scope for improvement, this new protocol is a very promising way to coat a layer on top of an organic dense support.

7) D. Supporting information

Figure S7.1 shows the TGA and DSC curves for both PA6 F136 and FLE40 substrates. They were provided by the DSM company.

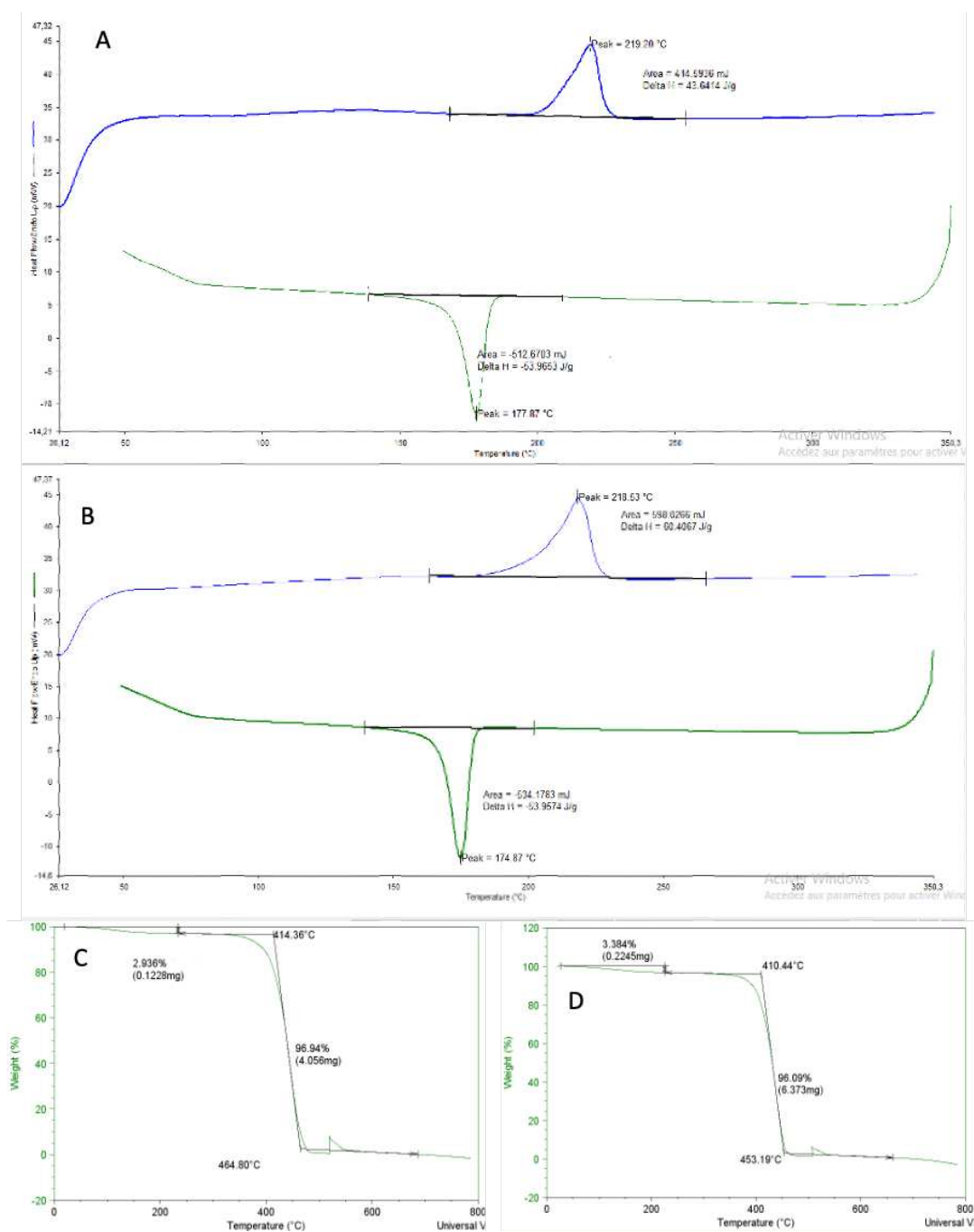


Figure S7.1 DSC curves of PA6 F136 (A), FLE40 (B) and TGA curves of F136 (C) and FLE40 (D).

Table S7.1 indicates the calculations made for the potassium hydroxide mass, which are defined with respect to the ratio of Phg hydroxyl groups to the KOH hydroxyl groups.

Table S7.1 Potassium hydroxide mass calculations.

KOH molecular weight – g/mol	56.11	Fixed
Phg molecular weight – g/mol	126.11	Variable
Number of OH groups in Phg	3	Intermediate results
Number of OH groups in KOH	1	Desired result
Ratio OHPhg/OHKOH	3.5	
m of Phg – g	2.5	
n of Phg - mol	$n_{\text{Phg}} = m_{\text{Phg}}/M_{\text{Phg}}$	
n of OH in Phg - mol	$n_{\text{OHPhg}} = n_{\text{Phg}} * \text{OH}_{\text{Phg}}$	
n of OH in KOH - mol	$n_{\text{OHKOH}} = n_{\text{OHPhg}} * \text{Ratio}$	
n of KOH - mol	$n_{\text{KOH}} = n_{\text{OHKOH}}/\text{OH}_{\text{KOH}}$	
m of KOH - g	$m_{\text{KOH}} = n_{\text{KOH}} * M_{\text{KOH}}$	

Figure S7.2 shows an FTIR measurement measured on sample S10-10 on top of the F136 substrate, and more precisely, the part which looks like crystals. It was compared to the pure HCCP spectrum. It is clearly an agglomerate of unreacted HCCP.

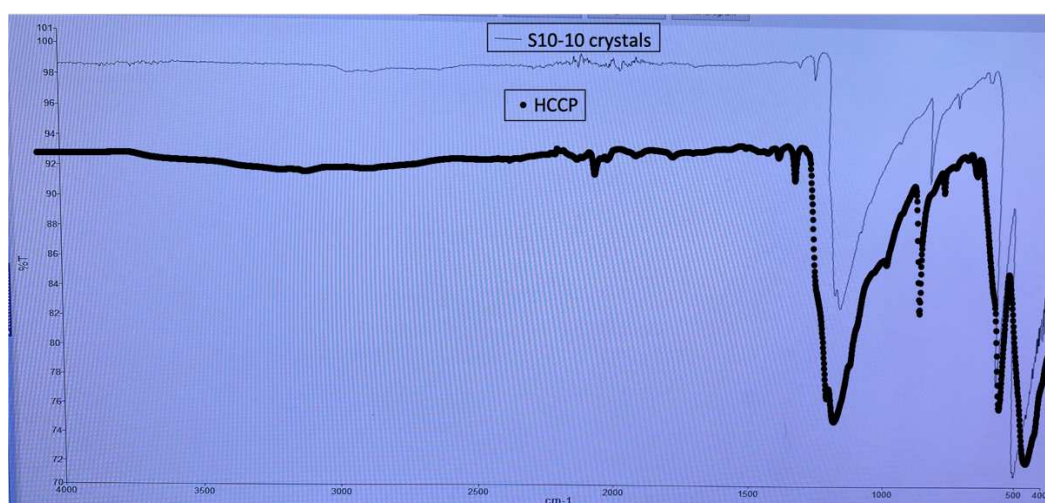


Figure S7.2 FTIR spectrum of sample S10-10. The thin black curve corresponds to the part which looks like crystals on the surface of the sample and the thick black curve to HCCP alone.

The devices not used in the previous chapters are listed in Table S7.1

Table S7.1 Information and parameters of the devices not already presented in previous chapter.

Analysis	Device	Information
Polishing machine	Tegramin 30, Struers, USA	Polishing machine used as surface mechanical treatment
Low-pressure/vacuum plasma cleaner	Femto model 1A, Diener electronics, Germany	Plasma device used as surface chemical treatment
High-density plasma with a low heating effect /Atmospheric plasma	Manual treatment pen MTP2, STTS, France	

Figure S7.3 displays the first set of samples obtained after the addition of a surface treatment in the IP process of Phg-HCCP. They consist of a PA6 substrate along with a “layer” on top. There are two different PA6, both having undergone a different treatment, and the coloured circles correspond to the points where the FTIR measurements were taken.

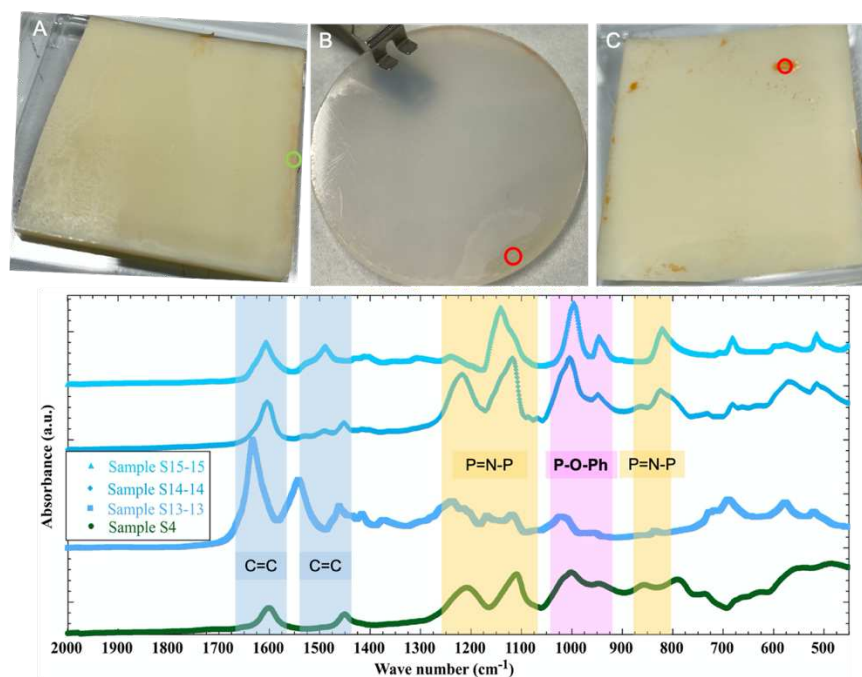


Figure S7.3 Samples S13-13 (A), S14-14 (B) and S15-15 (C) of Phg-HCCP IP on PA6 substrates and their corresponding FTIR spectra. Sample S4 shows a Phg-HCCP film spectrum.

Figure S7.4 presents the SEM pictures of two samples made with the new IP process. They show the granular aspect of the Phg-HCCP film formed on the first samples. This new process includes a plasma treatment and a deprotonation step of the modified surface.

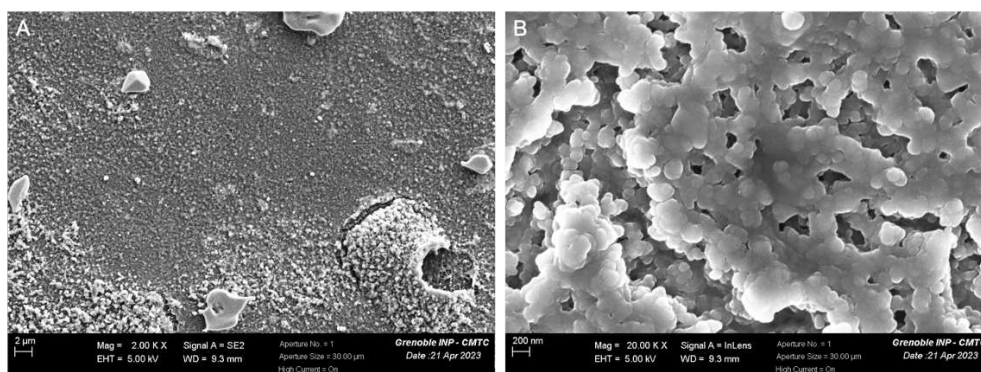


Figure S7.4 SEM pictures of the granular aspect of the film for samples S20-20 (A) and S22-22 (B), which are similar to samples S21-21 and S23-23. They were made with the new IP process.

Figure S7.5 and Tables S7.2, S7.3 and S7.4 define the gas permeation calculations, which were used to estimate the permeability coefficient of hydrogen in a combined Phg-HCCP film on a PA6 substrate. The intrinsic value of the permeability coefficient of hydrogen in the Phg-HCCP film was taken from the result of a gas permeance measurement of the layer on top of a porous ceramic support (cf. Chapter 6). If all the calculations are not detailed here, they are based on the fact that, in a combined system of a layer/support barrier subject to a pressure differential (Figure S7.5), the flux through the support is the same as that through the layer, even if the pressure gradients are not necessarily the same in both, which implies an intermediate pressure, p_I , at the junction between the two layers.

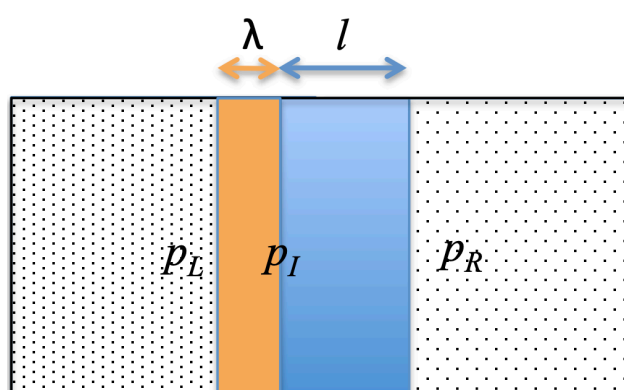


Figure S7.5 A combined layer/support system with different thicknesses (blue and orange rectangles), subject to a pressure differential between their two sides, where $p_L > p_R$ and p_I is the pressure at the interface.

Table S7.2 Gas permeation calculations based on the drawing above.

<ul style="list-style-type: none"> Flux, J, is defined by the amount of gas, Q, passing through the membrane <i>per unit time and per unit surface area</i>. 	S7.1.
$J = \frac{Q}{A \times t}$	
<p>With A, the cross-sectional area of the layer and t, the time it takes for, say, n moles of gas to pass through the membrane. This quantity of gas can also be expressed as an equivalent volume of ideal gas held at the standard temperature and pressure (STP) conditions, $V_{STP} = nRT_{STP}/p_{STP}$, which leads to the unit $\text{cm}^3(\text{STP}) \text{ cm}^{-2} \text{ s}^{-1}$ for the flux.</p>	
<ul style="list-style-type: none"> Permeability coefficient, P_c^s, is the flux divided by the pressure gradient, $\Delta p/l$, applied to the layer of thickness l. Typical units are $(\text{cm}^3(\text{STP}) \text{ cm cm}^{-2} \text{ s}^{-1} \text{ Pa}^{-1})$. 	S7.2.
$P_c^s = \frac{J}{\left(\frac{\Delta p}{l}\right)} = \frac{J \times l}{(p_L - p_R)}$	
<p>With p_L and p_R, the pressure on the left side and right side of the layer and $p_L > p_R$.</p>	
<ul style="list-style-type: none"> Theoretical permeability coefficient, \bar{P}_c, of a system combining a polymer substrate (layer s) of thickness l and a barrier layer, b, of thickness λ, where the pressure $p_R \approx 0$ and their respective flux are the same. 	S7.3.
$\bar{P}_c = \frac{P_c^s \times P_c^b \times (l + \lambda)}{\lambda \times P_c^s + l \times P_c^b} = \frac{(l + \lambda)}{\left(\frac{\lambda}{P_c^b} + \frac{l}{P_c^s}\right)}$	
<p>Where \bar{P}_c^s is the permeability coefficient of the substrate and \bar{P}_c^b is the permeability coefficient of the barrier layer.</p>	

Table S7.3 Experimental values required for the calculation of the effective permeability coefficient of a combined support plus barrier layer system.

Permeability coeff. ($\text{cm}^3(\text{STP}) \text{ cm cm}^{-2} \text{ s}^{-1} \text{ Pa}^{-1}$)	
Polyamide 6 FLE40	Phg-HCCP film alone (supported by a porous ceramic substrate)
Thickness = 0.2 cm (A)	Thickness = 2.5×10^{-6} cm (C)
76.8×10^{-15} (B)	0.0182×10^{-15} (D)

Table S7.4 Calculated value presented in the text, with the references given in the table above.

25 nm Phg-HCCP film on PA6

$$\bar{P}_c = \frac{B \times D \times (A + C)}{C \times B + A \times D} = \frac{7.68E10^{-14} \times 1.82E10^{-17} \times (0.2 + 2.5E10^{-6})}{2.5E10^{-6} \times 7.68E10^{-14} + 0.2 \times 1.82E10^{-17}} = 73.0E10^{-15} \text{ cm}^3(\text{STP}) \text{ cm cm}^{-2} \text{ s}^{-1} \text{ Pa}^{-1}$$

7) E. Acknowledgments

This research forms part of the research programme of Dutch Polymer Institute (DPI), project DINGOES #845. It had access to the resources of the University of Twente, faculty of Science and Technology (TNW), The Netherlands.

7) F. Abbreviations list

➤ BSD	Backscattered detector (BSD)
➤ C/N	Carbon and Nitrogen (elemental analysis)
➤ DMSO	Dimethyl sulfoxide
➤ EDS	Energy dispersive X-ray spectroscopy
➤ FTIR	Fourier transform infrared
➤ HCCP	Hexachlorocyclotriphosphazene
➤ IP	Interfacial polymerization
➤ KOH	Potassium hydroxide
➤ PA	Polyamide
➤ Phg	Phloroglucinol
➤ SE2	Second electron detectors
➤ SEM	Scanning electron microscope
➤ <i>t</i> -BuOK	Potassium <i>tert</i> -butoxide
➤ UV	Ultra-violet
➤ WCA	Water contact angle
➤ XRF	X-Ray Fluorescence

Chapter 8 : Conclusion and Perspectives

8) A. General conclusion and remarks

This work was aimed at improving the hydrogen impermeability of the walls of lightweight composite-based high-pressure gas storage tanks for mobile applications. Indeed, so far, the three-layer type IV tanks (Figure 1.19) are mature enough in terms of technology to be commercialized, but there is still room for improvement in terms of their barrier properties against the permeation of hydrogen. If depressurization occurs rapidly, the mobility of H_2 through the tank walls can lead to severe deformations, delamination and cracking of the reservoirs. Therefore, two possibilities arise to solve this problem: either completely change the inner liner, *i.e.* the layer in direct contact with the hydrogen, or incorporate a hydrogen-barrier coating between the first and the second layer of the tank. This last option was the guideline of this project, which was conducted using two different but complementary approaches: molecular modelling and laboratory experiments.

On the experimental side, the interfacial polymerization (IP) technique was used to synthesize the coating. IP is relatively straightforward to put into operation, it can in principle produce defect-free thin films and it is suitable for large-scale production. However, it can be somewhat laborious to optimize because of its numerous interconnected parameters. For this reason, atomistic simulations were carried out in parallel in order to support the experimental approach by selecting the most suitable parameters for the required barrier application. The former work [260] conducted by the team of Professor Nieck E. Benes at the University of Twente (The Netherlands), and especially, by Dr. Farzaneh Radmanesh, suggested the selection of two candidate monomers for this application: 1,3,5-benzotriol, more commonly referred to as phloroglucinol (Phg), and phosphonitrilic chloride trimer, also known as hexachlorotriphosphazene (HCCP). Indeed, preliminary cross-linked polyphosphazene films synthesized from these two monomers by IP on a porous substrate had shown relatively good hydrogen barrier properties [260]. Therefore, the intention was to confirm the former results, to optimize the hydrogen barrier properties and then coat the polyphosphazene layer on a dense support corresponding to the walls of a hydrogen tank. The work was organised in several steps corresponding to the different Chapters of this document.

8) A. 1. Molecular modelling

The simulation part started with the testing and selection of a suitable hydrogen model amongst the many models available in the literature for this gas [212-229]. Due to their incompatibility with common polymer force fields, some of these models were discarded before making any tests. Eight well-known models based on the Lennard-Jones 12-6 terms for the Van der Waals interactions [212, 215, 217, 218, 221, 222, 225, 228], were checked for their ability to reproduce accurately the experimental data relevant to H_2

storage tanks. The properties of particular interest here are the hydrogen pVT phase diagram and the solubility in its gas phase over a wide range of temperatures (-50°C to 90°C) and pressures (50 to 2000 bars), which are pertinent with respect to the operating conditions of hydrogen-powered vehicles. The models were of various complexity with the number of interaction sites ranging from one to five (Figure 3.1) and 600 MD simulations were conducted. Depending on the models, there were discrepancies of 0.4 to 6.7% with respect to the experimental pVT phase diagram (Figure 3.3 and Table 3.2), whereas differences of 0.9 to 27.9% were found with respect to the experimental gas solubilities (Figure 3.5 and Table 3.4). This study identified the hydrogen model of Yang and Zhong [221] as being the best compromise between realism, simplicity and computational efficiency. It was then used in the last step of the modelling to estimate the permeation properties of H_2 in dense Phg-HCCP models.

However, before building the complex film models, accurate force fields for the intermediates, *i.e.* the pure monomers and small fragments of linked monomers had to be optimized and validated (Figures 4.1 or 5.1). The work was distributed between different members of the USMB team. Separate force fields for both monomers, Phg and HCCP, were developed with respect to their respective crystal structures. These monomer models were further combined to generate dense homogeneous mixtures with different Phg:HCCP stoichiometric ratios, which were the starting points for mimicking the polycondensation reaction. Initial tests were made on an equimolar 1:1 mixture, which gave a density close to that expected for ideal mixing (Figure 4.13). The next stage was the development of potentials for different fragments of the combined monomers. Indeed, when HCCP and Phg are bonded together, changes occur in the “chemical environment” of the atoms. Within the context of producing a molecular network, knowing how the partial charges q vary for each atom is very important. These changes were assessed by considering progressively larger fragments defined by one type of monomer linked to one or more monomers of the opposite type. Knowing that Phg and HCCP can make a maximum of three and six bonds, respectively, different representative fragments were generated (Table 4.5). Since a fragment can have different structures depending on the torsion angle(s) of its linking bridge(s), several conformers had to be considered for each fragment. Their geometries were optimized by *Gaussian09* [203] and the new charges were extracted as a function of the connectivity between the monomers (Table 4.14). Along with parameters taken from the TRIPOS force field [239] and those optimized for the pure monomers, a complete force field was thus obtained for all possible permutations of linked Phg-HCCP molecules.

Starting from homogeneous monomer mixtures and using an algorithm which performed different connectivity changes, atom eliminations and partial charge reassignments, a procedure was developed to mimic the reaction of HCCP with Phg. Over a dozen networks corresponding to different initial monomer

ratios were generated but only seven of them are detailed here. They correspond to the following Phg:HCCP ratios: 1:1, 5:4, 4:3 (two different size systems), 3:2, 2:1 and 3:1. For all of them, their complete connectivity was extracted, *i.e.* how many molecules are present in the systems, how many monomers of each type are in the biggest molecule (\approx network), how many “active atoms” have reacted (Cl or OH), etc. Besides giving a precise idea of the network structure, this can also be compared to available experimental information, as shown in Table 8.1.

Table 8.1 Comparison of the information on the structures of the networks obtained experimentally by IP (Chapters 6 and 7) and by molecular modelling (Chapter 5) starting from mixtures with different monomer ratios. For the experimental results, the average is given when two values are available.

Experimental	Initial or Bulk ratio Phg:HCCP	2:1 = 2 (S6)		4:1 = 4 (S5)		8:1 = 8 (S4)	
	Network ratio Phg/HCCP (estimated, Eq. 6.1)	1.6		1.3		1.4	
	No. of reacted Cl <i>per</i> HCCP – (upper estimate from C/N, Eq. 6.3)	4.8		3.9		4.1	
	No. of reacted Cl <i>per</i> HCCP – all in the network (estimated from P/Cl, Eq. 6.5)	3.8		3.6		3.9	
Simulations	Initial or “Local” ratio Phg:HCCP	1:1 = 1	5:4 = 1.25	4:3 = 1.33	3:2 = 1.5	2:1 = 2	3:1 = 3
	Network ratio Phg/HCCP	1.041	1.285	1.344	1.499	1.969	2.721
	Real no. of reacted Cl <i>per</i> HCCP	3.061	3.689	3.783	4.088	4.859	5.557
	No. of reacted Cl <i>per</i> HCCP – upper (estimated from C/N, Eq. 6.3)	3.0	3.750	4.002	4.500	6.000	9.000
	No. of reacted Cl <i>per</i> HCCP – all in the network (estimated from P/Cl, Eq. 6.5)	2.941	3.588	3.754	4.080	4.859	5.557
	Average ring connectivity	3.000	3.228	3.228	3.272	3.274	2.987

The estimations based on the P/Cl and C/N ratios include all the molecules in the system, *i.e.* the Phg-HCCP network, the excess monomers, the solvents, the by-products, the contaminants, etc. However, the presence of *e.g.* salts in the experiments or unreacted monomers in the models demonstrates that these estimates have their limitations. The experimental elemental analyses cannot resolve between atoms in a network and those that are not. However, in simulations, it is possible to check the estimations against the actual values for the network, *e.g.* the true number of reacted Cl *per* HCCP ring in the network.

Of course, it must be pointed out that a simulated polymerization is much simpler to control than an experimental one. Amongst the simplifications, the most important one is the monomer ratio at the interface. Although the experimental IP can control the starting concentration of each monomer in its separate solution, *i.e.* the bulk ratio, the “local ratio at the interface” leading to the network is unknown. This was confirmed by experimental samples, whose bulk ratios were different but ended up having almost the same estimated ratio in the network (Table 8.1). On the other hand, in a simulated system, the Phg:HCCP ratio set by the user *is* the “local ratio at the interface” and the one really involved in the reaction. In the range of initial monomer model ratios shown in Table 8.1, this clearly leads to a close correspondence to the Phg/HCCP ratio in the network. At higher ratios, Phg is more and more in excess and the correlation inevitably tails away.

Therefore, the connectivity results obtained from an experimental bulk ratio for the initial mixture and a simulation with nominally the same (but a ratio which is more “local”) are not necessarily comparable. However, the experimental results suggest that, when the bulk ratio is 8:1 or 4:1, the Phg/HCCP ratio in the network is ~ 1.3 , *i.e.* $\sim 4:3$. This can be compared to the simulated 4:3 system. Using either the C/N or P/Cl ratio, this leads to experimental estimations between 3.6 and 4.1 out of 6 Cl *per* HCCP, which are perfectly consistent with the value of 3.8 found for the model network. In both cases, not all the Cl react. In the models, increasing the local ratio in the initial monomer mixtures up to 3:1 increases the number of reacted Cl *per* HCCP ring in the network up to over 5.5, *i.e.* close to the maximum possible. Experimentally, adjusting the bulk ratios appears to have much less of an effect on the resulting films. Varying the local ratio in the simulated systems also reveals that the average indiscriminate ring connectivity, or degree of cross-linking, passes through a maximum for a ratio of 2:1 (Table 8.1). This maximum has interesting correlations with other measures made on the network polymers.

Amongst the results extracted from the model networks, there are some mechanical parameters: the elasticity behaviour, Young’s modulus and Poisson’s ratio. They were evaluated from uniaxial compression tests and the networks were all found to have elastic recovery (Figure 5.14). Young’s modulus generally increases with the initial monomer ratio in the mixtures before passing through a maximum at a ratio of 2:1 (Figure 5.15). This correlates well with the cross-linking degree. Poisson’s ratio shows no clear trend with the initial ratio but does have a minimum value at a ratio of 2:1 (Figure 5.15). This suggests that there is a close correlation between the high degree of cross-linking and the structural response of the network polymer.

Finally, the hydrogen permeation behaviour inside these networks was also modelled and it was found that (Figure 5.21 and Tables 5.6 and 5.7):

- The H₂ solubility coefficient varies by no more than a factor of two between the various networks simulated but at the higher Phg/HCCP ratios it starts to decrease.
- The H₂ diffusion coefficient is very sensitive to the Phg/HCCP ratio and decreases by a factor ~16 between the 1:1 and 2:1 systems. Indications from simulations in progress suggest strongly this trend continues at even higher ratios.
- The trend for the H₂ permeability coefficient is largely set by that of the diffusion coefficient but is reinforced also at the higher ratios by the decreasing solubility coefficient. There is a twentyfold decrease in going from the 1:1 to the 2:1 system and the indications from work in progress are that the minimum value of the permeability coefficient clearly occurs at ratios higher than the 2:1 ratio presented here.

To conclude, the atomistic level simulations allowed a detailed investigation of the connectivity of the model networks and an assessment of their highly sensitive dependence on the local ratio of the initial monomer mixture at the interface. The impact on the behaviour of H₂ in the Phg-HCCP networks was also investigated and found to be highly related to the underlying details of the various structures tested. A clear trend was identified of a rapid decrease in diffusion, and hence permeability, at the higher Phg/HCCP ratios studied suggesting that the optimum intrinsic barrier properties of the network occur at a Phg/HCCP ratio greater than 2:1. The discrepancies with the experimental values for the permeability coefficient suggest that trapped molecules, such as contaminants, excess monomers, by-products and salts, may also play a significant role in defining the effective barrier properties of the Phg-HCCP film.

8) A. 2. Interfacial polymerization

The first step was to repeat the experiments done by Radmanesh *et al.* [260] so as to verify the reproducibility of the results. The selection of the monomers was based on this work because the polyphosphazene film produced earlier had shown quite good barrier properties with a hydrogen permeability coefficient of $2.5 \times 10^{-15} \text{ cm}^3 \text{ cm cm}^{-2} \text{ s}^{-1} \text{ Pa}^{-1}$. Before trying to improve these properties, it was found that when the same process was strictly followed, it gave a similar product in terms of composition but slightly better in terms of crosslinking. This led to a much lower permeability coefficient of $0.0182 \times 10^{-15} \text{ cm}^3 \text{ cm cm}^{-2} \text{ s}^{-1} \text{ Pa}^{-1}$ for H₂ (Figure 6.17). It really illustrates the sophistication and sensitivity of the IP technique.

A second study using a one-solution polymerization approach led to the conclusion that a similar product seemed to be formed using either bulk or interfacial polymerization, *i.e.* a Phg-HCCP polymer. The advantages of IP are that it is in principle able to produce directly a defect-free thin film on a support, but

the aim of testing also bulk polymerization was to produce a thicker layer, which is easier to analyse than a thinner one. Analyses of the amount of each type of element suggested a Phg/HCCP ratio in the network of about 4:3 and that not all the -Cl or -OH react, which means a film with an intermediate cross-linking degree (Tables 7.2 and 7.3). As noted in the previous Section, the maximum number of chlorine groups reacting *per* HCCP ring is about 4, out of 6, a value consistent with the simulated network having a 4:3 ratio. Molecular modelling strongly suggests that if the Phg/HCCP ratio is higher than the 2:1 ratio, that which gives the maximum amount of cross-linking, the permeability coefficient should be even lower and the barrier properties better. It should be noted that, in some cases, a higher degree of cross-linking also introduces a higher steric hindrance and can lead to a lower-density material with higher free-volume [76, 351]. Guided by the molecular modelling results on Phg-HCCP networks, increasing the experimental cross-linking degree towards higher values was seen as the most promising way to improve the existing Phg-HCCP layer. The intention was to do this by modifying specific IP parameters.

In addition, part of the work focused on attempting to deposit with IP a continuous and homogeneous film on a dense polyamide support, as used in the inner liners of hydrogen storage tanks. Up to this point, the IP layers had only been successfully produced on substrates, which do not correspond at all to the current hydrogen tanks wall (Figure 1.19). For this reason, attempts to grow the film on the surface of two different polyamide 6 (PA6) supports, one of them being actually used in the hydrogen type IV tanks, were made. Following several trials with various surface treatments of the PA6 supports, a new optimized IP process was designed. It included a plasma treatment of the surface of the support, a deprotonation step of this new activated surface using a very strong base (Figure 7.12) as well as an inversion of the order of application of the monomers. It allowed films of different qualities to be produced on the surface of the PA6 supports. Although the precise mechanism of this new process is unclear, it is known that the plasma treatment affects the substrate surface by either introducing new functions or breaking bonds and introducing new reaction sites *via organic* bonds. This new protocol would probably not work on *inorganic* dense substrates such as silicon wafers, but it is certainly highly adapted to applications such as the H₂ storage tanks.

Another important comment about this new process is that, if it is still an IP, it most likely does not involve a “liquid-liquid” interface but rather a “solid-liquid” interface. Indeed, IP is not limited to two liquid phases [146], since the reaction can occur as long as an interface is present between the immiscible medias containing the monomers. This different type of interface could be between the HCCP crystals, which are first coated on the surface, and the Phg in a solution of DMSO, which is added afterwards. Indeed, performing a “solid-liquid” interfacial polymerization has already been reported by Qi *et al.* [352]. They

used a slightly different process with the solvents being crystallized and the monomers forming a layer on these crystals. They were then put into contact with the other reactants dissolved in another solvent. Therefore, modifying the type of interface generated could be one of the ways to improve the layer.

8) B. Future work

The project was clearly larger than what could be reasonably accomplished within a thesis. Therefore, there are several on-going studies that have to be finished and there are a number of follow-up studies that could be done, either on the modelling or on the experimental side. Some of the propositions are presented hereafter.

8) B. 1. Molecular modelling

Amongst the studies carried out to adapt and develop models for the various types of molecules tested, there is certainly room for improvement.

For hydrogen, the tests made on a range of pressures and temperatures related to the gas storage application already revealed some shortcomings in the available empirical models. There is certainly a possibility to refine an existing model to have a better agreement between simulation and experiment.

For the pure Phg and HCCP monomers, the refinements led to a good stability of the crystal structures. Nevertheless, there is sufficient experimental data on the crystal structures against which to test the models at more temperatures than attempted.

For the combined-monomer fragments, many were tested, but examining more of them would lead to more precision, especially now that the study revealed that the double links of a phosphorus are more than likely. Indeed, Tables S5.2 and S5.3 show that the percentage of P-O₂ groups is never below 22% and can go up to 86%, *i.e.* the probability of having several P bonded to two O is not negligible. Considering that all the Cl can react, whether they are on the same P or not, would increase the number of fragments from the initial 6 considered (Table 4.5) to 10, including all their conformers.

For the networks, some work is under progress with additional Phg:HCCP ratios, such as 4:1, 5:1 and 8:1, but with the maximum distance criterion used to define the reaction between an O and a Cl atom being set to 2.8 Å (Figure 5.2). This work should establish more precisely at what ratio the intrinsic barrier properties of the network are optimal. Another point is that unreacted monomers were found to remain in the final configurations and they are likely to participate to the barrier property of the network. If experimentally excess monomers are not present in the networks or if they are washed out during the IP

procedure, some simulations should be run without this excess, in order to check whether this affects the permeation behaviour.

8) B. 2. Interfacial polymerization

Unlike the simulation part, no future work has been started yet for the experimental part. However, several questions remain as well as prospects for improving the Phg-HCCP layer. Indeed, even if very promising results were obtained (especially for samples S20-20 to S23-23), the layers are still not totally defect-free, perfectly attached to the surface and their barrier properties have not been tested.

Some questions, which still need to be answered, are:

- On some samples made with the new process (cf. Chapter 7), whatever the plasma used, the layer also grew on the underside of the substrate despite a very low probability that this part was treated by the plasma. The deprotonation step was found to be insufficient to allow the attachment of the layer to the substrate. This is thus the combination of both steps which allows the promising results. Therefore, how can a layer which seems quite well-formed and attached on some samples, *e.g.* S20-20 to S23-23, be produced on this “hidden” face?
- It was noticed that particles tend to remain on the surface of some of the substrates after the first two steps of the new process and that they can be removed from this surface during either the final washing and/or drying step, thus leaving hollows, holes and cracks in the film. Beside the nature of those contaminants (salts? *t*-BuOK? solvent?), why are they eliminated on some samples and not on others?

The quality of the layer could be improved by working either on the “usual” process, on the “new” process, or by completely changing the process of polymerization.

The “usual” process is the one used so far for IP on top of a support and described in Figures: 2.9, 6.13 and 7.6. Some of the parameters changed were both soaking times in the monomer solutions, *i.e.* in HCCP/cyclohexane and in Phg/KOH/DMSO, the temperature and the drying step between the addition of each solution. Continuing with changes to these conditions is an option. Temperatures below ambient could be tested. Removing the excess of the first solution, *i.e.* the drying step, is definitely critical and could be studied more in-depth. Another factor of improvement is the deprotonation step of Phg, in KOH/DMSO. It sets the extent of conversion of hydroxyl groups into active O⁻, which then will react with HCCP to form the network. However, KOH is poorly soluble in DMSO and several changes, such as increasing the time and temperature or varying the KOH concentration, have already been investigated, both in this work and

before [260]. An option to favour the deprotonation of Phg would be to replace either the base, by *e.g.* triethylamine, or the solvent, by *e.g.* acetonitrile [285], as reported by Zhang *et al.* [312]. Furthermore, IP has a lot of other interconnected parameters which can be modified to tune the film properties (Figure 2.10). If some of them are fixed as long as the same chemistry is used (for example the diffusivity of the monomers), some others can always be varied. In addition to the ones mentioned above, these include the reaction times or the cleanliness and pore size of the substrate, the type of additional product or solvent or even the stirring during the reaction which could regulate the local concentration at the interface. A last option is the production of another type of interface, such as one reactant in solution and the other in the gas form. This would require other monomers, but Du *et al.* [353] have reported the synthesis of polyaniline microtubes with a gas-liquid IP using supercritical CO₂ to supply the vapour phase reactant. Lei *et al.* [354] have used an aqueous solution of one monomer to fill the pores of a substrate, which was then exposed to an inert gas stream containing the second monomer.

The “new” process (Figure 7.12) can also be enhanced. Its factors of improvement can be categorized into two groups: the ones already modified in this work, but for which more values could be tested, and the ones never changed and which could be adjusted. As the new process mainly focuses on the first two steps, the factors discussed here are only specific to the surface treatment and the deprotonation and they are summarized in Table 8.2.

Table 8.2 Factors of improvements for the new IP process defined for the HCCP and Phg monomers.

Already modified	Surface treatment	➤ In the last part of the study with the new process, the surface treatment was provided by atmospheric plasma. This device allows to change only the speed, number of passes and distance to the surface of the sample. If the effect of the latter was found to be not significant, the two others could still be adjusted and indeed, their increase seems to give good results. Therefore, continuing in that direction could be interesting.
		➤ Although quite a good layer was obtained with the atmospheric plasma, an even better film was produced with a vacuum plasma. Therefore, going further with the vacuum device and adjusting its parameters, <i>i.e.</i> time and power, is also an option.
	Deprotonation	➤ The step following the surface treatment was found to be a key point for the quality of the layer, <i>e.g.</i> it could control the formation of contaminants on the surface. The increase of the <i>t</i> -BuOK base concentration gives good results, it must be further investigated.
		➤ The extent of washing of the alkaline solution after the soaking also strongly impacts the quality of the film. This washing should be quantified precisely and then adjusted to have the best compromise between removing enough of the solution to avoid contaminants without disturbing the activation of the surface.

Never modified	Surface treatment	➤ A mechanical surface treatment could be used instead of a chemical one. Preliminary results were interesting, especially for the PA6 FLE40 substrate (cf. Chapter 7).
		➤ The chemical treatment could be kept, but changing the device or technique used is an alternative.
	Deprotonation	➤ If <i>t</i> -BuOK was chosen for its ability to deprotonate the groups newly deposited on the surface of the support and its availability, using another base with the same properties is possible as long as it can be dissolved in DMSO or, if the solvent must be changed, that it does not damage the substrate.

The last scope for improvement is completely changing the “manufacturing technique” (see Chapter 1) to replace the interfacial polymerization. However, certain difficulties can arise from the monomers used. Indeed, an attempt was made to spin-coat the solution containing the bulk polymerization product, but its viscosity was too high. It is also expected that, similar to spin-coating, the solution would also most likely be too viscous for tape casting or dip-coating. Inversely, this solution obtained by bulk polymerization could be involved in a phase inversion process, since regardless of whether it is very liquid or viscous, it will be converted into a solid layer. However, there is still most likely a viscosity limit and, depending on the process used, the solvent will probably have to be changed, *e.g.* for precipitation by controlled evaporation (Figure 1.52). The grafting approach could probably work as it also implies a treatment of the surface and, therefore, it could be adapted to the new IP process defined in this work. Then, the self-assembly by charged surface technique could be carried out if the deprotonation of Phg is enough to consider the monomer as an ion, which can then react with the surface. To conclude, the methods that are most likely to work are those placed in the same category as the IP, *i.e.* the bottom-up approach (Figure 1.45).

Résumé en français

Depuis le milieu des années 1900, l'influence de l'Homme sur la planète est devenue le principal facteur du réchauffement climatique et a déjà altéré le fonctionnement de la nature.

Le **Chapitre 1** de ce manuscrit fait un rapide état de l'art de la situation écologique dans le monde et rappelle que la civilisation humaine doit maintenant effectuer une transition des énergies fossiles vers les énergies renouvelables. Cela passe notamment par une décarbonisation de son industrie des transports. Dans ce contexte, l'hydrogène émerge comme une solution logique en raison de son abondance, sa haute capacité énergétique et le fait qu'il n'émette pas de CO₂ lors de sa combustion. Dans le cadre de la mobilité, il est utilisé comme vecteur d'énergie dans les voitures à piles à combustibles. En effet, avec seulement 5 kg de ce gaz, ces véhicules peuvent *a priori* rouler jusqu'à 600 km. Cependant, le principal inconvénient de l'hydrogène est son volume à température et pression ambiante, puisque 5 kg correspondent à environ 60 m³. Si trois méthodes principales existent pour réduire le volume[22, 48, 49, 54], seul le stockage à haute pression peut être utilisé dans les voitures à hydrogène. Elles sont donc équipées de réservoirs à H₂ comprimé jusqu'à 700 bars (Figure R.1).

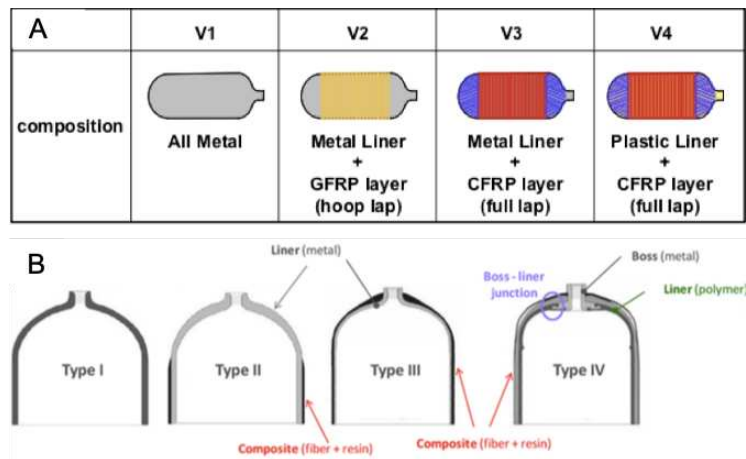


Figure R.1 Les différents types de réservoirs à haute pression d'hydrogène. GFRP signifie "Glass Fibre Reinforced Plastic" et CFRP à "Carbon Fibre Reinforced Plastic". On distingue les types I (ou V1), II (ou V2), III (ou V3) et IV (ou V4).

Seuls les réservoirs de Type IV sont utilisés pour les voitures légères et ils sont constitués de trois couches : un liner intérieur en plastique et deux parois extérieures en composites renforcés par des fibres de verre. Si contrairement aux types I, II et III, la couche intérieure en polymère n'est pas sensible au problème de fragilisation par l'hydrogène, elle est en revanche sujette à des déformations permanentes et parfois à des fissures, dû à une dépressurisation du réservoir trop rapide. Il s'agit d'un phénomène rencontré

quand la pression diminue d'un coup et que la vitesse de décompression excède celle à laquelle le gaz absorbé dans le polymère s'échappe par diffusion. Des fractures et contraintes internes sont alors générées et finissent par endommager le liner. Afin de réduire ces problèmes, il a donc été proposé d'incorporer dans ces réservoirs à hydrogène un film mince polymère additionnel à propriétés barrières pour H₂. Cette nouvelle couche doit être stable dans une large gamme de températures (-40°C à 80°C) et de pressions (50 à 700 bars). Si des matériaux « barrières » existent déjà, leurs propriétés sont souvent limitées dans de telles conditions. Ils doivent aussi pouvoir être fabriqués sous formes de films. Différentes techniques existent, dont la polymérisation interfaciale (IP).

L'IP est utilisée pour les synthèses de ce projet et elle est décrite dans le **Chapitre 2**. Elle permet d'obtenir des films minces, résistants et sans défauts en formant un réseau polymère à l'interface de deux solvants non miscibles, comme le montre la Figure R.2.

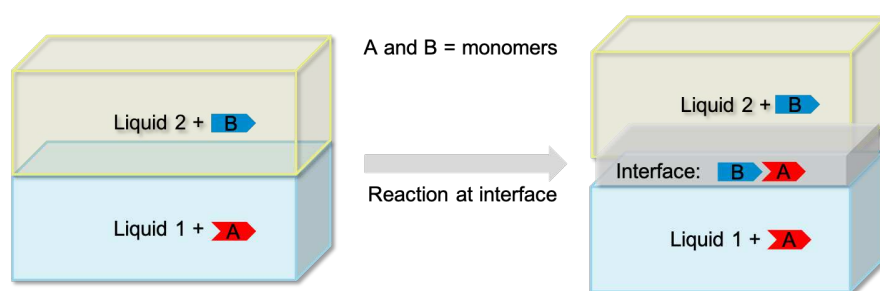


Figure R.2 La polymérisation interfaciale (IP) a lieu à l'interface entre un liquide 1 contenant le monomère A et un liquide 2 contenant le monomère B, les deux liquides étant immiscibles.

Deux types de films peuvent être obtenus avec l'IP. La première approche concerne des « free-standing films » qui, une fois collectés, rincés et filtrés, donnent une poudre qui peut être caractérisée par des analyses élémentaires pour la composition ou par gravimétrie pour le comportement thermique. La seconde approche concerne des films qui sont déposés à la surface d'un substrat à la manière d'un revêtement, aussi appelés « films on support ». Elle apporte de la résistance mécanique aux films et permet de les caractériser avec des techniques nécessitant des échantillons plus robustes telles que la spectroscopie infrarouge, visible, ultraviolet et à résonance magnétique nucléaire ou encore l'ellipsométrie, la microscopie électronique à balayage et les mesures de perméance. Si la polymérisation interfaciale est une technique facile à utiliser et applicable à une large gamme de polymères, elle dépend cependant beaucoup de paramètres interconnectés qui affectent les propriétés du film produit. Sa mise en œuvre peut donc s'avérer complexe en raison des difficultés associées à ces nombreux paramètres, par exemple la pureté des monomères qui ne peut pas être contrôlée *in situ*.

Le but du projet étant de déposer un film avec des propriétés barrières à H₂ les meilleures possibles, des simulations de modélisation moléculaire ont été menées en parallèle pour aider à la sélection des paramètres-clés susceptibles d'influencer les propriétés des membranes synthétisées par IP. La technique principale de modélisation est la dynamique moléculaire (DM), qui permet d'étudier les propriétés statiques et dynamiques des polymères à l'échelle atomique. Les lois du mouvement de Newton sont résolues numériquement pour tous les atomes d'un système, afin d'obtenir leurs positions en fonction du temps, c'est-à-dire leurs trajectoires. Pour cela, il est nécessaire de modéliser l'énergie potentielle résultant des interactions de chaque atome avec ses voisins (Figure R.3).

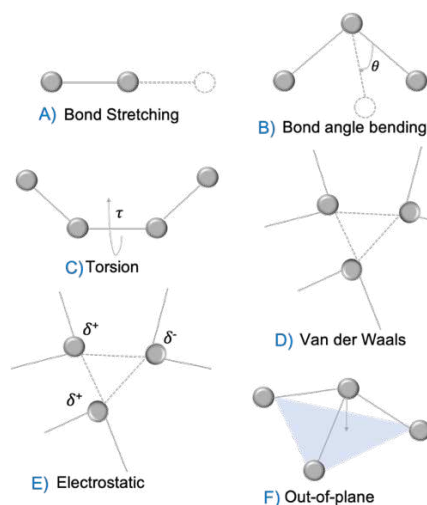


Figure R.3 Principales interactions atomiques dans les molécules. Elles correspondent aux potentiels typiques utilisés dans les simulations de DM.

Chaque type d'interaction est représenté par des équations mathématiques (ou potentiel) contenant plusieurs paramètres variables ainsi que certaines constantes physiques. Les termes variables dépendent de la nature chimique et de la position des atomes et définissent le « champ de force » ou modèle spécifique pour les molécules considérées. Les paramètres peuvent être obtenus à partir de données expérimentales, de calculs *ab initio* ou être déjà disponibles dans la littérature, comme pour l'hydrogène.

Afin de pouvoir modéliser des films complexes de polymères, il a fallu construire ou sélectionner, parmi les existants, des modèles pour chaque composant et les confronter aux données expérimentales disponibles. Pour la première étape, décrite dans le **Chapitre 3**, plusieurs modèles de H₂ dans la littérature ont été envisagés afin de trouver le plus adapté sur l'ensemble d'une gamme étendue de températures et de pressions des réservoirs, c'est-à-dire $-50^\circ\text{C} < T < +90^\circ\text{C}$ et $0 < P < 2000$ bars. 600 simulations de DM basées sur huit modèles classiques ont été comparées avec des données expérimentales sur H₂, telles que le

diagramme de phase pVT et la solubilité en phase gazeuse. À l'issue de cette sélection, le modèle de Yang et Zhong a été choisi comme le meilleur compromis entre réalisme, simplicité et efficacité de calcul.

Dans une seconde étape correspondant au **Chapitre 4**, les champs de forces des monomères sélectionnés pour l'IP, le phloroglucinol (Phg) et l'hexachlorocyclotriphosphazène (HCCP), ont été optimisés séparément sur les structures cristallines des deux composés. Ces deux monomères ont été choisis car ils avaient précédemment montré de bonnes capacités barrières. En plus de la DM, cette optimisation a nécessité le recours aux méthodes de théorie fonctionnelle de la densité (DFT) et de minimisation énergétique (EM). Les modèles de Phg et de HCCP ont alors permis de créer des mélanges sans séparation de phase nécessaires avant d'aborder la polymérisation. Il a également fallu compléter le développement du champ de forces global en étudiant et en optimisant de nombreux fragments de monomères liés, tout en tenant compte de la multiplicité de leurs conformères (Figure R.4). En effet, les paramètres, et en particulier les charges partielles, sont susceptibles de varier quand l'environnement chimique des atomes est modifié.

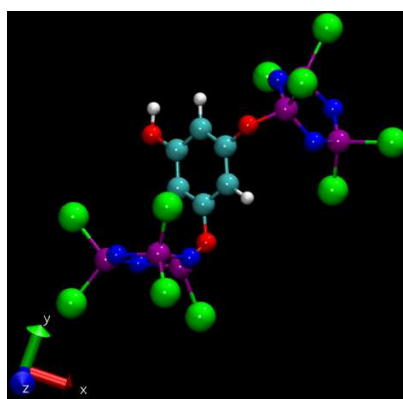


Figure R.4 Un Phg lié à deux HCCP formant un fragment de monomères liés (cyan = C ; rouge = O ; blanc = H ; bleu = N ; violet = P and vert = Cl).

La création de réseaux polyphosphazènes Phg-HCCP à partir de mélanges de monomères avec des ratios différents est décrite dans le **Chapitre 5**. Une fois ces réseaux générés, leurs propriétés mécaniques, de sorption et barrières à l'hydrogène ont été testées afin de caractériser les ratios susceptibles de conduire expérimentalement aux meilleures propriétés. En plus de la DM, les méthodes utilisées pour cette phase sont l'insertion de particules-tests (TPI) ainsi que les simulations de Monte Carlo dans l'ensemble grand-canonique (GCMC). Ces tests ont notamment démontré que le degré de réticulation dépend fortement du ratio initial des monomères et qu'il augmente par corrélation positive avec ce ratio. De même, le coefficient de perméabilité diminue très significativement quand le ratio des monomères augmente. Le ratio optimal prédit par la modélisation est le mélange avec le ratio Phg:HCCP le plus élevé.

En parallèle de ces modélisations, le **Chapitre 6** montre que plusieurs films minces de polyphosphazène Phg-HCCP ont été synthétisés par IP, à la fois sous forme free-standing et sur des supports poreux, afin de reproduire des résultats préliminairement obtenus. Ils ont été caractérisés pour estimer l'effet des différents paramètres sur les morphologies et les propriétés des films. Leurs capacités barrières ont été évaluées et sont très prometteuses puisqu'un coefficient de perméabilité à l'hydrogène assez bas ($1.8 \times 10^{-17} \text{ cm}^3 \text{ (STP) cm cm}^{-2} \text{ s}^{-1} \text{ Pa}^{-1}$) a pu être obtenu. Cependant, le degré de polymérisation ainsi que la qualité globale de ces films restent à améliorer.

Le **Chapitre 7** rend compte du travail mené pour améliorer les films Phg-HCCP, selon 3 axes: (1) produire une couche sur un support dense représentatif des réservoirs (2) qui doit être aussi continue et homogène que possible et (3) avec un réseau polymère ayant un degré de réticulation plus élevé ou, à défaut, un coefficient de perméabilité le plus bas possible pour H_2 . Le premier objectif a été atteint avec des films minces déposés sur des supports de polyamides denses fournis par des industriels. Il s'agit de matériaux déjà utilisés comme liners dans les réservoirs. Pour produire ces films, un nouveau protocole de dépôt, incluant un traitement de surface par plasma et une étape de déprotonation, a été développé (Figure R.6).

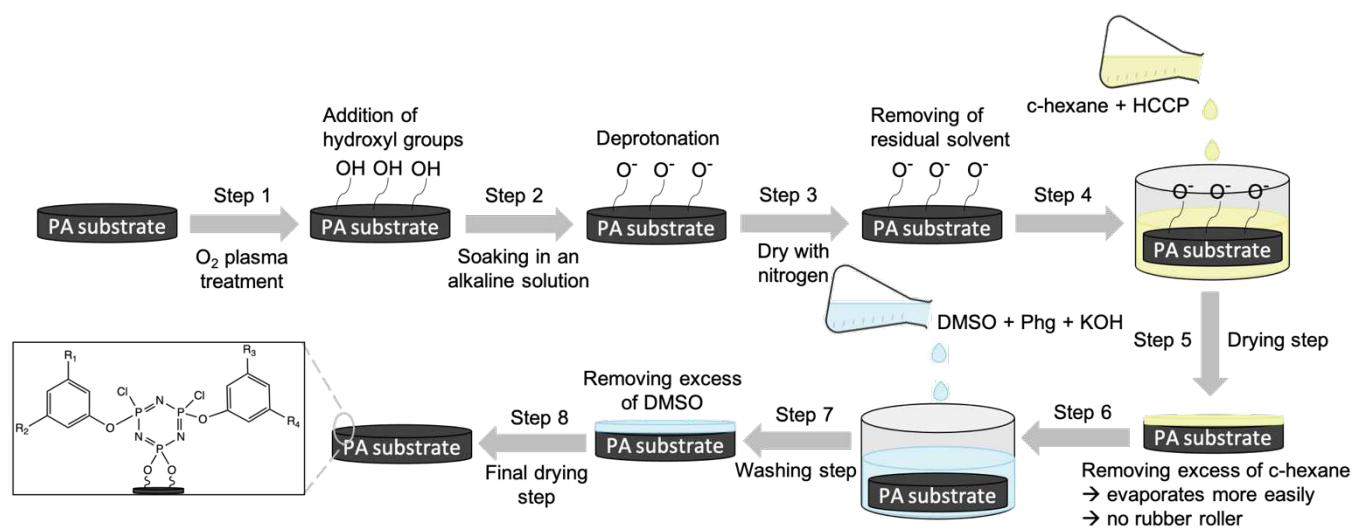


Figure R.5 Le nouveau procédé de polymérisation interfaciale d'un film Phg-HCCP sur un substrat dense en polyamide.

Le deuxième objectif a aussi été atteint pour certains des échantillons synthétisés avec le nouveau procédé. Si le degré de polymérisation est difficilement évaluable expérimentalement, dû à la présence de sous-produits de la réaction ou de monomères n'ayant pas réagi, une valeur théorique pour le coefficient de perméabilité à l'hydrogène a pu être calculée. La Figure R.6 compare cette valeur avec certains matériaux barrières existant pour l'hydrogène, ainsi que les films obtenus sur supports poreux (Chapitre 5). Il est

important de noter que les méthodes de mesure et les épaisseurs sont différentes pour tous les points, et qu'il aurait été nécessaire d'avoir plus de temps pour améliorer le troisième objectif, c'est-à-dire le film barrière sur le support polyamide.

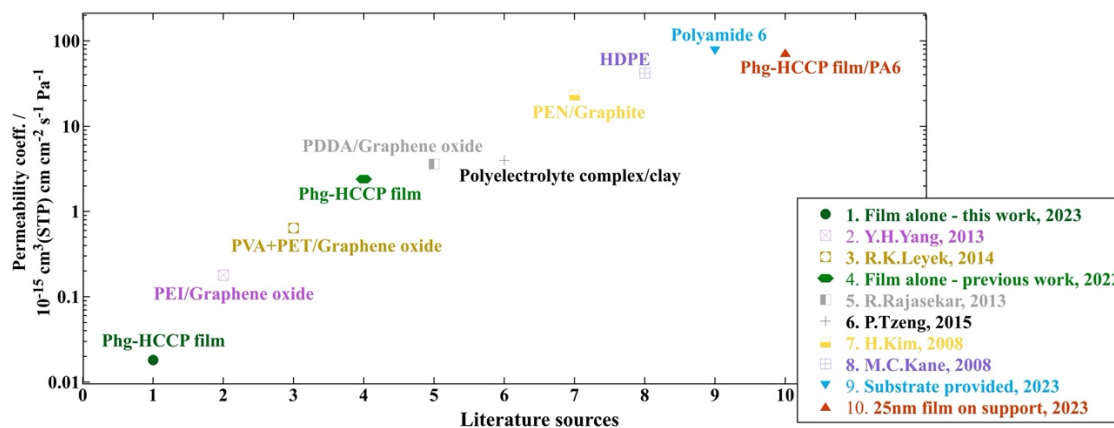


Figure R.6 Coefficients de perméabilité à l'hydrogène de différents matériaux barrières. Les films Phg-HCCP sur des supports poreux (issus des travaux actuels et antérieurs) sont en vert. Le substrat polyamide 6 fourni est en bleu et la valeur théorique du support avec le film est en rouge : « Film 25 nm sur support, 2023 ».

Le **Chapitre 8**, conclut ce manuscrit et récapitule les études encore en cours ainsi que les perspectives à suivre pour améliorer encore les films Phg-HCCP.

References

- [1] E. Hemingway, *For whom the bell tolls*, Scribner, New York, 1940.
- [2] IPCC, 2023: *Climate change 2023: Synthesis report. Contribution of working groups I, II and III to the sixth assessment report of the intergovernmental panel on climate change [core writing team, H. Lee and J. Romero (eds.)]*, IPCC, Geneva, Switzerland, 1-34 pp., <https://www.ipcc.ch/report/sixth-assessment-report-cycle/>.
- [3] IPCC, 2018: *Summary for Policymakers. In: Global Warming of 1.5°C. An IPCC Special Report on the impacts of global warming of 1.5°C above pre-industrial levels and related global greenhouse gas emission pathways, in the context of strengthening the global response to the threat of climate change, sustainable development, and efforts to eradicate poverty [Masson-Delmotte, V., P. Zhai, H.-O. Pörtner, D. Roberts, J. Skea, P.R. Shukla, A. Pirani, W. Moufouma-Okia, C. Péan, R. Pidcock, S. Connors, J.B.R. Matthews, Y. Chen, X. Zhou, M.I. Gomis, E. Lonnoy, T. Maycock, M. Tignor, and T. Waterfield (eds.)]*, World Meteorological Organization, Geneva, Switzerland, 32 pp., <https://www.ipcc.ch/sr15/>.
- [4] French government, 2015 *Paris Climate Conference (COP21)*, <https://www.diplomatie.gouv.fr/en/french-foreign-policy/climate-and-environment/2015-paris-climate-conference-cop21/>, (last accessed 12th October 2023).
- [5] National Geographic Society, *Fossil fuels*, <https://www.nationalgeographic.org/encyclopedia/fossil-fuels/>, (last accessed 12th October 2023).
- [6] IPCC, 2014: *Climate Change 2014: Synthesis Report. Contribution of Working Groups I, II and III to the Fifth Assessment Report of the Intergovernmental Panel on Climate Change [Core Writing Team, R.K. Pachauri and L.A. Meyer (eds.)]*, IPCC, Geneva, Switzerland, 151 pp., <https://www.ipcc.ch/report/ar5/syr/>.
- [7] Université Paris-Saclay, ENSTA IP Paris, *MOlecules and Materials for the ENergy of TOMorrow (MOMENTOM)*, <https://www.fun-mooc.fr/en/courses/molecules-and-materials-energy-tomorrow-momentom/>, (last accessed 11th October 2023).
- [8] Air Liquide, *Hydrogen energy*, <https://www.airliquide.com/fr/science-nouvelles-energies/energie-hydrogene>, (last accessed 12th October 2023).
- [9] Hydrogen Europe, *Welcome to Hydrogen Europe*, <https://hydrogeneurope.eu/>, (last accessed 12th October 2023).
- [10] H₂ mobility Deutschland, *H₂ mobility*, <https://h2.live/en/h2mobility>, (last accessed 27th January 2021).
- [11] DSM, *Climate & Energy*, <https://www.dsm.com/corporate/solutions/climate-energy.html>, (last accessed 27th January 2021).
- [12] French government, *Stratégie nationale pour l'hydrogène décarboné : lancement de deux appels à projets pour constituer des écosystèmes territoriaux autour de l'hydrogène*, <https://www.enseignementsup-recherche.gouv.fr/cid154923/strategie-nationale-pour-l-hydrogene-decarbone-lancement-de-deux-appels-a-projets-pour-constituer-des-ecosystemes-territoriaux-autour-de-l-hydrogene.html>, (last accessed 12th October 2023).
- [13] Royal Society of Chemistry, *Periodic table*, <https://www.rsc.org/periodic-table/element/1/hydrogen>, (last accessed 12th October 2023).
- [14] Air Liquide, *Gas encyclopedia by Air Liquide*, <https://encyclopedia.airliquide.com/hydrogen>, (last accessed 12th October 2023).
- [15] IFP Energies nouvelles, *All about hydrogen*, <https://www.ifpenergiesnouvelles.com/issues-and-foresight/decoding-keys/renewable-energies/all-about-hydrogen>, (last accessed 12th October 2023).
- [16] Fatih Birol, 2019: *The Future of Hydrogen*, IEA, Paris, <https://www.iea.org/reports/the-future-of-hydrogen>.
- [17] P. Nikolaidis, A. Poullikkas, *A comparative overview of hydrogen production processes*, *Renew. Sust. Energ. Rev.*, 67 (2017) 597-611, <https://doi.org/10.1016/j.rser.2016.09.044>.

- [18] U.S. Office of Energy Efficiency & Renewable Energy, *Hydrogen production: electrolysis*, <https://www.energy.gov/eere/fuelcells/hydrogen-production-electrolysis>, (last accessed 12th October 2023).
- [19] CEA, *Découvrir & Comprendre - l'hydrogène*, <https://www.cea.fr/comprendre/Pages/energies/renouvelables/hydrogene.aspx>, (last accessed 12th October 2023).
- [20] AFHYPAC, 2018: *Developing hydrogen for the French Economy : A prospective study*, AFHYPAC, Paris, France, 20 pp., http://www.afhypac.org/documents/publications/rapports/Afhypac_Etude%20H2%20Fce%20GB_def.pdf.
- [21] Air Liquide, *Destination: Hydrogen*, <https://energies.airliquide.com/destination-hydrogen>, (last accessed 12th October 2023).
- [22] I. Cumalioglu, A. Ertas, Y. Ma, T. Maxwell, *State of the art: hydrogen storage*, J. Fuel Cell Sci. Technol., 5 (2008) 034001, <https://doi.org/10.1115/1.2894462>.
- [23] AFHYPAC, *Tout savoir sur - applications, démonstration et réalisation dans le monde*, <https://www.afhypac.org/documentation/tout-savoir/>, (last accessed 27th January 2021).
- [24] BMW, *The BMW i Hydrogen NEXT*, https://www.bmwgroup.com/en/company/bmw-group-news/artikel/BMWi_Hydrogen_NEXT.html, (last accessed 27th January 2021).
- [25] Honda, *2021 Clarity fuel cell*, <https://automobiles.honda.com/clarity-fuel-cell>, (last accessed 12th October 2023).
- [26] Hyundai, *Hyundai NEXO*, <https://www.hyundai.com/fr/modeles/nexo.html>, (last accessed 12th October 2023).
- [27] Mazda, *Hydrogen vehicle*, <https://www.mazda.com/en/innovation/technology/env/hre/>, (last accessed 27th January 2021).
- [28] Nissan, *New X-TRAIL Fuel Cell Vehicle (FCV)*, <https://www.nissan-global.com/EN/TECHNOLOGY/OVERVIEW/fcv.html>, (last accessed 27th January 2021).
- [29] Renault Group, *Kangoo Z.E. Hydrogen et Master Z.E. Hydrogen*, <https://easyelectriclife.groupe.renault.com/fr/vehicules/kangoo-z-e-hydrogen-et-master-z-e-hydrogen/>, (last accessed 27th January 2021).
- [30] Toyota, *Brochure Mirai*, <https://www.toyota.fr/new-cars/mirai/brochure>, (last accessed 12th October 2023).
- [31] DAIMLER, *Mercedes-Benz GLC F-CELL*, <https://www.daimler.com/products/passenger-cars/mercedes-benz/glc-f-cell.html>, (last accessed 27th January 2021).
- [32] *Photos&360° Views*, <https://www.toyota.com/mirai/2023/photo-gallery/section/exterior/slide/1>, (last accessed 23rd September 2023).
- [33] U.S. Department of Energy, *Alternative fuels data center*, <https://afdc.energy.gov/vehicles/how-do-fuel-cell-electric-cars-work>, (last accessed 12th October 2023).
- [34] Toyota, *Electrification*, <https://www.toyota-europe.com/world-of-toyota/feel/environment/better-air/fuel-cell-vehicle>, (last accessed 12th October 2023).
- [35] G. Karthik Pandiyan, T. Prabakaran, *Implementation of nanotechnology in fuel cells*, Mater. Today: Proc., 33 (2020) 2681-2685, <https://doi.org/10.1016/j.matpr.2020.01.368>.
- [36] L. Antoni, J.-P. Poirot-Crouvezier, F. Roy, X. Glipa, *GENEPAC : pile à combustible à membrane échangeuse de protons PEMFC*, Techniques de l'ingénieur, (2013), <https://www.techniques-ingenieur.fr/base-documentaire/ingenierie-des-transport-th14/carburants-et-materiaux-alleges-pour-vehicule-42629210/genepac-pile-a-combustible-a-membrane-echangeuse-de-protons-pemfc-in52/systeme-pile-a-combustible-in52v2niv10004.html>.
- [37] M. Torregrossa, *Différences entre voiture électrique, voiture hybride et voiture hydrogène*, (2018), <https://www.automobile-propre.com/dossiers/differences-voiture-electrique-voiture-hybride-hydrogene/#:~:text=Alors%20qu'une%20voiture%20%C3%A9lectrique,%20stockant%20de%20l'hydrog%C3%A8ne.>

- [38] GM, *GM Hydrogen Fuel Cell Vehicles*, https://www.gmheritagecenter.com/featured/Fuel_Cell_Vehicles.html, (last accessed 12th October 2023).
- [39] Confucius, *The Analects*, Penguin Classics; 1st edition (September 3, 1998), 1998.
- [40] ISO, *TC197 Hydrogen Technologies*, <https://www.iso.org/committee/54560/x/catalogue/>.
- [41] Air Liquide, *Storing hydrogen*, <https://energies.airliquide.com/resources-planet-hydrogen/how-hydrogen-stored>, (last accessed 27th January 2021).
- [42] G. Gondor, *Pour le stockage de l'hydrogène : analyse thermodynamique de la formation d'hydrure métalliques et optimisation du remplissage d'un réservoir*, Ph.D. thesis, Université de Franche-Comté, 2008, <https://tel.archives-ouvertes.fr/tel-00782271/document>.
- [43] AFHYPAC, *Stockage solide de l'hydrogène*, <https://www.afhypac.org/documentation/tout-savoir/>, (last accessed 27th January 2021).
- [44] U.S. Department of Energy, *Hydrogen storage - basics*, <https://www.energy.gov/eere/fuelcells/hydrogen-storage-basics-0>, (last accessed 27th January 2021).
- [45] T. Brestovič, L. Bednarova, N. Jasminská, M. Lázár, R. Dobáková, *Hydrogen compressor utilizing of metal hydride*, *Acta Technologia*, 5 (2019) 37-41, <https://doi.org/10.22306/atec.v5i2.52>.
- [46] H. Barthelemy, M. Weber, F. Barbier, *Hydrogen storage: Recent improvements and industrial perspectives*, *Int. J. Hydrog. Energy*, 42 (2017) 7254-7262, <https://doi.org/10.1016/j.ijhydene.2016.03.178>.
- [47] M. Latroche, *De l'hydrogene stocké sous forme solide*, *Connaissance des énergies*, <https://www.connaissancedesenergies.org/videos-energies/videos-ruptures/de-l-hydrogene-stocke-sous-forme-solide>, (last accessed 12th October 2023).
- [48] G. Sandi, *Hydrogen storage and its limitations*, *Electrochem. Soc. Interface*, 13 (2004) 40-44, <https://doi.org/10.1149/2.F06043IF>.
- [49] K. L. Lim, H. Kazemian, Z. Yaakob, W. R. W. Daud, *Solid-state materials and methods for hydrogen storage: a critical review*, *Chem. Eng. Technol.*, 33 (2010) 213-226, <https://doi.org/10.1002/ceat.200900376>.
- [50] *Connaissance des énergies*, *De l'énergie stockée sous forme d'hydrogène solide*, <https://www.connaissancedesenergies.org/de-l-energie-stockee-sous-forme-d-hydrogene-solide-130222>, (last accessed 12th October 2023).
- [51] M. Piesing, *The epic attempts to power planes with hydrogen*, (2022), <https://www.bbc.com/future/article/20220316-the-epic-attempts-to-power-planes-with-hydrogen>.
- [52] P.-M. Heuser, D. S. Ryberg, T. Grube, M. Robinius, D. Stolten, *Techno-economic analysis of a potential energy trading link between Patagonia and Japan based on CO₂ free hydrogen*, *Int. J. Hydrog. Energy*, 44 (2019) 12733-12747, <https://doi.org/10.1016/j.ijhydene.2018.12.156>.
- [53] S. Kamiya, M. Nishimura, E. Harada, *Study on introduction of CO₂ free energy to Japan with liquid hydrogen*, *Phys. Procedia*, 67 (2015) 11-19, <https://doi.org/10.1016/j.phpro.2015.06.004>.
- [54] J. Gallarda, *Liquéfaction de l'hydrogène*, *Techniques de l'ingénieur*, base documentaire : TIB485DUO (2001), <https://www.techniques-ingenieur.fr/base-documentaire/procedes-chimie-bio-agro-th2/operations-unitaires-traitement-des-gaz-42485210/liquefaction-de-l-hydrogene-j3603/>.
- [55] AFHYPAC, *Liquéfaction de l'hydrogène*, <https://www.afhypac.org/documentation/tout-savoir/>, (last accessed 28th January 2021).
- [56] W. Liu, T. Gottschall, F. Scheibel, E. Bykov, N. Fortunato, A. Aubert, H. Zhang, K. Skokov, O. Gutfleisch, *Designing magnetocaloric materials for hydrogen liquefaction with light rare-earth Laves phases*, *J. Phys. Energy*, 5 (2023) 034001, <https://doi.org/10.1088/2515-7655/acb0b>.
- [57] M. A. Shampo, R. A. Kyle, D. P. Steensma, William F. Giauque—Nobel Prize for low-temperature research, *Mayo Clinic Proceedings*, [https://www.mayoclinicproceedings.org/article/S0025-6196\(11\)61700-X/fulltext](https://www.mayoclinicproceedings.org/article/S0025-6196(11)61700-X/fulltext).
- [58] A. Züttel, *Materials for hydrogen storage*, *Mater. Today*, 6 (2003) 24-33, [https://doi.org/10.1016/S1369-7021\(03\)00922-2](https://doi.org/10.1016/S1369-7021(03)00922-2).
- [59] Air Liquide, *Thermal protection equipment*, <https://advancedtech.airliquide.com/thermal-protection-equipment>, (last accessed 12th October 2023).

- [60] Air Liquide, *Space*, <https://www.airliquide.com/industry/space>, (last accessed 28th January 2021).
- [61] AFHYPAC, *Stockage de l'hydrogène sous forme de gaz comprimé*, <https://www.afhypac.org/documentation/tout-savoir/>, (last accessed 28th January 2021).
- [62] McPhy, *Fill up on clean energy in just a few minutes!*, <https://mcphy.com/en/equipment-services/hydrogen-stations/>, (last accessed 12th October 2023).
- [63] D. Mori, K. Hirose, *Recent challenges of hydrogen storage technologies for fuel cell vehicles*, Int. J. Hydrog. Energy, 34 (2009) 4569-4574, <https://doi.org/10.1016/j.ijhydene.2008.07.115>.
- [64] A. Air, M. Shamsuddoha, B. Gangadhara Prusty, *A review of Type V composite pressure vessels and automated fibre placement based manufacturing*, Compos. B Eng., 253 (2023) 110573, <https://doi.org/10.1016/j.compositesb.2023.110573>.
- [65] A. Züttel, *Hydrogen storage methods*, Naturwissenschaften, 91 (2004) 157-172, <https://doi.org/10.1007/s00114-004-0516-x>.
- [66] E. W. Lemmon, M. O. McLinden, D. G. Friend, *Thermophysical Properties of Fluid Systems*, in: NIST Chemistry WebBook, NIST Standard Reference Database Number 69, P. J. Linstrom, W. G. Mallard (Eds.) NIST, Gaithersburg MD, 20899, USA, 2021, <https://doi.org/10.18434/T4D303>.
- [67] E. Rivard, M. Trudeau, K. Zaghieb, *Hydrogen storage for mobility: A review*, Materials, 12 (2019), 1973, <https://www.mdpi.com/1996-1944/12/12/1973>.
- [68] M. Creighton, *Factor of safety in design and engineering: the basics*, <https://www.creativemechanisms.com/blog/factor-of-safety-in-design-and-engineering-the-basics>, (last accessed 12th October 2023).
- [69] U.S. Department of Energy, *Hydrogen and fuel cell technologies office multi-year research, development, and demonstration plan*, <https://www.energy.gov/eere/fuelcells/articles/hydrogen-and-fuel-cell-technologies-office-multi-year-research-development>, (last accessed 12th October 2023).
- [70] J. Zheng, X. Liu, P. Xu, P. Liu, Y. Zhao, J. Yang, *Development of high pressure gaseous hydrogen storage technologies*, Int. J. Hydrog. Energy, 37 (2012) 1048-1057, <https://doi.org/10.1016/j.ijhydene.2011.02.125>.
- [71] Luxfer Gas Cylinders, *G-Stor™ Carbon Composite Cylinder User Manual Alternative Fuel Cylinders*, <https://www.luxfercylinders.com/support/g-stor-carbon-composite-cylinder-user-manual-alter/alternative-fuel>, (last accessed 12th October 2023).
- [72] J. Wozniak, 2003: *Development of a compressed hydrogen gas integrated storage system (CH₂-ISS) for fuel cell vehicles*, Johns Hopkins University Applied Physics Laboratory, USA, 4 pp., https://www1.eere.energy.gov/hydrogenandfuelcells/pdfs/iiia2_wozniak.pdf.
- [73] ISO, *14687:2019 Hydrogen fuel quality — Product specification*, <https://www.iso.org/standard/69539.html>.
- [74] M. Silvanus, O. Frånberg, *Permeability properties of a pressure induced compacted polymer liner in gas cylinder*, J. Appl. Polym. Sci., 138 (2021) 50335, <https://doi.org/10.1002/app.50335>.
- [75] H. Fujiwara, H. Ono, K. Onoue, S. Nishimura, *High-pressure gaseous hydrogen permeation test method -property of polymeric materials for high-pressure hydrogen devices (1)*, Int. J. Hydrog. Energy, 45 (2020) 29082-29094, <https://doi.org/10.1016/j.ijhydene.2020.07.215>.
- [76] M. C. Kane, 2008: *Permeability, solubility, and interaction of hydrogen in polymers- An assesment of materials for hydrogen transport*, United States, <https://www.osti.gov/biblio/927901>.
- [77] G. Barbieri, *Permeance*, in: Encyclopedia of Membranes, Enrico Drioli, Lidietta Giorno (Eds.) Springer Berlin Heidelberg, Berlin, Heidelberg, 2016, pp. 1484-1485, https://doi.org/10.1007/978-3-662-44324-8_445.
- [78] I. Yeo, H. Jung, T.-H. Song, *Gas permeation characteristics through heat-sealed flanges of vacuum insulation panels*, Vacuum, 104 (2014) 70-76, <https://doi.org/10.1016/j.vacuum.2014.01.008>.
- [79] Y. Sun, H. Lv, W. Zhou, C. Zhang, *Research on hydrogen permeability of polyamide 6 as the liner material for type IV hydrogen storage tank*, Int. J. Hydrog. Energy, 45 (2020) 24980-24990, <https://doi.org/10.1016/j.ijhydene.2020.06.174>.

- [80] W. Balasooriya, C. Clute, B. Schritteser, G. Pinter, *A review on applicability, limitations, and improvements of polymeric materials in high-pressure hydrogen gas atmospheres*, Polym Rev, 62 (2022) 175-209, <https://doi.org/10.1080/15583724.2021.1897997>.
- [81] T. A. Yersak, D. R. Baker, Y. Yanagisawa, S. Slavik, R. Immel, A. Mack-Gardner, M. Herrmann, M. Cai, *Predictive model for depressurization-induced blistering of type IV tank liners for hydrogen storage*, Int. J. Hydrog. Energy, 42 (2017) 28910-28917, <https://doi.org/10.1016/j.ijhydene.2017.10.024>.
- [82] J. Pepin, E. Lainé, J.-C. Grandidier, S. Castagnet, P. Blanc-Vannet, P. Papin, M. Weber, *Determination of key parameters responsible for polymeric liner collapse in hyperbaric type IV hydrogen storage vessels*, Int. J. Hydrog. Energy, 43 (2018) 16386-16399, <https://doi.org/10.1016/j.ijhydene.2018.06.177>.
- [83] T. A. Edison, *Quotes*, <https://www.goodreads.com/quotes/57198-there-s-a-way-to-do-it-better---find-it>, (last accessed 12th October 2023).
- [84] Y. Yampolskii, I. Pinnau, B. D. Freeman, *Materials Science of Membranes for Gas and Vapor Separation*, John Wiley & Sons Ltd., Chichester, UK, 2006.
- [85] M. Deilmann, H. Halfmann, S. Steves, N. Bibinov, P. Awakowicz, *Silicon oxide permeation barrier coating and plasma sterilization of PET bottles and foils*, Plasma Process. Polym., 6 (2009) S695-S699, <https://doi.org/10.1002/ppap.200930907>.
- [86] K. Pang, R. Kotek, A. Tonelli, *Review of conventional and novel polymerization processes for polyesters*, Prog. Polym. Sci., 31 (2006) 1009-1037, <https://doi.org/10.1016/j.progpolymsci.2006.08.008>.
- [87] N. K. Acharya, V. Kulshrestha, K. Awasthi, A. K. Jain, M. Singh, Y. K. Vijay, *Hydrogen separation in doped and blend polymer membranes*, Int. J. Hydrog. Energy, 33 (2008) 327-331, <https://doi.org/10.1016/j.ijhydene.2007.07.030>.
- [88] P. Bandyopadhyay, T. T. Nguyen, X. Li, N. H. Kim, J. H. Lee, *Enhanced hydrogen gas barrier performance of diaminoalkane functionalized stitched graphene oxide/polyurethane composites*, Compos. B. Eng., 117 (2017) 101-110, <https://doi.org/10.1016/j.compositesb.2017.02.035>.
- [89] P. Bandyopadhyay, W. B. Park, R. K. Layek, M. E. Uddin, N. H. Kim, H.-G. Kim, J. H. Lee, *Hexylamine functionalized reduced graphene oxide/polyurethane nanocomposite-coated nylon for enhanced hydrogen gas barrier film*, J. Membr. Sci., 500 (2016) 106-114, <https://doi.org/10.1016/j.memsci.2015.11.029>.
- [90] J. S. Bunch, S. S. Verbridge, J. S. Alden, A. M. van der Zande, J. M. Parpia, H. G. Craighead, P. L. McEuen, *Impermeable atomic membranes from graphene sheets*, Nano Lett., 8 (2008) 2458-2462, <https://doi.org/10.1021/nl801457b>.
- [91] H. Kim, Y. Miura, C. W. Macosko, *Graphene/polyurethane nanocomposites for improved gas barrier and electrical conductivity*, Chem. Mater., 22 (2010) 3441-3450, <https://doi.org/10.1021/cm100477v>.
- [92] H. Liu, P. Bandyopadhyay, T. Kshetri, N. H. Kim, B.-C. Ku, B. Moon, J. H. Lee, *Layer-by-layer assembled polyelectrolyte-decorated graphene multilayer film for hydrogen gas barrier application*, Compos. B. Eng., 114 (2017) 339-347, <https://doi.org/10.1016/j.compositesb.2017.02.007>.
- [93] W. B. Park, P. Bandyopadhyay, T. T. Nguyen, T. Kuila, N. H. Kim, J. H. Lee, *Effect of high molecular weight polyethyleneimine functionalized graphene oxide coated polyethylene terephthalate film on the hydrogen gas barrier properties*, Compos. B. Eng., 106 (2016) 316-323, <https://doi.org/10.1016/j.compositesb.2016.09.048>.
- [94] Y.-H. Yang, L. Bolling, M. A. Priolo, J. C. Grunlan, *Super gas barrier and selectivity of graphene oxide-polymer multilayer thin films*, Adv. Mater., 25 (2013) 503-508, <https://doi.org/10.1002/adma.201202951>.
- [95] L. Zhao, H. Zhang, N. H. Kim, D. Hui, J. H. Lee, Q. Li, H. Sun, P. Li, *Preparation of graphene oxide/polyethyleneimine layer-by-layer assembled film for enhanced hydrogen barrier property*, Compos. B. Eng., 92 (2016) 252-258, <https://doi.org/10.1016/j.compositesb.2016.02.037>.

- [96] H. Liu, P. Bandyopadhyay, N. H. Kim, B. Moon, J. H. Lee, *Surface modified graphene oxide/poly(vinyl alcohol) composite for enhanced hydrogen gas barrier film*, Polym. Test., 50 (2016) 49-56, <https://doi.org/10.1016/j.polymertesting.2015.12.007>.
- [97] F. Xiang, S. M. Ward, T. M. Givens, J. C. Grunlan, *Structural tailoring of hydrogen-bonded poly(acrylic acid)/poly(ethylene oxide) multilayer thin films for reduced gas permeability*, Soft Matter, 11 (2015) 1001-1007, <https://doi.org/10.1039/C4SM02363C>.
- [98] R. K. Layek, A. K. Das, M. U. Park, N. H. Kim, J. H. Lee, *Layer-structured graphene oxide/polyvinyl alcohol nanocomposites: dramatic enhancement of hydrogen gas barrier properties*, J. Mater. Chem. A, 2 (2014) 12158-12161, <http://dx.doi.org/10.1039/C4TA02346C>.
- [99] P. Li, K. Chen, L. Zhao, H. Zhang, H. Sun, X. Yang, N. H. Kim, J. H. Lee, Q. J. Niu, *Preparation of modified graphene oxide/polyethyleneimine film with enhanced hydrogen barrier properties by reactive layer-by-layer self-assembly*, Compos. B. Eng., 166 (2019) 663-672, <https://doi.org/10.1016/j.compositesb.2019.02.058>.
- [100] O. B. Seo, S. Saha, N. H. Kim, J. H. Lee, *Preparation of functionalized MXene-stitched-graphene oxide/poly(ethylene-co-acrylic acid) nanocomposite with enhanced hydrogen gas barrier properties*, J. Membr. Sci., 640 (2021) 119839, <https://doi.org/10.1016/j.memsci.2021.119839>.
- [101] K. L. Simmons R.R. Barth, C. San Marchi, 2013: *Polymers for hydrogen infrastructure and vehicle fuel systems: Applications, properties, and gap analysis*, Sandia National Laboratories, <https://prod-ng.sandia.gov/techlib-noauth/access-control.cgi/2013/138904.pdf>.
- [102] S. A. Stern, J. R. Fried, *Permeability of polymers to gases and vapors*, in: Physical Properties of Polymers Handbook, J. E. Mark (Ed.) Springer, New York, 2007, pp. 1033-1047, https://doi.org/10.1007/978-0-387-69002-5_61.
- [103] M. W. Fitch, W. J. Koros, R. L. Nolen, J. R. Carnes, *Permeation of several gases through elastomers, with emphasis on the deuterium/hydrogen pair*, J. Appl. Polym. Sci., 47 (1993) 1033-1046, <https://doi.org/10.1002/app.1993.070470610>.
- [104] R. M. Barrer, E. K. Rideal, *Permeation, diffusion and solution of gases in organic polymers*, Trans. Faraday Soc., 35 (1939) 628-643, <https://doi.org/10.1039/TF9393500628>.
- [105] P. A. Lessing, *Polymeric hydrogen diffusion barrier, high-pressure storage tank so equipped, method of fabricating a storage tank and method of preventing hydrogen diffusion*, United States Patent (2008), <https://www.osti.gov/biblio/984455>.
- [106] U.S. Department of Energy, 2002: *Hydrogen, fuel cells and infrastructure technologies program, 2002 annual progress report*, United States, <https://www.osti.gov/biblio/15003052>.
- [107] L. B. Cataquiz P. A. Lessing, R. P. Anderson, 2003: *Low permeation liner for hydrogen gas storage tanks*, https://www1.eere.energy.gov/hydrogenandfuelcells/pdfs/iiia5_lessing.pdf.
- [108] N. K. Zhevago, V. I. Glebov, *Hydrogen storage in capillary arrays*, Energy Convers. Manag., 48 (2007) 1554-1559, <https://doi.org/10.1016/j.enconman.2006.11.017>.
- [109] M. Prewitz, M. Gaber, R. Müller, C. Marotzke, K. Holtappels, *Polymer coated glass capillaries and structures for high-pressure hydrogen storage: Permeability and hydrogen tightness*, Int. J. Hydrog. Energy, 43 (2018) 5637-5644, <https://doi.org/10.1016/j.ijhydene.2017.12.092>.
- [110] N. Hilal, A. F. Ismail, C. Wright, *Membrane Fabrication*, CRC Press, 2015.
- [111] D. T. Clausi, W. J. Koros, *Formation of defect-free polyimide hollow fiber membranes for gas separations*, J. Membr. Sci., 167 (2000) 79-89, [https://doi.org/10.1016/S0376-7388\(99\)00276-8](https://doi.org/10.1016/S0376-7388(99)00276-8).
- [112] M. R. Kosuri, W. J. Koros, *Defect-free asymmetric hollow fiber membranes from Torlon®, a polyamide-imide polymer, for high-pressure CO₂ separations*, J. Membr. Sci., 320 (2008) 65-72, <https://doi.org/10.1016/j.memsci.2008.03.062>.
- [113] H. Z. Chen, Y. C. Xiao, T.-S. Chung, *Multi-layer composite hollow fiber membranes derived from poly(ethylene glycol) (PEG) containing hybrid materials for CO₂/N₂ separation*, J. Membr. Sci., 381 (2011) 211-220, <https://doi.org/10.1016/j.memsci.2011.07.023>.
- [114] H. W. Ballew, F. J. Martinez, C. Markee, R. T. Eddleman, *The ABCs of filtration and bioprocessing for the third millenium*, Spectrum Laboratories Inc., 2002,

<https://www.yumpu.com/en/document/read/28617071/abcs-of-filtration-bioprocessing-spectrum-laboratories-inc>.

[115] N. Abdullah, M. A. Rahman, M. H. Dzarfan Othman, J. Jaafar, A. F. Ismail, *Chapter 2 - Membranes and Membrane Processes: Fundamentals*, in: *Current Trends and Future Developments on (Bio-) Membranes*, Angelo Basile, Sylwia Mozia, Raffaele Molinari (Eds.) Elsevier, 2018, pp. 45-70, <https://doi.org/10.1016/B978-0-12-813549-5.00002-5>.

[116] M. Sadrzadeh, T. Mohammadi, *Nanocomposite Membranes for Water and Gas Separation*, Elsevier Science, 2019.

[117] J.-C. Remigy, S. Desclaux, *Filtration membranaire (OI, NF, UF) Présentation des membranes et modules*, Techniques de l'ingénieur Procédés de traitement des eaux potables, industrielles et urbaines, base documentaire : TIB318DUO (2007), <https://www.techniques-ingenieur.fr/base-documentaire/environnement-securite-th5/procedes-de-traitement-des-eaux-potables-industrielles-et-urbaines-42318210/filtration-membranaire-oi-nf-uf-w4090/>.

[118] K. Xie, Q. Fu, G. G. Qiao, P. A. Webley, *Recent progress on fabrication methods of polymeric thin film gas separation membranes for CO₂ capture*, J. Membr. Sci., 572 (2019) 38-60, <https://doi.org/10.1016/j.memsci.2018.10.049>.

[119] S. Zhao, G. Zhang, W. Shen, X. Wang, F. Liu, *Design and fabrication of highly selective and permeable polymer membranes*, J. Appl. Phys., 128 (2020) 131102, <https://doi.org/10.1063/5.0015975>.

[120] D. Purchas, K. Sutherland, *Handbook of Filter Media*, Elsevier Science, 2002.

[121] V. Abetz, T. Brinkmann, M. Sözbilir, *Fabrication and function of polymer membranes*, Chemistry Teacher International, 3 (2021) 141-154, <https://doi.org/10.1515/cti-2020-0023>.

[122] I. A. Neacșu, A. I. Nicoară, O. R. Vasile, B. Ș. Vasile, *Chapter 9 - Inorganic micro- and nanostructured implants for tissue engineering*, in: *Nanobiomaterials in Hard Tissue Engineering - Applications of Nanobiomaterials Volume 4*, Alexandru Mihai Grumezescu (Ed.) William Andrew Publishing, 2016, pp. 271-295, <https://doi.org/10.1016/B978-0-323-42862-0.00009-2>.

[123] R. Zhang, Y. Liu, M. He, Y. Su, X. Zhao, M. Elimelech, Z. Jiang, *Antifouling membranes for sustainable water purification: strategies and mechanisms*, Chem. Soc. Rev., 45 (2016) 5888-5924, <https://doi.org/10.1039/C5CS00579E>.

[124] O. Shibaeva, *Investigation of copper wire-mediated controlled/living radical polymerization: development of greener solvent systems & grafting to cellulose via thio-bromo click reaction*, Master of Applied Science thesis, Queen's University, Kingston, Ontario, Canada, 2014, https://qspace.library.queensu.ca/bitstream/handle/1974/12501/Shibaeva_Oxana_201409_MASC.pdf;jsessionid=406860C126D83F852E4F24A3E90042F7?sequence=1.

[125] B. S. Lalia, V. Kochkodan, R. Hashaikeh, N. Hilal, *A review on membrane fabrication: structure, properties and performance relationship*, Desalination, 326 (2013) 77-95, <https://doi.org/10.1016/j.desal.2013.06.016>.

[126] Synder filtration, *Definition of phase inversion membrane*, <https://synderfiltration.com/learning-center/articles/introduction-to-membranes/phase-inversion-membranes-immersion-precipitation/>, (last accessed 12th October 2023).

[127] M. Zahid, A. Rashid, S. Akram, Z. A. Rehan, W. Razzaq, *A comprehensive review on polymeric nano-composite membranes for water treatment*, J. Membr. Sci. Technol, 8 (2018) 1-20, <https://doi.org/10.4172/2155-9589.1000179>.

[128] A. Aytimur, S. Kocyigit, I. Uslu, *Calcium Stabilized Ceria Doped Zirconia Nanocrystalline Ceramic*, J. Inorg. Organomet. Polym. Mater., 24 (2014) 927-932, <https://doi-org.camphrier-1.grenet.fr/10.1007/s10904-014-0064-6>.

[129] L.-Y. Chen, R.-H. Chen, *Influence of sequential biaxial stretching parameters on the interior structure of polypropylene membrane*, Adv. Mater. Process., 3 (2017) 206-221, <https://doi.org/10.1080/2374068X.2016.1247342>.

- [130] Z.-X. Low, Y. T. Chua, B. M. Ray, D. Mattia, I. S. Metcalfe, D. A. Patterson, *Perspective on 3D printing of separation membranes and comparison to related unconventional fabrication techniques*, *J. Membr. Sci.*, 523 (2017) 596-613, <https://doi.org/10.1016/j.memsci.2016.10.006>.
- [131] M. J. T. Raaijmakers, N. E. Benes, *Current trends in interfacial polymerization chemistry*, *Prog. Polym. Sci.*, 63 (2016) 86-142, <https://doi.org/10.1016/j.progpolymsci.2016.06.004>.
- [132] J. Tian, H. Chang, S. Gao, R. Zhang, *How to fabricate a negatively charged NF membrane for heavy metal removal via the interfacial polymerization between PIP and TMC?*, *Desalination*, 491 (2020) 114499, <https://doi.org/10.1016/j.desal.2020.114499>.
- [133] F. Radmanesh, *Advances in hybrid thin film composite membranes: The untraveled route of non-aqueous interfacial polymerization*, Ph.D. thesis, University of Twente, 2022, <https://research.utwente.nl/en/publications/advances-in-hybrid-thin-film-composite-membranes-the-untraveled-r>.
- [134] F. Zhang, J.-B. Fan, S. Wang, *Interfacial polymerization: From chemistry to functional materials*, *Angew. Chem. Int. Ed.*, 59 (2020) 21840-21856, <https://doi.org/10.1002/anie.201916473>.
- [135] Y. Song, J.-B. Fan, S. Wang, *Recent progress in interfacial polymerization*, *Mater. Chem. Front.*, 1 (2017) 1028-1040, <https://doi.org/10.1039/C6QM00325G>.
- [136] M. Kobašlija, D. T. McQuade, *Polyurea microcapsules from Oil-in-Oil emulsions via interfacial polymerization*, *Macromolecules*, 39 (2006) 6371-6375, <https://doi.org/10.1021/ma061455x>.
- [137] F. I. Chowdhury, *4 - Sustainable resin systems for polymer composites*, in: *Advances in Sustainable Polymer Composites*, Md Rezaur Rahman (Ed.) Woodhead Publishing, 2021, pp. 89-108, <https://doi.org/10.1016/B978-0-12-820338-5.00004-7>.
- [138] IUPAC, *functionality*, in: *Compendium of Chemical Terminology*, International Union of Pure and Applied Chemistry, 2019, <https://doi.org/10.1351/goldbook.FT07505>.
- [139] G. Bhat, V. Kandagor, *1 - Synthetic polymer fibers and their processing requirements*, in: *Advances in Filament Yarn Spinning of Textiles and Polymers*, Dong Zhang (Ed.) Woodhead Publishing, 2014, pp. 3-30, <https://doi.org/10.1533/9780857099174.1.3>.
- [140] V. R. Sastri, *7 - Engineering Thermoplastics: Acrylics, Polycarbonates, Polyurethanes, Polyacetals, Polyesters, and Polyamides*, in: *Plastics in Medical Devices (Second Edition)*, Vinny R. Sastri (Ed.) William Andrew Publishing, Oxford, 2014, pp. 121-172, <https://doi.org/10.1016/B978-1-4557-3201-2.00007-0>.
- [141] J.-B. Fan, H. Liu, Y. Song, Z. Luo, Z. Lu, S. Wang, *Janus particles synthesis by emulsion interfacial polymerization: polystyrene as seed or beyond?*, *Macromolecules*, 51 (2018) 1591-1597, <https://doi.org/10.1021/acs.macromol.7b02304>.
- [142] Y. Liang, Y. Zhu, C. Liu, K.-R. Lee, W.-S. Hung, Z. Wang, Y. Li, M. Elimelech, J. Jin, S. Lin, *Polyamide nanofiltration membrane with highly uniform sub-nanometre pores for sub-1 Å precision separation*, *Nat. Commun.*, 11 (2020) 2015, <https://doi.org/10.1038/s41467-020-15771-2>.
- [143] A. Nowbahar, V. Mansard, J. M. Mecca, M. Paul, T. Arrowood, T. M. Squires, *Measuring interfacial polymerization kinetics using microfluidic interferometry*, *J. Am. Chem. Soc.*, 140 (2018) 3173-3176, <https://doi.org/10.1021/jacs.7b12121>.
- [144] S. Neyertz, D. Brown, M. J. T. Raaijmakers, N. E. Benes, *A molecular characterization of hyper-cross-linked hybrid polyPOSS-imide networks*, *Comp. Mater. Sci.*, 117 (2016) 338-353, <https://doi.org/10.1016/j.commatsci.2016.02.015>.
- [145] M. J. T. Raaijmakers, M. A. Hempenius, P. M. Schön, G. J. Vancso, A. Nijmeijer, M. Wessling, N. E. Benes, *Sieving of hot gases by hyper-cross-linked nanoscale-hybrid membranes*, *J. Am. Chem. Soc.*, 136 (2014) 330-335, <https://doi.org/10.1021/ja410047u>.
- [146] M. J. T. Raaijmakers, *Hyper-cross-linked, hybrid membranes via interfacial polymerization*, Ph.D. thesis, University of Twente, 2015, [https://research.utwente.nl/en/publications/hypercrosslinked-hybrid-membranes-via-interfacial-polymerization\(98def830-a93b-4006-9f30-e314f89030ce\).html](https://research.utwente.nl/en/publications/hypercrosslinked-hybrid-membranes-via-interfacial-polymerization(98def830-a93b-4006-9f30-e314f89030ce).html).

- [147] E. Maaskant, H. Gojzewski, M. A. Hempenius, G. J. Vancso, N. E. Benes, *Thin cyclomatrix polyphosphazene films: interfacial polymerization of hexachlorocyclotriphosphazene with aromatic biphenols*, Polym. Chem., 9 (2018) 3169-3180, <https://doi.org/10.1039/C8PY00444G>.
- [148] M. J. T. Raaijmakers, M. Wessling, A. Nijmeijer, N. E. Benes, *Hybrid polyhedral oligomeric silsesquioxanes-imides with tailored intercage spacing for sieving of hot gases*, Chem. Mater., 26 (2014) 3660-3664, <https://doi.org/10.1021/cm500691e>.
- [149] D. Wu, Y. Huang, S. Yu, D. Lawless, X. Feng, *Thin film composite nanofiltration membranes assembled layer-by-layer via interfacial polymerization from polyethylenimine and trimesoyl chloride*, J. Membr. Sci., 472 (2014) 141-153, <https://doi.org/10.1016/j.memsci.2014.08.055>.
- [150] D. H. Shin, N. Kim, Y. T. Lee, *Modification to the polyamide TFC RO membranes for improvement of chlorine-resistance*, J. Membr. Sci., 376 (2011) 302-311, <https://doi.org/10.1016/j.memsci.2011.04.045>.
- [151] M. Z. Asuncion, R. M. Laine, *Fluoride rearrangement reactions of polyphenyl- and polyvinylsilsesquioxanes as a facile route to mixed functional phenyl, vinyl T₁₀ and T₁₂ silsesquioxanes*, J. Am. Chem. Soc., 132 (2010) 3723-3736, <https://doi.org/10.1021/ja9087743>.
- [152] K. Bouchemal, F. Couenne, S. Briançon, H. Fessi, M. Tayakout, *Polyamides nanocapsules: Modeling and wall thickness estimation*, AIChE J., 52 (2006) 2161-2170, <https://doi.org/10.1002/aic.10828>.
- [153] V. Enkelmann, G. Wegner, *Mechanism of interfacial polycondensation and the direct synthesis of stable polyamide membranes*, Makromol. Chem., 177 (1976) 3177-3189, <https://doi.org/10.1002/macp.1976.021771106>.
- [154] J. Zhao, Y. Zhang, Y. Su, J. Liu, X. Zhao, J. Peng, Z. Jiang, *Cross-linked bovine serum albumin composite membranes prepared by interfacial polymerization with stimuli-response properties*, J. Membr. Sci., 445 (2013) 1-7, <https://doi.org/10.1016/j.memsci.2013.05.050>.
- [155] S. K. Karode, S. S. Kulkarni, A. K. Suresh, R. A. Mashelkar, *Molecular weight distribution in interfacial polymerization—model development and verification*, Chem. Eng. Sci., 52 (1997) 3243-3255, [https://doi.org/10.1016/S0009-2509\(97\)00138-3](https://doi.org/10.1016/S0009-2509(97)00138-3).
- [156] Y. Arai, M. Watanabe, K. Sanui, N. Ogata, *Effect of polycondensation methods on molecular weight distribution of nylon 610*, J. Polym. Sci. Polym. Chem. Ed., 23 (1985) 3081-3093, <https://doi.org/10.1002/pol.1985.170231216>.
- [157] A. V. Berezkin, Y. V. Kudryavtsev, *Effect of cross-linking on the structure and growth of polymer films prepared by interfacial polymerization*, Langmuir, 31 (2015) 12279-12290, <https://doi.org/10.1021/acs.langmuir.5b03031>.
- [158] A. V. Berezkin, Y. V. Kudryavtsev, *Linear interfacial polymerization: theory and simulations with dissipative particle dynamics*, J. Chem. Phys., 141 (2014) 194906, <https://doi.org/10.1063/1.4901727>.
- [159] M. B. Ang, S.-H. Huang, S.-W. Wei, Y.-H. Chiao, R. R. Aquino, W.-S. Hung, H.-A. Tsai, K.-R. Lee, J.-Y. Lai, *Surface properties, free volume, and performance for thin-film composite pervaporation membranes fabricated through interfacial polymerization involving different organic solvents*, Polymers, 12 (2020) 2326, <https://doi.org/10.3390/polym12102326>.
- [160] A. K. Ghosh, B.-H. Jeong, X. Huang, E. M. V. Hoek, *Impacts of reaction and curing conditions on polyamide composite reverse osmosis membrane properties*, J. Membr. Sci., 311 (2008) 34-45, <https://doi.org/10.1016/j.memsci.2007.11.038>.
- [161] F. Yuan, Z. Wang, S. Li, J. Wang, S. Wang, *Formation–structure–performance correlation of thin film composite membranes prepared by interfacial polymerization for gas separation*, J. Membr. Sci., 421-422 (2012) 327-341, <https://doi.org/10.1016/j.memsci.2012.07.035>.
- [162] G.-Y. Chai, W. B. Krantz, *Formation and characterization of polyamide membranes via interfacial polymerization*, J. Membr. Sci., 93 (1994) 175-192, [https://doi.org/10.1016/0376-7388\(94\)80006-5](https://doi.org/10.1016/0376-7388(94)80006-5).
- [163] M. J. T. Raaijmakers, T. Schmidt, M. Barth, M. Tutus, N. E. Benes, M. Wessling, *Enzymatically active ultrathin pepsin membranes*, Angew. Chem. Int. Ed., 54 (2015) 5910-5914, <https://doi.org/10.1002/anie.201411263>.

- [164] M. F. Jimenez-Solomon, Q. Song, K. E. Jelfs, M. Munoz-Ibanez, A. G. Livingston, *Polymer nanofilms with enhanced microporosity by interfacial polymerization*, *Nat. Mater.*, 15 (2016) 760-767, <https://doi.org/10.1038/nmat4638>.
- [165] B. Khorshidi, T. Thundat, B. A. Fleck, M. Sadrzadeh, *A novel approach toward fabrication of high performance thin film composite polyamide membranes*, *Sci Rep*, 6 (2016) 22069, <https://doi.org/10.1038/srep22069>.
- [166] S. Jianliang, *Thermal-facilitated interfacial polymerization toward high-performance polyester desalination membrane*, *J. Mater. Chem. A*, 9 (2021) 8470-8479, <https://doi.org/10.1039/D0TA12283A>.
- [167] M. You, W. Li, Y. Pan, P. Fei, H. Wang, W. Zhang, L. Zhi, J. Meng, *Preparation and characterization of antibacterial polyamine-based cyclophosphazene nanofiltration membranes*, *J. Membr. Sci.*, 592 (2019) 117371, <https://doi.org/10.1016/j.memsci.2019.117371>.
- [168] P. S. Goh, A. F. Ismail, S. M. Sanip, B. C. Ng, M. Aziz, *Recent advances of inorganic fillers in mixed matrix membrane for gas separation*, *Sep. Purif.*, 81 (2011) 243-264, <https://doi.org/10.1016/j.seppur.2011.07.042>.
- [169] M. Dalwani, J. Zheng, M. Hempenius, M. J. Raaijmakers, C. M. Doherty, A. J. Hill, M. Wessling, N. E. Benes, *Ultra-thin hybrid polyhedral silsesquioxane-polyamide films with potentially unlimited 2D dimensions*, *J. Mater. Chem.*, 22 (2012) 14835-14838, <https://doi.org/10.1039/C2JM31941A>.
- [170] D. Li, H. Wang, *Recent developments in reverse osmosis desalination membranes*, *J. Mater. Chem.*, 20 (2010) 4551-4566, <https://doi.org/10.1039/B924553G>.
- [171] M. Matsumoto, L. Valentino, G. M. Stiehl, H. B. Balch, A. R. Corcos, F. Wang, D. C. Ralph, B. J. Mariñas, W. R. Dichtel, *Lewis-Acid-Catalyzed interfacial polymerization of covalent organic framework films*, *Chem*, 4 (2018) 308-317, <https://doi.org/10.1016/j.chempr.2017.12.011>.
- [172] J. Xiang, Z. Xie, M. Hoang, D. Ng, K. Zhang, *Effect of ammonium salts on the properties of poly(piperazineamide) thin film composite nanofiltration membrane*, *J. Membr. Sci.*, 465 (2014) 34-40, <https://doi.org/10.1016/j.memsci.2014.03.074>.
- [173] S. D. Naik, L. K. Doraiswamy, *Phase transfer catalysis: Chemistry and engineering*, *AIChE J.*, 44 (1998) 612-646, <https://doi.org/10.1002/aic.690440312>.
- [174] G. Z. Ramon, M. C. Y. Wong, E. M. V. Hoek, *Transport through composite membrane, part 1: Is there an optimal support membrane?*, *J. Membr. Sci.*, 415-416 (2012) 298-305, <https://doi.org/10.1016/j.memsci.2012.05.013>.
- [175] G. Gong, H. Nagasawa, M. Kanezashi, T. Tsuru, *Facile and scalable flow-induced deposition of organosilica on porous polymer supports for reverse osmosis desalination*, *ACS Appl. Mater. Interfaces*, 10 (2018) 14070-14078, <https://doi.org/10.1021/acsami.7b19075>.
- [176] X. Zhu, X. Zhang, J. Li, X. Luo, D. Xu, D. Wu, W. Wang, X. Cheng, G. Li, H. Liang, *Crumple-textured polyamide membranes via MXene nanosheet-regulated interfacial polymerization for enhanced nanofiltration performance*, *J. Membr. Sci.*, 635 (2021) 119536, <https://doi.org/10.1016/j.memsci.2021.119536>.
- [177] S. Wang, Y. Zhang, Y. Han, Y. Hou, Y. Fan, X. Hou, *Design of porous membranes by liquid gating technology*, *Acc. Mater. Res.*, 2 (2021) 407-419, <https://doi.org/10.1021/accounsmr.1c00024>.
- [178] F. Liu, L. Wang, D. Li, Q. Liu, B. Deng, *A review: the effect of the microporous support during interfacial polymerization on the morphology and performances of a thin film composite membrane for liquid purification*, *RSC Adv.*, 9 (2019) 35417-35428, <https://doi.org/10.1039/C9RA07114H>.
- [179] J.-A.-D. Sharabati, S. Guclu, S. Erkoc-Ilter, D. Y. Koseoglu-Imer, S. Unal, Y. Z. Menciloglu, I. Ozturk, I. Koyuncu, *Interfacially polymerized thin-film composite membranes: Impact of support layer pore size on active layer polymerization and seawater desalination performance*, *Sep. Purif.*, 212 (2019) 438-448, <https://doi.org/10.1016/j.seppur.2018.11.047>.
- [180] P. S. Singh, S. V. Joshi, J. J. Trivedi, C. V. Devmurari, A. P. Rao, P. K. Ghosh, *Probing the structural variations of thin film composite RO membranes obtained by coating polyamide over polysulfone membranes of different pore dimensions*, *J. Membr. Sci.*, 278 (2006) 19-25, <https://doi.org/10.1016/j.memsci.2005.10.039>.

- [181] S. Neyertz, D. Brown, S. Salimi, F. Radmanesh, N. E. Benes, *Molecular characterization of polyOAPS-imide isomer hyper-cross-linked membranes: Free-volume morphologies and sorption isotherms for CH₄ and CO₂*, *J. Membr. Sci.*, 636 (2021) 119531, <https://doi.org/10.1016/j.memsci.2021.119531>.
- [182] W. L. Vos, A. d. Kuijper, J. L. Barrat, J. A. Schouten, *High pressure phase diagram of helium-hydrogen calculated through fluid integral equations and density functional theory of freezing*, *J. Phys.: Condens. Matter*, 3 (1991) 1613, <https://doi.org/10.1088/0953-8984/3/11/019>.
- [183] E. Ricci, N. Vergadou, G. G. Vogiatzis, M. G. De Angelis, D. N. Theodorou, *Molecular simulations and mechanistic analysis of the effect of CO₂ sorption on thermodynamics, structure, and local dynamics of molten atactic polystyrene*, *Macromolecules*, 53 (2020) 3669-3689, <https://doi.org/10.1021/acs.macromol.0c00323>.
- [184] S. A. Hollingsworth, R. O. Dror, *Molecular dynamics simulation for all*, *Neuron*, 99 (2018) 1129-1143, <https://doi.org/10.1016/j.neuron.2018.08.011>.
- [185] A. R. Leach, *Molecular modelling: principles and applications*, Second ed., Pearson education, 2001.
- [186] D. Frenkel, B. Smit, *Understanding molecular simulation : from algorithms to applications*, Second ed., Academic Press, 2002, <https://doi.org/10.1016/B978-0-12-267351-1.X5000-7>.
- [187] S. Pandiyan, *A molecular-level understanding of CO₂ permeability in polymer membranes*, Ph.D. thesis, Université de Savoie, 2009, <http://hdl.handle.net/11858/00-001M-0000-000F-7488-6>.
- [188] I. Newton, *Philosophiae naturalis principia mathematica*, 1687.
- [189] S. Neyertz, *Gas transport in dense polymeric membranes, molecular dynamics simulations*, in: *Encyclopedia of Membrane Science and Technology*, E. M. V. Hoek, V. V. Tarabara (Eds.) John Wiley & Sons, Hoboken, NJ, USA, 2013, pp. 1-21, <https://doi.org/10.1002/9781118522318.emst101>.
- [190] M. P. Allen, D. J. Tildesley, *Computer simulation of liquids*, Clarendon Press, Oxford, UK, 1987, <https://doi.org/10.1093/oso/9780198803195.001.0001>.
- [191] D. Brewer, S. Pankavich, *Computational methods for a one-directional plasma model with transport field*, *J. Undergrad. Res.*, 4 (2011), <https://doi.org/10.1137/11S010906>.
- [192] M. P. Allen, *Introduction to molecular dynamics simulation*, in: *Computational soft matter: from synthetic polymers to proteins*, Norbert Attig, Kurt Binder, Helmut Grubmüller, Kurt Kremer (Eds.) NIC-Directors, Jülich, Germany, 2004, pp. 1-28, <https://juser.fz-juelich.de/record/35298/files/nic-series-23.pdf>.
- [193] W. H. Westphal, *Mechanics of point masses and rigid bodies*, in: *A short textbook of physics: not involving the use of higher mathematics*, Wilhelm H. Westphal (Ed.) Springer Berlin Heidelberg, Berlin, Heidelberg, 1968, pp. 6-57, https://doi.org/10.1007/978-3-642-85476-7_2.
- [194] D. Brown, *The gmq User Manual Version 6*, 2021, available at <http://www.lmops.univ-smb.fr/brown/gmq.html>.
- [195] M. Lal, M. L. Klein, G. Zerbi, B. W. H. Van Beest, C. Chachaty, J. H. R. Clarke, P. L. Nordio, G. J. T. Tiddy, K. Kremer, J. P. Ryckaert, M. G. Brereton, Y. Michopoulos, E. T. Samulski, J. Yarwood, S. L. Price, T. Boublik, A. H. Windle, H. D. Burrows, S. Sellers, G. R. Luckhurst, C. Zannoni, J. W. Emsley, R. W. Pastor, D. J. Osguthorpe, G. J. Moro, D. Brown, A. J. Stone, C. A. Reynolds, J. J. C. Teixeira-Dias, K. Yu, I. W. Hamley, D. J. Photinos, *General discussion*, *Journal of the Chemical Society, Faraday Transactions*, 88 (1992) 1775-1789, <https://doi.org/10.1039/FT9928801775>.
- [196] Université en ligne, *La dynamique moléculaire*, https://uel.unisciel.fr/chimie/modelisation/modelisation_ch05/co/1-1_calcul_d_une_trajectoire.html, (last accessed 12th October 2023).
- [197] S. Neyertz, D. Brown, M. J. T. Raaijmakers, N. E. Benes, *The influence of the dianhydride precursor in hyper-cross-linked hybrid polyPOSS-imide networks*, *Phys. Chem. Chem. Phys.*, 18 (2016) 28688-28703, <https://doi.org/10.1039/C6CP06184B>.
- [198] I. Tanis, D. Brown, S. Neyertz, R. Heck, R. Mercier, M. Vaidya, J.-P. Ballaguet, *A comparison of pure and mixed-gas permeation of nitrogen and methane in 6FDA-based polyimides as studied by*

- molecular dynamics simulations*, *Comput. Mater. Sci.*, 141 (2018) 243-253, <https://doi.org/10.1016/j.commatsci.2017.09.028>.
- [199] S. Pandiyan, D. Brown, S. Neyertz, N. F. A. van der Vegt, *Carbon dioxide solubility in three fluorinated polyimides studied by molecular dynamics simulations*, *Macromolecules*, 43 (2010) 2605-2621, <https://doi.org/10.1021/ma902507d>.
- [200] H. Kumar, P. K. Maiti, *Introduction to molecular dynamics simulation*, in: *Computational Statistical Physics*, Sitangshu Bikas Santra, Purusattam Ray (Eds.) Hindustan Book Agency, New Delhi, India, 2011, pp. 161-197.
- [201] J. M. Wernik, S. A. Meguid, *Atomistic-based continuum modeling of the nonlinear behavior of carbon nanotubes*, *Acta Mech.*, 212 (2010) 167-179, <https://doi.org/10.1007/s00707-009-0246-4>.
- [202] F. Wang, R. Latour, T. Boland, D. Bruce, J. Steven, Stuart, A. Vertegel, *Non-Boltzmann sampling for the accurate calculation of peptide-surface adsorption free energy*, Clemson University, 2023, <https://www.proquest.com/openview/b7d70d12fb6810402369e72f21ce75ef/1.pdf?pq-origsite=gscholar&cbl=18750&diss=y>.
- [203] M. J. Frisch, G. W. Trucks, H. B. Schlegel, G. E. Scuseria, M. A. Robb, J. R. Cheeseman, G. Scalmani, V. Barone, B. Mennucci, G. A. Petersson, H. Nakatsuji, M. Caricato, X. Li, H. P. Hratchian, A. F. Izmaylov, J. Bloino, G. Zheng, J. L. Sonnenberg, M. Hada, M. Ehara, K. Toyota, R. Fukuda, J. Hasegawa, M. Ishida, T. Nakajima, Y. Honda, O. Kitao, H. Nakai, T. Vreven, J. A. Montgomery Jr., J. E. Peralta, F. Ogliaro, M. Bearpark, J. J. Heyd, E. Brothers, K. N. Kudin, V. N. Staroverov, R. Kobayashi, J. Normand, K. Raghavachari, A. Rendell, J. C. Burant, S. S. Iyengar, J. Tomasi, M. Cossi, N. Rega, J. M. Millam, M. Klene, J. E. Knox, J. B. Cross, V. Bakken, C. Adamo, J. Jaramillo, R. Gomperts, R. E. Stratmann, O. Yazyev, A. J. Austin, R. Cammi, C. Pomelli, J. W. Ochterski, R. L. Martin, K. Morokuma, V. G. Zakrzewski, G. A. Voth, P. Salvador, J. J. Dannenberg, S. Dapprich, A. D. Daniels, O. Farkas, J. B. Foresman, J. V. Ortiz, J. Cioslowski, D. J. Fox, *Gaussian 09, Revision A.02*, 2009, available at <https://gaussian.com/glossary/g09/>.
- [204] S. Salimi, *Experimental characterization and modelling of OAPS as a precursor for polyOAPS-imide membranes*, Ph.D. thesis, Université Savoie Mont Blanc, 2022, <https://hal.science/tel-03614953>.
- [205] A. M. Helmenstine, ThoughtCo., *Geometric isomer definition (cis-trans Isomers)*, <https://www.thoughtco.com/definition-of-geometric-isomer-cis-trans-604481>, (last accessed 10th August 2021).
- [206] M. M. Hirtz, *Surface structuring by bottom-up and top-down approaches*, Ph.D. thesis, University of Münster, 2009, <https://nbn-resolving.de/urn:nbn:de:hbz:6-19489462864>.
- [207] S. R. Alam, J. S. Vetter, P. K. Agarwal, A. Geist, Performance characterization of molecular dynamics techniques for biomolecular simulations, PPOPP '06: ACM SIGPLAN 2006 Symposium on Principles and Practice of Parallel Programming 2006, New York, <https://dl.acm.org/doi/10.1145/1122971.1122983>.
- [208] F. Taslimi, *End-functionalized rodlike colloid suspensions under shear flow*, Ph.D. thesis, University of California, Irvine, 2013, <http://publications.rwth-aachen.de/record/229178/files/4815.pdf>.
- [209] P. P. Ewald, *Die Berechnung optischer und elektrostatischer Gitterpotentiale*, *Ann. Phys.*, 369 (1921) 253-287, <https://doi.org/10.1002/andp.19213690304>.
- [210] D. Fincham, *Optimisation of the Ewald sum for large systems*, *Mol. Simul.*, 13 (1994) 1-9, <https://doi.org/10.1080/08927029408022180>.
- [211] H. J. C. Berendsen, J. P. M. Postma, W. F. Van Gunsteren, A. DiNola, J. R. Haak, *Molecular dynamics with coupling to an external bath*, *J. Chem. Phys.*, 81 (1984) 3684-3690, 10.1063/1.448118.
- [212] J. O. Hirschfelder, C. F. Curtiss, R. B. Bird, *Molecular Theory of Gases and Liquids*, John Wiley & Sons Ltd., New York, 1954.
- [213] I. F. Silvera, V. V. Goldman, *The isotropic intermolecular potential for H₂ and D₂ in the solid and gas phases*, *J. Chem. Phys.*, 69 (1978) 4209-4213, <https://doi.org/10.1063/1.437103>.
- [214] J. D. Poll, L. Wolniewicz, *The quadrupole moment of the H₂ molecule*, *J. Chem. Phys.*, 68 (1978) 3053-3058, <https://doi.org/10.1063/1.436171>.

- [215] G. C. Maitland, M. Rigby, E. B. Smith, W. A. Wakeham, *Intermolecular Forces*, Clarendon Press, Oxford, 1981.
- [216] D. Marx, P. Nielaba, *Path-integral Monte Carlo techniques for rotational motion in two dimensions: quenched, annealed, and no-spin quantum-statistical averages*, *Phys. Rev. A*, 45 (1992) 8968-8971, <https://doi.org/10.1103/PhysRevA.45.8968>.
- [217] J.-P. Bouanich, *Site-site Lennard-Jones potential parameters for N₂, O₂, H₂, CO and CO₂*, *J. Quant. Spectrosc. Radiat. Transf.*, 47 (1992) 243-250, [https://doi.org/10.1016/0022-4073\(92\)90142-Q](https://doi.org/10.1016/0022-4073(92)90142-Q).
- [218] V. Buch, *Path integral simulations of mixed para-D₂ and ortho-D₂ clusters: The orientational effects*, *J. Chem. Phys.*, 100 (1994) 7610-7629, <https://doi.org/10.1063/1.466854>.
- [219] R. F. Cracknell, *Molecular simulation of hydrogen adsorption in graphitic nanofibres*, *Phys. Chem. Chem. Phys.*, 3 (2001) 2091-2097, <https://doi.org/10.1039/B100144M>.
- [220] W. F. Wang, *Atomic-potential parameters for H₂ and D₂: quantum corrections in the calculation of second-virial coefficients*, *J. Quant. Spectrosc. Radiat. Transf.*, 76 (2003) 23-30, [https://doi.org/10.1016/S0022-4073\(02\)00043-2](https://doi.org/10.1016/S0022-4073(02)00043-2).
- [221] Q. Yang, C. Zhong, *Molecular simulation of adsorption and diffusion of hydrogen in metal-organic frameworks*, *J. Phys. Chem. B*, 109 (2005) 11862-11864, <https://doi.org/10.1021/jp051903n>.
- [222] J. L. Belof, A. C. Stern, B. Space, *A predictive model of hydrogen sorption for metal-organic materials*, *J. Phys. Chem. C*, 113 (2009) 9316-9320, <https://doi.org/10.1021/jp901988e>.
- [223] K. McLaughlin, C. R. Cioce, J. L. Belof, B. Space, *Erratum: "A molecular H₂ potential for heterogeneous simulations including polarization and many-body van der Waals interactions" [J. Chem. Phys. 136, 194302 (2012)]*, *J. Chem. Phys.*, 137 (2012) 129901, <https://doi.org/10.1063/1.4755289>.
- [224] L. Sun, L. Yang, Y.-D. Zhang, Q. Shi, R.-F. Lu, W.-Q. Deng, *Accurate van der Waals force field for gas adsorption in porous materials*, *J. Comput. Chem.*, 38 (2017) 1991-1999, <https://doi.org/10.1002/jcc.24832>.
- [225] A. Köster, M. Thol, J. Vrabec, *Molecular models for the hydrogen age: hydrogen, nitrogen, oxygen, argon, and water*, *J. Chem. Eng. Data*, 63 (2018) 305-320, <https://doi.org/10.1021/acs.jced.7b00706>.
- [226] S. Stephan, M. T. Horsch, J. Vrabec, H. Hasse, *MolMod - an open access database of force fields for molecular simulations of fluids*, *Mol. Simul.*, 45 (2019) 806-814, <https://doi.org/10.1080/08927022.2019.1601191>.
- [227] R. A. C. Bartolomeu, L. F. M. Franco, *Thermophysical properties of supercritical H₂ from molecular dynamics simulations*, *Int. J. Hydrog. Energy*, 45 (2020) 16372-16380, <https://doi.org/10.1016/j.ijhydene.2020.04.164>.
- [228] Y. Sun, R. F. DeJaco, Z. Li, D. Tang, S. Glante, D. S. Sholl, C. M. Colina, R. Q. Snurr, M. Thommes, M. Hartmann, J. I. Siepmann, *Fingerprinting diverse nanoporous materials for optimal hydrogen storage conditions using meta-learning*, *Sci. Adv.*, 7 (2021) eabg3983, <https://doi.org/10.1126/sciadv.abg3983>.
- [229] S. Wang, K. Hou, H. Heinz, *Accurate and compatible force fields for molecular oxygen, nitrogen, and hydrogen to simulate gases, electrolytes, and heterogeneous interfaces*, *J. Chem. Theory Comput.*, 17 (2021) 5198-5213, <https://doi.org/10.1021/acs.jctc.0c01132>.
- [230] UNFCCC, *The Paris Agreement - Publication*, Paris Climate Change Conference - November 2015, Paris, 29th November 2018, <https://unfccc.int/documents/184656>.
- [231] IPCC, 2022: *Climate change 2022: Mitigation of climate change. Contribution of working group III to the sixth assessment report of the intergovernmental panel on climate change* [P.R. Shukla, J. Skea, R. Slade, A. Al Khourdajie, R. van Diemen, D. McCollum, M. Pathak, S. Some, P. Vyas, R. Fradera, M. Belkacemi, A. Hasija, G. Lisboa, S. Luz, J. Malley, (eds.)], Cambridge University Press, Cambridge, UK and New York, NY, USA, <https://www.ipcc.ch/report/ar6/wg3/>.
- [232] D. C. Rosenfeld, J. Lindorfer, K. Fazeni-Fraisl, *Comparison of advanced fuels - Which technology can win from the life cycle perspective?*, *J. Clean. Prod.*, 238 (2019) 117879, <https://doi.org/10.1016/j.jclepro.2019.117879>.
- [233] MAHYTEC, *Compressed hydrogen storage*, <https://www.mahytec.com/en/compressed-hydrogen-storage/>, (last accessed 12th October 2023).

- [234] Advanced Structural Technologies Inc., *Hydrogen storage and transportation solutions*, <https://astforgetech.com/alternative-energy/>, (last accessed 12th October 2023).
- [235] S. Neyertz, D. Brown, S. Salimi, F. Radmanesh, N. E. Benes, *Molecular characterization of membrane gas separation under very high temperatures and pressure: single- and mixed-gas CO₂/CH₄ and CO₂/N₂ permselectivities in hybrid networks*, *Membranes*, 12 (2022) 526, <https://doi.org/10.3390/membranes12050526>.
- [236] M. Lal, M. L. Klein, G. Zerbi, B. W. H. Van Beest, C. Chachaty, J. H. R. Clarke, P. L. Nordio, G. J. T. Tiddy, K. Kremer, J. P. Ryckaert, M. G. Brereton, Y. Michopoulos, E. T. Samulski, J. Yarwood, S. L. Price, T. Boublik, A. H. Windle, H. D. Burrows, S. Sellers, G. R. Luckhurst, C. Zannoni, J. W. Emsley, R. W. Pastor, D. J. Osguthorpe, G. J. Moro, D. Brown, A. J. Stone, C. A. Reynolds, J. J. C. Teixeira-Dias, K. Yu, I. W. Hamley, D. J. Photinos, *General discussion*, *J. Chem. Soc., Faraday trans.*, 88 (1992) 1775-1789, <https://doi.org/10.1039/FT9928801775>.
- [237] A. Aasen, M. Hammer, Å. Ervik, E. A. Müller, Ø. Wilhelmsen, *Equation of state and force fields for Feynman–Hibbs-corrected Mie fluids. I. Application to pure helium, neon, hydrogen and deuterium*, *J. Chem. Phys.*, 151 (2019) 064508, <https://doi.org/10.1063/1.5111364>.
- [238] A. Rahbari, J. Brenkman, R. Hens, M. Ramdin, L. J. P. van den Broeke, R. Schoon, R. Henkes, O. A. Moulton, T. J. H. Vlugt, *Solubility of water in hydrogen at high pressures: a molecular simulation study*, *J. Chem. Eng. Data*, 64 (2019) 4103-4115, <https://doi.org/10.1021/acs.jced.9b00513>.
- [239] M. Clark, R. D. Cramer, N. Van Opdenbosch, *Validation of the general purpose tripes 5.2 force field*, *J. Comput. Chem.*, 10 (1989) 982-1012, <https://doi.org/10.1002/jcc.540100804>.
- [240] A. A. Gusev, S. Arizzi, U. W. Suter, D. J. Moll, *Dynamics of light gases in rigid matrices of dense polymers*, *J. Chem. Phys.*, 99 (1993) 2221-2227, <https://doi.org/10.1063/1.465283>.
- [241] N. F. A. Van der Vegt, *A molecular dynamics simulation study of solvation thermodynamical quantities of gases in polymeric solvents*, *J. Membr. Sci.*, 205 (2002) 125-139, [https://doi.org/10.1016/S0376-7388\(02\)00071-6](https://doi.org/10.1016/S0376-7388(02)00071-6).
- [242] N. F. A. Van der Vegt, W. J. Briels, M. Wessling, H. Strathmann, *Free energy calculations of small molecules in dense amorphous polymers. Effect of the initial guess configuration in molecular dynamics studies*, *J. Chem. Phys.*, 105 (1996) 8849-8857, <https://doi.org/10.1063/1.472614>.
- [243] F. Darkrim, D. Levesque, *Monte Carlo simulations of hydrogen adsorption in single-walled carbon nanotubes*, *J. Chem. Phys.*, 109 (1998) 4981-4984, <https://doi.org/10.1063/1.477109>.
- [244] R. Patel, J. Castro, M. Tsapatsis, J. I. Siepmann, *Molecular simulations probing the adsorption and diffusion of ammonia, nitrogen, hydrogen, and their mixtures in bulk MFI zeolite and MFI nanosheets at high temperature and pressure*, *J. Chem. Eng. Data*, 67 (2022) 1779-1791, <https://doi.org/10.1021/acs.jced.2c00086>.
- [245] J. L. Belof, A. C. Stern, B. Space, *An accurate and transferable intermolecular diatomic hydrogen potential for condensed phase simulation*, *J. Chem. Theory Comput.*, 4 (2008) 1332-1337, <https://doi.org/10.1021/ct800155q>.
- [246] G. Ciccotti, M. Ferrario, J. P. Ryckaert, *Molecular dynamics of rigid systems in cartesian coordinates: a general formulation*, *Mol. Phys.*, 47 (1982) 1253-1264, <https://doi.org/10.1080/00268978200100942>.
- [247] W. Smith, *A replicated data molecular dynamics strategy for the parallel Ewald sum*, *Comput. Phys. Commun.*, 67 (1992) 392-406, [https://doi.org/10.1016/0010-4655\(92\)90048-4](https://doi.org/10.1016/0010-4655(92)90048-4).
- [248] W. Humphrey, A. Dalke, K. Schulten, *VMD: Visual molecular dynamics*, *J. Mol. Graph.*, 14 (1996) 33-38, [https://doi.org/10.1016/0263-7855\(96\)00018-5](https://doi.org/10.1016/0263-7855(96)00018-5).
- [249] S. Neyertz, D. Brown, *Single- and mixed-gas sorption in large-scale molecular models of glassy bulk polymers. Competitive sorption of a binary CH₄/N₂ and a ternary CH₄/N₂/CO₂ mixture in a polyimide membrane*, *J. Membr. Sci.*, 614 (2020) 118478, <https://doi.org/10.1016/j.memsci.2020.118478>.
- [250] B. Widom, *Some topics in the theory of fluids*, *J. Chem. Phys.*, 39 (1963) 2808-2812, <https://doi.org/10.1063/1.1734110>.

- [251] J. P. Hansen, I. R. McDonald, *Theory of Simple Liquids (4th edition)*, Academic Press, Amsterdam, 2013, 10.1016/c2010-0-66723-x.
- [252] F. Müller-Plathe, *Permeation of polymers — a computational approach*, *Acta Polymerica*, 45 (1994) 259-293, <https://doi.org/10.1002/actp.1994.010450401>.
- [253] T. Spyriouni, G. C. Boulougouris, D. N. Theodorou, *Prediction of sorption of CO₂ in glassy atactic polystyrene at elevated pressures through a new computational scheme*, *Macromolecules*, 42 (2009) 1759-1769, 10.1021/ma8015294.
- [254] W. J. Worlton C. E. Holley Jr., R. K. Zeigler, 1958: *Compressibility factors and fugacity coefficients calculated from the Beattie-Bridgeman equation of state for hydrogen, nitrogen, oxygen, carbon dioxide, ammonia, methane, and helium*, Los Alamos Scientific Lab., Los Alamos, NM, USA, <https://www.osti.gov/biblio/4289497>.
- [255] J. A. Beattie, O. C. Bridgeman, *A new equation of state for fluids. I. Application to gaseous ethyl ether and carbon dioxide*, *J. Am. Chem. Soc.*, 49 (1927) 1665-1667, <https://doi.org/10.1021/ja01406a005>.
- [256] M. E. Kainourgiakis, E. S. Kikkinides, G. C. Charalambopoulou, A. K. Stubos, *Simulation of adsorption in 3-D reconstructed mesoporous materials by a simulated annealing algorithm*, in: *Studies in Surface Science and Catalysis*, F. Rodriguez-Reinoso, B. McEnaney, J. Rouquerol, K. Unger (Eds.) Elsevier, 2002, pp. 147-154, [https://doi.org/10.1016/S0167-2991\(02\)80231-2](https://doi.org/10.1016/S0167-2991(02)80231-2).
- [257] L. Chen, T. Groß, H. Krienke, H.-D. Lüdemann, *T,p-Dependence of the self-diffusion and spin-lattice relaxation in fluid hydrogen and deuterium*, *Phys. Chem. Chem. Phys.*, 3 (2001) 2025-2030, <http://dx.doi.org/10.1039/B101215K>.
- [258] J. F. Lee, F. W. Sears, D. L. Turcotte, *Statistical Thermodynamics*, 2nd ed., Addison-Wesley Publishing Company, Inc., Philippines, 1973.
- [259] Q. Yang, C. Zhong, *Molecular simulation of adsorption and diffusion of hydrogen in metal-organic frameworks*, *J. Phys. Chem. B*, 109 (2005) 11862-11864, <https://doi.org/10.1021/jp051903n>.
- [260] F. Radmanesh, A. Tena, E. J. R. Sudhölter, M. A. Hempenius, N. E. Benes, *Nonaqueous interfacial polymerization-derived polyphosphazene films for sieving or blocking hydrogen gas*, *ACS Appl. Polym. Mater.*, 5 (2023) 1955-1964, <https://doi.org/10.1021/acsapm.2c02022>.
- [261] A. Karadağ, H. Akbaş, *Phosphazene-Based Ionic Liquids*, in: *Recent Advances in Ionic Liquids*, Mohammed Muzibur Rahman (Ed.) IntechOpen, Rijeka, 2018, <https://doi.org/10.5772/intechopen.76613>.
- [262] F. Radmanesh, M. G. Elshof, N. E. Benes, *Polyoctahedral silsesquioxane hexachlorocyclotriphosphazene membranes for hot gas separation*, *ACS Appl. Mater. Interfaces*, 13 (2021) 8960-8966, <https://doi.org/10.1021/acsami.0c21968>.
- [263] P. Elmer, *ChemDraw Prime*, available at <https://perkinelmerinformatics.com/products/research/chemdraw/>.
- [264] MERCK, *Phosphonitrilic chloride trimer*, <https://www.sigmaaldrich.com/FR/fr/product/aldrich/481947#>, (last accessed 12th October 2023).
- [265] TCI, *Phosphonitrilic chloride trimer*, <https://www.tcichemicals.com/BE/fr/p/C0584>, (last accessed 12th October 2023).
- [266] G. J. Bullen, *An improved determination of the crystal structure of hexachlorocyclotriphosphazene (phosphonitrilic chloride)*, *J. Chem. Soc. A*, (1971) 1450-1453, <https://doi.org/10.1039/J19710001450>.
- [267] M. Yildiz, B. Duelger, S. Yilmaz, *Synthesis, spectroscopic studies and antimicrobial activity of phosphazenes derivatives*, *Asian J. Chem.*, 20 (2008) 2719-2732, https://asianjournalofchemistry.co.in/user/journal/viewarticle.aspx?ArticleID=20_4_34.
- [268] H. R. Allcock, *Polyphosphazene elastomers, gels, and other soft materials*, *Soft Matter*, 8 (2012) 7521-7532, <https://doi.org/10.1039/C2SM26011E>.
- [269] FooDB, *Showing compound phloroglucinol*, <https://foodb.ca/compounds/FDB013879>, (last accessed 12th March 2023).
- [270] D. Pádua, E. Rocha, D. Gargiulo, A. A. Ramos, *Bioactive compounds from brown seaweeds: Phloroglucinol, fucoxanthin and fucoidan as promising therapeutic agents against breast cancer*, *Phytochem. Lett.*, 14 (2015) 91-98, <https://doi.org/10.1016/j.phytol.2015.09.007>.

- [271] MERCK, *Phloroglucinol*, https://www.merckmillipore.com/FR/fr/product/Phloroglucinol,MDA_CHEM-818887#overview, (last accessed 12th October 2023).
- [272] National Library of Medicine, *Phloroglucinol*, <https://pubchem.ncbi.nlm.nih.gov/compound/Phloroglucinol>, (last accessed 12th October 2023).
- [273] K. Maartmann-Moe, *The crystal and molecular structure of phloroglucinol*, *Acta Cryst.*, 19 (1965) 155-157, <https://doi.org/10.1107/S0365110X65002992>.
- [274] S. Sun, M. Jin, X. Zhou, J. Ni, X. Jin, H. Liu, Y. Wang, *The application of quantitative ¹H-NMR for the determination of Orlistat in tablets*, *Molecules*, 22 (2017) 1517, <https://doi.org/10.3390/molecules22091517>.
- [275] C. H. Görbitz, M. Kaboli, M. L. Read, K. Vestli, *Benzene-1,3,5-triol at 105 K*, *Acta Cryst.*, E64 (2008) o2023, <https://doi.org/10.1107/S1600536808030638>.
- [276] D. E. Braun, D. A. Tocher, S. L. Price, U. J. Griesser, *The complexity of hydration of phloroglucinol: a comprehensive structural and thermodynamic characterization*, *J. Phys. Chem. B*, 116 (2012) 3961-3972, <https://doi.org/10.1021/jp211948q>.
- [277] S. W. Bartlett, S. J. Coles, D. B. Davies, M. B. Hursthouse, H. Ibisoglu, A. Kilic, R. A. Shaw, I. Un, *Structural investigations of phosphorus-nitrogen compounds. 7. Relationships between physical properties, electron densities, reaction mechanisms and hydrogen-bonding motifs of N₃P₃Cl_(6-n)(NHBu^t)_n derivatives*, *Acta Cryst.*, B62 (2006) 321-329, <https://doi.org/10.1107/S0108768106000851>.
- [278] R. H. Boyd, L. Kesner, *Conformational analysis of phosphazenes. A force field for the calculation of the molecular structures of halophosphazenes*, *J. Am. Chem. Soc.*, 99 (1977) 4248-4256, <https://doi.org/10.1021/ja00455a006>.
- [279] H. G. M. De Wit, J. A. Bouwstra, J. G. Blok, C. G. de Kruif, *Vapor pressures and lattice energies of oxalic acid, mesotartaric acid, phloroglucinol, myoinositol, and their hydrates*, *J. Chem. Phys.*, 78 (1983) 1470-1475, <https://doi.org/10.1063/1.444836>.
- [280] H. Sun, P. Ren, J. R. Fried, *The COMPASS force field: parameterization and validation for phosphazenes*, *Comput. Theor. Polym. Sci.*, 8 (1998) 229-246, [https://doi.org/10.1016/S1089-3156\(98\)00042-7](https://doi.org/10.1016/S1089-3156(98)00042-7).
- [281] R. Steinman, F. B. Schirmer, L. F. Audrieth, *The preparation and physical properties of trimeric phosphonitrilic chloride*, *J. Am. Chem. Soc.*, 64 (1942) 2377-2378, <https://doi.org/10.1021/ja01262a044>.
- [282] S. Neyertz, S. Salimi, F. Radmanesh, N. E. Benes, D. Brown, *High-temperature molecular screening of hybrid poly(OAPS-imide) networks based on octa(aminophenyl)silsesquioxane for increased thermomechanical resistance*, *Phys. Chem. Chem. Phys.*, 23 (2021) 11438-11454, <http://dx.doi.org/10.1039/D1CP01052B>.
- [283] M. Ahmad, T. Nawaz, I. Hussain, X. Chen, M. Imran, R. Hussain, M. A. Assiri, S. Ali, Z. Wu, *Phosphazene cyclomatrix network-based polymer: chemistry, synthesis, and applications*, *ACS Omega*, 7 (2022) 28694-28707, <https://doi.org/10.1021/acsomega.2c01573>.
- [284] X. Guo, Y. Li, M. Zhang, K. Cao, Y. Tian, Y. Qi, S. Li, K. Li, X. Yu, L. Ma, *Collyiform crystalline 2D covalent organic frameworks (COFs) with quasi-3D topologies for rapid I₂ adsorption*, *Angew. Chem. Int. Ed.*, 59 (2020) 22697-22705, <https://doi.org/10.1002/anie.202010829>.
- [285] X. Wei, D. Zheng, M. Zhao, H. Chen, X. Fan, B. Gao, L. Gu, Y. Guo, J. Qin, J. Wei, Y. Zhao, G. Zhang, *Cross-linked polyphosphazene hollow nanosphere-derived N/P-doped porous carbon with single nonprecious metal atoms for the oxygen reduction reaction*, *Angew. Chem. Int. Ed.*, 59 (2020) 14639-14646, <https://doi.org/10.1002/anie.202006175>.
- [286] C. Ramakrishnan, *Ramachandran and his map*, *Reson.*, 6 (2001) 48-56, <https://doi.org/10.1007/BF02836967>.
- [287] M. Bulacu, N. Goga, W. Zhao, G. Rossi, L. Monticelli, X. Periole, D. P. Tieleman, S. J. Marrink, *Improved angle potentials for coarse-grained molecular dynamics simulations*, *J. Chem. Theory Comput.*, 9 (2013) 3282-3292, <https://doi.org/10.1021/ct400219n>.

- [288] G. L. Deitrick, L. E. Scriven, H. T. Davis, *Efficient molecular simulation of chemical potentials*, J. Chem. Phys., 90 (1989) 2370-2385, <https://dx.doi.org/10.1063/1.455979>.
- [289] Y. Tamai, H. Tanaka, K. Nakanishi, *Molecular simulation of permeation of small penetrants through membranes. 2. Solubilities*, Macromolecules, 28 (1995) 2544-2554, <https://doi.org/10.1021/ma00111a058>.
- [290] G. Dömötör, R. Hentschke, *Atomistically modeling the chemical potential of small molecules in dense systems*, J. Phys. Chem. B, 108 (2004) 2413-2417, <https://doi.org/10.1021/jp0367427>.
- [291] J. Farahbakhsh, V. Vatanpour, M. Khoshnam, M. Zargar, *Recent advancements in the application of new monomers and membrane modification techniques for the fabrication of thin film composite membranes: A review*, React. Funct. Polym., 166 (2021) 105015, <https://doi.org/10.1016/j.reactfunctpolym.2021.105015>.
- [292] R. Weng, X. Huang, D. Liao, S. Xu, L. Peng, X. Liu, *A novel cellulose/chitosan composite nanofiltration membrane prepared with piperazine and trimesoyl chloride by interfacial polymerization*, RSC Adv., 10 (2020) 1309-1318, <http://dx.doi.org/10.1039/C9RA09023A>.
- [293] Y. Mo, A. Tiraferri, N. Y. Yip, A. Adout, X. Huang, M. Elimelech, *Improved antifouling properties of polyamide nanofiltration membranes by reducing the density of surface carboxyl groups*, Environ. Sci. Technol., 46 (2012) 13253-13261, <https://doi.org/10.1021/es303673p>.
- [294] Y. Zhang, N. E. Benes, R. G. H. Lammertink, *Visualization and characterization of interfacial polymerization layer formation*, Lab Chip, 15 (2015) 575-580, <https://doi.org/10.1039/C4LC01046A>.
- [295] M. D. Jalageri, A. Nagaraja, Y. M. Puttaiahgowda, *Piperazine based antimicrobial polymers: a review*, RSC Adv., 11 (2021) 15213-15230, <https://doi.org/10.1039/D1RA00341K>.
- [296] Biosynth, *Trimesoyl chloride*, <https://www.biosynth.com/p/FT165516/4422-95-1-trimesoyl-chloride>, (last accessed 12th October 2023).
- [297] E. W. Lemmon, M. O. McLinden, D. G. Friend, *Piperazine*, in: NIST Chemistry WebBook, NIST Standard Reference Database Number 69, P. J. Linstrom, W. G. Mallard (Eds.) NIST, Gaithersburg MD, 20899, USA, 2023, <https://doi.org/10.18434/T4D303>.
- [298] E. W. Lemmon, M. O. McLinden, D. G. Friend, *1,3,5-Benzenetricarbonyl trichloride*, in: NIST Chemistry WebBook, NIST Standard Reference Database Number 69, P. J. Linstrom, W. G. Mallard (Eds.) NIST, Gaithersburg MD, 20899, USA, 2023, <https://doi.org/10.18434/T4D303>.
- [299] PubChem, National Library of Medicine, *Piperazine*, <https://pubchem.ncbi.nlm.nih.gov/compound/4837#section=Information-Sources>, (last accessed 11th October 2023).
- [300] MERCK, *1,3,5-Benzenetricarbonyl trichloride*, <https://www.sigmaaldrich.com/NL/en/product/aldrich/147532>, (last accessed 11th October 2023).
- [301] C. Liu, J. Yang, B.-B. Guo, S. Agarwal, A. Greiner, Z.-K. Xu, *Interfacial polymerization at the alkane/ionic liquid interface*, Angew. Chem. Int. Ed., 60 (2021) 14636-14643, <https://doi.org/10.1002/anie.202103555>.
- [302] Z. Yang, L. Li, C. Jiang, N. Zhao, S. Zhang, Y. Guo, Y. Chen, S. Xue, C. Ji, S. Zhao, R. R. Gonzales, H. Matsuyama, J. Xia, Q. J. Niu, *Tailored thin film nanocomposite membrane incorporated with Noria for simultaneously overcoming the permeability-selectivity trade-off and the membrane fouling in nanofiltration process*, J. Membr. Sci., 640 (2021) 119863, <https://doi.org/10.1016/j.memsci.2021.119863>.
- [303] W. Ogieglo, *In-situ spectroscopic ellipsometry for studies of thin films and membranes*, Ph.D. thesis, University of Twente, 2014, <https://research.utwente.nl/en/publications/in-situ-spectroscopic-ellipsometry-for-studies-of-thin-films-and->.
- [304] Y. Dahman, C. Halim, O. Matos, L. Chan, *Generic methodologies for characterization*, in: Nanotechnology and Functional Materials for Engineers, Yaser Dahman (Ed.) Elsevier, 2017, pp. 19-45, <https://doi.org/10.1016/B978-0-323-51256-5.00002-2>.
- [305] X. Wang, P. Karakiliç, X. Liu, M. Shan, A. Nijmeijer, L. Winnubst, J. Gascon, F. Kapteijn, *One-pot synthesis of high-flux b-oriented MFI zeolite membranes for Xe recovery*, ACS Appl. Mater. Interfaces, 10 (2018) 33574-33580, <https://doi.org/10.1021/acsami.8b12613>.

- [306] P. Karakiliç, C. Huiskes, M. W. J. Luiten-Olieman, A. Nijmeijer, L. Winnubst, *Sol-gel processed magnesium-doped silica membranes with improved H₂/CO₂ separation*, *J. Membr. Sci.*, 543 (2017) 195-201, <https://doi.org/10.1016/j.memsci.2017.08.055>.
- [307] R. Hayashi, T. Ueno, S. Migita, Y. Tsutsumi, H. Doi, T. Ogawa, T. Hanawa, N. Wakabayashi, *Hydrocarbon deposition attenuates osteoblast activity on titanium*, *J. Dent. Res.*, 93 (2014) 698-703, <https://doi.org/10.1177/0022034514536578>.
- [308] J. S. Dhaliwal, S. R. N. David, N. R. Zulhilmi, S. K. Sodhi Dhaliwal, J. Knights, R. F. de Albuquerque Junior, *Contamination of titanium dental implants: a narrative review*, *SN Appl. Sci.*, 2 (2020) 1011, <https://doi.org/10.1007/s42452-020-2810-4>.
- [309] S. Yan, M. Li, S. A.-O. Komasa, A. Agariguchi, Y. Yang, Y. Zeng, S. Takao, H. Zhang, Y. Tashiro, T. Kusumoto, Y. Kobayashi, L. Chen, K. Kashiwagi, N. Matsumoto, J. Okazaki, T. Kawazoe, *Decontamination of titanium surface using different methods: an in vitro study*, *Materials*, 13 (2020) 2287, <https://doi.org/10.3390/ma13102287>.
- [310] C. Yoshihara, T. Ueno, P. Chen, Y. Tsutsumi, T. Hanawa, N. Wakabayashi, *Inverse response of osteoblasts and fibroblasts to growth on carbon-deposited titanium surfaces*, *J. Biomed. Mater. Res. Part B Appl. Biomater.*, 106 (2018) 1869-1877, <https://doi.org/10.1002/jbm.b.33996>.
- [311] L. Sun, T. Liu, H. Li, L. Yang, L. Meng, Q. Lu, J. Long, *Fluorescent and cross-linked organic-inorganic hybrid nanoshells for monitoring drug delivery*, *ACS Appl. Mater. Interfaces*, 7 (2015) 4990-4997, <https://doi.org/10.1021/acsami.5b00175>.
- [312] M. Zhang, Y. Li, C. Bai, X. Guo, J. Han, S. Hu, H. Jiang, W. Tan, S. Li, L. Ma, *Synthesis of microporous covalent phosphazene-based frameworks for selective separation of uranium in highly acidic media based on size-matching effect*, *ACS Appl. Mater. Interfaces*, 10 (2018) 28936-28947, <https://doi.org/10.1021/acsami.8b06842>.
- [313] G. Tang, X. Zeng, L. Hou, T. Song, S. Yin, B. Long, A. Ali, G.-J. Deng, *Cross-linked ultrathin polyphosphazene-based nanosheet with promoted charge separation kinetics for efficient visible light photocatalytic CO₂ reforming to CH₄*, *Appl. Catal. B: Environ.*, 306 (2022) 121090, <https://doi.org/10.1016/j.apcatb.2022.121090>.
- [314] H. R. Allcock, C. Chen, *Polyphosphazenes: phosphorus in inorganic-organic polymers*, *J. Org. Chem.*, 85 (2020) 14286-14297, <https://doi.org/10.1021/acs.joc.0c01710>.
- [315] R. Rajasekar, N. H. Kim, D. Jung, T. Kuila, J. K. Lim, M. J. Park, J. H. Lee, *Electrostatically assembled layer-by-layer composites containing graphene oxide for enhanced hydrogen gas barrier application*, *Compos. Sci. Technol.*, 89 (2013) 167-174, <https://doi.org/10.1016/j.compscitech.2013.10.004>.
- [316] P. Tzeng, E. L. Lugo, G. D. Mai, B. A. Wilhite, J. C. Grunlan, *Super Hydrogen and Helium Barrier with Polyelectrolyte Nanobrick Wall Thin Film*, *Macromol. Rapid Commun.*, 36 (2015) 96-101, <https://doi.org/10.1002/marc.201400559>.
- [317] H. Kim, C. W. Macosko, *Morphology and properties of polyester/exfoliated graphite nanocomposites*, *Macromolecules*, 41 (2008) 3317-3327, <https://doi.org/10.1021/ma702385h>.
- [318] R. J. Mayer, M. Breugst, N. Hampel, A. R. Ofial, H. Mayr, *Ambident reactivity of phenolate anions revisited: a quantitative approach to phenolate reactivities*, *J. Org. Chem.*, 84 (2019) 8837-8858, <https://doi.org/10.1021/acs.joc.9b01485>.
- [319] T. B. Phan, C. Nolte, S. Kobayashi, A. R. Ofial, H. Mayr, *Can one predict changes from S_N1 to S_N2 mechanisms?*, *J. Am. Chem. Soc.*, 131 (2009) 11392-11401, <https://doi.org/10.1021/ja903207b>.
- [320] Chemical Book, *Phloroglucinol(108-73-6) ¹H NMR*, https://www.chemicalbook.com/SpectrumEN_108-73-6_1HNMR.htm, (last accessed 12th October 2023).
- [321] D. L. Pavia, G. M. Lampman, G. S. Kriz, J. A. Vyvyan, *Introduction to spectroscopy*, 5th ed., Cengage learning, 2014.
- [322] G. R. Fulmer, A. J. M. Miller, N. H. Sherden, H. E. Gottlieb, A. Nudelman, B. M. Stoltz, J. E. Bercaw, K. I. Goldberg, *NMR chemical shifts of trace impurities: common laboratory solvents, organics*,

- and gases in deuterated solvents relevant to the organometallic chemist, *Organometallics*, 29 (2010) 2176-2179, <https://doi.org/10.1021/om100106e>.
- [323] F. Radmanesh, A. Tena, E. J. R. Sudhölter, N. E. Benes, *Low temperature pyrolysis of thin film composite polyphosphazene membranes for hot gas separation*, *Mater. Today Nano*, 24 (2023) 100379, <https://doi.org/10.1016/j.mtnano.2023.100379>.
- [324] Y. W. Chen-Yang, S. J. Cheng, B. D. Tsai, *Preparation of the partially substituted (phenoxy)chlorocyclotriphosphazenes by phase-transfer catalysis*, *Ind. Eng. Chem. Res.*, 30 (1991) 1314-1319, <https://doi.org/10.1021/ie00054a036>.
- [325] S. Caron, E. McInturff, *Nucleophilic Aromatic Substitution*, in: *Practical synthetic organic chemistry*, Stéphane Caron (Ed.), 2020, pp. 231-246, <https://doi.org/10.1002/9781119448914.ch4>.
- [326] F. Terrier, *Modern nucleophilic aromatic substitution*, John Wiley & Sons, 2013, <https://doi.org/10.1002/9783527656141>.
- [327] D. Wang, K. Hildenbrand, J. Leitich, H.-P. Schuchmann, C. v. Sonntag, *pH-dependent tautomerism and pKa values of phloroglucinol (1,3,5-trihydroxybenzene), studied by ¹³C NMR and UV spectroscopy*, *Z. Naturforsch. B.*, 48 (1993) 478-482, <https://doi.org/10.1515/znb-1993-0413>.
- [328] P.-G. De Gennes, F. Brochard-Wyart, D. Quéré, *Capillarity: deformable Interfaces*, in: *Capillarity and Wetting Phenomena*, Pierre-Gilles de Gennes, Françoise Brochard-Wyart, David Quéré (Eds.) Springer New York, New York, NY, 2004, pp. 1-31, https://doi.org/10.1007/978-0-387-21656-0_1.
- [329] T. Zhang, Y. Zhao, H. Li, B. Zhang, *Effect of polyurethane sizing on carbon fibers surface and interfacial adhesion of fiber/polyamide 6 composites*, *J. Appl. Polym. Sci.*, 135 (2018) 46111, <https://doi.org/10.1002/app.46111>.
- [330] Y. Son, *Measurement of interfacial tension between polyamide-6 and poly(styrene-co-acrylonitrile) by breaking thread method*, *Polymer*, 42 (2001) 1287-1291, [https://doi.org/10.1016/S0032-3861\(00\)00497-3](https://doi.org/10.1016/S0032-3861(00)00497-3).
- [331] J. R. Vig, *UV/ozone cleaning of surfaces*, *J. Vac. Sci. Technol. A*, 3 (1985) 1027-1034, <https://doi.org/10.1116/1.573115>.
- [332] K. Gotoh, S. Kikuchi, *Improvement of wettability and detergency of polymeric materials by excimer UV treatment*, *Colloid Polym. Sci.*, 283 (2005) 1356-1360, <https://doi.org/10.1007/s00396-005-1308-3>.
- [333] S. Man Lung, L. Jing, M. Peng Cheng, J.-K. Kim, *Cleaning and functionalization of polymer surfaces and nanoscale carbon fillers by UV/Ozone treatment: A review*, *J. Compos. Mater.*, 43 (2009) 1537-1564, <https://doi.org/10.1177/0021998308337740>.
- [334] J. B. Koo, S. Y. Kang, I. K. You, K. S. Suh, *Effect of UV/ozone treatment on hysteresis of pentacene thin-film transistor with polymer gate dielectric*, *Solid-State Electronics*, 53 (2009) 621-625, <https://doi.org/10.1016/j.sse.2009.04.005>.
- [335] S. Mukhopadhyay, S. S. Roy, R. A. D'Sa, A. Mathur, R. J. Holmes, J. A. McLaughlin, *Nanoscale surface modifications to control capillary flow characteristics in PMMA microfluidic devices*, *Nanoscale Res. Lett.*, 6 (2011) 411, <https://doi.org/10.1186/1556-276X-6-411>.
- [336] I. Novák, A. Popelka, M. Valentín, I. Chodák, M. Špírková, A. Tóth, A. Kleinová, J. Sedláčik, M. Lehocký, M. Marônek, *Surface behavior of polyamide 6 modified by barrier plasma in oxygen and nitrogen*, *Int. J. Polym. Anal. Charact.*, 19 (2014) 31-38, <https://doi.org/10.1080/1023666X.2014.850907>.
- [337] C. Canal, R. Molina, E. Bertran, P. Erra, *Wettability, ageing and recovery process of plasma-treated polyamide 6*, *J. Adhes. Sci. Technol.*, 18 (2004) 1077-1089, <https://doi.org/10.1163/1568561041257487>.
- [338] G. Primc, *Surface modification of polyamides by gaseous plasma—Review and scientific challenges*, *Polymers*, 12 (2020) 3020, <https://doi.org/10.3390/polym12123020>.
- [339] J. Yip, K. Chan, K. M. Sin, K. S. Lau, *Low temperature plasma-treated nylon fabrics*, *J. Mater. Process. Technol.*, 123 (2002) 5-12, [https://doi.org/10.1016/S0924-0136\(02\)00024-9](https://doi.org/10.1016/S0924-0136(02)00024-9).
- [340] V. Štěpánová, P. Šrámková, S. Sihelník, M. Stupavská, J. Jurmanová, D. Kováčik, *The effect of ambient air plasma generated by coplanar and volume dielectric barrier discharge on the surface characteristics of polyamide foils*, *Vacuum*, 183 (2021) 109887, <https://doi.org/10.1016/j.vacuum.2020.109887>.

- [341] D. Pappas, A. Bujanda, J. D. Demaree, J. K. Hirvonen, W. Kosik, R. Jensen, S. McKnight, *Surface modification of polyamide fibers and films using atmospheric plasmas*, Surf. Coat. Technol., 201 (2006) 4384-4388, <https://doi.org/10.1016/j.surfcoat.2006.08.068>.
- [342] Z. Gao, S. Peng, J. Sun, L. Yao, Y. Qiu, *Influence of processing parameters on atmospheric pressure plasma etching of polyamide 6 films*, Appl. Surf. Sci., 255 (2009) 7683-7688, <https://doi.org/10.1016/j.apsusc.2009.04.137>.
- [343] Z. Gao, *Modification of surface properties of polyamide 6 films with atmospheric pressure plasma*, Appl. Surf. Sci., 257 (2011) 6068-6072, <https://doi.org/10.1016/j.apsusc.2011.01.132>.
- [344] S. Suresh, V. C. Srivastava, I. M. Mishra, *Adsorption of catechol, resorcinol, hydroquinone, and their derivatives: a review*, Int. J. Energy Environ. Eng., 3 (2012) 32, <https://doi.org/10.1186/2251-6832-3-32>.
- [345] MERCK, *Cyclohexane*, <https://www.sigmaaldrich.com/NL/en/product/sial/227048>, (last accessed 12th October 2023).
- [346] A. V. Rayer, K. Z. Sumon, L. Jaffari, A. Henni, *Dissociation constants (pKa) of tertiary and cyclic amines: structural and temperature dependences*, J. Chem. Eng. Data, 59 (2014) 3805-3813, <https://doi.org/10.1021/je500680q>.
- [347] M. Â. F. Perez, D. Daniel, M. Padula, C. L. do Lago, C. B. G. Bottoli, *Determination of primary aromatic amines from cooking utensils by capillary electrophoresis-tandem mass spectrometry*, Food Chem., 362 (2021) 129902, <https://doi.org/10.1016/j.foodchem.2021.129902>.
- [348] STTS, *Plasma treatment*, <https://www.stts-surface.fr/en/plasma/>, (last accessed 12th October 2023).
- [349] Z. Károly, G. Kalácska, L. Zsidai, M. Mohai, S. Klébert, *Improvement of adhesion properties of polyamide 6 and polyoxymethylene-copolymer by atmospheric cold plasma treatment*, Polymers, 10 (2018) 1380, <https://doi.org/10.3390/polym10121380>.
- [350] J. Hanusová, D. Kováčik, M. Stupavská, M. Černák, I. Novák, *Atmospheric pressure plasma treatment of polyamide-12 foils*, Open Chem., 13 (2015) 382-388, <https://doi.org/10.1515/chem-2015-0049>.
- [351] D. Brown, S. Neyertz, M. J. T. Raaijmakers, N. E. Benes, *Sorption and permeation of gases in hyper-cross-linked hybrid poly(POSS-imide) networks: An in silico study*, J. Membr. Sci., 577 (2019) 113-128, <https://doi.org/10.1016/j.memsci.2019.01.039>.
- [352] G. Qi, L. Huang, H. Wang, *Highly conductive free standing polypyrrole films prepared by freezing interfacial polymerization*, Chem. Commun., 48 (2012) 8246-8248, <https://doi.org/10.1039/C2CC33889K>.
- [353] J. Du, J. Zhang, B. Han, Z. Liu, M. Wan, *Polyaniline microtubes synthesized via supercritical CO₂ and aqueous interfacial polymerization*, Synth. Met., 155 (2005) 523-526, <https://doi.org/10.1016/j.synthmet.2005.07.336>.
- [354] J. Lei, W. Liang, C. J. Brumlik, C. R. Martin, *A new interfacial polymerization method for forming metal/ conductive polymer Schottky barriers*, Synth. Met., 47 (1992) 351-359, [https://doi.org/10.1016/0379-6779\(92\)90374-R](https://doi.org/10.1016/0379-6779(92)90374-R).